Published in Journals: Applied Sciences, Coatings,
Materials and Metals

Topic Reprint

Environmental Sensitivity and Safety Assessment of Materials

Edited by
Jian Chen, Daokui Xu, Fanjiang Meng and James Noël

mdpi.com/topics

MDPI

Environmental Sensitivity and Safety Assessment of Materials

Environmental Sensitivity and Safety Assessment of Materials

Topic Editors

Jian Chen
Daokui Xu
Fanjiang Meng
James Noël

MDPI

Basel • Beijing • Wuhan • Barcelona • Belgrade • Novi Sad • Cluj • Manchester

Topic Editors

Jian Chen
Department of Chemistry
University of Western Ontario
London, ON
Canada

Daokui Xu
Institute of Metal Research
Chinese Academy of Science
Shenyang
China

Fanjiang Meng
Shanghai Nuclear
Engineering Research and
Design Institute
Shanghai
China

James Noël
Department of Chemistry
University of Western Ontario
London, ON
Canada

Editorial Office
MDPI AG
Grosspeteranlage 5
4052 Basel, Switzerland

This is a reprint of the Topic, published open access by the journals *Applied Sciences* (ISSN 2076-3417), *Coatings* (ISSN 2079-6412), *Materials* (ISSN 1996-1944) and *Metals* (ISSN 2075-4701), freely accessible at: https://www.mdpi.com/topics/Environ_Mat.

For citation purposes, cite each article independently as indicated on the article page online and as indicated below:

Lastname, A.A.; Lastname, B.B. Article Title. *Journal Name* **Year**, *Volume Number*, Page Range.

ISBN 978-3-7258-4219-3 (Hbk)
ISBN 978-3-7258-4220-9 (PDF)
https://doi.org/10.3390/books978-3-7258-4220-9

© 2025 by the authors. Articles in this book are Open Access and distributed under the Creative Commons Attribution (CC BY) license. The book as a whole is distributed by MDPI under the terms and conditions of the Creative Commons Attribution-NonCommercial-NoDerivs (CC BY-NC-ND) license (https://creativecommons.org/licenses/by-nc-nd/4.0/).

Contents

Junguo Cui, Yuyin Wu, Zhongqi Lu and Wensheng Xiao
Studying Corrosion Failure Prediction Models and Methods for Submarine Oil and Gas Transport Pipelines
Reprinted from: *Appl. Sci.* **2023**, *13*, 12713, https://doi.org/10.3390/app132312713 . . . . . **1**

Cuilan Lu, Daokui Xu, Lan Zhang, Shuo Wang, Xiangbo Xu and Dongliang Wang
High-Temperature Mechanical Behavior of an As-Extruded Al-5Zn-2Mg-0.3Cu (in wt.%) Alloy
Reprinted from: *Coatings* **2023**, *13*, 1758, https://doi.org/10.3390/coatings13101758 . . . . . **17**

Sebastian Topliceanu, Monica Almeida, Miguel Oliveira, Dan Cogălniceanu and Isabel Lopes
The Number of Ethylene Oxide Groups of Sulphate-Based Surfactants Influences the Cytotoxicity of Mixed Micelles to an Amphibian Cell Line
Reprinted from: *Appl. Sci.* **2023**, *13*, 8745, https://doi.org/10.3390/app13158745 . . . . . **28**

Jinxin Gou, Xiao Xing, Gan Cui, Zili Li, Jianguo Liu and Xiangyuan Deng
Hydrogen-Induced Cracking in CGHAZ of Welded X80 Steel under Tension Load
Reprinted from: *Metals* **2023**, *13*, 1325, https://doi.org/10.3390/met13071325 . . . . . **38**

Giuseppa Ancione, Rebecca Saitta, Paolo Bragatto, Giacomo Fiumara and Maria Francesca Milazzo
The Use of Augmented Reality for the Management of Equipment Ageing with a Virtual Sensor
Reprinted from: *Appl. Sci.* **2023**, *13*, 7843, https://doi.org/10.3390/app13137843 . . . . . **54**

Victor Malachy Udowo, Maocheng Yan, Fuchun Liu and Enhou Han
Effect of Redox Switch, Coupling, and Continuous Polarization on the Anti-Corrosion Properties of PEDOT Film in NaCl Solution
Reprinted from: *Coatings* **2023**, *13*, 944, https://doi.org/10.3390/coatings13050944 . . . . . **70**

Zhen He, Chen Yu, Jiaming Liu, Zengcheng Miao and Yuxin Wang
Effects of Preparation Parameters on the Structural and Morphologic Properties of SnO_2-Sb Coatings
Reprinted from: *Coatings* **2023**, *13*, 866, https://doi.org/10.3390/coatings13050866 . . . . . **89**

Jianfen Zhou, Zhiyong Dong, Yinzhen Dong, Xiaohui He, Hongmei Wu, Bin Chen and Qian Mao
Experimental Study on Repairing the Mechanical Characteristics of Oil-Contaminated Silty Clay in Ancient Dike with Modified Lime Mortar
Reprinted from: *Materials* **2023**, *16*, 3449, https://doi.org/10.3390/ma16093449 . . . . . **101**

Shuo Wang, Daokui Xu, Baojie Wang, Dongliang Wang, Zhiqiang Zhang and Xiangbo Xu
Effect of the Surface Film Formed by Hydrogen Charging on the Corrosion Behavior of an As-Cast Mg–8%Li (in wt. %) Alloy
Reprinted from: *Coatings* **2023**, *13*, 800, https://doi.org/10.3390/coatings13040800 . . . . . **123**

Yuxin Wang, Zengcheng Miao, Songlin Zheng, Jiahuan Chen and Zhen He
An Investigation into Electrodeposited Co−Ni−TiO_2 Films with Improved Mechanical and Corrosion Properties
Reprinted from: *Coatings* **2023**, *13*, 783, https://doi.org/10.3390/coatings13040783 . . . . . **139**

Yingqi Huang, Can Tang, Wenfeng Hao and Guoqi Zhao
Acoustic Source Localization in Metal Plates Using BP Neural Network
Reprinted from: *Metals* **2023**, *13*, 755, https://doi.org/10.3390/met13040755 . . . . . **149**

Soo-Jin Cho, Ha-Na Jang, Sung-Jin Cho, Young-Sam Yoon and Heung-Min Yoo
Material Recycling for Manufacturing Aggregates Using Melting Slag of Automobile Shredder Residues
Reprinted from: *Materials* **2023**, *16*, 2664, https://doi.org/10.3390/ma16072664 . . . . . **171**

Li-Ming Wu, Zi-Jian Wang, Yong-Zai Chang, Feng Gao, Bin Zhang, Yi Wu and Han-Xiu Fan
Vibration Performance of Steel Fiber Concrete Tunnel Lining by Adjacent Tunnel Blasting Construction
Reprinted from: *Appl. Sci.* **2023**, *13*, 4201, https://doi.org/10.3390/app13074201 . . . . . **191**

Zhidai Zhou, Jiahuan Chen, Chen Yu, Yuxin Wang and Yu Zhang
Failure Analysis of Printed Circuit Board Solder Joint under Thermal Shock
Reprinted from: *Coatings* **2023**, *13*, 572, https://doi.org/10.3390/coatings13030572 . . . . . **211**

Lan Liu, Weidong Chen, Shengzhuo Lu, Yanchun Yu, Shibo Wu and Peiwen Wu
Study on Shock Initiation Randomness of Energetic Materials on a Macroscopic Scale
Reprinted from: *Appl. Sci.* **2023**, *13*, 2534, https://doi.org/10.3390/app13042534 . . . . . **221**

Sheng Chen, Xinbao Wang, Zhiqiu Guo, Changjun Wu, Yongxiong Liu, Ya Liu and Xuping Su
Investigation of the Microstructure, Thermal Properties, and Mechanical Properties of Sn-Bi-Ag and Sn-Bi-Ag-Si Low Temperature Lead-Free Solder Alloys
Reprinted from: *Coatings* **2023**, *13*, 285, https://doi.org/10.3390/coatings13020285 . . . . . **248**

Chan Yao, Hongliang Ming, Jian Chen, Jianqiu Wang and En-Hou Han
Effect of Cold Deformation on the Hydrogen Permeation Behavior of X65 Pipeline Steel
Reprinted from: *Coatings* **2023**, *13*, 280, https://doi.org/10.3390/coatings13020280 . . . . . **265**

Hui Su, Yawei Luan, Qiujuan Ma, Baowen Hu, Shaoxing Liu and Yanjie Bai
Effect of Different Temperatures on the Hydration Kinetics of Urea-Doped Cement Pastes
Reprinted from: *Materials* **2022**, *15*, 8343, https://doi.org/10.3390/ma15238343 . . . . . **276**

Xiang-Yun Zhang, Liang-Liang He, Jin-Ying Du and Zi-Zhou Yuan
Removal of Pb(II) from Water by FeSiB Amorphous Materials
Reprinted from: *Metals* **2022**, *12*, 1740, https://doi.org/10.3390/met12101740 . . . . . **289**

Rafał Krakowski
Influence of Effective Microorganisms, Colloidal Nanosilver and Silver Compounds on Water Content in New and Used Engine Oil: A Preliminary Study
Reprinted from: *Appl. Sci.* **2022**, *12*, 10234, https://doi.org/10.3390/app122010234 . . . . . **304**

Rihua Yang, Yiming Yang, Xuhui Zhang and Xinzhong Wang
Experimental Study on Performance of Local Bond-Slip Test of Steel Strand Tendons and Concrete
Reprinted from: *Coatings* **2022**, *12*, 1494, https://doi.org/10.3390/coatings12101494 . . . . . **320**

Jiyu Hou, Baojie Wang, Daokui Xu, Liji Cui and Jie Sun
Effect of Surfactants on the Corrosion Protectability of Calcium Phosphate Conversion Coatings on Duplex Structured Mg-8Li (in Wt.%) Alloy
Reprinted from: *Coatings* **2022**, *12*, 1182, https://doi.org/10.3390/coatings12081182 . . . . . **333**

Yongzeng Jiang, Jing Dong, Xiaoyu Qi and Fazhi Wang
Improvement of Monitoring Technology for Corrosive Pollution of Marine Environment under Cloud Computing Platform
Reprinted from: *Coatings* **2022**, *12*, 938, https://doi.org/10.3390/coatings12070938 . . . . . **347**

Jun Li, Yayun He, Xi Zhao and Chankyung Kim
Evolution of Microstructure and Mechanical Properties of Al-Zn-Mg-Cu Alloy by Extrusion and Heat Treatment
Reprinted from: *Coatings* **2022**, *12*, 787, https://doi.org/10.3390/coatings12060787 . . . . . **359**

Ang Gao and Mengxi Zhang
Performance and Application of Geocell Reinforced Sand Embankment under Static and Cyclic Loading
Reprinted from: *Coatings* **2022**, *12*, 767, https://doi.org/10.3390/coatings12060767 . . . . . **370**

applied sciences

MDPI

Article

Studying Corrosion Failure Prediction Models and Methods for Submarine Oil and Gas Transport Pipelines

Junguo Cui [1,2,*], Yuyin Wu [1,2], Zhongqi Lu [3] and Wensheng Xiao [1,2]

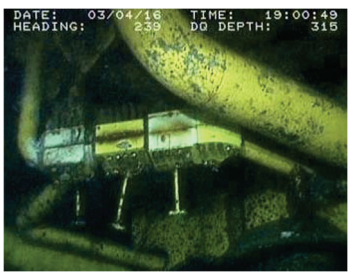
[1] College of Mechanical and Electrical Engineering, China University of Petroleum, Qingdao 266580, China; z22040105@s.upc.edu.cn (Y.W.); xiaows@upc.edu.cn (W.X.)
[2] National Engineering Research Center of Marine Geophysical Prospecting and Exploration and Development Equipment, Qingdao 266580, China
[3] Offshore Oil Engineering (Qingdao) Co., Ltd., Qingdao 266520, China; luzhq7@cooec.com.cn
* Correspondence: cuijunguo@upc.edu.cn

Abstract: To predict the corrosion failure of carbon steel oil and gas pipelines more accurately, a new corrosion failure prediction model for submarine oil and gas transport pipelines was constructed. A corrosion failure prediction management system was also developed based on the constructed model. To construct the model, corrosion experiments were carried out to analyze the influences of temperature, partial pressure of CO_2, pH value, and flow rate acting on the corrosion rate. Based on the analysis results and the corrosion experiment data, a new corrosion failure prediction model containing the time and flow rate for oil and gas pipelines was constructed. The model is based on the existing corrosion prediction model and has a determination coefficient, R^2, of 0.9573, which indicates good prediction accuracy. A machine learning prediction model was also used to predict, and the prediction results are compared with that of the proposed model, which further verifies the accuracy and feasibility of the proposed model. A corrosion failure prediction management system for carbon steel oil and gas pipelines was developed based on the constructed model, which makes corrosion failure prediction more convenient and faster and provides a reference for the accurate prediction and efficient control of oil and gas pipeline corrosion failure.

Keywords: submarine oil and gas transport pipeline; corrosion experiment; corrosion prediction model; corrosion prediction management system

1. Introduction

Carbon steel pipelines are the main facilities for submarine oil and gas transportation. The economic losses and environmental pollution caused by the failure of oil and gas transport pipelines are severe, and corrosion caused by the transportation medium is the main cause of pipeline failure, as shown in Figure 1. Therefore, studying the corrosion failure prediction model and method for submarine oil and gas pipelines is important to the safety of submarine oil and gas transportation.



(**a**) Corrosion of pipeline.



(**b**) Leak position.

Figure 1. Corrosion of submarine oil and gas transport pipeline.

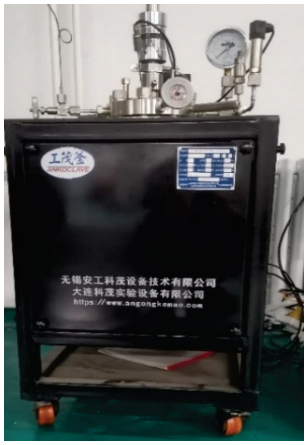
Until recently, research on the corrosion failure prediction of carbon steel rigid oil and gas pipelines at home and abroad has undergone four stages [1]: an initial empirical model, a semi-empirical model, a mechanism model, and a corrosion failure prediction model established using machine learning algorithms. The initial empirical model was proposed based on experiments and field data [2]. Many improvements have been made since its establishment, such as parameter optimization and making prediction software easier to apply [3–5]. However, this type of model cannot be widely used in practice because it does not consider electrochemical reaction kinetics, which increases prediction error. Based on the empirical model, fluid dynamics and other factors must be considered to study the transfer law of corrosive mediums inflow [6]; this is the semi-empirical model. Continuous improvement involves considering the pH value of the medium, corrosion product film, and specific gravity of crude oil for prediction accuracy [7,8]. With the development of computer technology, experts have combined computational methods with experimental and theoretical analysis to reveal the mechanism of corrosion and the established mechanism model. We considered the influence of factors such as the pH value, medium flow rate, and temperature on the reduction reaction of hydrogen ions, water, and oxygen at the cathode and the dissolution process of iron at the anode in the mechanism model [9–12]. In addition, we propose dimensionless film-forming tendency factors based on the circulation experiment to establish a kinetic model of deposition growth for corrosion product films and better understand the corrosion process [13]. Since data processing has become easier and more efficient, researchers have used machine learning algorithms to analyze experimental or statistical data, building a variety of corrosion prediction models. These algorithms are widely used in numerical modeling and predicting interest fields [14–16]. El-Abbasy et al. [17] established a prediction model based on a regression analysis and neural networks [18], where they analyzed the sensitivity of each influencing factor to pipeline corrosion failure. Ossai et al. [19] established a Markov model with non-uniform linear growth in continuous time to predict pit depth distribution after pipeline corrosion. Larin et al. [20] proposed a new algorithm by determining which model of the pipeline's corrosion area could be established directly. A mechanistic model and an electrochemical model for the carbon dioxide corrosion of mild steel are proposed in [21,22], respectively. Xu et al. [23] conducted failure pressure prediction for pipelines containing corrosion defects based on a DE-BPNN model. However, a predictive model based on machine learning algorithms cannot obtain an explicit reaction formula; it has poor adaptability and requires repeated training. Although the empirical model and semi-empirical model have relational expressions between factors influencing corrosion and corrosion rate, these factors are not fully considered.

Uniform corrosion is the main corrosion form of carbon steel oil and gas pipelines in an acidic solution. We discuss the influence of various factors on uniform corrosion rate in this paper based on carbon steel corrosion simulations and reactor experiments. Considering time and flow rate [24,25], we established a new corrosion prediction model for carbon steel oil and gas pipelines and developed a corrosion prediction management system, providing a reference for the accurate prediction and efficient control of oil and gas pipeline corrosion failures.

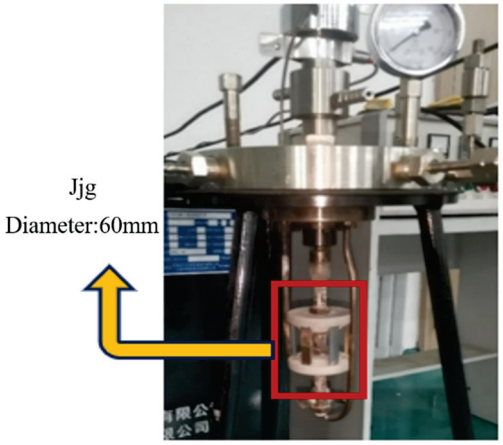
2. Corrosion Test

2.1. Arrangement and Experimental Procedure

We applied an FCZ2-10-300 high-temperature and high-pressure reactor to the experiment. The main material of the reactor body was 316 L stainless steel. In order to improve its corrosion resistance, an anti-corrosion lining was added to the innermost layer. The reactor equipment and reactor body are shown in Figure 2a,b, respectively.



(**a**) High-temperature and high-pressure reactor equipment.



(**b**) High-temperature and high-pressure reactor body.

Figure 2. High-temperature and high-pressure reactor equipment.

The experimental material was X60 pipeline steel, which was made as a corrosion coupon with dimensions of 50 × 10 × 3 mm, as shown in Figure 3. The influence of the partial CO_2 pressure, temperature, flow rate, and corrosion time on its corrosion rate was studied next.

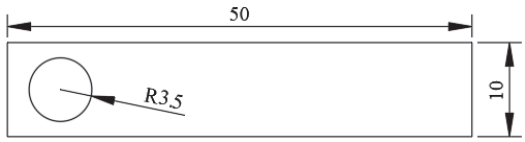


Figure 3. Size of the corrosion coupon (mm).

The working principle of high-temperature and high-pressure reactor equipment is shown in Figure 4. The temperature in the reactor, stirring speed, and start and stop control of the circulating water pump for the jacket cooling are all controlled by the corresponding knobs on the control cabinet. The pressure in the reactor is displayed by the pressure gauge, which synchronizes with the display screen of the control cabinet.

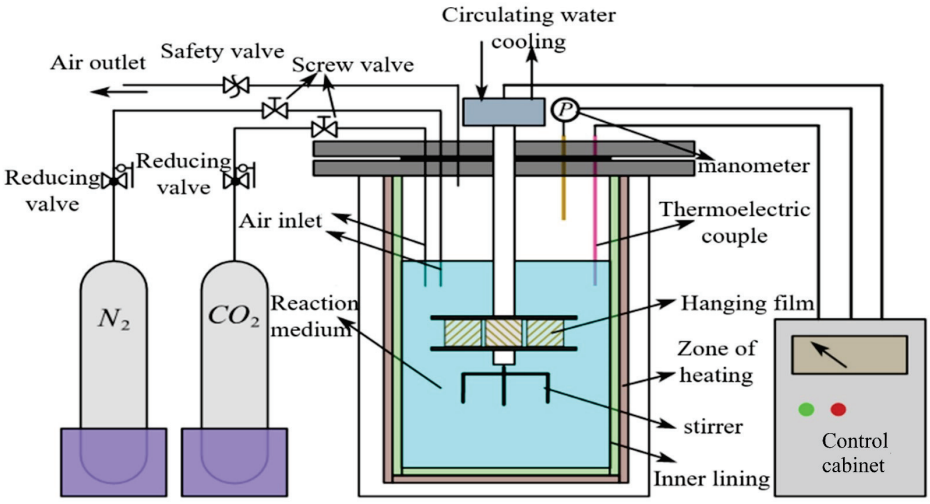


Figure 4. Schematic diagram of a high-temperature and high-pressure reactor.

In this experiment, the corrosion of the experimental material was mainly affected by the CO_2 aqueous solution, so the pH value of the solution was only affected by the partial

CO_2 pressure and temperature. Equation (1) calculates the pH value of a 1 L aqueous solution injected into CO_2 [26].

$$pH_{CO_2} = 3.82 + 0.00384Tem - 0.51log(P_{CO_2}) \quad (1)$$

In this formula, pH_{CO2} is the pH value of the solution under partial CO_2 pressure and temperature, *Tem* (°C) is temperature, and P_{CO2} (MPa) is the partial CO_2 pressure.

We arranged experimental plans using the Response Surface Method [27] according to different experimental requirements. We conducted the experiment, obtained experimental data, and used these data to fit a multivariate function reflecting the relationship between the response and the factor. Finally, we obtained a mathematical model describing the relationship between the experimental factor and the response. When arranging the experimental plans, the axial point of the face-centered cubic design fell on the cube plane but did not exceed the original design level. The estimation of various items was also relatively accurate. In addition, based on the three-level design principle, we used this method to design. We adopted a 1/2 face-centered cubic design and set up 25 groups of experiment plans with a resolution V. Table 1 shows the level values of each factor, and Table 2 shows the design and experimental arrangement.

Table 1. Level table of experimental factors.

Experimental Factor		P_{CO2} (MPa)	*Tem* (°C)	V_l (m·s^{-1})	*T* (day)
level	Low	0.1	30	1	3
	High	0.3	90	3	7

Table 2. Experimental schedule.

Serial Number	Ordinal Factor					Respond
	P_{CO2} (MPa)	*Tem* (°C)	V_l (m·s^{-1})	*t* (day)	pH_{CO2}	*H* (mm)
1	0.3	90	3	7	4.4	0.00493
2	0.2	60	2	5	4.5	0.00295
3	0.3	90	1	3	4.4	0.00382
4	0.1	30	1	7	4.5	0.00289
5	0.1	30	1	3	4.5	0.00228
6	0.2	90	2	5	4.6	0.00294
7	0.2	60	1	5	4.4	0.00325
8	0.3	30	3	3	4.2	0.00303
9	0.2	60	2	7	4.4	0.00313
10	0.1	90	1	3	4.7	0.00246
11	0.2	30	2	5	4.3	0.00277
12	0.3	30	3	7	4.2	0.00405
13	0.1	60	2	5	4.6	0.00272
14	0.1	30	3	3	4.5	0.00229
15	0.1	30	3	7	4.5	0.00239
16	0.1	90	1	7	4.7	0.00268
17	0.2	60	2	3	4.4	0.00296
18	0.1	90	3	7	4.7	0.00275
19	0.1	90	3	3	4.7	0.00254
20	0.3	90	1	7	4.4	0.00456
21	0.3	30	1	3	4.2	0.00347
22	0.3	90	3	3	4.4	0.00398
23	0.2	60	3	5	4.5	0.00306
24	0.3	60	2	5	4.3	0.00392
25	0.3	30	1	7	4.2	0.00385

Annotation: *H* is the uniform corrosion depth.

The experiment system was set up to conduct the following experiment arrangements, as shown in Figure 5.

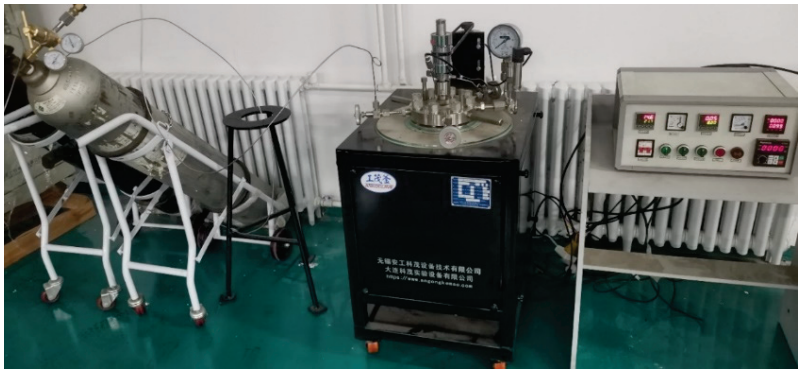
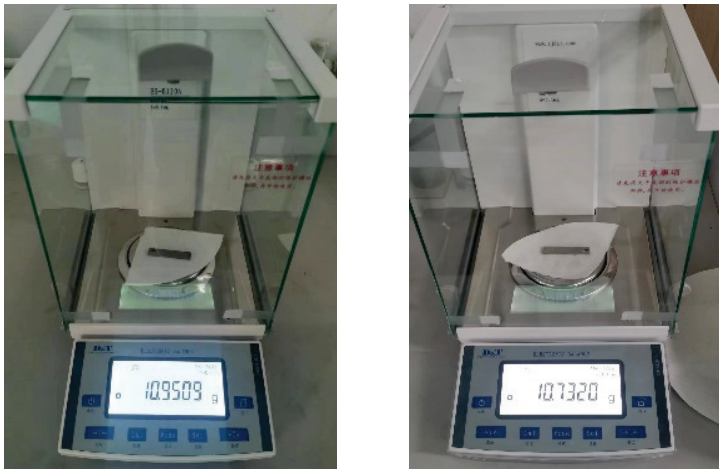


Figure 5. High-temperature and high-pressure reactor experimental device.

The experimental steps were as follows:

(1) Sealing test of the reactor. Tighten the bolts three to four times according to the reactor's loading procedure, and then inject nitrogen into the air inlet to control the pressure in the reactor to a certain value. After 12 h, observe whether the pressure in the reactor decreases. If the pressure remains stable, the reactor seal is effective;
(2) Proceed with the experiment after confirming the seal. Clean the corrosion coupons using filter papers, and then remove surface grease using absorbent cotton. Finally, immerse the coupons in anhydrous ethanol for further degreasing and dehydration;
(3) Wrap the coupons in filter paper after cold air drying and put them in the dryer for 1 h to ensure that they are completely dried;
(4) Prepare the solution. The reactor container has a capacity of 2 L. To ensure safety, the experimental simulation liquid should not exceed 2/3 of the container's capacity. At the same time, to ensure complete immersion of the coupons in the solution, the simulated solution in this experiment was limited to 1 L;
(5) Remove the coupons from the dryer. To ensure the accuracy of the experiment, a vernier caliper should be used to measure the size of the coupons with an accuracy of 0.01 mm. Calculate and record the coupons area, weigh the coupons with an accuracy of 0.1 mg, and record the weight as 'm_1';
(6) Pour the configured solution into the reactor, then fix the coupons to the clamp of the reactor body. Install and fix the reactor body, open the exhaust port, and inject nitrogen for 1 h to facilitate deoxygenation treatment;
(7) Tighten the exhaust port after deoxygenation, set the appropriate conditions according to the working conditions, and open the exhaust port when the experimental time is up. Remove the pressure in the reactor, discharge the gas in the reactor, and remove the coupons after cooling;
(8) Submerge the coupons after the experiment in anhydrous ethanol, and then use absorbent cotton to degrease and remove water. Finally, clean the oxidized sediment on the surface, and then soak the coupons in anhydrous ethanol again. Remove the coupons, wipe them clean, and dry them in the dryer. After drying, record the weighing data (m_2), as shown in Figure 6;
(9) Clean the reactor body and conduct the next set of experiments.



(**a**) Before corrosion. (**b**) After corrosion.

Figure 6. Electronic balance weighing.

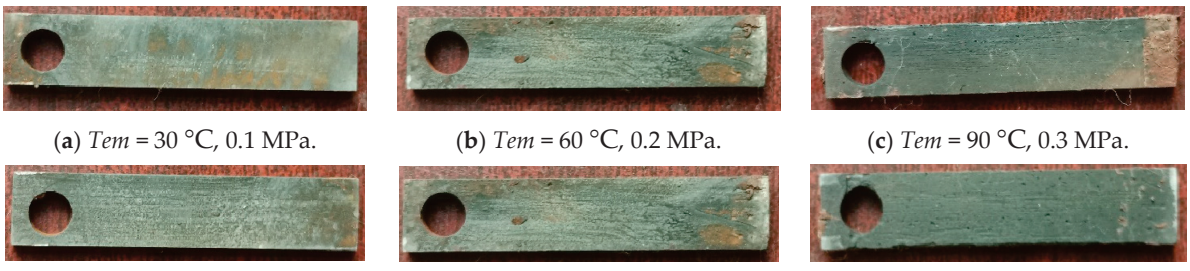
2.2. Experimental Results and Discussion

The uniform corrosion depth can be calculated according to the weighing data before and after the corrosion experiment, namely the surface area and density of the coupons, as shown in Equation (2):

$$H = \frac{10\Delta W}{S \times \rho} \tag{2}$$

where H (mm) is the uniform corrosion depth; ΔW is poor quality before and after the corrosion experiment, $\Delta W = m_1 - m_2$ (g); S (cm^2) is the surface area of the coupons; and ρ ($g \cdot cm^{-3}$) is the density of the corrosion material.

The experiment was conducted following a face-centered cubic design arrangement. The corrosion depth of the coupons under 25 different working conditions is listed in the last column of Table 2. According to the existing literature, the temperature and partial CO_2 pressure have the greatest influence on corrosion. Figure 7 shows part of the coupons under experimental conditions for three days, with *Tem* = 30 °C, 60 °C, and 90 °C; P_{CO2} = 0.1 MPa, 0.2 MPa, and 0.3 MPa; and V_l = 2 $m \cdot s^{-1}$.



(**a**) *Tem* = 30 °C, 0.1 MPa. (**b**) *Tem* = 60 °C, 0.2 MPa. (**c**) *Tem* = 90 °C, 0.3 MPa.

(**d**) *Tem* = 60 °C, 0.1 MPa. (**e**) *Tem* = 90 °C, 0.2 MPa. (**f**) *Tem* = 30 °C, 0.3 MPa.

Figure 7. Coupons after experiment.

Figure 7 shows significant local corrosion under the working conditions. The weight loss of the coupons under all experimental working conditions is depicted, as shown in Figure 8.

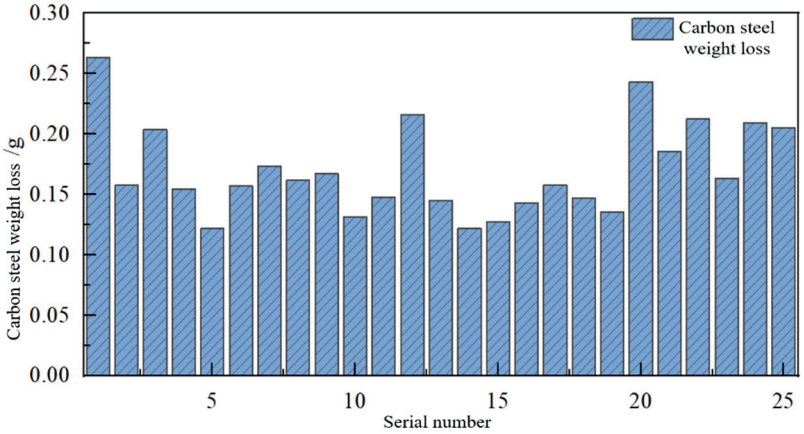


Figure 8. Weight loss record under 25 different working conditions.

According to the weight loss recorded in Figure 8, the corrosion rate can be calculated by Equation (3).

$$v_s = \frac{365 \times H}{t} \tag{3}$$

where v_s (mm·a^{-1}) is the corrosion rate obtained via the experiment, and t (day) is the corrosion time.

3. Construction of Carbon Steel Corrosion Prediction Model

3.1. Model Establishment

The existing carbon steel corrosion prediction model evolved based on semi-empirical models, as shown in Equation (4) [28].

$$logRc = -7.545 - \frac{3359.5}{T + 273} - 2.4622log(P_{CO_2}) + 5.9977(7 - pH_{CO_2}) \tag{4}$$

where Rc is the corrosion rate obtained by model.

The shortcoming of this model is that it predicts a fixed corrosion rate, assuming that the corrosion depth is a linear function of time. However, the corrosion morphology continuously evolves throughout the corrosion process, leading to changes in the corresponding corrosion rate. Experiments and simulations demonstrate the impact of the medium flow rate on the pipeline, which cannot be ignored when evaluating the corrosion rate. Therefore, considering time and flow rate, we propose a new corrosion prediction parametric model, as shown in Equation (5).

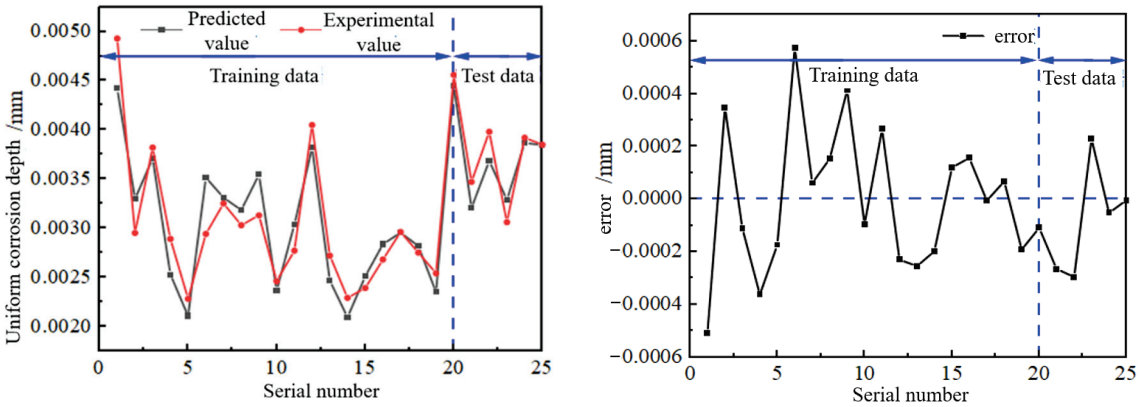
$$h = \begin{cases} At^{b1} \\ ln(A) = b_2 + \frac{b_3}{Tem+273.15} + b_4 ln(P_{CO_2}) + b_5(7 - pH_{CO_2}) + b_6 ln(V_l) \end{cases} \tag{5}$$

where h (mm) is the remaining thickness of the tube wall, and b_1 to b_6 are the undetermined coefficients.

The sampling method of the face-centered cubic design cannot be used to simulate the segmental phenomenon caused by temperature adequately. Therefore, only the one-stage model was fitted, which verified the feasibility of the constructed model. These results laid the foundation for developing a more precise segmental corrosion prediction model for carbon steel pipelines. Based on the experimental corrosion data listed in Table 2, the least squares method was used to obtain the undetermined coefficients, as shown in Equation (6).

$$h = \begin{cases} At^{0.14761} \\ A = e^{(-5.6126 - \frac{472.9539}{Tem+273.15} + 0.096 ln(P_{CO2}) - 0.5827(7 - pH_{CO2}) - 0.0408 ln(V_l))} \end{cases} \tag{6}$$

The determination coefficient, R^2, of the fitted model is 0.9573, close to "1", thus indicating the model's is accuracy. The carbon steel uniform corrosion depth and error curve calculated by this model are shown in Figure 9.



(**a**) Corrosion rate predicted value. (**b**) Prediction error.

Figure 9. Predicted corrosion depth of carbon steel and error curve.

Figure 9a shows that the experimental and simulation values are similar in terms of variation trend and value. In addition, the prediction error curve in Figure 9b shows minimal variation, fluctuating around "0", with a maximum error of 0.0006. This result confirms the feasibility of the proposed method and accuracy of the fitted model.

3.2. Verification of Prediction Model

To further verify the feasibility and accuracy of the constructed model, BP neural network and random forest regression models based on corrosion data were established for prediction. The BP neural network prediction model was further optimized using the improved particle swarm optimization method based on the prediction results. The prediction results of the established BP neural network prediction model, random forest regression prediction model, and optimized BP neural network prediction model were compared to the prediction model constructed in this paper.

3.2.1. BP (Backpropagation) Neural Network Prediction Model

BP neural networks, also called backpropagation networks, were proposed in the late 1980s, when there was a calculation error lag on the Internet. To improve transmission, it propagates in the opposite direction after reaching the input layer through the calculation [29].

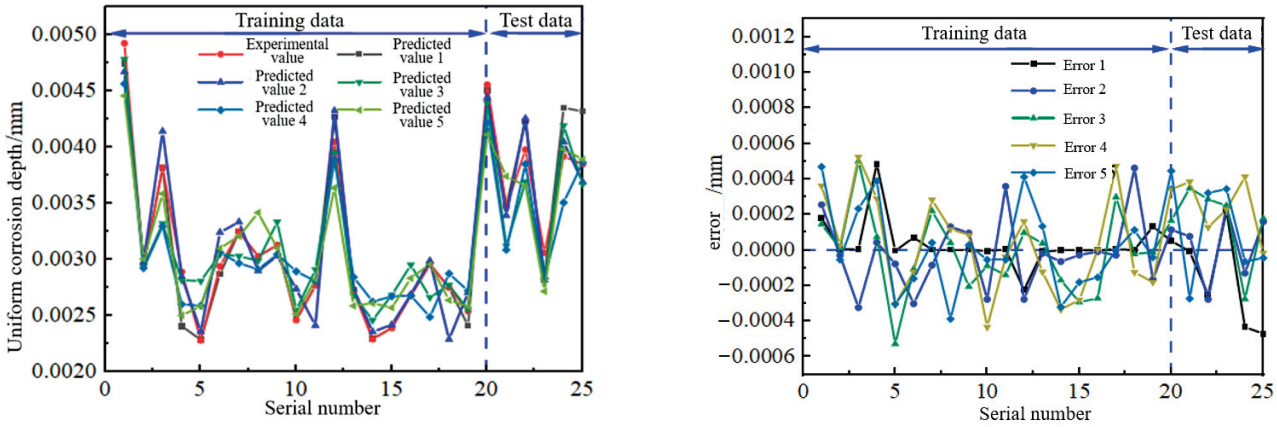
We separated the experimental data into training and test sets according to a certain proportion. If the training set is too small, insufficient training strength is likely to occur. If the training set is too large and the test set is relatively small, the model cannot be verified. Therefore, 80% of the total data was selected as the training set, and the remaining 20% as the test set to build the model. According to the experimental data, five influencing factors were received as inputs, and the uniform corrosion depth of the carbon steel served as output. Therefore, the input layer had five neurons, and the output layer had one neuron. Determining the number of neurons in the hidden layer is crucial to the accuracy of the model, which is calculated according to the following empirical formula:

$$l = \sqrt{m+n} + a \tag{7}$$

where l is the number of hidden layer neurons; m is the number of neurons in the input layer; n is the number of neurons in the output layer; and a indicates the empirical parameter, $1 \leq a \leq 10$.

We found that using the BP neural network prediction model achieved better accuracy with nine hidden layer neurons. According to the experimental sample size and desired accuracy, the maximum number of iterations was set to 300, with an expected error of 0.0001 and a learning rate of 0.01.

Due to the inherent randomness in the training process of machine learning algorithms, the results vary each time. In this study, the model was trained 30 times, and the top five results were selected for plotting the predicted corrosion depth of carbon steel and the error curve, as shown in Figure 10.



(**a**) Carbon steel corrosion depth prediction. (**b**) Prediction error.

Figure 10. BP neural network model corrosion prediction.

3.2.2. Random Forest Regression Prediction Model

The key parameters affecting the accuracy of the random forest regression prediction model are the leaf size and the number of decision trees. In this paper, the leaf size was set to 5, 10, 20, 50, and 100, and the number of decision trees was set to 200. Figure 11 shows the mean square error of carbon steel corrosion prediction under varying numbers of decision trees and leaf sizes.

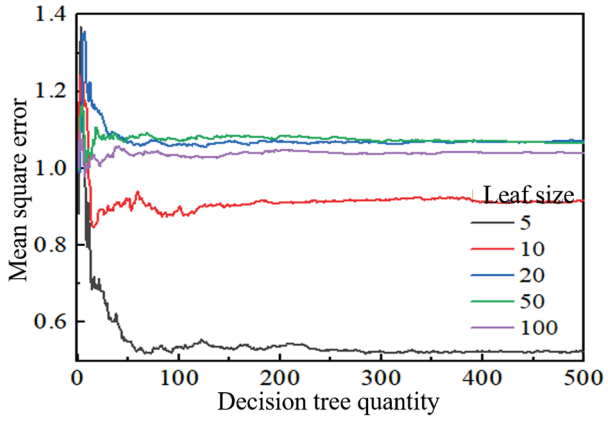
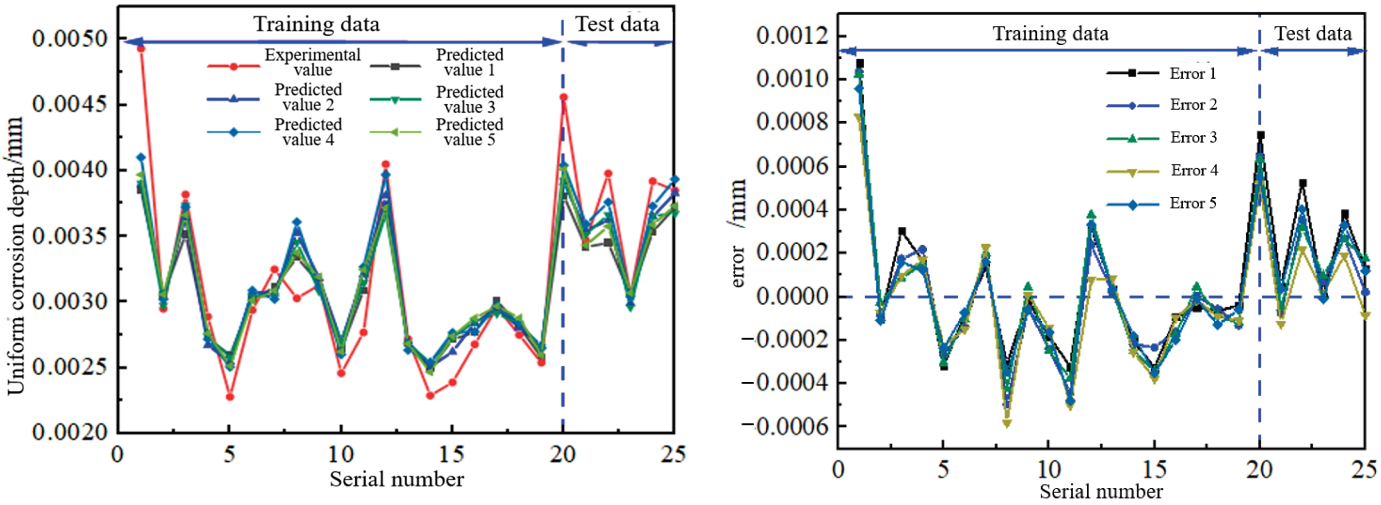


Figure 11. Parameter selection of random forest regression.

Figure 11 shows that errors in prediction models trained using corrosion data are minimized when the leaf size is set to five. According to the fundamental principle of the random forest regression algorithm, the prediction output of the model represents the average predictions from all decision trees. As the number of decision trees increases, the predicted values tend to stabilize. If the decision trees are sequentially built after stability, the computation time will only increase and even lead to "overfitting". As Figure 11 illustrates, the number of decision trees stabilizes at around 60 for carbon steel corrosion

prediction. Based on the analysis, the leaf size was set to five, and the number of decision trees to 60, when the random forest regression corrosion prediction model was established for this paper. If the number of samples is large enough while developing the random forest regression prediction model, the "overfitting" phenomenon will not occur, because the algorithm adopts a back-sampling cross-experiment for verification. If less data are available, dividing the data into training and test sets is necessary. Therefore, 80% of the total experimental data was selected as the training set, while the remaining 20% served as the test set for building the random forest regression corrosion prediction model.

Similar to the BP neural network prediction model, the model underwent 30 training iterations, and the top 5 results were selected for plotting the predicted corrosion depth of carbon steel and the error curve, as shown in Figure 12.



(**a**) Carbon steel corrosion depth prediction.

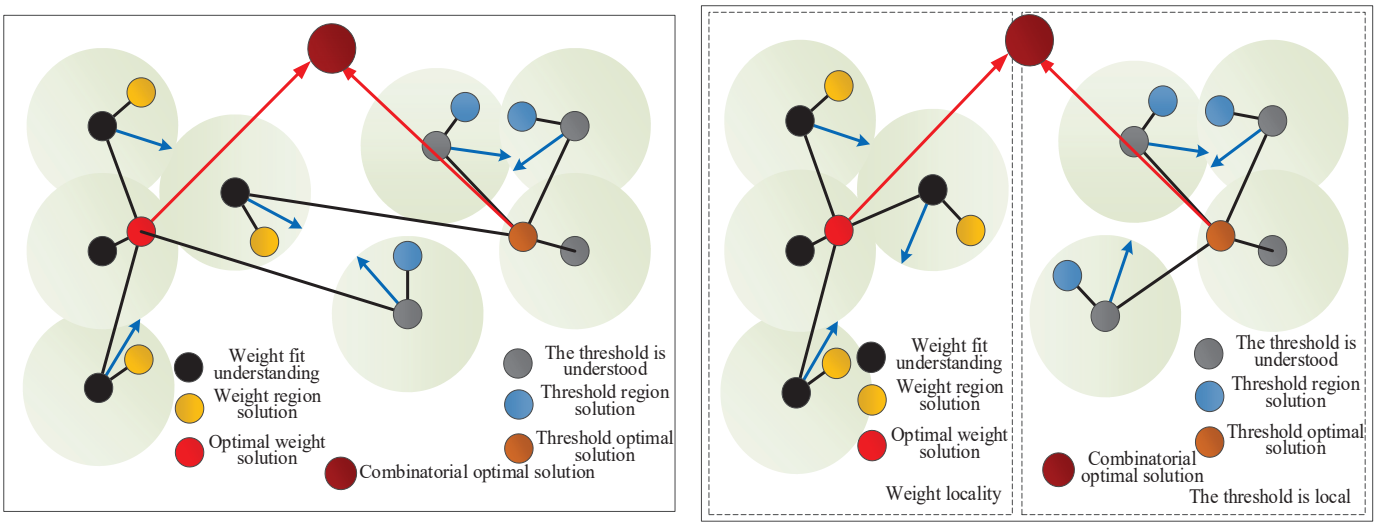
(**b**) Prediction error.

Figure 12. Corrosion prediction by random forest regression model.

3.2.3. Optimized BP Neural Network Prediction Model

Figures 10 and 12 show that the error of the two machine learning prediction models, the BP neural network model and the random forest regression model, is minor when predicting the corrosion of carbon steel. Nevertheless, the training results of random forest regression predictions are remarkably consistent among the five training runs, whereas those of the BP neural network prediction model exhibit significant variability. This discrepancy is also evident in the error curve charts. The error trend curve of the random forest regression prediction model follows a consistent pattern, whereas the error curve of the BP neural network prediction model appears relatively chaotic. This discrepancy indicates that the random forest regression prediction model demonstrates greater stability, albeit with a marginally higher overall error, whereas the BP neural network model exhibits a lower overall error despite requiring a longer training period. Moreover, the BP neural network prediction model achieves superior accuracy, albeit at the expense of a lengthy optimization process during training. According to the fundamental principles of the BP neural network algorithm, its prediction accuracy hinges significantly on the appropriate tuning of weights and thresholds between layers. The suitability of these values directly impacts training efficiency and the precision of prediction calculations. Therefore, in this paper, we used the enhanced particle swarm optimization algorithm to fine-tune these parameters. According to the principle of the particle swarm optimization algorithm [30,31], the initial position, velocity, particle range, and expected fitness value for single-factor optimization can be iteratively calculated to obtain the optimal value. In this part, the optimization of the two factors, weight and threshold, may be difficult due to the different value ranges of the two factors [32]. Local optimality or long iteration times may occur, as shown in Figure 13a. In light of these challenges, the particle swarm optimization algorithm

was refined first. It assigns specific value ranges to the weight and threshold, allowing them to search for optimization within their respective local domains. The mean square error serves as the fitness value, and the combined values of the two factors, which comprise the smallest fitness value, represent the optimal solution, as shown in Figure 13b.



(**a**) Before improvements. (**b**) After improvement.

Figure 13. Optimization schematic diagram of improved pre- and post-particle swarm optimization algorithms.

In addition, when the inertia weight factor is introduced into the particle velocity updating formula, the larger the value is, the better the global search effect will be. Otherwise, it will be conducive to local searches. To balance the two situations, the algorithm has a strong global search ability in the early stages of operation, conducts accurate searches after locking the approximate optimal solution range, and introduces dynamic inertia weight factors [33,34]. Its calculation formula is as follows:

$$w = w_s - (w_s - w_e)(\frac{i}{m})^2 \tag{8}$$

where w_s is the initial inertia weight, w_e is the inertia weight when iteration reaches the maximum, i is the current iterations, and m is the total number of iterations.

Generally speaking, when the initial and final inertia weights are 0.9 and 0.4, respectively, the PSO performance is the best. When the progress of iteration shows a parabolic decline, the optimization ability gradually changes from global to local.

The dynamic inertia weight factor is introduced into the velocity update formula of the particle swarm optimization algorithm, as shown in Equation (9).

$$v_i = w \times v_i + c_1 \times rand() \times (pbest_i - x_i) + c_2 \times rand() \times (gbest_i - x_i) \tag{9}$$

where w is the inertia factor; v_i is the particle velocity; i = 1,2 ... N, N is the total number of particles; c_1 and c_2 are learning factors that are usually set to 2; and *rand*() is a random number between 1 and 2.

Figure 14 shows the flowchart of optimization in this model.

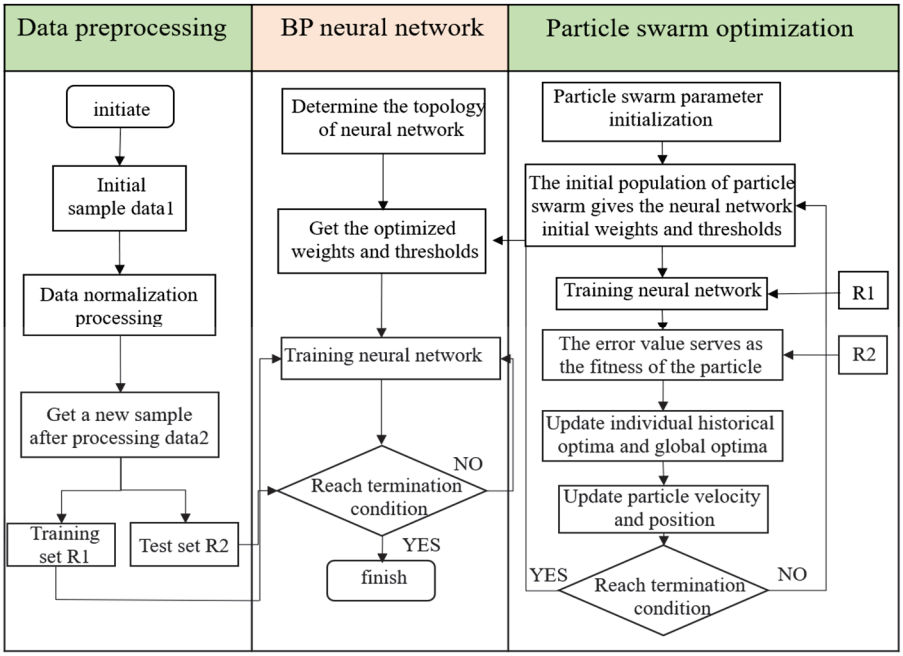


Figure 14. Flowchart of optimization model establishment.

We established this model based on the data obtained from a corrosion experiment with a high-temperature and high-pressure reactor. According to the scale of corrosion data, the population size of the particle swarm optimization algorithm was set to 30, the number of iterations was 500, and both c_1 and c_2 were set to 2. The value range of the neural network weight and threshold was set to $[-1, 3.8]$ and $[-1, 8]$, respectively.

After the parameters were set, the iterative optimization of the particle swarm optimization algorithm was started by reading the carbon steel corrosion data. The iterative weight and threshold parameters were input into the neural network prediction model, and the corrosion of carbon steel materials was predicted again. The training was conducted 30 times, and the prediction curve was drawn based on the top 5 times, as shown in Figure 15.

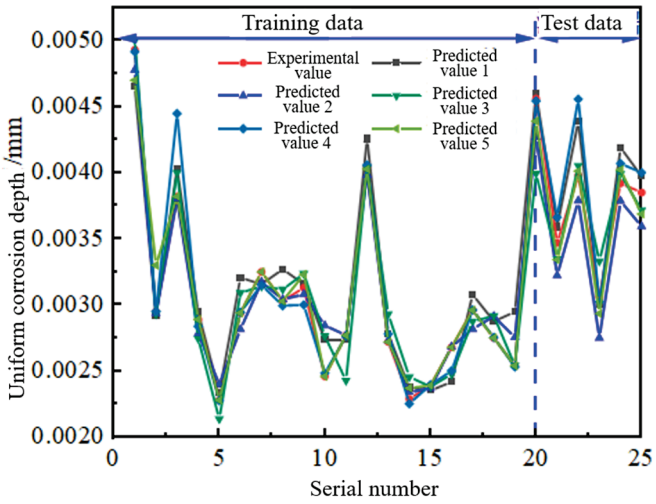


Figure 15. Corrosion prediction of optimized BP neural network model.

Figure 15 shows that the five optimal training results of the optimized model exhibit smaller fluctuations, greater stability, and increased accuracy.

3.2.4. Model Comparison Test

We selected group data with higher accuracy from each established machine learning prediction model and compared them to the model established in this paper. The prediction curves of each model are shown in Figure 16.

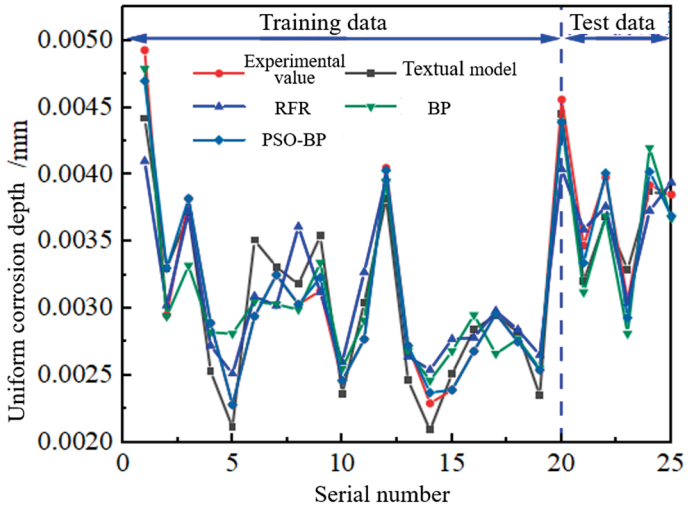


Figure 16. Comparison and prediction test of each model.

Figure 16 shows that the prediction model results are consistent with the prediction trend of the machine learning prediction model. Furthermore, it has high accuracy, so it can be applied to the corrosion prediction of carbon steel materials.

3.3. Management System Development

We developed a corrosion failure prediction management system for carbon steel oil and gas pipelines to broaden the application scope of this model. The main interface of the system is shown in Figure 17.

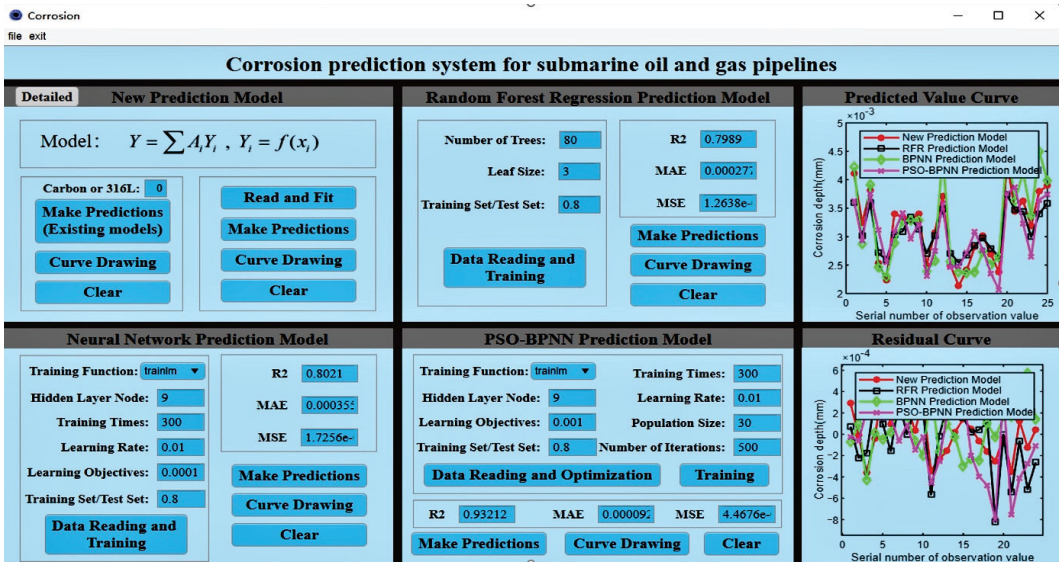


Figure 17. Main interface of oil and gas pipeline corrosion prediction management system.

The model constructed in this paper is integrated and compiled, and so is the parameterized model [35]. Users can import corrosion data and train parameters to improve the model's prediction accuracy. In addition, our model's feasibility can be tested by compiling three machine learning algorithm prediction models, namely the BP neural network,

random forest regression, and optimized neural network model, into the management system. Users can also use different prediction models to make more convenient and efficient predictions.

As seen in Figure 17, the prediction results of the management system are consistent with Figure 16, proving the feasibility of using the developed management system for prediction. Moreover, the prediction results of the machine learning algorithm are similar to the model described in this paper, thus confirming the accuracy of our prediction model.

3.4. Determination of Corrosion Failure Criteria

At present, according to the oil and gas industry standard SY/T6151 [36], safety parameters affecting carbon steel oil and gas pipeline transportation include the depth of the corrosion pit, the longitudinal length of the corrosion pit, and the circumferential length. We used the maximum depth of the corrosion pit to classify pipelines with different corrosion degrees into five states: light, medium, heavy, severe, and perforated. Table 3 list the parameters.

Table 3. Corrosion failure criteria for carbon steel oil and gas pipelines.

Corrosion Condition	Mild	Moderate	Severe	Extremely Severe	Perforation
Maximum depth of corrosion pit/mm	<1	1~2	2~50% Wall thickness	50~80% Wall thickness	>80% Wall thickness

As seen in Table 3, carbon steel oil and gas pipelines are divided into five corrosion levels, namely five corrosion states, according to the maximum depth of the corrosion pit and wall thickness of oil and gas pipelines. The corrosion state of the pipeline can be determined by calculating the corrosion depth.

4. Conclusions

We arranged 25 orthogonal experiment plans, using face-centered cubic designs derived from the response surface method to improve the shortcomings of existing oil and gas pipeline corrosion prediction models. Corrosion experiments with high-temperature and high-pressure reactors were performed according to experimental arrangements. The corrosion depths of the coupons under different working conditions were obtained. We developed a new corrosion failure prediction model for carbon steel oil and gas pipelines, using the least squares method on corrosion experiment data. This model introduced two variables: time and flow rate. The determination coefficient, R^2, of the model was 0.9573, which illustrates a good fitting effect. Three machine learning algorithm prediction models, namely the BP neural network, random forest regression, and optimized neural network, were constructed and compared with the new prediction model proposed in this paper. The prediction model results described in this paper are consistent with the prediction trend of the machine learning prediction models, which had high accuracy, verifying the feasibility and accuracy of the proposed prediction model. Finally, based on the constructed prediction model, we developed a corrosion failure prediction management system for carbon steel oil and gas pipelines, making corrosion prediction for submarine oil and gas transport pipelines more convenient and faster. Based on the uniform corrosion failure prediction model in this paper, the pitting corrosion failure prediction model of the stainless-steel pipeline for oil and gas transmission can be studied further.

Author Contributions: Conceptualization, J.C.; methodology, Z.L.; software, Z.L.; validation, Y.W. and Z.L.; formal analysis, Y.W.; investigation, J.C.; resources, W.X.; data curation, Y.W.; writing—original draft preparation, Y.W. and Z.L.; writing—review and editing, J.C.; visualization, Y.W.; supervision, W.X. All authors have read and agreed to the published version of the manuscript.

Funding: This research was funded by the high-tech ship research project of the Ministry of Industry and Information Technology of the People's Republic of China (grant no. 2018GXB01-02-003), the Strategic Research and Consulting project of the Chinese Academy of Engineering (grant no. 2022-DFZD-36), and the Fundamental Research Funds for the Central Universities (grant no. 22CX01003A-1).

Institutional Review Board Statement: Not applicable.

Informed Consent Statement: Not applicable.

Data Availability Statement: The data presented in this study are available upon request from the corresponding author. The data are not publicly available due to privacy.

Acknowledgments: We sincerely acknowledge Kuitao Wang and Feng Yin for their administrative and technical support and guidance.

Conflicts of Interest: Author Zhongqi Lu was employed by the company Offshore Oil Engineering (Qingdao) Co., Ltd. The remaining authors declare that this research was conducted without any commercial or financial relationships that could be construed as a potential conflict of interest.

References

1. Yao, Q.K. Research on Internal Corrosion Prediction Method of Gas Collecting Pipeline in Moxi Gas Field. Master's Thesis, Southwest Petroleum University, Chengdu, China, 2012.
2. Olsen, S.; Halvorsen, A.M.; Lunde, P.G.; Nyborg, R. CO_2 corrosion prediction model—Basic principles. *Corrosion* **2005**, *55*, 223.
3. Liu, W.W. Research on CO_2 Corrosion Law and Prediction Model of Oil Field Gathering and Transportation Pipeline. Master's Thesis, China University of Petroleum, Qingdao, China, 2010.
4. Feng, C.Q. Research on CO_2 Corrosion Prediction Method and Anti-Corrosion Measure of Gas Well Tubing. Master's Thesis, Southwest Petroleum University, Chengdu, China, 2015.
5. Sun, Q. Study on CO_2 corrosion prediction and anti-corrosion countermeasures of gas well tubing. *Pet. Chem. Equip.* **2018**, *21*, 71–74.
6. De, W.C.; Lotz, U. Prediction of CO_2 corrosion of carbon steel. *Corrosion* **1993**, *51*, 69.
7. de Waard, C.; Lotz, U.; Milliams, D.E. Predictive Model for CO_2 Corrosion Engineering in Wet Natural Gas Pipelines. *Corrosion* **1991**, *47*, 976–985. [CrossRef]
8. Cui, Y.; Lan, H.Q.; Kang, Z.L.; He, R.Y.; Huang, H.; Lin, N. Improvement of a CO_2 corrosion prediction model for natural gas pipelines based on flow field calculation. *Acta Pet. Sin.* **2013**, *34*, 386–392.
9. Nešić, S.; Nordsveen, M.; Nyborg, R.; Stangeland, A. A Mechanistic Model for Carbon Dioxide Corrosion of Mild Steel in the Presence of Protective Iron Carbonate Films—Part 2: A Numerical Experiment. *Corrosion* **2003**, *59*, 489–497. [CrossRef]
10. Kiani, K.; Shodja, H.M. Response of reinforced concrete structures to macrocell corrosion of reinforcements. Part I: Before propagation of microcracks via an analytical approach. *Nucl. Eng. Des.* **2011**, *241*, 4874–4892. [CrossRef]
11. Ožbolt, J.; Oršanić, F.; Balabanić, G.; Kušter, M. Modeling damage in concrete caused by corrosion of reinforcement coupled 3D FE model. *Int. J. Fract.* **2012**, *178*, 233–244. [CrossRef]
12. Otieno, M.B.; Beushausen, H.D.; Alexander, M.G. Modelling corrosion propagation in reinforced concrete structures—A critical review. *Cem. Concr. Compos.* **2010**, *33*, 240–245. [CrossRef]
13. Nešić, S.; Lee, K.-L.J. A Mechanistic Model for Carbon Dioxide Corrosion of Mild Steel in the Presence of Protective Iron Carbonate Films—Part 3: Film Growth Model. *Corrosion* **2003**, *59*, 616–628. [CrossRef]
14. Zhang, Z.M.; Luca, G.D.; Archambault, B.; Chavez, J.; Rice, B. Traffic Dataset for Dynamic Routing Algorithm in Traffic Simulation. *J. Artif. Intell. Technol.* **2022**, *2*, 111–122. [CrossRef]
15. Hu, X.; Kuang, Q.; Cai, Q.; Xue, Y.; Zhou, W.; Li, Y. A Coherent Pattern Mining Algorithm Based on All Contiguous Column Bicluster. *J. Artif. Intell. Technol.* **2022**, *2*, 80–92. [CrossRef]
16. Jia, Z.; Wang, W.; Zhang, J.; Li, H. Contact high-temperature strain automatic calibration and precision compensation research. *J. Artif. Intell. Technol.* **2022**, *2*, 69–76.
17. El-Abbasy, M.S.; Senouci, A.; Zayed, T.; Mirahadi, F.; Parvizsedghy, L. Artificial neural network models for predicting condition of offshore oil and gas pipelines. *Autom. Constr.* **2014**, *45*, 50–65. [CrossRef]
18. Du, H.; Du, S.; Li, W. Probabilistic time series forecasting with deep non-linear state space models. *CAAI Trans. Intell. Technol.* **2022**, *8*, 3–13. [CrossRef]
19. Ossai, C.I.; Boswell, B.; Davies, I. Markov chain modelling for time evolution of internal pitting corrosion distribution of oil and gas pipelines. *Eng. Fail. Anal.* **2016**, *60*, 209–228. [CrossRef]
20. Larin, O.; Barkanov, E.; Vodka, O. Prediction of reliability of the corroded pipeline considering the randomness of corrosion damage and its stochastic growth. *Eng. Fail. Anal.* **2016**, *66*, 60–71. [CrossRef]
21. Nordsveen, M.; Nešić, S.; Nyborg, R.; Stangeland, A. A Mechanistic Model for Carbon Dioxide Corrosion of Mild Steel in the Presence of Protective Iron Carbonate Films—Part 1: Theory and Verification. *Corrosion* **2003**, *59*, 443–456. [CrossRef]

22. Nesic, S.; Postlethwaite, J.; Olsen, S. An Electrochemical Model for Prediction of Corrosion of Mild Steel in Aqueous Carbon Dioxide Solutions. *Corrosion* **1996**, *52*, 280–294. [CrossRef]
23. Xu, L.S.; Ling, X.; Ma, J.J.; Ma, H.Q.; Fu, X.H. Prediction on failure pressure of pipeline containing corrosion defects based on DE-BPNN. *J. Saf. Sci. Technol.* **2021**, *17*, 91–96.
24. Kiani, K.; Shodja, H.M. Prediction of the penetrated rust into the microcracks of concrete caused by reinforcement corrosion. *Appl. Math. Model.* **2011**, *35*, 2529–2543. [CrossRef]
25. Kiani, K.; Shodja, H.M. Response of reinforced concrete structures to macrocell corrosion of reinforcements. Part II: After propagation of microcracks via a numerical approach. *Nucl. Eng. Des.* **2012**, *242*, 7–18. [CrossRef]
26. Zhang, S.C.; Lv, Y.H.; Pei, T.G.; Deng, P.; Chen, B.; Fu, Y.K.; Lai, W.J.; Yao, X.Q.; Lin, X.Z. Failure Analysis of Corrosion and Perforation and Life Prediction of Natural Gas Pipeline. *Corros. Prot.* **2020**, *41*, 74–78.
27. Wang, Y.F.; Wang, C.G. Theory and application of response surface method. *J. Minzu Univ. China (Nat. Sci. Ed.)* **2005**, *3*, 236–240.
28. Feng, H.Z.; Xing, X.J.; Yan, W. Research on CO_2 stage corrosion prediction model for offshore oil casing in China. *China Pet. Mach.* **2015**, *43*, 87–92.
29. Chen, J.; Zhao, X.Y.; Cai, L.L.; Zheng, C.; Peng, M. Application of BP neural network in internal corrosion direct assessment methodology for pipelines. *Total Corros. Control* **2023**, *37*, 97–102.
30. Zhao, H.; Ma, L. Several rough set models in quotient space. *CAAI Trans. Intell. Technol.* **2021**, *7*, 69–80. [CrossRef]
31. Chen, J.; Yu, S.; Wei, W.; Ma, Y. Matrix-based method for solving decision domains of neighbourhood multi-granulation decision-theoretic rough sets. *CAAI Trans. Intell. Technol.* **2022**, *7*, 313–327. [CrossRef]
32. Hossein, M.S.; Keivan, K.; Alireza, H. A model for the evolution of concrete deterioration due to reinforcement corrosion. *Math. Comput. Model.* **2010**, *52*, 1403–1422.
33. Alhudhaif, A.; Saeed, A.; Imran, T.; Kamran, M.; Alghamdi, A.S.; Aseeri, A.O.; Alsubai, S. A Particle Swarm Optimization Based Deep Learning Model for Vehicle Classification. *Comput. Syst. Sci. Eng.* **2022**, *40*, 223–235. [CrossRef]
34. Cao, J. *Theory and Method of Emergency Collaborative Decision*, 1st ed.; Science Press: Beijing, China, 2015; pp. 32–88.
35. Hsiao, I.; Chung, C.-Y. AI-Infused Semantic Model to Enrich and Expand Programming Question Generation. *J. Artif. Intell. Technol.* **2022**, *2*, 47–54. [CrossRef]
36. Hua, C. Contrastive study on new and old evaluation standards of SY/T 6151 for corrosion pipeline. *Contemp. Chem. Ind.* **2016**, *45*, 1476–1479.

Disclaimer/Publisher's Note: The statements, opinions and data contained in all publications are solely those of the individual author(s) and contributor(s) and not of MDPI and/or the editor(s). MDPI and/or the editor(s) disclaim responsibility for any injury to people or property resulting from any ideas, methods, instructions or products referred to in the content.

coatings

MDPI

Article

High-Temperature Mechanical Behavior of an As-Extruded Al-5Zn-2Mg-0.3Cu (in wt.%) Alloy

Cuilan Lu [1,2], Daokui Xu [1,2,*], Lan Zhang [1,2], Shuo Wang [1], Xiangbo Xu [1,2] and Dongliang Wang [1,2]

[1] Key Laboratory of Nuclear Materials and Safety Assessment, Institute of Metal Research, Chinese Academy of Sciences, Shenyang 110016, China; cllu21s@imr.ac.cn (C.L.); lz534651520@163.com (L.Z.); wangs1909@foxmail.com (S.W.); xiangbo@zju.edu.cn (X.X.); dlwang19s@imr.ac.cn (D.W.)

[2] School of Materials Science and Engineering, University of Science and Technology of China, Shenyang 110016, China

* Correspondence: dkxu@imr.ac.cn

Abstract: To ensure that Al alloys are being served as the high-temperature structural components for applications in aerospace and transportation, it is necessary to investigate their high-temperature mechanical behavior and failure mechanism. In this paper, the mechanical behavior of the as-extruded Al-5Zn-2Mg-0.3Cu (in wt.%) alloy was studied and compared under different high-temperature tensile-testing conditions. It was found that the yield strength and the ultimate tensile strength of the alloy gradually decreased with the increase in temperature, but its elongation ratio showed a slightly increasing trend. Failure analysis demonstrated that there were a lot of ductile dimples on the fracture surfaces and that obvious necking occurred for the samples being tensile-tested at different temperatures. Surface observation revealed that the initiation of micro-cracks was mainly attributed to the self-cracking of the brittle phase particles. Moreover, when the testing temperature was between 450 °C and 550 °C, micro-cracks could also occur at the interface between phase particles and the Al matrix.

Keywords: aluminum alloy; high temperature; mechanical behavior; failure analysis; micro-crack

1. Introduction

Since aluminum (Al) alloys have many advantages, such as low density, good strong plasticity, corrosion resistance, and good electrical and thermal conductivity, they have a wide application prospect in the fields of rail transit, ship, and aerospace [1–5]. At room temperature, their mechanical properties can well meet the standard of material selection for light-weight and high-strength structural materials [6]. However, with the rapid development of aerospace technology and transportation, the service temperature of Al alloys being the high-temperature structural components in engine blocks, cylinder heads, and engine room components is becoming harsher and harsher [7,8]. For example, the temperature of the Al alloy for its application as a missile shell can reach 400 °C (0.6 T_m) or above during the operation in question [9]. In high-temperature conditions, the mechanical degradation of Al alloys has become a key constraint to their application [10]. Therefore, it is of great significance to develop high-strength and heat-resistant Al alloys for ensuring their service reliability at elevated temperatures.

Compared with other Al alloys, the Al-Zn-Mg-Cu (7xxx) series alloys have a relatively high specific strength, good workability and corrosion resistance, and are often used as part of an aircraft's skin and wing frame [11–13]. In addition, the high-temperature mechanical properties of the 7xxx series Al alloys are good [14–16]. In the research regarding the mechanical behavior of 7015 and 6061 Al alloys at temperatures ranging from room temperature to 500 °C, Oñoro et al. reported that the tensile strength of the 7015 Al alloy was significantly higher than that of the 6061 Al alloy, but that the tensile strength of the 7015 Al alloy at 400 °C was still lower than 100 MPa [14]. Yang et al. reported that

the main softening mechanisms of the 7050 Al alloy at 350 °C/0.01 s^{-1} were dynamic recovery, dynamic precipitation, and coarsening of precipitates, while the main softening mechanisms at 450 °C/10 s^{-1} were dynamic recovery, dynamic recrystallization, and deformation heating [15]. Due to these reasons, the tensile strength of the as-extruded 7075 Al alloy at 550 °C was only 20 MPa [16]. So far, although the mechanical behavior of the 7xxx series Al alloys at elevated temperatures above 400 °C has been investigated, few studies about the effect of temperature on the micro-damage mechanisms at elevated temperatures can be referred.

In this work, through investigating and comparing the mechanical behavior of an as-extruded Al-5Zn-2Mg-0.3Cu (in wt.%) (7N01) Al alloy at the elevated temperature of above 400 °C, the effects of temperature on the mechanical properties and failure mechanisms were disclosed. The study of this topic would significantly deepen the understanding of the relationship between the microstructure and cracking mechanism of Al alloys at elevated temperatures. Moreover, the obtained high-temperature mechanical data can be used for guiding whether the investigated alloy is suitable for application in engine components.

2. Experimental Procedures

2.1. Material and Sample Preparation

The material used in this experiment is a commercial as-extruded 7N01 Al alloy sheet with a thickness of 10 mm and an extrusion ratio of 10:1, which was provided by the CSR Qingdao Sifang Co. Ltd. of Qingdao, China. The concrete chemical composition of the alloy was determined using an inductively coupled plasma spectrometer (ICP-AES) (Agilent, Beijing, China), as listed in Table 1.

Table 1. Chemical composition of the 7N01 Al alloy (in wt.%).

Chemical Composition	Zn	Mg	Cu	Mn	Cr	Ti	Zr	Si	Fe	Al
Content	4.96	1.95	0.28	0.45	0.25	0.08	0.22	0.28	0.35	91.18

The bulk metallographic specimens with a dimension of 10 mm × 10 mm × 3.5 mm were cut from the as-extruded 7N01 Al alloy sheet using a wire, electrical discharge cutting machine. Here, samples with their exposed large surface being perpendicular to the extrusion direction (ED), transverse direction (TD) and normal direction (ND) were defined as ED sample, ND sample and TD sample, respectively. Similarly, the plate-shaped tensile specimens were cut from the sheet along the extrusion direction and their surfaces were parallel to the sheet surface. The shape and dimensions of the tensile specimen are shown in Figure 1. Then, the surfaces of the bulk metallographic specimens and tensile specimens were ground by sequentially using 400, 800, 2000 and 5000 grit papers, followed by mechanical polishing with 2.5 μm and 1.0 μm of diamond grinding paste until no small scratches could be observed on the polished surfaces using an optical microscope (OM, VHX-900F) (Keyence, Osaka, Japan) with a magnification of 500×. After that, the polished surfaces of the metallographic specimens were etched with 16 mL HNO_3 + 1 mL HF + 3 g Cr_2O_3 + 83 mL H_2O.

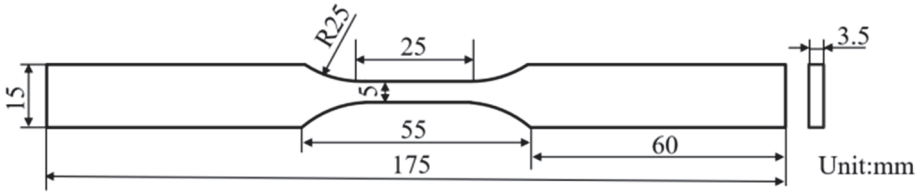


Figure 1. The shape and dimensions of the high-temperature tensile specimen.

2.2. Microstructural Observations

X-ray diffraction (XRD; D/Max 2400) (Rigaku, Tokyo, Japan) with a radiation source of monochromatic Cu-Ka (wavelength of 0.154056 nm), a step length of 0.02°, a scanning

range of 10° to 90°, a scanning rate of 10°/min and an accelerated voltage of 40 kv was employed for analyzing the phase component of the alloy. Based on the MDI Jade 9 software, the diffraction peak was calibrated and the existing phases in the alloy were determined. The etched surfaces of differently orientated samples were observed using an optical microscope (OM, VHX-900F) (Keyence, Osaka, Japan). The size, morphology and distribution of phase particles were observed using a scanning electron microscope (SEM, EM Crafts Cube II) (EmCrafts, Hanam-si, Republic of Korea). Based on the energy dispersive spectrum (EDS, Oxford Xplore Compact 30) (Oxford instruments, Oxford, UK) analysis and elemental scanning, the main chemical components and their distribution of phase particles were determined.

2.3. High-Temperature Tensile Testing

The tensile testing of the as-extruded 7N01 Al alloy at 400 °C, 450 °C, 500 °C and 550 °C were carried out using a tensile testing machine (MTS, 370.10) (Mechanical Testing & Simulation, Eden Prairie, MN, USA) equipped with a high-temperature environmental furnace. The tensile samples were loaded on the test machine with their gauge sections being located in the middle of the environmental furnace. After the temperature had reached the set values, the samples were held at the temperature for 2 h to ensure that they would reach the set temperature. During the heat preservation process, the temperature fluctuation in the high-temperature environmental furnace was ±1 °C. Then, the samples were subjected to high-temperature tensile tests at the tensile rate of 1×10^{-3} s^{-1}. In order to reflect the error range of the high-temperature mechanical properties of samples, three parallel samples were used for each condition.

2.4. Failure Analysis

After the high-temperature tensile testing, the tensile fracture surfaces were washed with alcohol and air-dried. Then, the fracture morphologies of the samples which had failed at 400 °C, 450 °C, 500 °C and 550 °C were observed using SEM. A three-dimensional (3D) metallographic microscope (OM, VHX-900F) (Keyence, Osaka, Japan) was used to observe the 3D morphologies of the tensile fracture surfaces. In order to characterize the plastic deformation and failure mechanisms of the samples that had been tensile-tested at different elevated temperatures the side surfaces with a distance of 2 mm and 5 mm from the fracture surfaces on the basis of their corresponding cross-sectional shrinkage ratios were observed using SEM.

3. Results

3.1. Microstructural Characterization

Figure 2 shows the microstructure of ED, TD and ND oriented samples. It can be seen that the grain structures of the samples with different orientations are equiaxed and the grain sizes are quite uniform. The average grain sizes of the ED, ND and TD samples were determined to be 6.9 μm, 7.5 μm and 7.9 μm, respectively. In comparison, the grain size of the ED sample was slightly smaller than that of the other two samples. Figure 3 is the result of the SEM observations and EDS analysis of the as-extruded 7N01 Al alloy. It can be seen that there are some bright, white, irregular particles with a size of less than 5 μm, in the matrix (Figure 3a). Moreover, these particles are aggregated and preferentially distributed along the extrusion direction. The EDS spectrum and elemental scanning reveal that the main components of these particles are Al, Fe, Mn and Si (Figure 3b,c). The XRD phase analysis of the as-extruded 7N01 Al alloy is shown in Figure 4. It can be seen that the alloy is mainly composed of an α-$Al_{15}(MnFe)_3Si_2$ phase and the Al matrix, because the low solubility of the Fe and Mn elements can easily cause the formation of the α-$Al_{15}(MnFe)_3Si_2$ phase [17].

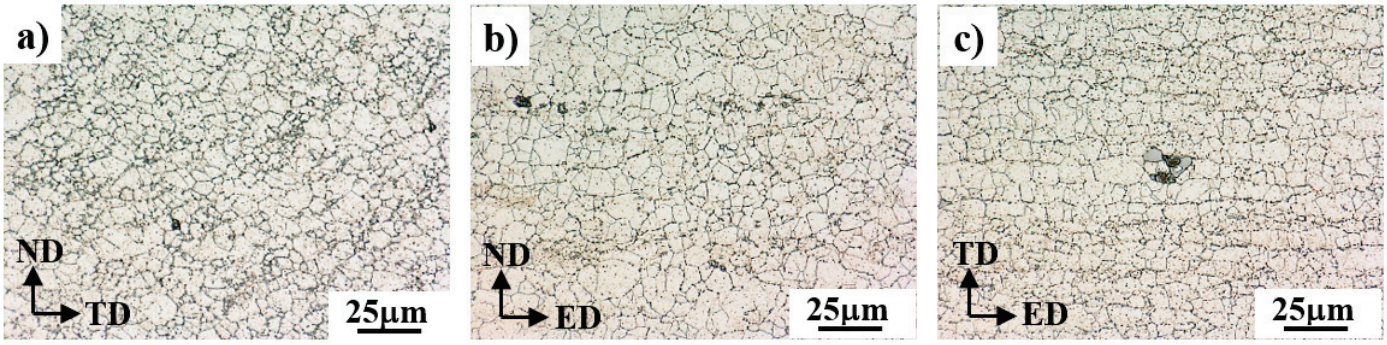


Figure 2. Microstructure observation of the as-extruded 7N01 Al alloy: (**a**) ED sample, (**b**) TD sample and (**c**) ND sample.

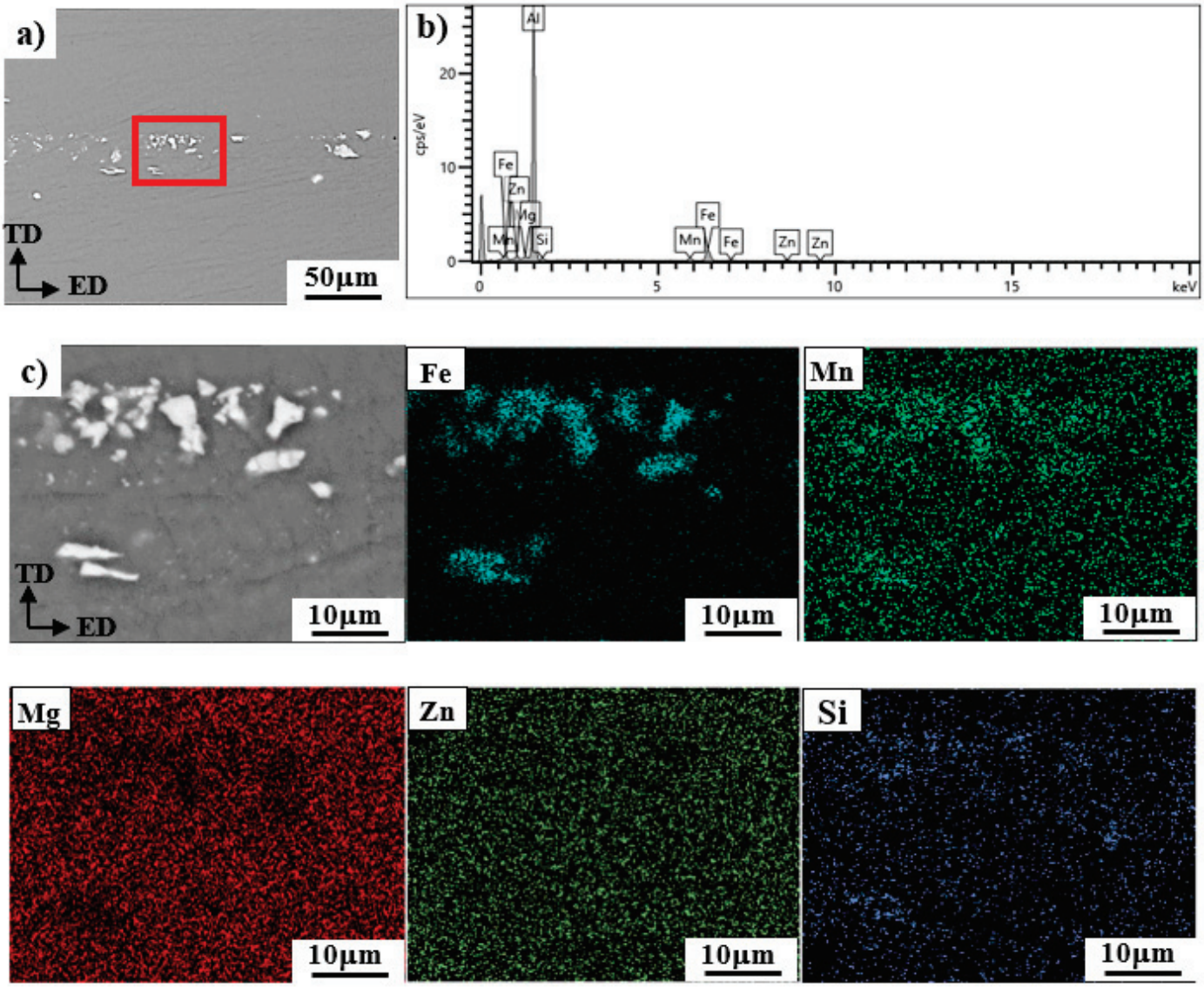


Figure 3. SEM observations and EDS analysis of the as-extruded 7N01 Al alloy: (**a**) distribution of phase particles, (**b**) EDS result of phase particles, and (**c**) EDS scanning and elemental distribution of the squared region in image (**b**).

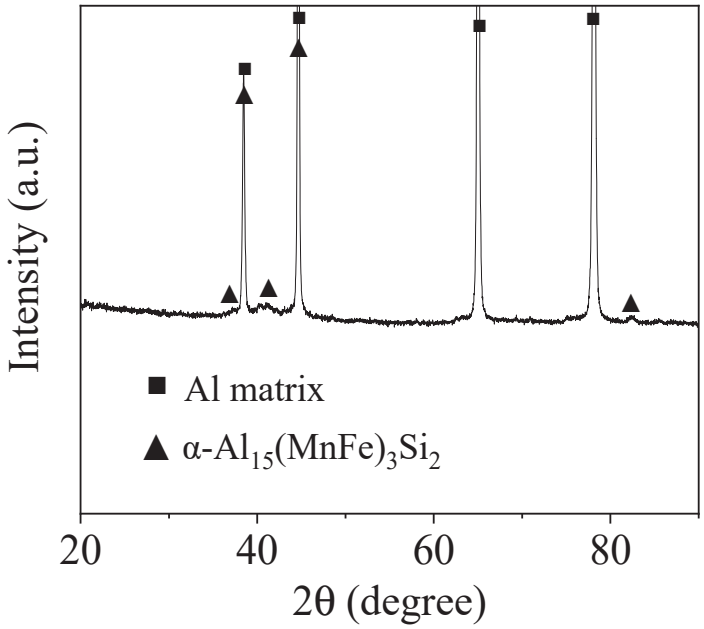


Figure 4. XRD phase analysis of the as-extruded 7N01 Al alloy.

3.2. Mechanical Properties at Elevated Temperatures

Figure 5 shows the high-temperature tensile-stress–strain curves of the as-extruded 7N01 Al alloy at temperatures of 400 °C, 450 °C, 500 °C and 550 °C. In order to describe and compare their mechanical properties at different elevated temperatures, the yield strength ($\sigma_{0.2}$), ultimate tensile strength (UTS) and elongation ratio (ε_f) are determined, as listed in Table 2. It can be seen that the $\sigma_{0.2}$ and UTS values of the alloy decrease with the increase in testing temperature, but the alloy's plasticity changes slightly at different temperatures. At the temperatures of 400 °C, 450 °C, 500 °C and 550 °C, the $\sigma_{0.2}$ values of the alloy are, respectively, 269 MPa, 260 MPa, 256 MPa and 255 MPa; the UTS values are, respectively, 308 MPa, 286 MPa, 276 MPa and 273 MPa and the ε_f values are, respectively 18%, 21%, 20% and 23%. It is demonstrated that the alloy has good high-temperature mechanical strength because its yield strength can be higher than 250 MPa at an elevated temperature ranging from 400 °C to 550 °C.

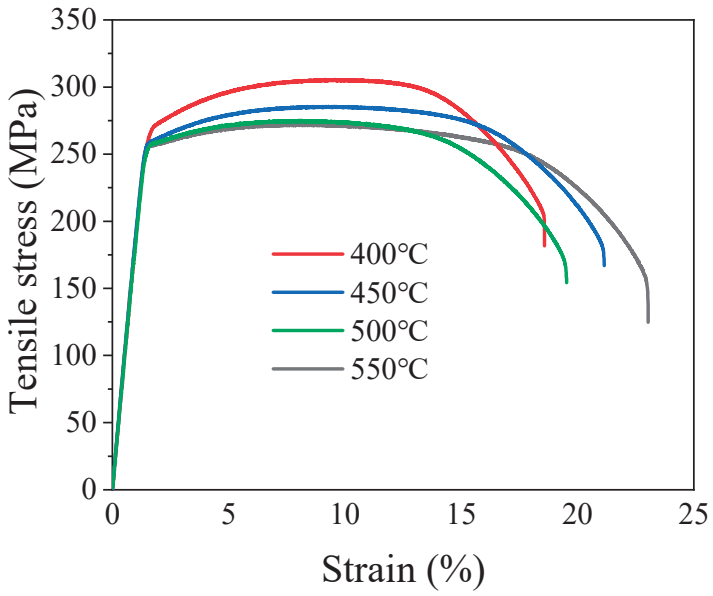


Figure 5. High-temperature tensile-stress–strain curve of the as-extruded 7N01 Al alloy.

Table 2. Yield strength, tensile strength and elongation ratio of the as-extruded 7N01 Al alloy.

Testing Temperature	$\sigma_{0.2}$/MPa	UTS/MPa	ε_f/%
400 °C	269 ± 6	308 ± 2	18 ± 1
450 °C	260 ± 1	286 ± 1	21 ± 1
500 °C	256 ± 1	276 ± 1	20 ± 1
550 °C	255 ± 2	273 ± 2	23 ± 1

3.3. Fracture Mechanism

Figure 6 shows the tensile fracture morphologies of the as-extruded 7N01 Al alloy tested at 400 °C, 450 °C, 500 °C and 550 °C. It can be seen that the tensile samples at different temperatures show the obvious necking phenomenon and that their fracture surfaces are distributed with a large number of plastic dimples, indicating their typical ductile fracture characteristics. Meanwhile, the size of plastic dimples on the fracture surfaces increases with the testing temperature. In addition, phase particles can be observed at the bottom of the dimples. Figure 7 shows the optical observations of the fracture surfaces and the three-dimensional morphologies of the alloy at different temperatures. It can be seen that the maximum height-difference values caused by the plastic dimples on the fracture surfaces of samples tensile-tested at 400 °C, 450 °C, 500 °C and 550 °C are 214.76 μm, 281.83 μm, 256.78 μm and 347.68 μm, respectively. Generally, the size and depth of plastic dimples can reflect the plastic-deformation capability of metallic materials, in which larger and deeper plastic dimples correspond to a better plasticity [15]. In contrast, for the sample being tensile-tested at 400 °C, the plastic dimples on its fracture surface have the smallest size and the shallowest depth, resulting in the lowest elongation ratio. For the sample being tensile-tested at 550 °C, the largest size and the deepest plastic dimples on the fracture surface ensure the highest elongation ratio.

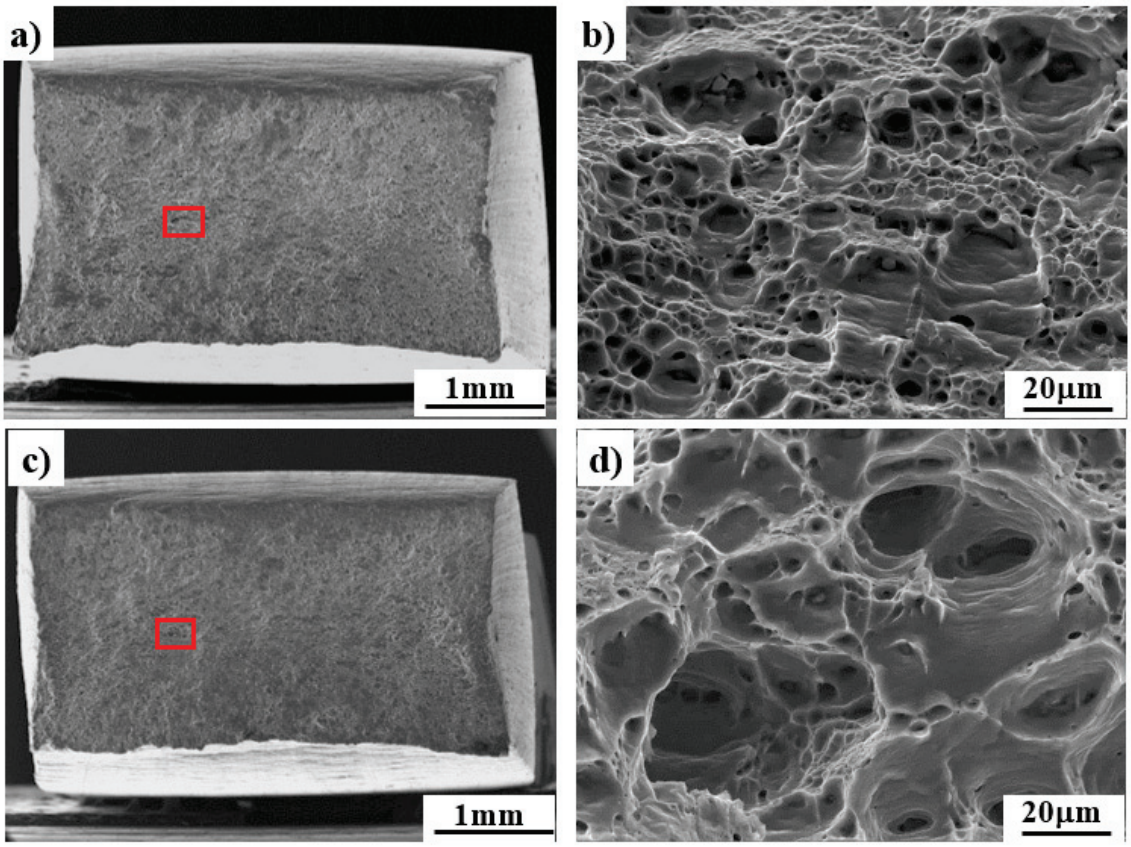


Figure 6. *Cont.*

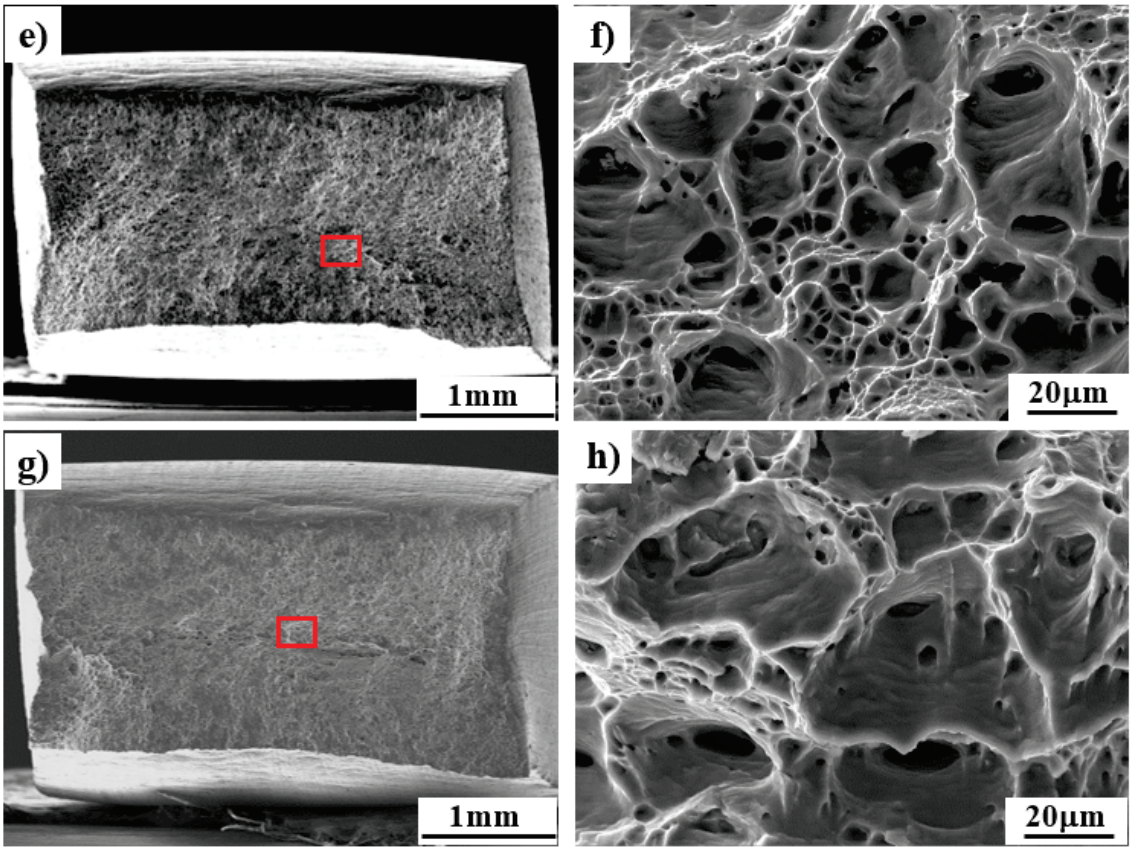


Figure 6. Low- and high-magnification SEM observations of the tensile fracture surfaces of the as-extruded 7N01 Al alloy tensile-tested at the following temperatures: (**a**,**b**) 400 °C, (**c**,**d**) 450 °C, (**e**,**f**) 500 °C, (**g**,**h**) 550 °C. The locations of the images (**b**,**d**,**f**,**h**) are squared in the images (**a**,**c**,**e**,**g**), respectively.

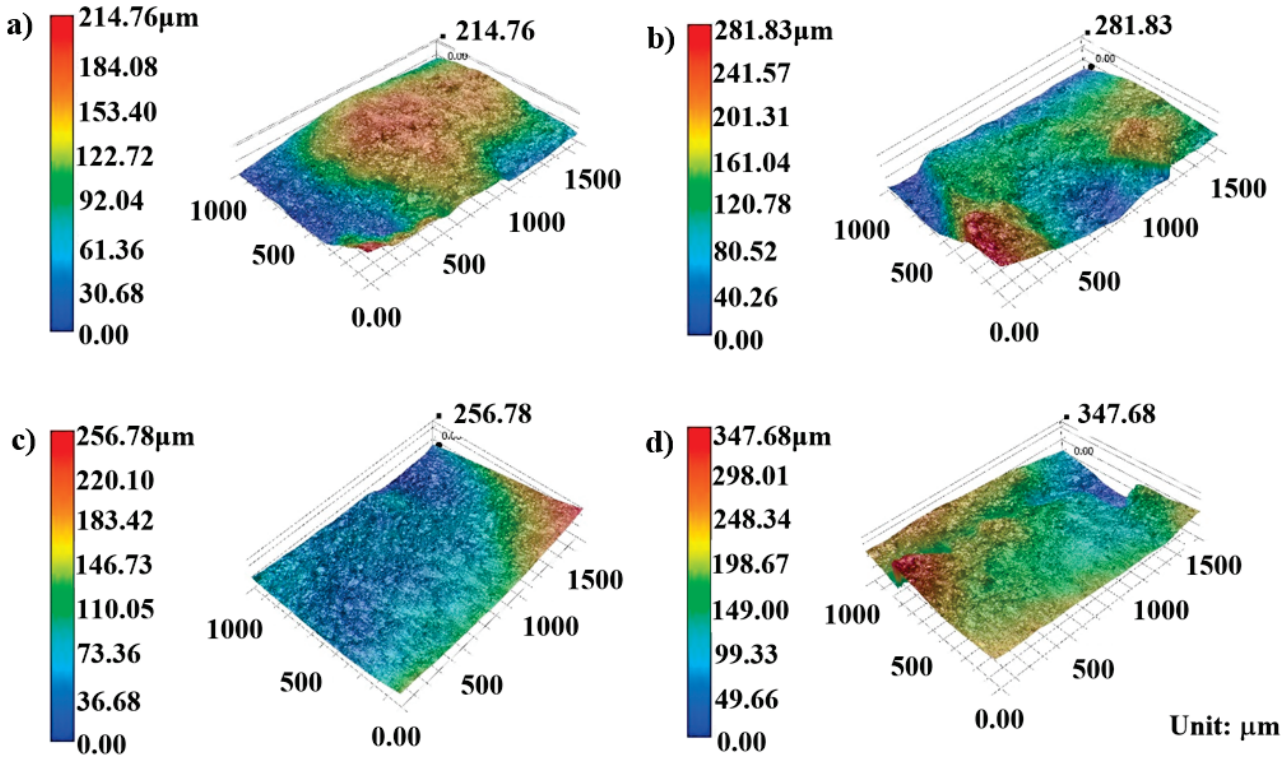


Figure 7. Three-dimensional morphologies of the as-extruded 7N01 Al alloy tensile-tested at the following high-temperatures: (**a**) 400 °C, (**b**) 450 °C, (**c**) 500 °C, (**d**) 550 °C.

In order to disclose the micro-damage mechanism of the alloy at different temperatures, the side surfaces 2 mm and 5 mm away from the fractures were observed using SEM, as shown in Figure 8. It can be seen that, for the tensile samples tested at different temperatures, slip traces are not obvious and the plastic deformation is weak in the area 5 mm away from the fractures and their corresponding cross-sectional shrinkage ratios of 7%~8%. However, micro-cracks can be observed in this area and their initiation is mainly due to the self-cracking of coarse phase particles. For the area 2 mm away from the fracture surfaces, the cross-sectional shrinkage ratios of the corresponding sections of tensile samples are 36%~38%. In this area, a large number of slip traces can be observed, indicating that severe plastic deformation occurs. In addition, the initiated micro-cracks are mainly located in the interior of the phase particles. However, when the testing temperature is between 450 °C and 550 °C, micro-cracks can also occur at the interface between the phase particles and the Al matrix.

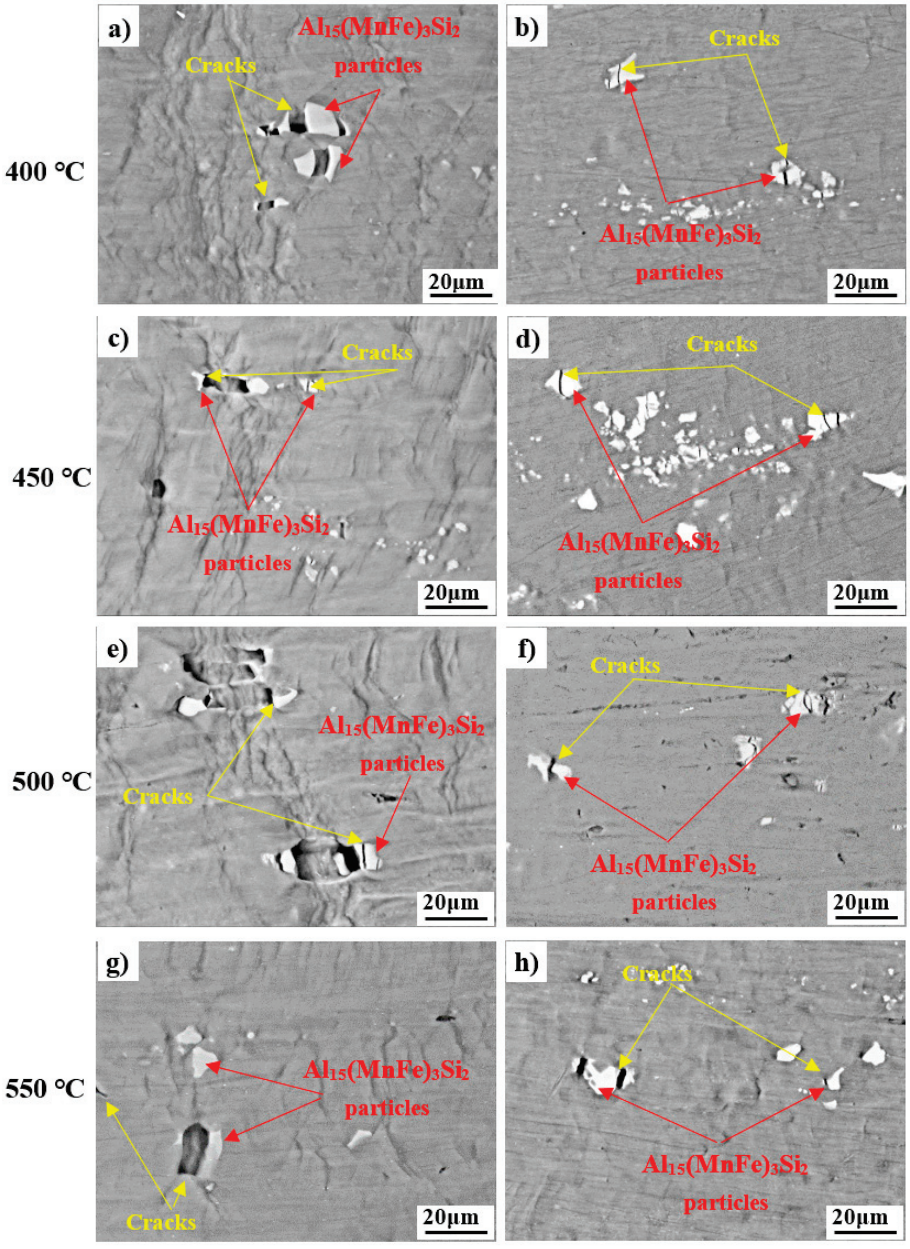


Figure 8. Backscattered scanning electron (BSE) observations to the surface areas with a distance of 2 mm and 5 mm from the tensile fractures after being tensile-tested at the following temperatures: (**a**,**b**) 400 °C, (**c**,**d**) 450 °C, (**e**,**f**) 500 °C, (**g**,**h**) 550 °C, respectively.

4. Discussion

4.1. Effect of Temperature on the High-Temperature Mechanical Properties

Based on the measured mechanical properties at high temperatures, it can be seen that the mechanical strength of the 7N01 Al alloy decreases with the increase in temperature. It has been reported that the main strengthening mechanisms of the 7xxx series Al alloys were the dislocation strengthening and the second-phase strengthening [11,18]. Among these, the second-phase strengthening mechanism includes the cut-through mechanism and the Orowan mechanism [19]. When the size of the second-phase particles exceeds 3 nm, the main strengthening mechanism of the alloy will change from the cut-through mechanism to the Orowan bypass mechanism [11,19]. In this work, the size of the phase particles in the 7N01 Al alloy is about 5 μm, much larger than 3 nm. Therefore, the strengthening mechanism should be mainly ascribed to the Orowan bypassing mechanism. However, with the temperature increasing, the enhancement degree due to the Orowan bypassing mechanism gradually weakens [11]. In addition, although the phase particles can effectively pin the dislocation movement and play an important role in strengthening the alloy [18,19], their pinning effect on the dislocation movement and grain boundaries sliding is remarkably degraded at elevated temperatures [18]. Therefore, the high-temperature yield strength and ultimate tensile strength of the as-extruded 7N01 Al alloy exhibit a decreasing trend with the increase in temperature.

4.2. Effect of Temperature on the Failure Mechanisms

In general, casting defects and brittle phases in Al alloys can easily cause stress concentration and subsequently induce crack initiation and propagation at elevated temperatures, which could remarkably reduce their high-temperature mechanical properties [20–22]. In the investigation about the mechanical behavior of the die-cast Al–10Si–Mn–Mg alloy at high temperatures, Ahna et al. reported that the initiation of micro-cracks was mainly attributed to the self-cracking of brittle Si-containing phase particles during the tensile-testing process [23]. Similarly, Han et al. studied the mechanical behavior of the TiB_2/Al-Si composite at high temperatures and found that the fracture mechanism was mainly ascribed to the breaking of the silicon particles and the debonding of the TiB_2 particle–matrix [24]. For the as-extruded 7N01 Al alloy investigated in this study, the phase particles formed are mainly α-$Al_{15}(MnFe)_3Si_2$, also existing in other Al–Zn–Mg alloys [25]. Qian et al. reported that, when the amount of Mn was higher than 0.4 wt.% in the Al–Si alloys, the formed α-$Al_{15}(MnFe)_3Si_2$ phase could effectively pin the grain boundary sliding and then induce the enhancement of the high-temperature tensile strength of the alloys [26]. It has been reported that the addition of Mn in Al–Si alloys with lower Fe content can cause the transformation of the brittle β-Al_5SiFe phase into the plastic α-$Al_{15}(MnFe)_3Si_2$ phase [26,27]. However, compared with the Al matrix, the α-$Al_{15}(MnFe)_3Si_2$ phase is still brittle and highly susceptible to fragmentation during the extrusion, resulting in the zonal aggregation and preferential distribution of broken α-$Al_{15}(MnFe)_3Si_2$ phase particles along the extrusion direction (Figure 3a). Therefore, the stress concentration in the α-$Al_{15}(MnFe)_3Si_2$ phase particles leads to their preferential cracking in order to coordinate the plastic deformation of the Al matrix during the high-temperature tensile process. In addition, in the investigation of the mechanical behavior of the Ti-2Al-Nb-based alloys at elevated temperatures, Wu et al. reported that the interfacial bonding strength of the interfaces between the high-strength TiB-reinforced phase and the matrix decreases with increasing temperature [28]. Therefore, for the tensile samples tested at temperatures above 400 °C, besides the self-cracking of the α-$Al_{15}(MnFe)_3Si_2$ phase particles, the initiation of microcracks can be observed at the interface between the α-$Al_{15}(MnFe)_3Si_2$ phase particles and the Al matrix in the area 2 mm away from the fracture surfaces. However, for the area 5 mm away from the fracture surfaces, the cross-sectional shrinkage ratio is only 7%~8% and the occurred plastic deformation is quite small. Thus, the incompatible plastic deformation at the interface between the α-$Al_{15}(MnFe)_3Si_2$ phase particles and the Al matrix is weak and can hardly cause the interfacial cracking. Then, only the self-cracking

of the α-$Al_{15}(MnFe)_3Si_2$ phase particles can be observed far from the fracture surfaces. On the basis of the results of this work, it seems that controlling the size and quantity of phase particles should effectively enhance the high-temperature mechanical properties of Al alloys.

5. Conclusions

Through investigating and comparing the mechanical behavior and micro failure mechanisms of the as-extruded 7N01 Al alloy at high temperatures, the main conclusions are as follows:

(1) The as-extruded 7N01 Al alloy is mainly composed of α-$Al_{15}(MnFe)_3Si_2$ particles and Al matrix; its yield strength and ultimate tensile strength decrease with the increase in temperature, but its elongation ratio changes slightly.
(2) For the samples being tensile-tested at different temperatures, a lot of ductile dimples on the fracture surfaces and obvious necking can be observed.
(3) The initiation of micro-cracks is mainly attributed to the self-cracking of the α-$Al_{15}(MnFe)_3Si_2$ particles and the interfacial cracking at the interface between the phase particles and the Al matrix.

Author Contributions: Conceptualization, D.X.; Methodology, C.L., X.X. and D.W.; Software, S.W.; Validation, X.X.; Formal analysis, D.W.; Investigation, C.L., L.Z. and S.W.; Data curation, L.Z.; Writing—original draft, C.L.; Writing—review & editing, D.X.; Project administration, D.X. All authors have read and agreed to the published version of the manuscript.

Funding: This research was funded by the National Natural Science Foundation of China Projects under Grants (Nos. 52071220, U21A2049, 51871211, 51701129, and 51971054), the China Postdoctoral Science Foundation (No. 2023M733572), the Liaoning Province's project of "Revitalizing Liaoning Talents" (No. XLYC1907062), the Doctor Startup Fund of Natural Science Foundation Program of the Liaoning Province (No. 2019-BS-200), the high-level achievement construction project of Shenyang Ligong University (No. SYLUXM202105), the Liaoning BaiQianWan Talents Program, the Domain Foundation of Equipment Advance Research of 13th Five-year Plan (No. 61409220118), the National Key Research and Development Program of China under Grants (Nos. 2017YFB0702001 and 2016YFB0301105), the Innovation Fund of the Institute of Metal Research (IMR), the Chinese Academy of Sciences (CAS), the National Basic Research Program of China (973 Program)'s project under Grant (No. 2013CB632205), the Fundamental Research Fund for the Central Universities under Grant (No. N2009006), and the Bintech-IMR R&D Program (No. GYY-JSBU-2022-009).

Institutional Review Board Statement: Not applicable.

Informed Consent Statement: Not applicable.

Data Availability Statement: Not applicable.

Conflicts of Interest: The authors declare no conflict of interest.

References

1. Han, W.H.; Li, Y.; Li, P.; Su, G.P.; Zhang, C.Z.; Sun, C.F.; Chen, C.G.; Yang, F.; Guo, Z.M. Microstructure and Mechanical Properties at Elevated Temperature of Powder Metallurgy Al-Zn-Mg-Cu Alloy Subjected to Hot Extrusion. *Metals* **2022**, *12*, 259. [CrossRef]
2. Vijayakumar, M.D.; Dhinakaran, V.; Sathish, T.; Muthu, G.; Ram, P.M.B. Experimental study of chemical composition of aluminium alloys. *Mater. Today* **2021**, *37*, 1790–1793. [CrossRef]
3. Zhao, P.H.; Wu, X.L.; Liu, Y.; Gao, K.Y.; Wen, S.P.; Wei, W.; Rong, L.; Huang, H.; Wu, H.; Zhou, D.J.; et al. Microstructure, mechanical properties and corrosion behavior of commercial 7N01 alloys. *Trans. Nonferrous Met. Soc. China* **2022**, *32*, 778–789. [CrossRef]
4. Rahimi, S.; Khiabani, A.B.; Yarmand, B.; Kolahi, A. Comparison of corrosion and antibacterial properties of Al alloy treated by plasma electrolytic oxidation and anodizing methods. *Mater. Today* **2018**, *5*, 15667–15676. [CrossRef]
5. Ura-Binczyk, E. Improvement of pitting-corrosion resistance of Ultrafine-Grained 7475 Al alloy by aging. *Materials* **2022**, *15*, 360. [CrossRef]
6. Anyasodor, G.; Koroschetz, C. Industrial based volume manufacturing of lightweight aluminium alloy panel components with high-strength and complex-shape for car body and chassis structures. *J. Phys. Conf. Ser.* **2017**, *896*, 012093. [CrossRef]

7. Czerwinski, F. A search for the eutectic system of high-temperature cast aluminium alloys. *Mater. Sci. Technol.* **2021**, *37*, 683–692. [CrossRef]
8. Yang, H.N.; Duan, X.N.; Wang, G.Q.; Gao, S.P.; Xiao, Z. Microstructure and mechanical properties of Al-18Si-10Cu-10Ni-5Mn(-5Mg) heat-resistant aluminium alloys prepared by laser-directed energy deposition. *Mater. Sci. Eng. A* **2023**, *883*, 145512. [CrossRef]
9. Belov, N.A.; Akopyan, T.K.; Korotkova, N.O.; Shurkin, P.K.; Timofeev, V.N.; Raznitsyn, O.A.; Sviridova, T.A. Structure and heat resistance of high strength Al-3.3%Cu-2.5%Mn-0.5%Zr (wt%) conductive wire alloy manufactured by electromagnetic casting. *J. Alloys Compd.* **2021**, *891*, 161948. [CrossRef]
10. Chakraborty, P.; Singha, M.K.; Tiwari, V. Dynamic tensile and compressive behaviour of AA7475-T7351 alloy under different strain rates and temperatures. *Structures* **2022**, *46*, 49–63. [CrossRef]
11. Dai, P.; Luo, X.; Yang, Y.Q.; Kou, Z.D.; Huang, B.; Zang, J.X.; Ru, J.G. High temperature tensile properties, fracture behaviors and nanoscale precipitate variation of an Al-Zn-Mg-Cu alloy. *Prog. Nat. Sci.* **2020**, *30*, 63–73. [CrossRef]
12. Paulisch, M.C.; Treff, A.; Driehorst, I.; Reimers, W. The influence of natural aging and repeated solution annealing on microstructure and mechanical properties of hot extruded alloys Al 7020 and Al 7175. *Mater. Sci. Eng. A* **2018**, *709*, 203–213. [CrossRef]
13. Leon, S.J.; Bharathiraja, G.; Jayakumar, V. A review on friction stir welding in Aluminium alloys. *IOP Conf. Ser. Mater. Sci. Eng.* **2020**, *954*, 012007. [CrossRef]
14. Onoro, J. High-temperature mechanical properties of aluminium alloys reinforced with titanium diboride (TiB_2) particles. *Rare Metals* **2011**, *30*, 200–205. [CrossRef]
15. Yang, Q.Y.; Liu, X.Y.; Liu, Y.X.; Fan, X.Z.; Shu, M. The flow softening behavior and deformation mechanism of AA7050 aluminum alloy. *Mater. Trans.* **2019**, *60*, 2041–2047. [CrossRef]
16. Chen, G.; Jiang, J.F.; Du, Z.M.; Han, F.; Atkinson, H.V. Hot tensile behavior of an extruded Al-Zn-Mg-Cu alloy in the solid and in the semi-solid state. *Mater. Des.* **2014**, *54*, 1–5. [CrossRef]
17. Liu, B.; Ma, C.C.; Li, L.; Yang, C.H.; Yu, N.; Wang, W.M.; Gao, T. Morphologies and compositions of α-$Al_{15}Fe_3Si_2$-Type intermetallics in Al-Si-Fe-Mn-Cr alloys. *Int. J. Met.* **2023**, *17*, 1156–1164. [CrossRef]
18. Huo, W.T.; Hou, L.G.; Zhang, Y.S.; Zhang, J.S. Warm formability and post-forming microstructure/property of high-strength AA7075-T6 Al alloy. *Mater. Sci. Eng. A* **2016**, *675*, 44–54. [CrossRef]
19. Jin, W.M.; Yu, J.H.; Zhang, Z.Q.; Jia, H.J.; Ren, M.W. Study on Ultra-High Temperature Contact Solution Treatment of Al-Zn-Mg-Cu Alloys. *Metals* **2021**, *11*, 842. [CrossRef]
20. Jaglinski, T.; Lakes, R. Creep behavior of Al-Si die-cast alloys. *J. Eng. Mater. Technol.* **2004**, *126*, 378–383. [CrossRef]
21. Zhang, B.; Cockcroft, S.L.; Maijer, D.M.; Zhu, J.D.; Phillion, A.B. Casting defects in low-pressure die-cast aluminum alloy wheels. *JOM* **2005**, *57*, 36–43. [CrossRef]
22. Avalle, M.; Belingardi, G.; Cavatorta, M.P.; Doglione, R. Casting defects and fatigue strength of a die cast aluminium alloy: A comparison between standard specimens and production cpmponents. *Int. J. Fatigue* **2002**, *24*, 1–9. [CrossRef]
23. Ahn, C.; Jo, I.; Ji, C.; Cho, S.; Mishra, B.; Lee, E. Creep behavior of high-pressure die-cast AlSi10MnMg aluminum alloy. *Mater. Charact.* **2020**, *167*, 110495. [CrossRef]
24. Han, G.; Zhang, W.Z.; Zhang, G.H.; Peng, Z.J.; Wang, Y.J. High-temperature mechanical properties and fracture mechanisms of Al-Si piston alloy reinforced with in situ TiB2 particles. *Mater. Sci. Eng. A* **2015**, *633*, 161–168. [CrossRef]
25. Li, S.; Dong, H.G.; Li, P.; Chen, S. Effect of repetitious non-isothermal heat treatment on corrosion behavior of Al-Zn-Mg alloy. *Corros. Sci.* **2018**, *131*, 278–289. [CrossRef]
26. Qian, Z.; Liu, X.F.; Zhao, D.G.; Zhang, G.H. Effects of trace Mn addition on the elevated temperature tensile strength and microstructure of a low-iron Al-Si piston alloy. *Mater. Lett.* **2008**, *62*, 2146–2149. [CrossRef]
27. Narayanan, L.A.; Samuel, F.; Gruzleski, J.E. Crystallization behavior of iron-containing intermetallic compounds in 319 aluminum alloy. *Metall. Mater. Trans. A* **1994**, *25*, 1761–1773. [CrossRef]
28. Wu, T.F.; Fan, R.L.; Wu, Y.; Wu, D.P.; Yang, J.L.; Chen, M.H. Microstructure, densification and mechanical properties of in situ TiBw/Ti_2AlNb composites fabricated by spark plasma sintering. *J. Mater. Sci.* **2023**, *58*, 8359–8378. [CrossRef]

Disclaimer/Publisher's Note: The statements, opinions and data contained in all publications are solely those of the individual author(s) and contributor(s) and not of MDPI and/or the editor(s). MDPI and/or the editor(s) disclaim responsibility for any injury to people or property resulting from any ideas, methods, instructions or products referred to in the content.

applied sciences

MDPI

Communication

The Number of Ethylene Oxide Groups of Sulphate-Based Surfactants Influences the Cytotoxicity of Mixed Micelles to an Amphibian Cell Line

Sebastian Topliceanu [1,2], Monica Almeida [3], Miguel Oliveira [3], Dan Cogălniceanu [1] and Isabel Lopes [3,*]

[1] Faculty of Natural and Agricultural Sciences, Ovidius University Constanţa, 1 Universităţii Street, 900470 Constanţa, Romania; topliceanu.sebastian@gmail.com (S.T.); dan_cogalniceanu@yahoo.com (D.C.)
[2] Centre for Research and Development of the Morphological and Genetic Studies of Malignant Pathology, Ovidius University Constanţa, 145 Tomis Blvd., 900591 Constanţa, Romania
[3] Centre for Environmental and Marine Studies (CESAM), Department of Biology, University of Aveiro, 3810-193 Aveiro, Portugal; monica.alm@ua.pt (M.A.); migueloliveira@ua.pt (M.O.)
* Correspondence: ilopes@ua.pt

Abstract: Sodium lauryl ether sulphate (SLEnS) is an anionic surfactant that is widely used in many fields, such as cosmetics and detergents, among others. This study evaluated the influence of the number of ethylene oxide (EO) units, present in the head group of SLEnS, on its cytotoxicity to the A6 cell line of *Xenopus laevis* using MTT and resazurin assays. The A6 cell line was exposed for 48 h to six SLE_nS variants: SLE_0S, SLE_1S, SLE_4S, $SLE_{11}S$, $SLE_{30}S$, and $SLE_{50}S$ (subscript values correspond to the number of EO units). Overall, the six variants impaired the A6 cells' viability at low concentrations for the MTT assay, with the median lethal concentrations ($LC_{50,48h}$) ranging between 0.398 and 0.554 mg/L and for the resazurin assay between 0.557 and 0.969 mg/L. Further, the obtained results indicate SLE_nS variants with fewer EO units to be the most cytotoxic in the resazurin assay; although a similar cytotoxicity pattern was observed with the MTT assay, a significant association between the number of EO units and the values of LC_{50} was not found. This result highlights the usefulness of in vitro assays with A6 cell lines as a first screening tool for assessing the structure–toxicity relationship of this type of surfactant, also providing a baseline for the development of environmentally friendlier chemical compounds while still maintaining their efficiency.

Keywords: in vitro assay; *Xenopus laevis*; cell viability; sodium lauryl ether sulphate; structure–toxicity assessment; A6 cell line

1. Introduction

Sodium lauryl ether sulphates (SLE_nS) consist of anionic surfactants that are used worldwide in pharmaceutical and cosmetic products, cleaning products and detergents [1,2], pesticides [3], and land excavation processes [4], among others. Given the wide use of these surfactants, their occurrence in the environment is expected. Whereas information on the concentrations of $SLE_{n>1}S$ in the aquatic environment is scarce, concentrations of sodium lauryl sulphate (SL_0S) ranging from 0.018 to 5.94 mg/L have been measured in urban effluents, agriculture, and industrial sewages [5,6], and concentrations from 40 to 500 mg/kg were measured in soil near excavation industries [4]. The presence of SLE_nS in these abiotic components raises environmental concerns since it can have adverse effects on the environment, with concentrations ranging from 0.004 to 3509 mg/L known to cause toxicity to biota, namely, aquatic species [7,8]. This reported toxicity has been proven to be dependent on many biological (e.g., species sensitivity) and physicochemical (e.g., water hardness, temperature) factors [9,10]. Specifically, the chemical structure of SLE_nS, as it regards the degree of ethyl oxidation (i.e., number of ethylene oxide groups on its headgroup), has been shown by Martins et al. [1] to change its toxicity, when present in

mixed micelles, to the marine bacterium *Vibrio fischeri*. The study showed that the bioluminescence of *V. fischeri* was less affected by micelles containing SLE_nS variants with a higher number of EO units. Also, Wong et al. [11] reported that a fewer number of EO units in nine alcohol ethoxylate surfactants led to increased acute toxicity to the zooplankton species *Daphnia magna* and the fish *Pimephales promelas*. Despite these two examples, few studies addressing the influence of the structure of SLE_nS on its toxicity to aquatic biota have been published. But understanding the structure–toxicity relationship of these types of polymers is of the most relevance to make predictions of their toxicity when conducting risk assessments using frameworks and supporting the design of more ecofriendly structures. With this type of study, when targeting the characterization of the effects on freshwater vertebrates, ethical issues arise related to the welfare and protection of animals used in scientific procedures, as regulated by the European Directive for animal protection (Directive 2010/63/EU). In this context, in vitro toxicity assays have been proposed as a good first screening alternative to the use of in vivo assays, thus minimizing the use of animal experimentation. Further, in vitro testing is considered a high-throughput, fast, and cheap methodology [12], allowing for the testing of a wider range of substances simultaneously at a higher number of concentrations, characteristics that are a major advantage when performing screenings of the influence of the structure–toxicity relationships of chemicals. The effect of surfactants on cells involves destabilizing the cell membrane through flip-flop movements, leading to phospholipid hydrolysis, protein denaturation, and membrane leakage [13,14]. This in vitro approach was used in the present work to predict the effects of SLE_nS variants on amphibian cell lines. Among the four classes of vertebrates, Amphibia is considered the most threatened, with 41% of extant species classified as threatened with extinction [15]. Chemical pollution has been pointed out as being amongst the most relevant factors contributing to this conservation status of amphibians, namely, because these organisms have highly permeable skin and a rudimentary immune system [16]. Nevertheless, amphibians typically have aquatic early life stages, which make them high-risk targets for exposure to surfactant contamination, since water is considered the ultimate fate of most surfactants [17]. Therefore, studying the potential risks that different surfactants pose to this group of organisms is highly relevant. The present study assessed the influence of the number of EO units present in the polar head group of SLE_nS on the cytotoxicity of mixed micelles, which is formed with alkylbenzene sulfonic acid, to the A6 cell line, which was derived from a male *Xenopus laevis*. This in vitro methodology was used as a preliminary and high-throughput approach to infer the possible impacts that these surfactants may have on amphibians, as recommended by several legislative guidelines regarding animal experimentation (e.g., EU Directive 63/2010). This cell line, A6, is one of the most used models for in vitro studies regarding amphibians and is responsive to several toxins (e.g., cadmium) [18,19] and mitogens (e.g., flavonoids) [20]. In addition, since the tissue of origin is the kidney, all processes concerning membrane dynamics are well studied [21,22], making this model suitable for this study.

2. Materials and Methods

2.1. Test Substance

The cytotoxicity of six variants of mixed micelles made of two anionic surfactants (sodium lauryl ether sulfate (SLE_nS) and alkyl benzene sulfonate (LAS)) was tested (Figure 1). A mixture of these two anionic surfactants was selected because it has been shown that together they self-assemble at a lower critical micelle concentration compared to when they are found alone, thus requiring a lower concentration of the surfactants, which leads to a higher viscosity of the final mixture, decreasing skin irritability (e.g., [23]). These micelles were obtained according to Martins et al. [1]. In brief, SLE_nS and LAS were mixed in distilled water using a ratio of 1:2 with 3300 mg/L of SLE_nS and 6600 mg/L of LAS. While LAS was kept constant in each micelle variant, SLE_nS varied in the number of ethylene oxide units. Micelles with six types of SLE_nS were produced: SLE_0S, SLE_1S, SLE_4S, $SLE_{11}S$, $SLE_{30}S$, and $SLE_{50}S$, where the subscript number corresponds to the number of EO units.

Since all of these types of SLE_nS were added to the exact same concentration of LAS, the differences in the observed cytotoxicity can be assumed to be a function of SLE_nS, and all of tested concentrations are presented in mg/L of SLE_nS. Therefore, SLE_nS notation is used to refer to the six variants of mixed micelles tested in this work. The company Greendet Lda. (Coimbra, Portugal) provided the surfactant LAS, while SLE_nS were acquired from BASF SE (BASF GmbH, Dusseldorf, Germany).

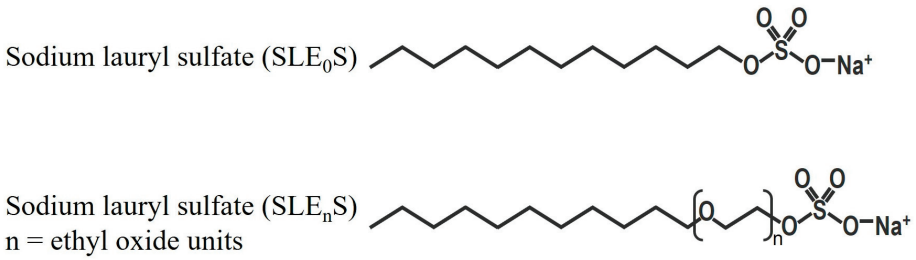


Figure 1. Chemical structure of sodium lauryl ether sulphate (SLE_nS) with and without ethylene oxide units.

2.2. Biological Model

The cell line used in this study was the A6 epithelial cell line (ECACC 89072613), which was isolated from the kidney of an adult male *Xenopus laevis* [24]. This cell type was selected to perform this study because it is an easy-to-culture cell line, and it is extensively used to study the impact of chemicals on amphibians (e.g., [18]). Furthermore, some of the processes involved in membrane dynamics (which may be altered by the chemicals tested in this study) with this cell line, especially concerning the opening of sodium and calcium channels, are already known. This cell line was kindly provided by Professor Peter Lorenz from the University of Rostock (Rostock, Germany). Cells were grown in 55% Leibovitz (L-15) culture medium (Biowest, Nuaillé, France), diluted with 35% ultrapure water, and supplemented with 10% fetal bovine serum (Capricorn, Düsseldorf, Germany), 100 U/mL penicillin G, 100 µg/mL streptomycin, and 25 µg/mL amphotericin B (Biowest, France) [25]. Cells were subcultured twice a week using Tryple Express (ThermoFisher Scientific, Porto Salvo, Portugal) as a dissociation agent and 70% phosphate-buffered saline (PBS) as washing solution [26], and they were routinely maintained in T75 flasks at 25 °C under atmospheric air.

2.3. Cytotoxicity Assays

To assess the cytotoxicity of the six SLE_nS variants to A6 cell lines, two different viability assays were performed, namely, the thiazolyl blue tetrazolium bromide (MTT) and resazurin assays, according to the National Institute of Health's (NIH) guidelines [27], which were adapted to the A6 cell line. Briefly, cells were plated on 96-well plates at a density of 1×10^4 cells per well (Countess® II FL Automated Cell Counter (ThermoFisher Scientific®)) and allowed to adhere overnight at 25 °C. On the following day, test solutions of each SLE_nS variant were made, immediately before exposure, through the dilution of the initially prepared stock solution (3300 mg/L of SLE_nS and 6600 mg/L of LAS) in complete cell culture medium. Then, the cell lines were exposed to the following SLE_nS concentrations, which were selected based on prior range finding tests: 0.132, 0.264, 0.396, 0.528, 0.66, 0.792, 0.924, 1.056, 1.188, and 1.32 mg/L of SLE_nS. The duration of the tests was 48 h, with observations of the viability of the cells made after 24 h and 48 h of exposure. Three independent assays were performed, each containing four replicates per concentration and type of SLE_nS. For the MTT assay, 3-(4,5-dimethylthiazol-2-yl)-2,5-diphenyltetrazolium bromide (TCI, Brussels, Belgium) was diluted in PBS (pH 7.36) at a concentration of 5 mg/mL, while for the resazurin assay, 7-hydroxy-3H-phenoxazin-3-one-10-oxide sodium salt (Serva, Heidelberg, Germany) was diluted in PBS of pH 7.36 at a concentration of 0.15 mg/mL, and both reagents were sterilized by filtration (pore: 0.22 µm), stored at −20 °C, and protected from light. After the exposure period, the cells

were washed with PBS, 100 µL of 10% MTT solution was added to each well, and the plates were incubated for 4 h at 25 °C. At this stage, the cells with an active metabolism transform the MTT to purple-colored formazan. Then, the MTT solution was removed and DMSO was added to the wells. The amount of formazan produced was measured through absorbance (at 570 nm and 690 nm using MultiSkan Spectrum ThermoFisher Scientific®). The cell viability was calculated as a percentage of the control. After the 24 and 48 h exposure periods, 10 µL of resazurin was added to each well, and the cells were incubated for 4 h at 25 °C. After this period, the media were transferred to black 96-well plates. Viable cells will reduce resazurin to resorufin. The fluorescence was measured (Ex. 530.0—Em. 590.0 nm) with a fluorescence spectrophotometer (Hitachi F-7000; ©Hitachi, Ltd.; WVR, Lisbon, Portugal). The cell viability was calculated as a percentage of the control.

2.4. Data Analysis

Lethal concentrations causing a 10, 25, 50, and 90% effect on the cell viability (LC_{10}, LC_{25}, LC_{50}, and LC_{90}, respectively) were estimated by fitting the data to a sigmoidal nonlinear regression model with four parameters and are expressed in the text in mg/L of SLE_nS. A two-way analysis of variance (ANOVA) was conducted to analyze the cytotoxic interaction between the exposure time and SLE_nS concentrations. The assumptions to conducted the ANOVA were checked with the Shapiro–Wilk test (for normality) and Bartlett's test (for homogeneity of variance). The coefficient of correlations (r) for linear regressions were determined to identify associations between the values of computed LC_{50} (with MTT and RES assays) and the number of EO groups in the SLE_nS variants. To check for associations between the LC_{50} computed using the MTT and the resazurin assays, coefficient correlations were computed after running Pearson correlations. The significance level for the ANOVA, linear regressions, and Pearson correlations was set at $p < 0.05$. All statistical analyses was performed using GraphPad Prism v9.1.0 for Windows (GraphPad Software, San Diego, CA, USA).

3. Results

3.1. MTT Assay

The cell viability showed a significant difference between the 24 h and 48 h exposure periods for SLE_1S and $SLE_{11}S$ ($p < 0.05$), while there were no significant differences in the exposure periods for SLE_0S, SLE_4S, $SLE_{30}S$, and $SLE_{50}S$ ($p > 0.05$; Figure 2; Table S2).

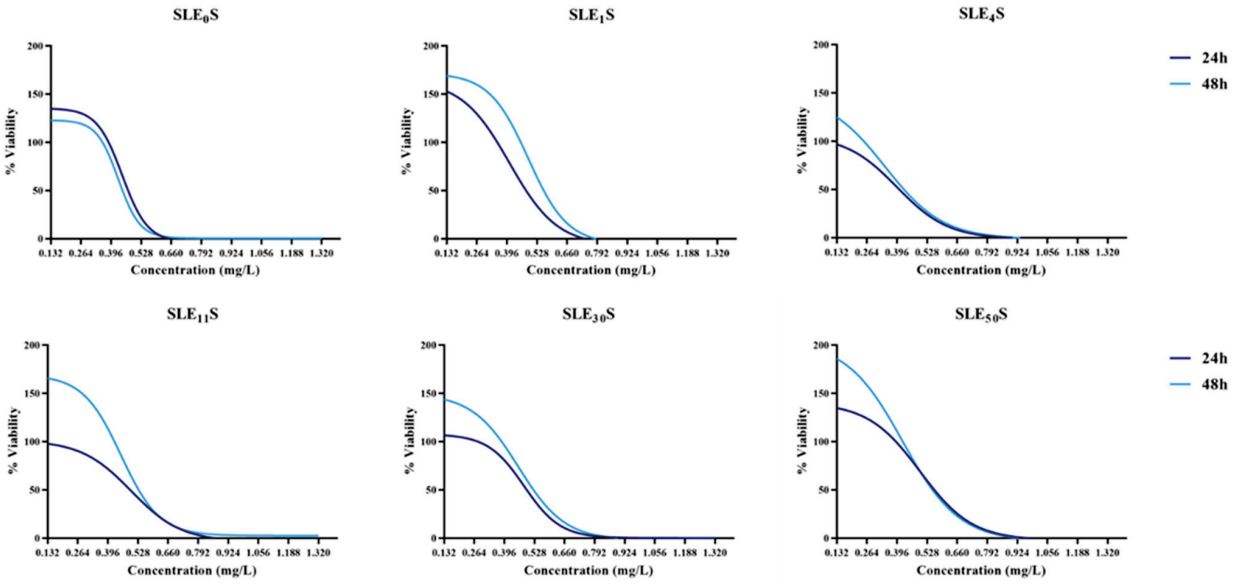


Figure 2. Fitted curves of the cell viability of the A6 cell line to the six variants of SLE_nS after 24 and 48 h of exposure based on the MTT cell viability assay.

Based on the estimated LC_{50} values at both the 24 h and 48 h exposure times, the variants with lower EO units, SLE_0S, SLE_1S, and SLE_4S (the values ranged between 0.398 and 0.475 and 0.417 and 0.552 mg/L, respectively), exhibited slightly higher cytotoxicity than $SLE_{11}S$, $SLE_{30}S$, and $SLE_{50}S$ (the values ranged between 0.488 and 0.554 and 0.517 and 0.548 mg/L, respectively) (Figure 3; Table S1). Despite this tendency of the SLE_nS variants with higher EO units to exhibit a lower cytotoxicity, a significant positive association between the number of EO units and the values of LC_{50} after 24 and 48 h of exposure was not observed ($p \geq 0.07$; $r \leq 0.55$; Table S3).

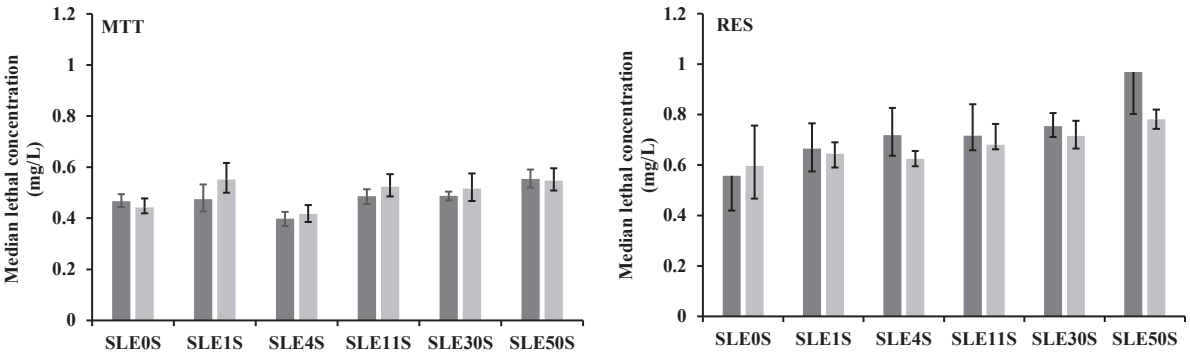


Figure 3. Median lethal concentrations calculated for the six SLE_nS variants after 24 h (dark grey bars) and 48 h (light grey bars) of exposure based on the MTT and resazurin (RES) assays. Error bars represent the 95% confidence limits, and missing upper bars mean that the upper 95% confidence limit could not be computed.

3.2. Resazurin Assay

The cell viability showed no significant differences between 24 h and 48 h of exposure for all six variants of SLE_nS ($p > 0.05$; Figure 4; Table S2).

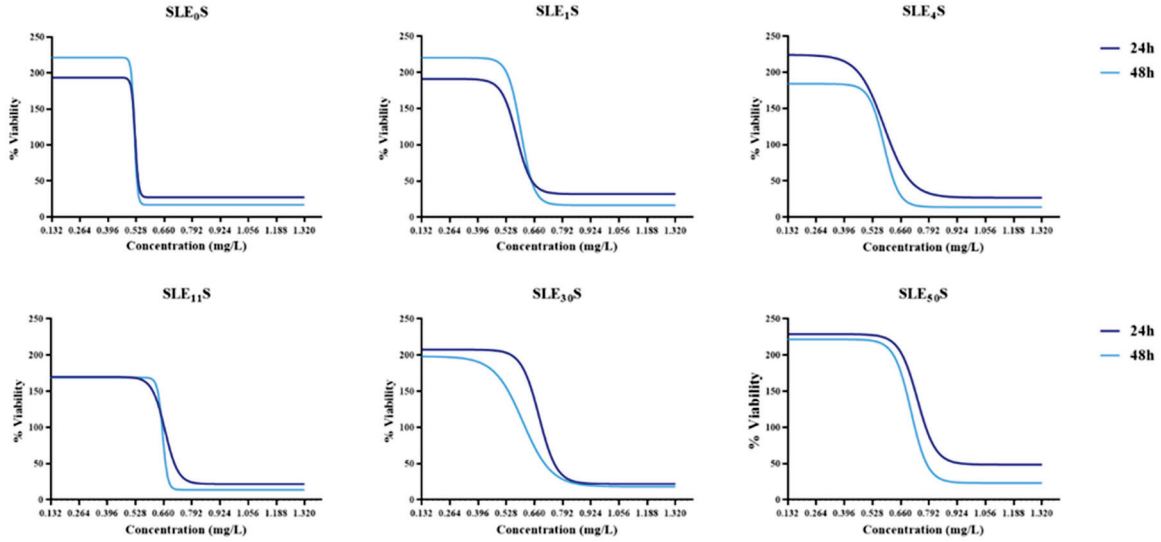


Figure 4. Fitted curves of the cell viability of the A6 cell line to the six variants of SLE_nS after 24 and 48 h of exposure based on the resazurin cell viability assay.

The estimated LC_{50} values increased with the number of EO units of the SLE_nS variants, ranging from 0.557 to 0.969 mg/L, at 24 h exposure, and from 0.597 to 0.782 mg/L, at 48 h of exposure, respectively, for SLE_0S and $SLE_{50}S$ (Figure 3; Table S1). A significant positive association was found at 24 h and 48 h of exposure between the number of EO units of the SLE_nS variants and the computed values of the LC_{50} ($p \leq 0.011$; $r \geq 0.91$; Table S3).

When comparing the computed LC_x for the six SLE_nS variants from the MTT and resazurin assays, no significant correlations were observed between the two assays at 24 and 48 h of exposure ($r \leq 0.688$, $p \geq 0.131$; Table S3). But, the MTT assay generally resulted in lower values of LC_x, suggesting its higher sensitivity to these surfactants (Table S1). Namely, the LC_{50} values obtained from the resazurin assay were 1.2- to 1.8-fold higher than those measured using the MTT assay (Figure 3).

4. Discussion

The ethoxylation of sodium lauryl sulphate (i.e., the addition of ethylene oxide (EO) groups) has been proven to reduce its hazards to humans regarding the skin irritation effects of this surfactant while maintaining its functionalities [28], although a parallel assessment of the influence of such ethoxylation on the toxicity of SLE_nS to the biota has rarely been conducted, even though this chemical is commonly discharged in freshwater ecosystems. Thus, the present work aimed to elucidate the effects of different degrees of ethoxylation (number of EO groups) of SLE_nS on the viability of the *X. laevis* kidney cell line A6 through MTT and resazurin assays. Although both assays estimate cellular viability due to the reduction of the active ingredient by oxidoreductases present in the cell, there is a preference for the enzymes that catalyze this reaction towards MTT or resazurin [29]. While MTT is mainly reduced by the oxidoreductases, dehydrogenases, oxidases, and peroxidases using NADH, NADPH, succinate, or pyruvate as electron donors that are present in the mitochondria and plasma membrane, resazurin is mainly reduced by reductases present in the cytosol, mitochondrial, or microsomal enzymes; by enzymes in the respiratory chain; or by electron transfer agents, preferably N-methylphenazinium methosulfate [27,30]. The results obtained varied according to the assay used. The resazurin assay indicated that SLE_nS variants with a fewer number of EO units were the most toxic to A6 cell lines, exhibiting lower values of LC_{50}. Though the results from the MTT assay showed a similar pattern of fewer EO units associated with higher toxicity, no significant association was observed between the computed LC_{50} values and the number of EO groups. This pattern of toxicity is in line with previously published works. Martins et al. [1] assessed the effects of SLE_nS on the bioluminescence of the marine bacterium *Vibrio fischeri* and reported that SLE_nS with a greater number of EO units were comparatively less toxic to the bacterium than those with a fewer number of EO units. These authors reported acute toxicity ranges (LC_{50}) from 0.56 to 2.81 mg/L^{-1} for SLE_0S, SLE_1S, SLE_2S, and SLE_4S, while $SLE_{11}S$, $SLE_{30}S$, and $SLE_{50}S$ showed an acute toxicity from 8.09 to 8.60 mg/L^{-1} [1]. Possible mechanisms for SLE_nS with a fewer number of EO units being more toxic were suggested by Martins et al. [1]. First, a higher number of EO units is linked with a high stabilization of micelles due to the screening of headgroup repulsion, which contributes to the presence of a lower quantity of monomers in the suspension. Therefore, this mechanism lowers the amount of surfactant (i.e., monomers) able to penetrate the cell membrane, resulting in lower toxicity [1]. The second mechanism is represented by the fact that surfactants with a fewer number of EO units are more hydrophobic and, consequently, more efficient at associating with cellular membranes, thus being more bioavailable [1]. Similarly, Wong et al. [11] determined the acute toxicity of nine variants of alcohol ethoxylate surfactants with different alkyl chain lengths and different numbers of EO groups on *P. promelas* and on *D. magna*. The authors reported increasing toxicity with decreasing number of EO units; for example, for *D. magna* the $EC_{50,48hs}$ ranged from 0.46 mg/L (for the variant with 5 EOs) to 1.2 mg/L (for the variant with 13 EOs) [11]. The exposure duration had no significant effect on the cell viability for any variant of SLE_nS in the resazurin assay, but a significant influence was registered for SLE_1S and $SLE_{11}S$ when the MTT assay was performed. This latter assay also showed a higher sensitivity to the variants of SLE_nS compared to the resazurin assay. One of the possibilities for the lower values of LC_{50} computed with the data obtained from the MTT assay may be due to the mode of action of the surfactants, since membrane destabilization and hydrolysis of cell membrane proteins and enzymes might impair the conversion of MTT to formazan by cellular membrane enzymes. The work from Magalhães

et al. [31] demonstrates that SLE_0S promotes denaturation of lipase with the consequent loss of function, but the increase in the number of EO units of the polar head of SLE_2S stabilizes the enzyme, maintaining its function. Surfactants that are prone to forming micelles, including SLE_0S, tend to induce curvature stress, causing membrane disordering and culminating in cellular lysis [32]; but recent developments have demonstrated that this effect is diminished with the incorporation of EO, with SLE_1S having a critical micelle concentration of 0.7 mM in comparison to SLE_0S with 8.7 mM and a membrane stiffness that increases instead of decreasing, diminishing membrane disordering [33].

Despite the differential sensitivity between the MTT and resazurin assays, the micelles composed of each of the six variants of SLE_nS and LAS were able to impair the viability of the A6 cells at low concentrations: for MTT the $LC_{50,48h}$ ranged from 0.398 to 0.554 mg/L and for resazurin from 0.557 to 0.969 mg/L. These values are within the range of toxicity reported by Martins et al. [1] for the bacterium *V. fisherii*; as mentioned above, $EC_{50,15min.}$ values were between 0.56 and 8.60 mg/L. Though, comparing the toxicity of SLE_0S here reported with that of other studies, a higher toxicity was observed in the present work. Song et al. [34] tested SLE_0S on the mouse fibroblast-like cells L-929 (ATCC, CCL-1) and reported an LC_{50} of 173.6 mg/L in 72 h of exposure (converted from the original result of 602 µM reported in their article), which is considerably higher than the values estimated for the A6 cells in the present study. Bondi et al. [7] report LC_{50} values ranging between 1 mg/L and 13.9 mg/L for aquatic organisms (invertebrates and fish) exposed for 96 h to sodium lauryl sulphate (SLE_0S). Nevertheless, this toxicity was influenced, apart from the target species, by several environmental factors such as water temperature and hardness [10,35]. Vater et al. [36] showed that human keratinocytes and fibroblasts cell lines, when exposed to 1.65 mg/L of SLE_0S (converted from the original result of 5% concentration reported in their article), have no active metabolism and, therefore, no viability after 24 h of exposure, with our work demonstrating far lower concentrations for LC_{90}, but this higher cytotoxicity may be due to the presence of LAS. Several studies focusing on the effect of SLE_nS and LAS in keratinocytes and other cellular models demonstrate that the exerted cytotoxic effects are not exclusive to membrane damage but also involve the formation of reactive oxygen species (ROS) together with altered calcium metabolism [37–39]. Bjerregaard et al. [37] using the same cellular model, A6 cell line, demonstrated that LAS was able to activate calcium channels in the apical membrane and destabilize ion homeostasis, contributing to a higher chloride secretion due to the activation of calcium-dependent chloride channels from the apical membrane [37]. Alterations to calcium metabolism induced by sodium lauryl sulphate (SLS) at concentrations higher than 7.21 mg/L (converted from the original result of 25 µM reported in the article) were also found in keratinocytes and in a reconstructed human epidermal skin model [38]. Mizutani et al. [39] demonstrated that membrane damage due to SLE_0S activates calcium channels, inducing an increase in intracellular calcium promoting the formation of ROS and the activation of IL-1, leading to skin roughness. Responses to surfactants are also dependent on the cellular membrane constitution, namely, the presence of cholesterol that induces rigidness to the membrane and, therefore, interferes with the penetration capability of surfactants [40–42]. This is also important for evaluating the effect of surfactants that are able to transverse the plasma membrane and interfere with organellar membranes, which have different compositions in comparison to the plasma membrane [43,44]. Such an example was found regarding ammonium lauryl sulphate (ALS), which promoted apoptosis through mitochondrial dysfunction, with alterations in mitochondrial membrane potential, reticulum, lysosomal shrinking, and LDH release [45].

5. Conclusions

Overall, this study showed that SLE_nS with a fewer number of EO units were more toxic, as previously shown by other studies at the organismal level. This result highlights the importance and usefulness of in vitro tests as first screenings for this type of study, which can be performed rapidly, are reliable, and do not require animal experimentation. For future works, experiments with other cell lines that exibit different active metabolic

pathways (e.g., XTC-2), is recommended, targeting the establishment of better structure–toxicity relationships of these SLE_nS variants,. Once established, this relationship between EO groups and toxicity may be explored using in vivo assays with amphibians with the variants identified as the least toxic to further assess their risks for this class of vertebrates and to confirm that the variants with a greater number of EO units are more ecofriendly.

Supplementary Materials: The following supporting information can be downloaded at: https://www.mdpi.com/article/10.3390/app13158745/s1, Table S1: Concentrations of the six variants of SLE_nS causing 10, 25, 50, and 90% effect (LC_{10}, LC_{25}, LC_{50}, and LC_{90}) and the respective 95% confidence limits within parenthesis after 24 and 48 h of exposure for the MTT and resazurin (RES) assays. Table S2. p-Values concerning two-way ANOVA followed by Tukey's multiple comparisons test to distinguish differences between exposure times (significant differences are in bold, $p < 0.05$). Table S3. Parameters of the linear regressions performed between the median lethal concentrations and the number of EO units (significant differences are in bold, $p < 0.05$) and the Pearson correlations performed between the cell viabilities measured with the MTT and resazurin methods.

Author Contributions: S.T.: Investigation, Conceptualization, Methodology, Data curation, Formal analysis, Software, and Writing—original draft; M.A.: Methodology, Data curation, Formal analysis, Software, and Writing—Reviewing and Editing; M.O.: Funding acquisition, Conceptualization, Visualization, Investigation, and Writing—Reviewing and Editing; D.C.: Funding acquisition, Conceptualization, Validation, and Writing—Reviewing and editing; I.L.: Funding acquisition, Supervision, Investigation, Conceptualization, Methodology, Data curation, Formal analysis, Validation, and Writing—Reviewing and editing. All authors have read and agreed to the published version of the manuscript.

Funding: This work was possible with the financial support of Short-Term Scientific Missions (STSM) part of The COST (European Cooperation in Science and Technology) action PERIAMAR (PEsticide RIsk AssessMent for Amphibians and Reptiles; CA18221), National Funds through the Portuguese Foundation for Science and Technology, and the Ministry of Education and Science and by European Regional Development Fund (FEDER) funds within the PT2020 Partnership Agreement and Compete 2020 (POFC) by the Center of Environmental and Marine Studies (CESAM) (UIDP/50017/2020+UIDB/50017/2020+ LA/P/0094/2020) through strategic programs and research project GOGOFROG (POCI-01-0145-FEDER-030718).

Institutional Review Board Statement: Not applicable.

Informed Consent Statement: Not applicable.

Data Availability Statement: Data are available upon request only because of restrictions.

Acknowledgments: We would like to thank to Sónia Coelho, Carolina Frazão, and Fábio Gomes for their support with the laboratory work. Thanks are due to Filipe Antunes and Greendet Lda for providing the SLE_nS-LAS micelles.

Conflicts of Interest: The authors declare no conflict of interest.

References

1. Martins, N.; Pereira, J.L.; Antunes, F.E.; Melro, E.; Duarte, C.M.G.; Dias, L.; Soares, A.M.V.M.; Lopes, I. Role of surfactant headgroups on the toxicity of SLEnS-LAS mixed micelles: A case study using microtox test. *Sci. Total Environ.* **2018**, *643*, 1366–1372. [CrossRef] [PubMed]
2. de Seixas-Junior, C.H.; de Carvalho, M.M.; Jacumazo, J.; Piazza, R.D.; Parchen, G.P.; de Freitas, R.A. Interaction of guar gum galactomannans with the anionic surfactant sodium lauryl ether sulphate. *Int. J. Biol. Macromol.* **2020**, *165*, 713–721. [CrossRef] [PubMed]
3. Mohamad, S.F.S.; Mohamad, S.; Aziz, A.A. The susceptibility of aphids, Aphis gossypii Glover to lauric acid based natural pesticide. *Procedia Eng.* **2013**, *53*, 20–28. [CrossRef]
4. Caracciolo, A.B.; Cardoni, M.; Pescatore, T.; Patrolecco, L. Characteristics and environmental fate of the anionic surfactant sodium lauryl ether sulphate (SLES) used as the main component in foaming agents for mechanized tunnelling. *Environ. Pollut.* **2017**, *226*, 94–103. [CrossRef]
5. Sar, S.K.; Verma, C.; Pandey, P.K. Spectrophotometric determination of sodium lauryl sulphate as a prime anionic surfactant and contaminant in central East Chhattisgarh (Durg-Bhilai Region). *Rasayan J. Chem.* **2008**, *1*, 236–245.

6. Bergé, A.; Wiest, L.; Baudot, R.; Giroud, B.; Vulliet, E. Occurrence of multi-class surfactants in urban wastewater: Contribution of a healthcare facility to the pollution transported into the sewerage system. *Environ. Sci. Pollut. Res.* **2018**, *25*, 9219–9229. [CrossRef]
7. Bondi, C.A.; Marks, J.L.; Wroblewski, L.B.; Raatikainen, H.S.; Lenox, S.R.; Gebhardt, K.E. Human and environmental toxicity of sodium lauryl sulfate (SLS): Evidence for safe use in household cleaning products. *Environ. Health Insights* **2015**, *9*, 27–32. [CrossRef]
8. Asio, J.R.G.; Garcia, J.S.; Antonatos, C.; Sevilla-Nastor, J.B.; Trinidad, L.C. Sodium lauryl sulfate and its potential impacts on organisms and the environment: A thematic analysis. *Emerg. Contam.* **2023**, *9*, 100205. [CrossRef]
9. Mariani, L.; Grenni, P.; Barra Caracciolo, A.; Donati, E.; Rauseo, J.; Rolando, L.; Patrolecco, L. Toxic response of the bacterium Vibrio fischeri to sodium lauryl ether sulphate residues in excavated soils. *Ecotoxicology* **2020**, *29*, 815–824. [CrossRef]
10. Lewis, M.A. The effects of mixtures and other environmental modifying factors on the toxicities of surfactants to freshwater and marine life. *Water Res.* **1992**, *26*, 1013–1023. [CrossRef]
11. Wong, D.C.; Dorn, P.B.; Chai, E.Y. Acute toxicity and structure-activity relationships of nine alcohol ethoxylate surfactants to fathead minnow and Daphnia magna. *Environ. Toxicol. Chem.* **1997**, *16*, 1970–1976. [CrossRef]
12. Van Norman, G.A. Limitations of animal studies for predicting toxicity in clinical trials: Is it time to rethink our current approach? *JACC Basic Transl. Sci.* **2019**, *4*, 845–854. [CrossRef] [PubMed]
13. Ahyayauch, H.; Bennouna, M.; Alonso, A.; Goni, F.M. Detergent effects on membranes at subsolubilizing concentrations: Transmembrane lipid motion, bilayer permeabilization, and vesicle lysis/reassembly are independent phenomena. *Langmuir* **2010**, *26*, 307–313. [CrossRef] [PubMed]
14. Otzen, D. Protein–surfactant interactions: A tale of many states. *BBA-Proteins Proteom.* **2011**, *1814*, 562–591. [CrossRef] [PubMed]
15. IUCN. The IUCN Red List of Threatened Species. Version 2022-2. Available online: https://www.iucnredlist.org (accessed on 8 April 2023).
16. Wake, D.B.; Vredenburg, V.T. Are we in the midst of the sixth mass extinction? A view from the world of amphibians. *Proc. Natl. Acad. Sci. USA* **2008**, *105* (Suppl. 1), 11466–11473. [CrossRef]
17. Ivanković, T.; Hrenović, J. Surfactants in the environment. *Arh. Hig. Rada Toksikol.* **2010**, *61*, 95–109. [CrossRef]
18. Shirriff, C.S.; Heikkila, J.J. Characterization of cadmium chloride-induced BiP accumulation in *Xenopus laevis* A6 kidney epithelial cells. *Comp. Biochem. Physiol. C Toxicol. Pharmacol.* **2017**, *191*, 117–128. [CrossRef]
19. Khan, S.; Khamis, I.; Heikkila, J.J. The small heat shock protein, HSP30, is associated with aggresome-like inclusion bodies in proteasomal inhibitor-, arsenite-, and cadmium-treated *Xenopus* kidney cells. *Comp. Biochem. Physiol. A Mol. Integr. Physiol.* **2015**, *189*, 130–140. [CrossRef]
20. Sun, H.; Niisato, N.; Nishio, K.; Hamilton, K.L.; Marunaka, Y. Distinct action of flavonoids, myricetin and quercetin, on epithelial Cl^- secretion: Useful tools as regulators of Cl^- secretion. *BioMed Res. Int.* **2014**, *2014*, 902735. [CrossRef]
21. Thai, T.L.; Yu, L.; Eaton, D.C.; Duke, B.J.; Al-Khalili, O.; Lam, H.Y.; Ma, H.; Bao, H.F. Basolateral $P2X_4$channels stimulate ENaC activity in *Xenopus* cortical collecting duct A6 cells. *Am. J. Physiol. Renal. Physiol.* **2014**, *307*, F806-13. [CrossRef]
22. Tokuda, S.; Niisato, N.; Nakajima, K.; Marunaka, Y. Regulation of the paracellular Na^+ and Cl^- conductances by the $NaCl^-$ generated osmotic gradient in a manner dependent on the direction of osmotic gradients. *Biochem. Biophys. Res. Commun.* **2008**, *366*, 464–470, Erratum in *Biochem. Biophys. Res. Commun.* **2009**, *384*, 274. [CrossRef]
23. Liley, J.R.; Penfold, J.; Thomas, R.K.; Tucker, I.M.; Petkov, J.T.; Stevenson, P.S.; Banat, I.M.; Marchant, R.; Rudden, M.; Terry, A.; et al. Self-assembly in dilute mixtures of non-ionic and anionic surfactants and rhamnolipd biosurfactants. *J. Colloid Interface Sci.* **2017**, *487*, 493–503. [CrossRef]
24. Rafferty, K.A., Jr. Mass culture of amphibian cells: Methods and observations concerning stability of cell type. In *Biology of Amphibian Tumors*; Mizell, M., Ed.; Recent Results in Cancer Research; Springer: Berlin/Heidelberg, Germany, 1969; Volume 1969, pp. 52–81.
25. Born, N.; Thiesen, H.J.; Lorenz, P. The B-subdomain of the Xenopus laevis XFIN KRAB-AB domain is responsible for its weaker transcriptional repressor activity compared to human ZNF10/Kox1. *PLoS ONE* **2014**, *9*, e87609. [CrossRef]
26. Bui-Marinos, M.P.; Varga, J.F.; Vo, N.T.; Bols, N.C.; Katzenback, B.A. Xela DS2 and Xela VS2: Two novel skin epithelial-like cell lines from adult African clawed frog (Xenopus laevis) and their response to an extracellular viral dsRNA analogue. *Dev. Comp. Immunol.* **2020**, *112*, 103759. [CrossRef]
27. Riss, T.L.; Moravec, R.A.; Niles, A.L.; Duellman, S.; Benink, H.A.; Worzella, T.J.; Minor, L. Cell Viability Assays. Assay Guidance Manual. Company and the National Center for Advancing Translational Sciences. 2016. Available online: https://www.ncbi.nlm.nih.gov/books/NBK144065/ (accessed on 6 April 2023).
28. Löffler, H.; Happle, R. Profile of irritant patch testing with detergents: Sodium lauryl sulfate, sodium laureth sulfate and alkyl polyglucoside. *Contact Dermat.* **2003**, *48*, 26–32. [CrossRef] [PubMed]
29. Lavogina, D.; Lust, H.; Tahk, M.J.; Laasfeld, T.; Vellama, H.; Nasirova, N.; Vardja, M.; Eskla, K.-L.; Salumets, A.; Rinken, A.; et al. Revisiting the Resazurin-Based Sensing of Cellular Viability: Widening the Application Horizon. *Biosensors* **2022**, *12*, 196. [CrossRef] [PubMed]
30. Präbst, K.; Engelhardt, H.; Ringgeler, S.; Hübner, H. Basic colorimetric proliferation assays: MTT, WST, and resazurin. In *Cell Viability Assays: Methods and Protocols*; Gilbert, D., Friedrich, O., Eds.; Humana Press: New York, NY, USA, 2017; Volume 1601, pp. 1–17.

31. Magalhães, S.S.; Alves, L.; Sebastiao, M.; Medronho, B.; Almeida, Z.L.; Faria, T.Q.; Brito, M.M.R.; Moreno, J.M.; Antunes, F.E. Effect of ethyleneoxide groups of anionic surfactants on lipase activity. *Biotechnol. Prog.* **2016**, *32*, 1276–1282. [CrossRef] [PubMed]
32. Nazari, M.; Kurdi, M.; Heerklotz, H. Classifying surfactants with respect to their effect on lipid membrane order. *Biophys. J.* **2012**, *102*, 498–506. [CrossRef]
33. Lee, S.W.; Tettey, K.E.; Yarovoy, Y.; Lee, D. Effects of anionic surfactants on the water permeability of a model stratum corneum lipid membrane. *Langmuir* **2014**, *30*, 220–226. [CrossRef]
34. Song, H.Y.; Kim, Y.H.; Seok, S.J.; Gil, H.W.; Yang, J.O.; Lee, E.Y.; Hong, S.Y. Cellular toxicity of surfactants used as herbicide additives. *J. Korean Med. Sci.* **2012**, *27*, 3–9. [CrossRef]
35. El-Dossoki, F.I.; Gomaa, E.A.; Hamza, O.K. Solvation thermodynamic parameters for sodium dodecyl sulfate (SDS) and sodium lauryl ether sulfate (SLES) surfactants in aqueous and alcoholic-aqueous solvents. *SN Appl. Sci.* **2019**, *1*, 933. [CrossRef]
36. Vater, C.; Adamovic, A.; Ruttensteiner, L.; Steiner, K.; Tajpara, P.; Klang, V.; Elbe-Burger, A.; Wirth, M.; Valenta, C. Cytotoxicity of lecithin-based nanoemulsions on human skin cells and ex vivo skin permeation: Comparison to conventional surfactant types. *Int. J. Pharm.* **2019**, *566*, 383–390. [CrossRef]
37. Bjerregaard, H.F.; Stærmose, S.; Vang, J. Effect of linear alkylbenzene sulfonate (LAS) on ion transport and intracellular calcium in kidney distal epithelial cells (A6). *Toxicol. In Vitro* **2001**, *15*, 531–537. [CrossRef] [PubMed]
38. Choi, H.; Shin, M.K.; Ahn, H.J.; Lee, T.R.; Son, Y.; Kim, K.S. Irritating effects of sodium lauryl sulfate on human primary keratinocytes at subtoxic levels of exposure. *Microsc. Res. Tech.* **2018**, *81*, 1339–1346. [CrossRef] [PubMed]
39. Mizutani, T.; Mori, R.; Hirayama, M.; Sagawa, Y.; Shimizu, K.; Okano, Y.; Masaki, H. Sodium lauryl sulfate stimulates the generation of reactive oxygen species through interactions with cell membranes. *J. Oleo Sci.* **2016**, *65*, 993–1001. [CrossRef] [PubMed]
40. Apel-Paz, M.; Doncel, G.F.; Vanderlick, T.K. Impact of membrane cholesterol content on the resistance of vesicles to surfactant attack. *Langmuir* **2005**, *21*, 9843–9849. [CrossRef]
41. Morris, S.A.; Bobbitt, J.R.; Ananthapadmanabhan, K.P.; Kasting, G.B. The effect of prolonged exposure on sodium dodecyl sulfate penetration into human skin. *Toxicol. In Vitro* **2021**, *77*, 105246. [CrossRef]
42. Nigam, P. Thermodynamic quantification of sodium dodecyl sulfate penetration in cholesterol and phospholipid monolayers. *Chem. Phys. Lipids* **2020**, *232*, 104974. [CrossRef]
43. Casares, D.; Escribá, P.V.; Rosselló, C.A. Membrane lipid composition: Effect on membrane and organelle structure, function and compartmentalization and therapeutic avenues. *Int. J. Mol. Sci.* **2019**, *20*, 2167. [CrossRef]
44. Klose, C.; Surma, M.A.; Simons, K. Organellar lipidomics—Background and perspectives. *Curr. Opin. Cell Biol.* **2013**, *25*, 406–413. [CrossRef]
45. Park, E.J.; Seong, E.; Kim, Y.; Lee, K. Ammonium lauryl sulfate-induced apoptotic cell death may be due to mitochondrial dysfunction triggered by caveolin-1. *Toxicol. In Vitro* **2019**, *57*, 132–142. [CrossRef] [PubMed]

Disclaimer/Publisher's Note: The statements, opinions and data contained in all publications are solely those of the individual author(s) and contributor(s) and not of MDPI and/or the editor(s). MDPI and/or the editor(s) disclaim responsibility for any injury to people or property resulting from any ideas, methods, instructions or products referred to in the content.

metals

MDPI

Article

Hydrogen-Induced Cracking in CGHAZ of Welded X80 Steel under Tension Load

Jinxin Gou [1,2], Xiao Xing [1,2,*], Gan Cui [1,2], Zili Li [1,2,*], Jianguo Liu [1,2] and Xiangyuan Deng [1,2]

[1] College of Pipeline and Civil Engineering, China University of Petroleum (East China), Qingdao 266580, China
[2] Shandong Key Laboratory of Oil & Gas Storage and Transportation Safety, Qingdao 266580, China
* Correspondence: 20170079@upc.edu.cn (X.X.); zilimenhuzu@163.com (Z.L.)

Abstract: X80 steel is extensively used in hydrogen environments and is susceptible to hydrogen embrittlement (HE). This paper studied the hydrogen-induced cracking (HIC) behavior in the coarse-grained heat-affected zone (CGHAZ) of X80 steel welds, through applying in situ hydrogen-charging tensile experiments, hydrogen permeation experiments, and various surface analysis techniques. It is shown that a few hydrogen atoms can significantly decrease a material's elongation and reduction of area. When the heat input (HI) was 29.2 kJ/cm, the material had minor sensitivity to hydrogen embrittlement. The tensile fractures were ductile without hydrogen. However, the fracture surface exhibited brittle fracture with hydrogen. With increased HI, the HE fracture showed a transition of intergranular fracture→intergranular and transgranular mixed fracture→transgranular fracture. In the presence of hydrogen, the grain boundaries of elongated strips were prone to the formation of intergranular cracks under a tension load, and the hydrogen embrittlement resistance of the bulk lath bainite (LB) was weak. The hydrogen embrittlement susceptibility of pure granular bainite (GB) was lower. Fine LB and GB composite structures could remarkably inhibit intergranular cracks, giving the steel a superior resistance to hydrogen embrittlement.

Keywords: carbon steel; tensile; hydrogen diffusion; SEM; hydrogen embrittlement

1. Introduction

The development of the hydrogen energy industry is a vital engine in optimizing the energy structure and promoting the transformation and upgrading of traditional industries [1–4]. Hydrogen storage and transportation is the bridge between hydrogen production and hydrogen energy applications [5,6]. China plans to build the first west-to-east hydrogen pipeline, with a total length of more than 400 km. In order to save transportation costs, X80 steel, suitable for large-diameter and high-pressure pipelines, will be widely used in hydrogen environments. In addition, the X80 steel pipelines currently in service are affected by cathodic overprotection and high-voltage transmission line interference, which causes hydrogen generation and penetration into the pipeline [7–10]. All these factors expose X80 steel to the risk of hydrogen embrittlement [11–13].

Whether exposed to high-pressure hydrogen or cathodic hydrogen evolution, once the hydrogen atoms are adsorbed on the metal surface and enter the pipeline [14], they accumulate in the hydrogen trap [15,16], which will cause hydrogen embrittlement (HE), especially in the weld area of a pipeline [17,18]. The multiplicity of grain orientations, grain boundaries, and dislocations caused by welding changes the mechanical properties of the material [19–22]. Pipe fracture failure due to insufficient toughness of the girth weld is one of the main failure modes of high-strength steel pipes. The welded joint's heat-affected zone (HAZ) [23–25] is a unique area between the weld and the base material (BM). Due to a non-uniformity of organization [26,27], it is easy to produce local defects and stress concentrations. This is the most vulnerable failure zone in the weld [28–30].

To date, the susceptibility of different metallographic structures of the X80 steel coarse-grained heat-affected zone (CGHAZ) to HE under tension load has not been fully characterized and understood. This knowledge is critical in helping to prevent hydrogen-induced cracking (HIC) in X80 steel hydrogen pipelines. This work investigated the HIC behavior in the CGHAZ of X80 steel welds using in situ hydrogen-charging tensile tests, hydrogen permeation experiments, and various surface analysis techniques. These results are expected to be used as the reference for the design and fabrication process of hydrogen pipelines.

2. Experimental

2.1. Materials and Specimens

Test specimens used in this work were taken from a sheet of X80 steel pipeline. The chemical composition of the steel contains (wt.%): C 0.07, Cu 0.221, Cr 0.266, Si 0.216, Mn 1.8, Ni 0.168, Mo 1.82, Nb 0.105, P 0.0137, Ti 0.013, Al 0.026, N 0.003, S 0.0009 and Fe balance.

The process of specimen machining is shown in Figure 1. First, slices of 16 × 180 × 2.2 mm^3 and 34 × 150 × 2.2 mm^3 were axially cut from X80 pipeline steel using wire cutting. Subsequently, the Gleeble 3500 thermal simulator (DSI, New York, NY, USA) was employed to conduct the heat treatment of the sheet [31]. The red part was the uniform temperature zone in the simulated welding heat treatment. Then, the heat-treated specimens were processed into tensile and hydrogen-permeable specimens with wire cutting. The surface of the specimen was ground with silicon carbide sandpaper to a grain size of 600, 800, and 1200, then polished with W5 diamond slurry. The specimen was then degreased with acetone and dehydrated with ethanol.

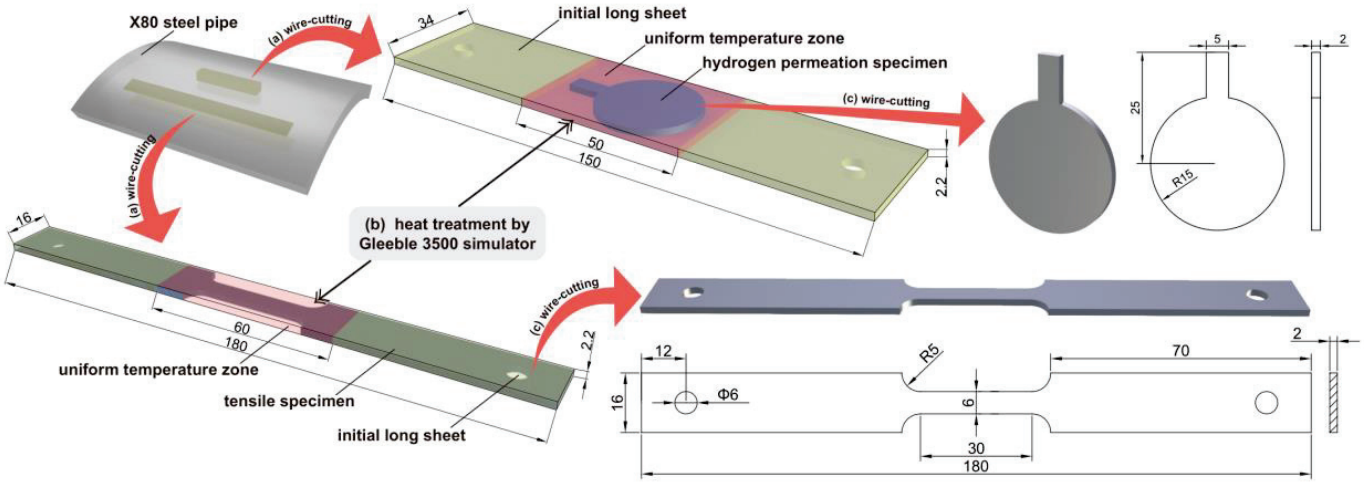


Figure 1. Schematic diagram illustrating the processes for specimen manufacturing and the specimen dimensions, adapted with permission from [32] (unit: mm).

Through a spiral submerged arc welding experiment of X80 steel, heat input curves were obtained from thermocouples pre-buried at different positions from the weld [29]. The cooling time from 800 °C to 500 °C ($t_{8/5}$) was obtained according to the heat input curve of CGHAZ [32,33]. The actual $t_{8/5}$ was 15.5s, and the corresponding welding heat input was 18.1 kJ/cm. We changed the cooling time $t_{8/5}$ and calculated the heat input corresponding to different cooling times, according to the theoretical and empirical formula of welding. The calculated thermal simulation parameters are shown in Table 1.

Table 1. CGHAZ thermal simulation parameters adapted from [34].

Label	Heating Rate (°C/s)	Peak Temperature (°C)	Holding Time (s)	Cooling Time $t_{8/5}$ (s)	Heat Input (kJ/cm)
HI08.5	150	1350	1	4.5	8.5
HI18.1				15.5	18.1
HI29.2				39.0	29.2
HI38.3				68.5	38.3
HI48.5				109.0	48.5

2.2. Metallographic Observation

The specimens were etched in a mixed solution of 4% nitric acid and ethanol and then observed with a ZEISS Axio Imager A2m (Carl Zeiss AG, Oberkochen, Germany) metallurgical microscope. The microstructures of CGHAZ under different heat inputs are shown in Figure 2. HI08.5 and HI18.1 were mainly composed of bulk lath bainite (LB), and LB was more finely interwoven in HI08.5. In HI29.2, LB was divided by granular bainite (GB), the composite structure was mainly composed of fine LB and GB. As the heat input continued to increase, the HI38.2 and HI48.5 were mainly composed of GB. With the increase in the heat input, the content of LB gradually decreased, while that of GB increased gradually [35].

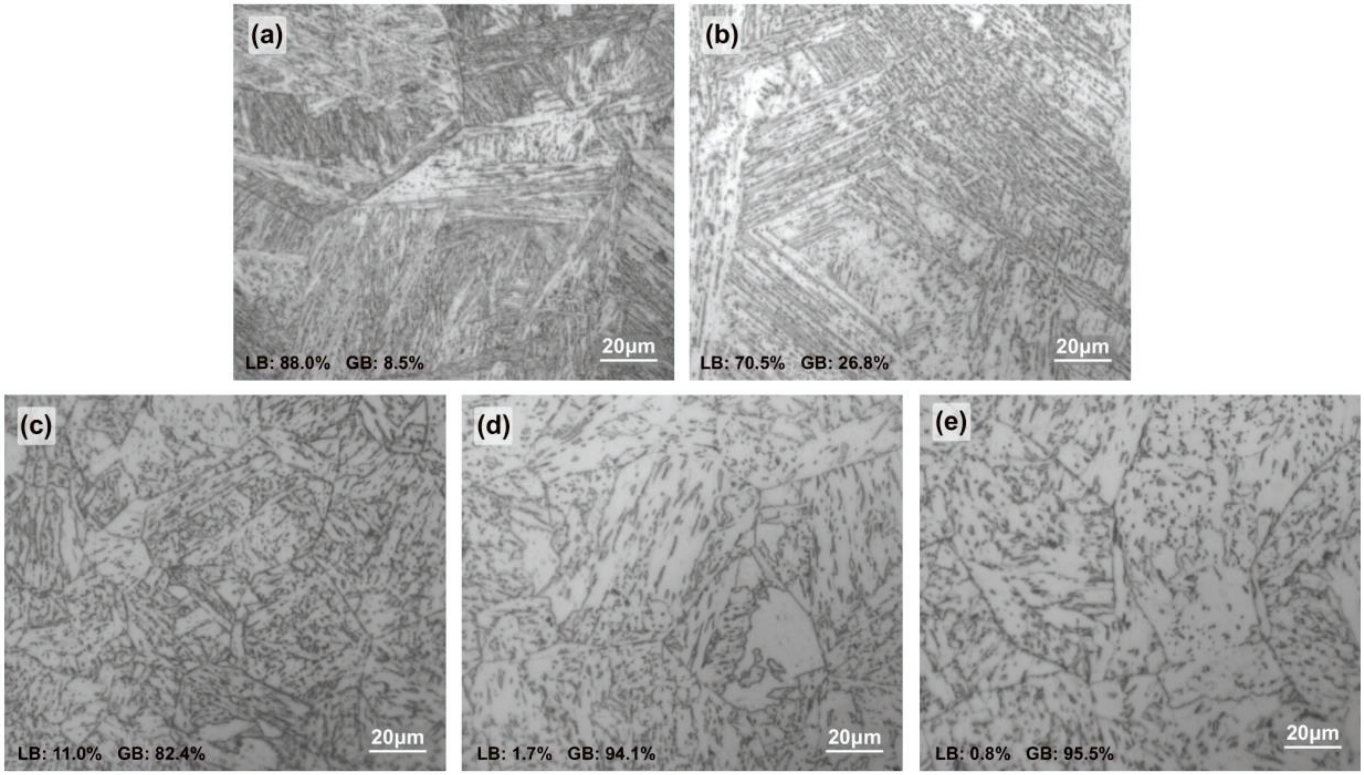


Figure 2. Metallographic structure of CGHAZ in welded X80 steel: (**a**) HI08.5, (**b**) HI18.1, (**c**) HI29.2, (**d**) HI38.3, and (**e**) HI48.5.

2.3. Tensile and Hydrogen Permeation Testing

The in situ hydrogen charging tensile device [34] is shown in Figure 3a. The type of tensile machine used in the tensile experiment in this paper was a slow strain stress testing machine WDML-50, which was manufactured by LETRY in 2020, and the in situ electrochemical hydrogen charging method was used to charge the specimen with hydrogen during the stretching process [36]. The electrochemical charging solution contained

0.5 mol/L H_2SO_4 + 0.2 g/L CH_4N_2S [37]. The hydrogen charging current densities were 5 mA/cm^2, 10 mA/cm^2, 20 mA/cm^2, 30 mA/cm^2, and 40 mA/cm^2; the hydrogen charging temperature was 20 °C; and the pre-charging time was 1.5 h. Stretching was performed at 20 °C, with a strain rate of 10^{-6} s^{-1}. After the specimen was broken, the fracture was ultrasonically cleaned for 10 min in acetone and absolute ethanol solutions and dried and sealed for SEM observation.

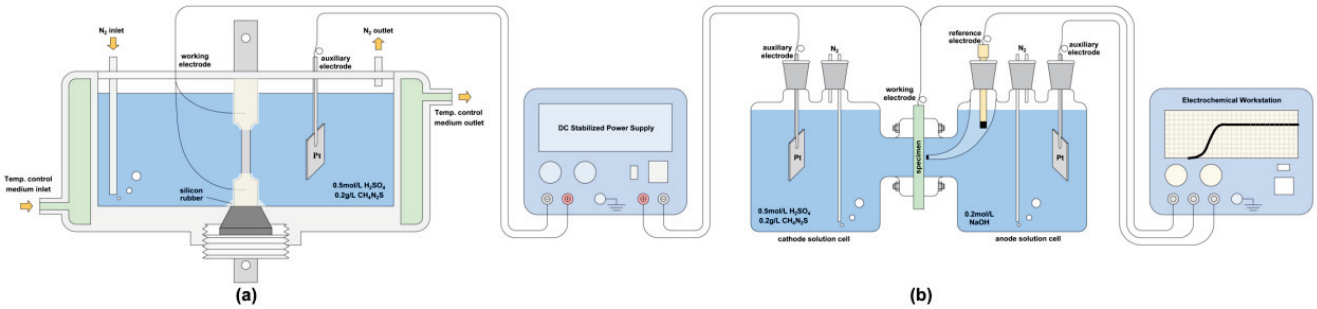


Figure 3. Schematic diagram of the device: (**a**) in situ hydrogen charging tensile, (**b**) D-S double electrolytic cell for hydrogen permeation.

Hydrogen permeation experiments [38,39] were carried out using the D-S double electrolytic cell shown in Figure 3b. The working electrode and the auxiliary electrode on the cathode side were connected to a DC stable power supply. The working electrode on the anode side, the auxiliary electrode, and the saturated calomel reference electrode constituted a three-electrode system connected to an electrochemical workstation. The electrochemical workstation recorded the hydrogen permeation current density change with time. The hydrogen permeation test temperature was 20 °C.

2.4. Characterization of the Fracture Surface

The fractured section was cut from the specimen using wire cutting, ultrasonically cleaned with acetone and anhydrous ethanol, and dried with cold air. The fracture surface was observed using a Hitachi S4800 cold field emission SEM (Hitachi, Tokyo, Japan).

3. Results and Discussion

3.1. Effect of Heat Input on Tensile Properties

To analyze the effect of heat input on the tensile properties of CGHAZ, engineering stress–strain curves of BM and CGHAZ without hydrogen were measured, as shown in Figure 4. The mechanical performance parameters were measured, and the results are shown in Table 2. The tensile curve of BM had an obvious yield point, while CGHAZ had no obvious yield point. As the heat input increased, the material's ultimate tensile strength (*UTS*) gradually decreased, but there was a slight increase for HI29.2. Simultaneously, the elongation (*EL*) of the material decreased with the increase in heat input, indicating that the higher the tensile strength, the worse the tensile toughness. When the heat input was $\leq$29.2 kJ/cm, the *UTS* of CGHAZ was significantly higher than BM. When the heat input was increased to 38.3 kJ/cm, the mechanical properties of CGHAZ were similar to BM. When the heat input continued to increase to 48.5 kJ/cm, the strength of CGHAZ was lower than that of BM, but the *EL* was higher than that of BM, showing a more substantial tensile toughness. The reduction in area (*RA*) in the CGHAZ was smaller than that of the BM.

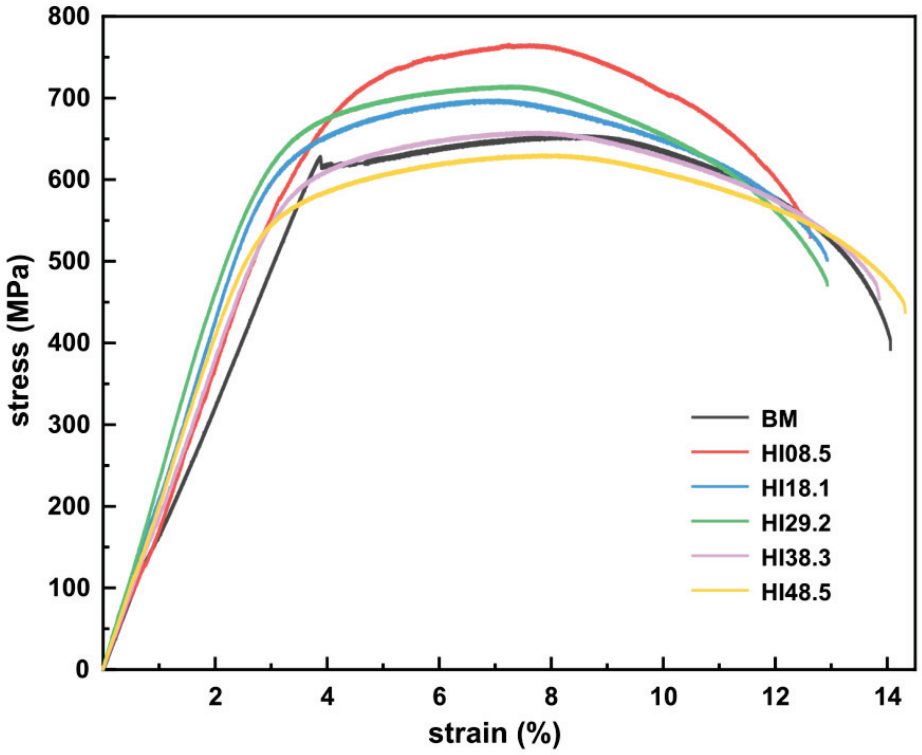


Figure 4. Stress–strain curve of BM and CGHAZ under different heat inputs.

Table 2. Tensile parameters of BM and CGHAZ under different heat inputs.

Label	*UTS* (MPa)	*RA* (%)	*EL* (%)
BM	654.28	36.61	14.06
HI08.5	766.21	25.70	12.65
HI18.1	697.95	25.87	13.14
HI29.2	714.97	26.56	13.25
HI38.3	658.58	28.20	14.05
HI48.5	630.68	28.76	14.48

3.2. Tensile Properties of CGHAZ with Different Heat Inputs at Different Hydrogen Concentrations

Slow tensile tests were performed on BM and CGHAZ under different heat inputs and hydrogen concentrations (including no hydrogen). The engineering stress–strain curves are shown in Figure 5. For BM, in the elastic stretching stage, the slope of the stress–strain curve increased obviously with the increase in hydrogen charging current density. Furthermore, the Young's modulus of the material gradually increased, and the stiffness of the material gradually increased. Nevertheless, for CGHAZ, in the elastic stretching stage, the Young's modulus of the material was less affected by hydrogen. In the presence of hydrogen atoms, whether BM or CGHAZ, the tensile specimens broke rapidly in the elastic stage. Hydrogen reduced the tensile properties of the materials, but there were apparent differences in the hydrogen embrittlement susceptibility among the different materials.

To clarify the effect of hydrogen on the tensile properties of the materials, we should pay attention to the concentration of hydrogen atoms rather than the hydrogen charging current density. Therefore, we used electrochemical hydrogen permeation experiments to determine the concentration of hydrogen atoms in the different materials at different hydrogen-charging current densities [40–43]. The hydrogen permeation curves of the materials with different heat inputs at different hydrogen charging current densities are shown in Figure 6.

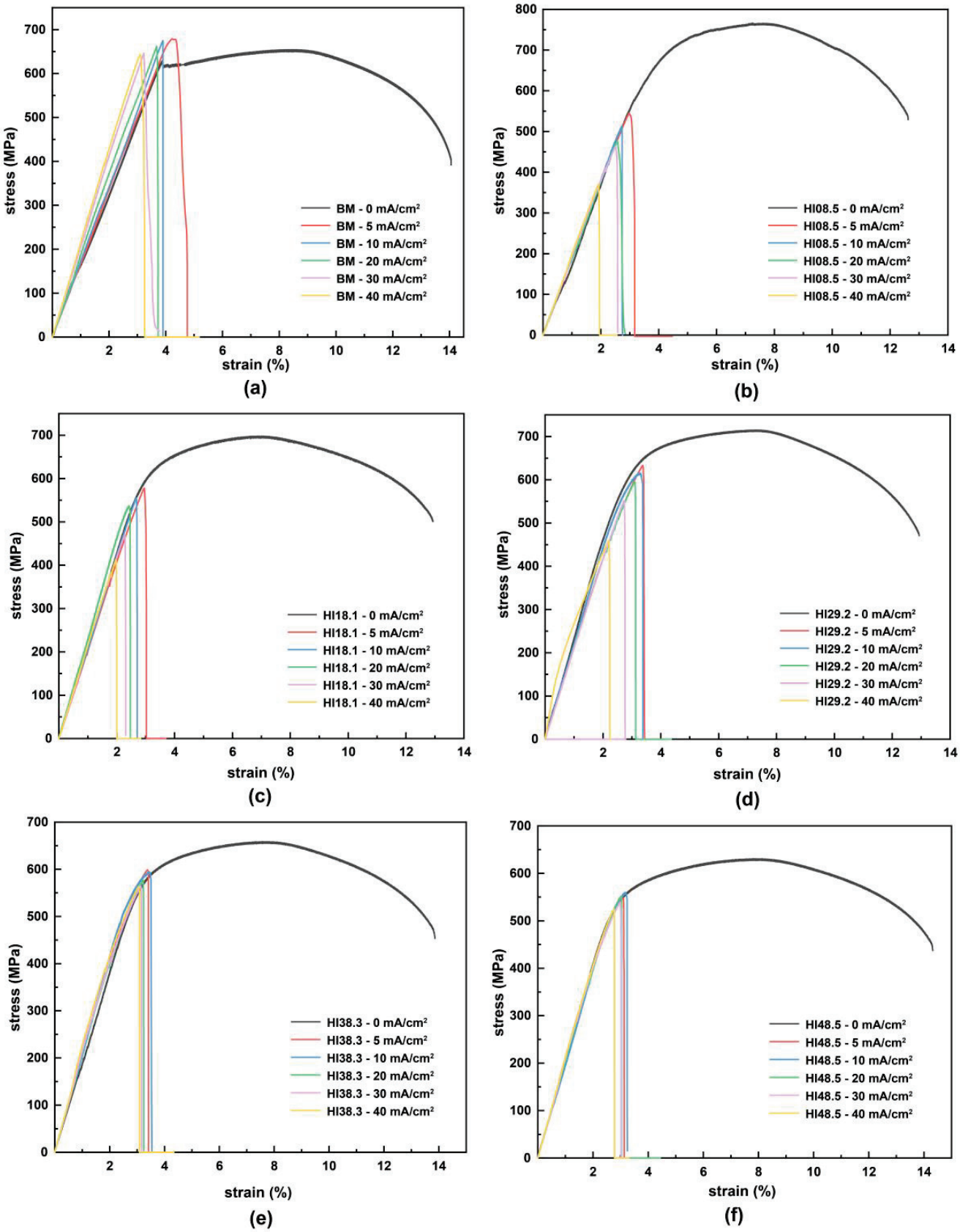


Figure 5. Stress–strain curves of materials with different heat inputs at different hydrogen charging current densities: (**a**) BM, (**b**) HI08.5, (**c**) HI18.1, (**d**) HI29.2, (**e**) HI38.3, (**f**) HI48.5.

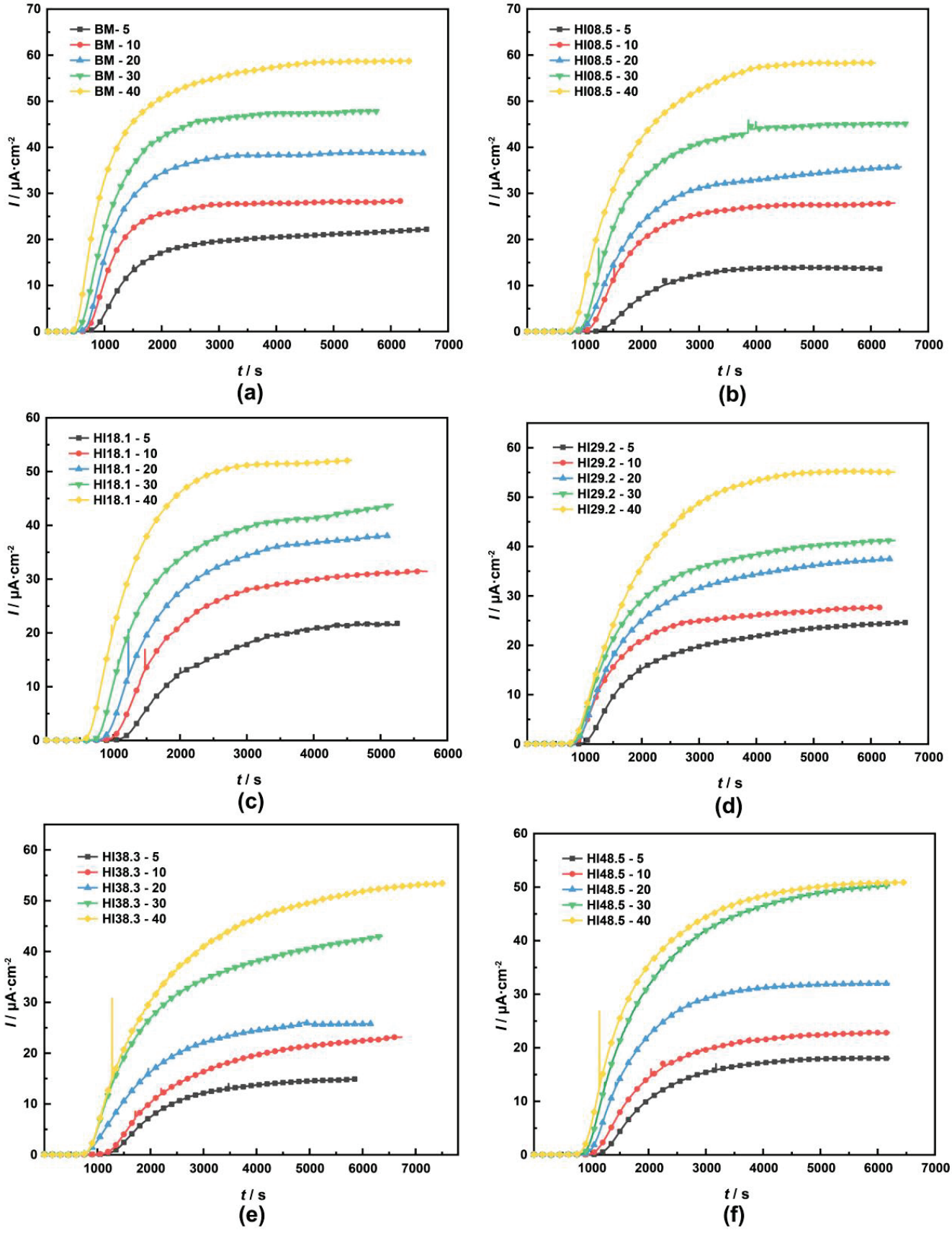


Figure 6. Hydrogen permeation curves of materials with different heat inputs at different hydrogen charging current densities: (**a**) BM, (**b**) HI08.5, (**c**) HI18.1, (**d**) HI29.2, (**e**) HI38.3, (**f**) HI48.5 [34].

The constant concentration (CC) model was chosen as the hydrogen permeation model [44–46]. For the CC model, the theoretical seepage transient current follows the dimensionless Formula (1):

$$\frac{I_t}{I\infty} = \frac{2}{\sqrt{\pi\tau}} \sum_{n=0}^{\infty} \exp\left(-\frac{(2n+1)^2}{4\tau}\right) \quad (1)$$

where I_t is the transient current density at time t; I_∞ is the steady-state current density; $\tau = Dt/L^2$ is a dimensionless parameter; D is the hydrogen diffusivity; and L is the thickness of the specimen.

The hydrogen diffusion coefficient D in this experiment was calculated using the Laplace method [47–49]. Moreover, the hydrogen concentration C_0 was calculated using the following formula:

$$C_0 = \frac{I_\infty L}{D\mathrm{F}} \quad (2)$$

where F is the Faraday constant, and its value is 96,485 C/mol. The calculation results are shown in Table 3.

Table 3. Calculation results of hydrogen concentration for different heat input specimens at different hydrogen charging current densities.

Label	D (10^{-6} cm^2·s^{-1}) C_0 (10^{-5} mol·cm^{-3})									
	I = 5 mA/cm^2		I = 10 mA/cm^2		I = 20 mA/cm^2		I = 30 mA/cm^2		I = 40 mA/cm^2	
	D	C_0	D	C_0	D	C_0	D	C_0	D	C_0
BM	3.978	1.123	4.932	1.131	4.863	1.606	4.991	1.914	5.304	2.227
HI08.5	3.123	0.928	3.025	1.72	3.454	2.144	3.687	2.554	3.834	3.115
HI18.1	2.725	1.626	3.248	1.911	3.586	2.113	4.043	2.162	4.881	2.177
HI29.2	3.287	1.553	3.348	1.699	3.440	2.252	3.641	2.323	3.953	2.897
HI38.3	2.477	1.236	2.755	1.725	3.010	1.757	3.100	2.847	3.247	3.411
HI48.5	3.079	1.203	3.152	1.474	3.157	2.080	3.447	2.995	3.521	3.036

The *UTS* and *EL* were obtained according to the stress–strain curve in Figure 5. *RA* was obtained from fracture dimension measurements. Measurements were taken at three locations of the fracture surface, to obtain an average value. According to the hydrogen concentrations of the different heat input specimens at different hydrogen charging current densities in Table 3, the hydrogen charging current density was replaced by the hydrogen concentration. The *UTS*, *EL*, and *RA* under different hydrogen charging current densities, hydrogen concentrations, and HI were obtained, as shown in Figures 7–9. As depicted in Figure 7c, it can be observed that a minor welding heat input led to an improvement in the *UTS*, with HI08.5 exhibiting the highest *UTS* value under a tension load. However, when hydrogen atoms were present, as shown in Figure 7b, the *UTS* of the CGHAZ gradually decreased with the increase in hydrogen concentration, and the smaller the heat input, the more significant the decrease in *UTS*. For this scenario, the *UTS* of HI08.5 and HI18.1 was the worst.

In the absence of hydrogen atoms, the CGHAZ achieved desirable elongation characteristics, with *EL* gradually increasing with the increase in welding heat input. Notably, at HI48.5, the elongation rate reached 14.48%, surpassing BM. Figure 8c shows that the elongation rate dropped significantly once the hydrogen atoms entered the material. From Figure 8d,b, with the increase in the hydrogen charging current density, the elongation of the material decreased. The *UTS* of HI08.5 and HI18.1 was the worst. *EL* refers to the ability of a material to deform when stretched. The greater the elongation, the better the toughness of the material. Hydrogen atoms can cause a material to lose its toughness rapidly, especially when the material microstructure has a substantial content of LB.

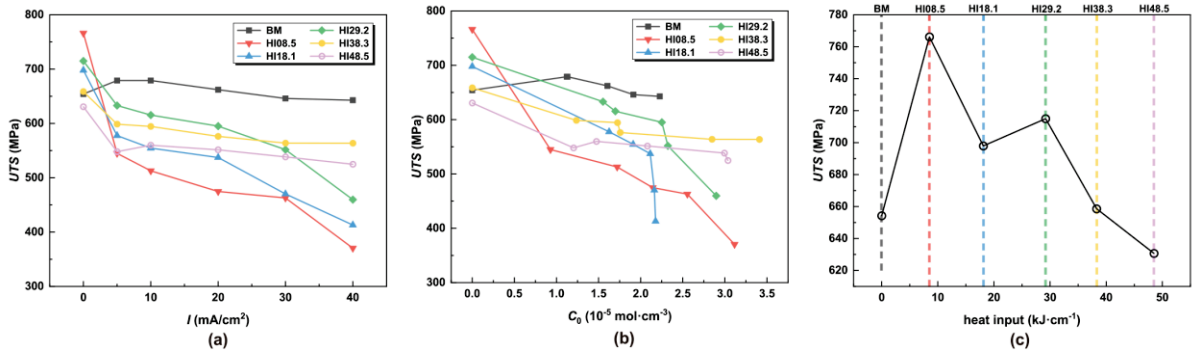


Figure 7. *UTS* at different hydrogen charging current densities, hydrogen concentrations, and HI (**a**) under different I, (**b**) under different C_0, and (**c**) under different HI.

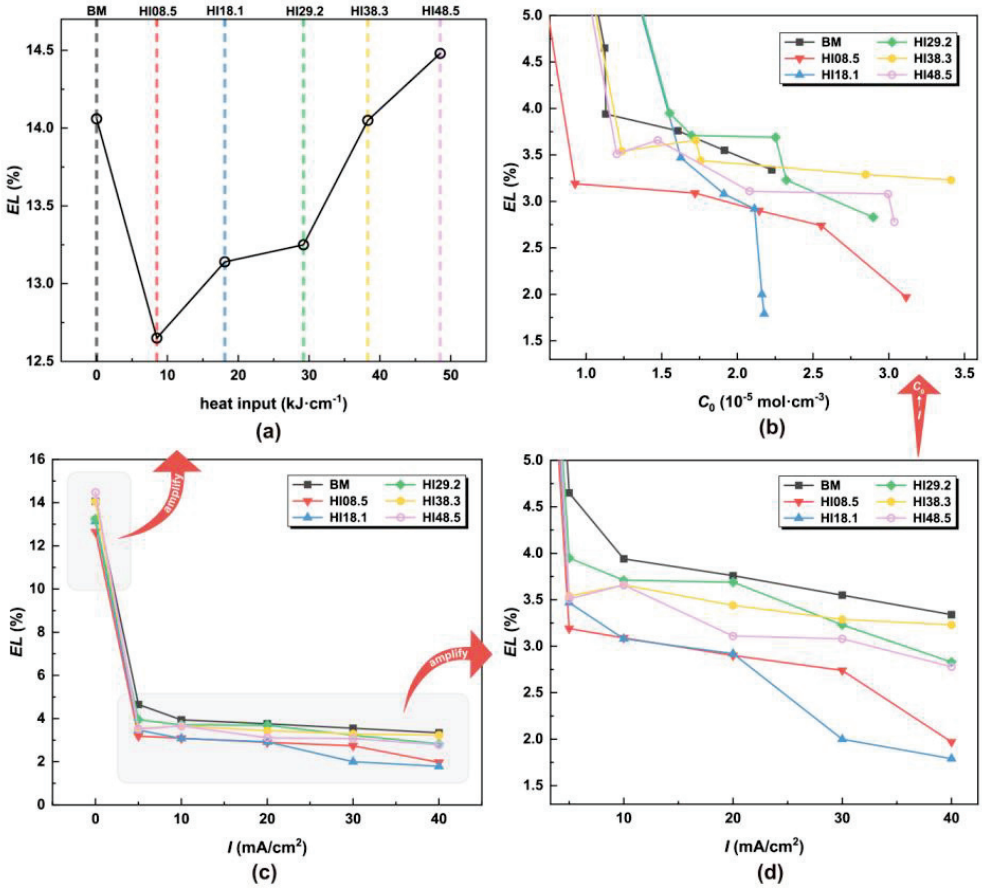


Figure 8. *EL* under different HI, hydrogen charging current density, and hydrogen concentration (**a**) under different HI, (**b**) under different C_0, (**c**) under different I, and (**d**) local amplification under different I.

As shown in Figure 9a, in the absence of hydrogen atoms, the *RA* of CGHAZ was lower than that of the BM. For CGHAZ, with the increase in HI, *RA* gradually increased, indicating that the plasticity of the material was enhanced. As shown in Figure 9c, the *RA* dropped significantly once the material came into contact with hydrogen atoms. From Figure 9d,b, with the increase in hydrogen concentration, the *RA* of the material decreased gradually, indicating a loss of plasticity of the material. The *EL* and *RA* of HI18.1 showed a continuous and sharp drop around the hydrogen concentrations of 1.5×10^{-5} mol·cm^{-3} and 2.2×10^{-5} mol·cm^{-3}. This proves that the plasticity of the material dropped sharply.

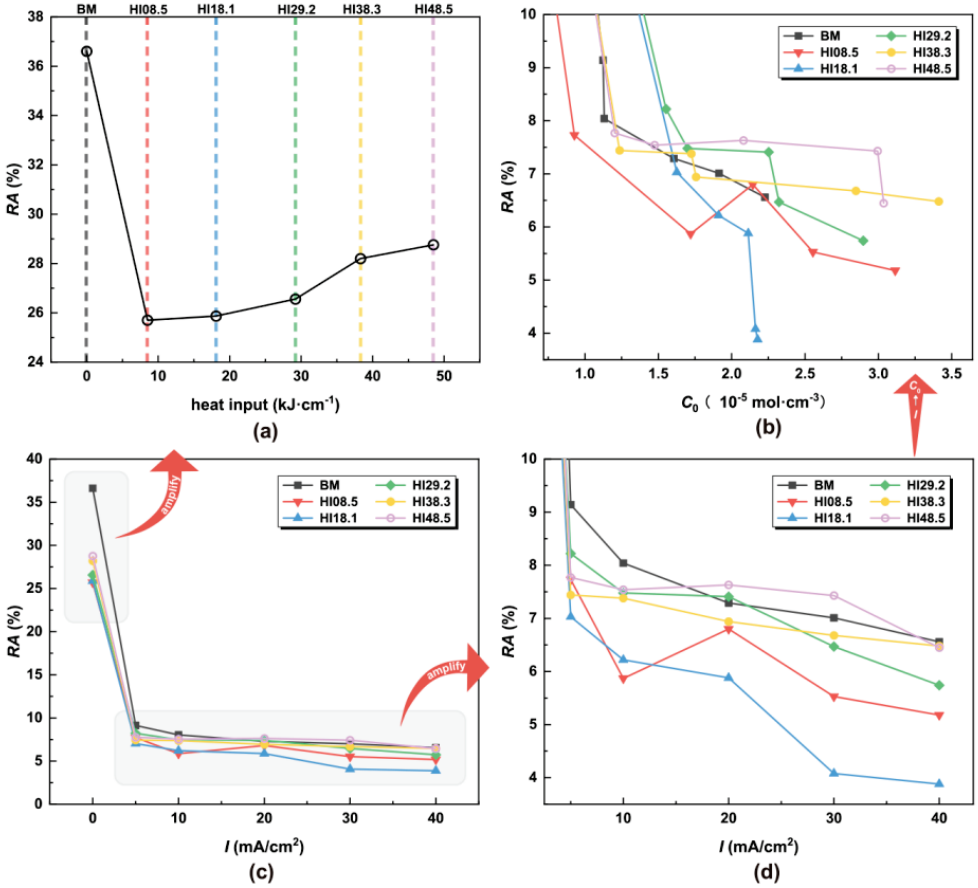


Figure 9. *RA* under different HI, hydrogen charging current densities, and hydrogen concentrations: (**a**) under different HI, (**b**) under different C_0, (**c**) under different I, and (**d**) local amplification under different I.

The relative elongation ΔEL was used to characterize the hydrogen embrittlement susceptibility of the material, and its expression is

$$\Delta EL = \frac{EL_{w/oH} - EL_{withH}}{EL_{w/oH}} \times 100\% \quad (3)$$

where $EL_{w/oH}$ is the elongation without hydrogen, and EL_{withH} is the elongation with hydrogen. The ΔEL of CGHAZ with different heat inputs at different hydrogen concentrations was calculated, respectively. The calculation results are shown in Figure 10.

When the heat input was set to 29.2 kJ/cm, CGHAZ had the lowest hydrogen embrittlement sensitivity under tensile load, even lower than the BM. When HI > 29.2 kJ/cm, the susceptibility to hydrogen embrittlement of CGHAZ was less affected by the hydrogen concentration gradient. At this stage, the susceptibility to hydrogen embrittlement was slightly higher than that of BM, steadily increasing with an escalating hydrogen concentration. When HI <29.2 kJ/cm, the hydrogen embrittlement susceptibility of HI18.1 was the highest, and the susceptibility to hydrogen embrittlement increased rapidly with the increase in the hydrogen concentration. The welding heat input associated with HI18.1 precisely matched the welding parameter used in the current operational pipeline.

3.3. Fracture Surface Analysis of CGHAZ with Different Heat Inputs

The tensile fracture surfaces of the CGHAZ specimens under different heat inputs without hydrogen charging and at a hydrogen charging current density of 20 mA/cm^2 are shown in Figure 11.

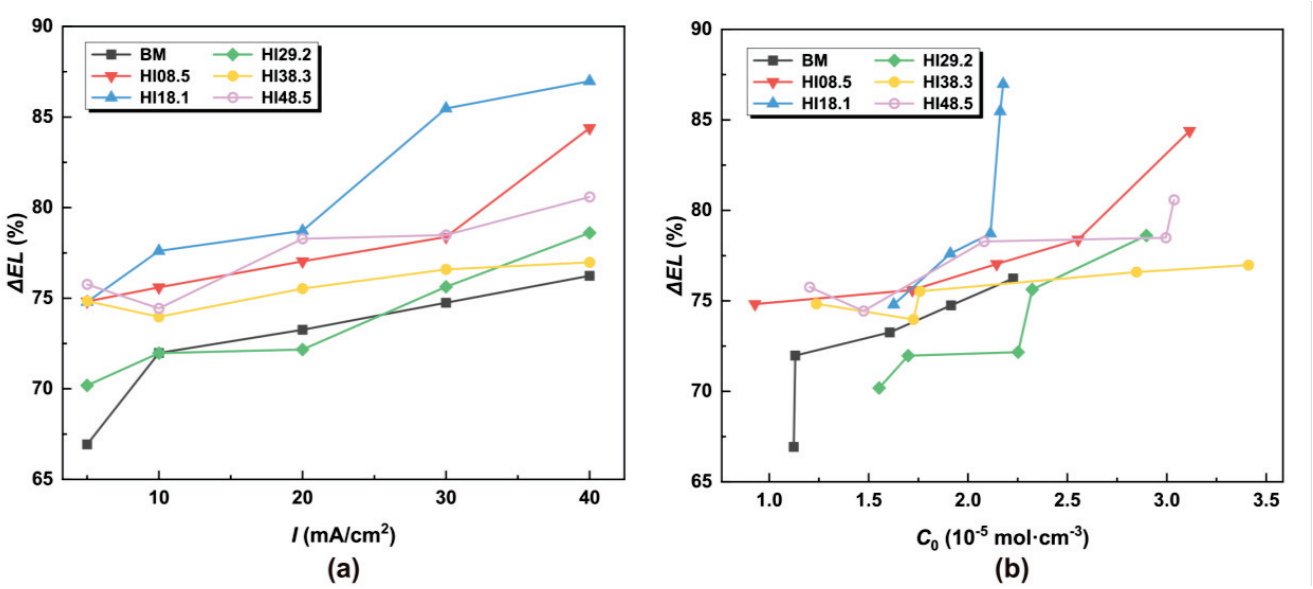


Figure 10. ΔEL under different hydrogen charging current densities and hydrogen concentrations: (**a**) under different I, (**b**) under different C_0.

Without hydrogen, the tensile fracture surfaces under different heat inputs were characterized by ductile fracture. Dimple structures dominated the fracture surface, and dense small dimples were distributed around large ones. Furthermore, there was an apparent necking phenomenon. With the increase in heat input, the area and content of large dimples in the fracture surface increased, indicating that the material's toughness had increased. When it reached HI29.2, small cracks and inclusion holes appeared on the fracture surface. In the presence of hydrogen, the fracture surface showed brittle fracture characteristics. HI08.5 exhibited intergranular fractures, and deep cracks were observed on the fracture surface. The hydrogen accumulated in the specimen reduced the critical stress of crack initiation and had a specific auxiliary effect on crack propagation [50–52]. Therefore, the large cracks propagated in different directions, leading to the rapid fracturing of the specimen under hydrogen charging. At HI18.1, intergranular and transgranular fractures existed in the fracture surface, and a clear boundary between them could be observed. At HI29.2, the fracture surface mainly showed a transgranular fracture, but there were apparent tearing edges on the fracture surface. The surface of the transgranular fracture was truncated at multiple points, and there were apparent step structures between the river-like patterns. The fracture surfaces resulting from HI38.3 and HI48.5 exhibited transgranular brittle fractures, with the surfaces becoming progressively flatter. The step area of the river-like pattern also gradually increased, and the secondary cracks gradually became more extensive and deeper.

3.4. Mechanism of the Difference in Sensitivity of LB and GB to HIC under a Tensile Load

HIC analysis was performed of the metallographic structure of CGHAZ with different heat inputs and of its tensile properties under different hydrogen concentrations. In the absence of hydrogen, the bulk LB enhanced the tensile strength of CGHAZ and improved the material performance [53,54]. Nevertheless, when hydrogen was present, the bulk LB exhibited a high sensitivity to hydrogen embrittlement, and the materials predominantly composed of bulk LB demonstrated a weak resistance to hydrogen embrittlement. In the presence of hydrogen, the composite structure of fine LB and GB had the best resistance to hydrogen embrittlement. The susceptibility to hydrogen embrittlement of the pure GB structure was less affected by changes in the hydrogen concentration. The mechanism of the influence of LB and GB on HIC under tensile load was analyzed, as shown in Figure 12. Hydrogen atoms tended to accumulate in the grain boundaries [55]. When the

hydrogen atoms gathered in the bulk LB grain boundaries, the grain boundaries of long strips tended to initiate intergranular cracks under a tensile load, as shown in Figure 12a. When the microstructure became a composite microstructure of fine LB and GB, as shown in Figure 12b, the extended grain boundaries in the original bulk LB were divided by GB. Segmentation made the intergranular cracks more likely to be blocked, so the fracture surface presented mixed intergranular and transgranular fractures. The fracture was transgranular when the metallographic structure became pure GB, as shown in Figure 12c. Hydrogen atoms only acted on cracks passing through the grain boundaries, so their susceptibility to hydrogen embrittlement was less affected by changes in the hydrogen concentration. Therefore, under a tension load, the fine LB and GB composite structure in Figure 12b shows a better resistance to hydrogen embrittlement. This is a more desirable structure in metal metallurgy and welding processes.

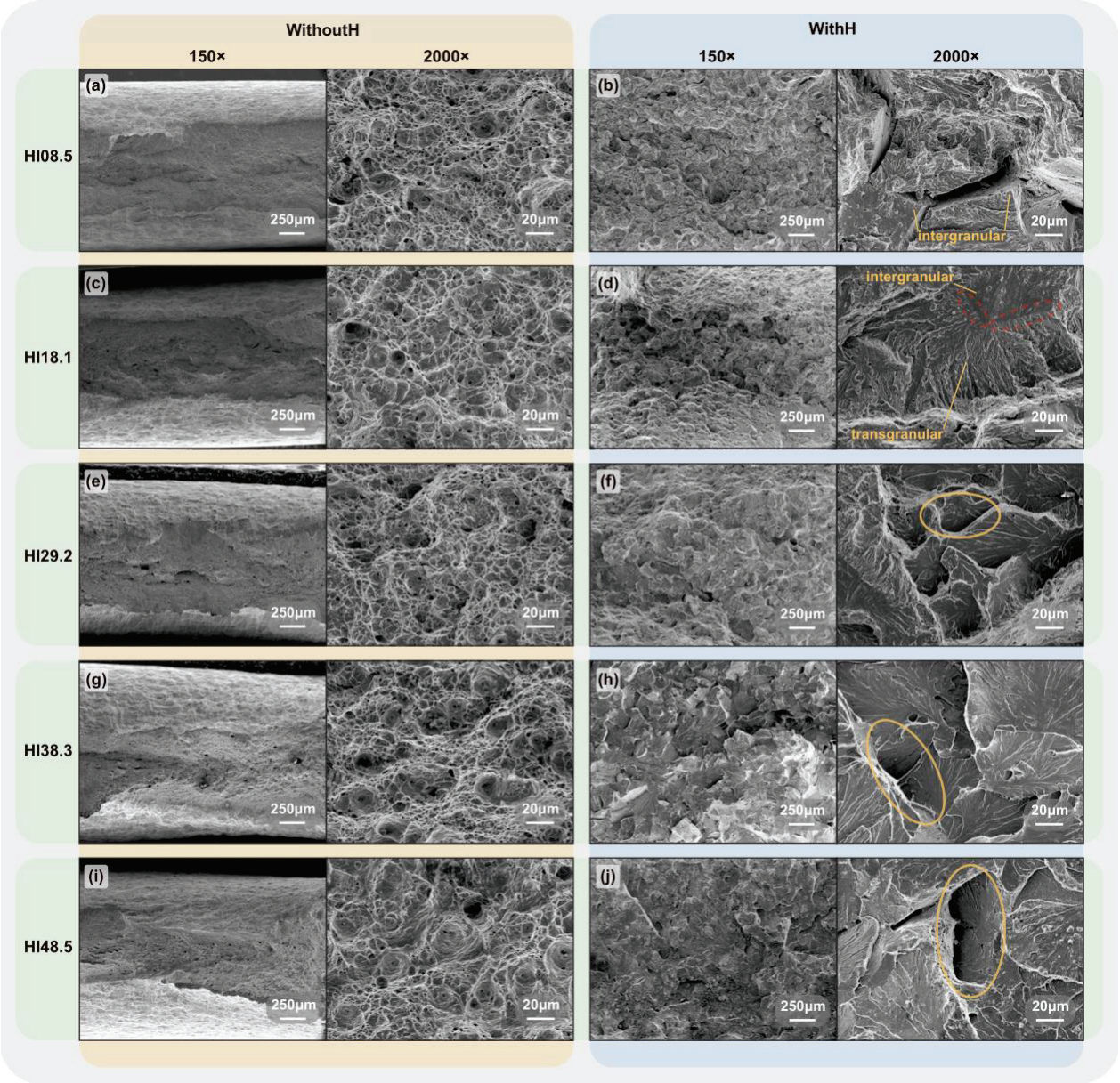


Figure 11. Fracture surface of X80 Steel CGHAZ: without hydrogen—(**a**) HI08.5, (**c**) HI18.1, (**e**) HI29.2, (**g**) HI38.3, (**i**) HI48.5; with hydrogen—(**b**) HI08.5, (**d**) HI18.1, (**f**) HI29.2, (**h**) HI38.3, (**j**) HI48.5.

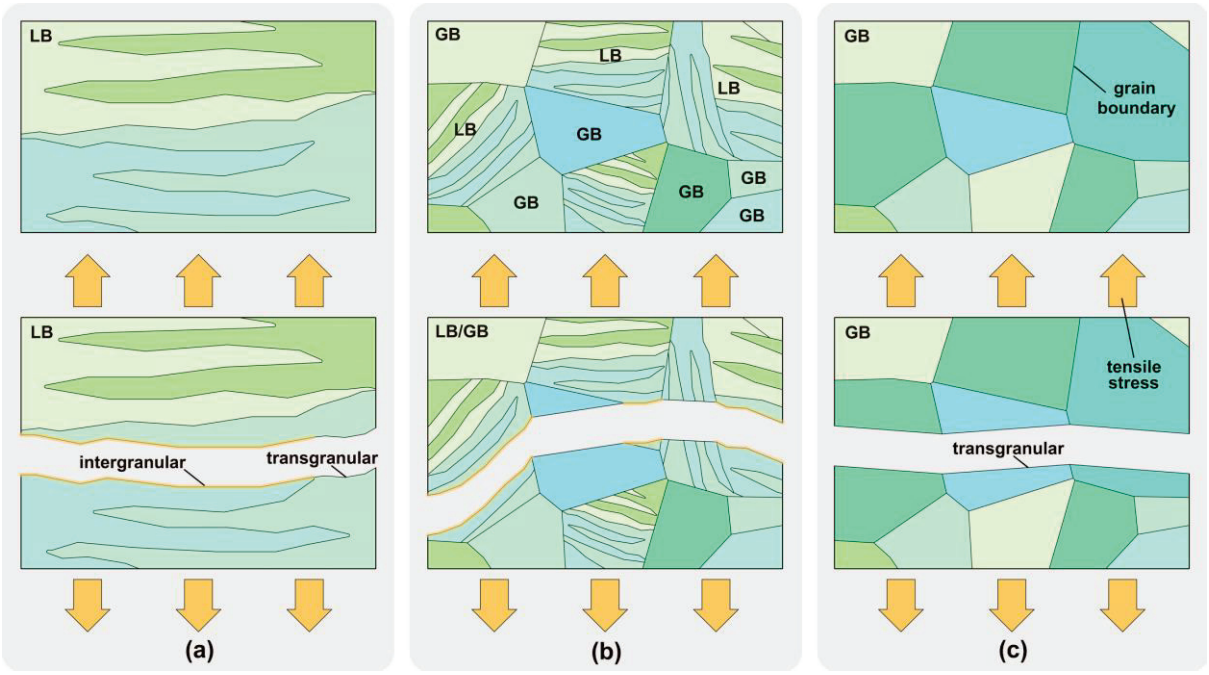


Figure 12. HIC of LB and GB under tension load: (**a**) LB, (**b**) LB and GB, (**c**) GB.

According to the microstructure content and the arresting effect of the different structures on HIC, a comparison of HIC resistance of the different microstructures is summarized in Table 4. This verifies that 11% LB steel had a better HE resistance. Moreover, these LBs should be scattered in GB.

Table 4. Comparison of the microstructure and HIC resistance of CGHAZ.

Label	LB and GB Content	Microstructure Distribution	Fracture Characteristics with Hydrogen	HE Resistance
HI08.5	LB: 88.0% GB: 8.5%	mainly LB, finely intertwined	intergranular fracture	high susceptibility to HE
HI18.1	LB: 70.5% GB: 26.8%		intergranular and transgranular mixed fracture	
HI29.2	LB: 11.0% GB: 82.4%	LB mixed with GB, LB dispersed in GB	transgranular fracture with stepped truncation	minimal susceptibility to HE
HI38.3	LB: 1.7% GB: 94.1%	mainly GB	flat transcrystalline fracture	less affected by hydrogen concentration
HI48.5	LB: 0.8% GB: 95.5%			

4. Conclusions

1. An increment in hydrogen concentration resulted in an increased Young's modulus of BM during the elastic stretching stage. However, this effect was not prominent in CGHAZ. The *UTS* of CGHAZ gradually decreased with the increase in hydrogen concentration. Once the material was exposed to hydrogen, the material plasticity dropped sharply at first and then decreased slowly with the increased hydrogen concentration.
2. The HI 29.2 specimen had the lowest sensitivity to HE under tensile load. The HE sensitivity of HI38.3 and HI48.5 became less affected by the hydrogen concentration gradient. The HE susceptibility of HI18.1 was the highest, and its HE susceptibility increased rapidly with the hydrogen concentration.

3. In the presence of hydrogen, the fracture surface showed brittle fracture characteristics. HI08.5 demonstrated intergranular fracture behavior. HI18.1 showed mixed transgranular and intergranular fractures. For HI29.2, the fracture surface mainly showed a transgranular fracture with stepped truncation. For HI38.3 and HI48.5, the fracture surfaces exhibited transgranular brittle fracture, with the surfaces becoming progressively flatter.
4. Steels predominantly composed of bulk LB were vulnerable to hydrogen embrittlement and exhibit intergranular cracking. A fine LB and GB composite structure can remarkably obstruct intergranular cracks, giving a superior resistance to hydrogen embrittlement. The LB content of hydrogen-resistant steels is expected to be about 11%, and LB should be scattered in GB.

Author Contributions: Conceptualization, J.G. and G.C.; Data curation, J.G. and X.D.; Funding acquisition, X.X. and Z.L.; Methodology, J.G. and J.L.; Resources, X.X. and Z.L.; Supervision, J.L.; Writing—original draft, J.G. and X.D.; Writing—review and editing, J.G., X.X., G.C., Z.L. and J.L. All authors have read and agreed to the published version of the manuscript.

Funding: This research was funded by the Natural Science Foundation of Shandong Province [ZR2020ME094], National Natural Science Foundation of China [52004323], Senior Foreign Expert Project Foundation [G2022152003L], and CNPC Innovation Foundation [2022DQ02-0502].

Data Availability Statement: The data supporting this study's findings are available from the corresponding author upon reasonable request.

Conflicts of Interest: The authors declare that they have no known competing financial interest or personal relationships that could have appeared to influence the work reported in this paper.

References

1. Koohi-Fayegh, S.; Rosen, M.A. A Review of Energy Storage Types, Applications and Recent Developments. *J. Energy Storage* **2020**, *27*, 101047. [CrossRef]
2. Smith, C.; Hill, A.K.; Torrente-Murciano, L. Current and Future Role of Haber–Bosch Ammonia in a Carbon-Free Energy Landscape. *Energy Environ. Sci.* **2020**, *13*, 331–344. [CrossRef]
3. Abdin, Z.; Zafaranloo, A.; Rafiee, A.; Mérida, W.; Lipiński, W.; Khalilpour, K.R. Hydrogen as an Energy Vector. *Renew. Sustain. Energy Rev.* **2020**, *120*, 109620. [CrossRef]
4. Dawood, F.; Anda, M.; Shafiullah, G.M. Hydrogen Production for Energy: An Overview. *Int. J. Hydrogen Energy* **2020**, *45*, 3847–3869. [CrossRef]
5. Messaoudani, Z.L.; Rigas, F.; Binti Hamid, M.D.; Che Hassan, C.R. Hazards, Safety and Knowledge Gaps on Hydrogen Transmission via Natural Gas Grid: A Critical Review. *Int. J. Hydrogen Energy* **2016**, *41*, 17511–17525. [CrossRef]
6. Jaworski, J.; Kułaga, P.; Blacharski, T. Study of the Effect of Addition of Hydrogen to Natural Gas on Diaphragm Gas Meters. *Energies* **2020**, *13*, 3006. [CrossRef]
7. Zhang, P.; Laleh, M.; Hughes, A.E.; Marceau, R.K.W.; Hilditch, T.; Tan, M.Y. A Systematic Study on the Influence of Electrochemical Charging Conditions on the Hydrogen Embrittlement Behaviour of a Pipeline Steel. *Int. J. Hydrogen Energy* **2023**, *48*, 16501–16516. [CrossRef]
8. Zhang, L.; Shen, H.; Lu, K.; Cao, W.; Sun, Y.; Fang, Y.; Xing, Y.; Du, Y.; Lu, M. Investigation of Hydrogen Concentration and Hydrogen Damage on API X80 Steel Surface under Cathodic Overprotection. *Int. J. Hydrogen Energy* **2017**, *42*, 29888–29896. [CrossRef]
9. Singh, V.; Singh, R.; Arora, K.S.; Mahajan, D.K. Hydrogen Induced Blister Cracking and Mechanical Failure in X65 Pipeline Steels. *Int. J. Hydrogen Energy* **2019**, *44*, 22039–22049. [CrossRef]
10. Sanchez, L.; Cong, H. AC Interference on Hydrogen Absorption in Low Carbon Steel under Cathodic Protection. *Int. J. Hydrogen Energy* **2023**, *48*, 1202–1217. [CrossRef]
11. Zhang, T.; Zhao, W.; Li, T.; Zhao, Y.; Deng, Q.; Wang, Y.; Jiang, W. Comparison of Hydrogen Embrittlement Susceptibility of Three Cathodic Protected Subsea Pipeline Steels from a Point of View of Hydrogen Permeation. *Corros. Sci.* **2018**, *131*, 104–115. [CrossRef]
12. An, T.; Zhang, S.; Feng, M.; Luo, B.; Zheng, S.; Chen, L.; Zhang, L. Synergistic Action of Hydrogen Gas and Weld Defects on Fracture Toughness of X80 Pipeline Steel. *Int. J. Fatigue* **2019**, *120*, 23–32. [CrossRef]
13. Zhou, D.; Li, T.; Huang, D.; Wu, Y.; Huang, Z.; Xiao, W.; Wang, Q.; Wang, X. The Experiment Study to Assess the Impact of Hydrogen Blended Natural Gas on the Tensile Properties and Damage Mechanism of X80 Pipeline Steel. *Int. J. Hydrogen Energy* **2021**, *46*, 7402–7414. [CrossRef]

14. Li, X.; Ma, X.; Zhang, J.; Akiyama, E.; Wang, Y.; Song, X. Review of Hydrogen Embrittlement in Metals: Hydrogen Diffusion, Hydrogen Characterization, Hydrogen Embrittlement Mechanism and Prevention. *Acta Metall. Sin. (Engl. Lett.)* **2020**, *33*, 759–773. [CrossRef]
15. Zhao, H.; Chakraborty, P.; Ponge, D.; Hickel, T.; Sun, B.; Wu, C.-H.; Gault, B.; Raabe, D. Hydrogen Trapping and Embrittlement in High-Strength Al Alloys. *Nature* **2022**, *602*, 437–441. [CrossRef] [PubMed]
16. Liu, Q.; Venezuela, J.; Zhang, M.; Zhou, Q.; Atrens, A. Hydrogen Trapping in Some Advanced High Strength Steels. *Corros. Sci.* **2016**, *111*, 770–785. [CrossRef]
17. Sun, Y.; Cheng, Y.F. Hydrogen Permeation and Distribution at a High-Strength X80 Steel Weld under Stressing Conditions and the Implication on Pipeline Failure. *Int. J. Hydrogen Energy* **2021**, *46*, 23100–23112. [CrossRef]
18. Sun, Y.; Cheng, Y.F. Thermodynamics of Spontaneous Dissociation and Dissociative Adsorption of Hydrogen Molecules and Hydrogen Atom Adsorption and Absorption on Steel under Pipelining Conditions. *Int. J. Hydrogen Energy* **2021**, *46*, 34469–34486. [CrossRef]
19. Köse, C. Effect of Heat Input and Post Weld Heat Treatment on the Texture, Microstructure and Mechanical Properties of Laser Beam Welded AISI 317L Austenitic Stainless Steel. *Mater. Sci. Eng. A* **2022**, *855*, 143966. [CrossRef]
20. Köse, C. Heat Treatment and Heat Input Effects on the Dissimilar Laser Beam Welded AISI 904L Super Austenitic Stainless Steel to AISI 317L Austenitic Stainless Steel: Surface, Texture, Microstructure and Mechanical Properties. *Vacuum* **2022**, *205*, 111440. [CrossRef]
21. Köse, C.; Topal, C. Texture, Microstructure and Mechanical Properties of Laser Beam Welded AISI 2507 Super Duplex Stainless Steel. *Mater. Chem. Phys.* **2022**, *289*, 126490. [CrossRef]
22. Panin, S.V.; Maruschak, P.O.; Vlasov, I.V.; Syromyatnikova, A.S.; Bolshakov, A.M.; Berto, F.; Prentkovskis, O.; Ovechkin, B.B. Effect of Operating Degradation in Arctic Conditions on Physical and Mechanical Properties of 09Mn2Si Pipeline Steel. *Procedia Eng.* **2017**, *178*, 597–603. [CrossRef]
23. Yang, Y.; Shi, L.; Xu, Z.; Lu, H.; Chen, X.; Wang, X. Fracture Toughness of the Materials in Welded Joint of X80 Pipeline Steel. *Eng. Fract. Mech.* **2015**, *148*, 337–349. [CrossRef]
24. Li, R.; Zuo, X.; Hu, Y.; Wang, Z.; Hu, D. Microstructure and Properties of Pipeline Steel with a Ferrite/Martensite Dual-Phase Microstructure. *Mater. Charact.* **2011**, *62*, 801–806. [CrossRef]
25. Li, J.; Li, H.; Peng, W.; Xiang, T.; Xu, Z.; Yang, J. Effect of Simulated Welding Thermal Cycles on Microstructure and Mechanical Properties of Coarse-Grain Heat-Affected Zone of High Nitrogen Austenitic Stainless Steel. *Mater. Charact.* **2019**, *149*, 206–217. [CrossRef]
26. Sun, Y.; Fujii, H.; Imai, H.; Kondoh, K. Suppression of Hydrogen-Induced Damage in Friction Stir Welded Low Carbon Steel Joints. *Corros. Sci.* **2015**, *94*, 88–98. [CrossRef]
27. Duan, R.H.; Wang, Y.Q.; Luo, Z.A.; Wang, G.D.; Xie, G.M. Hydrogen Embrittlement Behavior in the Nugget Zone of Friction Stir Welded X100 Pipeline Steel. *Int. J. Hydrogen Energy* **2023**, *48*, 8296–8309. [CrossRef]
28. Zhao, W.; Zhang, T.; Zhao, Y.; Sun, J.; Wang, Y. Hydrogen Permeation and Embrittlement Susceptibility of X80 Welded Joint under High-Pressure Coal Gas Environment. *Corros. Sci.* **2016**, *111*, 84–97. [CrossRef]
29. Zhang, T.; Zhao, W.; Deng, Q.; Jiang, W.; Wang, Y.; Wang, Y.; Jiang, W. Effect of Microstructure Inhomogeneity on Hydrogen Embrittlement Susceptibility of X80 Welding HAZ under Pressurized Gaseous Hydrogen. *Int. J. Hydrogen Energy* **2017**, *42*, 25102–25113. [CrossRef]
30. Deng, Q.; Zhao, W.; Jiang, W.; Zhang, T.; Li, T.; Zhao, Y. Hydrogen Embrittlement Susceptibility and Safety Control of Reheated CGHAZ in X80 Welded Pipeline. *J. Mater. Eng. Perform.* **2018**, *27*, 1654–1663. [CrossRef]
31. Zhang, Y.; Liu, N.; Li, Z.; Zhang, G.; Yuan, H.; Xu, W.; Gao, Z.; Mi, J. Gleeble Experiments Concerning Dendrite Re-Melting and Its Role in Microstructural Evolution in Spray Formed High-Alloy Metals. *Rare Met.* **2011**, *30*, 401–404. [CrossRef]
32. Sirin, K.; Sirin, S.Y.; Kaluc, E. Influence of the Interpass Temperature on T8/5 and the Mechanical Properties of Submerged Arc Welded Pipe. *J. Mater. Process. Technol.* **2016**, *238*, 152–159. [CrossRef]
33. Xu, W.W.; Wang, Q.F.; Pan, T.; Su, H.; Yang, C.F. Effect of Welding Heat Input on Simulated HAZ Microstructure and Toughness of a V-N Microalloyed Steel. *J. Iron Steel Res. Int.* **2007**, *14*, 234–239. [CrossRef]
34. Gou, J.; Nie, R.; Xing, X.; Li, Z.; Cui, G.; Liu, J.; Deng, X.; Cheng, Y.F. Hydrogen-Induced Cracking of Welded X80 Steel Studies by Experimental Testing and Molecular Dynamics Modeling. *Corros. Sci.* **2023**, *214*, 111027. [CrossRef]
35. Huda, N.; Midawi, A.; Gianetto, J.A.; Gerlich, A.P. Continuous Cooling Transformation Behaviour and Toughness of Heat-Affected Zones in an X80 Line Pipe Steel. *J. Mater. Res. Technol.* **2021**, *12*, 613–628. [CrossRef]
36. Xing, X.; Cheng, R.; Cui, G.; Liu, J.; Gou, J.; Yang, C.; Li, Z.; Yang, F. Quantification of the Temperature Threshold of Hydrogen Embrittlement in X90 Pipeline Steel. *Mater. Sci. Eng. A* **2021**, *800*, 140118. [CrossRef]
37. Li, X.; Wang, Y.; Zhang, P.; Li, B.; Song, X.; Chen, J. Effect of Pre-Strain on Hydrogen Embrittlement of High Strength Steels. *Mater. Sci. Eng. A* **2014**, *616*, 116–122. [CrossRef]
38. Gou, J.; Deng, X.; Cui, G.; Xing, X.; Li, Z. Research on Hydrogen Permeation in the X80 Steel Heat-Affected Zone with Different Heat Inputs. *J. Phys. Conf. Ser.* **2022**, *2383*, 012140. [CrossRef]
39. Koren, E.; Hagen, C.M.; Wang, D.; Lu, X.; Johnsen, R.; Yamabe, J. Experimental Comparison of Gaseous and Electrochemical Hydrogen Charging in X65 Pipeline Steel Using the Permeation Technique. *Corros. Sci.* **2023**, *215*, 111025. [CrossRef]

40. Van den Eeckhout, E.; Verbeken, K.; Depover, T. Methodology of the Electrochemical Hydrogen Permeation Test: A Parametric Evaluation. *Int. J. Hydrogen Energy* **2023**. [CrossRef]
41. Peral, L.B.; Amghouz, Z.; Colombo, C.; Fernández-Pariente, I. Evaluation of Hydrogen Trapping and Diffusion in Two Cold Worked CrMo(V) Steel Grades by Means of the Electrochemical Hydrogen Permeation Technique. *Theor. Appl. Fract. Mech.* **2020**, *110*, 102771. [CrossRef]
42. Cheng, Y.F. Analysis of Electrochemical Hydrogen Permeation through X-65 Pipeline Steel and Its Implications on Pipeline Stress Corrosion Cracking. *Int. J. Hydrogen Energy* **2007**, *32*, 1269–1276. [CrossRef]
43. Addach, H.; Berçot, P.; Rezrazi, M.; Takadoum, J. Study of the Electrochemical Permeation of Hydrogen in Iron. *Corros. Sci.* **2009**, *51*, 263–267. [CrossRef]
44. Zhao, W.; Zhang, T.; He, Z.; Sun, J.; Wang, Y. Determination of the Critical Plastic Strain-Induced Stress of X80 Steel through an Electrochemical Hydrogen Permeation Method. *Electrochim. Acta* **2016**, *214*, 336–344. [CrossRef]
45. Xu, Z.; Zhang, P.; Meng, G.; Wang, Y.; Wang, J.; Shao, Y.; Wang, F. Influence of Low Tensile Stress on the Kinetics of Hydrogen Permeation and Evolution Behavior in Alkaline Environment. *Int. J. Hydrogen Energy* **2022**, *47*, 33803–33812. [CrossRef]
46. Díaz, A.; Zafra, A.; Martínez-Pañeda, E.; Alegre, J.M.; Belzunce, J.; Cuesta, I.I. Simulation of Hydrogen Permeation through Pure Iron for Trapping and Surface Phenomena Characterisation. *Theor. Appl. Fract. Mech.* **2020**, *110*, 102818. [CrossRef]
47. Jebaraj, J.J.M.; Morrison, D.J.; Suni, I.I. Hydrogen Diffusion Coefficients through Inconel 718 in Different Metallurgical Conditions. *Corros. Sci.* **2014**, *80*, 517–522. [CrossRef]
48. Meng, G.; Sun, F.; Wang, S.; Shao, Y.; Zhang, T.; Wang, F. Effect of Electrodeposition Parameters on the Hydrogen Permeation during Cu–Sn Alloy Electrodeposition. *Electrochim. Acta* **2010**, *55*, 2238–2245. [CrossRef]
49. Izadi, H.; Tavakoli, M.; Moayed, M.H. Effect of Thermomechanical Processing on Hydrogen Permeation in API X70 Pipeline Steel. *Mater. Chem. Phys.* **2018**, *220*, 360–365. [CrossRef]
50. Olden, V.; Alvaro, A.; Akselsen, O.M. Hydrogen Diffusion and Hydrogen Influenced Critical Stress Intensity in an API X70 Pipeline Steel Welded Joint-Experiments and FE Simulations. *Int. J. Hydrogen Energy* **2012**, *37*, 11474–11486. [CrossRef]
51. Kumai, B.; Hojo, T.; Koyama, M.; Akiyama, E.; Waki, H.; Nagasaka, A. Pre-Strain Effects on Critical Stress and Hydrogen Content for Hydrogen-Induced Quasi-Cleavage Fracture in a TRIP-Aided Bainitic Ferrite Steel: Martensitic Transformation, Matrix Damage, and Strain Aging. *Int. J. Hydrogen Energy* **2020**, *45*, 27920–27928. [CrossRef]
52. Sun, Y.; Frank Cheng, Y. Hydrogen-Induced Degradation of High-Strength Steel Pipeline Welds: A Critical Review. *Eng. Fail. Anal.* **2022**, *133*, 105985. [CrossRef]
53. Krauss, G.; Thompson, S.W. Ferritic Microstructures in Continuously Cooled Low- and Ultralow-Carbon Steels. *ISIJ Int.* **1995**, *35*, 937–945. [CrossRef]
54. Li, C.; Wang, Y.; Han, T.; Han, B.; Li, L. Microstructure and Toughness of Coarse Grain Heat-Affected Zone of Domestic X70 Pipeline Steel during in-Service Welding. *J. Mater. Sci.* **2011**, *46*, 727–733. [CrossRef]
55. Xing, X.; Gou, J.; Li, F.; Zhang, Y.; Cheng, J.; Wang, Y.; Liu, J.; Cui, G.; Li, Z.; Zhang, P.; et al. Hydrogen Effect on the Intergranular Failure in Polycrystal Ɑ-Iron with Different Crystal Sizes. *Int. J. Hydrogen Energy* **2021**, *46*, 36528–36538. [CrossRef]

Disclaimer/Publisher's Note: The statements, opinions and data contained in all publications are solely those of the individual author(s) and contributor(s) and not of MDPI and/or the editor(s). MDPI and/or the editor(s) disclaim responsibility for any injury to people or property resulting from any ideas, methods, instructions or products referred to in the content.

applied sciences

MDPI

Article

The Use of Augmented Reality for the Management of Equipment Ageing with a Virtual Sensor

Giuseppa Ancione [1,*], Rebecca Saitta [1], Paolo Bragatto [2], Giacomo Fiumara [3] and Maria Francesca Milazzo [1]

[1] Dipartimento di Ingegneria, University of Messina, 98166 Messina, Italy; mfmilazzo@unime.it (M.F.M.)
[2] Dipartimento di Ingegneria, Università Campus Biomedico, 00128 Roma, Italy
[3] Dipartimento di Scienze Matematiche e Informatiche, Scienze Fisiche e Scienze della Terra, University of Messina, 98166 Messina, Italy
* Correspondence: giusi.ancione@unime.it

Abstract: Much of the equipment that is used in the chemical and process industry and for handling or treating hazardous substances is subject to deterioration. To manage the risk of major accidents due to this deterioration, the current legislation requires periodic controls that must be carried out to verify the health conditions (ageing). To support the inspectors performing this task, a virtual sensor has been designed and developed. It is a system composed of hardware and software that uses mathematical models and augmented reality to assist in on-field inspections for monitoring and predicting equipment ageing. Currently, there are no AR devices to perform inspections aimed at verifying the integrity of equipment. The virtual sensor collects ageing-related information and returns the corrosion rate, the probability of the critical pit, the corrosion evolution through iso-contour corrosion maps, and the RUL; finally, it allows visualising the equipment condition through augmented reality, (e.g., by means of thickness maps and tables that overlay the equipment). The aim of this paper is to present the graphical interface of the software application, which has been improved to minimise errors due to human–machine interaction. A large diesel storage tank has been used to show how the virtual sensor works.

Keywords: equipment ageing; inspection; augmented reality; safety; chemical industry

1. Introduction

Innovative technologies, such as the Internet of Things, artificial intelligence, big data, cloud computing, cyber–physical systems, interconnectivity, augmented reality, etc., characterise the development of Industry 4.0 by means of the integration of physical and digital systems. They bring many advantages throughout the industrial sector, which take the form of increasing efficiency, profitability, innovation, customisation, and performance [1]. Another important aspect to note, as a strength element for Industry 4.0, is the potential support in the improvement of the safety management, even if, currently, there are only a few studies that analyse the integration of safety management and Industry 4.0 [2]. Among them, Gisbert et al. [3] considered that information technology and wireless communication allow for continuous and effective detection of workplace hazards, while Beetz et al. [4] stated that the development of robots dedicated to safety may be able to recognise actions that can cause injury to workers. Podgorski et al. [5] observed that personal protective equipment (PPE) supplied with automation technology is being adopted in smart factories to achieve better safety management. Other authors instead highlighted that artificial intelligence and its applications have a lot of potential, especially as regards predictive maintenance, for example, by improving the diagnostics of critical equipment failures [6,7] and of rotating machines [8] or transport systems [9] by reducing or eliminating threats to the safety of people, goods, and the environment.

Industry 4.0 aims to digitise production by sharing and analysing information as well as connecting humans and machines [10]. The machine–machine and human–machine

interactions represent fundamental aspects of this digitalisation process [2], but these are not free from having disadvantages. Emerging and experimental technologies cause a deep change in society, which needs time to adapt and normalise itself through new paradigms, procedures, and labour laws. This requires companies to continuously update, but it often becomes unsustainable for most of them, especially for small and medium ones. Another aspect to be considered is that these systems create absolute dependence on the technology since within these interactions, the machines no longer only represent the arm that carries out the heavy, repetitive, and/or dangerous work, but increasingly play a decision-making role [11]. Particular attention must be given to these technologies, especially when they are involved in safety. In many cases, technology improves safety, but it can also add new industrial and occupational risks to the traditional ones, in which the human factor can be considered the main link between both types of risk [12]. Siemieniuch et al. [13] also highlight that safety management, in the context of Industry 4.0, requires more research efforts on human factors and ergonomics. In this context, particular attention must be given to the establishments under the Seveso Directive [14], in which the release of hazardous materials could be the cause of severe accidents, the so-called major accident hazards (e.g., fires, explosions, and toxic dispersions) impacting people and the environment. Seveso establishments include refineries, petrochemical plants, and oil-derived depots. All these sites feature several large aboveground storage tanks, which are always critical for the control of major accident hazards.

Some scholars have discussed the potential of smart systems for improving the control of major accident hazards due to the use of hazardous materials in different industries (energy, chemical and manufacturing sectors, oil and gas, transportation, etc.) [15]. Some innovative solutions have been presented in the literature: Bragatto et al. [16] defined RFID technology supporting effective risk management in chemical warehouses; Ancione et al. [17] developed a real-time visual guidance system for cranes to manage risks due to collisions during the lifting of loads in working places; Gnoni et al. [18] defined an IOT-based system to prevent injuries in assembling line production systems; Mennuti et al. [19] used wireless sensor networks based on acoustic emissions to monitor some damages in various structures. As regards the use of innovative technologies, evidence justifies a particular interest towards augmented reality (AR) in the industrial context. These works highlight the increasing request to make industrial activities more efficient, safe, and economic. In this context, coupled with other technologies, AR contributes to the achievement of this goal.

The literature outlines the main applications of AR, referring to various industrial sectors. However, there are some limitations that are mainly related to human–machine interactions [20]. Egger and Masood [21] described the recent spread of AR technologies and stated that these are not yet ready for industrial implementation in some areas, whereas they are in other sectors. The most common applications of AR concern training for the management of operations [22–24] and assisting in the routine maintenance of industrial equipment by following visual instructions and interactive guides superimposed on the real equipment for a more effective workflow, even with remote assistance [25–29]. Yang et al. [30] described how AR, combined with instant messaging and image recognition technologies, could greatly assist chemical plant inspections to solve the problems associated with low efficiency and poor standardisation.

The use of AR in the inspection sector appears as one of the most important in the industrial context, where AR represents a promising technique for improving the transfer of information from the digital to the operator in a smart and non-intrusive way [31,32]. Depending on the industrial sector and the scope, inspections could typically involve controls to be performed on products [33,34] or equipment; in the first case, it concerns the detection of design discrepancies, while in the second one, it is used to intercept possible causes of malfunction. The execution of this activity is therefore essential in the manufacturing process, especially where many factors, such as the complexity of the products and the inability of the operator to comply with certain assembly sequences,

can potentially lead to mistakes or design changes. The control of the equipment for maintenance purposes or due to malfunctions is important for the production continuity and safety purposes, especially in the chemical industry due to the reasons discussed above. A critical aspect related to the inspections concerns the annotation and formalisation of detected errors and design changes, and the subsequent sharing of the information with the technical office; these activities require a high mental workload [35].

In the context of major accident hazard industries, it is possible to find applications of AR for the following scopes:

- to overcome the limit of using paper-based checklists during on-site inspections. The use of AR technologies makes the inspection more efficient and advanced than the conventional approaches [36,37];
- to help operators in performing tasks and operations by means of man–machine interaction through the addition of information to the real work environment [32,34,38,39] (such as live video streams, pictures, or instructions);
- to support education for managers and employees with computer-generated 3D environments [40,41] and train in hazardous materials handling by means of simulations [38].

Therefore, the literature shows that currently, this technology is not mature enough to perform inspections aimed at verifying the integrity of equipment and visualising the deterioration level. As part of a recently concluded research project [42], a virtual sensor has been developed to elaborate and visualise information relating to the deterioration of critical equipment; it also produces prognostic estimates of the corrosion rate, the critical pit probability, the evolution of the material corrosion, and the residual useful life (RUL) of the equipment. The virtual sensor supports on-field inspections by visualising the information in AR via a mobile device display, such as a smartphone or a tablet or via wearable device (e.g., smart glasses). During the first phase of the development of this virtual sensor, greater importance has been given to the optimisation of the processes for the implementation of the mathematical models that use several different types of input data. In this manuscript, the investigation of the human–machine interaction (HMI) in using this device is presented; this work resulted in a user-friendly interface, which improved the usability of the software, making it accessible even to personnel that are not experts in advanced technologies. The manuscript is organised as follows. Section 2 provides a short description of the models and the software that represents the virtual sensor; Section 3 describes the methodology for the development of a user-friendly interface of the virtual sensor, reducing the errors due to HMI; Section 4 illustrates the results, discusses them, and presents some future improvements; finally, Section 5 gives the conclusions of this work.

2. Architecture of the Virtual Sensor

A virtual sensor for ageing management is a tool supporting inspectors in major accident hazard establishments. Inspectors usually need to understand the actual deterioration level of critical equipment, acquire information that cannot be found with a visual inspection, and finally, elaborate the metrics related to the ageing status and about the adequacy of the ageing management.

The system has been designed to collect various information, process the acquired data, produce prognostic estimates regarding the corrosion rate, the critical pit probability, the evolution of the corrosion surface, and the RUL of the equipment, and finally, it allows visualising the results by using AR. Therefore, the sensor is composed of four elements: the dataset, which is fed through the collection of information about the equipment to be analysed; the set of the models; the software for the management of the data and the elaboration of ageing-related metrics; the tool for the visualisation of the results in AR.

The models used by the virtual sensor are:

- the ageing fishbone model for the estimation of the overall adequacy index (also simply named ageing index) [43];

- the failure frequency model for the quantification of the failure frequency due to the equipment deterioration by taking into account the ageing management;
- the model for the identification of the probability of the critical pit, based on the extreme values theory (Gumbel distribution model) [44];
- the model for the calculation of the residual useful lifetime based on a combination of the Gumbel distribution and the Bayes theorem [45];
- an advanced spatial interpolation technique of the thickness data to produce corrosion maps (the kriging interpolation model) [46].

More details about these models are given by Ancione et al. [42].

The virtual sensor is made up of an "App Desktop" that acquires and processes inputs (the equipment information) and an "App Mobile" for the AR visualisation of the acquired and processed data.

2.1. Methodology for Ageing Monitoring and Prediction

The methodology for the ageing monitoring and prediction consists of the three steps, shown in Figure 1. In the first phase, the data for the definition of the ageing conditions of the equipment are collected from various sources (e.g., thickness measurements of the material's equipment, accelerating and slowing down factors with respect to the ageing, etc.). After being acquired, these data are pre-processed (second phase) to be ready for the subsequent phase (processing). The data processing (third phase) consists of the execution of the above-mentioned models.

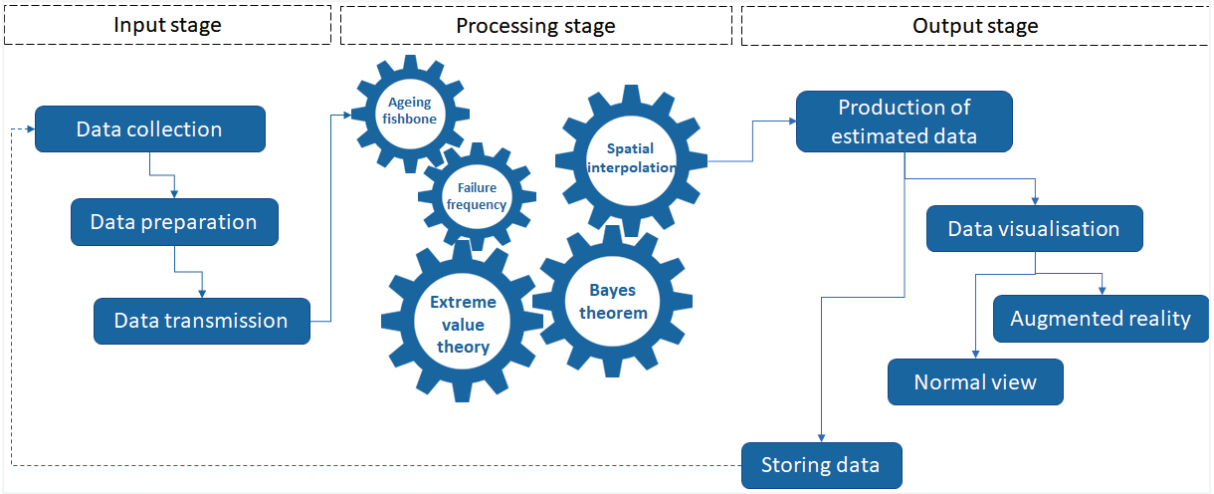


Figure 1. Methodology of data elaboration of the virtual sensor.

The outputs of these models can be displayed by using a PC, which is the common way to view the results, or by means of a smartphone, a tablet, or finally, by a wearable device, such as smart glasses. A QR code (placed on the equipment) is used as marker for the equipment identification and to associate the elaborated outcomes. Smart glasses allow an increased view of the produced information to be displayed by overlapping the iso-level corrosion maps on the surface of the corresponding equipment (augmented reality); other outputs are accessible through tables and graphs and shown on the sides of the equipment. The third phase includes the data storage.

2.2. Hardware

The hardware used for the construction of the virtual sensor includes:

- PC with CPU: Intel® Core™ i5 (3 GHz); RAM DDR4: 16 GB, connectivity: USB Type C™, Wi-Fi 6, Bluetooth® 5; operative system: Windows 10 pro 64 bit;
- Smartphone with operating system: Android v.11, compatible with Google Play Service for AR;

- Smart glasses: Epson Moverio BT-40S.

2.3. Software

The programming language used to create the App Desktop was Python [47], along with some of its support libraries such as Matplotlib [48] for the creation of graphs, Numpy [49] and Pandas [50] for data processing, and PyKrige [51] for data interpolation through the kriging technique. Several different types of technology were used to realise the mobile application:

- Unity 2021.1.13.f1, which is a multiplatform graphic engine, allowed us to create interactive content and live 3D visualisation [52];
- The C# programming language was used within Unity to make the content dynamic and allow the user to interact with it;
- Blender 2.93 [53] was used as software for modelling and was chosen to reproduce the equipment to study and upload the 3D model on Unity.

3. Development of a User-Friendly Interface of the Virtual Sensor

The development of the interface for the virtual sensor is based on a procedure that aims at the reduction in errors due to HMI. It consists of:

1. Virtual sensor testing;
2. Assessment of human–machine interaction and identification of criticalities in human–machine interaction;
3. Interface development;
4. Virtual sensor testing.

3.1. Human–Machine Interaction

Figure 2 shows the flow diagram of the interaction between the inspector (user) and the App Desktop. The dotted line indicates a path that can be omitted, i.e., the case when the user does not elaborate future estimates but only visualises the corrosion surface and the parameters related to the current and past inspections. Figure 3 illustrates the interaction between the inspector and the App Mobile.

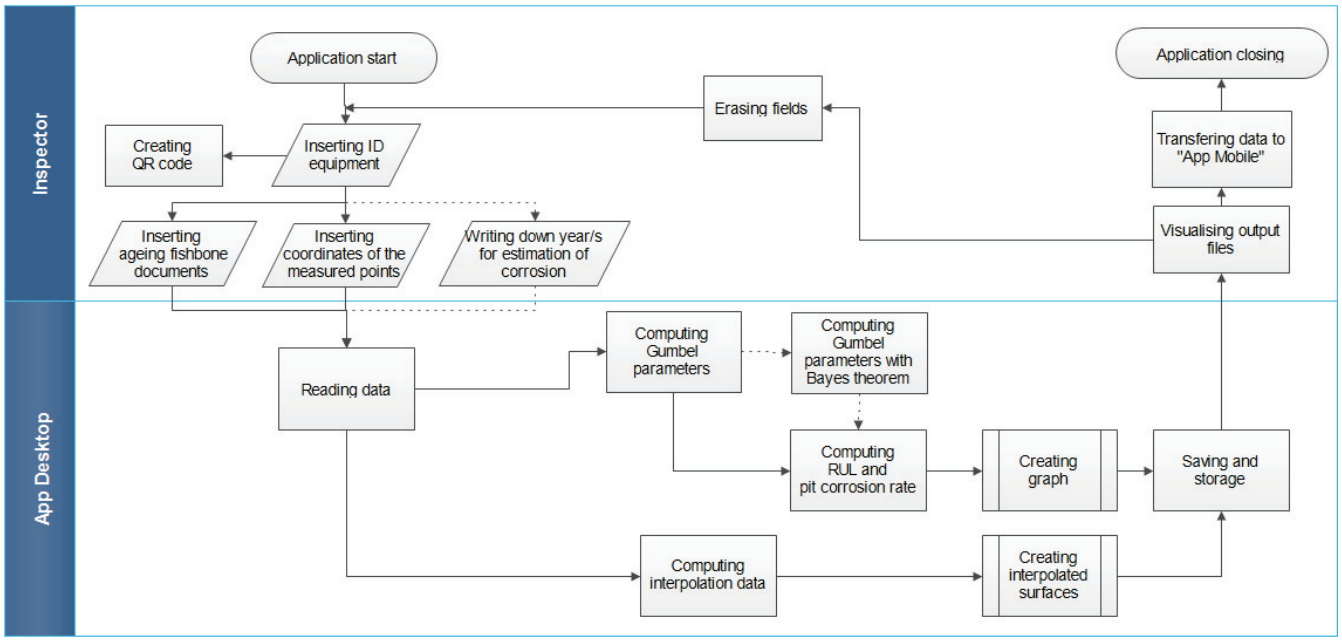


Figure 2. Flow diagram interaction between the inspector and the App Desktop.

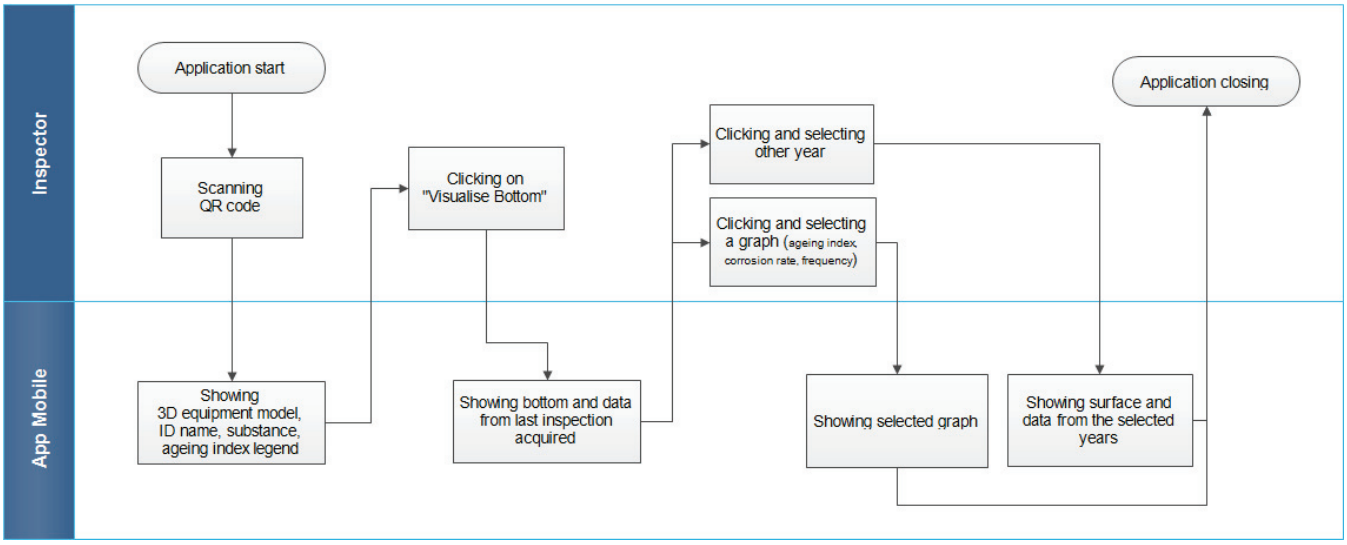


Figure 3. Flow diagram interaction between the inspector and the App Mobile.

To use the virtual sensor, the inspector starts the App Desktop and enters the equipment ageing data. This requires that he/she uploads:

- the Excel files of the inspection carried out by means the ageing fishbone model [21] (ageing index method, whose application is suggested by the Italian Ministry of the Environment);
- the text files containing the thickness measurements sampled during the inspections with the relative spatial coordinates.

Finally, the inspector can choose whether to elaborate information relating only to the current state of the equipment, to the past, or to the future, i.e., by referring to the dates of the previous inspections or selecting from 1 to 5 different future years. He/she can choose to also produce the estimates of the ageing-related metrics (critical pit probability, RUL, corrosion rate, etc.) and the corrosion surfaces at the same time.

Then, the application reads and codes these data, processes them according to the implemented models (see Section 2.1), and creates graphs and tables of the ageing parameters for a selected year. Once the processing is complete, the application automatically stores the documents in the defined path. Next, the inspector can visualise the information produced to migrate it to the App Mobile, or reset the interface fields to make a new entry and perform a new process. A further operation that the inspector can perform by using the App Desktop, after entering the name of the equipment, is the generation of the QR code to be placed close to the equipment to be examined if it has not been coded yet. The final step is to exit the App Desktop and then start the App Mobile.

3.2. Interface Testing

To test the virtual sensor, a hydrocarbon storage tank included in a tank farm was selected. The vessel is an atmospheric tank with a fixed roof made of carbon steel and containing diesel. It has been operating for over 55 years. Two bottom inspection datasets from different years were available (1990 was the first inspection year and 2019 the second one). During both inspections, the thickness was measured at a number of points. The nominal thickness of the bottom is 8 mm, while the minimum detected thickness was 6.1 mm in 1990 and 2.8 mm in 2019. Figure 4 shows the location of the sampled points on the tank bottom.

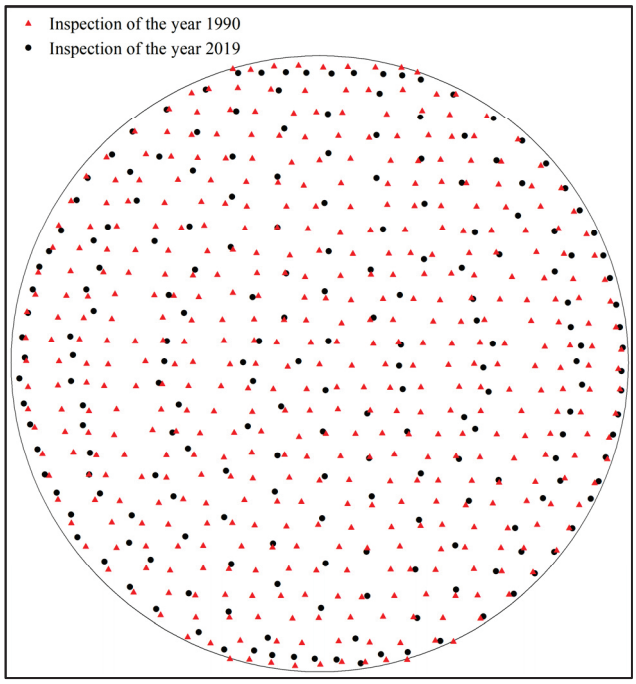


Figure 4. Spatial distribution of sampled points.

A 3D model of the vessel was created as a basic support for the AR, and was adapted to be overlapped on a miniature of the storage tank that is available in the laboratory of the TREES-MAT (Technology and Research on Energy, Environment and Safety Materials) Group of the University of Messina. Figure 5 shows the 3D model created.

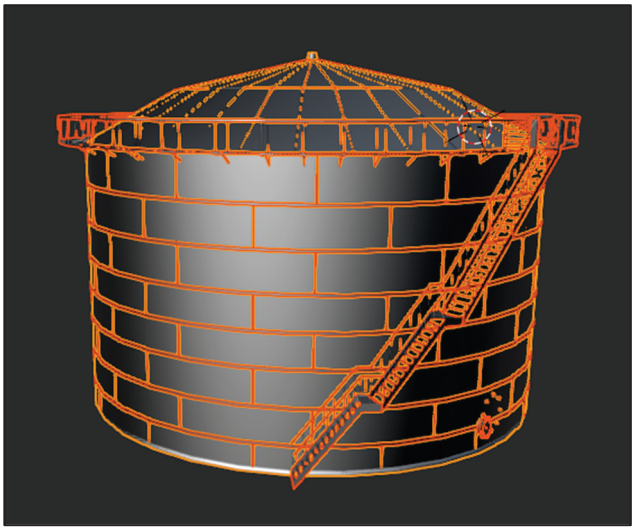


Figure 5. 3D model of the atmospheric storage tank.

A safety walk was carried out in order to observe the inside of the tank in AR. A "safety walk" is an inspection of a unit of an establishment, which has the aim of checking the conditions from a safety point of view. In this manuscript, the AR results are shown by overlapping them on a photograph of the tank in its real location.

4. Results

4.1. Identification of Criticalities in Human–Machine Interaction

The tests were carried out by at least 40 users by using the miniature of the tank described in [42]. The results were homogenous by referring to three groups classified as

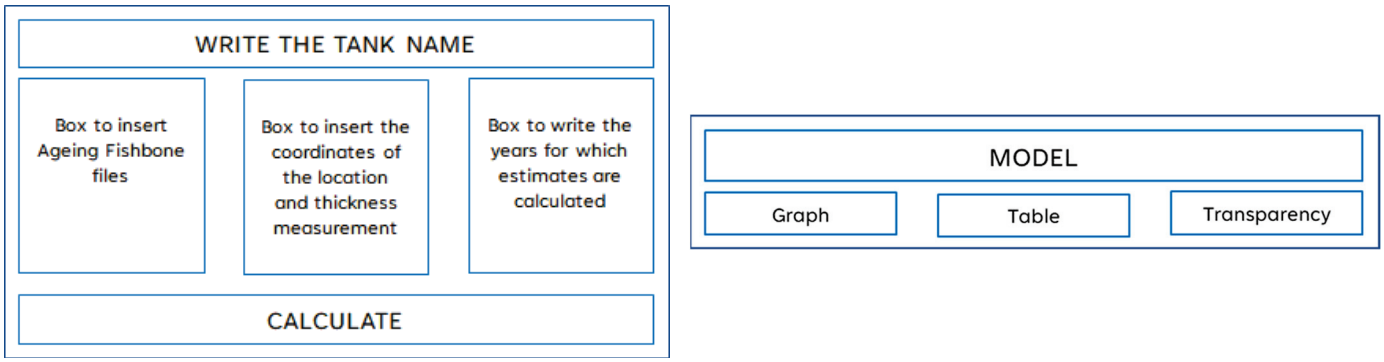
follows: group 1 users with a strong background in computer science but no background in safety, group 2 users with only knowledge of safety and chemical plants, and group 3 users with solid experience in computers science and safety. The usability tests were conducted by carrying out a safety walk in the laboratory and asking participants to list the critical issues that emerged during the use of the virtual sensor.

The following criticalities were highlighted:

- the migration from the App Desktop to the App Mobile was complex and possible only for experts in informatics;
- the App Mobile had a very crowded interface, with limited space for AR visualisation;
- the use of a mobile phone to give instructions to the virtual sensor caused the distraction of the user.

4.2. Interface Development

The critical issues highlighted led to the development of a user-friendly interface. Figure 6 illustrates a preview of the main elements, included in the interface of both the desktop and the Mobile applications, in order to manage the criticalities highlighted during the testing of the virtual sensor.



(**a**) (**b**)

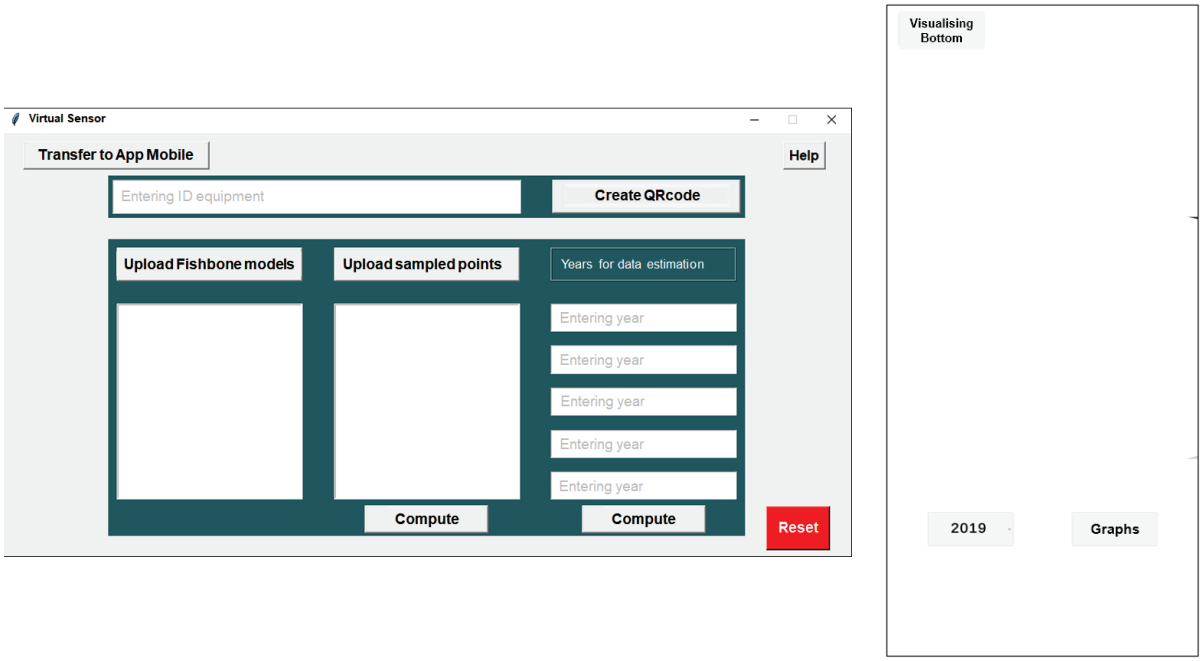
Figure 6. Scheme of the interface: (**a**) App Desktop, (**b**) App Mobile.

The GUI of the App Desktop is used to generate the information, which is subsequently overlapped via AR. It allows the creation of a dedicated space for the data storage of the equipment to be inspected, i.e., a folder identified with the name or the code of the equipment. It has a section dedicated to entering the historical data about ageing, i.e., the ageing fishbone files and the collected thicknesses at the different points from previous inspections. A box where it is possible to enter the year (or years) for which the parameters related to deterioration are expected to be estimated is included, as well as a section dedicated to the calculation.

The GUI of the App Mobile was designed to be very minimalist to leave as much free space as possible on the display to frame the objects by means of the camera. This view also allows other information to be shown by AR.

The App Desktop performs the data processing and management. It enables the user to load the input data in the system and to migrate them to the model, then to elaborate and store the outputs.

The interface of the App Desktop (Figure 7a) includes six fields to enter text and eight buttons acting as described below. The interface of the App Mobile essentially has only three buttons (Figure 7b), to leave the screen free from useless elements that could interfere with the AR vision. AR consists of the overlapping of the outputs on the reality framed by the camera in the right position.



(**a**) (**b**)

Figure 7. GUI of the (**a**) App Desktop (**b**) and App Mobile.

Table 1 reports the description of the functionalities for each button (or input box) included in the App Desktop interface.

Table 1. Functionality of the buttons included in the App Desktop.

Button (or Text Box)	Functionality Description
Transfer to App Mobile	Output migration (together with the 3D model of the equipment) from the App Desktop to the mobile device.
Help	To provide explanation about how to use the app.
Upload fishbone modules	Uploading fishbone modules of the equipment. These modules must be uploaded in chronological order.
Upload sampled points (inspection data)	Uploading thickness measurements carried out on the equipment associated with the relative spatial coordinates. Files must be uploaded in chronological order.
Create QR code	Generation of the QR code of the equipment.
Compute (on the GUI's centre)	Calculation of the current condition of the equipment.
Compute (on the GUI's right)	Calculate future condition of the equipment.
Reset	To remove data from all fields.
Entering ID equipment	To enter the name of the equipment being analysed (this text box must always be filled in).
Year for data estimation	To enter the years for the prediction of the equipment condition.

Before using the app, other configurations must be made directly in the "config_vs" file (located in the software folder); these are (i) the substance contained in the equipment; (ii) the nominal thickness of the equipment material (bottom of the tank), (iii) the knowledge derived from previous inspections of similar equipment (i.e., the parameters of the probability distribution function, for details see [42]); (iv) the number of inspections carried out for the tank.

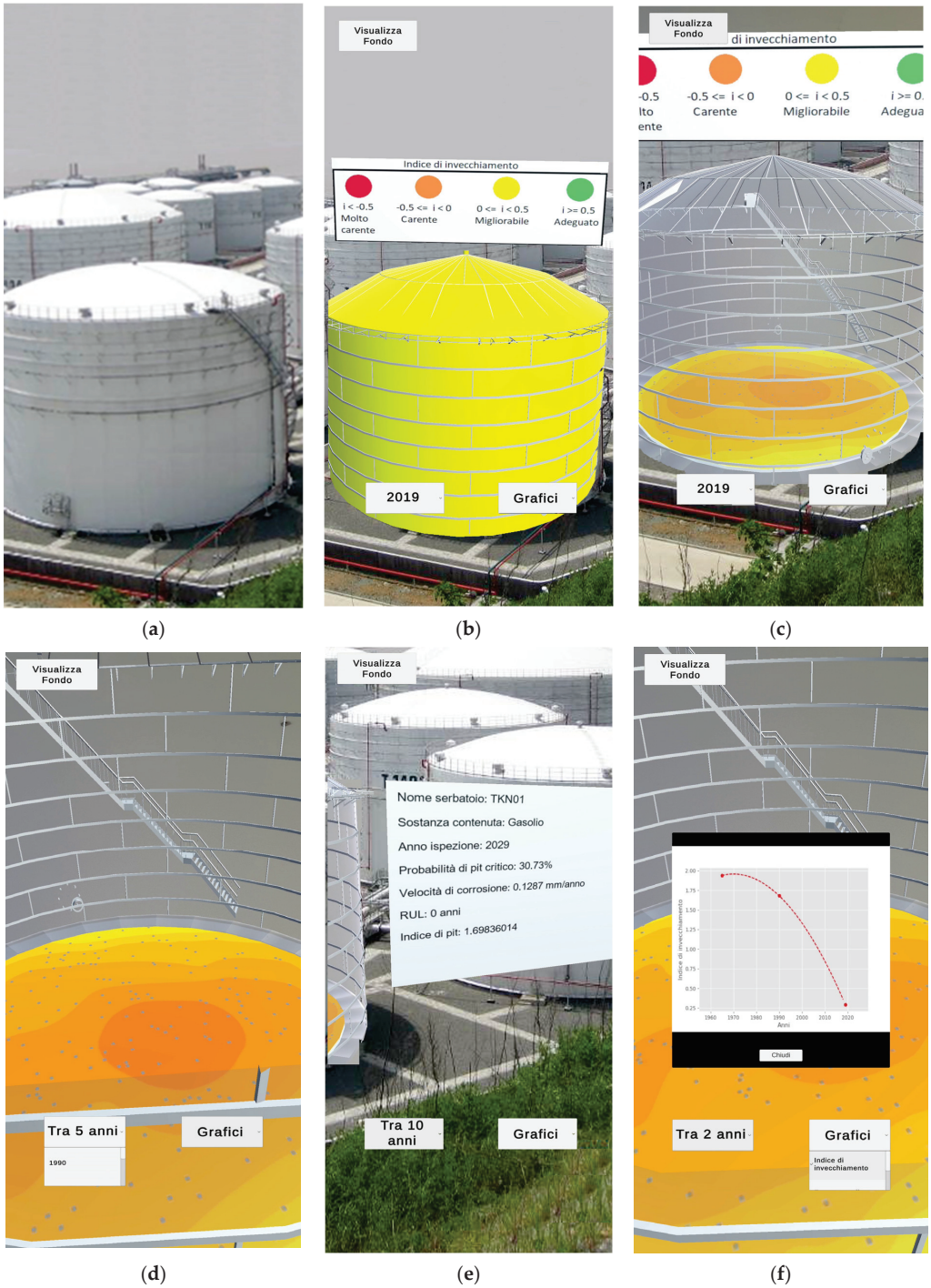
The App Mobile allows the visualisation of the outputs, also in augmented reality, on-field (during a safety walk). The app permits recognising the equipment and superimposing the iso-contour corrosion maps, the table containing the ageing parameters, and other general information about the equipment (such as name, identification code, substance contained, year of commissioning or reconditioning). As mentioned above, its GUI has only three buttons, since the sensors of the mobile device (e.g., position sensor, etc.), allow,

following the physical movement of the inspector, the exploration of the equipment in a fluid and immersive way. The buttons, on the other hand, permit the selection of the year for which the inspector wants to know the ageing metrics and the corrosion map, to make the equipment parts transparent (those not analysed), and finally, to choose the graph to be visualised.

After the improvement of the GUI, the virtual sensor was tested again by the same users. The data migration step was automatised and the elements of the App Mobile were reduced in number and dimensions (according to the users' suggestions). The users found the new version very user-friendly. The issue related to the use of a mobile device to give instructions to the virtual sensor is still not solved because this requires the introduction of other technologies or a further improvement of the software. (i.e., the finger on the screen of the mobile device should leave a trace in such a way that the inspector, while looking at the smart glasses, is aware about the position of his/her finger on the screen). Voice command could be another potential way to manage the graphical interface. The use of vocal registrations could be another possible implementation to collect useful information on-field. The consideration above is not an obstacle to the adoption of the technology for the proposed scope, but it represents a potential future development of this research.

4.3. Augmented Reality Results

Figure 8 shows some screenshots of the results provided by the virtual sensor during an inspection made for the case study. The first operation to be carried out to use the virtual sensor is to frame the QR code of the equipment (Figure 8a). The code is positioned at a certain distance and at a certain height, depending on the orography of the territory as well as the arrangement of the unit of the establishment, to allow an easy overview during the walk of the inspector inside the plant. The device instantly recognises the vessel and shows the 3D model of the tank on the display in AR (Figure 8b). The colour of the equipment depends on its ageing state, i.e., the value of the ageing index during the last inspection; a legend to identify this state is available above the tank. Subsequently, by clicking on the "Visualizza fondo" (which translates to "View bottom") button at the top of the interface (Figure 8c), all the slabs making up the mantle and roof of the 3D model become transparent, even if the structure of the tank remains visible; at the same time, an iso-contour map is overlapped on the bottom, which represents the corrosion surface associated with the last performed inspection. The next step is to choose the year (past or future) for which the corrosion trend must be estimated (Figure 8d); this can be chosen by means of a pop-up menu on the bottom left button. For the same year, the ageing-related metrics (the corrosion rate, the pit density, the RUL, the probability of the critical pit, the ageing index, and the updated failure rate) and other general equipment information (name of the tank and the stored substance) are also displayed in a table placed on the right side of the equipment (Figure 8e). Finally, the last step of the use of the App Mobile concerns the visualisation of the graphs showing the trend of the ageing index, the corrosion rate, and the failure frequency vs. the time (year); this can be achieved by using a small pop-up menu on the "Graphics" button at the bottom right of the GUI (Figure 8f).



(**a**) (**b**) (**c**)

(**d**) (**e**) (**f**)

Figure 8. Screenshots of the mobile display visualising augmented reality during a simulated safety walk in the establishment. (**a**) holistic view of equipment; (**b**) overlay 3D model; (**c**) bottom thickness map; (**d**) thickness map enlargement and scrolling of a pop-up menu; (**e**) table box information; (**f**) example of graph given and scrolling of the graphs pop-up menu. Below the translation is given for all the words (or phrases) that appear in this Figure: Visualizza fondo = View bottom. Molto carente = Very lack. carente = lack. Migliorabile = Improvable. adeguato = Adequate. Indice di invecchiamento = Ageing index. Grafici = Graphs. Tra = Between. Anni = Years. Nome serbatoio = Tank name. Sostanza contenuta = Substance contained. Gasolio = Diesel. Anno ispezione = Inspection year. Probabilità di pit critico = Critical pit probability. Velocità di corrosione = Corrosion rate. Indice di pit = Pit index. Chiudi = Close.

For each movement of the inspector (i.e., the movement of the camera), the AR view updates according to the movement; for example, it allows zooming when he/she is approaching the framed area or shrinking if he/she moves away.

The dots that can be observed on the tank bottom maps in Figure 8f are not the sampled points, but a graphical representation of the pit density, which increases over time due to the worsening of the material due to the corrosion [42]. The number of points displayed is correlated with the scale parameter of the distribution probability function used to model the phenomenon (note that for each 0.1 increment in the scale parameter, there is an increase of 50 points randomly scattered and displayed on the map).

Some considerations must be made about the image resolution. It is certainly conditioned by the number of sampled points (points where the measurement was made during the last inspections). To obtain better results, a geostatistical technique (i.e., kriging) was used to interpolate or predict values at unsampled places in space [54]. This technique is based on a statistical model that evaluates the spatial autocorrelation of the data and estimates the value of a variable at a given location by combining nearby measured values of that variable and assigning them weights based on the spatial correlation between them. Weights are determined using a variogram or covariance function.

The accuracy of the AR overlay depends on the technique used to implement AR in the virtual sensor. The tracking Image technique (contained within Unity) was used. For this purpose, a grid composed of a large set of vertices was created. The grid is a circumference with its centre at the origin of the axes (0, 0), which coincides with the centre of the bottom of the tank, and has a radius of 1. The dimensions of the real bottom are readapted to this grid. This allows the sampled points to be inserted inside the image in the correct position with respect to the centre.

The accuracy of the RUL estimation is related to the corrosion model. It is derived from experimental tests when numerous inspection data are not available. These tests reproduce the conditions inside the tanks for the specific case study (i.e., fuel, impurity, trend of temperature, bottom material, etc.). The corrosion rate is correlated with the measure of the thickness of the samples of the bottom tank carried out in the laboratory. A microscope was used to measure the depth of the pits, but clearly, in a real case (i.e., tank miniature and large storage tank), it is not possible to use such an instrument and the accuracy is related to techniques applied (i.e., ultrasound or magnetic flux leakage).

The visualisation of the corrosion map, combined with the estimation of the RUL and the other ageing-related parameters, allows the inspector to focus attention on the critical points when he/she is on-field. The whole system (virtual sensor) makes it possible to combine visual deductions with forecasts obtained from the models in order to understand the real expected evolution of the phenomenon, also on the basis of how it is managed.

4.4. Discussion

A comparison with other solutions that use AR in the inspection sector has been made. The virtual sensor allows the equipment integrity to be controlled, while other widespread systems support checking the correct connection of fittings and performing routine maintenance by using information superimposed on the equipment. The developed sensor shows the information that is useful for quantifying ageing metrics and permits the integration of new information acquired on-field. In this way, new information can be annotated without using a paper notebook, and such information is included in the application, which appropriately organises the input file for the models. then, it is also possible to process input data in order to elaborate ageing indexes and generate iso-corrosion maps. The advantage is having a lot of information, in tabular and visual form, through a minimalist and intuitive interface. This availability would not otherwise be possible on-field because this information is generally archived on paper.

In summary, the comparison with AR solutions reported in the literature shows similarities with the use of AR in the virtual sensor. These are related to the opportunity to overcome the limit of using paper-based annotations during inspections and to help

operators in performing tasks and operations by the addition of information to the real work environment. This is possible without adding new risks for the worker. As regards the monitoring and assessment of equipment ageing, the virtual sensor appears to use AR in an innovative way within the inspection sector.

Based on what has been discussed above, the virtual sensor appears innovative as there are no AR-based tools for the monitoring and assessment of equipment ageing. This allows the virtual sensor to be positioned within the broader context of existing systems but with this specific peculiarity. The virtual sensor helps in running numerical models for ageing assessment, the application of some of which is useful to the establishment operator in order to comply with the Seveso legislation. The evaluation of the adequacy of ageing management is a crucial matter, especially when the equipment is close to the end of its lifetime. Therefore, having tools that help in the acquisition and management of input data to the models represents a valid support for the operator. Unfortunately, the use of these tools requires experimental validation tests in the laboratory to ensure that their development does not introduce new risks, such as those associated with human–machine interaction. The test results of the virtual sensor demonstrated the effectiveness of the support provided by the system to the inspector. This effectiveness was quantified through interviews with the users. The questions led to the following evidence: (1) the system allows the operator to be able to manage a lot of information and to combine visual deductions with forecasts obtained from the models, in order to understand the real expected evolution of the phenomenon, also on the basis of how it is managed. (2) the developed interface allows the information to be managed without creating confusion for the user.

5. Conclusions

The scientific literature and websites of various companies developing AR technologies to support industrial activities do not mention the use of the technology for ageing inspections of critical equipment. Current AR applications are designed for the training of workers. In addition, AR is commonly used in equipment maintenance and repair, which can be through displaying guides and operative instructions concerning assembly/disassembly especially in places that are difficult to access. Based on this evidence, AR use proposed in this work is definitely innovative.

The virtual sensor is a useful tool for the inspector as well as for the establishment operator to access information that could be needed on-field during inspections. AR provides information about the condition of parts of the equipment that cannot be captured during a visual inspection. Other advantages are related to the elaboration of ageing-related metrics, and their update and storage. The virtual sensor supports performing these operations for all the equipment included in the establishment.

In this work, the system, which was developed in a previous version, was improved to make its GUI more user-friendly. The investigation of the HMI supported the implementation process and allowed the improvement of the usability of the software by making it accessible, even to personnel that are not experts in advanced technologies.

Currently, the virtual sensor is designed to inspect very large storage tanks for the management of the integrity of some parts of this type of equipment. In particular, the bottom of the tank is not easy to monitor, as its inspection requires the vessel to be emptied and then cleaned to carry out the thickness measurements. These activities are executed at long time intervals to avoid extended stops and repeated exposure of the inspector to unhealthy environments. The use of this system aims to extend the inspection interval by means of the estimation of the expected conditions. The virtual sensor is a particularly useful tool for the inspector, who can benefit from further information during a safety walk, beyond that captured through a direct observation.

In addition, the current experimentation has been carried out in the laboratory. Therefore, to address how the terrain and the weather conditions could affect the accuracy and

effectiveness of the use of the technology, it is necessary to test it in a real establishment (future development of the system).

By means of the laboratory tests, it has been possible to improve the system and its GUI. However, larger-scale implementation requires further improvements. Using mobile devices suitable for difficult environments (e.g., explosive atmospheres) and the ability to work without using wireless connections are both necessary. There may be problems related to scalability, i.e., related to the framing of very extensive equipment, for which it will be necessary to study appropriate solutions. The use of more recent models of smartphones and smart glasses will improve the performance. However, it becomes necessary to update the part of the software that manages the transfer between the App Desktop and the App Mobile. As far as costs are concerned, a preliminary estimate suggests a total expense that includes the cost of smartphones, smart glasses, and software and its maintenance. There are limitations associated with different types of equipment, mainly related to the geometry and complexity of the systems, where it may be difficult to distinguish one piece of equipment from another. The complexity refers to systems with multiple walls or undulating surfaces or with complex intersections, which causes a crowded view. In addition, the virtual sensor appears especially significant in cases where it is difficult to interrupt system operating to monitor a part of it (as in the case of tank bottoms).

Author Contributions: Conceptualisation, G.A., R.S., G.F., P.B. and M.F.M.; methodology, G.A., R.S. and M.F.M.; software, R.S.; validation, M.F.M., G.F. and P.B.; formal analysis, G.A. and R.S.; investigation, G.A. and R.S.; resources, M.F.M.; data curation, G.A. and R.S.; writing—original draft preparation, G.A.; writing—review and editing, M.F.M.; visualisation, R.S. and G.A.; supervision, G.F., P.B. and M.F.M.; project administration, M.F.M.; funding acquisition, M.F.M. All authors have read and agreed to the published version of the manuscript.

Funding: This research was funded by INAIL, project DYN-RISK (BRiC 2019/ID2).

Institutional Review Board Statement: Not applicable.

Informed Consent Statement: Not applicable.

Data Availability Statement: Not applicable.

Conflicts of Interest: The authors declare no conflict of interest.

References

1. Brettel, M.; Friederichsen, N.; Keller, M.; Rosenberg, M. How virtualization, decentralization and network building change the manufacturing landscape: An Industry 4.0 perspective. *Int. J. Inf. Commun. Eng.* **2014**, *8*, 37–44.
2. Liu, Z.; Xie, K.; Li, L.; Chen, Y. A paradigm of safety management in Industry 4.0. *Syst. Res. Behav. Sci.* **2020**, *37*, 632–654. [CrossRef]
3. Gisbert, J.R.; Palau, C.; Uriarte, M.; Prieto, G.; Palazón, J.A.; Esteve, M.; Moyano, A. Integrated system for control and monitoring industrial wireless networks for labor risk prevention. *J. Netw. Comput. Appl.* **2014**, *39*, 233–252. [CrossRef]
4. Beetz, M.; Bartels, G.; Albu-Schäffer, A.; Bálint-Benczédi, F.; Belder, R.; Beßler, D.; Haddadin, S.; Maldonado, A.; Mansfeld, N.; Wiedemeyer, T.; et al. Robotic agents capable of natural and safe physical interaction with human co-workers. In Proceedings of the 2015 IEEE/RSJ International Conference on Intelligent Robots and Systems (IROS), Hamburg, Germany, 28 September–2 October 2015; pp. 6528–6535.
5. Podgorski, D.; Majchrzycka, K.; Dąbrowska, A.; Gralewicz, G.; Okrasa, M. Towards a conceptual framework of OSH risk management in smart working environments based on smart PPE, ambient intelligence and the Internet of Things technologies. *Int. J. Occup. Saf. Ergon.* **2017**, *23*, 1–20. [CrossRef]
6. Zhang, Y. Diagnosis and Detection Method of Critical Equipment Failure Based on Electronic Nose Technology. *Chem. Eng. Trans.* **2018**, *68*, 241–246.
7. Nadai, N.; Melani, A.H.A.; Souza, G.F.M.; Nabeta, S.I. Equipment failure prediction based on neural network analysis incorporating maintainers inspection findings. In Proceedings of the Annual Reliability and Maintainability Symposium (RAMS), Orlando, FL, USA, 23–26 January 2017.
8. Liu, R.; Yang, B.; Zio, E.; Chen, X. Intelligenza artificiale per la diagnosi dei guasti delle macchine rotanti: Una revisione. *Sist. Mecc. Ed Elabor. Del Segnale* **2018**, *108*, 33–47. (In Italian)
9. Ersöz, O.Ö.; Inal, A.F.; Aktepe, A.; Türker, A.K.; Ersöz, S. A Systematic Literature Review of the Predictive Maintenance from Transportation Systems Aspect. *Sustainability* **2022**, *14*, 14536. [CrossRef]

10. Wee, D.; Kelly, R.; Cattel, J.; Breunig, M. *Industry 4.0-How to Navigate Digitization of the Manufacturing Sector*; McKinsey & Company: Munich, Germany, 2015; p. 58.
11. Carra, S.; Monica, L.; Vignali, G. Decision Making Approaches for Safety Purposes in Working Environments with Human-Technology Interaction. In Proceedings of the 31st European Safety and Reliability Conference, Angers, France, 19–23 September 2021.
12. Brocal, F.; González, C.; Komljenovic, D.; Katina, P.F.; Miguel, A.; Sebastián, M.A. Emerging risk management in Industry 4.0: An approach to improve organizational and human performance in the complex systems. *Complex. Manuf. Process Syst.* **2019**, *2019*, 2089763. [CrossRef]
13. Siemieniuch, C.E.; Sinclair, M.A.; Henshaw, M.D. Global drivers, sustainable manufacturing and systems ergonomics. *Appl. Ergon.* **2015**, *51*, 104–119. [CrossRef]
14. EU Council. Directive 2012/18/EU on the control of major-accident hazards involving dangerous substances. *Off. J. Eur. Union* **2012**, *L197*, 1–37.
15. Ansaldi, S.M.; Agnello, P.; Bragatto, P.A. Smart safety systems: Are they ready to control the hazard of major accidents? *WIT Trans. Built Environ.* **2018**, *174*, 169–180.
16. Bragatto, P.A.; Pirone, A.; Gnoni, M.G. Application of RFID technology for supporting effective risk management in chemical warehouses. In *Safety, Reliability and Risk Analysis: Beyond the Horizon*; Taylor & Francis Group: London, UK, 2014.
17. Ancione, G.; Kavasidis, I.; Merlino, G.; Milazzo, M.F. Real-time guidance system for cranes to manage risks due to releases of hazardous materials. In *Risk, Reliability and Safety: Innovating Theory and Practice*; Taylor & Francis Group: London, UK, 2017.
18. Gnoni, M.G.; Elia, V.; Bragatto, P.A. An IOT based system to prevent injuries in assembly line production systems. In Proceedings of the IEEE International Conference on Industrial Engineering and Engineering Management (IEEM), Bali, Indonesia, 4–7 December 2016; pp. 1889–1892.
19. Mennuti, C.; Augugliaro, G.; De Petris, C.; Cardarilli, G.; Di Nunzio, L.; Fazzolari, R. Tecniche per la localizzazione di danni strutturali per mezzo di AE: Algoritmi e possibili soluzioni HW per WSN. In Proceedings of the SAFAP Conference, Milan, Italy, 15–6 November 2016. (In Italian).
20. Arena, F.; Collotta, M.; Pau, G.; Termine, F. An Overview of Augmented Reality. *Computers* **2022**, *11*, 28. [CrossRef]
21. Egger, J.; Masood, T. Augmented reality in support of intelligent manufacturing—A systematic literature review. *Comput. Ind. Eng.* **2020**, *140*, 106195. [CrossRef]
22. Lu, X.; Zhang, J.; Chen, K.; Ma, D.; Zhang, Y.; Wan, Y. Efficiency and Safety Improvement of Power Equipment Smart Inspection and Operation via Augmented Reality Glasses based on AI Technology. In Proceedings of the 4th World Symposium on Artificial Intelligence (WSAI), Jilin, China, 23–25 June 2022; pp. 18–23.
23. Garcia, C.A.; Naranjo, J.E.; Ortiz, A.; Garcia, M.V. An Approach of Virtual Reality Environment for Technicians Training in Upstream Sector. *IFAC-PapersOnLine* **2019**, *52*, 285–291. [CrossRef]
24. Salman, N.; Colombo, S.; Manca, D. Testing and Analyzing Different Training Methods for Industrial Operators: An Experimental Approach. In *Computer Aided Chemical Engineering*; Kraslawski, A., Turunen, I., Eds.; European Symposium on Computer Aided Process Engineering; Elsevier: Amsterdam, The Netherlands, 2013; Volume 32, pp. 667–672.
25. Koteleva, N.I.; Zhukovskiy, Y.L.; Valnev, V. Augmented Reality Technology as a Tool to Improve the Efficiency of Maintenance and Analytics of the Operation of Electromechanical Equipment. *J. Phys. Conf. Ser.* **2021**, *1753*, 012058. [CrossRef]
26. Website Infosys.com. 'AR & VR Technology-Solving Many Core Oil & Gas Challenges'. Available online: https://www.infosys.com/insights/industry-stories/ar-vr-in-oil-gas.html (accessed on 10 May 2023).
27. Website Nsflow.com. 'Augmented Reality (AR) Training Platform in Oil and Gas Industry'. Available online: https://nsflow.com/industries/augmented-reality-in-the-oil-gas-industry#industry (accessed on 10 May 2023).
28. Website www.fusionvr.in. 'Augmented Reality Solutions for Chemicals, Oil & Industries'. Available online: https://www.fusionvr.in/ar-chemicals-oil-and-gas (accessed on 10 May 2023).
29. Website of Council of Petroleum Accountants Societies. 'The Use of Augmented Reality in the Oil and Gas Industry'. Available online: https://copas.org/augmented-reality-oil-and-gas-industry/ (accessed on 10 May 2023).
30. Yang, L.I.Z.; Zhang, D.S.; Bang, D.U.Y. An Intelligent Safety Inspection System Based on AR Technology. *J. Beijing Univ. Chem. Technol.* **2022**, *49*, 59.
31. Romero, D.; Stahre, J.; Taisch, M. The Operator 4.0: Towards socially sustainable factories of the future. *Comput. Ind. Eng.* **2020**, *139*, 106128. [CrossRef]
32. Marino, E.; Barbieri, L.; Colacino, B.; Kum Fleri, A.; Bruno, F. An Augmented Reality inspection tool to support workers in Industry 4.0 environments. *Comput. Ind.* **2021**, *127*, 103412. [CrossRef]
33. Chen, Y.J.; Lai, Y.S.; Lin, Y.H. BIM-based augmented reality inspection and maintenance of fire safety equipment. *Automat. Constr.* **2020**, *110*, 103041. [CrossRef]
34. Shin, D.H.; Dunston, P.S. Evaluation of Augmented Reality in steel column inspection. *Automat. Constr.* **2009**, *18*, 118–129. [CrossRef]
35. Wickens, C.D.; Hollands, J.G.; Banbury, S.; Parasuraman, R. *Engineering Psychology & Human Performance*; Psychology Press: New York, NY, USA, 2015.
36. Lee, K. Augmented Reality in Education and Training. *TechTrends* **2012**, *56*, 13–21. [CrossRef]

37. Ramakrishna, P.; Hassan, E.; Hebbalaguppe, R.; Sharma, M.; Gupta, G.; Vig, L.; Sharma, G.; Shroff, G. An AR Inspection Framework: Feasibility Study with Multiple AR Devices. In Proceedings of the 2016 IEEE International Symposium on Mixed and Augmented Reality (ISMAR-Adjunct), Merida, Mexico, 19–23 September 2016; pp. 221–226.
38. Vignali, G.; Bertolini, M.; Bottani, E.; Di Donato, L.; Ferraro, A.; Longo, F. Design and Testing of an Augmented Reality Solution to Enhance Operator Safety in the Food Industry. *Int. J. Food Eng.* **2018**, *14*, 20170122. [CrossRef]
39. Fjeld, M.; Voegtli, B.M. Augmented chemistry: An interactive educational workbench. In Proceedings of the International Symposium on Mixed and Augmented Reality (ISMAR '02), Darmstadt, Germany, 1 October 2002.
40. Husár, J.; Knapčíková, L. Implementation of Augmented Reality in Smart Engineering Manufacturing: Literature Review. In *Mobile Networks and Applications*; Springer: Berlin/Heidelberg, Germany, 2023.
41. Lester, S.; Hofmann, J. Some pedagogical observations on using augmented reality in a vocational practicum. *Br. J. Educ. Technol.* **2020**, *51*, 645–656. [CrossRef]
42. Ancione, G.; Saitta, R.; Bragatto, P.; Fiumara, G.; Milazzo, M.F. An Advanced System for the Visualisation and Prediction of Equipment Ageing. *Sustainability* **2022**, *14*, 6156. [CrossRef]
43. Ministero dell'Ambiente e della Sicurezza Energetica. Valutazione Sintetica Dell'adeguatezza del Programma di Gestione dell' Invecchiamento Delle Attrezzature Negli Stabilimenti Seveso. Available online: https://www.mase.gov.it/notizie/valutazione-sintetica-dell-adeguatezza-del-programma-di-gestione-dell-invecchiamento-delle (accessed on 17 April 2023).
44. Gumbel, E.J. Statistical Theory of Extreme Values and Some Practical Applications. US Department of Commerce, National Bureau of Standards. *Appl. Math. Ser.* **1954**, *33*, 1–51.
45. Milazzo, M.F.; Ancione, G.; Bragatto, P.; Mennuti, C. Simplified modelling of the remaining useful lifetime of atmospheric storage tanks in major hazard establishments. *Chem. Engineer. Trans.* **2020**, *82*, 175–180.
46. Bailey, T.C.; Gatrell, A.C. *Interactive Spatial Data Analysis*; Longman Scientific & Technical: Essex, UK, 1995.
47. Website "Python Software Foundation". Available online: https://www.python.org/ (accessed on 20 January 2023).
48. Hunter, J.D. Matplotlib: A 2D Graphics Environment. *Comput. Sci. Eng.* **2007**, *9*, 90–95. [CrossRef]
49. Harris, C.M. Array programming with NumPy. *Nature* **2020**, *585*, 357–362. [CrossRef]
50. McKinney, W. Data structures for statistical computing in python. In Proceedings of the 9th Python in Science Conference, Austin, TX, USA, 28 June–3 July 2010; Volume 445, pp. 9951–9956.
51. Murphy, B.; Müller, S.; Yurchak, R. GeoStat-Framework/PyKrige: v1.6.1. *Zenodo* **2021**. [CrossRef]
52. Haas, J.K. *A History of the Unity Game Engine*; Worcester Polytechnic Institute: Worcester, MA, USA, 2014.
53. Blender Online Community. *A 3D Modelling and Rendering Package*; Stichting Blender Foundation: Amsterdam, The Netherlands, 2018. Available online: http://www.blender.org (accessed on 1 February 2023).
54. Ancione, G.; Bragatto, P.; Milazzo, M.F. Visualization of the Bottom Deterioration of Atmospheric Storage Tanks by Combining Prediction and Interpolation Models. *Chem. Eng. Trans.* **2022**, *91*, 271–276.

Disclaimer/Publisher's Note: The statements, opinions and data contained in all publications are solely those of the individual author(s) and contributor(s) and not of MDPI and/or the editor(s). MDPI and/or the editor(s) disclaim responsibility for any injury to people or property resulting from any ideas, methods, instructions or products referred to in the content.

coatings

MDPI

Article

Effect of Redox Switch, Coupling, and Continuous Polarization on the Anti-Corrosion Properties of PEDOT Film in NaCl Solution

Victor Malachy Udowo [1,2], Maocheng Yan [1,*], Fuchun Liu [1,3,*] and En-Hou Han [1,3]

[1] Institute of Metal Research, Chinese Academy of Sciences, Shenyang 110016, China; victorudowo@mail.ustc.edu.cn (V.M.U.)
[2] School of Materials Science and Engineering, University of Science and Technology of China, Hefei 230026, China
[3] Institute of Corrosion Science and Technology, Guangzhou 510530, China
* Correspondence: yanmc@imr.ac.cn (M.Y.); fliu@imr.ac.cn (F.L.)

Abstract: Conjugated poly(3,4-ethylenedioxythiophene) (PEDOT) film was electrochemically synthesized on stainless steel (SS). Redox interactions between the PEDOT film and the SS substrate were examined in 3.5 wt.% NaCl aqueous solution with the aid of electrochemical and spectroscopic analyses. The results show that the PEDOT film exhibited a barrier effect and mediated the oxygen reduction reaction, thus hindering ion diffusion to the steel substrate. Localized electrochemical impedance spectroscopy (LEIS) of the scratched area on the polymer film shows that PEDOT healed the defect by coupling with redox reactions on the steel surface to prevent charge localization and concentration. The electroactivity of the polymer film declined when PEDOT was polarized at potentials >−0.7 V. Prolonged exposure of the PEDOT film to dissolved oxygen in NaCl solution resulted in the polymer's over-oxidation (degradation), evidenced by the formation of a carbonyl group in the spectroscopic result. The degradation of PEDOT was attributed to chain scissoring due to hydroxide ion attacks on the polymer chain.

Keywords: conducting polymer; coating; stainless steel; electrochemical interaction; degradation

1. Introduction

Owing to high conductivity and the ability to protect metals under a defective coating, conducting polymers (CPs) such as polyaniline (PANI), polypyrrole (PPy), and polythiophene (PTh) derivatives are still choice materials for use in corrosion prevention. They are considered environmentally friendly substitutes for the hazardous hexavalent chromium in conventional coatings [1,2]. CPs may exist in the semiconducting neutral form, where electrons are added to the polymer backbone and/or conducting oxidized states when electrons are removed [3–5]. It is postulated that the redox processes on the CP stabilize the steel potential in the passive regime and aid the formation of a protective oxide layer on the metal [4]. In the process, the CP charge lost to metal oxidation is replenished by oxygen reduction, thereby stabilizing the steel potential in the passive region to hinder further corrosion reactions.

CPs are shown to protect against metal corrosion via mechanisms such as the barrier effect, anodic passivation, and release of dopant ions [5–8]. Galvanic coupling is an important aspect of corrosion protection by CPs, and oxidants (such as dissolved oxygen) are vital to sustaining the effect on CPs [6–11]. Torresi et al. [5] found that the galvanic coupling between PANI and metals (Fe, Ni, Cu, and Zn) strongly depends on the redox states of the CP. Most recently, Yan et al. [6,7] reported the cathodic protection of Al alloy by undoped CPs. Reports show that almost all p-doped CPs are oxidant toward Fe and its alloys [5–8].

However, the prolonged exposure of CPs to oxygen may result in decreased efficiency and over-oxidation (degradation) of the polymer film. In fact, oxygen catalyzes the oxidation/doping of PANI and Ppy [6–8]. The degradation of PANI is found to release carcinogenic toxins while Ppy is unstable, especially in the conducting state [8]. Research on metal corrosion inhibition by CPs has since been achieved using polythiophene derivatives. Among PTh derivatives, poly(3,4-ethylenedioxythiophene) (PEDOT) is remarkably known for its mechanical flexibility, excellent conductivity, and environmental stability, making it suitable for use in antistatic coatings, electrode material in batteries, supercapacitors, and fuel cells [8–11]. Following decades of research, PEDOT has been found to inhibit the corrosion of steel and Al alloys [8–16].

Zhang et al. [12] and Gao et al. [13] reported the significant corrosion inhibition effects of PEDOT on SS and Al alloy in aqueous solutions. Su et al. [14] showed that reduced PEDOT could promote passivation of the metal–CP interface, thus suppressing further corrosion reactions. Zhu et al. [15] demonstrated the corrosion mitigation of SS in a chloride solution by PEDOT, which served as the electron exchange medium to passivize the metal and reduce oxygen availability on the surface. Although the use of PEDOT in the corrosion protection of active metals has been reported in the literature [12–16], the research scope has been limited, and the underlying mechanisms have not been thoroughly investigated. Furthermore, the effect of redox processes on the corrosion protection mechanism of the PEDOT film has not been completely investigated.

In this work, PEDOT was electrochemically synthesized on SS. The redox behavior of the SS covered by PEDOT film was examined in NaCl aqueous solution at different polarization levels via electrochemical and spectroscopic analyses. The corrosion protection mechanism of the PEDOT film is also discussed.

2. Materials and Methods

2.1. Material and Substrate Preparation

The substrate used in this work was 316L stainless steel (SS), which has the nominal composition given in Table 1 [17]. Samples of 316L SS cut to 10 mm × 10 mm × 5 mm sizes were embedded in epoxy resin, leaving just 1 cm^2 of exposed surface area for use in the electrochemical tests as the working electrode (WE). The work surface of the samples was polished with 400-, 600-, 800-, and 1000-grit SiC paper. All the chemicals were analytical grade and bought from Sigma Aldrich, China. The PEDOT film was synthesized from an aqueous mixture containing 30 mM EDOT, 0.1 M $LiClO_4$, and 30 mM sodium dodecyl sulfate (SDS) as the dopant anion and electron-transfer mediator.

Table 1. Chemical composition of 316L stainless steel (wt.%).

Element	C	Mn	P	S	Cr	Ni	Mo	Si	N	Fe
Weight (%)	0.03	1.62	0.04	0.01	18.1	11.9	2.40	0.28	0.10	Bal.

The PEDOT film was electrodeposited on 316L SS at a deposition current of 5 mA cm^{-2} for 120 s and then left to dry naturally at room temperature. The choice of the current density was based on previous reports on the effects of polymerization potentials on the synthesis of PEDOT [16]. Electrodeposition was performed via a potentiostat (Reference 600+, Gamry Instruments, Warminster, PA, USA) in a three-electrode configuration comprising a platinum (Pt) mesh as the counter electrode (CE) and a saturated calomel electrode (SCE) as the reference electrode (RE). The SS covered by PEDOT film was the working electrode during the electrochemical tests. The chemical structures of the EDOT monomer and the neutral and oxidized forms of PEDOT are given in Figure 1.

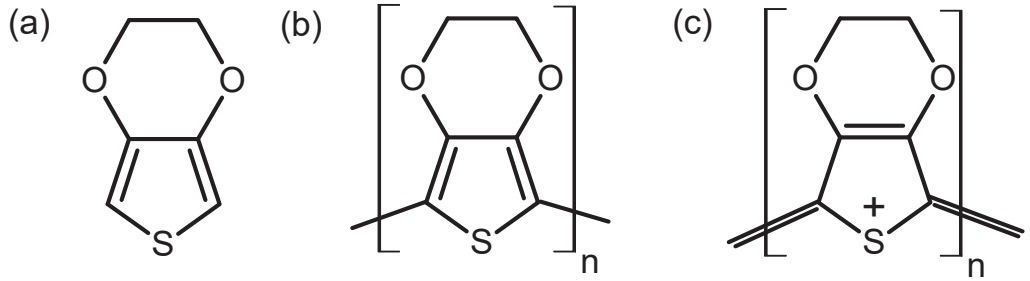


Figure 1. Chemical structures of EDOT monomer (**a**), neutral (**b**), and oxidized (**c**) forms of PEDOT.

2.2. Electrochemical Measurements

The electrochemical tests were performed in an aqueous solution of 3.5 wt.% NaCl as the electrolyte via the Gamry Reference/600+ potentiostat in a 3-electrode electrochemical cell configuration fabricated in a glass jar [18]. The cover of the glass cell had three openings for inserting the WEs (PEDOT-coated SS and bare SS) and a saturated calomel electrode (SCE) inserted in a Luggin capillary and Pt mesh as the CE [18]. Cyclic voltammetry (CV) was measured at a potential scan rate of 50 mV/s. The slow scan rate was chosen to allow sufficient time for the products of the reduction reaction in the forward scan to participate in the reverse reaction and generate clear anodic and cathodic reversible peaks. The electrochemical impedance spectroscopy (EIS) spectra were acquired at an open-circuit potential over the 110–0.1 Hz frequency range at 10 points per decade using an AC signal of 5 mV RMS amplitude.

Localized electrochemical impedance spectroscopy (LEIS) measurements were carried out using a VersaSCAN scanning electrochemical system (AMETEK, Berwyn, IL, USA) with low conductivity (approximately 70 μS/cm) to maximize resolution. A twin-electrode in a fixed position was placed above the defective coating surface measuring (1 cm^2) in NaCl aqueous solution. The microprobe tip travelled over the micro-defect on the coating surface at a separation distance of about 100 μm, stimulation frequency of 1 kHz, and disturbance amplitude of 10 mV. The generated LEIS data were converted to impedance using Origin software.

The PEDOT-coated electrode and bare SS were electrically coupled via the potentiostat in a zero-resistance ammeter (ZRA). In the second coupling experiment, the ability of oxygen to recharge (re-oxidize) the reduced PEDOT was examined. PEDOT was first reduced by coupling with bare SS, and the mixed potential and discharge current were recorded simultaneously. On decoupling, the individual electrode potentials were recorded to study the polymer reoxidation by DO. After a steady-state electrode potential was attained, the electrodes were coupled again, and the cycle was repeated three more times.

2.3. Surface Characterization

The morphology of the PEDOT coating after testing was observed using an optical microscope, scanning electron microscopy (SEM) with the aid of the SEM XL30-FEG spectrometer, and energy-dispersive spectrometer (EDS). After electrochemical tests, the PEDOT film was submitted to spectroscopic analysis with the aid of a (Jobin Yvon High resolution) Raman spectrometer equipped with a confocal microscope and a liquid-N_2 cooled charge-coupled device (CCD) detector and a He-Ne laser (632.8 nm). The chemical changes in the PEDOT film were further assessed by X-ray photoelectron spectroscopy (XPS, ESCALAB250). The details of the XPS analytical process can be found in the reference [19].

3. Results

3.1. Electrodeposition of PEDOT on SS

The potential–time plot reveals the nucleation process of the PEDOT film on SS. Figure 2a presents two distinct regions. The electropolymerization process starts around 1.2 V, and at potentials higher than 1.6 V, the polymer passes into the oxidized state (Figure 2a). The SEM image of the freshly prepared PEDOT (Figure 2b) presents cauliflower morphology typical of electrochemically polymerized films [14–16]. The cauliflower-like islands show that the regions closer to the SS substrate have similar morphology (Figure 2b).

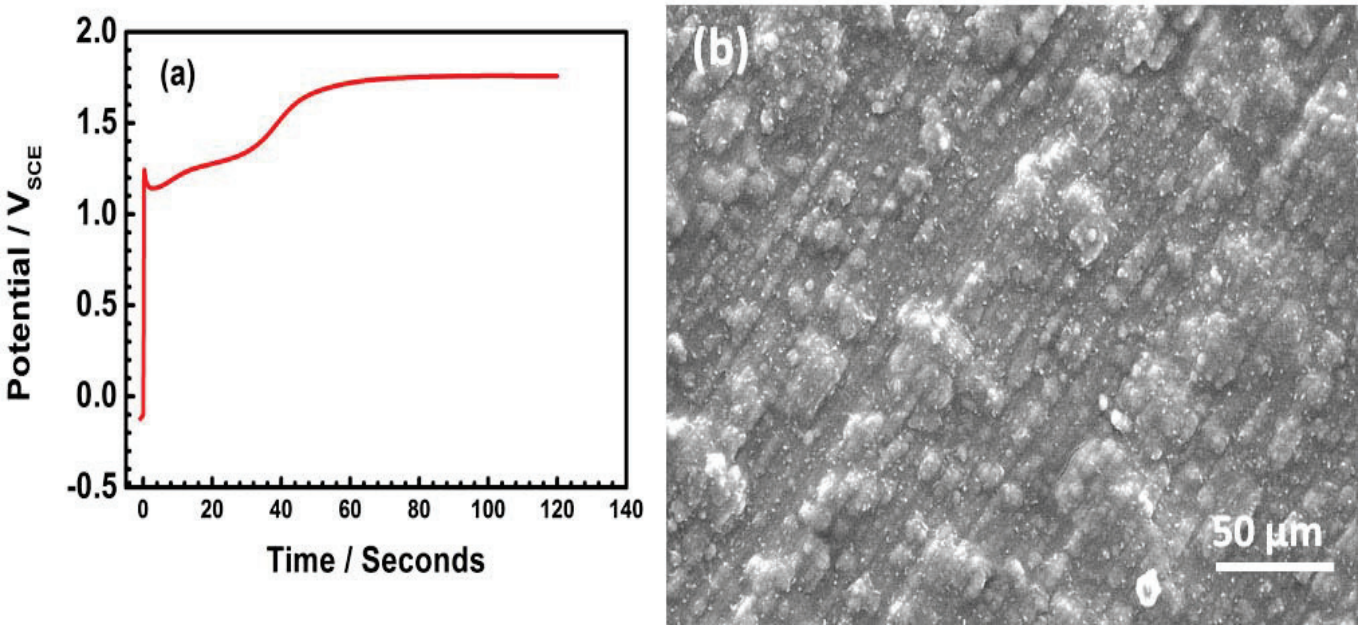


Figure 2. Potential–time plot recorded during electrodeposition of PEDOT on SS (**a**) and SEM image of freshly prepared PEDOT film (**b**).

3.2. Cyclic Voltammetry

The CV of CPs in an electrolyte has been frequently used to evaluate their threshold reduction and oxidation potentials [20,21]. Figure 3 shows the CV curve of PEDOT film obtained in an aqueous solution of 3.5 wt.% NaCl. By visual inspection of the CV curve, the oxidation peak is observed around –0.2 V, while the reduction peak appears around –0.6 V. The peak separation and the decrease in the current density corresponding to the reduction peak (around −0.6 V) as the number of cycles increases indicates that the redox process on the polymer is quasi-reversible [21]. After 20 consecutive oxidation–reduction cycles, the CP's redox properties are almost unaltered. Such electrochemical stability makes PEDOT favorable for application in anti-corrosion coatings.

3.3. Open-Circuit Potential

Figure 4 shows the open-circuit potential (E_{OCP}) of PEDOT and bare SS recorded as a function of the immersion period in NaCl solution. Protection of the PEDOT coating on 316L SS is evident (Figure 4) by the stabilization of the potential at about −0.0019 V after 43 h of testing, while that of bare SS evolves to correspond with iron dissolution. Whereas the early negative shift in the E_{OCP} of PEDOT suggests a partial reduction of the CP by coupling with the SS substrate, reoxidation of the CP by oxygen may be involved in the later ennoblement [8–10]. Moreover, the potential difference between PEDOT and bare SS electrodes strongly suggests the existence of a galvanic effect, where the former is likely the anodic member.

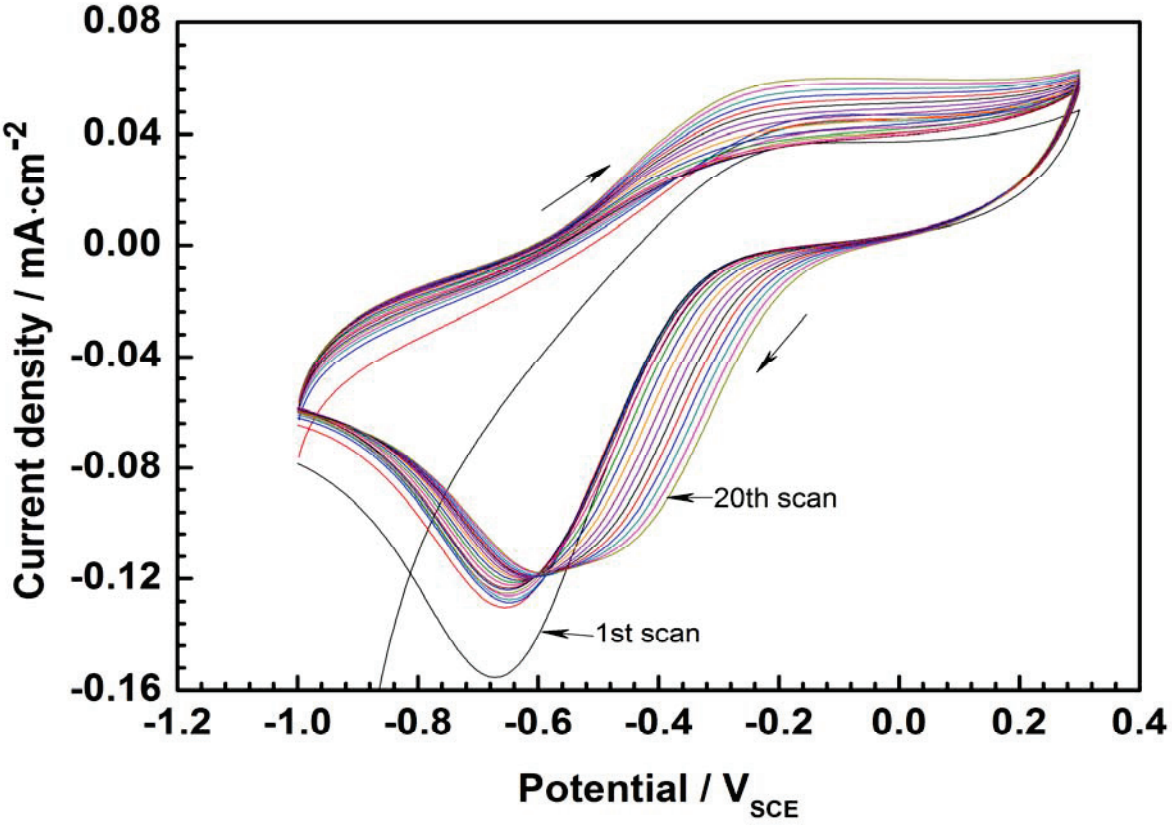


Figure 3. Cyclic voltammetry curves of PEDOT-coated electrode in 3.5% NaCl solution after 1 h of immersion to stabilize the electrode potential (scan rate is 50 mV/s).

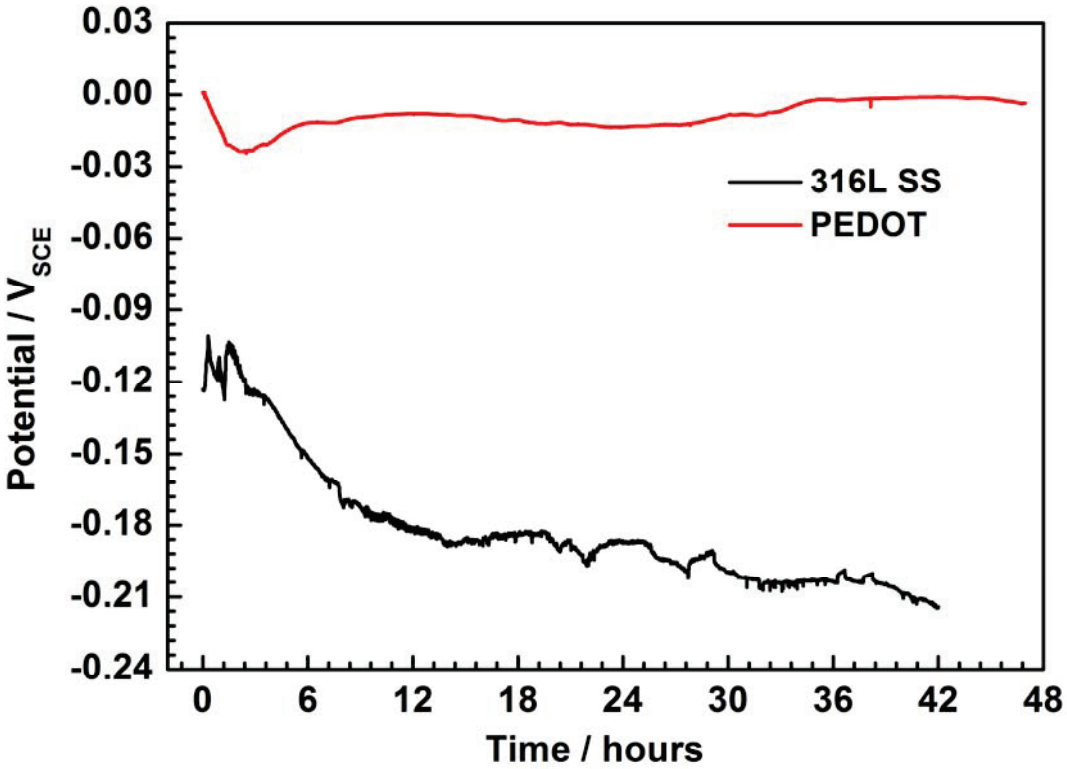


Figure 4. Evolution of open-circuit potential (E_{OCP}) of PEDOT-coated electrode and bare SS recorded as a function of immersion time in 3.5% NaCl solution.

3.4. Galvanic Coupling

The PEDOT-coated electrode (WE) and the bare SS (CE) were electrically coupled in NaCl solution via the potentiostat in ZRA mode, resulting in a steady coupling current of about 0.012 µA (Figure 5). The mixed potential (*E*mix) of PEDOT decreases from −0.060 to −0.168 V in 6 h (Figure 5), demonstrating the reduction of the polymer to its semi-conducting form. The extent of reduction is determined by the potential drift of the bare SS exposed to corrosion reactions in NaCl solution. After 6 h, an inflection is observed, and then the *E*mix ennobles significantly (Figure 5), suggesting reoxidation of the CP by coupling with the oxygen reduction reaction on the polymer film. Fluctuations in the mixed potential of PEDOT during coupling (Figures 5 and 6) suggest ionic exchanges occurring between the CP film and the electrolyte.

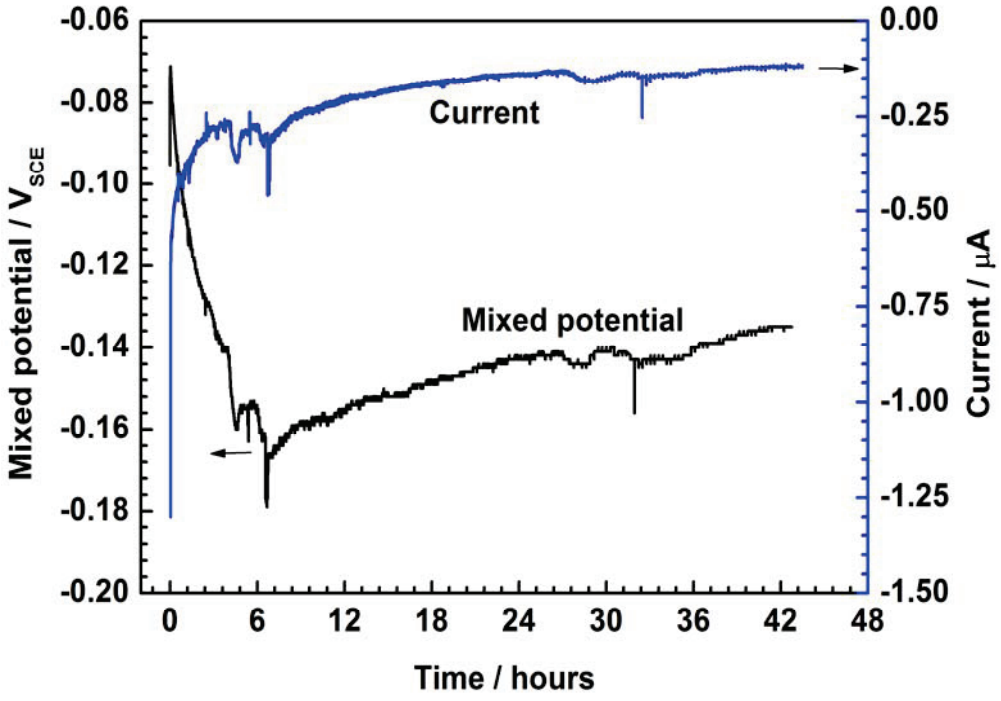


Figure 5. Galvanic coupling between the PEDOT and bare SS electrodes immersed in 3.5% NaCl solution.

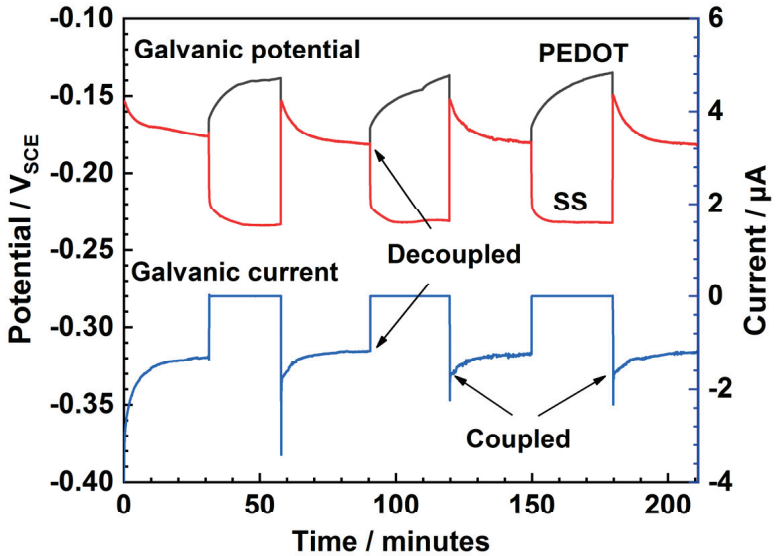


Figure 6. Dynamic galvanic corrosion in 3.5% NaCl solution, where PEDOT serves as the working electrode and SS is the counter electrode.

The capacity of DO to reoxidize the polymer film was examined with the aid of the classical charging/discharging experiments. First, PEDOT was reduced by coupling with bare SS for 30 min in NaCl solution and then reoxidized/recharged by decoupling while the *E*OCP of both electrodes was recorded concurrently. As seen in Figure 6, a discharge current of about 0.0736 μA is observed after 30 min. After four discharging/charging cycles, no noticeable change in the coupling current can be observed (Figure 6). However, the potential of PEDOT exhibits significant positive shifts on decoupling, while that of the bare SS shifts negatively, indicating that the electrodes exist in different oxidation states.

When two electronic conductors (such as the bare SS and PEDOT) are electrically connected, a purely electronic (i.e., non-redox) interaction is anticipated whereby the Fermi energy (or electrochemical potential of electrons) of each conductor is altered. As a result, electrons move from the (more active) SS into the PEDOT-coated electrode until the Fermi energies in the two phases are equal [8,9]. The immediate ennoblement in the potential of the PEDOT electrode upon decoupling reflects the Fermi level shift, owing to redox reactions on the polymer, which strongly buffer its electron activity (or Fermi energy).

The electrochemical behavior of the coated SS during the coupling experiments (Figures 5 and 6) is similar to that of the uncoupled PEDOT observed in Figure 4, which confirms that the initial potential decline is due to the coupling of redox reactions between the CP and the steel substrate in NaCl solution. However, the *E*OCP of the uncoupled PEDOT is more positive (Figure 4) because redox reactions on the coated substrate weakly discharge the charge stored in the CP film during electrodeposition. The E_{OCP} of PEDOT is further discussed in Section 4.1.

3.5. EIS

The healing effect of the CP was studied using the LEIS maps of a simulated defect on the PEDOT film. The LEIS map of the defective coating displays a funnel shape after 0 h of testing in the NaCl solution (Figure 7a). In the early corrosion phase, the impedance at the defect is the minimum of the plot, about 768 Ω. Plateaus are observed around the defect in the areas covered by the coating, and the impedance is one order of magnitude higher than that of the defective area.

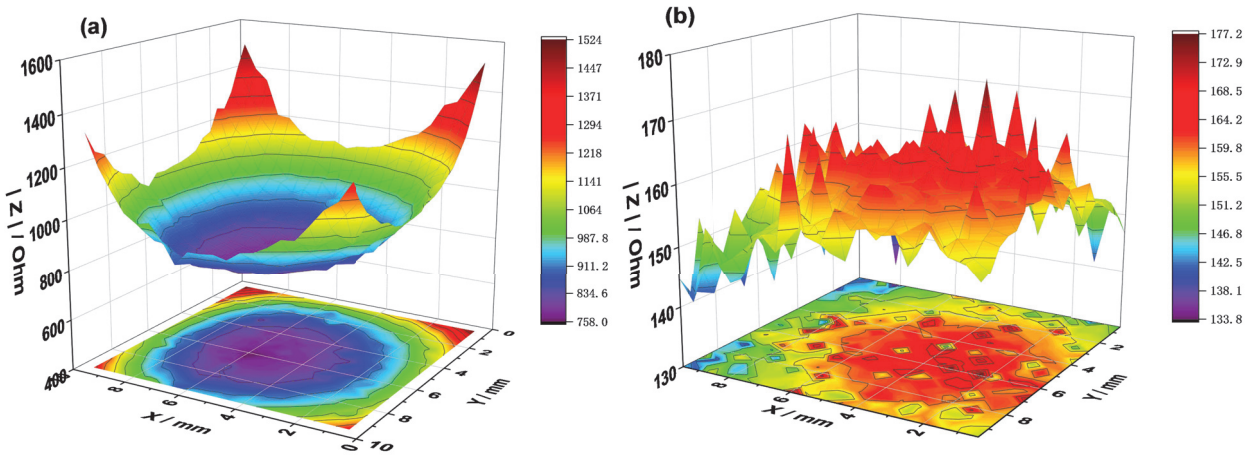


Figure 7. Localized EIS maps around the defect on PEDOT-coated SS after 1 h (**a**) and 6 h (**b**) of immersion in 3.5% NaCl solution.

After 6 h of immersion, the plateaus disappear due to redox interactions between the conductive polymer film and the steel substrate in NaCl solution. As expected, the impedance of the coated surface declines by an order of magnitude (Figure 7b). The uniformity in the impedance map of the defective coating after 6 h demonstrates the healing of the polymer film, which is partly due to the release of SDS anions when the polymer is reduced by coupling with the steel substrate. The formation of oxide corrosion products at the defect may also account for the effect observed in Figure 7b. Most importantly, the

PEDOT film prevents surface charge localization and concentration at the defect owing to its ability to conduct electrons and ions, resulting in the electrochemical protection of SS (Figure 7b).

The PEDOT film was subjected to conventional EIS tests in NaCl solution to examine the average impedance response of the entire surface. Figure 8 shows that the impedance of PEDOT decreases after 24 h of testing (Figure 8a,b). Such an evolution of impedance of CP-coated metals may not be entirely due to the barrier effect of the polymer film [22–24]. The galvanic coupling results show that PEDOT initially couples with the steel substrate (Figures 4 and 5), which will likely promote substrate oxidation, particularly in the early corrosion phase. The evolved cations will couple with the oxygen reduction reaction (ORR) in the NaCl solution to form a protective oxide layer, which hinders ion diffusion at the CP/steel interface [22–24].

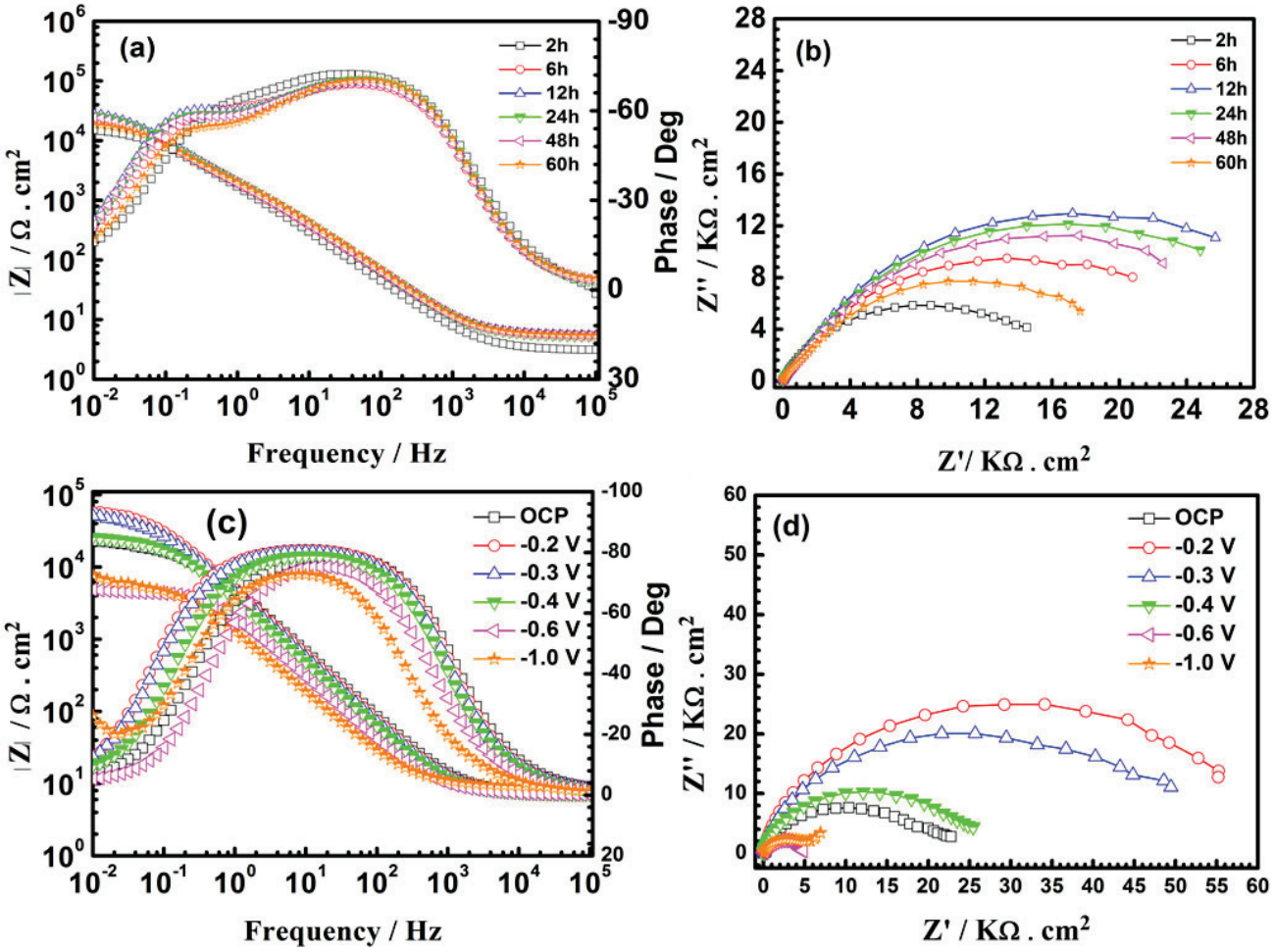


Figure 8. Bode and Nyquist plots of PEDOT-coated SS at open-circuit potential (OCP) (**a**,**b**), and the sample polarized at different potentials (**c**,**d**) in 3.5% NaCl solution.

The EIS data were further analyzed by fitting with the equivalent electric circuit in Figure 9, and the fitting parameters are given in Table 2. R_s is the electrolyte resistance, and R_{ct} represents the charge transfer resistance. The R_{ct} arises from a kinetically controlled electrochemical reaction, such as electron transfer between the substrate and the CP [25,26]. The constant-phase element (CPE), denoted as Q_{dl}, replaces the capacitance due to the non-ideal capacitive response of the metal/coating interface. The CPE describes the heterogeneity, porosity, and roughness of the coating [25], which can be evaluated by the following equation:

$$\mathrm{CPE} = Y_0 \, (\omega_m)^{n-1} \quad (1)$$

where Y_0 is the admittance of the CPE and ω_m is the frequency where the imaginary component of the impedance (Z″) has a maximum. The dispersion index (n) describes the system's deviation from a capacitor's ideal behavior. The value of n is such that $0 \leq n \leq -1$. Smaller n values imply more dispersion, while the effect ceases when n equals unity. Hence, the CPE behaves as an ideal capacitance [26]. The decreased R_{ct} values of PEDOT after 24 h of testing in NaCl solution (Table 2) indicate penetration of the electrolyte through to the steel surface after the protectiveness of the oxide layer declines.

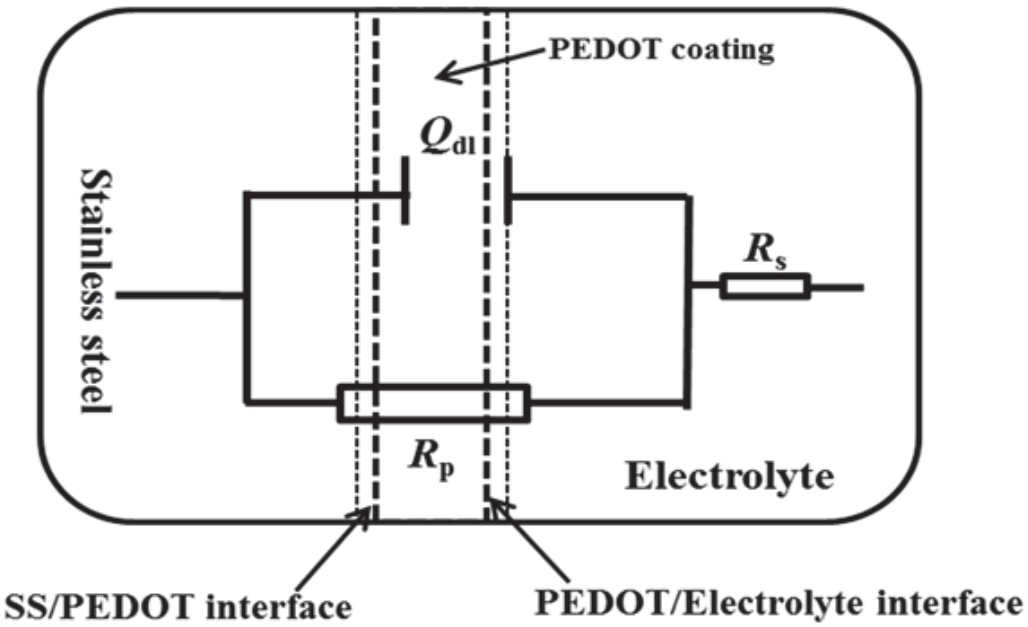


Figure 9. Equivalent electrical circuit used for fitting the EIS data of PEDOT-coated SS electrode using the ZSimpWin software. The chi square of the fit was 5.83×10^{-4}.

Table 2. Fitted electrochemical parameters of PEDOT from corrosion immersion test in 3.5% NaCl solution.

Time/ Hours	R_s $\Omega \cdot cm^2$	Q_{dl} Y_0 $Ss^n cm^{-2}$	n	R_{ct} $K\Omega \cdot cm^2$
2	3.139	9.974×10^{-5}	0.8394	14.63
6	5.374	7.661×10^{-5}	0.8312	22.29
12	5.425	7.177×10^{-5}	0.8330	26.09
24	5.334	7.738×10^{-5}	0.8283	28.34
48	5.383	7.577×10^{-5}	0.8402	19.35

The redox behavior of PEDOT at various applied potentials was studied in NaCl solution. The PEDOT-coated SS was polarized at each potential for 300 s in NaCl solution before acquiring the impedance spectrum, starting from the OCP (0 V) to higher cathodic potentials (Table 3). At lower cathodic potentials (from −0.2 V to −0.3 V), the magnitude of R_{ct} is double that of the undoped PEDOT (0 V). This may be related to the permeation of the electrolyte through the PEDOT film to the steel surface. In this potential range, the reduction of PEDOT and DO in the NaCl solution will occur, whereby OH^- ions generated by the oxygen reduction reaction (ORR) can attack the PEDOT chains [27,28], resulting in the loss of electroactivity and conductivity.

Table 3. Fitted electrochemical parameters of the PEDOT polarized at different potentials in 3.5 wt.% NaCl.

Polarized Potential V_{SCE}	R_s $\Omega \cdot cm^2$	Q_{dl} Y_0 $Ss^n cm^{-2}$	n	R_{ct} $K\Omega \cdot cm^2$
OCP	6.618	4.045×10^{-5}	0.9098	22.92
−0.200	7.413	3.847×10^{-5}	0.9071	56.63
−0.300	7.380	4.308×10^{-5}	0.9010	50.66
−0.400	7.354	5.071×10^{-5}	0.8929	25.81
−0.600	7.212	8.780×10^{-5}	0.8757	4.836
−0.700	6.947	7.194×10^{-5}	0.8742	2.393
−0.800	7.152	4.775×10^{-4}	0.8224	4.018
−1.000	8.844	2.756×10^{-4}	0.8438	7.728

The R_{ct} of PEDOT exhibits a pronounced decrease after PEDOT was polarized from –0.4 V to –0.7 V, indicating a progressive reduction and loss of counterions from the polymer film (Table 3). The R_{ct} gradually increases at potentials >–0.7 V, similar to the position of the cathodic peak in Figure 2, indicating a decline in the electroactivity and conductivity of the coated electrode. The diminishing electroactivity and conductivity at potentials >-0.7 V correspond to the abundance of OH^- ions generated from the excessive reduction of dissolved oxygen in this potential regime, which can attack the PEDOT chains and retard the electroactivity [27–30]. Fortunately, most electroactivity on CP can be preserved within the potential range from -0.4 V to -0.7 V, where the PEDOT electrode exhibits good conductivity and stability.

3.6. Raman Spectroscopy

The molecular changes in the polarized PEDOT film at different applied potentials were examined by Raman spectroscopy to clarify the observations in the EIS data. Sharp and well-defined bands characterize the spectra of polarized PEDOT (Figure 10). The most intense band at 1432 cm^{-1} is assigned to the C_α=C_β symmetric stretch, and that at 1512 cm^{-1} is the C_α=C_β asymmetric stretch [31–35]. The bands at 1364 and 1269 cm^{-1} correspond to the C_β=C_β symmetric stretch and C_α–C'_α stretch, respectively [35]. The peak at 1095 cm^{-1} corresponds to the C–O–C deformation, while the peaks between 440 cm^{-1} and 991 cm^{-1} are related to the oxyethylene ring deformation of PEDOT [35–37]. The decrease in the overall band intensity of the sample polarized at –1.0 V shows the loss of SDS due to the dedoping process.

In Figure 11, the peaks observed at 1417 cm^{-1} and 1432 cm^{-1} correspond to the neutral (quinoid) C_α=C_β and oxidized (benzoid) C_α–C_β symmetric stretching modes, respectively. The undoped PEDOT film (0 V) is highly oxidized as it contains the highest amount of the benzoid (oxidized) structures (Figure 11a). The oxidation level decreases as the polymer film is polarized from –0.2 to –0.6 V, demonstrating the dedoping process of the CP on the application of cathodic potentials (Figure 11c,d). The band shift from 1424 to 1417 cm^{-1} (redshift) in the spectra of polarized samples on stepping to higher cathodic potentials indicates the change in the doping level, as the benzoid-predominated PEDOT (at 0 V) transforms to a quinoid-structure-dominant polymer film at –0.6 V and –1.0 V [35–37]. The percentage of the benzoid structure in the polymer increases to approximately 40% (Table 4) after the sample was polarized at –1.0 V (in agreement with the EIS data) to accelerate nucleophilic attacks (by O_2 and OH^- ions) on the PEDOT chains due to excessive oxygen reduction at higher cathodic potentials.

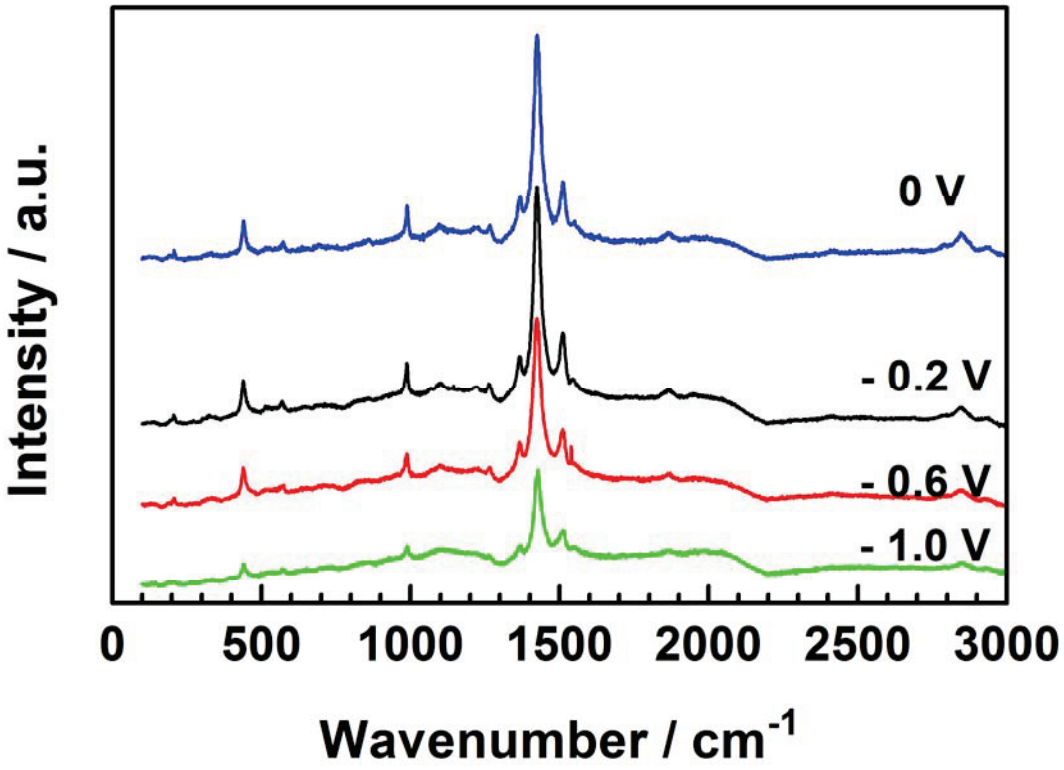


Figure 10. Raman spectra of PEDOT polarized at each potential for 300 s in NaCl solution.

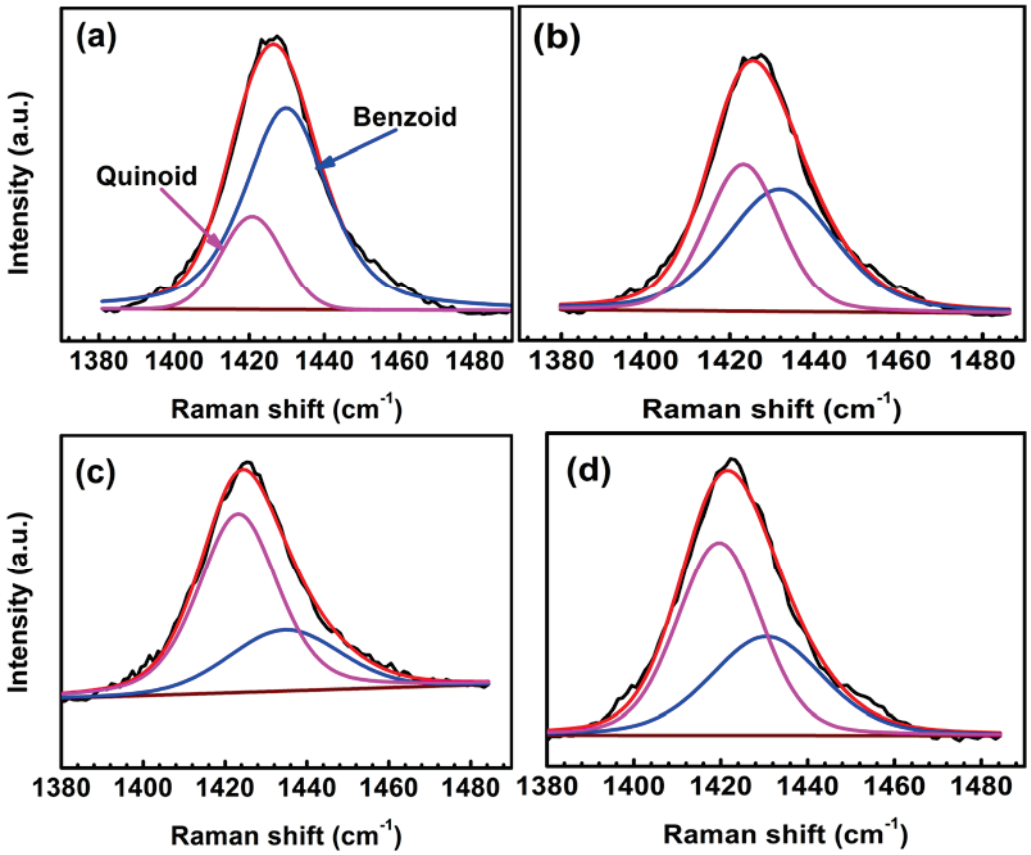


Figure 11. Micro-Raman spectra showing the neutral (quinoid) and oxidized (benzoid) regions of the PEDOT film polarized at 0 V (**a**), −0.2 V (**b**), −0.6 V (**c**), and −1.0 V (**d**) in NaCl solution. The black and red lines represent the raw data and fitted lines, respectively.

Table 4. Percentage composition of the oxidized (benzoid) structures in the polarized PEDOT film.

Polarization Potential	0 V	–0.2 V	–0.6 V	–1.0 V
Percentage	77%	46%	34%	40%

3.7. Surface Characterization

Figure 12 shows the surface of the undoped PEDOT film examined by SEM after 60 h of corrosion tests in NaCl solution. The PEDOT film exhibits non-uniform porosity with swellings and micro-cracks (Figure 12c,d), characteristic of PEDOT film in an over-oxidized state. Corrosion products are observed on the PEDOT film, which evolves from the substrate via the coating pores (Figure 12c). EDS analysis of the spot marked by a red rectangle on the PEDOT film (Figure 12d) shows that the elemental composition in weight % includes 67.3 C, 22.4 O, 7.20 S, 1.11 Na, 0.91 Cl, 0.48 Fe, 0.33 Cr, and 0.27 Mo. The high S-content is attributed to SDS dopant anions in the polymer matrix, which are released during the reduction of PEDOT by galvanic coupling with the steel substrate (Figures 5 and 6).

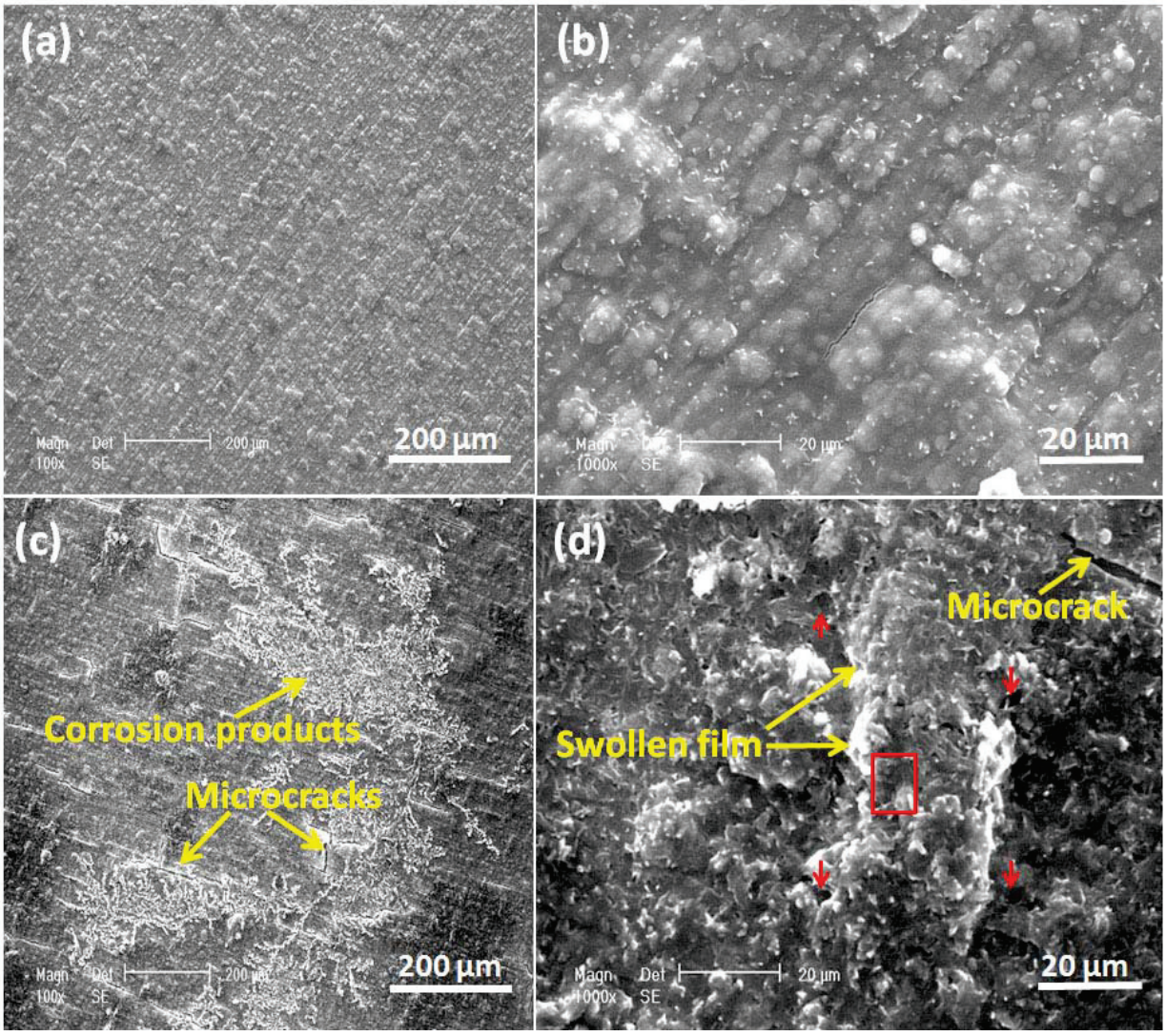


Figure 12. SEM images of freshly prepared PEDOT coating (**a**,**b**) and after corrosion immersion tests in 3.5% NaCl solution (**c**,**d**). Red arrows mark the pores on the PEDOT film, while the red box represents the area of the surface analyzed by EDS.

3.8. XPS

The chemical states of tested PEDOT films were further examined by XPS analysis. Both thiophenes and sulfonates are detected in the S 2p spectra of PEDOT (Figure 13a). The sub-peaks located at 168.5 and 169.6 correspond to the sulfonate components of the SDS dopant, while the sub-peaks located at 163.7 and 164.6 are attributed to the S of the thiophene rings (C–S–C) [14]. The peak at 165.4 eV is assigned to the oxidized thiophene sulfur (with a positive partial charge, $S^{\delta+}$) due to polarons and bipolarons [30,31]. The peak at 169.0 eV indicates sulfur oxidation in the PEDOT thiophene ring [30]. S=O groups can form after prolonged exposure to dissolved oxygen due to oxidation of the thiophene sulfur [29–33].

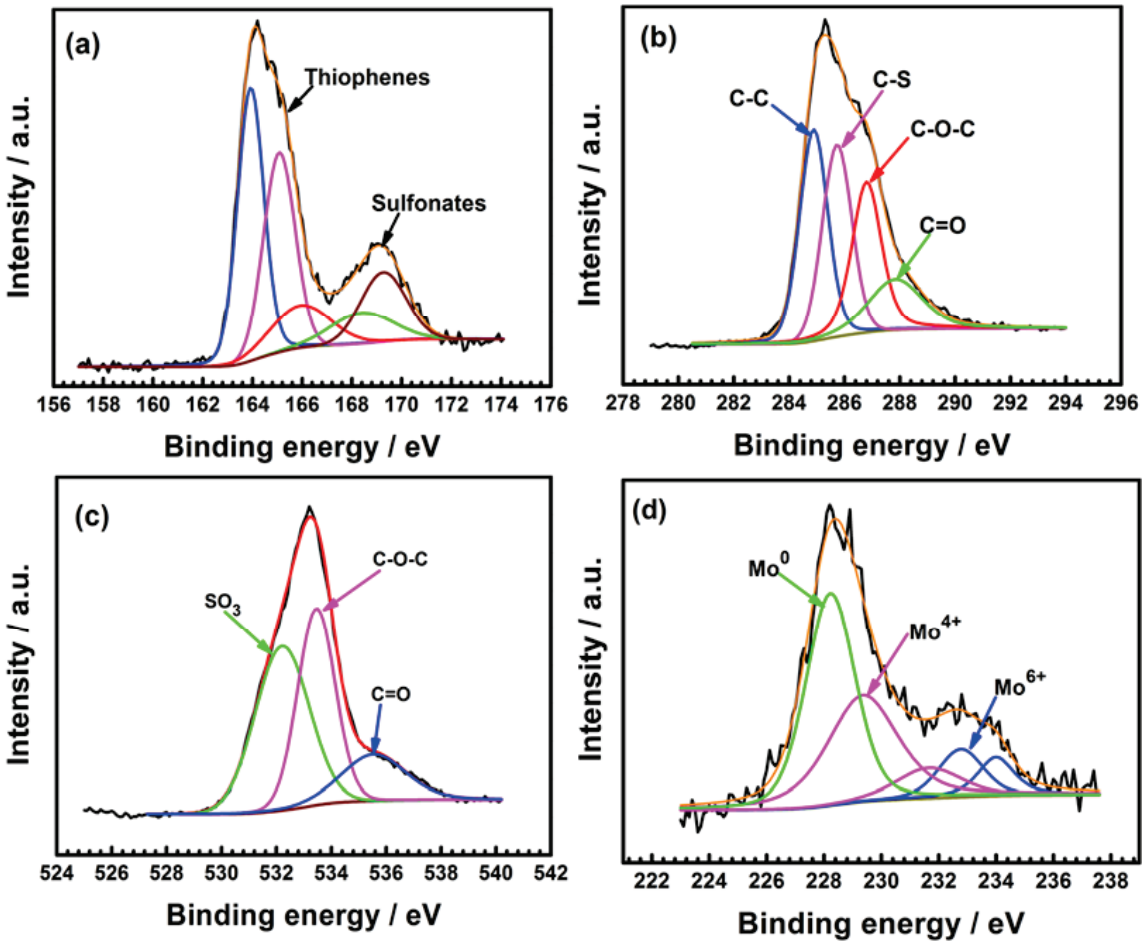


Figure 13. XPS spectra of C 1s (**a**), S 2p (**b**), O 1s (**c**), and Mo 3d (**d**) of PEDOT coating after corrosion tests in 3.5% NaCl solution at open circuit potential. The black and red lines represent the raw data and fitted lines, respectively.

In the C 1s spectrum (Figure 13b), the intense peak at 285.6 eV corresponds to carbon atoms belonging to C–C and C–H groups at α and β positions of the thiophene rings [28]. The peak at 285.6 eV corresponds to the C–S bonds of thiophene and the C–C bonds of the SDS anions [14,38]. A fourth peak in the C 1s spectrum at 287.9 eV and the O 1S signal at 535.7 eV (Figure 13b,c) indicate the formation of C=O groups associated with the degradation of the polymer film [33]. The formation of the C=O bond implies the breaking of the π-conjugation of the thiophene ring [29,32,33]. DO in the test media can attack the PEDOT chain during the prolonged immersion test period to promote their degradation [34–37]. Similar degradation mechanisms have been reported in the references [34–37].

Figure 13d shows that Mo enriched the oxide layer of the steel substrate. The spectrum of Mo 3d (Figure 13d) indicates the presence of Mo^0, Mo^{4+}, and Mo^{6+}. The two peaks at 232.87 eV and 235.99 eV are attributed to MoO_4^{2-} and MoO_3, respectively [39]. It is well known that Mo^{6+} promotes the formation of MoO_3 and MoO_4^{2-} in the passive film of 316L SS. The Mo-enriched oxide layer hinders ion diffusion to the steel substrate, resulting in the increased resistance of coated electrode after 60 h of testing (Table 2).

4. Discussion

The effect of the redox switch and coupling on the anti-corrosion properties of PEDOT film in NaCl solution is discussed under the following subheadings: corrosion protection mechanism and polarization behavior of the PEDOT film, as depicted in Figure 14.

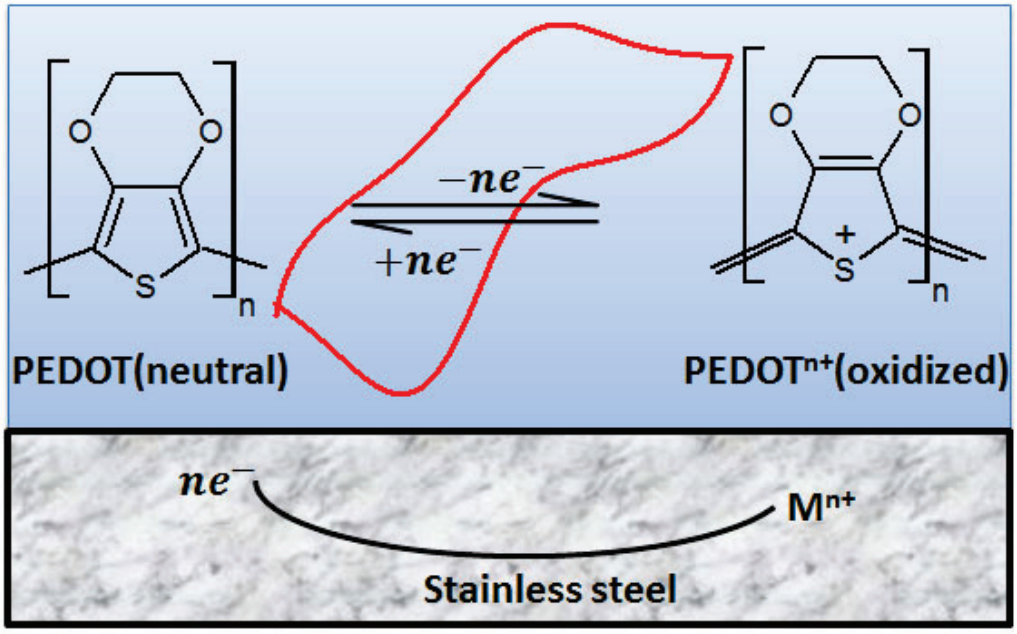


Figure 14. Proposed mechanism for the redox behavior of PEDOT film immersed in 3.5% NaCl solution.

4.1. Corrosion Protection Mechanism

The electrochemical polymerization of EDOT on SS generates positive charge carriers, which means the freshly prepared PEDOT film is in the oxidized state ($PEDOT^{n+}$). When the electrolyte reaches the steel surface, anodic substrate oxidation occurs, which yields electrons that partially reduce/discharge PEDOT at the cathode (Figures 4 and 5). At the same time, cations (M^{n+}) evolve to react with the corrosive medium to form an oxide layer [27,38–40]:

Anodic reactions:

$$M \longrightarrow M^{n+} + ne^- \quad (2)$$

Cathodic reactions:

$$PEDOT^{n+} + ne^- \longrightarrow PEDOT \quad (3)$$

The discharged PEDOT in reaction (3) is later recharged/reoxidized by mediating ORR:

$$\frac{n}{4}O_2 + \frac{n}{2}H_2O + ne^- \longrightarrow nOH^- \quad (4)$$

$$PEDOT + \frac{n}{4}O_2 + \frac{n}{2}H_2O \longrightarrow PEDOT^{n+} + nOH^- \quad (5)$$

$$Mn^+ \frac{n}{4}O_2 + \frac{n}{2}H_2O \longrightarrow M(OH)_n \quad (6)$$

Reactions (1) and (4) will couple to produce $M(OH)_n$, which represent the unstable hydroxides of Fe or Mo that are converted to more stable Fe_3O_4/Fe_2O_3 and MoO_3/MoO_4^{2-} in the oxide layer, which hinders the diffusion of corrosive anions to the steel substrate at the coating pores and defects (Figures 12 and 13).

The reduction/dedoping of PEDOT by galvanic coupling with the steel substrate could initiate a self-healing process in the scratched area of the coating by releasing SDS anions, which cannot diffuse out of the polymer matrix, due to its large size (Figure 11). The dopant anions may react with metal ions to form a "complex" (reaction (7)):

$$\{PEDOT^{n+}/SDS^{-}\} + e^{-} + M^{+} \rightleftharpoons \{PEDOT/SDS^{-}/M^{+}\} \quad (7)$$

The on-demand release of inhibitors is exploited in smart coatings to heal defective areas on coatings. Documented reports show that an aqueous SDS solution inhibits steel corrosion in acidic and alkaline solutions [41,42]. Dealloyed cations can also chelate with the CP via the thiophene sulfur to form $PEDOT/SDS/M^+$ "complexes" [38].

Furthermore, Figure 2 shows that PEDOT exhibits excellent stability after 20 charging–discharging cycles, which is attained mainly by the charge compensation phenomenon. Counterions, X^- (mainly OH^- and Cl^-), are incorporated into the polymer film from the electrolyte upon reoxidation to form the $PEDOT^+/SDS^-/M^+/X^-$ "complex" and maintain charge neutrality [42]:

$$\{PEDOT/SDS^{-}/M^{+}\} + nX^{-} \rightleftharpoons \{PEDOT^{n+}/SDS^{-}/M^{+}/X^{-}\} \quad (8)$$

The XPS and EDS results (Figure 13) demonstrate that reactions (7) and/or (8) are favored during the test.

By mediating ORR, the PEDOT film limits the amount of oxygen available at the surface of SS (reaction (8)). However, the fluctuations in the potential of the coated electrode (Figures 4 and 5) show that reactions (2)–(6) influenced the stability and performance of the PEDOT film. The Nernst equation expresses the E_{OCP} of CPs [43]:

$$E_{OCP} = E^0 + \frac{RT}{F}\ln\frac{[PEDOT^{n+}]}{[PEDOT]} + \Delta\varphi_D \quad (9)$$

where E^0 is the standard potential of the redox system; $[PEDOT^{n+}]$ and [PEDOT] are the concentrations of the oxidized (benzoid) and neutral (quinoid) forms of PEDOT, respectively. The standard gas constant is denoted as R, T is the temperature, F is the Faraday constant, and $\Delta\varphi_D$ is the Donnan potential at the polymer/solution interface.

The charging–discharging processes of the PEDOT film affect its potential by changing the ratio of $[PEDOT^{n+}]/[PEDOT]$. As the potential stabilizes, the rates of charging and discharging on the polymer film become equal [38,42]:

$$K_{OX}[O_2]^{n/4}[PEDOT] = K_{red}[PEDOT^{n+}][OH^-]^n \quad (10)$$

where K_{ox} and K_{red} are rate constants of the oxidation and reduction reactions, respectively. $[O_2]$ and $[OH^-]$ are the concentrations of O_2 and OH^-, respectively:

$$\frac{[PEDOT^{n+}]}{[PEDOT]} = \frac{K_{ox}[O_2]^{n/4}}{K_{red}[OH^-]^n} \quad (11)$$

From relationship (11), it can be deduced that $[O_2]$ and $[OH^-]$ are important factors that influence the stability and conductivity evidenced by the E_{OCP} of PEDOT. Prolonged exposure of the PEDOT film to O_2 and OH^- in NaCl solution results in the formation of C=O groups associated with the over-oxidation (degradation) of the polymer film (Figure 4). The non-uniform porosity of the over-oxidized PEDOT film could also create gradients of molecules (e.g., O_2, H_2O) and ions (Cl^-, OH^-), resulting in the formation of micro-galvanic cells, which could enhance the corrosion process of the steel substrate (Figure 12).

4.2. Polarization Behavior

PEDOT exhibits a p-type semi-conductor (i.e., holes extracting) characteristic [9,11], which implies that the polymer film could hinder electron transport [27]. Interactions between the polymer unit segment and the neighboring oxide layer on SS lead to the formation of electronic bands, which are separated by an energy gap (Figure 6). Charge transportation through the oxide layer to the PEDOT film and vice versa may be difficult owing to the difference in the position of their valence bands and the energy gaps (Figure 8). During electrochemical doping, ions are incorporated into or extracted from the PEDOT film (reactions (7) and (8)). The band gap energy is effectively minimized due to electrons transferred from redox reactions on the polymer, which manifests as improved electrical conductivity (Figures 7, 8, 10 and 11). The conductivity increase in these materials arises from the introduction of polaronic (cation) and/or bipolaronic (dication) species into the polymer backbone, which are charge-compensated by counterions [43].

When the PEDOT film is polarized at sufficiently high cathodic potentials (from –0.4 V to −0.7 V), the polarization of the polymer in this potential regime causes several changes in the polymer. PEDOT is dedoped, with the release of dopant (SDS) anions, while cations in the test solution (e.g., Na^+) are inserted for charge compensation. In addition, the PEDOT volume will shrink to close ion channels [28,29], thus making the invasion of corrosive anions difficult (Figures 7 and 9). The percentage of benzoid structures in the PEDOT film decreases to mitigate attacks by nucleophiles (mainly OH^- ions and intermediate products are formed from ORR), which can cause degradation of the PEDOT film by breaking the π-conjugation of the thiophene ring. Alternatively, ORR may directly consume the electrons on the PEDOT film, a pathway that does not involve dedoping the polymer [27]. However, when PEDOT is polarized at cathodic potentials >–0.7 V, the polymer is deeply reduced/dedoped, and more OH^- ions are generated from the excessive oxygen reduction in this potential range. Fast ejection of the abundant OH^- ions generated by the high applied force causes a loss of electroactivity and possibly deformation of the PEDOT chain (Figures 7 and 9). In addition, the increased percentage of the oxidized quinoid structures on the PEDOT chains (Table 4) could promote nucleophile attack on the polymer.

In summary, the PEDOT film is reduced by coupling with redox reactions on the SS substrate, while evolved cations react with OH^- to form an insoluble oxide layer enriched by Mo species. Whereas the PEDOT film becomes cathodic, the steel region under the rust layer is anodic. PEDOT is reoxidized by mediating ORR, which limits the amount of oxygen available at the substrate while the porosity of the coating increases, thus opening up ion channels in the coating to attacks by corrosive anions. Attacks on the polymer chain by OH− ions generated from ORR cause degradation of the polymer film after prolonged exposure to dissolved oxygen. When PEDOT is polarized at sufficiently high cathodic potentials (ranging from –0.4 V to –0.7 V), the polymer is dedoped, and the volume shrinks to prevent nucleophile attacks. There is a need for an additional reservoir of negative charges to be integrated into the coating to supply electrons for reduction and sustain the CP in the reduced state, which offers better protection of the steel substrate.

5. Conclusions

Strongly adherent PEDOT film was electrodeposited on stainless steel (SS), and redox interactions of the CP-coated electrode were examined in NaCl aqueous solution at various polarization potentials. The following conclusions can be inferred:

(1) The PEDOT film exhibited barrier protection and mediated the oxygen reduction reaction on SS.
(2) The PEDOT film was initially reduced by coupling with the SS substrate and then re-oxidized by dissolved O_2.
(3) The scratched PEDOT film prevented surface charge localization, resulting in the electrochemical protection of SS.

(4) With polarization at cathodic potentials from –0.4 V to –0.7 V, PEDOT was dedoped, which caused the polymer structure to shrink, thereby preventing nucleophile attacks.
(5) The electroactivity and conductivity of the polymer film declined when PEDOT was polarized at potentials >–0.7 V.
(6) OH^- ions generated from the oxygen reduction reaction attacked the polymer chain, causing the formation of carbonyl and sulfone groups, evidenced by XPS results of the degraded film. Degradation (over-oxidation) of the PEDOT coating due to attacks by OH^- ions was favored by prolonged exposure to oxygen.

Author Contributions: Conceptualization, M.Y.; methodology, M.Y.; validation, M.Y. and F.L.; formal analysis, V.M.U.; investigation, V.M.U.; resources, M.Y.; data curation, V.M.U.; writing—original draft, V.M.U.; writing—review and editing, V.M.U., M.Y. and F.L.; visualization, V.M.U.; supervision, F.L. and E.-H.H.; project administration, M.Y.; funding acquisition, M.Y. All authors have read and agreed to the published version of the manuscript.

Funding: This work was supported by the "National Natural Science Foundation of China" (No. 52071320).

Institutional Review Board Statement: Not applicable.

Informed Consent Statement: Not applicable.

Data Availability Statement: Not applicable.

Acknowledgments: The authors are grateful to Bright Okonkwo for improving the grammar in the manuscript and Gao Bowen for technical support during the laboratory experiments.

Conflicts of Interest: The authors declare no conflict of interest.

References

1. Namsheer, K.; Rout, C.S. Conducting polymers: A comprehensive review on recent advances in synthesis, properties and applications. *RSC Adv.* **2021**, *11*, 5659–5697.
2. Tallman, D.E.; Pae, Y.; Bierwagen, G.P. Conducting polymers and corrosion: Part 2—Polyaniline on aluminum alloys. *Corrosion* **2000**, *56*, 401–410. [CrossRef]
3. Rebetez, G.; Bardagot, O.; Affolter, J.; Réhault, J.; Banerji, N. What Drives the Kinetics and Doping Level in the Electrochemical Reactions of PEDOT:PSS? *Adv. Funct. Mater.* **2022**, *32*, 2105821. [CrossRef]
4. Gomez-Carretero, S.; Libberton, B.; Svennersten, K.; Persson, K.; Jager, E.; Berggren, M.; Rhen, M.; Richter-Dahlfors, A. Redox-active conducting polymers modulate Salmonella biofilm formation by controlling availability of electron acceptors. *NPJ Biofilms Microbiomes* **2017**, *3*, 19. [CrossRef]
5. Torresi, R.M.; Souza, S.D.; Silva, J.E.; Da, P.; Torresi, S.; De, I.C. Galvanic coupling between metal substrate and polyaniline acrylic blends: Corrosion protection mechanism. *Electrochim. Acta* **2005**, *50*, 2213–2218. [CrossRef]
6. Yan, M.C.; Tallman, D.E.; Rasmussen, S.C.; Bierwagen, G.P. Corrosion Control Coatings for Aluminum Alloys Based on Neutral and n-Doped Conjugated Polymers. *J. Electrochem. Soc.* **2009**, *156*, C360. [CrossRef]
7. Yan, M.; Tallman, D.E.; Bierwagen, G.P. Role of oxygen in the galvanic interaction between polypyrrole and aluminum alloy. *Electrochim. Acta* **2008**, *54*, 220–227. [CrossRef]
8. Khomenko, V.G.; Barsukov, V.Z.; Katashinskii, A.S. The catalytic activity of conducting polymers toward oxygen reduction. *Electrochim. Acta* **2005**, *50*, 1675. [CrossRef]
9. Mitraka, E.; Jafari, M.J.; Vagin, M.; Liu, X.; Fahlman, M.; Ederth, T.; Berggren, M.; Jonsson, M.P.; Crispin, X. Oxygen-induced doping on reduced PEDOT. *J. Mater. Chem. A* **2017**, *5*, 4404–4412. [CrossRef]
10. Ma, Q.; Pu, K.B.; Cai, W.F.; Wang, Y.H.; Chen, Q.Y.; Li, F.J. Characteristics of Poly(3,4-ethylenedioxythiophene) Modified Stainless Steel as Anode in Air-Cathode Microbial Fuel Cells. *Ind. Eng. Chem. Res.* **2018**, *57*, 6633–6638. [CrossRef]
11. Vázquez, M.; Bobacka, J.; Ivaska, A.; Lewenstam, A. Influence of oxygen and carbon dioxide on the electrochemical stability of poly(3,4-ethylenedioxythiophene) used as ion-to-electron transducer in all-solid-state ion-selective electrodes. *Sens. Actuators B Chem.* **2002**, *82*, 7–13. [CrossRef]
12. Zhang, S.; Li, M.; Zhai, L. Preparation and corrosion inhibition of single and biphase composite coating based on PEDOT in 0.1 M NaOH. *Int. J. Electrochem. Sci.* **2019**, *14*, 4828–4837. [CrossRef]
13. Gao, B.; Wang, M.; Yan, M.; Zhao, H.; Wei, Y.; Lei, H. Electrochemical Preparation and Corrosion Resistance of PEDOT Coatings on Surface of 2024 Aluminum Alloy. *Acta Metall. Sin.* **2020**, *56*, 1541–1550.

14. Su, Y.; Qiu, S.; Liu, Y.; Yang, D.; Zhao, H.; Wang, L. PEDOT: PSS-exfoliated graphene to improve the corrosion resistance of waterborne epoxy coating. *Int. J. Electrochem. Sci.* **2019**, *14*, 4595–4610. [CrossRef]
15. Zhu, G.; Hou, J.; Zhu, H.; Qiu, R.; Xu, J. Electrochemical synthesis of poly(3,4-ethylenedioxythiophene) on stainless steel and its corrosion inhibition performance. *J. Coat. Technol. Res.* **2013**, *10*, 659–668. [CrossRef]
16. Sakmeche, N.; Aaron, J.J.; Aeiyach, S.; Lacaze, P.C. Usefulness of aqueous anionic micellar media for electrodeposition of poly-(3,4-ethylenedioxythiophene) films on iron, mild steel and aluminum. *Electrochim. Acta* **2000**, *45*, 1921–1931. [CrossRef]
17. Pujar, M.G.; Parvathavarthini, N.; Dayal, R.K. Some aspects of corrosion and film formation of austenitic stainless steel type 316LN using electrochemical impedance spectroscopy (EIS). *J. Mater. Sci.* **2007**, *42*, 4535–4544. [CrossRef]
18. Udowo, V.M.; Gao, Q.; Yan, M.; Liu, F. Sulfate-Reducing Bacteria Corrosion of Pipeline Steel in Polyacrylamide Gel Used for Enhanced Oil Recovery. *J. Mater. Eng. Perform.* **2023**. [CrossRef]
19. Wu, T.; Xu, J.; Sun, C.; Yan, M.; Yu, C.; Ke, W. Microbiological corrosion of pipeline steel under yield stress in soil environment, *Corros. Sci.* **2014**, *88*, 291–305.
20. Waelder, J.; Vasquez, R.; Liu, Y.; Maldonado, S.A. Description of the Faradaic Current in Cyclic Voltammetry of Adsorbed Redox Species on Semiconductor Electrodes. *J. Am. Chem. Soc.* **2022**, *144*, 6410–6419. [CrossRef]
21. Elgrishi, N.; Rountree, K.J.; McCarthy, B.D.; Rountree, E.S.; Eisenhart, T.T.; Dempsey, J.L. A Practical Beginner's Guide to Cyclic Voltammetry. *J. Chem. Educ.* **2018**, *95*, 197–206. [CrossRef]
22. Wang, C.; Whitten, P.G.; Too, C.O.; Wallace, G.G. A galvanic cell driven controlled release system based on conducting polymers. *Sens. Actuators B Chem.* **2008**, *129*, 605–611. [CrossRef]
23. Ocón, P.; Cristobal, A.B.; Herrasti, P.; Fatas, E. Corrosion performance of conducting polymer coatings applied on mild steel. *Corros. Sci.* **2005**, *47*, 649–662. [CrossRef]
24. Yan, M.; Vetter, C.A.; Gelling, V.J. Corrosion inhibition performance of polypyrrole Al flake composite coatings for Al alloys. *Corros. Sci.* **2013**, *70*, 37–45. [CrossRef]
25. Nwokolo, I.K.; Shi, H.; Ikeuba, A.I.; Gao, N.; Li, J.; Ahmed, S.; Liu, F. Synthesis, Characterization and Investigation of Anticorrosion Properties of an Innovative Metal–Organic Framework, ZnMOF-BTA, on Carbon Steel in HCl Solution. *Coatings* **2022**, *12*, 1288. [CrossRef]
26. Ikeuba, A.I.; Okafor, P.C. Green corrosion protection for mild steel in acidic media: Saponins and crude extracts of Gongronema latifolium. *Pigment. Resin Technol.* **2018**, *48*, 57–64. [CrossRef]
27. Qi, K.; Qiu, Y.; Chen, Z.; Guo, X. Corrosion of conductive polypyrrole: Effects of continuous cathodic and anodic polarisation. *Corros. Sci.* **2013**, *69*, 376–388. [CrossRef]
28. Wang, D.; Li, Z.; Qi, K.; Qiu, Y.; Guo, X. Insights on the capacitance degradation of polypyrrole nanowires during prolonged cycling. *Polym. Degrad. Stab.* **2022**, *202*, 110034. [CrossRef]
29. Wang, D.; Pillier, F.; Cachet, H.; Debiemme-Chouvy, C. One-pot electrosynthesis of ultrathin overoxidized poly(3,4-ethylenedioxythiophene) films. *Electrochim. Acta* **2022**, *401*, 139472. [CrossRef]
30. Ujvári, M.; Láng, G.G.; Vesztergom, S.; Szekeres, K.J.; Kovács, N.; Gubicza, J. Structural changes during the overoxidation of electro-chemically deposited poly(3,4-ethylenedioxythiophene) films. *J. Electrochem. Sci. Eng.* **2016**, *6*, 77–89. [CrossRef]
31. Bouabdallaoui, M.; Aouzal, Z.; Ben Jadi, S.; El Jaouhari, A.; Bazzaoui, M.; Lévi, G.; Aubard, J.; Bazzaoui, E.A. X-ray photoelectron and in situ and ex situ resonance Raman spectroscopic investigations of polythiophene overoxidation. *J. Solid State Electrochem.* **2017**, *21*, 3519–3532. [CrossRef]
32. Teixeira, H.J.; Dias, C.; Veloso, R.C.; Apolinário, A.; Ventura, J. Tuning PEDOT:PSS low-impedance thin films with high charge injection for microelectrodes applications. *Prog. Org. Coat.* **2022**, *168*, 106894. [CrossRef]
33. Kamil, M.P.; Suhartono, T.; Ko, Y.G. Corrosion behavior of plasma electrolysis layer cross-linked with a conductive polymer coating. *J. Mater. Res. Technol.* **2021**, *15*, 4672–4682. [CrossRef]
34. Gueye, M.N.; Carella, A.; Massonnet, N.; Yvenou, E.; Brenet, S.; Faure-Vincent, J.; Pouget, S.; Rieutord, F.; Okuno, H.; Benayad, A.; et al. Structure and Dopant Engineering in PEDOT Thin Films: Practical Tools for a Dramatic Conductivity Enhancement. *Chem. Mater.* **2016**, *28*, 3462–3468. [CrossRef]
35. Shi, Y.; Zhou, Y.; Che, Z.; Shang, J.; Wang, Q.; Liu, F.; Zhou, Y. Degradation phenomena and degradation mechanisms for highly conductive PEDOT: PSS films. *Mater. Lett.* **2022**, *308 Pt A*, 131106. [CrossRef]
36. Marciniak, S.; Crispin, X.; Uvdal, K.; Trzcinski, M.; Birgerson, J.; Groenendaal, L.; Louwet, F.; Salaneck, W.R. Light induced damage in poly(3,4-ethylenedioxythiophene) and its derivatives studied by photoelectron spectroscopy. *Synth. Met.* **2004**, *141*, 67–73. [CrossRef]
37. Khaldi, A.; Maziz, A.; Plesse, C.; Soyer, C.; Vidal, F.; Cattan, E. Sensors and Actuators B: Chemical Synergetic PEDOT degradation during a reactive ion etching process. *Sens. Actuators B Chem.* **2016**, *229*, 635–645. [CrossRef]
38. Deshpande, P.P.; Jadhav, N.G.; Gelling, V.J.; Sazou, D. Conducting polymers for corrosion protection: A review. *J. Coat. Technol. Res.* **2014**, *11*, 473–494. [CrossRef]
39. Wang, Z.; Seyeux, A.; Zanna, S.; Maurice, V.; Marcus, P. Chloride-induced alterations of the passive film on 316L stainless steel and blocking effect of pre-passivation. *Electrochim. Acta* **2020**, *329*, 135159. [CrossRef]
40. Tahir, M.; Din, I.U.; Zeb, M.; Aziz, F.; Wahab, F.; Gul, Z.; Alamgeer; Sarker, M.R.; Ali, S.; Ali, S.H.M.; et al. Thin Films Characterization and Study of N749-Black Dye for Photovoltaic Applications. *Coatings* **2022**, *12*, 1163. [CrossRef]

41. Zhang, J.; Meng, Y.; Tian, Y.; Zhang, X. Effect of concentration and addition of ions on the adsorption of sodium dodecyl sulfate on stainless steel surface in aqueous solutions. *Colloids Surf. A Physicochem. Eng. Asp.* **2015**, *484*, 408–415. [CrossRef]
42. Alam, R.; Mobin, M.; Aslam, J. Polypyrrole/graphene nanosheets/rare earth ions/dodecyl benzene sulfonic acid nanocomposite as a highly effective anticorrosive coating. *Surf. Coat. Technol.* **2016**, *307*, 382–391.
43. Qi, K.; Qiu, Y.; Chen, Z.; Guo, X. Corrosion of conductive polypyrrole: Effects of environmental factors, electrochemical stimulation, and doping anions. *Corros. Sci.* **2012**, *60*, 50–58. [CrossRef]

Disclaimer/Publisher's Note: The statements, opinions and data contained in all publications are solely those of the individual author(s) and contributor(s) and not of MDPI and/or the editor(s). MDPI and/or the editor(s) disclaim responsibility for any injury to people or property resulting from any ideas, methods, instructions or products referred to in the content.

coatings

MDPI

Article

Effects of Preparation Parameters on the Structural and Morphologic Properties of SnO_2-Sb Coatings

Zhen He, Chen Yu, Jiaming Liu, Zengcheng Miao and Yuxin Wang *

School of Materials Science and Engineering, Jiangsu University of Science and Technology, Zhenjiang 212003, China
* Correspondence: ywan943@163.com

Abstract: Sb-doped SnO_2 (SnO_2-Sb) coatings show superiority in degrading toxic and refractory organic pollutants. SnO_2-Sb coatings can be prepared by oxidizing electrodeposited Sn-Sb coatings through an annealing process. The properties and structure of SnO_2-Sb coatings can be tailored by adjusting the preparation parameters. This study examines the effects of crucial preparation parameters on the performance of SnO_2-Sb coatings, with the aim of enhancing their properties.Determining the coatings' cross-sectional and surface characteristics was accomplished using various characterization techniques. A thorough investigation of the prepared samples' phase and element components was also carried out. Based on the findings, the surface roughness of the prepared Sn-Sb precoating changed with increasing current density, yet the primary surface features of the SnO_2-Sb coatings were hardly altered by the annealing process. Without lowering the coating thickness, the appropriate current density of 30 mA/cm^2 produced a rough and active coating surface. Our study's proper annealing temperature of 600 °C transformed Sn-Sb precoating into SnO_2-Sb coating and achieved excellent coating quality.While changes in the Sb content affected the morphology of the prepared SnO_2-Sb coatings, the mixed oxide coatings' cassiterite SnO_2 phase was unaffected. These results may provide insights into the optimized use of SnO_2-Sb coatings in various applications.

Keywords: SnO_2-Sb; electrodeposition; structures

1. Introduction

Environmental pollution caused by industrial waste is regarded as a significant issue. The use of electrocatalytic oxidation for the treatment of refractory effluents has been extensively investigated along with rapid industrialization worldwide [1–3]. The anode material plays a vital role in electrocatalytic oxidation reactions, which determines the oxidation efficiency and final oxidation products [4,5]. Given its stable size, long life, high electrocatalytic performance, and low cost, the dimensional stable anode (DSA) electrode is a promising electrocatalytic anode material. Among the DSA electrodes, the titanium-based Sb-doped SnO_2 (Ti/SnO_2-Sb) electrode has shown superiority in degrading various organic pollutants, especially in treating toxic organic pollutants and some refractory organic pollutants [6–8].

So far, multiple preparation methods, including thermal decomposition, electrodeposition, and chemical vapor deposition, are available to obtain SnO_2-Sb coatings on a Ti substrate [9,10]. Although thermal decomposition has been used extensively to make SnO_2-Sb coatings, the complex procedures make preparation challenging, and its open structure results in an inferior service life. In contrast, the electrodeposition technique has recently been developed by researchers to create SnO_2-Sb coatings [11]. Electrodeposition demonstrates its high efficiency and compatibility in coating preparation. For instance, Ding and co-authors produced SnO_2-Sb coatings on a titanium substrate by cathodic electrodeposition and annealing, which revealed a cluster structure on the coatings' surface.Wu and colleagues created SnO_2-Sb coatings on TiO_2 nanotubes using pulse electrodeposition to achieve a solid electrochemical oxidation ability and high oxygen evolution potential.

SnO_2-Sb coatings' structure and properties could be carefully tailored by altering their preparation parameters [12–14]. Subtle variations in the electrodeposition process affect the resulting properties, and preparation parameters determine the structure and components of the coatings produced.When preparing SnO_2-Sb by the electrodeposition method, many crucial preparation parameters are present, including Sb concentration, current density, and annealing temperature [15–17]. For example, Qing Ni investigated the effects of Sb content on the degradation performance of SnO_2-Sb coatings prepared by the electrodeposition method [18]. Despite this, there are intricate correlations between coating properties and preparation conditions, as these parameters are not independent of each other [19,20]. Such correlations have been examined extensively, in which the outcomes from different studies may sometimes not be comparable due to the various preparation processes. The critical characteristics of prepared coatings, such as active areas and long-term stability, are directly determined by preparation parameters such as current density and annealing temperature. Therefore, in-depth research is still very much needed on the precise impact of these crucial preparation parameters on SnO_2-Sb coatings [21–24].

This work successfully prepared SnO_2-Sb coatings on Ti substrates by the electrodeposition method from a sulfate medium [25]. This study attempts to demonstrate a clear correlation between the essential parameters and characteristics of SnO_2-Sb coatings. The effects of Sb concentration, current density, and annealing temperature on the structure and constituents of the coatings produced were comprehensively investigated.This study's findings could advance the understanding of SnO_2-Sb electrodeposition preparation and pave the way for improving its electrochemical performance in the future.

2. Experiments and Materials

2.1. Pretreatments of Ti Substrates

Pure Ti sheets, which were 15 mm × 15 mm ×2 mm in size, were used in this study. The chemicals used were supplied by Aladdin Co. (Shanghai, China) as analytical reagents and used as received.Grounding and sandpaper polishing up to a 2000 mesh were used to finish the titanium sheet. The polished titanium sheet was placed in a 15 wt.% NaOH aqueous solution at 85 °C for 2 h at a constant temperature. The alkaline treated titanium sheet was immersed in a 12 wt.% oxalic acid solution at 85 °C for 3 h, followed by ultrasonic washing for 10 min.

2.2. Preparation of Sn-Sb Precoatings

By electrodeposition of the cathode current in a sulfate electroplating medium, SnO_2-Sb coatings were produced on pretreated Ti substrates. The sulfate electrolyte consisted of 65 mL/L H_2SO_4 (sulphuric acid), 10 g/L $SnSO_4$ (stannic sulfate), 0.25~0.75 g/L $SbCl_3$ (antimony chloride), 2 g/L $C_{12}H_{16}O_{11}$ (gelatin), and 1 g/L $C_6H_6O_2$ (p-dihydroxybenzene). The ratios of Sb/Sn in atomic percentages in the electrolytes were 2.5%, 5.0%, and 7.5% in the electrodeposition process. A pretreated titanium sheet served as the cathode and a tinplate (40 mm by 40 mm) served as the anode for the electrolytic cell.At a specific current density (10, 20, 30, 40, and 50 mA/cm^2), cathodic electrodeposition was performed at a stirring speed of 300 rpm. The electroplating time was 10 min and the temperature was 30 °C. After the cathodic electrodeposition, the Sn-Sb precoating was prepared on the Ti substrate.

2.3. Preparation of SnO_2-Sb Coatings

Further oxidation treatment was necessary to obtain the SnO_2-Sb coatings. The as-prepared Sn-Sb precoatings were transferred into oxides in a muffle furnace for annealing treatment at certain temperatures (500, 600, 700 °C) for 10 h, followed by air cooling to obtain the SnO_2-Sb coatings.

2.4. Characterization Tests

A scanning electron microscope (SEM, ProX, Phenom; Eindhoven, The Netherlands) was used to determine the coatings' surface and cross-sectional structures, and an embedded energy dispersive spectrometer (EDS) detector was used for elemental analysis. The phase components were identified using an X-ray diffraction (XRD-6000X; Shimadzu, Kyoto, Japan) machine with Cu Ka radiation (Rouse = 1.54056 Ü).X-ray photoelectron spectroscopy (XPS, ESCALAB 250Xi; Thermo Fisher Scientific, Waltham, MA, USA) was utilized to analyze elemental details.

3. Results and Discussion

3.1. Effects of Current Density

Figure 1 shows the surface morphologies and elemental compositions of the electrodeposited Sn-Sb precoatings and annealed SnO_2-Sb coatings. The prepared Sn-Sb precoatings' surface features were smooth and dense at low current densities (10 and 20 mA/cm^2), as depicted in Figure 1a,c. As the current density increased to 30 mA/cm^2, tiny pores began to appear on the precoating surface, resulting in a significant increase in surface roughness (Figure 1e). However, when the current density increased to 50 mA/cm^2, the Sn-Sb precoatings revealed a non-uniform surface morphology, making the coating quality inferior as shown in Figure 1i.

The surface characteristics of the SnO_2-Sb coatingswere hardly altered compared to the Sn-Sb precoatings, even though the precoatings were oxidized; their surface morphology was largely preserved. It can be seen that the SnO_2-Sb coatings had relatively flat surface features when prepared at 10 and 20 mA/cm^2, and their coating surface was dense and had few pores as indicated in Figure 1b,d. When the current density reached 30 mA/cm^2 as shown in Figure 1f, the SnO_2-Sb coatings exhibited a cluster-like surface structure, where the small crystallites coalesced into numerous surface clusters. However, by increasing the current density to 40 and 50 mA/cm^2, as shown in Figure 1h,j, the agglomeration process became more evident and prominent pores appeared. In the meantime, the surface clusters became smaller and their number increased.

Polarization behavior could explain the variations in surface morphology at the increasing current densities during the electrodeposition process [26]. Precisely, the polarization effect was enhanced due to the high overpotential caused by the high current density, during which the side reaction of hydrogen evolution was intensified. The release of hydrogen gas created surface pores and protrusions, significantly altering the surface morphology of the precoatings.

The attached elemental data support the preparation of the precoatings and SnO_2-Sb coatings [27]. Sn dominated the prepared precoatings, but it is noteworthy that an increasing current density resulted in higher Sb content in the Sn-Sb precoatings. This variation in elemental composition occurred due to the different reduction potentials of Sn and Sb. The increased Sb content during precoating at higher current densities could be attributed to a greater reduction overpotential of the Sb electrodeposition reactions [28].

Figure 2 shows the XRD diffractograms of the Sb-Sn precoatingsand SnO_2-Sb coatings prepared at different current densities. The positions of the diffraction peaks are consistent with the standard Sn (JCPDS:04-0673) and Sb (JCPDS:33-0118) diffractograms, which proves the successful electrodeposition of Sn and Sb on the Ti substrates. In all samples, the dominant peaks originated from Sn. It should be noted that the increased current density reduced the intensity of the most significant Sn diffraction peaks, which indicates the refined grain size under the high current density. It has extensively been reported that small grain sizes are correlated with the high overpotential at a high applied current density [29,30]. Inaddition, a higher current density above 30 mA/cm^2 led to a higher content of Sb in the precoatings, as indicated by more Sb peaks recorded in the profiles, which agrees with previous EDS data.

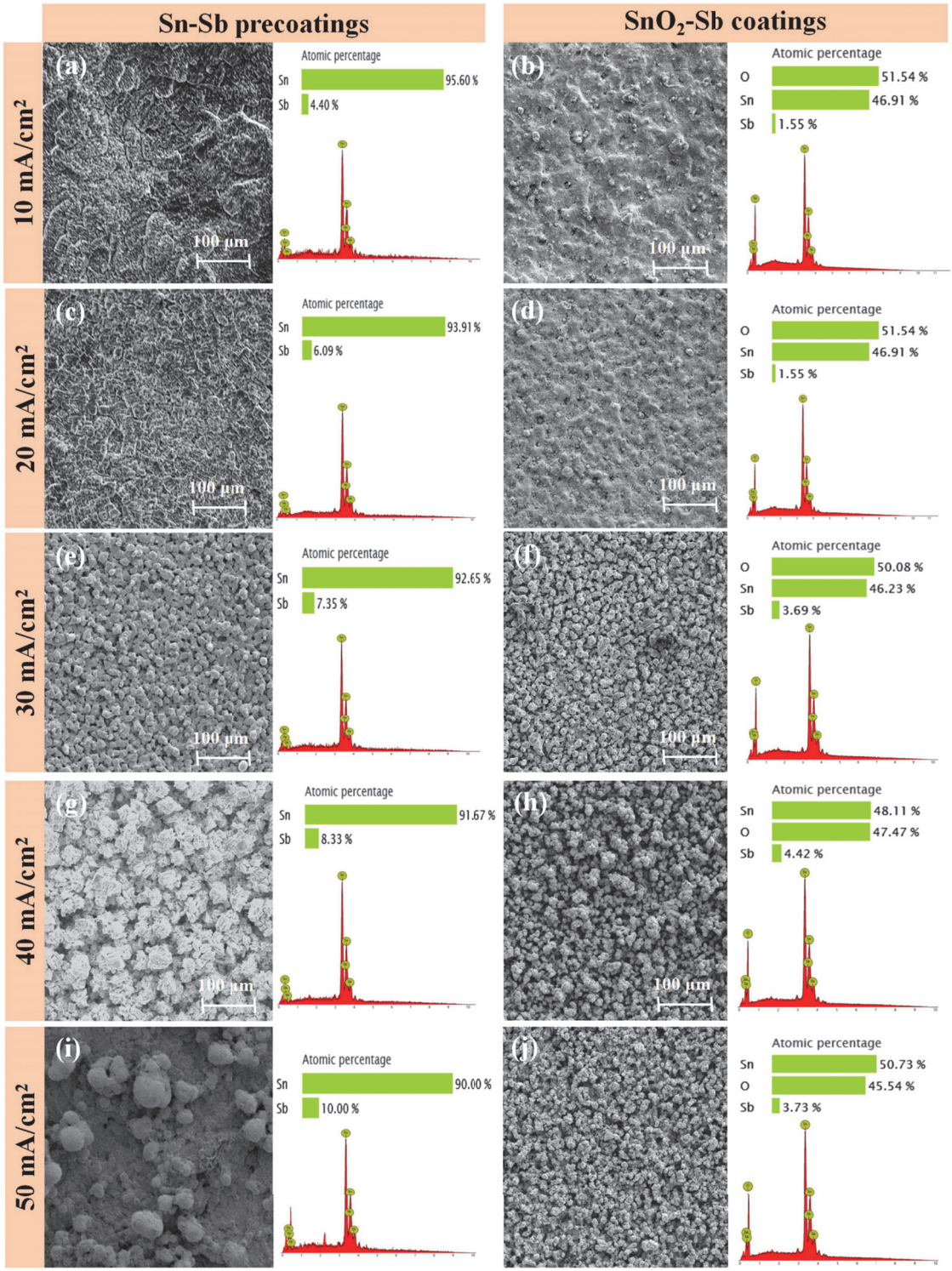


Figure 1. Surface morphologies and elemental compositions of Sn-Sb precoatings prepared at different current densities: (**a**) 10 mA/cm^2, (**c**) 20 mA/cm^2, (**e**) 30 mA/cm^2, (**g**) 40 mA/cm^2, (**i**) 50 mA/cm^2. Morphologies and elemental compositions ofSnO_2-Sb coatings prepared at different current densities: (**b**) 10 mA/cm^2, (**d**) 20 mA/cm^2, (**f**) 30 mA/cm^2, (**h**) 40 mA/cm^2, (**j**) 50 mA/cm^2.

Despitethe XRD pattern differences for the precoatings under different current densities, the annealed SnO_2-Sb coatings show similar phase constituents for all samples (Figure 2b). Most diffraction peaks belonged to SnO_2, while no peaks from the antimony oxide were detected in the coatings.

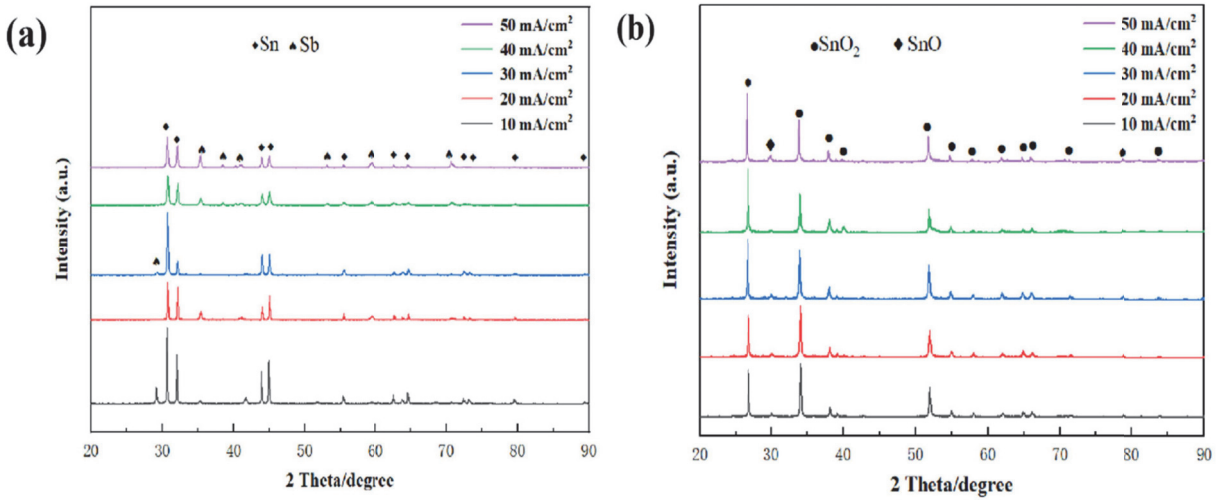


Figure 2. XRD diffractograms recorded of (**a**) Sn-Sb precoatings and (**b**) SnO_2-Sb coatings prepared at different current densities.

The cross-sectional morphologies of the samples prepared by different current densities were also determined, as depicted in Figure 3. The SnO_2-Sb layer was electrodeposited on the Ti substrates for all samples. When the current density was below 30 mA/cm^2, the prepared SnO_2-Sb coating was well-coated, fully covering the substrate with a good quality. The estimated thickness of the SnO_2-Sb coating increased from ~14 um at 10 mA/cm^2 to ~23 um at 30 mA/cm^2.

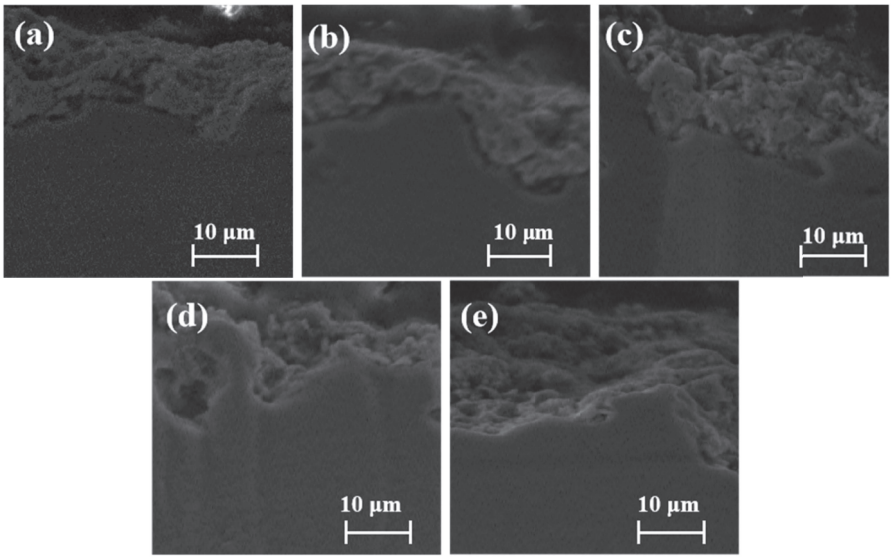


Figure 3. Cross-sectional morphologies of SnO_2-Sb coatings prepared at different current densities: (**a**) 10 mA/cm^2, (**b**) 20 mA/cm^2, (**c**) 30 mA/cm^2, (**d**) 40 mA/cm^2, (**e**) 50mA/cm^2.

When the current density was higher than 30 mA/cm^2, a notable morphologic change trend could be noted: the higher the applied current density, the thinner the coated SnO_2-Sb coating (i.e., 5~10 um). The observed phenomena match the surface observations of the samples, which suggests that an open coating surface correlates with a small coating thickness. To further verify such phenomena, we carried out the cross-sectional images for typical samples using a different preparation method. Specifically, we cut the plate sample directly and performed SEM observation without polishing or grounding, which helped to avoid the possible detachment of a porous coating. We found a consistent trend in that an excessively high current density resulted in a thinner coating and a relatively porous surface structure, as shown in Figure S1 in the Supplementary Materials.

Under a high current density, the intense hydrogen evolution consumedmuch of the charge in the electrodeposition process. The release of hydrogen gas gives an open surface and leads to a thinner coating. The subsequent annealing treatment hardly changed such variation trends.

XPS measurements were carried out to analyze the chemical state of the surface elements for the prepared SnO_2-Sb coatings, as shown in Figure 4. Figure 4a shows the overall spectrum. The annealing treatment oxidized the precoating into its oxide form. Figure 4b–d revealed that Sb^{3+} and Sb^{5+} were present in the SnO_2-Sb coatings, corresponding to the two oxidation states for Sb that existed in the SnO_2 lattice. Moreover, O_{lat} (i.e., lattice oxygen species) and O_{ads} (hydroxyl oxygen species) are the two oxygen species that were identified, consistent with previous research [31].

On the basis of the XPS analysis, Table 1 illustrates the calculated ratios of Sb^{5+}/Sb^{3+} and O_{ads}/O_{lat}. The higher proportion of Sb^{5+}/Sb^{3+} indicates that there was an adequate oxidation reaction during annealing. Generally speaking, Sb^{5+} is the prominent electron donor for SnO_2-Sb coatings. The current density of 30 mA/cm^2 generated a more conductive coating with a higher proportion of Sb^{5+}/Sb^{3+}. Increased Sb^{5+} content gave rise to improved conductivity and an active surface. The lattice oxygen was reduced at the same time as the natural suppliers of oxygen vacancies were suppressed.

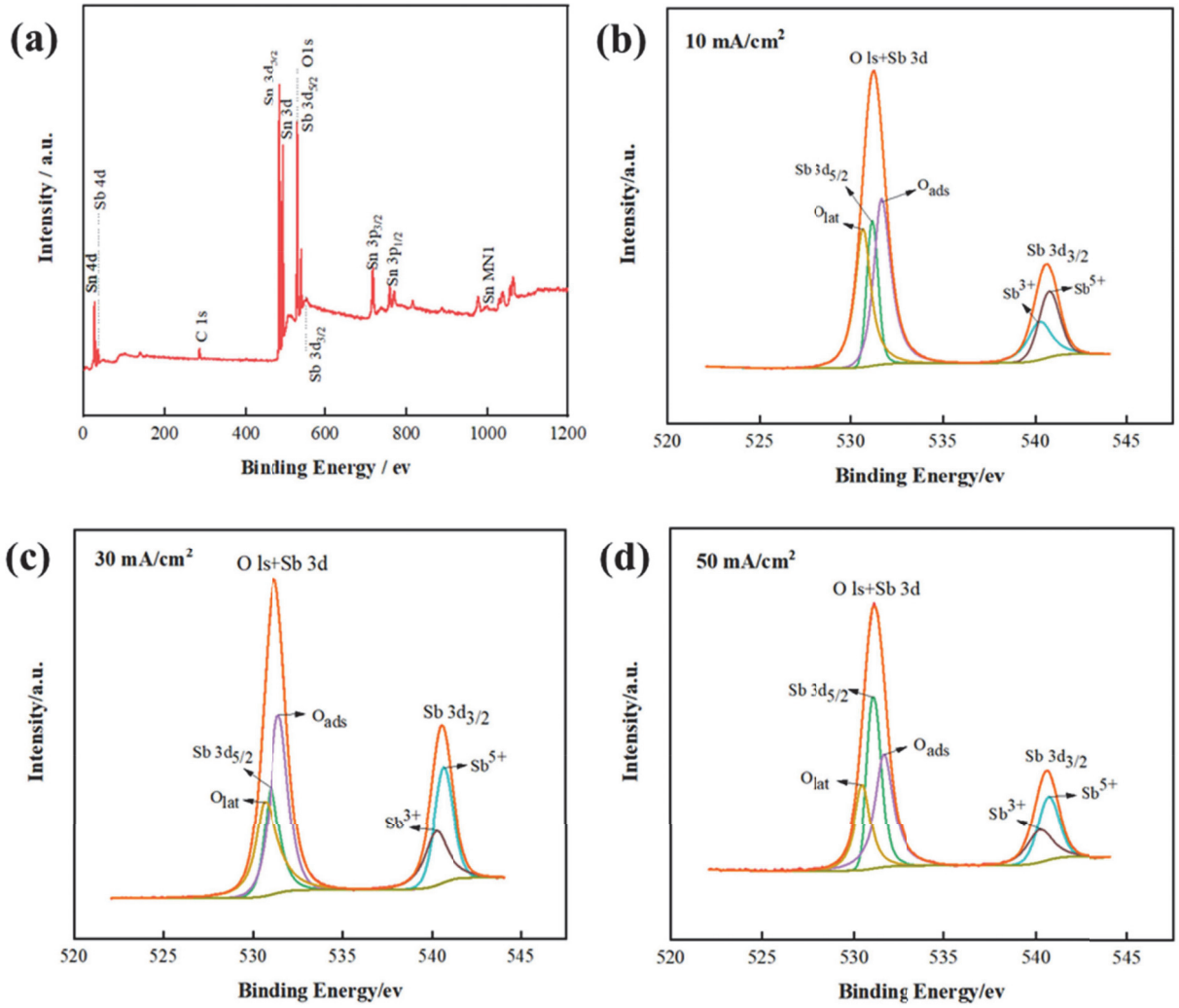


Figure 4. XPS spectra recorded of samples prepared at different current densities: (**a**) full spectrum; (**b**) O and Sbspectra detected of the samples prepared with the current density of 10 mA/cm^2, (**c**) 30 mA/cm^2, (**d**) 50 mA/cm^2.

Table 1. Calculated atomic ratios for the samples prepared at different current densities.

Applied Current Density	AtomicRatio	
	Sb^{5+}/Sb^{3+}	O_{ads}/O_{lat}
10 mA/cm^2	1.24	0.53
30 mA/cm^2	1.52	0.72
50 mA/cm^2	1.36	0.61

The surface characteristics of SnO_2-Sb coatings, such as roughness, conductivity, and active areas, are essential to determine for their potential applications, such as electrochemical catalysis and energy storage. Furthermore, the coatings' complete coverage of the substrate used is a premise in its applications. In this regard, it is possible to subtly customize SnO_2-Sb coatings' surface morphology for various usages by varying their electrodeposition parameters. In this regard, our study could be a reference for related research.

3.2. Effects of Annealing Temperature

Theeffects of annealing temperature on the oxide layers were also comprehensively investigated. The experiments used a current density of 30 mA/cm^2, considering their rough surface and good coating quality. Heat treatment temperatures of 500, 600, and 700 °C were applied to prepare the SnO_2-Sb_2O_x coatings.

Figure 5 presents the surface information of the oxide coatings. It should be noted that the annealing temperature of 500 °C could not fabricate a rough surface morphology, as indicated in Figure 5a,b, where a relatively flat surface consisting of rectangular crystals was observed for the SnO_2-Sb coatings. In contrast, a higher heating temperature of 600 °C gave a distinct surface morphology showing numerous cauliflower-shaped crystals. Further increasing the temperature to 700 °C turned the coating into a relatively non-uniform surface made up of separate spheres.

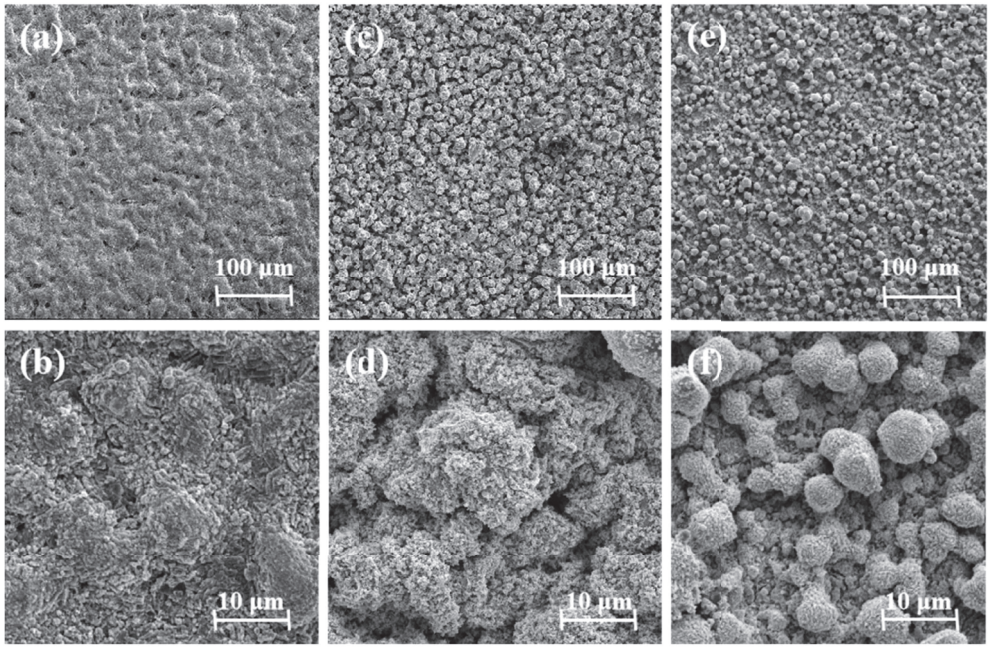


Figure 5. Surface morphologies and magnification plots of SnO_2-Sb coatings prepared at different annealing temperatures: (**a**) 500 °C, (**b**) 500 °C magnification, (**c**) 600 °C, (**d**) 600 °C magnification, (**e**) 700 °C, (**f**) 700 °C magnification.

The phase constituents for the samples prepared at different heating temperatures are presented in Figure 6. At the temperature of 500 °C, sharp SnO_2 peaks were detected, yet a minor Sn peak still existed in the coatings. This indicates an inadequate oxidation process at a low temperature, which harmed the coating performance. The annealing treatment under an increased temperature entirely changed the coatings into their oxide form. It sharpened the SnO_2 diffraction peaks due to the promoted grain growth process at a higher oxidation temperature.

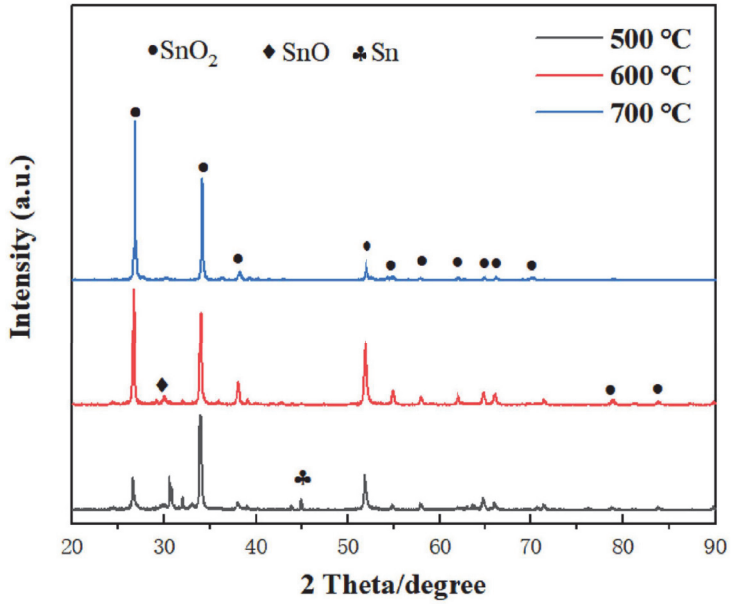


Figure 6. XRD patterns recorded of the SnO_2-Sb coatings prepared at different annealing temperatures.

Cross-sectional information was recorded and is displayed in Figure 7. The annealing treatment at a low temperature of 500 °C could not transform the precoatings into their oxide form, and a limited coating thickness of ~13 um was observed, as shown in Figure 7a. The annealing treatment at 600 °C resulted in a much thicker and uniform coating with a thickness of ~23 um, as depicted in Figure 7b. However, under an excessively high temperature at 700 °C, the thickness distribution of the oxide coating became much less uniform, as shown in Figure 7c, which agrees with the surface morphologic observations above.

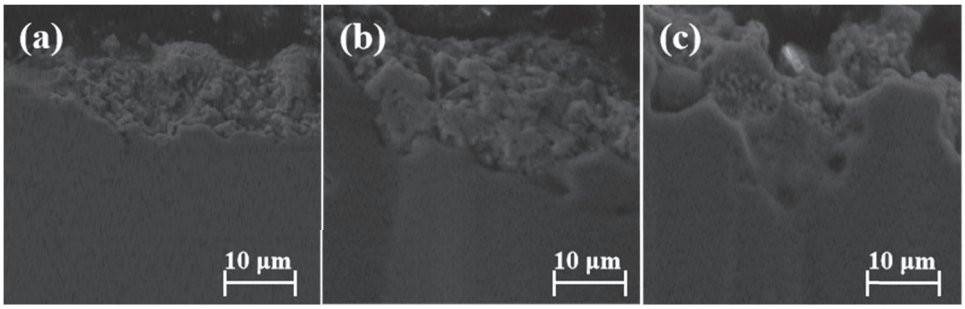


Figure 7. Cross-sectional morphologies of SnO_2-Sb coatings prepared at different annealing temperatures: (**a**) 500 °C, (**b**) 600 °C, (**c**) 700 °C.

The annealing temperature alters the oxidation process significantly [32–34], during which Sn-Sb precoatingsare transformed into SnO_2-Sb coatings. As proposed by our study, selecting a proper annealing temperature is of great importance: a low temperature cannot fully oxidize the precoatings and a high temperature causes severe non-uniformity. In contrast, our study's proper annealing temperature of 600 °C preparedSnO_2-Sb coatingsof an excellent quality.

3.3. Effectsof Sb Concentration on Electrolytes

This research also investigated the effects of Sb concentration on the electrolytes within the prepared coatings. Three different concentrations of 2.5%, 5.0%, and 7.5% (Sb: Sn in atomic percentagesof electrolytes) were selected for the experiments. Figure 8 presents the surface morphologies and elemental results recorded on the Sn-Sb precoatings and SnO_2-Sb coatings. A small concentration at 2.5% caused a relatively flat surface morphology with some spherical crystals. When a 5.0% Sb concentration was applied, more rough and open surface features were attained. However, upon further increasing the Sb concentration to 7.5%, a flatter surface morphology was obtained for the precoating, causing a non-uniform surface morphology for the oxide coating after the annealing treatment, as shown in Figure 8f.

In addition, the EDS results presented in Figure 8 indicate that the increasing Sb concentration in the electrodeposition directly resulted in higher Sb content in the prepared coatings. It should be noted that the Sb content in the Sn-Sb coatingswas higher than in the electrolytes, resulting from the higher overpotential of Sn reduction reactions [35].

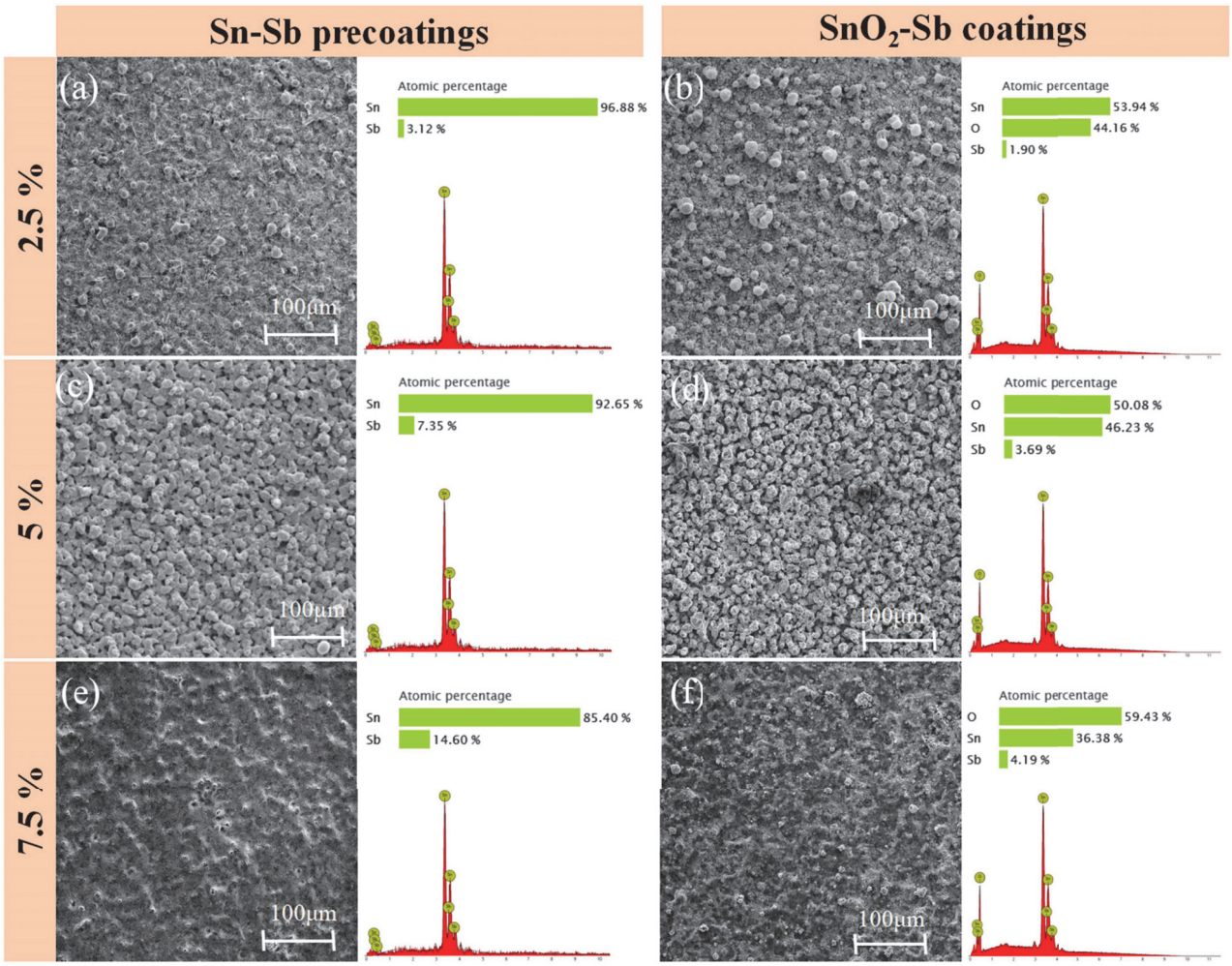


Figure 8. Surface morphologies and elemental compositions of Sn-Sb precoatingsandSnO_2-Sb coatings prepared at different Sb concentrations: (**a**) 2.5%, (**c**) 5.0%, (**e**) 7.5%.Morphologies and elemental compositions ofSnO_2-Sb coatings prepared at different Sb concentrations: (**b**) 2.5%, (**d**) 5.0%, (**f**) 7.5%.

The phase constituents of the prepared samples are presented in Figure 9. The Sn-Sb precoatings were electrodeposited on the Ti substrates for all samples, as shown in Figure 9a. The high Sb content in the electrolytes gave rise to several Sb peaks appearing for the Sn-Sb precoatings. Interestingly, the increased Sb concentration gave no Sb_2O_x diffraction peak

in the patterns, indicating that the Sb was doped by substituting the Sn in the lattice.The activity of mixed oxides was significantly affected by Sb doping. In the case of pure SnO_2, the non-conductivity made them unsuitable anode materials. The phase composition of the SnO_2-Sb coatings may be influenced by the doping level, which in turn, impacts electrical conductivity. The cassiterite SnO_2 was present in the mixed oxide. By substituting Sn^{4+} ions with doped Sb at their locations, the extra valence electrons in Sb acted as donors and SnO_2 was more conductive [36].

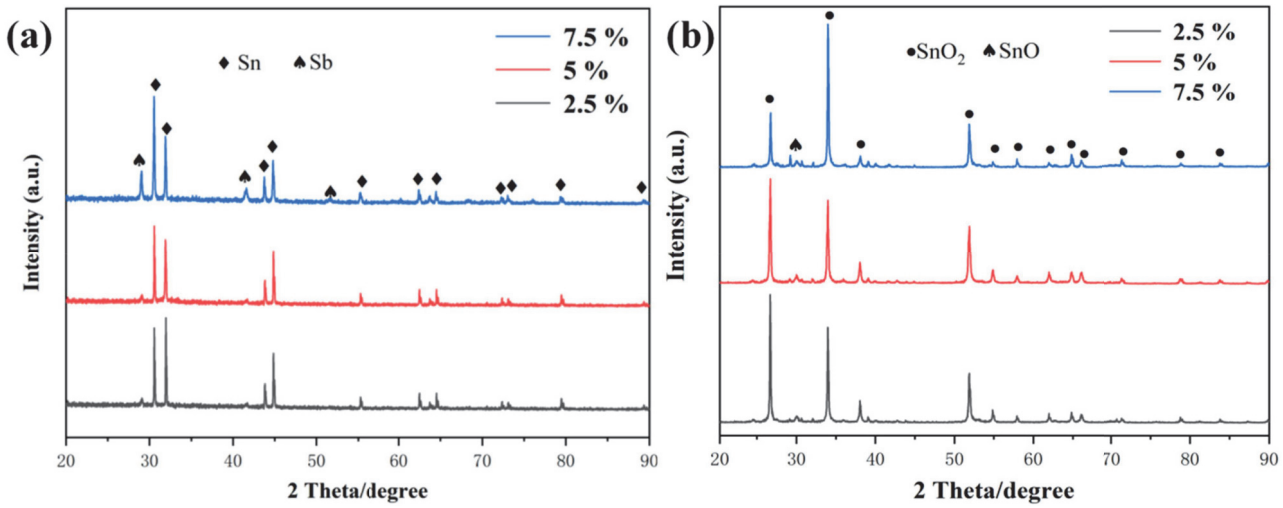


Figure 9. XRD diffractograms recorded of (**a**) Sn-Sb precoatings and (**b**) SnO_2-Sb coatings prepared at different Sb concentrations.

4. Conclusions

This study examined how the properties of SnO_2-Sb coatings are affected by different preparation parameters. Sn-Sb coatings were electrodeposited and then oxidized into SnO_2-Sb coatings through an annealing treatment. Increasing the current density altered the surface roughness of the prepared Sn-Sb precoatings, but the annealing treatment did not significantly alter the primary surface features of the SnO_2-Sb coatings. The suitable current density of 30 mA/cm^2 created a rough, active coating surface without a decrease in the coating thickness.

Our study's proper annealing temperature of 600 °C transformed Sn-Sb precoatings into SnO_2-Sb coatings and achieved an excellent coating quality. The change in Sb content affected the morphologic features of the prepared SnO_2-Sb coatings but did not vary the cassiterite SnO_2 phase in the mixed oxide coatings.

Supplementary Materials: The following supporting information can be downloaded at: https://www.mdpi.com/article/10.3390/coatings13050866/s1, Figure S1: The cross-sectional images taken on the samples made by different method: the plate sample was directly cut and vertically observed without polishing or grounding.

Author Contributions: Conceptualization, Z.H. and Y.W.; methodology, C.Y.; validation, Z.H.; formal analysis, Y.W.; investigation, C.Y.; resources, Z.H.; data curation, J.L.; writing—original draft preparation, Z.H.; writing—review and editing, C.Y., Z.M. and Y.W.; funding acquisition, Z.H. All authors have read and agreed to the published version of the manuscript.

Funding: This work was supported by the Natural Science Foundation of Jiangsu Province under Grant No. BK20201008.

Institutional Review Board Statement: Not applicable.

Informed Consent Statement: Not applicable.

Data Availability Statement: Not applicable.

Conflicts of Interest: The authors declare no conflict of interest.

References

1. Shao, D.; Yan, W.; Li, X.; Yang, H.; Xu, H. A Highly Stable Ti/TiHx/Sb–SnO_2 Anode: Preparation, Characterization and Application. *Ind. Eng. Chem. Res.* **2014**, *53*, 3898–3907. [CrossRef]
2. Zhang, B.; Chen, M.; Zhang, C.; He, H. Electrochemical oxidation of gaseous benzene on a Sb-SnO_2/foam Ti nano-coating electrode in all-solid cell. *Chemosphere* **2019**, *217*, 780–789. [CrossRef] [PubMed]
3. Shao, D.; Chu, W.; Li, X.; Yan, W.; Xu, H. Electrochemical oxidation of guaiacol to increase its biodegradability or just remove COD in terms of anodes and electrolytes. *RSC Adv.* **2016**, *6*, 4858–4866. [CrossRef]
4. Pahlevani, L.; Mozdianfard, M.R.; Fallah, N. Electrochemical oxidation treatment of offshore produced water using modified Ti/Sb-SnO_2 anode by graphene oxide. *J. Water Process Eng.* **2020**, *35*, 101204. [CrossRef]
5. Duan, T.; Chen, Y.; Wen, Q.; Duan, Y. Enhanced electrocatalytic activity of nano-TiN composited Ti/Sb–SnO_2 electrode fabricated by pulse electrodeposition for methylene blue decolorization. *RSC Adv.* **2014**, *4*, 57463–57475. [CrossRef]
6. Sun, Y.; Cheng, S.; Li, L.; Yu, Z.; Mao, Z.; Huang, H. Facile sealing treatment with stannous citrate complex to enhance performance of electrodeposited Ti/SnO_2-Sb electrode. *Chemosphere* **2020**, *255*, 126973. [CrossRef]
7. Sun, Y.; Cheng, S.; Mao, Z.; Lin, Z.; Ren, X.; Yu, Z. High electrochemical activity of a Ti/SnO_2-Sb electrode electrodeposited using deep eutectic solvent. *Chemosphere* **2020**, *239*, 124715. [CrossRef]
8. Mameda, N.; Park, H.; Shah, S.S.A.; Lee, K.; Li, C.-W.; Naddeo, V.; Choo, K.-H. Highly robust and efficient Ti-based Sb-SnO_2 anode with a mixed carbon and nitrogen interlayer for electrochemical 1,4-dioxane removal from water. *Chem. Eng. J.* **2020**, *393*, 124794. [CrossRef]
9. Shao, D.; Yan, W.; Cao, L.; Li, X.; Xu, H. High-performance Ti/Sb-SnO_2/Pb_3O_4 electrodes for chlorine evolution: Preparation and characteristics. *J. Hazard. Mater.* **2014**, *267*, 238–244. [CrossRef]
10. Shao, C.; Chen, A.; Yan, B.; Shao, Q.; Zhu, K. Improvement of electrochemical performance of tin dioxide electrodes through manganese and antimony co-doping. *J. Electroanal. Chem.* **2016**, *778*, 7–11. [CrossRef]
11. Song, Y.-F.; Liu, J.-M.; Ge, F.; Huang, X.; Zhang, Y.; Ge, H.-H.; Meng, X.-J.; Zhao, Y.-Z. Influence of Nd-doping on the degradation performance of Ti/Sb-SnO_2 electrode. *J. Environ. Chem. Eng.* **2021**, *9*, 105409. [CrossRef]
12. Rajasekhar, B.; Nambi, I.M.; Govindarajan, S.K. Investigating the degradation of $nC1_2$ to nC_{23} alkanes and PAHs in petroleum-contaminated water by electrochemical advanced oxidation process using an inexpensive Ti/Sb-SnO_2/PbO_2 anode. *Chem. Eng. J.* **2021**, *404*, 125268. [CrossRef]
13. Zhang, Y.; Zhang, C.; Shao, D.; Xu, H.; Rao, Y.; Tan, G.; Yan, W. Magnetically assembled electrodes based on Pt, RuO_2-IrO_2-TiO_2 and Sb-SnO_2 for electrochemical oxidation of wastewater featured by fluctuant Cl^- concentration. *J. Hazard. Mater.* **2022**, *421*, 126803. [CrossRef] [PubMed]
14. Shao, D.; Lyu, W.; Cui, J.; Zhang, X.; Zhang, Y.; Tan, G.; Yan, W. Polyaniline nanoparticles magnetically coated Ti/Sb-SnO_2 electrode as a flexible and efficient electrocatalyst for boosted electrooxidation of biorefractory wastewater. *Chemosphere* **2020**, *241*, 125103. [CrossRef]
15. Duan, Y.; Wen, Q.; Chen, Y.; Duan, T.; Zhou, Y. Preparation and characterization of TiN-doped Ti/SnO_2-Sb electrode by dip coating for Orange II decolorization. *Appl. Surf. Sci.* **2014**, *320*, 746–755. [CrossRef]
16. Guo, D.; Guo, Y.; Huang, Y.; Chen, Y.; Dong, X.; Chen, H.; Li, S. Preparation and electrochemical treatment application of Ti/Sb-SnO_2-Eu&rGO electrode in the degradation of clothianidin wastewater. *Chemosphere* **2021**, *265*, 129126. [CrossRef]
17. Bi, Q.; Zhang, Z.; Sun, Y.; Jiang, S.; Wang, Z.; Li, Y.; Xue, J. Preparation and performance of highly active and long-life mesopore Ti/SnO_2–Sb electrodes for electrochemical degradation of phenol. *J. Alloy. Compd.* **2021**, *889*, 161657. [CrossRef]
18. Ni, Q. Ti/SnO_2-Sb_2O_5 as an Anode Material in Electro-Oxidation of Organic Compounds for Wastewater Treatment. Ph.D. Thesis, University of Toronto, Toronto, ON, Canada, 2016.
19. Wai, T.P.; Yin, Y.; Zhang, X.; Li, Z.; Alakhras, F. Preparation of Ti/SnO_2-Sb/Rare Earth Electrodes Containing Different Contents of Ni Intermediate Layer for Efficient Electrochemical Decolorization of Rhodamine B. *J. Chem.* **2021**, *2021*, 2672674. [CrossRef]
20. Zhang, R.; Li, K.; Ren, S.; Chen, J.; Feng, X.; Jiang, Y.; He, Z.; Dai, L.; Wang, L. Sb-doped SnO_2 nanoparticle-modified carbon paper as a superior electrode for a vanadium redox flow battery. *Appl. Surf. Sci.* **2020**, *526*, 146685. [CrossRef]
21. Ansari, A.R.; Hammad, A.H.; Abdel-wahab, M.S.; Shariq, M.; Imran, M. Structural, optical and photoluminescence investigations of nanocrystalline CuO thin films at different microwave powers. *Opt. Quantum Electron.* **2020**, *52*, 426. [CrossRef]
22. Hone, F.G.; Ampong, F.K.; Abza, T.; Nkrumah, I.; Paal, M.; Nkum, R.K.; Boakye, F. The effect of deposition time on the structural, morphological and optical band gap of lead selenide thin films synthesized by chemical bath deposition method. *Mater. Lett.* **2015**, *155*, 58–61. [CrossRef]
23. Arandhara, G.; Bora, J.; Saikia, P.K. Effect of pH on the crystallite size, elastic properties and morphology of nanostructured ZnS thin films prepared by chemical bath deposition technique. *Mater. Chem. Phys.* **2020**, *241*, 122277. [CrossRef]
24. Ansari, A.R.; Imran, M.; Yahia, I.S.; Abdel-Wahab, M.S.; Alshahrie, A.; Khan, A.H.; Sharma, C. Effect of microwave power on morphology of AgO thin film grown using microwave plasma CVD. *Int. J. Surf. Sci. Eng.* **2018**, *12*, 1–12. [CrossRef]
25. Cui, Y.H.; Li, X.Y.; Chen, G. Electrochemical degradation of bisphenol A on different anodes. *Water Res.* **2009**, *43*, 1968–1976. [CrossRef] [PubMed]

26. Sun, Y.; Zhang, S.; Jin, B.; Cheng, S. Efficient degradation of polyacrylamide using a 3-dimensional ultra-thin SnO(2)-Sb coated electrode. *J. Hazard. Mater.* **2021**, *416*, 125907. [CrossRef] [PubMed]
27. Ansari, A.; Nematollahi, D. Convergent paired electrocatalytic degradation of p-dinitrobenzene by Ti/SnO_2-Sb/β-PbO_2 anode. A new insight into the electrochemical degradation mechanism. *Appl. Catal. B Environ.* **2020**, *261*, 118226. [CrossRef]
28. Asim, S.; Yin, J.; Yue, X.; Shah, M.W.; Zhu, Y.; Li, Y.; Wang, C. Controlled fabrication of hierarchically porous Ti/Sb–SnO_2 anode from honeycomb to network structure with high electrocatalytic activity. *RSC Adv.* **2015**, *5*, 28803–28813. [CrossRef]
29. He, Z.; Cao, D.; Wang, Y.; Yin, L.; Singh, H. Preparation of Co–P–TiO_2 nanocomposite coatings via a pulsed electrodeposition process. *Surf. Eng.* **2020**, *36*, 975–981. [CrossRef]
30. He, Z.; Zhou, Y.; Wang, Y.; Guo, P.; Jiang, W.; Yao, C.; Shu, X. Preparation and properties of Ni-W-P-TiO_2 nanocomposite coatings developed by a sol-enhanced electroplating method. *Chin. J. Chem. Eng.* **2022**, *44*, 369–376. [CrossRef]
31. Zhang, S.; Yu, C.; Tan, J.; Wang, Y.; He, Z. Ti/SnO_2-Sb_2Ox-TiO_2 Electrodeposited from Methanesulfonate Electrolytes: Preparation, Properties, and Performance. *Coatings* **2022**, *12*, 366. [CrossRef]
32. Özdal, T.; Chtouki, T.; Kavak, H.; Figa, V.; Guichaoua, D.; Erguig, H.; Mysliwiec, J.; Sahraoui, B. Effect of Annealing Temperature on Morphology and Optoelectronics Properties of Spin-Coated CZTS Thin Films. *J. Inorg. Organomet. Polym. Mater.* **2020**, *31*, 89–99. [CrossRef]
33. Manickam, K.; Muthusamy, V.; Manickam, S.; Senthil, T.S.; Periyasamy, G.; Shanmugam, S. Effect of annealing temperature on structural, morphological and optical properties of nanocrystalline TiO2 thin films synthesized by sol–gel dip coating method. *Mater. Today Proc.* **2020**, *23*, 68–72. [CrossRef]
34. Timofeev, V.A.; Mashanov, V.I.; Nikiforov, A.I.; Azarov, I.A.; Loshkarev, I.D.; Korolkov, I.V.; Gavrilova, T.A.; Yesin, M.Y.; Chetyrin, I.A. Effect of annealing temperature on the morphology, structure, and optical properties of nanostructured SnO_x films. *Mater. Res. Express* **2020**, *7*, ab6122. [CrossRef]
35. Xu, L.; Liang, G.; Yin, M. A promising electrode material modified by Nb-doped TiO_2 nanotubes for electrochemical degradation of AR 73. *Chemosphere* **2017**, *173*, 425–434. [CrossRef] [PubMed]
36. Yang, K.; Liu, Y.; Qiao, J. Electrodeposition preparation of Ce-doped Ti/SnO_2-Sb electrodes by using selected addition agents for efficient electrocatalytic oxidation of methylene blue in water. *Sep. Purif. Technol.* **2017**, *189*, 459–466. [CrossRef]

Disclaimer/Publisher's Note: The statements, opinions and data contained in all publications are solely those of the individual author(s) and contributor(s) and not of MDPI and/or the editor(s). MDPI and/or the editor(s) disclaim responsibility for any injury to people or property resulting from any ideas, methods, instructions or products referred to in the content.

materials

MDPI

Article

Experimental Study on Repairing the Mechanical Characteristics of Oil-Contaminated Silty Clay in Ancient Dike with Modified Lime Mortar

Jianfen Zhou [1,2], Zhiyong Dong [1,*], Yinzhen Dong [3], Xiaohui He [4], Hongmei Wu [2], Bin Chen [2] and Qian Mao [2]

[1] College of Civil Engineering, Zhejiang University of Technology, Hangzhou 310014, China; zhoujf@zjweu.edu.cn
[2] Key Laboratory for Technology in Rural Water Management of Zhejiang Province, Zhejiang University of Water Resources and Electric Power, Hangzhou 310018, China
[3] Lanxi Town Planning Office, Jinhua 321100, China
[4] Lanxi Water Affairs Bureau, Jinhua 321100, China
* Correspondence: dongzy@zjut.edu.cn

Abstract: Flood-controlled ancient dikes play a significant role in flood control and have received widespread attention as historical and cultural symbols. Flood-controlled ancient dikes often undergo disasters, and research on their repair is receiving increasing attention from experts and scholars. This article studies the control of seepage and bank slope instability in flood-controlled ancient dikes. Starting from the repair of ancient dike materials, three types of work are carried out: a test of soil's mechanical properties, finite element numerical simulation, and repair technology research. The research results show that the soil of the ancient dike site has hardened after being contaminated with waste oil from catering. The strength index of the ancient dike soil decreases and shows brittleness when the water content is 15% and the oil content exceeds 6%. The strength index and permeability coefficient of oil-contaminated soil improved using modified lime mortar (MLM), which was achieved using the method of MLM to repair oil contaminated soil. When the MLM content was 10% and the oil content was 6%, the friction angle of the soil sample reached its maximum value. When the MLM content was the same, the higher the density of the soil sample, the greater the friction angle and cohesion and the smaller the permeability coefficient. Establishing a finite element numerical model, through comparative analysis, it was found that after MLM remediation of oil-contaminated soil, the extreme hydraulic gradient of the ancient dike decreased by 31.3%, and the extreme safety factor of the bank slope stability increased by 31.2%. MLM pressure grouting technology was used to improve the soil during the remediation of contaminated soil at the ancient dike site. Through on-site drilling inspection, the effective diffusion radius of MLM grouting was obtained, and the plane layout and grouting depth of MLM pressure grouting were determined. The on-site water injection permeability test showed that using MLM pressure grouting technology can effectively repair oil-contaminated soil in the ancient dike while reducing the permeability coefficient by 8–15%.

Keywords: flood-controlled ancient dike; silty clay; oil pollution; mechanical characteristic of MLM soil; MLM pressure grouting; seepage coefficient of MLM soil

1. Introduction

The urbanization process in China has had a significant impact on the urban water system structure, and urban construction planning optimization based on flood control safety and historical water engineering protection is gradually becoming a research hotspot [1–5]. Many ancient embankments in southern China are adjacent to residential buildings, and rainwater and sewage pipelines are staggered. While ancient dike works play the role of flood control, they are affected by the leakage of waste oil from residents' catering, resulting in changes in the nature of the soil mass of the flood-control dike, resulting in the

aggravation of the damage of piping soil flow caused by flood scouring and changes in the soil strength, resulting in the change of the overall stability of the bank slope and even landslide damage. Lime is the main building material for ancient projects around the world. The repair of ancient dikes requires the use of lime, which has better compatibility with the materials of the original structure to be repaired. There are few reports on the remediation of oil-contaminated soil with lime. Previous research has mainly focused on two aspects: on the one hand, experimental research on the physical and mechanical properties of mineral oil-contaminated soil, and on the other hand, the research on lime-modified raw soil and the reparation of ancient building materials.

The mineral oil of common contaminated soil includes oil, gasoline, diesel, and gasoline, and the contaminated soil includes cohesive soil, fine sand, silty clay, etc. Oil-contaminated soil samples were prepared by mixing the residual soil and oil and were tested in the laboratory. The results showed that oil pollution led to the deterioration of the geotechnical properties of the soil samples. Compared with raw soil, its maximum dry density, optimum water content, permeability, and shear strength decreased [6–8]. The particle size distribution and density of soil samples have a great impact on the mechanical properties and permeability of oil-contaminated clayey silt. With the increase in oil content, the friction angle of soil samples decreases, the cohesion does not change significantly, and the permeability coefficient increases significantly [9]. After the gravel is polluted by oil, with the increase in oil content, the friction angle decreases and the cohesion increases significantly [10–12]. After the clay is polluted by gasoline, the pH value of the clay decreases significantly and the conductivity increases. Additionally, at first, with the increase in gasoline content, the friction angle slightly increased and the cohesion decreased significantly. However, with the increase in the lead content in gasoline, the friction angle and cohesion decreased [13,14]. Another study investigated the effect of petroleum-derived contaminants on the permeability, cohesion, friction angle, and shear strength of fine sand. An increase in cohesion was observed for sand with up to 1% oil contamination, after which the cohesion began to decrease, which also resulted in the reduction in the permeability [15]. After diesel contaminated the loess, the permeability coefficient of the loess decreased with the increase in diesel content, and the compression modulus and unconfined compressive strength were almost unchanged [16–18]. Gasoline pollution poorly graded sand, low-plasticity clay, and silt, and decrease in the friction angle and an increase in the cohesion of the soils were found with an increase in contamination. Unconfined compressive strength of silty soil decreased with increasing gas oil percentage, which is different from low plasticity clay [19,20]. The oil content also affects the bearing-capacity characteristics of sandy loam soil and the settlement of the footing, and was also found to significantly reduce the load settlement and ultimate bearing capacity of the footing [21]. Through the direct shear test and bearing capacity test of strip shallow foundation, it is shown that the oil content reduces the shear strength and bearing capacity of sand to varying degrees [22]. Based on the above research, the physical and mechanical behavior of different types of soil polluted by different kinds of mineral oil is complex, which is quite different from the original soil's properties. It is necessary to evaluate the changes in physical and mechanical properties of silty clay contaminated by oil and to analyze the impact of waste oil pollution on the stress–strain relationship, seepage characteristics, and microstructure characteristics of silty clay, providing basic data for the improvement in the contaminated soil.

Due to the special historical and cultural value of ancient dikes to be preserved during repair, the repair materials should be compatible with the raw materials, and lime should be the main material [23–27]. There are many experimental studies on adding lime and additives to change soil properties. Previous studies have obtained five properties of natural hydraulic lime mortar, namely the type of natural hydraulic lime [28–30]; the ratio of binder to aggregate [31]; the effect of the water–cement ratio on the fluidity of lime mortar [32,33]; the characteristics of aggregate, including composition, particle size, and distribution [34]; and the curing conditions [35]. The results show that when the ratio of binder to aggregate of lime mortar is 1:3, its mechanical properties can be improved and

better carbonation can be obtained [36–38]. Lime and binder can be used to change the mechanical properties and durability of raw soil, and the modification effect of raw soil will increase with the increase in lime content [39–44].

Many scholars have studied the effects of physical and mechanical properties of soil on the seepage and bank-slope stability of flood control dikes. Based on the change in the microstructural arrangement of soil particles, the microscopic change in the permeability coefficient of soil is studied experimentally [45–47]. The coupling equation of seepage and erosion shows that the pore water pressure in soil increases until the hydraulic gradient is greater than the critical hydraulic gradient, and the fine particle phase migrates and loosens from the soil, resulting in deformation and instability [48–51]. Research on bank-slope stability has shown that numerical analysis methods provide an appropriate and effective tool to establish numerical models. Based on changes in the intrinsic properties of soil and experimental data, the bank-slope stability remains to be analyzed [52–57]. Current research rarely involved the characteristics of lime to improve the oil-contaminated soil, and carrying out relevant research is urgently needed to repair the soil to reinforce the ancient dike.

2. Methodology and Materials

2.1. Methodology

There are many flood-controlled ancient dikes in China. These ancient dikes still play a role in flood control, and at the same time, they are often protected cultural relics and landmark buildings in towns. Representative flood-controlled ancient dikes in southern China are all distributed in densely populated towns along rivers (in Figure 1a). Take the Lanxi ancient dike as an example, which is located at the intersection of Qujiang, Jinhua, and Lanjiang rivers, as shown in Figure 1b. The ancient dike was first built in 1512 AD and consists of a wharf and an ancient dike [58], as shown in Figure 1c,d. The ancient dike is built of red sandstone, and the city gate hole is the entrance and exit from the ancient wharf to the town, as shown in Figure 1e,f.



Figure 1. Characteristics of flood-controlled ancient dikes in South China. (**a**) Typical ancient dike distribution; (**b**) aerial view of Lanxi Ancient Dike; (**c**) ancient dike boundary stele; (**d**) ancient wharf; (**e**) city gate hole in ancient dike; (**f**) side view of ancient dike.

Ancient dikes have suffered various forms of damage. The bank slope of Lanxi Ancient Dike is mainly filled with artificial soil, Figure 1a. During the rainy season, the confluence of river water often leads to a surge of river water (Figure 2b). In addition, rainfall and groundwater collection lead to leakage of the ancient dike wall, and waste oil from residential and catering pollutes the soil, as shown in Figure 2c,d. After the soil of the ancient dike was polluted by the waste oil from catering, the stability of the bank slope was reduced, and landslides and other damages occurred, as shown in Figure 2e.

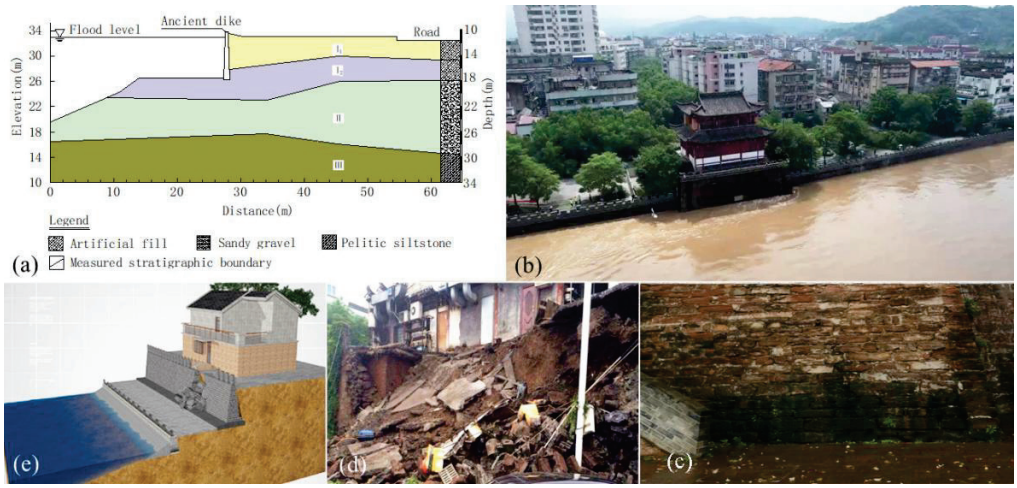


Figure 2. Damage to ancient dike. (**a**) Engineering geology of Lanxi ancient dike; (**b**) flood of Lanjiang river; (**c**) leakage; (**d**) oil pollution; (**e**) bank slope collapse.

Through experiments, the physical and mechanical parameters of soil were obtained, and changes in soil, oil content, and modified lime mortar (MLM) content on mechanical indicators were compared and analyzed. Then, the stability of flood-controlled ancient dike was studied using the finite element numerical analysis approach to take into account the intrinsic variability of the soil parameters. The research provides theoretical guidance for the study of ancient dike seepage, slope stability, and reinforcement measures, as shown in Figure 3.

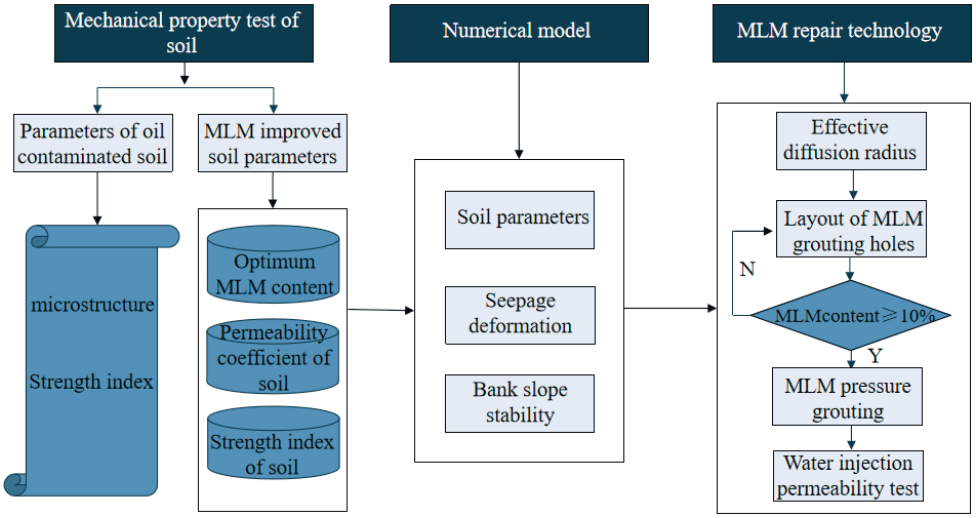


Figure 3. Flowchart of the proposed methodology.

2.2. Materials

2.2.1. Soil

The soil for the test was taken from a typical section of the Lanxi Ancient Dike. Figure 4a,b is a typical section of the Lanxi dike. It follows that the ancient dike's geology can be divided into three soil layers, namely newly filled layers I_1 and I_2 and sand gravel-filled layer II. The thickness of soil layers I_1 and I_2 is 2.5~4.5 m, the thickness of sand gravel layer II is 6.1~11.5 m, and the layer below layer II is the argillaceous silty sand layer. The soil of layer I_1 is newly artificially filled soil, mainly composed of silty cohesive soil with mixed rubble and a small number of broken bricks in the middle. In some embankment sections, there are still brick wall structures of previous houses left. This layer of soil has poor uniformity, complex material composition, unstable properties, and poor impermeability. The filling soil of layer I_2 is mainly composed of silty clay with sand gravel. Compared to layer I_1, this layer has a relatively long filling history. The structure of this layer is moderately dense, with general uniformity. This layer of soil has medium water permeability. Layer II is composed of sandy gravel pebbles, mixed with silty clay, and is moderately dense with medium water permeability. The impact range of waste oil leakage from catering is mostly in layer I_1 and layer I_2, and the impact range of seepage deformation is in layer I_1, layer I_2, and layer II. The soil used in this test is taken from this range, and after drying and screening, the soil with a particle size of less than 2 mm is taken for the remolded soil test.

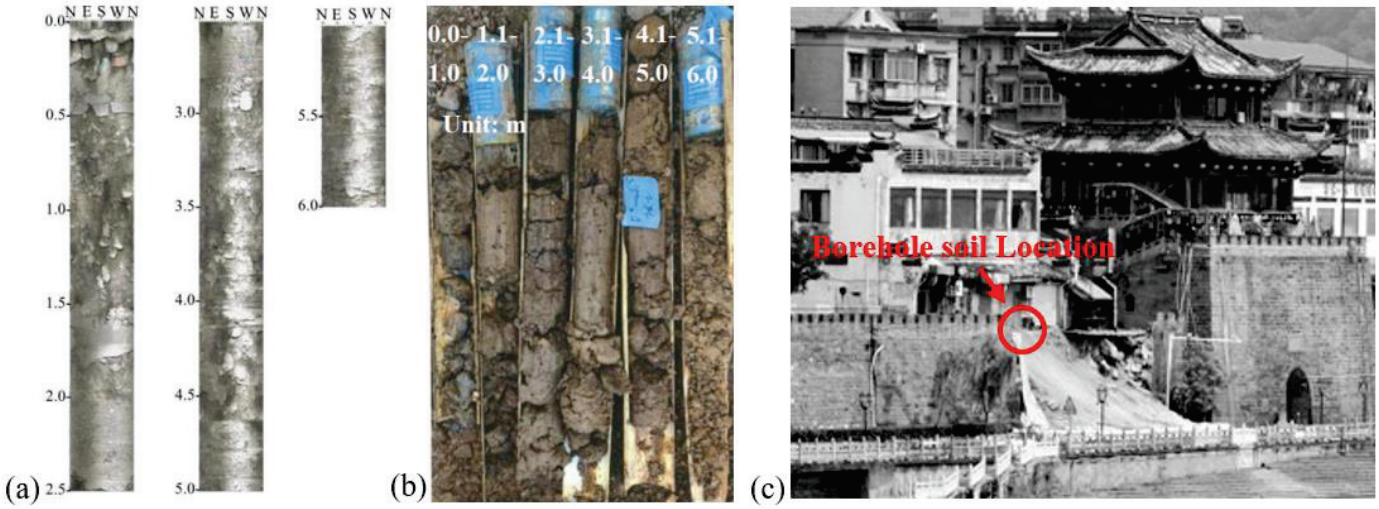


Figure 4. Soil sampling of a typical section of an ancient dike. (**a**) TV histogram of boreholes in strata I_1 and I_2; (**b**) bored soil core of soil layers I_1 and I_2; (**c**) bank slope collapse.

The ancient dike is adjacent to residential buildings and municipal facilities, and the bank slope often collapses suddenly, as shown in Figure 4c.

The dry density and moisture content of soil samples of soil layers I_1, I_2, and II were measured with the drying method, the specific gravity with the pycnometer method, and the liquid plastic limit and plastic limit of I_1 and I_2 soil samples with the combined liquid plastic limit method according to the Standard for Soil Test Methods (GB/T50123-2019), as shown in Table 1.

Table 1. Physical property parameters of silty clay.

Soil	Dry Density /g·cm^{-3}	Volumetric Water Content/%	Liquid Limit /%	Plastic Limit /%	Plasticity Index	Specific Gravity
I_1	1.53 ± 0.08	44.4 ± 2.1	44.4	27.4	17.6	2.70
I_2	1.68 ± 0.07	41.2 ± 1.5	43.5	26.2	18.4	2.65
II	1.79 ± 0.13	38.6 ± 1.1	/	/	/	2.72

After the soil sample was fully air-dried, it was fully rolled with a rubber rod and sieved through a 2 mm sieve, and the sieve residue was stored in a sealed bag for standing by. In order to analyze the composition and distribution of soil particles, a 0.075 mm sieve was used to divide the soil samples into two groups: coarse particles with a diameter of 0.075~2 mm and fine particles with a diameter of less than 0.075 mm. The soil samples were put into a self-sealing bag for standby, as shown in Figure 5a. Then, 0.075~2 mm soil sample were sieved with fine screen, and fine particles smaller than 0.075 mm were analyzed with a laser particle size analyzer (MS2000) (Hangzhou, Zhejiang province, China), as shown in Figure 5b,c. The instrument can analyze particles of 0.02~2000 μm, adopt a scanning speed of 1000 times/s, and perform platform conversion with intelligent dry and wet methods according to standard operating procedures (SOPs).



Figure 5. Particle size distribution test of soil sample. (**a**) Sandbagging at 0.075~2 mm; (**b**) fine particles less than 0.075 mm were packed separately; (**c**) laser particle size analyzer; (**d**) gradation curve of soil samples.

The particle grading curves of three soil samples were obtained, as shown in Figure 5d. The mass of 0.005~0.075 mm silt in soil samples exceeded 50% of the total mass of fine particles, and the mass of clay particles with a particle size of less than 0.005 mm was about 10%.

2.2.2. Oil

Through environmental field investigation and geological survey, according to the composition analysis of soil samples, it is found that the leakage of waste cooking oil causes soil contamination. With the change in waste oil content, soil properties change. The mechanism of the influence of waste cooking oil infiltration on soil properties is still unclear, and there are few relevant studies. This paper carried out an experimental study on this topic. Since the main component of waste cooking oil is edible oil, light and low-viscosity vegetable oil was selected as the test oil. See Table 2 for its physical parameters.

Table 2. Physical parameters of edible oil (normal temperature) [59,60].

Oil	Density/g·cm^{-3}	Viscosity Coefficient/Pa·s	Surface Tension/mN·m^{-1}	Freezing Point/°C
Vegetable oil	0.912	11.2	34.2	−5.0

2.2.3. Prepare Oil Contaminated Soil

The test is divided into two groups, namely, a consolidated undrained test and a saturated seepage test. The effect of oil content on the mechanical properties of soil was studied by measuring the stress–strain relationship of soil samples through a consolidated undrained triaxial test. The saturated seepage test was used to study the influence of reducing the fine particle content in soil samples on the permeability coefficient and to explore the change in the permeability coefficient in the process of seepage deformation.

Soil samples with a dry density of 1.53 g/cm^3, 1.68 g/cm^3, and 1.79 g/cm^3 and a grain size of 0.075~2 mm were each taken for preparing samples for the consolidated undrained test. The masses of soil, water, and oil were calculated according to Equations (1)–(3). The

reconstituted soil samples were configured with a water content of 15%; an oil content of 0%, 3%, 6%, 9%, and 12%; a diameter of 3.8 cm; and a height of 7.6 cm. GDS triaxial apparatus (DYNTTS) was used for he consolidated undrained compression test.

$$m_0 = (1 + 0.01w_0)\rho_d V \quad (1)$$

where m_0 denotes the mass of air dried soil, g; w_0 is air dried moisture content, %; ρ_d is the dry density of soil sample, g/cm^3; and V is the volume of soil sample compactor, cm^3.

$$\Delta m_w = 0.01(w' - w_0)\rho_d V \quad (2)$$

where Δm_w is the amount of water that should be added to the soil sample, g, and w' is the water content to be configured for the soil sample, %.

$$\Delta O = 0.01(O' - O_0)\rho_d V \quad (3)$$

where ΔO is the amount of oil that should be added to the soil sample, g; O' is the oil content to be configured for the soil sample, %; and O_0 is the initial oil content, which is generally zero.

2.3. Test Method

The soil sample was mixed with vegetable oil and left to stand for 24 h. The microstructure and main components of the soil sample were analyzed using scanning electronic microscopy (SEM) (Hangzhou, Zhejiang province, China) and energy-dispersive spectroscopy (EDS). Due to the poor conductivity of soil, it is necessary to perform sputtering with gold in advance, about 15 min before SEM scanning. After the sample stage is sent to the corresponding position of the instrument, the sample needs to be automatically evacuated for 20 min to avoid interference with the radiation signal of the scanned sample. A vacuum is maintained at 7.0×10^{-5} mbar, and then one moves to the sample stage using the relevant buttons and finds the best observation position, changes the magnification and focus, and adjusts the astigmatism until a satisfactory image is obtained. The voltage is 12~15 kV, and photos are taken at 1000 times magnification; then, satisfactory images are saved and printed.

The microscopic analysis adopts ZEIZZ-EVO15 (Hangzhou, Zhejiang province, China) scanning electron microscope for phase analysis, LaB6 electron gun, acceleration voltage EHT of 12~15 KV, probe current I probe of 20 pA, X-ray composition analysis current of 300~600 pA, and working distance WD of 8~15 mm. The EDS is used to determine the elemental composition of the sample by the back-scattered detector image. X-ray diffraction (XRD) was used to study the crystalline and amorphous phases of the original soil samples and the soil samples contaminated by vegetable oil.

According to *Standard for geotechnical testing method (GB/T50123-2019)*, after evenly mixing with water, the soil surface is covered with film and left to stand at room temperature, 20 °C, for 24 h, and then the oil and soil are mixed with an oil content of 3%, 6%, 9%, and 12% and left to stand for 7 d. Oil content soil samples are prepared densities of 1.53, 1.68, and 1.79 g/cm^3. After saturation in a vacuum in pure water in a vacuum cylinder for 8 h, the consolidated undrained test is carried out on the GDS triaxial tester. The test process is shown in Figure 6.

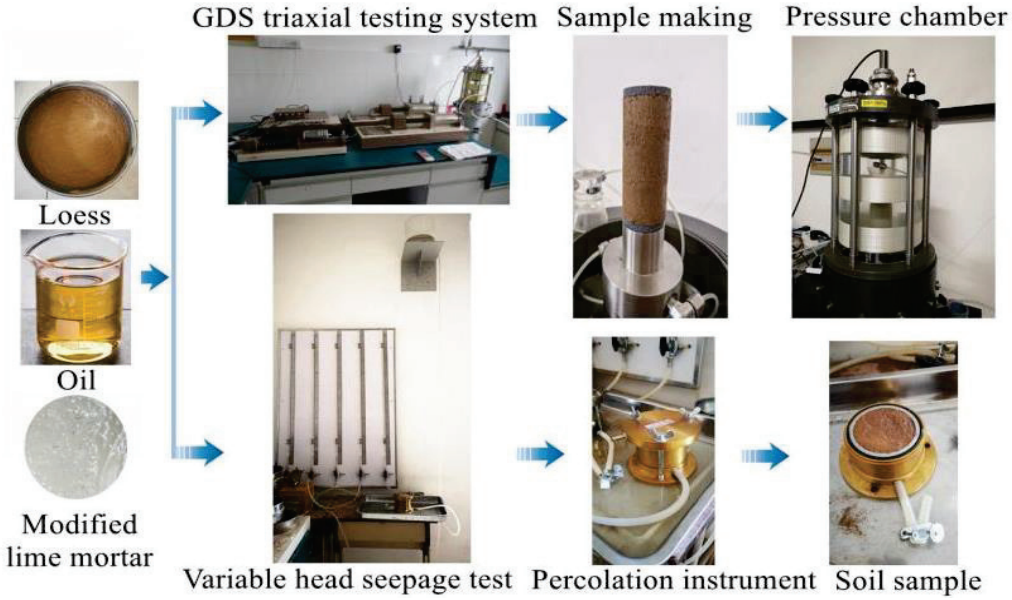


Figure 6. Schematic diagram of the experimentation process.

The MLM is then prepared. The main component of hydrated lime is Ca $(OH)_2$, and the mineral powder is S95-grade ground granulated blast furnace slag. The modified lime mortar (MLM) is prepared according to a ratio of hydrated lime to mineral powder of 2:3, the water–cement ratio is 0.43, and additives such as viscosity additives are added. The modified lime mortar is mixed evenly with 5%, 10%, and 15% content and 6% oil-content-contaminated soil after 24 h of static and cured at 20 °C and 90% relative humidity for 7 days for standby.

See Table 3 for the composition ratio of the two test soil samples.

Table 3. Test soil sample grouping and sample preparation ratio.

Soil	Dry Density/(g/cm^3)	Water Content/%	Oil Content/%	MLM Content/%
LO	1.53, 1.68, 1.79	15 ± 1	0, 3, 6, 9	0
LOM	1.53, 1.68, 1.79	15 ± 1	6	5, 10, 15

Note: LO is a mixed sample of silty clay and oil; LOM is a mixed sample of oil-contaminated silty clay treated with MLM.

The test flow of two soil samples is shown in Figure 7.

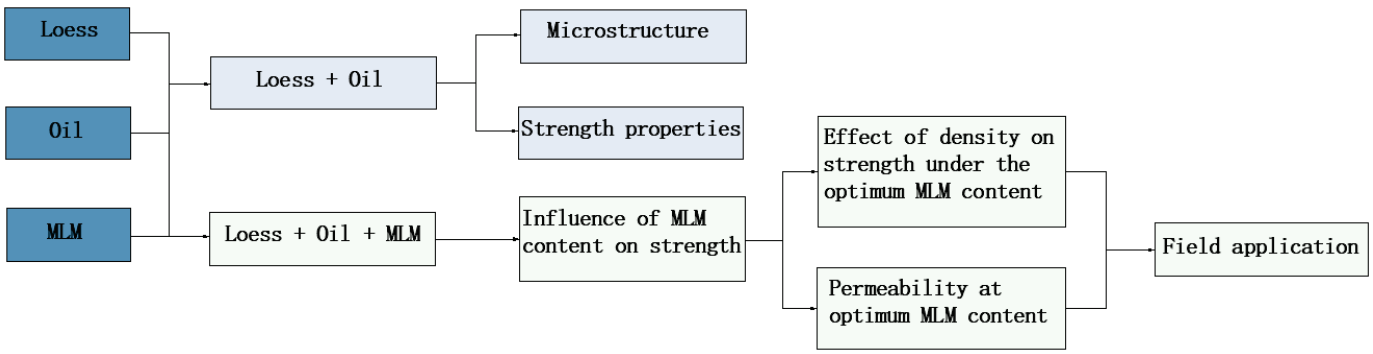


Figure 7. Flow chart of mechanical test for repairing oil-contaminated soil based on MLM.

3. Experiment and Analysis

The test was divided into two groups. For the first group, the results of microstructure and strength properties of oil-contaminated soil with 0%, 3%, 6%, and 9% oil content were analyzed, and for the second group, the changes in strength and permeability properties of MLM were analyzed to improve oil-contaminated soil.

3.1. Characteristics of Oil-Contaminated Soil

3.1.1. Microstructure Test

The microstructure and main constituent elements of soil samples were analyzed using scanning electron microscopy, and the microstructure of crystalline and amorphous materials of original soil samples and soil samples contaminated with vegetable oil were studied using phase analysis.

According to the image of the change in the SEM microstructure in Figure 8, it can be seen that the microstructures of silty clay with various oil content exhibit different characteristics. From Figure 8a, it can be observed that the microstructure of silty clay without oil is mainly granular. Figure 8b displays that the soil with an oil content of 3% is mainly scaly and massive. Figure 8c shows that when the oil concentration reaches 6%, the silty clay has a clear internal morphology of distinct flaky and block structures. The pores decrease and become compact. Figure 8d shows that silty clay with 9% oil content is granular, and small pores are obviously developed in it. In summary, energy spectrum analysis shows that the soil sample is mainly composed of O, Si, and Al and a small amount of Fe, K, Ca, and Mg. In the process of increasing the vegetable oil content, silty clay presents different structural properties. The undisturbed soil is powdery, and the scale-and-plate structure appears after the oil content increases. When the oil content continues to increase, the soil structure appears as porous cementation structures.

XRD diffraction analysis showed that there was no obvious change before versus after the crystal composition of the soil were contaminated by oil. It can be judged that there was no chemical reaction between vegetable oil and the soil, and no new substances were produced. Figure 9 shows that the main components of oil-contaminated soil samples were quartz (SiO_2), microcline ($KAlSi_3O_4$), muscovite ($K_{0.77}Al_{1.93}(Al_{0.5}SiO_{3.5})(OH)_2$), Albite ($AlSi_3O_4$) and chlorite-serpentine ($(Mg, Al)_4(Si, Al)_4O_{10}(OH)_4$). Among these, quartz accounted for 48%, microcline accounted for 24%, muscovite accounted for 17%, albite accounted for 8%, and chlorite-seripentine accounted for 1%.

3.1.2. Strength Property Test

When preparing soil samples, the dry density was 1.68 g/cm^3, the water content was 15%, and the oil contents of the different samples were 0%, 3%, 6%, and 9%. The soil volume, water volume, and oil volume were measured according to Equations (1)–(3). The soil particles were weighted, and the water and oil were fully mixed and then covered with film for storage and left to stand at room temperature for 24 h. After the soil, water, and oil were evenly mixed, the soil was taken for sample preparation. After the sample was saturated in a vacuum for 7 h in the saturator, the GDS triaxial apparatus was used for a consolidated undrained compression test. The system shall set the confining pressure and back pressure by levels, and the confining pressure and back pressure differences of the different groups were 30 kPa, 60 kPa, 90 kPa, and 120 kPa. The pressure difference was kept between the confining pressure and, the backpressure was kept as a constant in each test. After each stage of confining pressure and backpressure pressurization, a pore pressure coefficient B value test was conducted. The pore pressure coefficient B was the pore-pressure coefficient under the condition of equal isotropic stress, which is the increment of pore pressure caused by the unit increment of confining pressure when the soil is in the state of isotropic compressive stress. If the B value is greater than or equal to 0.95, the sample can be considered saturated. Under special circumstances, the B value of individual samples remains unchanged for a long time, which is also considered saturation. After consolidation, the next undrained shear test can be conducted. When the bias stress

reaches its peak value, 3~5% of the axial strain is then sheared. If the stress reading does not decrease significantly, it is sheared until the axial strain reaches 15~20%, and the whole test is complete. The peak value of deviatoric stress is taken. If there is no obvious peak value, the deviatoric stress corresponding to the axial strain of 15% is taken as the peak value.

Five parallel tests on each group of samples were carried out. Due to the influence of uncertain factors in the test, the data with large deviations were removed, the average values of 3–4 parallel test data were taken as the result; the deviatoric stress axial strain curves are drawn in Figure 10.

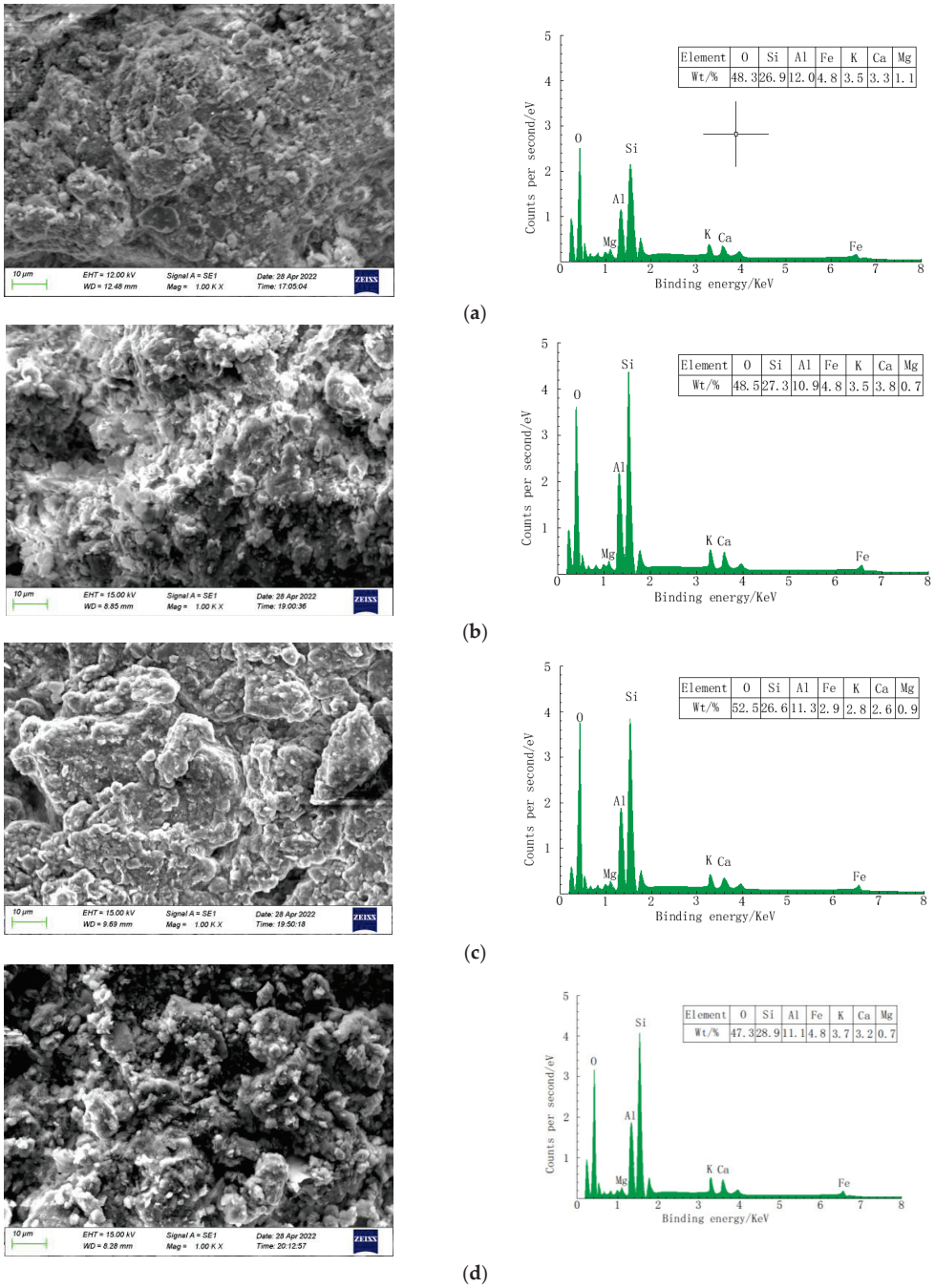


Figure 8. Microstructure and EDS of soil samples with oil content (ρ_d = 1.68 g/cm^3): (**a**) 0% oil content; (**b**) 3% oil content; (**c**) 6% oil content; (**d**) 9% oil content.

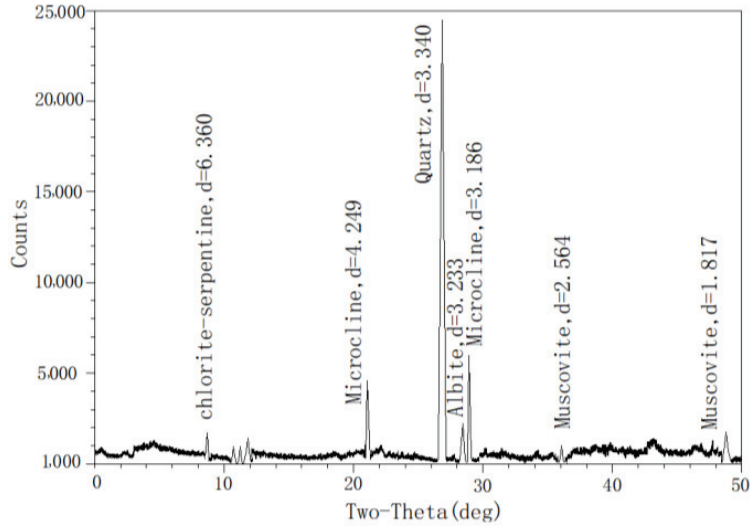


Figure 9. Mineralogical composition of silty clay sample at X-ray diffraction (XRD) test.

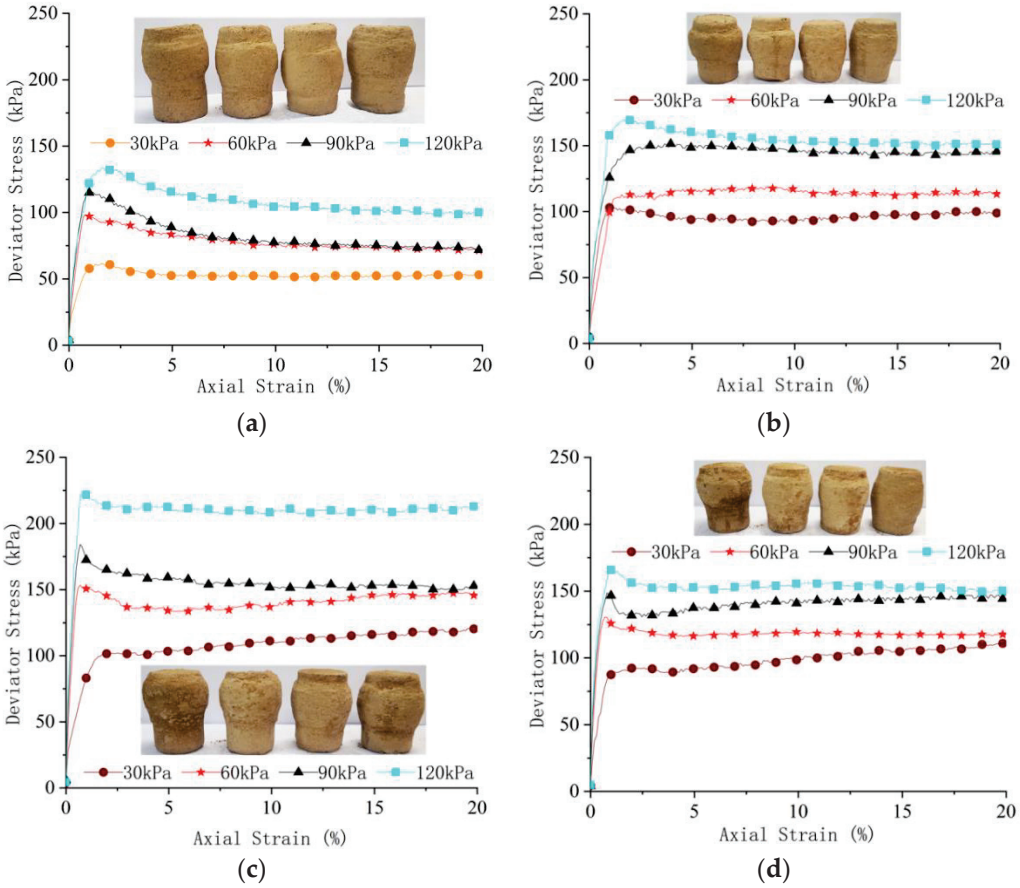


Figure 10. Relationship between principal stress deviation and strain: (**a**) 0% oil content; (**b**) 3% oil content; (**c**) 6% oil content; (**d**) 9% oil content.

It can be seen from Figure 10 that the peak value of the principal stress deviation also increases with the increase in the confining pressure. When the oil content is 6%, the peak value of the principal stress deviation reaches its maximum. The values under the four confining pressures are 110 kPa, 151 kPa, 185 kPa, and 221 kPa, which are 61.8%, 51.0%, 54.2%, and 62.5% higher than the oil-free soil samples, respectively. When the oil content increases to 9%, the peak value of the principal stress deviation of the soil sample decreases, showing a weakening trend of strength. It can be seen that with the increase

in oil content in soil samples, the peak value of principal stress deviation first increases and then decreases, reaching an extreme value when the oil content is 6%. The total stress failure circle is drawn according to the peak value of principal stress deviation under each confining pressure, and the strength envelope of each stress circle is drawn. Soil samples with a density of 1.79 g/cm^3 are taken to draw stress circle strength envelope lines with oil contents of 0%, 3%, 6%, and 9%, as shown in Figure 11. The dip angle and intercept of the envelope correspond to the friction angle and cohesion of soil samples, respectively. The friction angle and cohesion of soil samples with oil content are shown in Table 4. The friction angle of the soil sample increased with the increase in oil content. When the oil content increased to 6%, the friction angle reached a maximum value of 23.8° and then decreases. The cohesive force of the soil sample basically increased with the increase in oil content. The mechanical indicators of the soil show hardening.

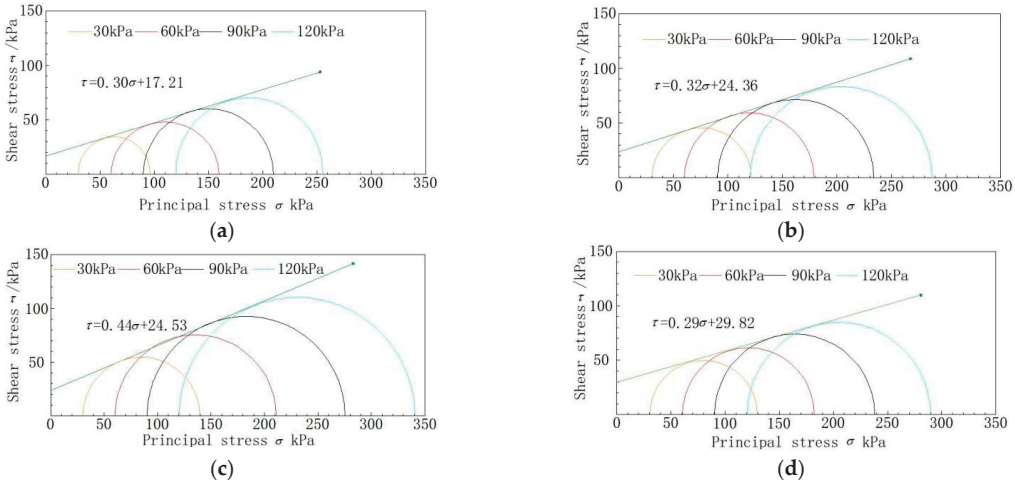


Figure 11. Mohr's circle for stresses and strength envelope of four oil contents of soil samples (ρ_d = 1.68 g/cm^3): (**a**) 0% oil content; (**b**) 3% oil content; (**c**) 6% oil content; (**d**) 9% oil content.

Table 4. Strength index of soil samples with oil content (1.68 g/cm^3).

Oil Content/%	Coulomb Line	Friction Angle/°	Cohesion/kPa
0	$\tau = 0.30\sigma + 17.21$	16.79	17.21
3	$\tau = 0.32\sigma + 24.36$	17.90	24.36
6	$\tau = 0.44\sigma + 24.53$	23.80	24.53
9	$\tau = 0.29\sigma + 29.82$	16.25	29.82

3.2. Properties of MLM with Oil-Contaminated Soil

3.2.1. Effect of MLM Content on Strength Index

In view of the large strength index of soil samples with an oil content of 6% and a density of 1.79 g/cm^3, the change in the strength index of oil-contaminated soil after treatment with MLM content was tested. The MLM accounted for 0%, 5%, 10%, and 15%, respectively, and the soil samples with 6% oil content were prepared. The consolidated undrained test was completed after 7 days of curing under standard conditions. Five parallel tests were carried out on each group of samples, the average value of 3–4 parallel test data were taken as the result, and the molar stress circle and strength envelope were drawn; see Table 5 for its strength index. It can be seen that for the soil sample with 1.68 g/cm^3 and an oil content of 6%, the friction angle gradually increased with the increase in the lime content. When the MLM content was 10%, the friction angle reached a maximum value of 30.07°, which is 1.26 times the friction angle of the non-lime-content-contaminated soil, and the maximum value of cohesion was 32.47 kPa, which was 1.32 times that of the non-lime content contaminated soil.

Table 5. Strength index of soil samples with MLM content (1.68 g/cm^3, oil content 6%).

MLM Content/%	Coulomb Line	Friction Angle/°	Cohesion/kPa
0	$y = 0.44x + 24.53$	23.80	24.53
5	$y = 0.48x + 26.71$	25.84	26.71
10	$y = 0.57x + 32.47$	30.07	32.47
15	$y = 0.55x + 32.32$	29.03	32.32

3.2.2. Impact of Contaminated Soil Density on Strength Index

According to 10% of MLM content, soil samples with densities of 1.53 g/cm^3, 1.68 g/cm^3, and 1.79 g/cm^3 were prepared. After the soil samples were cured under standard conditions for 7 days, five parallel tests and consolidated undrained shear tests were conducted on each group of samples, and the average value of 3–4 parallel test data was taken as the result. The peak value of the average principal stress deviation at each oil content is shown in Figure 11. The average friction angle and cohesion at each oil content are shown in Figure 12. It can be seen that the friction angle of the three densities of soil samples is the largest when the oil content is 6%, and the larger the density is, the larger the friction angle is, which is 25.59°, 27.72°, and 30.07°, with an increasing ratio of 8.3% and 8.5%.

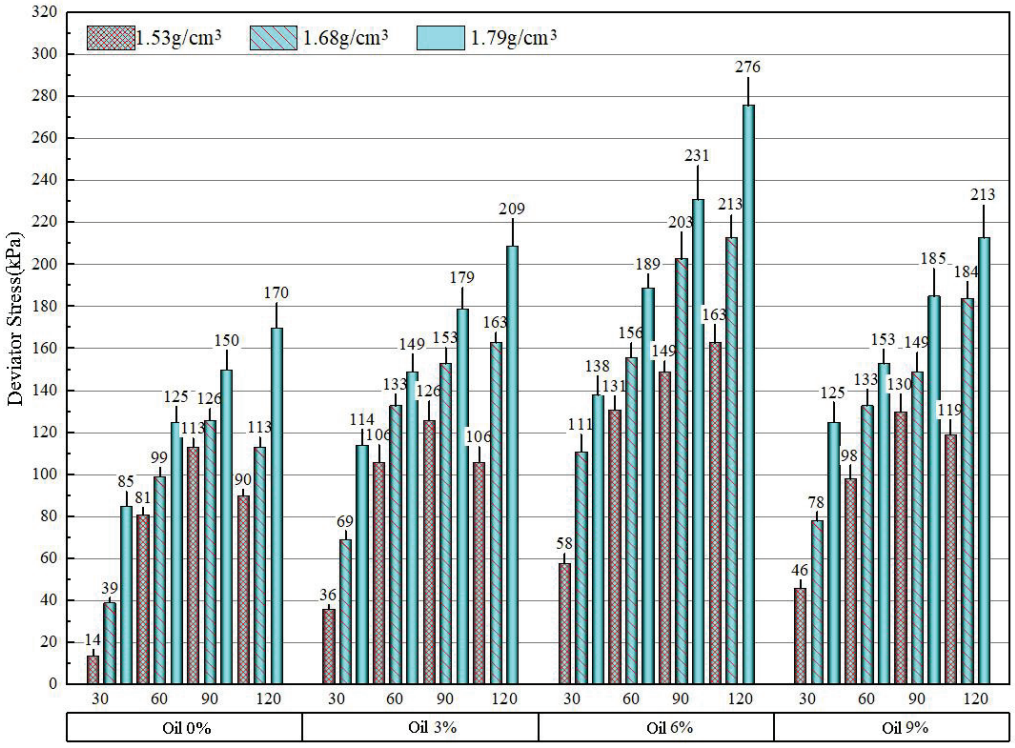


Figure 12. The mean values of the peak value of the principal stress deviation of three densities of MLM soil samples under different oil contents.

The peak value of the principal stress deviation of soil samples with densities of 1.53 g cm^3, 1.68 g/cm^3, and 1.79 g/cm^3 at each oil content is shown in Figure 12. The friction angle and cohesion at each oil content are shown in Figure 13. The cohesion of the three densities f soil samples increased with the increase in oil content. When the oil content was 9%, the cohesion was divided into 26.47 kPa, 27.67 kPa, and 29.82 kPa. The cohesion of the three densities of soil samples increased with the increase in oil content. When the oil content was 6%, the cohesion was divided into 28.63 kPa, 32.40 kPa, and 32.66 kPa.

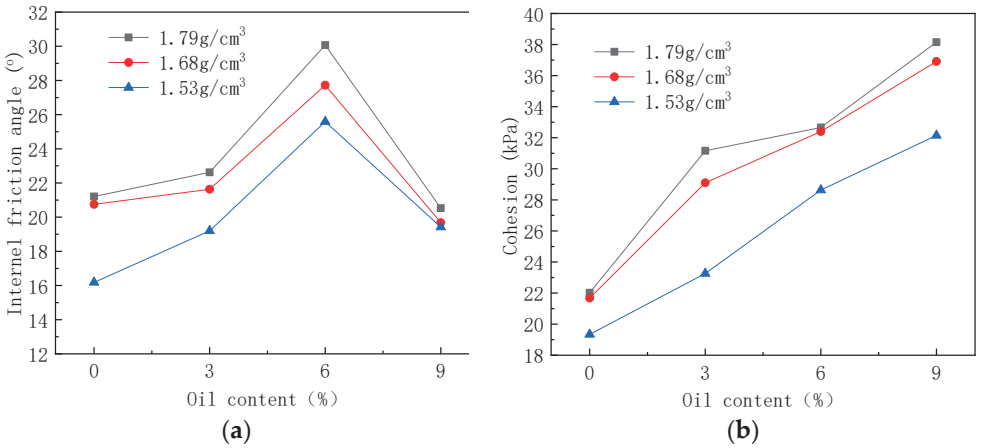


Figure 13. Strength index of three densities of MLM soil samples under each oil content (MLM content 10%). (**a**) Relationship between friction angle and oil content; (**b**) relationship between cohesion and oil content.

3.2.3. Permeability Test

(1) Influence of oil content on permeability

The permeability characteristics of soil samples with different oil content and 10% MLM content were studied. After the soil sample was saturated in a vacuum for 12 h, the permeability coefficient of the soil sample was measured using the variable-head permeability test. According to Darcy's law, the seepage flow through the soil sample at the same time was equal to the flow through the water head gauge. The seepage coefficient can be expressed as

$$k_T = 2.3\frac{\mathrm{aL}}{\mathrm{A}(t_2 - t_1)}\log\frac{H_1}{H_2} \tag{4}$$

where a denotes the sectional area of variable head pipe, a = 3 cm^2; L is seepage path, L = 4 cm; A is the cross-sectional area of the soil sample, A = 30 cm^2; t_1, t_2 are the starting and ending time of the measured water head, s; and H_1 and H_2 are the starting and ending head, cm.

The relationship between the permeability coefficient of the three densities of soil samples and the oil content is shown in Figure 14a. The permeability coefficient increases with the increase in the oil content. The maximum increase was in the soil samples with a density of 1.53 g/cm^3. The permeability coefficient of the soil samples with an oil content of 9% was 2.18 × 10^{-5} cm/s, which is 2.4 times the permeability coefficient of the 1.79 g/cm^3 soil sample. The soil sample used in this test was silty clay mixed with MLM. After vegetable oil pollution, a film is formed on the surface of soil particles, which shortens the seepage path of water between soil particles and increases the permeability coefficient.

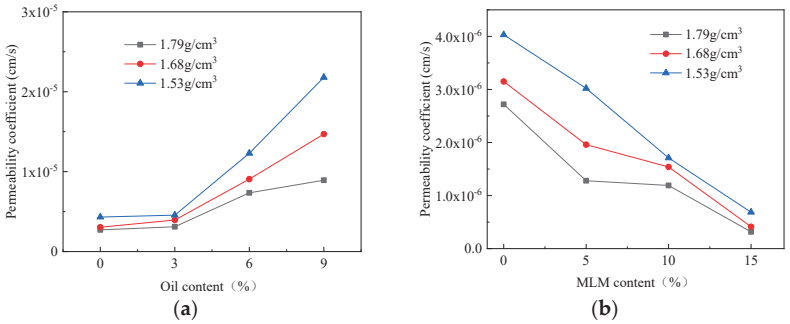


Figure 14. Permeability coefficient variation of three densities of soil samples. (**a**) Relationship between oil content and permeability coefficient (MLM content 10%); (**b**) relationship between MLM content and permeability coefficient (oil content 6%).

(2) Influence of MLM content on permeability

The permeability coefficient of the three densities o soil samples decreases gradually when the MLM content increases, and the relationship between the MLM content and the permeability coefficient is shown in Figure 14b. The permeability coefficient of the soil sample with a density of 1.53 g/cm^3 and an MLM content of 15% was 9.86 $\times$ 10^{-7} cm/s, which is 24% of the permeability coefficient of soil samples with an MLM content of 0%, namely 4.03 $\times$ 10^{-6} cm/s.

The permeability coefficient of the three densities of soil samples decreased gradually with the increase in lime content, and the relationship between MLM content and permeability coefficient is shown in Figure 14b. The permeability coefficient of the soil sample with a density of 1.53 g/cm^3 and MLM content of 15% was 9.86 $\times$ 10^{-7} cm/s and that of the soil sample with MLM content of 0% was 4.03 $\times$ 10^{-6} cm/s; the former is 24% of the latter.

4. Numerical Simulation Results and Discussion

4.1. Numerical Simulation Results

After the soil of the Lanxi ancient dike was contaminated with oil, the permeability coefficient and strength index of the soil changed, affecting the permeability deformation and stability of the bank slope. When using the finite element method to establish a numerical model [61], several diagonal lines are used to simplify the slope surface of the flood-controlled ancient dike. The elevation of the ancient dike top is 33.05 m, the elevation of the dike foot is 26.88 m, the elevation of the ancient dike foundation is 24.80 m, the height of the vertical section is 6.17 m, the width of the top is 0.22 m, the bottom height of the lower slope section of the upstream is 19.05 m, and the slope from bottom to top are 22° and 43°, respectively. The ancient dike is adjacent to the building, and the building foundation is a deep foundation. The upper load directly acts on the bearing layer, and its effect on the ancient dike can be ignored. The numerical model adopts quadrilateral continuous elastic-plastic elements with a grid edge length of 0.5 m, generating a total of 7023 nodes and 6877 elements. The numerical model of the ancient dike is shown in Figure 15. Point A_1 is located 2.10 m above the foundation behind the ancient dike, that is, at 26.90 m elevation. See Table 6 for mechanical parameters of ancient dike soil after oil pollution and MLM repair.

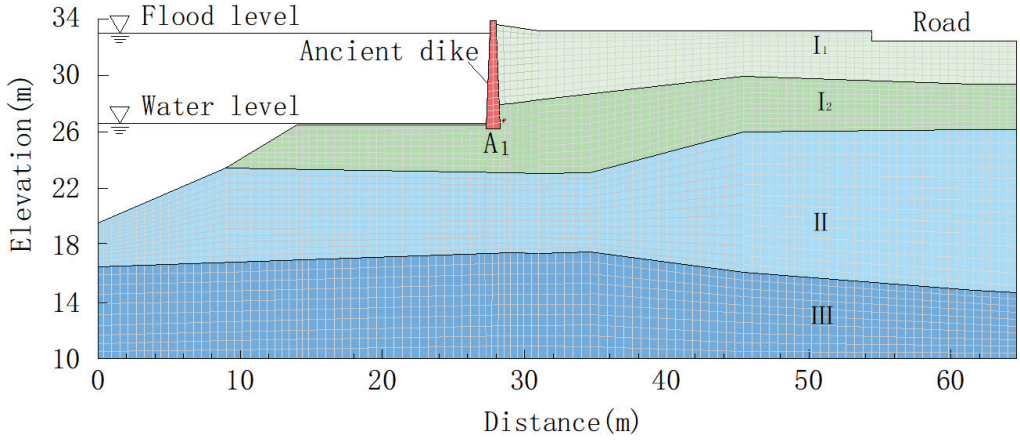


Figure 15. Numerical model of Lanxi ancient dike.

Table 6. Physical and mechanical indexes of soil layer in the typical section.

No.	Name	Thickness /m	Dry Density /kN·m^{-3}	Friction Angle (Oil Content 6%)/°	Cohesion (Oil Content 6%)/kPa	Initial Permeability Coefficient (Oil Content 6%)/cm·s^{-1}	Friction Angle (MLM Content 10%)/°	Cohesion (MLM Content 10%)/kPa	Initial Permeability Coefficient (MLM Content 10%)/cm·s^{-1}
I_1	Artificial fill-1	3.5	15.3	22.4	18.5	1.24×10^{-5}	26.5	22.3	1.83×10^{-6}
I_2	Artificial fill-2	4.1	16.8	23.8	24.5	9.70×10^{-4}	30.1	32.5	1.65×10^{-6}
II	Sandy gravel	10.6	17.9	35.0	0	4.12×10^{-4}	35.0	0	4.12×10^{-4}
III	Pelitic siltstone	>7	20.3	40.0	56.5	/	40.0	56.5	/

The numerical analysis results indicate that the seepage and slope stability of the ancient dike after being contaminated with oil are shown in Figure 16. Under external water level fluctuations, the hydraulic gradient of the soil varies with the location. Analyze the hydraulic gradient changes at point A_1 on the back of the wall. The results of finite computing show that the hydraulic gradient of the ancient dike soil changes with the rise and fall of the flood peak of the Lanjiang River. At the maximum rate of water pressure change, the hydraulic gradient of the soil reaches its maximum value. The distribution of gradient values corresponding to a 6% oil content in the soil is shown in Figure 16a. When the water level change rate continues to increase, the hydraulic gradient at point A_1 rapidly increases. When the water level is 26.58 m, the water level change rate reaches its maximum value, and the hydraulic gradient at point A_1 reaches its maximum value of 0.64. When the water level change rate decreases, the hydraulic gradient begins to decrease. As the growth rate of the Lanjiang River water level slows down, the hydraulic gradient at point A_1 gradually decreases. When the flood peak rapidly decreases, the hydraulic gradient decreases rapidly. When the water level changes slow down, the hydraulic gradient changes gradually stabilize. In the case of a sudden drop in water level in the Lanjiang River, when the rate of change reaches the stagnation point, the minimum stability safety coefficient of the ancient dike is 1.004. The typical calculated sliding surface is shown in Figure 16b. When using MLM to repair oil contaminated soil, when the MLM content is 10%, the permeability coefficient and mechanical parameters of the soil are changed, and the hydraulic gradient at point A_1 decreases to 0.44, which is 31.3% lower than the hydraulic gradient value of oil contaminated soil. The minimum stability coefficient of the bank slope is 1.317, which is 31.2% higher than the stability safety coefficient of oil contaminated soil. As shown in Figure 17.

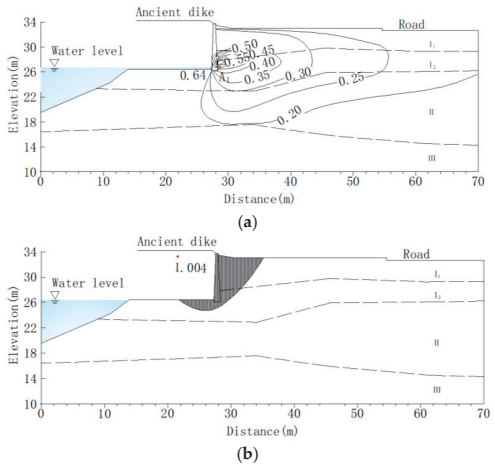


Figure 16. Analysis of seepage and bank slope stability of oil contaminated soil in ancient dikes (oil content of 6%). (**a**) Hydraulic gradient distribution map; (**b**) The minimum safety factor of bank slope stability and sliding surface.

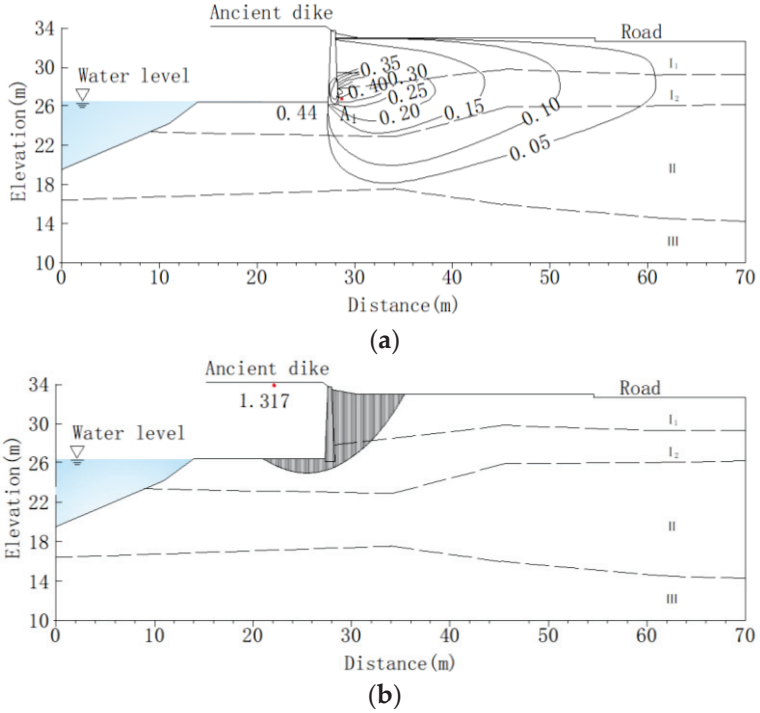


Figure 17. Analysis of seepage and bank slope stability in MLM repair of ancient dikes (MLM content 10%). (**a**) Hydraulic gradient distribution map; (**b**) The minimum safety factor of bank slope stability and sliding surface.

4.2. Repairing the Flood-Controlled Ancient Dike

The MLM pressure grouting measures were adopted to repair the oil-contaminated soil in the ancient dike. A modified lime grouting test was conducted on the ancient dike slope, and ZK1 grouting holes were set up with a diameter of 10 cm. The MLM shall be grouted in six steps. The MLM shall be prepared according to the proportion, and then the soil surface shall be treated, the position of the grouting nozzle shall be calibrated, and then the hole shall be drilled. After the grouting nozzle is installed, the pressure grouting shall be carried out, and the static curing shall be more than 24 h. After the joint is sealed, the secondary grouting shall be carried out, and the pressure shall be controlled at 0.1~0.5 MPa, so as to ensure that the slurry is full without leakage and dense without bubbles. Seventy-two hours after the completion of ZK1 grouting, inspection boreholes were set up at positions ZK2, ZK3, and ZK4 with a hole spacing of 40 cm, as shown in Figure 18a. After testing the drilled soil samples, it was determined that the ZK2 and ZK3 drilling soil samples were filled with MLM, and no MLM was found in the ZK4 drilling soil samples, as shown in Figure 18b–d. Therefore, the effective diffusion radius of MLM was determined as 20 cm.

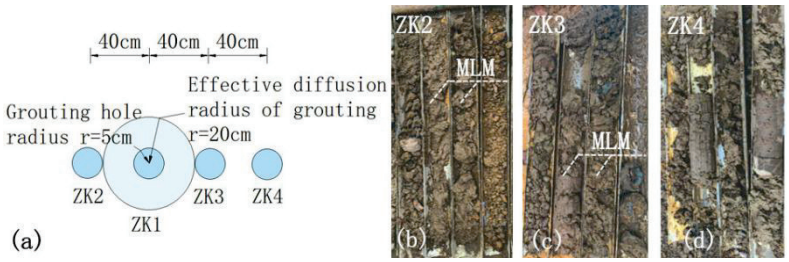


Figure 18. Grouting test of MLM. (**a**) Layout of grouting holes and inspection holes; (**b**) ZK2 borehole soil sample; (**c**) ZK3 borehole soil sample; (**d**) ZK4 borehole soil sample.

The layout of MLM pressure grouting is shown in Figure 19a, divided into two rows with a spacing of 100 cm and a spacing of 100 cm between each row of holes. Considering the effective diffusion radius of the grouting as 20 cm, the MLM content in the MLM pressure grouting area can be calculated to be about 14.6%. The drilling process is shown in Figure 19b,c. The drilling depth was 6.00 m, as shown in Figure 19d.

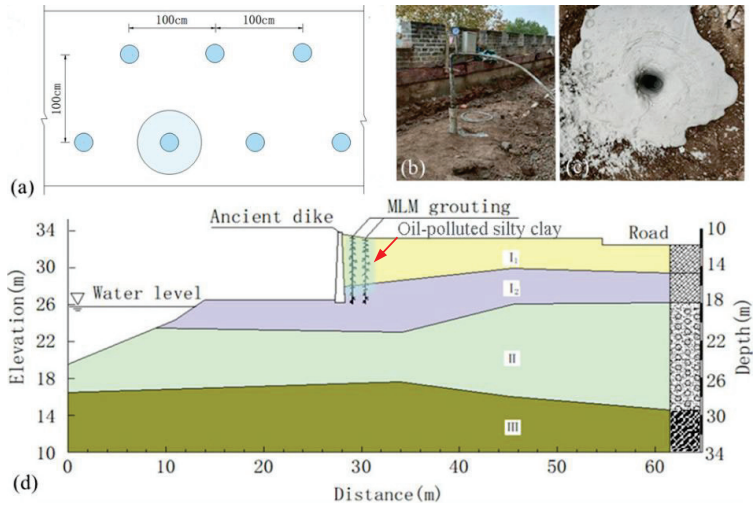


Figure 19. Repair measures of MLM pressure grouting: (**a**) distribution of grouting holes; (**b**) pressure grouting; (**c**) completion of grouting; (**d**) position and depth of pressure grouting.

After using MLM pressure grouting for ancient dikes, the pore water pressure and seepage ratio decreased significantly compared to the original structure section with good permeability. The results indicate that setting MLM pressure grouting can effectively reduce the permeability of the foundation soil, improve the cohesion of soil particles, and suppress the occurrence of piping in flood-controlled ancient dikes and repair engineering without changing the cultural relics. The compactness of the soil was improved inside the city wall, defects were treated, and leakage channels were blocked.

In order to verify the anti-seepage effect of MLM pressure grouting, on-site water injection permeability tests were conducted, with two inspection holes arranged as shown in Figure 20. The results of the water injection permeability test are shown in Table 7. According to the test, the permeability coefficient of the soil after pressure grouting with MLM was reduced by 8~15%.



Figure 20. On-site water-injection permeability test. (**a**) Arrangement of water-injection holes; (**b**) water-injection test for hole 1; (**c**) water-injection test for hole 2.

Table 7. List of water injection permeability test results of inspection holes 1 and 2.

No.	Oil-Contaminated Soil Test Results				MLM Grouting Repair Test Results
	Section	Hole Depth /m	Length /m	Permeability Coefficient/cm·s^{-1}	Permeability Coefficient/cm·s^{-1}
1	1	1.0–4.0	3.00	2.47×10^{-4}	2.11×10^{-4} (↓14.6%)
	2	4.0–8.0	4.00	6.21×10^{-5}	5.29×10^{-4} (↓14.8%)
	3	8.0–12.0	4.00	2.43×10^{-4}	2.38×10^{-4}
	4	12.0–16.0	4.00	1.11×10^{-4}	1.09×10^{-4}
2	1	1.0–4.0	3.00	2.15×10^{-4}	1.96×10^{-4} (↓8.8%)
	2	4.0–8.0	4.00	1.67×10^{-4}	1.46×10^{-4} (↓12.6%)
	3	8.0–12.0	4.00	1.58×10^{-4}	1.52×10^{-4}
	4	12.0–16.1	4.10	1.40×10^{-4}	1.39×10^{-4}

5. Conclusions

The physical properties, strength index, and permeability coefficients of oil-contaminated silty clay have changed, leading to the susceptibility of flood-controlled ancient dikes to disasters such as leakage and bank-slope instability. Through dynamic triaxial tests and variable head permeability tests, the strength index and permeability coefficient changes in oil-contaminated soil and MLM-improved soil were obtained. By using the finite element numerical simulation method for comparative analysis, the effect of MLM improvement on oil-contaminated soil on improving the leakage of flood-controlled ancient dikes and bank slope stability was obtained. Subsequently, MLM pressure grouting technology was used to repair the ruins of flood-controlled ancient dikes. The following conclusions were drawn from the above series of studies.

(1) After the silty clay was contaminated with oil, the relationship between the principal stress deviation and strain of the soil sample changed with the change in oil content, leading to stress hardening. When the oil content increased, the strength index also changed. When the oil content was 6%, the friction angle reached its maximum value, but as the oil content continued to increase, the friction angle decreased. When MLM was used to repair oil-contaminated soil, as the MLM content increased, the friction angle and cohesion of the soil sample also increased. When the MLM content was 10% and the oil content was 6%, the friction angle of the soil sample reached its maximum value. At the same MLM content, the higher the density of the soil sample, the greater the friction angle and cohesion, and the smaller the permeability coefficient.

(2) The finite element numerical simulation analysis shows that after the soil of the flood-controlled ancient dike was contaminated with oil, when the water level was at its maximum rate of change, and the water level was 26.58 m, the extreme hydraulic gradient of the ancient dike soil reached 0.64, and the extreme safety coefficient of bank slope stability was 1.004. When MLM was used to repair oil-contaminated soil, when the MLM content was 10%, the extreme hydraulic gradient of the ancient dike was 0.44, a decrease of 31.3%, and the extreme safety factor of bank slope stability was 1.317, an increase of 31.2%.

(3) MLM pressure-grouting technology was used to repair flood-controlled ancient dikes. The effective diffusion radius of MLM was detected through grouting tests, and then the distance, arrangement, and depth of MLM pressure grouting holes were determined. After the MLM grouting repair of oil-contaminated soil on the slope of the ancient dike was completed, on-site water injection permeability tests showed that the permeability coefficient of the ancient dike soil decreased by 8–12%.

Notably, this study can provide research methods and technical measures for the repair of similar flood-controlled ancient dikes.

Author Contributions: Conceptualization, data curation, methodology and writing—original draft preparation, J.Z.; Formal analysis, project administration, visualization and writing—review and editing, Z.D.; geological investigation, resources and visualization, Y.D. and X.H.; formal analysis

and supervision, H.W. and B.C.; validation and data curation, Q.M. All authors have read and agreed to the published version of the manuscript.

Funding: This research was Supported by Major Science and Technology Plan Project of Zhejiang Provincial Department of Water Resources (RA1904) and Basic Public Welfare Research Program of Zhejiang Province (LZJWD22E090001) and Scientific Research Foundation of Zhejiang University of Water Resources and Electric Power (xky2022010).

Institutional Review Board Statement: Not applicable.

Informed Consent Statement: Not applicable.

Data Availability Statement: Not applicable.

Acknowledgments: The authors thank Lanxi Water Construction Engineering Investment Limited Liability Company for their support and funding acquisition.

Conflicts of Interest: The authors declare that there are no conflict of interest regarding the publication of this paper.

References

1. Zhu, Q.; Tian, M.; Hu, D. Structural restoration of historic water systems and the prevention and mitigation of urban water logging for China's central region cities. *J. Hydraul. Eng.* **2022**, *53*, 798–810.
2. Bao, J.; Hou, X.; Wang, Y. An analysis of the principles in the restoration and protection of the ancient city wall of China. *Res. Herit. Preserv.* **2018**, *3*, 41–44.
3. Jia, T. The elements of flflood control of ancient city walls: Taking the ancient city wall of Taizhou Fu as an example. *Archit. J.* **2016**, *2*, 16–21.
4. Xia, M.; Yan, S.; Xia, Z. The ancient city of Ezhou and its barrier and the flflood control of the Yangtze River. *J. Ezhou Univ.* **2013**, *20*, 64–66.
5. Wu, Q. Technical Measures for Flood Control in Ancient Cities of China. *Anc. Build. Gard. Technol.* **1993**, *23*, 8–13.
6. Rahman, Z.A.; Hamzah, U.; Taha, M.R.; Ithnain, N.S.; Ahmad, N. Influence of Oil Contamination on Geotechnical Properties of Basaltic Residual Soil. *Am. J. Appl. Sci.* **2010**, *7*, 954–961. [CrossRef]
7. Iqbal, K.; Xu, C.; Nasir, H.; Alam, M.; Farooq, A.; Williams, E.J. Effect of Used Motor Oil and Bitumen as Additive on the Permeability and Mechanical Properties of Low Plastic Soil. *Adv. Mater. Sci. Eng.* **2020**, *2020*, 1360197. [CrossRef]
8. Ostovar, M.; Ghiassi, R.; Mehdizadeh, M.J.; Shariatmadari, N. Effects of Crude Oil on Geotechnical Specification of Sandy Soils. *Soil Sediment Contam. Int. J.* **2020**, *30*, 58–73. [CrossRef]
9. Abousnina, R.; Manalo, A.; Lokuge, W.; Zhang, Z. Effects of light crude oil contamination on the physical and mechanical properties of geopolymer cement mortar. *Cem. Concr. Compos.* **2018**, *90*, 136–149. [CrossRef]
10. Khamehchiyan, M.; Charkhabi, A.H.; Tajik, M. Effects of crude oil contamination on geotechnical properties of clayey and sandy soils. *Eng. Geol.* **2007**, *89*, 220–229. [CrossRef]
11. Chew, S.J.; Lee, C.Y. Simple shear behavior of palm biodiesel contaminated soil. *ARPN J. Eng. Appl. Sci.* **2010**, *5*, 6–9.
12. Heris, M.N.; Aghajani, S.; Hajialilue-Bonab, M.; Molamahmood, H.V. Effects of Lead and Gasoline Contamination on Geotechnical Properties of Clayey Soils. *Soil Sediment Contam. Int. J.* **2020**, *29*, 340–354. [CrossRef]
13. Sim, Y.L.; Lee, C.Y. Behavior of piles in palm biodiesel contaminated mining sand. *Int. J. Environ. Sci.* **2013**, *3*, 182230.
14. Safehian, H.; Rajabi, A.M.; Ghasemzadeh, H. Effect of diesel-contamination on geotechnical properties of illite soil. *Eng. Geol.* **2018**, *241*, 55–63. [CrossRef]
15. Abousnina, R.M.; Manalo, A.; Shiau, J.; Lokuge, W. Effects of light crude oil contamination on the physical and mechanical properties of fine sand. *Soil Sediment Contam. Int. J.* **2015**, *24*, 833–845. [CrossRef]
16. Kermani, M.; Ebadi, T. The Effect of Oil Contamination on the Geotechnical Properties of Fine-Grained Soils. *Soil Sediment Contam. Int. J.* **2012**, *21*, 655–671. [CrossRef]
17. Estabragh, A.; Beytolahpour, I.; Moradi, M.; Javadi, A. Mechanical behavior of a clay soil contaminated with glycerol and ethanol. *Eur. J. Environ. Civ. Eng.* **2015**, *20*, 503–519. [CrossRef]
18. Meegoda, N.J.; Rajapakse, R.A. Long-term and short-term hydraulic conductivities of contaminated clays. *J. Environ. Eng.* **1994**, *119*, 725–743. [CrossRef]
19. Nasehi, S.A.; Uromeihy, A.; Nikudel, M.R.; Morsali, A. Influence of Gas Oil Contamination on Geotechnical Properties of Fine and Coarse-Grained Soils. *Geotech. Geol. Eng.* **2016**, *34*, 333–345. [CrossRef]
20. Al-Adili, A.; Alsoudany, K.Y.; Shakir, A. Investigation of Crude Oil Pollution Effect on Stiffness Characteristics of Sandy and Gypseous Soil. *Soil Mech. Found. Eng.* **2017**, *54*, 276–282. [CrossRef]
21. Nasr, A.M.A. Experimental and Theoretical Studies for the Behavior of Strip Footing on Oil-Contaminated Sand. *J. Geotech. Geoenviron. Eng.* **2009**, *135*, 1814–1822. [CrossRef]
22. Bolouri-Bazaz, M.T.; Bolouri-Bazaz, J. Effect of Hydrocarbon Contamination on Biostabilization of Soil Contaminated with Motor Oil and Gasoline. *Geomicrobiol. J.* **2021**, *38*, 467–481. [CrossRef]

23. Kumar, D.N.; Kumar, P.R. Investigations on alternate lime-pozzolana based mortars for repair of heritage structures. *Constr. Build. Mater.* **2022**, *341*, 127776. [CrossRef]
24. Groot, C.J.W.P.; Gunneweg, J.T.M. Choosing Mortar Compositions for Repointing of Historic Masonry Under Severe Environmental Conditions. In *Historic Mortars*; Springer International Publishing: Cham, Switzerland, 2018; pp. 143–154. [CrossRef]
25. Veiga, R. Air lime mortars: What else do we need to know to apply them in conservation and rehabilitation interventions? A review. *Constr. Build. Mater.* **2017**, *157*, 132–140. [CrossRef]
26. Gulotta, D.; Goidanich, S.; Tedeschi, C.; Nijland, T.G.; Toniolo, L. Commercial NHLcontaining mortars for the preservation of historical architecture. Part 1: Compositional and mechanical characterization. *Constr. Build. Mater.* **2013**, *38*, 31–42. [CrossRef]
27. Song, Y.; Zhang, M.; Gan, X.; Dong, S.; Ding, S.; Geng, Y.; Li, J. Experimental Study on Mechanical Strength of Diesel-Contaminated Red Clay Solidified with Lime and Fly Ash. *Geofluids* **2022**, *2022*, 3891030. [CrossRef]
28. Zhang, D.; Zhao, J.; Wang, D.; Xu, C.; Zhai, M.; Ma, X. Comparative study on the properties of three hydraulic lime mortar systems: Natural hydraulic lime mortar, cement-aerial lime-based mortar and slag-aerial lime-based mortar. *Constr. Build. Mater.* **2018**, *186*, 42–52. [CrossRef]
29. Apostolopoulou, M.; Armaghani, D.J.; Bakolas, A.; Douvika, M.G.; Moropoulou, A.; Asteris, P.G. Compressive strength of natural hydraulic lime mortars using soft computing techniques. *Procedia Struct. Integr.* **2019**, *17*, 914–923. [CrossRef]
30. Figueiredo, C.; Ball, R.J.; Lawrence, M. Is BS EN 459-1: 2015 fit for purpose in the context of conservation? *J. Build. Limes Forum* **2016**, *23*, 46–52.
31. Vyšvařil, M.; Žižlavský, T.; Zimmermann, Š.; Bayer, P. Effect of aggregate type on properties of natural hydraulic lime-based mortars. In *Materials Science Forum*; Trans Tech Publications Ltd.: Wollerau, Switzerland, 2017. [CrossRef]
32. Hanley, R.; Pavia, S. A study of the work ability of natural hydraulic lime mortars and its influence on strength. *Mater. Struct.* **2008**, *41*, 373–381. [CrossRef]
33. Garijo, L.; Zhang, X.; Ruiz, G.; Ortega, J.J.; Wu, Z. The effects of dosage and production process on the mechanical and physical properties of natural hydraulic lime mortars. *Constr. Build. Mater.* **2018**, *169*, 325–334. [CrossRef]
34. Arizzi, A.; Martinez-Huerga, G.; Sebastian-Pardo, E.; Cultrone, G. Mineralogical, textural and physical-mechanical study of hydraulic lime mortars cured under different moisture conditions. *Mater. Constr.* **2015**, *65*, 053. [CrossRef]
35. Pozo-Antonio, J. Evolution of mechanical properties and drying shrinkage in lime-based and lime cement-based mortars with pure limestone aggregate. *Constr. Build. Mater.* **2015**, *77*, 472–478. [CrossRef]
36. Lanas, J.; Bernal, J.P.; Bello, M.; Galindo, J.A. Mechanical properties of natural hydraulic lime-based mortars. *Cem. Concr. Res.* **2004**, *34*, 2191–2201. [CrossRef]
37. Chever, L.; Pavía, S.; Howard, R. Physical properties of magnesian lime mortars. *Mater. Struct.* **2009**, *43*, 283–296. [CrossRef]
38. Ravi, R.; Thirumalini, S.; Taher, N. Analysis of ancient lime plasters—Reason behind longevity of the Monument Charminar, India a study. *J. Build. Eng.* **2018**, *20*, 30–41. [CrossRef]
39. Yang, Y.; Zhang, S.; Rong, H.; Zhang, L.; Zhang, Y.; Xue, L.; Wang, X.; Yang, J. Study on modification effect and mechanism of lime-based materials on raw soil. *J. Funct. Mater.* **2019**, *4*, 4067–4073. [CrossRef]
40. Ding, S.; Wang, W.; Yang, D.; Wu, C. Research progress and application of modification of raw soil building materials. *Build. Blocks Block Build.* **2014**, *5*, 45–48.
41. Ciancio, D.; Beckett, C.; Carraro, J. Optimum lime content identification for lime-stabilised rammed earth. *Constr. Build. Mater.* **2013**, *53*, 59–65. [CrossRef]
42. Ma, C.; Du, W.; Chen, B. Study on the strength development law of self-compacting soil-based modified materials. *New Build. Mater.* **2016**, *43*, 10–13.
43. Wang, D.; Zentar, R.; Abriak, N.E.; Di, S. Long-term mechanical performance of marine sediments solidified with cement, lime, and fly ash. *Mar. Georesources Geotechnol.* **2017**, *36*, 123–130. [CrossRef]
44. Liu, J.; Sheng, G.; Liu, Y. Effects of the Dosage of Solidified Agent on the Performance of Raw Soil Materials for Wall. *J. Shenyang Jianzhu Univ.* **2010**, *26*, 517–521.
45. Wang, Y.; Duan, X.; Gu, Y.; Wang, S. Experimental Investigation of the Seepage-Induced Failure Process in Granular Soils. *Geofluids* **2022**, *2022*, 5703151. [CrossRef]
46. Wang, Y.; Gu, Y.; Wang, S.; Duan, X. Permeability coeffificient investigation based on fractal characteristics of porous media soil. *Hydro Sci. Eng.* **2022**, *2022*, 50–58.
47. Lin, K.; Akihiro, T. Experimental investigations on suffusion characteristics and its mechanical consequences on saturated cohesionless soil. *Soils Found* **2014**, *54*, 713–730.
48. Richards, K.; Reddy, K. Experimental investigation of initiation of backward erosion piping in soils. *Geotechnique* **2012**, *62*, 933–942. [CrossRef]
49. Wang, Y.; Duan, X.; Gu, Y.; Wang, S. Fractal Characteristics of the Seepage Erosion Process in Porous Soil. *Geofluids* **2022**, *2022*, 3383773. [CrossRef]
50. Tao, H.; Tao, J. Quantitative analysis of piping erosion micro-mechanisms with coupled CFD and DEM method. *Acta Geotech.* **2017**, *12*, 573–592. [CrossRef]
51. Hu, Y.; Ma, P. Mechanism study and fifinite element simulation of three-phase coupling seepage erosion piping. *Rock Soil Mech.* **2013**, *34*, 913–921.

52. Baecher, G.B.; Christian, J.T. *Reliability and statistics in Geotechnical Engineering*; John Wiley & Sons Ltd.: West Sussex, UK, 2003; pp. 189–194.
53. Ching, J.; Phoon, K.-K. Establishment of generic transformations for geotechnical design parameters. *Struct. Saf.* **2012**, *35*, 52–62. [CrossRef]
54. Low, B. FORM, SORM, and spatial modeling in geotechnical engineering. *Struct. Saf.* **2014**, *49*, 56–64. [CrossRef]
55. Aguilar-López, J.; Warmink, J.; Schielen, R.; Hulscher, S. Soil stochastic parameter correlation impact in the piping erosion failure estimation of riverine flood defences. *Struct. Saf.* **2016**, *60*, 117–129. [CrossRef]
56. Zhao, T.; Montoya-Noguera, S.; Phoon, K.-K.; Wang, Y. Interpolating spatially varying soil property values from sparse data for facilitating characteristic value selection. *Can. Geotech. J.* **2018**, *55*, 171–181. [CrossRef]
57. Zhang, L.; Li, J.; Li, X.; Zhang, J.; Zhu, H. *Rainfall-Induced Soil Slope Failure: Stability Analysis and Probabilistic Assessment*; CRC Press, Taylor & Francis Ltd.: London, UK, 2019.
58. Lanxi Local Records Editorial Committee. *Lanxi City Records*; Zhejiang People's Publishing House: Hangzhou, China, 2013.
59. Wei, Y.; Ding, L. Experiments of the Castor Oil Viscosity Coefficient. *Exp. Sci. Technol.* **2014**, *12*, 29–30, 42.
60. Liang, C.; Wang, N.; Jin, Y.; Li, L. Study on the relation between viscosity and surface tension coefficient of castor oil. *Phys. Exp.* **2010**, *30*, 38–41.
61. Haeri, H.; Sarfarazi, V.; Ebneabbasi, P.; Maram, A.N.; Shahbazian, A.; Marji, M.F.; Mohamadi, A. XFEM and experimental simulation of failure mechanism of non-persistent joints in mortar under compression. *Constr. Build. Mater.* **2020**, *236*, 117500. [CrossRef]

Disclaimer/Publisher's Note: The statements, opinions and data contained in all publications are solely those of the individual author(s) and contributor(s) and not of MDPI and/or the editor(s). MDPI and/or the editor(s) disclaim responsibility for any injury to people or property resulting from any ideas, methods, instructions or products referred to in the content.

coatings

MDPI

Article

Effect of the Surface Film Formed by Hydrogen Charging on the Corrosion Behavior of an As-Cast Mg–8%Li (in wt. %) Alloy

Shuo Wang [1,2,3], Daokui Xu [2,4,5,*], Baojie Wang [6,*], Dongliang Wang [2], Zhiqiang Zhang [1,3,*] and Xiangbo Xu [2]

[1] Key Lab of Electromagnetic Processing of Materials, Ministry of Education, Northeastern University, Shenyang 110819, China; wangs1909@foxmail.com
[2] Key Laboratory of Nuclear Materials and Safety Assessment, Institute of Metal Research, Chinese Academy of Sciences, Shenyang 110016, China; dlwang19s@imr.ac.cn (D.W.); xiangbo@zju.edu.cn (X.X.)
[3] Engineering Research Center of Advanced Materials Preparing Technology, Ministry of Education, Northeastern University, Shenyang 110819, China
[4] Binzhou Institute of Technology, Binzhou 256606, China
[5] Shandong Key Laboratory of Advanced Aluminium Materials and Technology, Binzhou 256606, China
[6] School of Environmental and Chemical Engineering, Shenyang Ligong University, Shenyang 110159, China
* Correspondence: dkxu@imr.ac.cn (D.X.); bjwang@alum.imr.ac.cn (B.W.); zqzhang@mail.neu.edu.cn (Z.Z.)

Abstract: In this study, the effect of electrochemical hydrogen charging on the corrosion behavior of an as-cast Mg–8%Li alloy was investigated. It was revealed that after being cathodically hydrogen charged in a 0.1 M NaCl solution at a constant current density of 50 mA/cm^2 for 3 h, a product film with an average thickness of 20 μm was formed in the α-Mg phase, whilst the average thickness of the product film being formed in the β-Li phase was 6 μm. When the charging time was prolonged to 18 h, the thicknesses of the product films being formed on the α-Mg and β-Li phases were increased to 75 and 20 μm, respectively. The results of the grazing incidence X-ray diffraction (GIXRD) testing showed that the product films of the differently charged samples mainly consisted of $Mg(OH)_2$, LiOH and Li_2CO_3. The formed product films on the two matrix phases were dense and could hinder the erosion of Cl^- in a solution, and hence improved the corrosion resistance of the alloy. After being hydrogen charged for 3 h, the charge-transfer resistance (R_{ct}) value of the alloy was increased from 527 to 1219 Ω·cm^2. However, when the hydrogen charging time was prolonged to 18 h, the R_{ct} was slightly reduced to 1039 Ω·cm^2 due to the cracking of the surface product films and the interfacial cracking of the film/substrate matrix.

Keywords: magnesium–lithium alloy; hydrogen charging; product film; corrosion behavior

1. Introduction

As one of the lightest metallic structural materials, magnesium–lithium (Mg–Li) alloys have the high potential for reducing the weight of equipment and saving energy in industrial fields [1–5]. Generally, the mass fraction of Li determines the crystallographic structures of Mg–Li alloys [6]. Figure 1 shows the binary phase diagram of Mg–Li alloys calculated by Pandat software (CompuTherm LLC, Madison, WI, USA, version 8.0). It reveals that when the addition of Li ranges from 5.7 to 10.3 wt. %, the matrix of the Mg–Li alloys has a dual-phase structure with hexagonal close-packed (HCP) structured α-Mg and body-centered cubic (BCC) structured β-Li phases. Since dual-phase Mg–Li alloys usually have moderate mechanical strength, excellent ductility and good deformability, their development prospects in the aerospace, weapon and automotive industries are promising [7–11]. However, since the chemical activities of Mg and Li are high, the anodic dissolution of Mg–Li alloys can easily occur in aqueous environments and simultaneously cause hydrogen evolution [12–15]. It has been widely reported that hydrogen could influence the service properties of Mg alloys, such as the mechanical properties [16–28] and corrosion resistance [17–19,29–33]. For dual-phase structured Mg–Li alloys, Wang et al. [33]

reported that hydrogen charging could simultaneously deteriorate the tensile strength and ductility of an as-cast Mg–8%Li (in wt. %) alloy. However, few relevant investigations about the influence of hydrogen on the corrosion performance of Mg–Li alloys could hitherto be referenced. Song et al. [32] reported that for a Mg–2Zn alloy being hydrogen charged at 10 mA for 2 h in a 0.1 M NaCl solution, the measured corrosion current density (i_{corr}) was decreased by 80%. The higher corrosion resistance of the hydrogen-charged sample originated from the barrier effect of a compacter $Mg(OH)_2$ film being formed on the sample surface [32]. Similarly, Wang et al. [17] reported that for an as-cast Mg–7%Gd–5%Y–1%Nd–0.5%Zr alloy being hydrogen charged at -27.8 mA/cm^2 for 1 h in a 3.5 wt. % NaCl solution, an obvious surface product film could be formed. However, since the Mg_5Gd phase had a higher corrosion potential than the α-Mg matrix, the driving force for hydrogen evolution in the Mg_5Gd phase was stronger than that in the α-Mg phase under the same applied cathodic charging potential. This resulted in severe hydrogen-induced damages in the Mg_5Gd phases and then a deterioration of the protectiveness of the surface product film [17]. Similarly, for the Mg–8%Li alloy being conducted hydrogen charging at 50 mA/cm^2 for 3 h, obvious product films were also formed on the surface in the α-Mg and β-Li phases [33]. However, since the corrosion potentials in the α-Mg and β-Li phases were -1.75 V_{SCE} and -2.38 V_{SCE} [34], respectively, the driving force for hydrogen evolution in the α-Mg phase was stronger under the same applied hydrogen charging potential and the hydrogen-induced damage mainly presented in the α-Mg phase [33]. Li et al. [6] reported that for a dual-phase structured Mg–7.5%Li alloy immersed in a NaCl solution, the film formed in the β-Li phase had good protectiveness and could effectively prevent the corrosion attack of Cl^- anions. However, whether or not the product films that formed due to hydrogen charging could provide a similar protective effect on the dual-phase structured Mg–Li alloys requires further investigation.

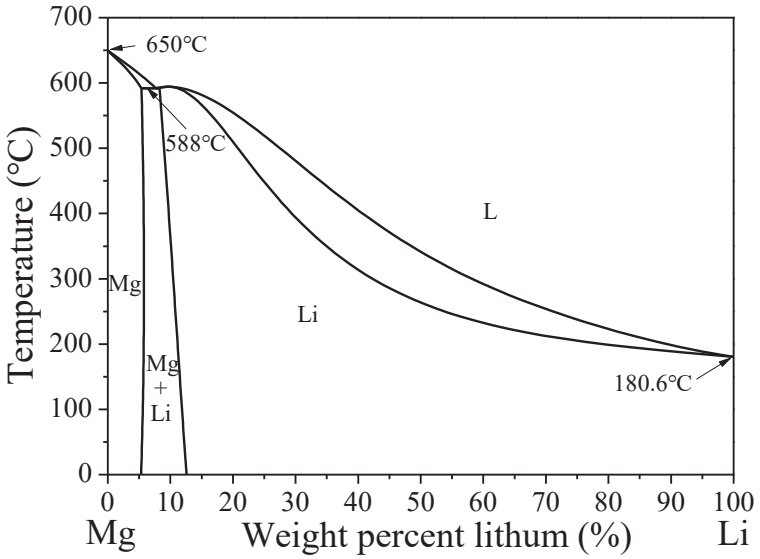


Figure 1. Binary phase diagram of Mg–Li alloys.

On the basis of the descriptions mentioned above, two questions can be proposed: (1) How do the product films formed by hydrogen charging influence the corrosion resistance of dual-phase structured Mg–Li alloys? (2) Do the product films prevent the α-Mg and β-Li phases from corrosion attack? In this study, these proposed questions are answered through an investigation of the corrosion behavior of an as-cast Mg–8%Li (in wt. %) alloy being electrochemically hydrogen charged for different durations of time. Moreover, the protection mechanism of the product film in the two matrix phases is discussed.

2. Materials and Methods

2.1. Material Preparation and Homogenization Treatment

The investigated material was an as-cast Mg–8%Li alloy, which was smelt in a vacuum resistance furnace under protective argon gas. After casting, the ingot with a dimension of 300 mm × 250 mm × 40 mm was obtained. Then, the ingot was held at 400 °C for 2 h to homogenize the microstructure. Using an inductively coupled plasma–atomic emission spectrum (ICP–AES) (Agilent, Beijing, China) apparatus, the determined chemical composition of the alloy was 8.2 wt. % Li and Mg balance. Moreover, the density and mechanical properties of the as-cast Mg–8%Li alloy were measured and listed in Table 1.

Table 1. Density and mechanical properties of the as-cast Mg–8%Li alloy.

Density (g/cm^3)	Yield Tensile Strength (MPa)	Ultimate Tensile Strength (MPa)	Elongation Ratio to Failure (%)
1.52 ± 0.04	65 ± 5	110 ± 5	38.5 ± 1.5

2.2. Microstructural Analysis

Samples with a dimension of 10 mm × 10 mm ×10 mm were sliced from the ingot. The sample surface was mechanically ground to a 5000-grit SiC paper first and then polished using diamond polishing paste to a 1.0 μm roughness. Thereafter, the polished surface was cleaned with alcohol and dried in air. X-ray diffraction (XRD; D/Max 2400) (Rigaku, Tokyo, Japan) was used for the phase analysis and scanning electron microscopy (SEM; EmCrafts CUBE II) (EmCrafts, Hanam-si, South Korea) was adopted to observe the microstructure.

2.3. Cathodic Hydrogen Charging Testing

Samples for cathodic hydrogen charging testing were connected to thin copper wires with conductive adhesive and mounted with epoxy resin. One surface with an area of 1 cm^2 was left exposed. Samples were polished to a 1.0 μm finish and then electrochemically hydrogen charged in a 0.1 M NaCl solution for 3, 6 and 18 h at a constant cathodic current density of 50 mA/cm^2 (yielding an electrode potential of approximately −4.50 V_{SCE}). The applied current density was consistent with previous studies [21,33]. All hydrogen charging tests were carried out using an electrochemical workstation (CorrTest CS350) (CorrTest, Wuhan, China) with a classical three-electrode system in which the reference electrode was the saturated calomel electrode (SCE) and the counter electrode was the Pt electrode. To clearly observe the formed surface product films, surface and three-dimensional (3D) morphologies of differently charged samples were observed using an optical microscope (OM; Keyence VHX 2000) (Keyence, Osaka, Japan) and their cross sections were observed using SEM. Moreover, a glancing incidence X-ray diffractometer (GIXRD; D/Max 2400) (Rigaku, Tokyo, Japan) under a glancing angle of 0.5° was used to analyze the compositions of product films. Compared with the X-ray photoelectron spectroscopy (XPS) method, the GIXRD method could be more suitable for determining whether the hydrates (such as $LiOH{\cdot}H_2O$) were contained in the product films [35].

2.4. Electrochemical Measurements

Electrochemical measurements for the differently charged samples were pursued in 0.1 M NaCl solution and the electrochemical workstation (CorrTest CS350) (CorrTest, Wuhan, China) with the same three-electrode system mentioned in Section 2.3 was used. The potentiodynamic polarization tests were scanned from −250 mV_{SCE} to 350 mV_{SCE} versus open-circuit potential (OCP) at a scanning rate of 0.1667 mV/s after being stabilized for 600 s at OCP. After the potentiodynamic polarization tests, the obtained curves were fitted using CorrView software (CorrTest, Wuhan, China, version 3.1c). Electrochemical impedance spectroscopy (EIS) measurements were conducted at OCP after 600 s stabilization with a sinusoidal potential destabilization of 5 mV and a frequency ranging from

100 kHz to 0.01 Hz. The obtained EIS data were fitted using Zsimpwin 3.30d software (Ametek, San Diego, CA, USA, version 3.30d).

2.5. Hydrogen Evolution and Immersion Testing

To observe the changes in hydrogen evolution volume for the sample being immersed in the 0.1 M NaCl solution, the hydrogen-charged samples were mounted with epoxy resin and only one surface with an area of 1 cm^2 was left exposed. Then, the mounted samples were immersed for up to 48 h at room temperature. During the testing, in order to guarantee the stable pH of the experimental environment, the solution volume was about 200 times larger than the sample volume. Furthermore, the solution was renewed every 24 h and possessed a stable pH value of about 6.7 ± 0.2, measured from a digital pH meter (INESA PHS-25) (INESA, Shanghai, China). To disclose the effect of hydrogen charging on the corrosion mechanism of the alloy, the macro corrosion morphologies of the uncharged and 3 h charged samples being immersed in 0.1 M NaCl solution for 0~48 h were observed using OM. Moreover, highly magnified and 3D observations of the corrosion morphologies in the uncharged and 3 h charged samples being immersed for 2, 4 and 8 h, respectively, were observed in situ using OM.

3. Results

3.1. Microstructural Characterization

Figure 2 shows the initial microstructure of the Mg–8%Li alloy. The XRD pattern exhibited that the alloy mainly consisted of α-Mg and β-Li phases (Figure 2a). The backscatter electron (BSE) image showed that the alloy had a dual-phase structure (Figure 2b). Figure 3 exhibits the surface and 3D morphologies of differently charged samples. On the basis of the 3D morphologies, it could be seen that the maximum surface height difference in the uncharged sample was 0.99 μm (Figure 3b). For the 3 h charged sample, an obvious white product film could be observed in the α-Mg phase and the surface in the β-Li phase was uniformly covered with a layer of dark product film (Figure 3c). Moreover, the maximum surface height difference was increased to 36.09 μm (Figure 3d). For the 6 h charged sample, the damage to the α-Mg phase became much more severe and the maximum surface height difference was increased to 54.78 μm (Figure 3e,f). After being charged for 18 h, the formed product film almost covered the whole sample surface and the maximum surface height difference increased to 100.60 μm (Figure 3g,h).

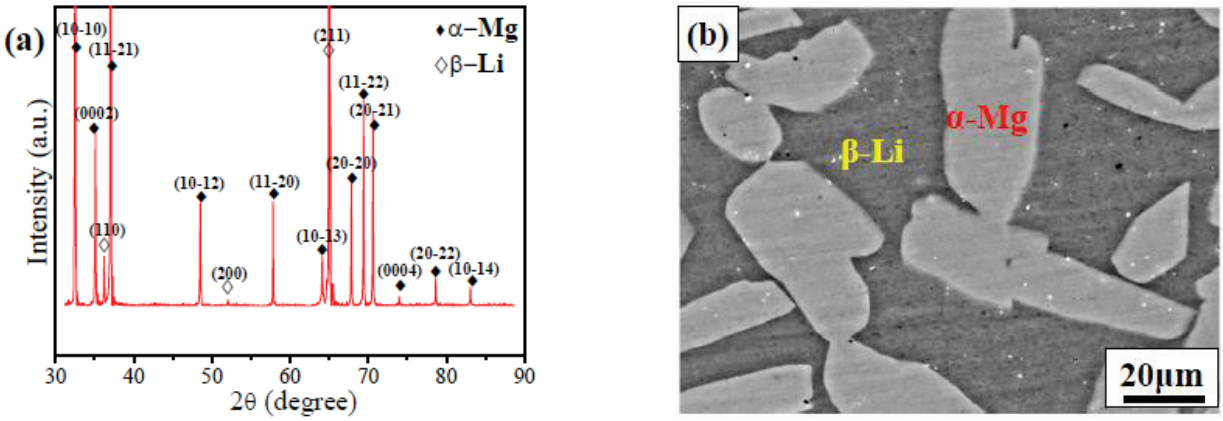


Figure 2. Microstructural characterization of the as-cast Mg–8%Li alloy: (**a**) XRD pattern, (**b**) BSE image.

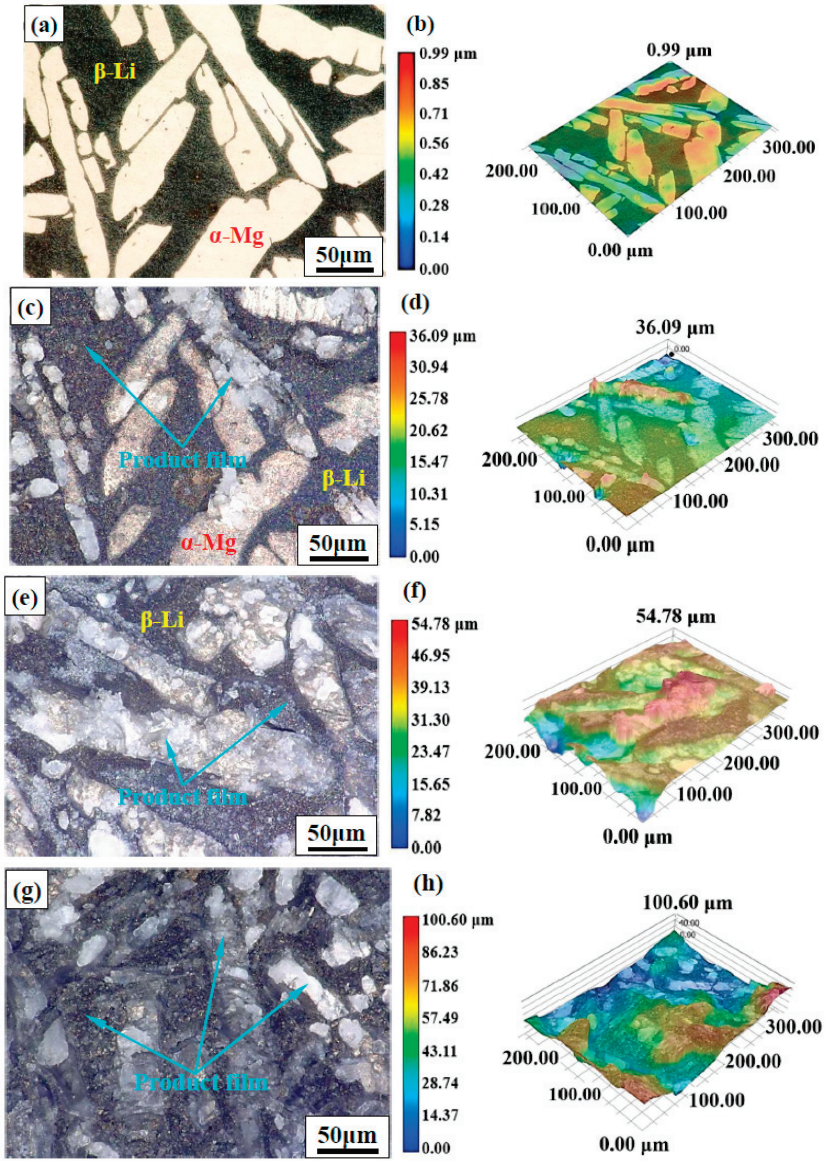


Figure 3. Surface and 3D morphologies of different samples after being hydrogen charged for: (**a**) 0 h, (**c**) 3 h, (**e**) 6 h and (**g**) 18 h. Images (**b**), (**d**), (**f**) and (**h**) are the corresponding 3D morphologies of images (**a**), (**c**), (**e**) and (**g**), respectively.

The GIXRD patterns in the formed product films are shown in Figure 4. For the 3 h, 6 h and 18 h charged samples, the product films were mainly constituted of $Mg(OH)_2$, LiOH and Li_2CO_3. Figure 5 presents the cross-sectional morphologies of the charged samples. It could be seen that for the 3 h charged sample, the average thickness of the product film formed in the α-Mg phase was 20 μm, whilst that in the β-Li phase was about 6 μm (Figure 5a,b). Moreover, the product films in the two phases were relatively uniform and only several microcracks could be seen in the product films (Figure 5b). The energy dispersive spectrum (EDS) results demonstrated that the product film in the α-Mg phase mainly contained Mg and O, whereas the main elements of the film in the β-Li phase were Mg, O and C (Figure 5b). With the prolongation of the hydrogen charging time, the thicknesses of the product films in the two phases were gradually increased (Figure 5c–f). For the 6 h charged sample, the average thickness of the product film formed in the α-Mg phase was about 40 μm and that in the β-Li phase was 10 μm (Figure 5c,d). Meanwhile, the number of cracks present in the interior of the product films increased (Figure 5d). Moreover, cracks could also be formed at the interfaces of the product film/substrate phases

(Figure 5d). In the 18 h charged sample, the average thickness values of the product films in the α-Mg and β-Li phases were further increased to 75 and 20 μm, respectively (Figure 5e,f). Furthermore, the number of cracks being presented in the interior of the product films and at the interfaces of the product film/substrate phases was further increased (Figure 5f).

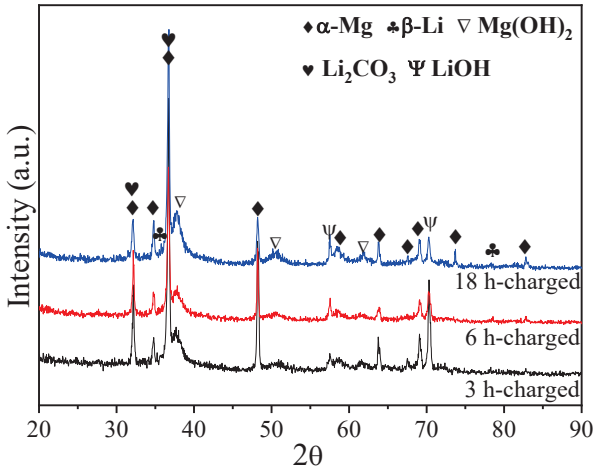


Figure 4. GIXRD patterns of the formed product films for differently charged samples.

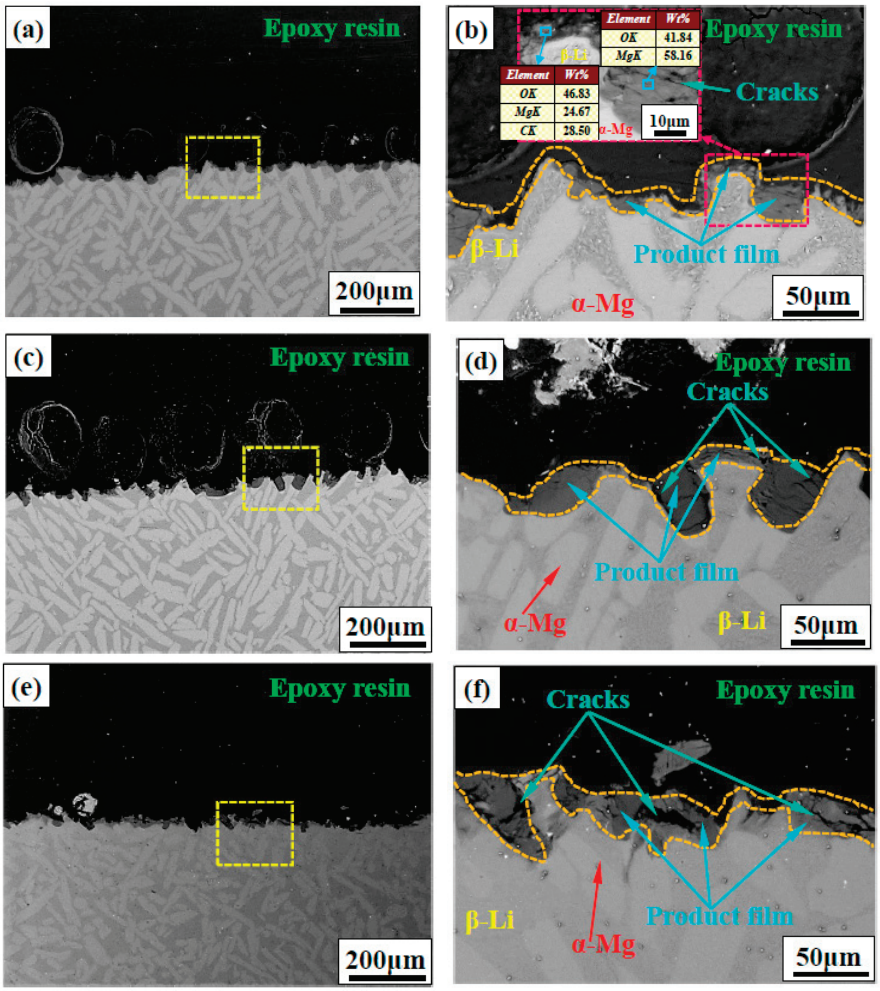


Figure 5. Cross-sectional morphologies of different samples after being hydrogen charged for: (**a**) 3 h, (**c**) 6 h and (**e**) 18 h. Images (**b**), (**d**) and (**f**) are high-magnified observations of the squared areas in images (**a**), (**c**) and (**e**), respectively.

3.2. Electrochemical Measurements

The potentiodynamic polarization curves for the differently charged samples are exhibited in Figure 6. This figure showed that the anodic and cathodic branches of the curves were not symmetric. Generally, for the Mg alloys, the cathodic branch corresponded to the occurrence of hydrogen evolution, whereas the anodic branch was concerned with the anodic dissolution of the α-Mg matrix [36]. Due to the occurrence of a negative difference effect (NDE) and pitting during the potentiodynamic polarization tests, the anodic branch was not suitable for fitting [13,14,36,37]. Therefore, the measured corrosion parameters of the differently charged samples were fitted from the cathodic branches using Tafel extrapolation. The fitting results are listed in Table 2. The results revealed that the corrosion potentials (E_{corr}) of the differently charged samples were basically the same (about −1.60 V_{SCE}) and the corrosion current density (i_{corr}) values of the 0, 3, 6 and 18 h charged samples were 51.9, 17.1, 18.2 and 19.1 μA/cm^2, respectively, indicating that the corrosion resistance of the Mg–8%Li alloy could be promoted by hydrogen charging. However, it should be noted that with the hydrogen charging time being prolonged from 3 to 18 h, the corrosion resistance of the alloy decreased slightly. Moreover, for the charged samples, an obvious film breakdown potential at about −1.45 V_{SCE} could be observed in their anodic branches.

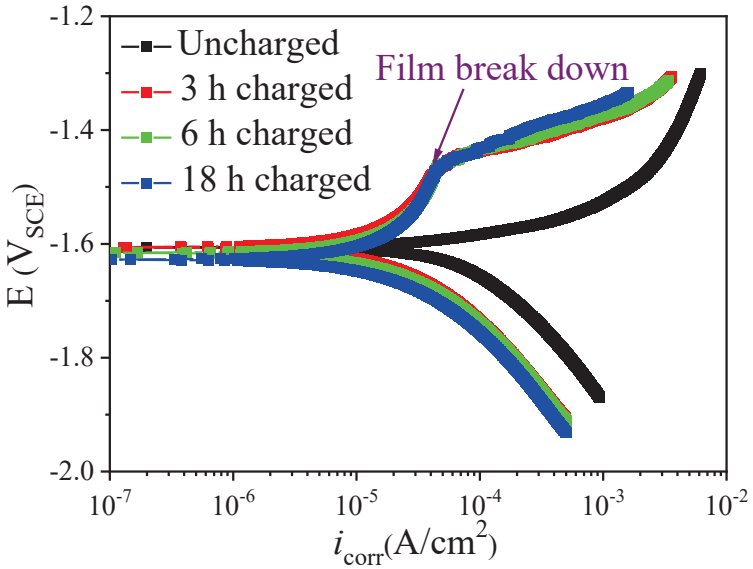


Figure 6. Potentiodynamic polarization curves of differently charged samples measured in a 0.1 M NaCl solution.

Table 2. Fitting results from the polarization curves of differently charged samples measured in a 0.1 M NaCl solution.

Hydrogen Charging Time (h)	i_{corr} (μA/cm^2)	E_{corr} (V_{SCE})
0	51.9 ± 8.1	−1.61 ± 0.01
3	17.1 ± 0.1	−1.61 ± 0.01
6	18.2 ± 0.3	−1.62 ± 0.01
18	19.1 ± 0.7	−1.62 ± 0.01

The EIS plots of the different samples are shown in Figure 7. The spectrum of the uncharged sample was composed of a high-frequency capacitive loop and a low- frequency inductive loop (Figure 7a). Generally, the low-frequency inductive loop was correlated with the occurrence of localized corrosion [16]. For the charged samples, the plots had a single capacitive loop and the impedance gradually decreased with the increase in charging

time. Moreover, in order to fit the EIS plots, two kinds of equivalent circuits were employed (Figure 7b,c) and the fitting results are listed in Table 3. The equivalent circuit in the uncharged sample consisted of the solution resistance (R_s), charge-transfer resistance (R_{ct}) and the double-layer capacitance at the alloy matrix/electrolyte interface (Q_{dl}) in the high-frequency capacitance loop, and the inductive resistance (R_L) and inductance (L) in the low-frequency inductance loop [16]. For the charged samples, the equivalent circuit was composed of the R_s, R_{ct} and Q_{dl}. Among them, the Q_{dl} was used to replace the ideal capacitor and account for the heterogeneity in the system [6,14]. Moreover, the Q_{dl} could be defined as Y_{dl} and n_{dl}, where n_{dl} is the dispersion coefficient [6,14]. Generally, the Q_{dl} was regarded as a capacitor when the n_{dl} value was 1 and could serve as the resistance when the n_{dl} value was 0 [6,13]. This finding revealed that when the hydrogen charging time was prolonged from 0 to 3 h, the determined R_{ct} values of the alloy increased from 527 to 1219 $\Omega \cdot cm^2$. After being hydrogen charged for 6 and 18 h, the R_{ct} values were slightly decreased to 1147 and 1039 $\Omega \cdot cm^2$, respectively.

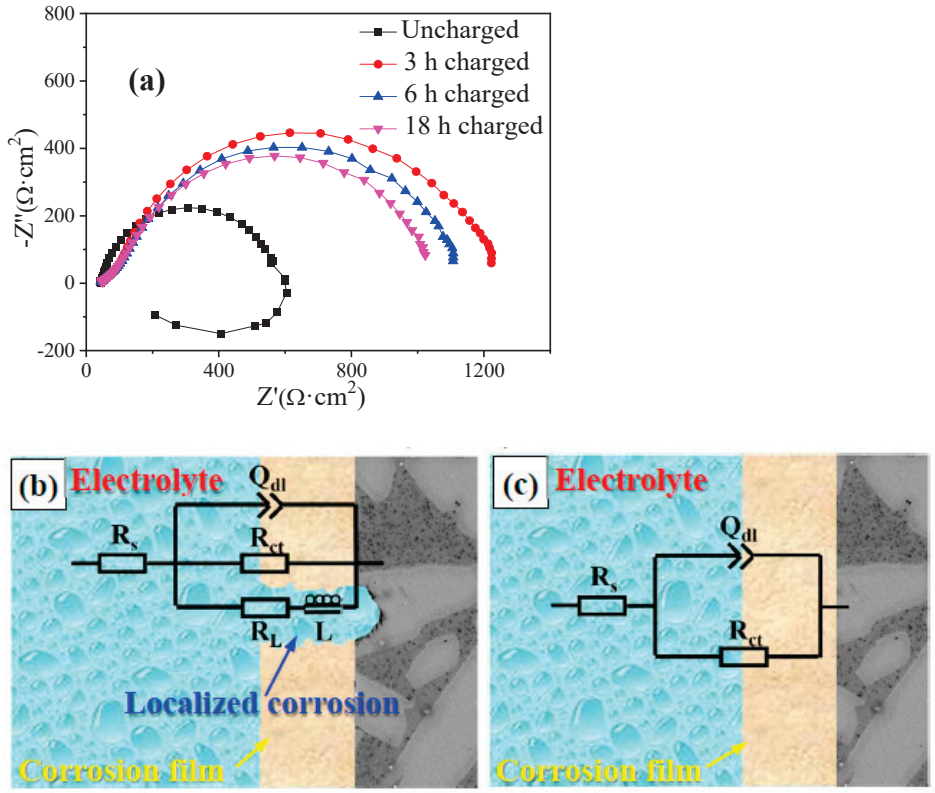


Figure 7. Nyquist plots and equivalent circuits of differently charged samples measured in a 0.1 M NaCl solution: (**a**) Nyquist plots, (**b**) equivalent circuit of uncharged sample and (**c**) equivalent circuit of 3, 6 and 18 h charged samples.

Table 3. The fitting EIS data of differently charged samples based on the equivalent circuits.

Hydrogen Charging Time (h)	R_s (Ω cm^2)	Y_{dl} (μF)	n_{dl}	R_{ct} (Ω cm^2)	L (H cm^{-2})	R_L (Ω cm^2)
0	42 ± 1	36.9 ± 3.6	0.88 ± 0.01	527 ± 22	3411 ± 854	256 ± 16
3	43 ± 2	24.3 ± 1.3	0.90 ± 0.01	1219 ± 40	-	-
6	46 ± 3	39.9 ± 1.5	0.87 ± 0.01	1147 ± 83	-	-
18	46 ± 7	31.8 ± 0.2	0.88 ± 0.01	1039 ± 62	-	-

3.3. Hydrogen Evolution

The hydrogen evolution curves of the differently charged samples immersed in a 0.1 M NaCl solution are presented in Figure 8. Following the gradients of the different curves, the results of the hydrogen evolution rates in the 3, 6 and 18 h charged samples were similar and were about 0.67 times lower than that of the uncharged sample. Since the electrochemical corrosion rates of the Mg–Li alloys were always proportional to the hydrogen evolution rates when immersed in the NaCl solution at OCP [13,14,17], this proved that the charged samples had the higher corrosion resistance, which was broadly consistent with the polarization and EIS data (Figures 6 and 7).

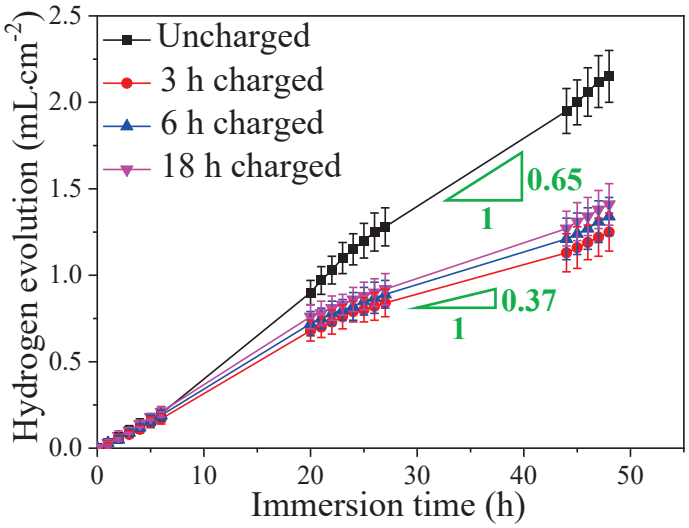


Figure 8. Hydrogen evolution curves of differently charged samples measured in a 0.1 M NaCl solution.

3.4. Corrosion Morphology

The macro corroded surfaces of the uncharged and 3 h charged samples immersed in the 0.1 M NaCl solution for different durations are exhibited in Figure 9. The results showed that for the uncharged sample, the localized corrosion mainly occurred at the edges of the sample when immersed for 2 h. The corroded area was significantly increased as the immersion time was prolonged. After being immersed for 48 h, substantial corrosion products almost covered the whole sample surface. In the 3 h charged sample, when the immersion time was less than 24 h, no obvious localized corrosion could be observed on the surface, demonstrating that the hydrogen-charged sample had a high corrosion performance in the NaCl solution. After being immersed for 48 h, the localized corrosion only occurred at the edges of the sample.

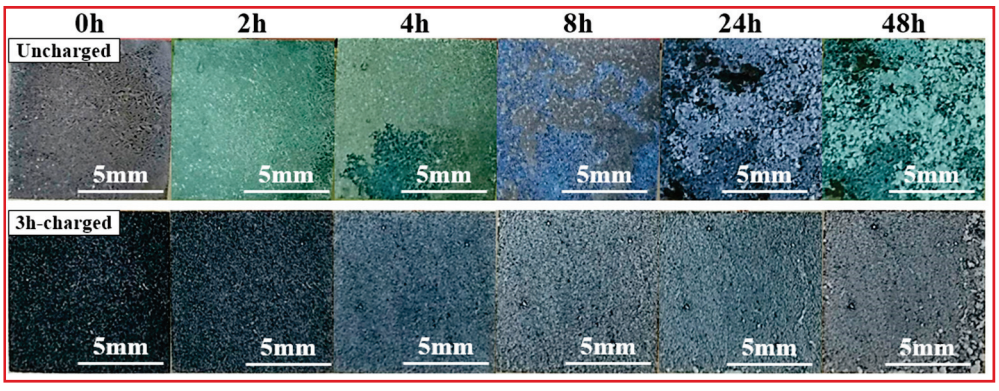


Figure 9. Macro corroded surfaces of the uncharged and 3 h charged samples after being immersed in the 0.1 M NaCl solution for different durations.

Figures 10 and 11, respectively, present the in situ observations of the evolution of the corroded regions on the surfaces of the uncharged and 3 h charged samples immersed for 2, 4 and 8 h in the 0.1 M NaCl solution. For the uncharged sample, at the early stage of corrosion, pits preferentially occurred at the α-Mg/β-Li interphases and in the α-Mg phase. The maximum surface height difference was almost unchanged (Figure 10c,d). After being immersed for 4 h, obvious localized corrosion propagated from the α-Mg phase to the β-Li phase and the maximum surface height difference due to the formed corrosion products was reached at 20.56 μm (Figure 10e,f). When the sample was immersed for 8 h, the corrosion severity further intensified and the maximum surface height difference of the localized corrosion was 35.87 μm (Figure 10g,h).

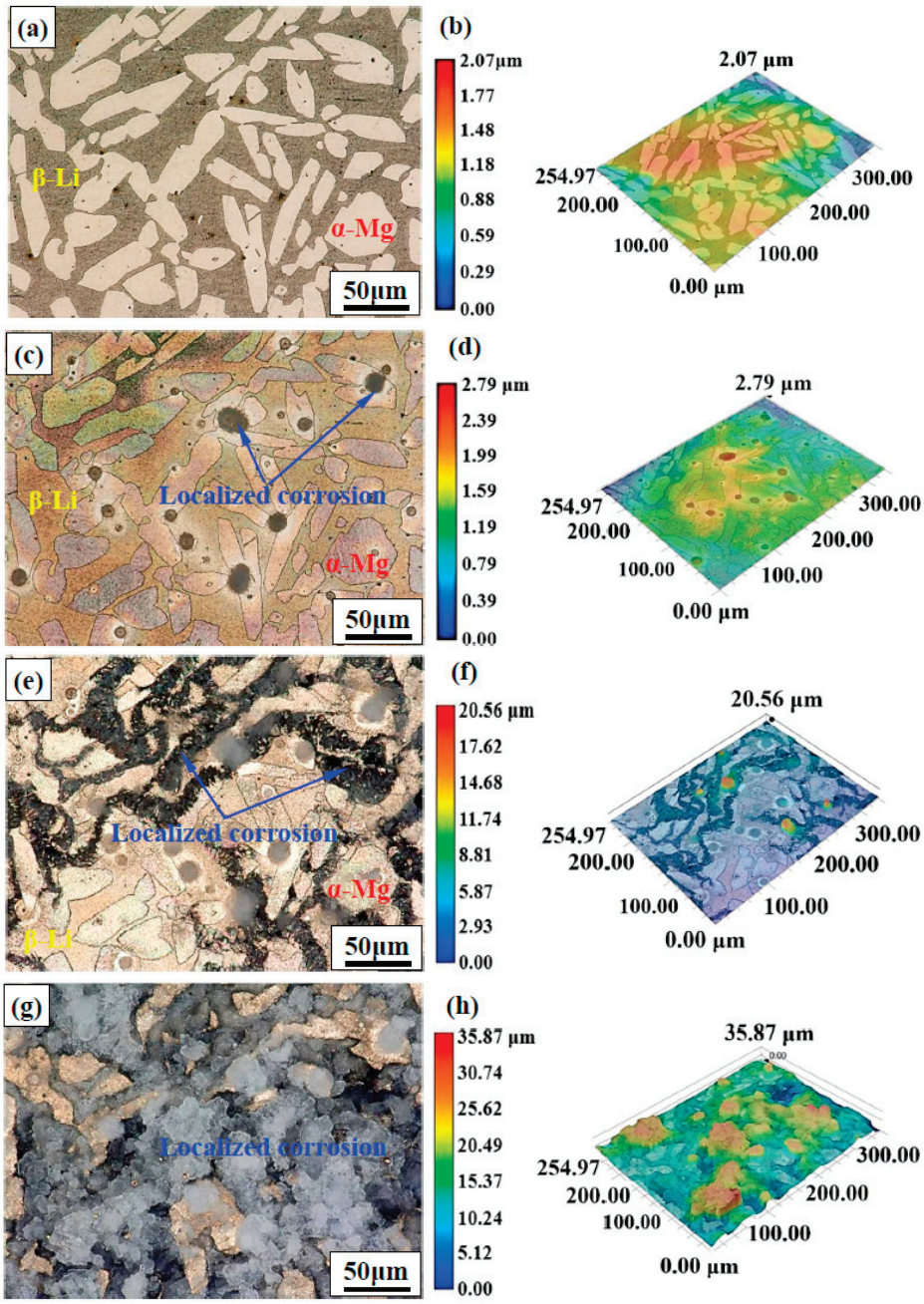


Figure 10. Surface corrosion morphologies and 3D images of the uncharged sample after being immersed in a 0.1 M NaCl solution for: (**a**) 0 h, (**c**) 2 h, (**e**) 4 h and (**g**) 8 h. Images (**b**), (**d**), (**f**) and (**h**) are the corresponding 3D morphologies of images (**a**), (**c**), (**e**) and (**g**), respectively.

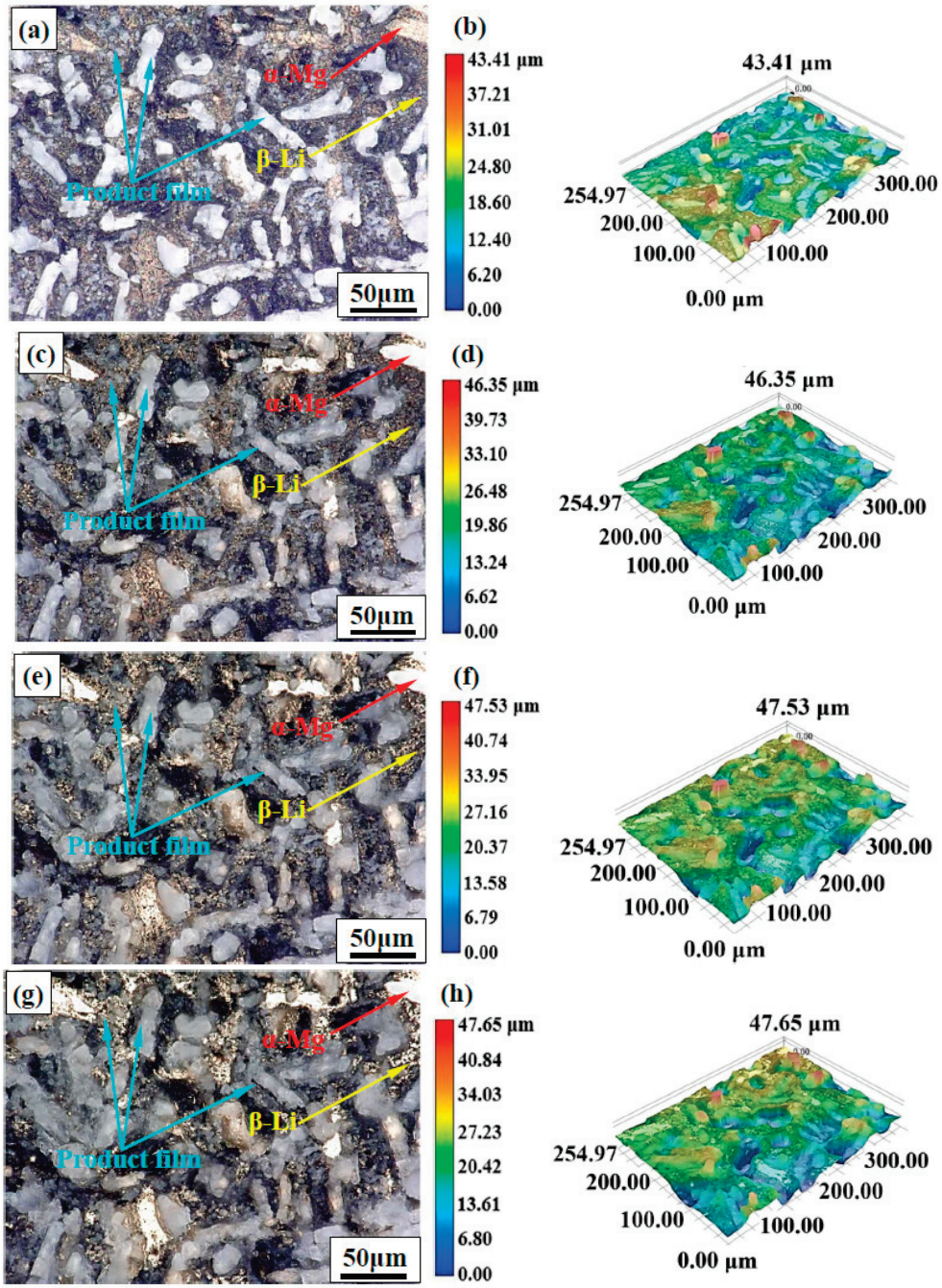


Figure 11. Surface corrosion morphologies and 3D images of the 3 h charged sample after being immersed in a 0.1 M NaCl solution for: (**a**) 0 h, (**c**) 2 h, (**e**) 4 h and (**g**) 8 h. Images (**b**), (**d**), (**f**) and (**h**) are the corresponding 3D morphologies of images (**a**), (**c**), (**e**) and (**g**), respectively.

In the 3 h charged sample, obvious product films were formed in the two matrix phases and the maximum surface height difference was 43.41 μm (Figure 11a,b). With the immersion time being prolonged from 2 to 8 h, no obvious localized corrosion occurred on the sample surface and the maximum surface height difference was slightly increased from 46.35 to 47.65 μm (Figure 11c–h), indicating that the product films being formed in the two matrix phases of the 3 h charged sample exhibited good corrosion protectiveness.

4. Discussion

In this study, the corrosion resistance of an Mg–8%Li alloy was effectively improved after hydrogen charging (Figures 6–8). Previous work demonstrated that for hydrogen-

charged Mg alloys, the change of their corrosion behavior was related to the formation of product films during the hydrogen charging process [17,29–32]. Therefore, in order to disclose the mechanism for improving corrosion resistance in the charged Mg–8%Li alloy, it was necessary to investigate the components and formation mechanisms of the formed product films in two matrix phases. Based on the Pourbaix diagram of the Mg–H_2O system, when the applied potential was lower than -2.36 V_{SCE}, the anodic dissolution of Mg could not occur in a neutral solution at 25 °C and an atmosphere of 1 atm [38]. Similarly, on the basis of the Pourbaix diagram of the Li–H_2O system in a neutral solution at 25 °C and an atmosphere of 1 atm, it was revealed that Li could not be corroded when the applied potential was lower than -3.25 V_{SCE} [39]. In the current investigation, since the applied charging potential was -4.50 V_{SCE}, the anodic dissolution in the α-Mg and β-Li phases could not occur during the hydrogen charging process. Therefore, the formation of the product films in the two matrix phases could be induced by hydrogen charging. Previous research reported that Mg and Li could react with charged hydrogen to form MgH_2 [38] and LiH hydrides [40], which are expressed in Reaction (1) and Reaction (2), respectively:

$$Mg + 2H \rightarrow MgH_2 \quad (1)$$

$$Li + H \rightarrow LiH \quad (2)$$

However, MgH_2 and LiH could be easily decomposed into $Mg(OH)_2$ and LiOH and generate H_2 when exposed to water [38,41], as expressed in Reaction (3) and Reaction (4). Moreover, LiOH could react with CO_2 in the air to form Li_2CO_3 [42], as expressed in Reaction (5):

$$MgH_2 + 2H_2O \rightarrow Mg(OH)_2 + 2H_2 \quad (3)$$

$$LiH + H_2O \rightarrow LiOH + H_2 \quad (4)$$

$$2LiOH + CO_2 \rightarrow Li_2CO_3 + H_2 \quad (5)$$

Therefore, it could be inferred that for the charged Mg–8%Li alloy, the formed product film in the α-Mg phase should mainly consist of $Mg(OH)_2$ (Figure 5) originating from the hydrolysis of the MgH_2 hydrides. Moreover, the product film in the β-Li phase should be composed of LiOH and Li_2CO_3, and the presence of Li_2CO_3 could be ascribed to the transformation of LiOH during long-time exposure to the air after the hydrogen charging processes. It was interesting to note that the thicknesses of the product films in the α-Mg phase were much larger than those in the β-Li phase for the differently charged samples (Figure 5). The main reason was that for the dual-phase structured Mg–Li alloys, the corrosion potentials in the α-Mg and β-Li phases were -1.75 V_{SCE} and -2.38 V_{SCE} [34], respectively, and the driving force for hydrogen evolution in the α-Mg phase was much stronger than that in β-Li phase under the same applied hydrogen charging potential of -4.50 V_{SCE}. This could lead to the formation of more product films in the α-Mg phase (Figure 5). It has been reported that when dual-phase Mg–Li alloys were immersed in a NaCl solution, the main component of the product film formed in the α-Mg phase was $Mg(OH)_2$ [6,13,14]. However, the Cl^- could react with the $Mg(OH)_2$ film to form $MgCl_2$, resulting in the degraded protectiveness of the $Mg(OH)_2$ film in the α-Mg phase [13,14]. For to this reason, Li et al. [6] reported that after being immersed in a 0.1 M NaCl solution for 4 h, the R_{ct} of the Mg–7.5Li alloy was reduced by 62% and pits mainly initiated in the α-Mg phase. However, in the current work, the R_{ct} of the Mg–8%Li alloy was increased by 57% after being hydrogen charged for 3 h (Figure 7). Furthermore, the product film in the α-Mg phase could effectively prevent the occurrence of localized corrosion after being immersed in the 0.1 M NaCl solution for 8 h (Figure 11). Therefore, it could be inferred that the $Mg(OH)_2$ film being formed by electrochemical hydrogen charging had a good corrosion performance in the NaCl solution. Wu et al. [43] reported that a dense

$Mg(OH)_2$ film, which could hinder the erosion of Cl^-, could be prepared on the surface of the AZ91D alloy using cathodic polarization. Thus, it could be conjectured that a $Mg(OH)_2$ film being prepared using a similar cathodic polarization method should also have the dense structure and the strong corrosion protectability. In addition to the product film in the α-Mg phase, the product film being formed in the β-Li phase also had good corrosion protectiveness (Figure 11). As mentioned previously, the product film in the β-Li phase should be constituted by LiOH and Li_2CO_3. However, for dual-phase Mg–Li alloys, Mg could exist in the β-Li phase as the solid solute [6]. Thus, it could be found that a small amount of $Mg(OH)_2$ could be formed in the β-Li phase during the hydrogen charging process. Zhang et al. [44] reported that the mixture of $LiOH/Mg(OH)_2$ could effectively promote the corrosion resistance of a Li–Mg electrode. Similarly, it could be speculated that the β-Li phase could also be protected by the $LiOH/Mg(OH)_2$ film. Moreover, Xu et al. [45] reported that a BCC structured Mg–10.95%Li–3.29%Al–0.59%Y–0.19%Zr alloy could have superior corrosion resistance due to the formation of the protective Li_2CO_3 film on the surface. Thus, it could be deduced that the Li_2CO_3 film in the β-Li phase should also have similarly high corrosion protectability.

However, it should be noted that the corrosion resistance of the charged samples gradually decreased with prolonged hydrogen charging time (Figures 6–8). The SEM observations of the cross-sections of the charged samples revealed that when the hydrogen charging time was prolonged, the number of cracks being presented in the interior of the surface product films and at the interfaces of the product film/substrate phases would be increased (Figure 5). In a previous study, Chen et al. [31] reported that during the hydrogen charging process of an AZ91 Mg alloy, the charged hydrogen atoms could combine into the H_2 gas in the interior of the corrosion film and react with the alloy matrix to form hydride. With the increase in hydrogen charging time, the hydrogen pressure induced by the H_2 gas and expansion stress caused by the formation of the hydrides could lead to the rupture of the corrosion film and degrade the corrosion resistance. Similarly, it can be speculated that for the charged Mg–8%Li alloy, cracking of the product film in the α-Mg phase should also be attributed to the formation of H_2 gas and hydrides. Moreover, it has been reported that the Pilling–Bedworth ratios (PBR) of the $Mg(OH)_2$, LiOH and Li_2CO_3 films were all larger than 1 [46], indicating that they had a larger volume than the Mg–Li matrix and their formation could induce local stresses [47]. Thus, for the sample being charged for a longer time, the gradually increased local stresses in the product films and at the product film/substrate phases could further promote the formation of cracks and degrade the corrosion protectability of the product films. In addition, previous studies demonstrated that although the yield strength, ultimate tensile strength and the elongation ratio to failure of the investigated Mg–8%Li alloy were gradually decreased with the increase in hydrogen charging time, the elongation ratio to failure of the alloy could still be 12.4 % even after being hydrogen charged at the cathodic current density of 50 mA/cm^2 for 18 h. This indicated that the Mg–8%Li alloy had a high resistance to hydrogen embrittlement [33]. Combined with the beneficial effect of hydrogen charging on the improvement of corrosion performance, this demonstrated that the Mg–8%Li alloy could be used as a candidate material in the hydrogen-containing service environment.

5. Conclusions

In this study, the effect of a product film formed by electrochemical hydrogen charging on the corrosion behavior of an as-cast Mg–8%Li alloy was investigated. The main conclusions were as follows:

(1) After being hydrogen charged at 50 mA/cm^2 for 3 h in a 0.1 M NaCl solution, an obvious product film composed of $Mg(OH)_2$, LiOH and Li_2CO_3 was formed in the two matrix phases of the Mg–8%Li alloy. Moreover, the thickness values of the formed product films in both of the phases increased with the prolongation of the hydrogen charging time.

(2) After being hydrogen-charged for 3 h, the formed product films in both of the two matrix phases were dense and had a high corrosion resistance in the NaCl solution.

Therefore, the matrix of the Mg–8%Li alloy underneath the product films could be protected. However, when the hydrogen charging time was increased to 18 h, the protectiveness of the product films was weakened because the number of cracks being presented in the interior of the films and at the interfaces of the product film/substrate phases was increased.

Author Contributions: Conceptualization, D.X. and S.W.; methodology, S.W.; software, S.W. and X.X.; validation, D.X., Z.Z. and B.W.; formal analysis, S.W. and D.W.; investigation, S.W.; resources, D.X.; data curation, D.X. and S.W.; writing—original draft preparation, S.W.; writing—review and editing, D.X., B.W. and S.W.; visualization, S.W., D.W. and X.X.; supervision, D.X.; project administration, D.X. and B.W.; funding acquisition, D.X. and Z.Z. All authors have read and agreed to the published version of the manuscript.

Funding: This research was supported by the National Natural Science Foundation of China Projects under Grant [Nos. U21A2049, 52071220, 51871211, 51701129 and 51971054], Liaoning Province's project of "Revitalizing Liaoning Talents" (XLYC1907062), the Doctor Startup Fund of the Natural Science Foundation Program of Liaoning Province (No. 2019-BS-200), the Strategic New Industry Development Special Foundation of Shenzhen (JCYJ20170306141749970), the funds of the International Joint Laboratory for Light Alloys, Liaoning BaiQianWan Talents Program, the Domain Foundation of Equipment Advance Research of the 13th Five-Year Plan (61409220118), the National Key Research and Development Program of China under Grant [Nos. 2017YFB0702001 and 2016YFB0301105], the Innovation Fund of the Institute of Metal Research (IMR), the Chinese Academy of Sciences (CAS), the National Basic Research Program of China (973 Program) project under Grant No. 2013CB632205 and the Fundamental Research Fund for the Central Universities under Grant [No. N2009006], Bintech-IMR R&D Program [No. GYY-JSBU-2022-009].

Institutional Review Board Statement: Not applicable.

Informed Consent Statement: Not applicable.

Data Availability Statement: Not applicable.

Conflicts of Interest: The authors declare no conflict of interest.

References

1. Wu, R.; Yan, Y.; Wang, G.; Murr, L.E.; Han, W.; Zhang, Z.; Zhang, M. Recent progress in magnesium-lithium alloys. *Int. Mater. Rev.* **2015**, *60*, 65–100. [CrossRef]
2. Yang, Y.; Xiong, X.M.; Chen, J.; Peng, X.D.; Chen, D.L.; Pan, F.S. Research advances in magnesium and magnesium alloys worldwide in 2020. *J. Magnes. Alloy.* **2021**, *9*, 705–747. [CrossRef]
3. Hou, J.Y.; Wang, B.J.; Xu, D.K.; Cui, L.J.; Sun, J. Effect of surfactants on the corrosion protectability of calcium phosphate conversion coatings on duplex structured Mg-8Li (in wt. %) alloy. *Coatings* **2022**, *12*, 1182. [CrossRef]
4. Wang, B.J.; Hou, J.Y.; Luan, J.Y.; Xu, D.K.; Sun, H.J.; Sun, J. The corrosion behaviors of an as-rolled Mg-8Li (in wt. %) alloy in two differently concentrated NaCl Solutions. *Coatings* **2022**, *12*, 406. [CrossRef]
5. Estrin, Y.; Nene, S.S.; Kashyap, B.P.; Prabhu, N.; Samman, T.A. New hot rolled Mg-4Li-1Ca alloy: A potential candidate for automotive and biodegradable implant applications. *Mater. Lett.* **2016**, *173*, 252–256. [CrossRef]
6. Li, C.Q.; Xu, D.K.; Chen, X.B.; Wang, B.J.; Wu, R.Z.; Han, E.H.; Birbilis, N. Composition and microstructure dependent corrosion behaviour of Mg-Li alloys. *Electrochim. Acta* **2018**, *260*, 55–64. [CrossRef]
7. Zhong, F.; Wu, H.J.; Jiao, Y.L.; Wu, R.Z.; Zhang, J.H.; Hou, L.G.; Zhang, M.L. Effect of Y and Ce on the microstructure, mechanical properties and anisotropy of as-rolled Mg-8Li-1Al alloy. *J. Mater. Sci. Technol.* **2020**, *39*, 124–134. [CrossRef]
8. Li, C.Q.; Xu, D.K.; Wang, B.J.; Sheng, L.Y.; Qiao, Y.X.; Han, E.H. Natural ageing responses of duplex structured Mg-Li based alloys. *Sci. Rep.* **2017**, *7*, 40078. [CrossRef]
9. Xu, D.K.; Li, C.Q.; Wang, B.J.; Han, E.H. Effect of icosahedral phase on the crystallographic texture and mechanical anisotropy of duplex structured Mg-Li alloys. *Mater. Des.* **2015**, *88*, 88–97. [CrossRef]
10. Xu, D.K.; Zu, T.T.; Yin, M.; Han, E.H. Mechanical properties of the icosahedral phase reinforced duplex Mg-Li alloy both at room and elevated temperatures. *J. Alloys Compd.* **2014**, *582*, 161–166. [CrossRef]
11. Xu, D.K.; Liu, L.; Xu, Y.B.; Han, E.H. The strengthening effect of icosahedral phase on as-extruded Mg-Li alloys. *Scr. Mater.* **2007**, *57*, 285–288. [CrossRef]
12. Dobkowska, A.; Adamczyk-Cieślak, B.; Kubásek, J.; Vojtěch, D.; Kuc, D.; Hadasik, E.; Mizera, J. Microstructure and corrosion resistance of a duplex structured Mg-7.5Li-3Al-1Zn. *J. Magnes. Alloy.* **2021**, *9*, 467–477. [CrossRef]
13. Wang, B.J.; Xu, D.K.; Cai, X.; Qiao, Y.X.; Sheng, L.Y. Effect of rolling ratios on the microstructural evolution and corrosion performance of an as-rolled Mg-8 wt. %Li alloy. *J. Magnes. Alloy.* **2021**, *9*, 560–568. [CrossRef]

14. Wang, B.J.; Xu, K.; Xu, D.K.; Cai, X.; Qiao, Y.X.; Sheng, L.Y. Anisotropic corrosion behavior of hot-rolled Mg-8 wt. %Li alloy. *J. Mater. Sci. Technol.* **2020**, *53*, 102–111. [CrossRef]
15. Song, Y.W.; Shan, D.Y.; Chen, R.S.; Han, E.H. Corrosion characterization of Mg-8Li alloy in NaCl solution. *Corros. Sci.* **2009**, *51*, 1087–1094. [CrossRef]
16. Wang, S.D.; Xu, D.K.; Wang, B.J.; Sheng, L.Y.; Han, E.H.; Dong, C. Effect of solution treatment on stress corrosion cracking behavior of an as-forged Mg-Zn-Y-Zr alloy. *Sci. Rep.* **2016**, *6*, 29471. [CrossRef]
17. Wang, S.D.; Xu, D.K.; Wang, B.J.; Sheng, L.Y.; Qiao, Y.X.; Han, E.H.; Dong, C. Influence of phase dissolution and hydrogen absorption on the corrosion behavior of Mg-7%Gd-5%Y-1%Nd-0.5%Zr alloy in 3.5 wt. % NaCl solution. *Corros. Sci.* **2018**, *142*, 185–200. [CrossRef]
18. Chen, J.; Wang, J.Q.; Han, E.H.; Ke, W. Effect of hydrogen on stress corrosion cracking of magnesium alloy in 0.1 M Na_2SO_4 solution. *Mater. Sci. Eng. A* **2008**, *488*, 428–434. [CrossRef]
19. Chen, J.; Wang, J.Q.; Han, E.H.; Ke, W. Electrochemical corrosion and mechanical behaviors of the charged magnesium. *Mater. Sci. Eng. A* **2008**, *494*, 257–262. [CrossRef]
20. Uematsu, Y.; Kakiuchi, T.; Nakajima, M. Stress corrosion cracking behavior of the wrought magnesium alloy AZ31 under controlled cathodic potentials. *Mater. Sci. Eng. A* **2012**, *531*, 171–177. [CrossRef]
21. Sozanska, M.; Moscicki, A. Investigation of the susceptibility of the WE54 Magnesium based alloy to stress corrosion cracking. *J. Mater. Eng. Perform.* **2020**, *29*, 949–963. [CrossRef]
22. Dubey, D.; Kadali, K.; Panda, S.S.; Kumar, A.; Jain, J.; Mondal, K.; Singh, S.S. Comparative study on the stress corrosion cracking susceptibility of AZ80 and AZ31 magnesium alloys. *Mater. Sci. Eng. A* **2020**, *792*, 139793. [CrossRef]
23. Merson, E.; Myagkikh, P.; Poluyanov, V.; Merson, D.; Vinogradov, A. On the role of hydrogen in stress corrosion cracking of magnesium and its alloys: Gas-analysis study. *Mater. Sci. Eng. A* **2019**, *748*, 337–346. [CrossRef]
24. Zhou, L.F.; Liu, Z.Y.; Wu, W.; Li, X.G.; Du, C.W.; Jiang, B. Stress corrosion cracking behavior of ZK60 magnesium alloy under different conditions. *Int. J. Hydrog. Energy* **2017**, *42*, 26162–26174. [CrossRef]
25. Shi, Z.M.; Hofstetter, J.; Cao, F.Y.; Uggowitzer, P.J.; Dargusch, M.S.; Atrens, A. Corrosion and stress corrosion cracking of ultra-high-purity Mg5Zn. *Corros. Sci.* **2015**, *93*, 330–335. [CrossRef]
26. Wang, S.; Xu, D.K.; Wang, D.L.; Zhang, Z.Q.; Wang, B.J. Effect of icosahedral phase formation on the stress corrosion cracking (SCC) behaviors of the as-cast Mg-8%Li (in wt. %) based alloys. *J. Magnes. Alloy.* 2022; *in press*. [CrossRef]
27. Kappes, M.; Iannuzzi, M.; Carranza, R.M. Hydrogen embrittlement of magnesium and magnesium alloys: A review. *J. Electrochem. Soc.* **2013**, *160*, C168–C178. [CrossRef]
28. Lynch, S. Hydrogen embrittlement phenomena and mechanisms. *Corros. Rev.* **2012**, *30*, 105–123. [CrossRef]
29. Zhang, T.; Shao, Y.W.; Meng, G.Z.; Li, Y.; Wang, F.H. Effects of hydrogen on the corrosion of pure magnesium. *Electrochim. Acta* **2006**, *52*, 1323–1328. [CrossRef]
30. Zhang, T.; Li, Y.; Wang, F.H. Roles of β phase in the corrosion process of AZ91D magnesium alloy. *Corros. Sci.* **2006**, *48*, 1249–1264. [CrossRef]
31. Chen, J.; Wang, J.Q.; Han, E.H.; Dong, J.H.; Ke, W. States and transport of hydrogen in the corrosion process of an AZ91 magnesium alloy in aqueous solution. *Corros. Sci.* **2008**, *50*, 1292–1305. [CrossRef]
32. Song, Y.W.; Han, E.-H.; Dong, K.H.; Shan, D.Y.; Yim, C.D.; You, B.S. Effect of hydrogen on the corrosion behavior of the Mg-xZn alloys. *J. Magnes. Alloy.* **2014**, *2*, 208–213. [CrossRef]
33. Wang, S.; Xu, D.K.; Wang, D.L.; Zhang, Z.Q.; Liu, L.; Wang, B.J. Effect of electrochemical hydrogen charging on the microstructure and mechanical behavior of an as-cast Mg-8%Li (in wt. %) alloy. *J. Magnes. Alloy.* 2023; *to be submitted*.
34. Morishige, T.; Doi, H.; Goto, T.; Nakamura, E.; Takenaka, T. Exfoliation Corrosion Behavior of Cold-Rolled Mg-14 mass% Li-1 mass% Al Alloy in NaCl Solution. *Mater. Trans.* **2013**, *54*, 1863–1866. [CrossRef]
35. Li, C.Q.; Deng, B.B.; Dong, L.J.; Shi, B.Q.; Dong, Y.; Peng, F.; Zhang, Z.R. Effect of Zn addition on the corrosion behaviours of as-cast BCC Mg-11Li based alloys in NaCl solution. *Mater. Design* **2022**, *221*, 111019. [CrossRef]
36. Atrens, A.D.; Gentle, I.; Atrens, A. Possible dissolution pathways participating in the Mg corrosion reaction. *Corros. Sci.* **2015**, *92*, 173–181. [CrossRef]
37. Zhao, M.C.; Liu, M.; Song, G.L.; Atrens, A. Influence of pH and chloride ion concentration on the corrosion of Mg alloy ZE41. *Corros. Sci.* **2008**, *50*, 3168–3178. [CrossRef]
38. Chen, J.; Dong, J.H.; Wang, J.Q.; Han, E.H.; Ke, W. Effect of magnesium hydride on the corrosion behavior of an AZ91 magnesium alloy in sodium chloride. *Corros. Sci.* **2008**, *50*, 3610–3614. [CrossRef]
39. Pourbaix, M. Atlas of electrochemical equilibria in aqueous solutions. *J. Electroanal. Chem.* **1967**, *13*, 471. [CrossRef]
40. Thakur, C.; Balasubramaniam, R. Hydrogen embrittlement of aged and retrogressed-reaged Al-Li-Cu-Mg alloys. *Acta Mater.* **1997**, *45*, 1323–1332. [CrossRef]
41. Dinh, L.N.; Grant, D.M.; Schildbach, M.A.; Smith, R.A.; Siekhaus, W.J.; Balazs, B.; Leckey, J.H.; Kirkpatrick, J.R.; McLean II, W. Kinetic measurement and prediction of the hydrogen outgassing from the polycrystalline LiH/Li_2O/LiOH system. *J. Nucl. Mater.* **2005**, *347*, 31–43. [CrossRef]
42. Cho, Y.M.; Lee, J.Y.; Bokare, A.D.; Kwon, S.B.; Park, D.S.; Jung, W.S.; Choi, J.S.; Yang, Y.M.; Lee, J.Y.; Choi, W.Y. LiOH-embedded zeolite for carbon dioxide capture under ambient conditions. *J. Ind. Eng. Chem.* **2015**, *22*, 350–356. [CrossRef]

43. Wu, F.X.; Li, W.X.; Liang, J. Electrochemical deposition and corrosion resistance of $Mg(OH)_2$ films on magnesium alloy. *Chin. J. Mater. Res.* **2014**, *28*, 703–709.
44. Zhang, Z.Y.; Chen, K.H.; Ni, E.F. Effect of magnesium on the electrochemical behavior of lithium anode in LiOH aqueous solution used for lithium-water battery. *Electrochim. Acta* **2010**, *55*, 3830–3837. [CrossRef]
45. Xu, W.Q.; Birbilis, N.; Sha, G.; Wang, Y.; Daniels, J.; Xiao, Y.; Ferry, M. A high-specific-strength and corrosion-resistant magnesium alloy. *Nat. Mater.* **2015**, *14*, 1229–1235. [CrossRef]
46. Zeng, R.C.; Sun, L.; Zheng, Y.F.; Cui, H.Z.; Han, E.H. Corrosion and characterisation of dual phase Mg-Li-Ca alloy in Hank's solution: The influence of microstructural features. *Corros. Sci.* **2014**, *79*, 69–82. [CrossRef]
47. Chen, J.; Ai, M.R.; Wang, J.Q.; Han, E.H.; Ke, W. Formation of hydrogen blister on AZ91 magnesium alloy during cathodic charging. *Corros. Sci.* **2009**, *51*, 1197–1200. [CrossRef]

Disclaimer/Publisher's Note: The statements, opinions and data contained in all publications are solely those of the individual author(s) and contributor(s) and not of MDPI and/or the editor(s). MDPI and/or the editor(s) disclaim responsibility for any injury to people or property resulting from any ideas, methods, instructions or products referred to in the content.

coatings

MDPI

Article

An Investigation into Electrodeposited Co−Ni−TiO_2 Films with Improved Mechanical and Corrosion Properties

Yuxin Wang, Zengcheng Miao, Songlin Zheng, Jiahuan Chen and Zhen He *

School of Materials Science and Engineering, Jiangsu University of Science and Technology, Zhenjiang 212000, China
* Correspondence: hezhen@just.edu.cn

Abstract: This investigation proposes the use of sol-enhanced electrodeposition to create a range of Co−Ni−TiO_2 films. The addition of TiO_2 sol controls the nucleation process and the properties of the composite films by generating TiO_2 nanoparticles in situ in the electrodeposition process. The transmission electron microscopy (TEM) and zeta potential analyses revealed a relatively homogenous distribution with particle size in the range below 100 nm for the TiO_2 nanoparticles produced. Microstructure, phase composition, hardness, friction, and corrosion resistance of Co−Ni−TiO_2 films were thoroughly investigated in relation to TiO_2 sol concentration. The results show that the addition of a limited content of TiO_2 sol upgraded Co−Ni films by producing a Co−Ni−TiO_2 film with a high dispersion of TiO_2 nanoparticles. On the other hand, too much TiO_2 sol could cause agglomeration and hinder the metal deposition process, resulting in surface pores and the deterioration of film performance.

Keywords: Co−Ni; electrodeposition; nanoparticles

1. Introduction

Due to their excellent mechanics, wear, corrosion, and other advantages, Co−Ni alloys are frequently used in protective coatings in various industries [1–4]. The main preparation techniques for cobalt-nickel coatings include electrodeposition, physical vapor deposition, chemical vapor deposition, and plasma spraying [5–8]. Electroplating technology has been regarded as a simple and efficient technique for preparing Co−Ni films [9,10]. The performance of a Co−Ni film cannot further satisfy the demands in some challenging service conditions, and it is of great scientific significance to further strengthen the Co−Ni film. Current methods for improving the performance of Co−Ni alloys include heat treatment, the pulse electrodeposition process, and composite electrodeposition technology [11–13]. Composite electrodeposition technology, one of the industry's most widely employed reinforcement methods, can significantly enhance the Co−Ni alloy's comprehensive properties [14,15].

Nanoparticles such as SiC [16], ZrO_2 [17], TN [18], WC [19], TiO_2 [20–22], and Al_2O_3 [23] have recently been utilized as the second reinforcing phase for composite electrodeposition. In traditional composite electrodeposition techniques, nanometer-sized inert particles are added to the electrolytes to create films. For instance, recent research by Rasooli et al. explored the influence of Cr_2O_3 nanoparticles on the Ni−Co−Cr_2O_3 coatings' microstructure, mechanical properties, and corrosion-related properties, and found the incorporation of Cr_2O_3 nanoparticles could increase the nucleation amount of Co and improve the coating's performance [24]. In another report, by examining the SiC-doped Ni−Co coating, Bakhit et al. stated that embedding SiC nanoparticles improved the Ni−Co film's compactness and corrosion resistance [25].

However, nanoparticles with a high specific surface region and surface energy can easily result in agglomeration in a bath and greatly impair the performance of the resultant composite coating. To overcome this issue, our research group developed TiO_2

sol-enhanced electrodeposition to reach nanoparticles' excellent dispersion and chemical stability in electrolytes. The TiO_2-incorporated composite coatings show improvements in mechanical and corrosion performance. When adding the TiO_2 sol to the plating bath, TiO_2 nanoparticles could be generated and directly co-deposited on the substrate's surface with metal ions, effectively preventing nanoparticle agglomeration. The excellent dispersion of nanoparticles gives rise to a uniform, compact surface structure and an excellent coating performance.

Diverse Co−Ni−TiO_2 films with superior performance were electrodeposited using TiO_2 sol at various contents. Microstructure, phase composition, mechanical properties, and corrosion performance of Co−Ni−TiO_2 films have been examined at diverse contents of TiO_2 sols. The Co−Ni film's mechanical properties and corrosion resistance can be greatly improved if TiO_2 sol is present in a suitable amount, enhancing its utility in industrial use.

2. Experimental

2.1. TiO_2 Sol Preparation

All reagents were purchased from Beijing Chemical Ltd. (Beijing, China) and used at analytical grade without further purification. The method of preparing TiO_2 sol comprises the following three steps: (1) preparation of solution A: adding 5.64 mL of $C_4H_{11}NO_2$ (diethanolamine) to 70 mL of C_2H_5OH (ethanol) with adequate stirring, followed by slowly dripping 19.74 mL of $C_{16}H_{36}O_4Ti$ (tetrabutyl titanate) into the as-prepared solution under a stirring speed of 300 rpm; (2) preparation of solution B: mix 9 mL of C_2H_5OH and 0.9 mL of distilled water; and (3) solution B was added dropwise into solution A, after which the bath was stirred 500 rpm for 30 min to produce TiO_2 sol.

This study mixed 10 mL of TiO_2 sol with 100 mL of di-ionized (DI) water under ultrasonic agitating, with the purpose of producing and determining the in situ created TiO_2 nanoparticles. After the solution was dropped on a copper mesh and dried, the fresh nanoparticle could be observed.

2.2. Electrodeposition of Co−Ni−TiO_2 Films

This experiment produced Co−Ni−TiO_2 films in the electrodeposition process and used the brass sheet as a cathode and the high-purity cobalt board as an anode. To generate TiO_2 nanoparticles in situ, TiO_2 sol was slowly added to the Co−Ni electrolyte at magnetic stirring prior to electrodeposition. It should be noted that the attached organic chains in the freshly formed nanoparticles further avoid possible agglomerations.

The electrolytes used in the experiment consisted of 70 g/L $NiSO_4$ (nickel sulfate), 50 g/L NiCl (nickel chloride), 60 g/L $CoSO_4$ (cobalt sulfate), 50 g/L H_3BO_3 (boric acid), 0.015 g/L $C_{12}H_{25}SO_4Na$ (sodium dodecyl sulfate), and 0.15 g/L $C_7H_5NO_3S$ (saccharin). The electrodepositing temperature was 50 °C and the stirring rate was 300 rpm. Composite electrodeposition was performed at the current density of 25 mA/cm^2 for 40 min with various concentrations of TiO_2 sol.

2.3. Sample Characterization

This work used a transmitting electron microscope to characterize the newly generated nanoparticles (HRTEM, FEI Talos F200X G2, Thermo Fisher Scientific, Santa Clara, CA, USA). The samples' surface morphology, cross-sectional morphology, and wear track morphology were observed using a Gemini SEM 300 electron microscope with an embedded EDS detector manufactured by Zeiss Company, Jena, Germany. A 90-plus zeta potential analyzer (Malvern Zetasizer Nano ZS, Malvern, UK) was employed to investigate the zeta potential of a composite plating solution in order to determine the dispersibility and stability of TiO_2 nanoparticles. The phase constituents of the Co−Ni−TiO_2 films were analyzed by Cu−Kα radiation (XRD, Bruker, Saarbrucken, Germany).

The Co−Ni−TiO_2 film's hardness was determined by a Vickers microhardness analyzer using 50 g for 15 s. The wear performance of the Co-Ni-TiO_2 films was determined

using a micro-tribometer (UMT−2, CETR, New York, NY, USA). In the wear tests, steel balls 4 mm in diameter and a load of 5 N were used under a wear speed of 10 mm/s.

With the aid of an electrochemical workstation (CS2350, Corrtest, Wuhan, China), the Co−Ni−TiO_2 films' electrochemical performance was evaluated. The platinum plate with dimensions of 10 mm × 10 mm × 0.3 mm served as the counter electrode, while a saturated KCl electrode served as the reference electrode. When the open circuit potential had been stabilized, the samples were tested at room temperature at a scanning speed of 1 mV/s using 3.5 wt.% NaCl solution.

3. Results and Discussion

3.1. Characterization of TiO_2 Sol

Figure 1 presents the TEM images recorded on the generated TiO_2 nanoparticles made by adding sol into DI water. Figure 1a shows that the TiO_2 nanoparticles are agglomerated in the drying process, but some individual nanoparticles can still be identified. The TiO_2 nanoparticles agglomerate into various-sized spheres under the TEM observations shown in Figure 1b. Some TiO_2 nanoparticle agglomerates can be found, and the separated TiO_2 nanoparticles show a particle diameter of no more than 100 nm.

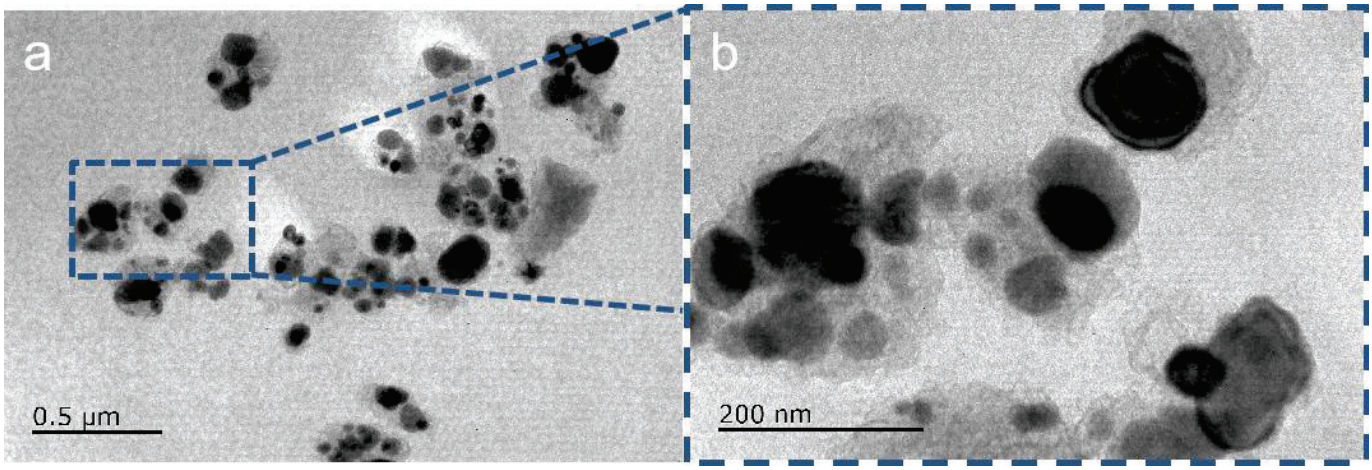


Figure 1. TEM images were taken on the generated TiO_2 nanoparticles made by adding sol into DI water. (**a**) TEM image, (**b**) Enlarged image for nanoparticles.

To confirm the existence of the produced nanoparticles, the individual TiO_2 nanoparticle was observed and analyzed. The particle size that was observed is approximately 80 nm, as illustrated in Figure 2a, with an interplanar space of 0.354 nm. Moreover, the electron diffraction pattern reveals the presence of anatase-type nanoparticles, as depicted in Figure 2b,c.

The particle size distribution of TiO_2 nanoparticles generated in DI water is further determined in Figure 3. The recorded size distribution map indicates that the average size of TiO_2 nanoparticles ranges from ~20 to ~100 nm in distilled water. This is consistent with the findings from the above TEM microscopic morphology observation. We note that the zeta potential measured a slightly smaller size distribution than the TEM images, which may be the result of aggregation occurring in the drying process prior to the TEM observation.

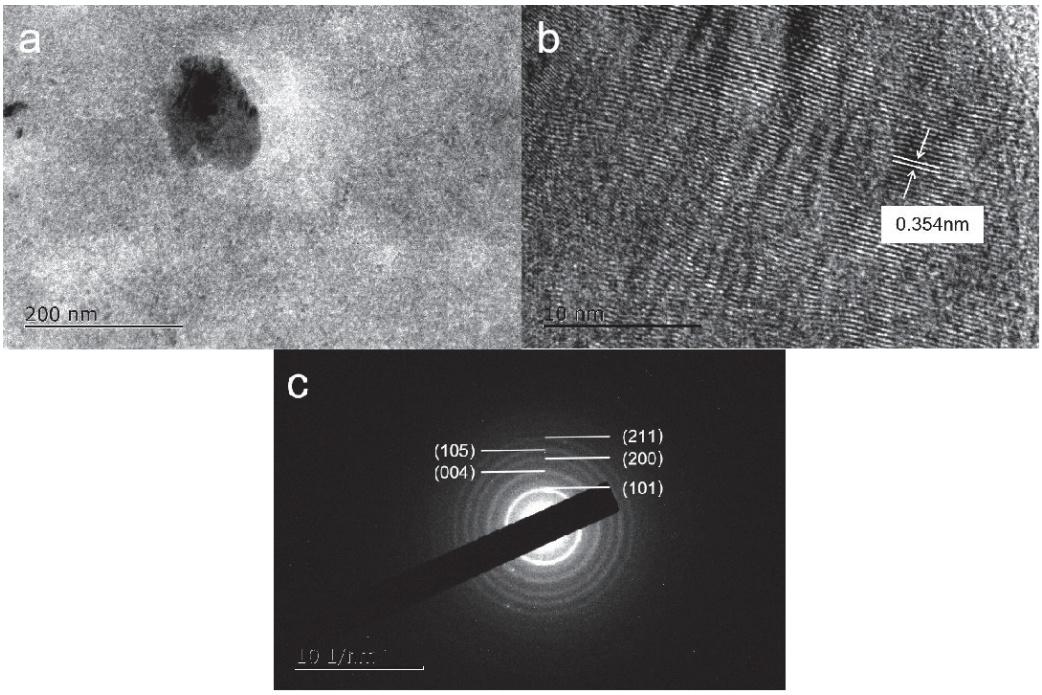


Figure 2. The microstructure of a single TiO_2 nanoparticle. (**a**) TEM image, (**b**) HR−TEM micrograph, (**c**) electron diffraction pattern.

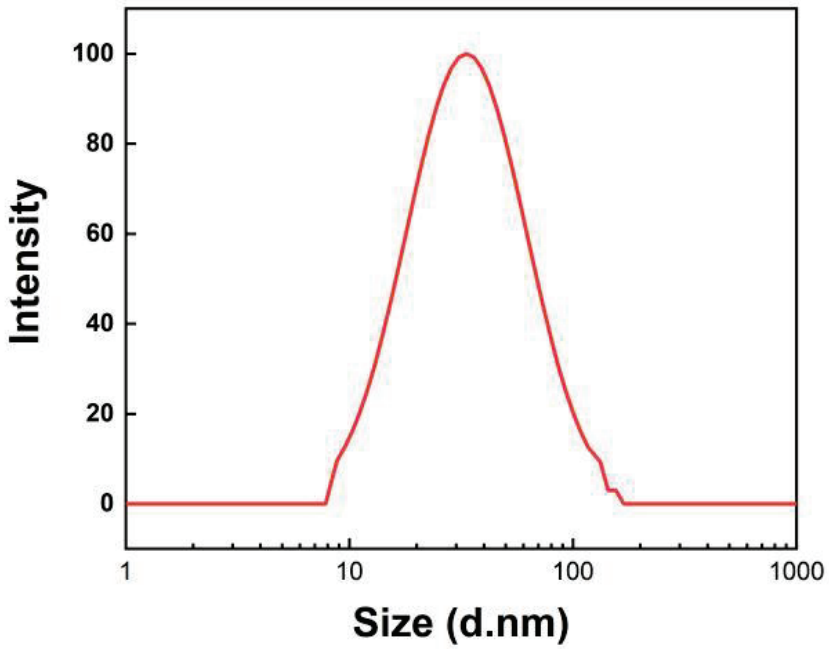


Figure 3. Size distribution of TiO_2 nanoparticles generated by adding sol into DI water.

3.2. Structural Characterizations of Co−Ni−TiO_2 Films

Figure 4 depicts the microscopic surface morphologies of Co−Ni−TiO_2 films produced by varied TiO_2 concentrations. The surface of the Co−Ni−TiO_2 films is refined and has the most significant surface uniformity and coverage at 12.5 mL/L TiO_2 sol. However, Co−Ni−50 mL/L TiO_2 film's grains are coarsened. In general, highly dispersed TiO_2 nanoparticles provide more nucleation sites, promoting nucleation processes and refining surface crystals. However, the excessive TiO_2 nanoparticles can result in agglomeration and coating coarsening under 50 mL/L TiO_2 sol.

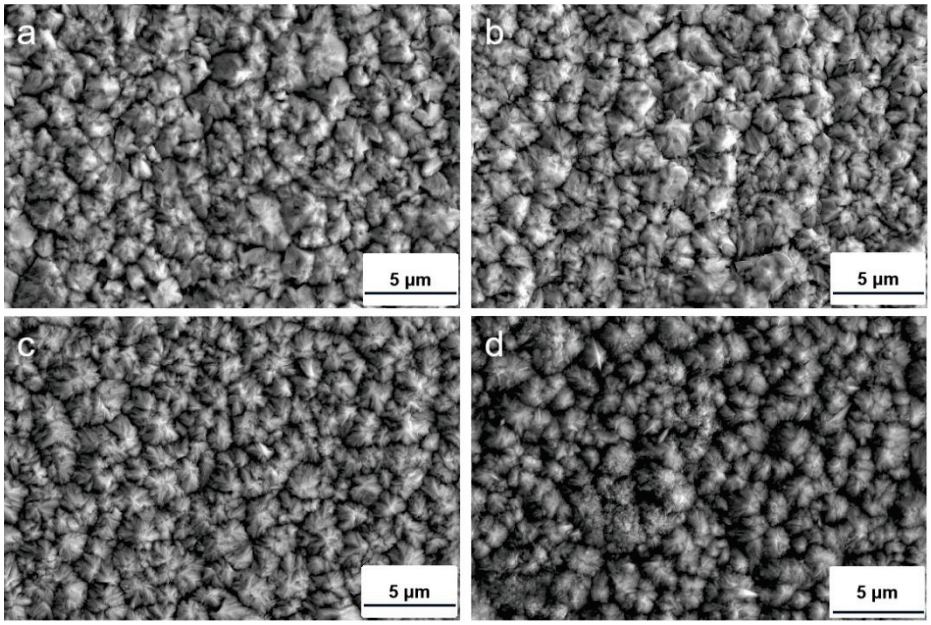


Figure 4. Surface morphology of Co−Ni−TiO_2 films prepared with different content of TiO_2 sol: (**a**) 0 mL/L; (**b**) 5 mL/L; (**c**) 12.5 mL/L; (**d**) 50 mL/L.

X-ray diffractograms of Co−Ni−TiO_2 films with diverse TiO_2 sol content are shown in Figure 5. The (220) diffraction peak is distinct in the Co−Ni−TiO_2 diffractograms. In addition, the location of the textured peak is a bit different from the standard peak due to the insertion of Ni atoms into the Co atom's structure, which is consistent with some previous papers [4,9,26]. Because there is very little content of TiO_2 nanoparticles incorporated in the Co−Ni film, no TiO_2 diffraction peak was observed in the profiles.

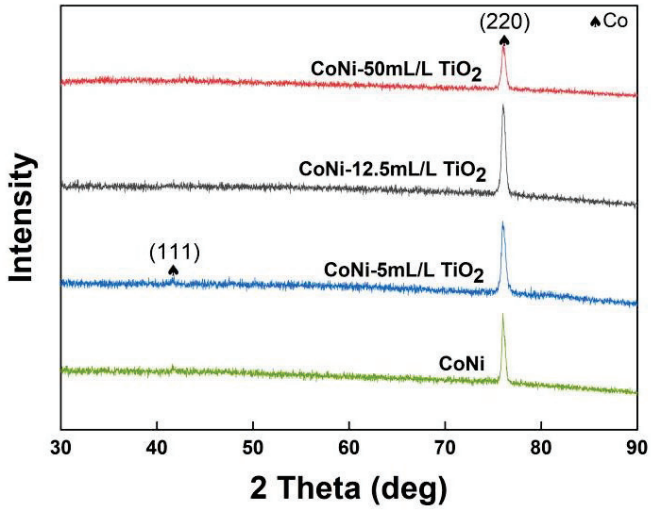


Figure 5. X-ray diffractograms recorded on the prepared Co−Ni−TiO_2 films.

Figure 6 shows the cross-sectional morphology of the composite films prepared. The coated composite film tightly adheres to the substrate with no defects, such as peeling and holes, indicating a good coating quality for all samples. In addition, no TiO_2 agglomeration regions are identified on the cross-sectional morphologies. However, the film thickness decreases at 50 mL/L sol addition. When excessive TiO_2 sol was added to the electrolyte, the electrodeposition process could be hindered and more charged current would be consumed in the side reaction of hydrogen evolution, thereby decreasing the film thickness.

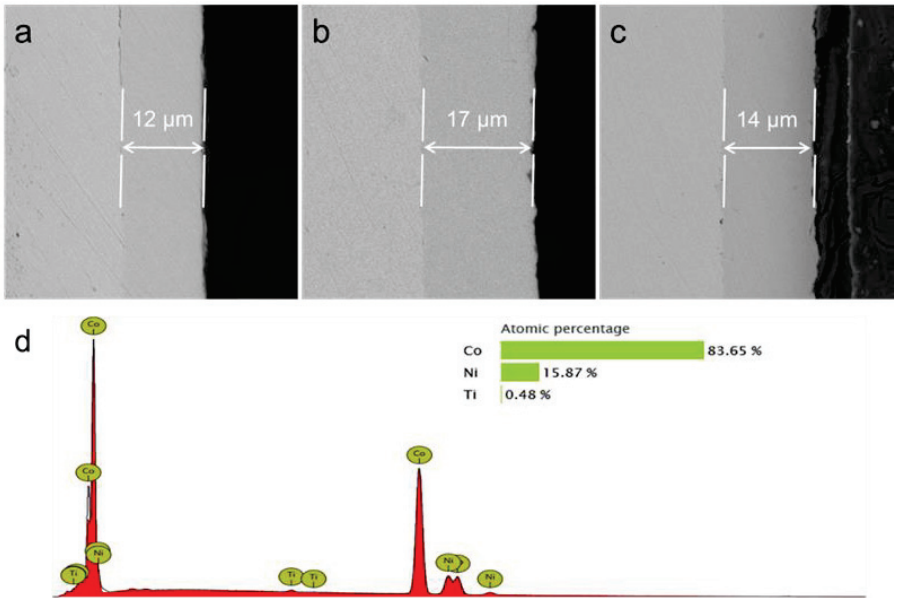


Figure 6. Cross-section of Co−Ni−TiO_2 films prepared with different content of TiO_2 sol: (**a**) 0 mL/L; (**b**) 12.5 mL/L; (**c**) 50 mL/L, and (**d**) the EDS results of the Co−Ni−12.5 mL/L TiO_2 sample.

The elemental composition obtained by EDS detection of the Co−Ni−12.5 mL/L TiO_2 sample is depicted in Figure 6d. The Co element, which has an atomic ratio of 83.78%, and the Ni element, which has an atomic ratio of 15.87%, are the main components in the prepared film according to the EDS results. There is a limited amount of Ti in the film, resulting from the incorporated TiO_2.

3.3. Mechanical Properties of Co−Ni−TiO_2 Films

The microhardness of Co−Ni−TiO_2 films at diverse TiO_2 sol content has been shown in Figure 7. The microhardness of the Co−Ni film is ~228 HV. Co−Ni-12.5 mL/L TiO_2 film possesses the highest microhardness of 323 HV, which is 41% higher than the Co−Ni film's hardness. However, adding 50 mL/L TiO_2 sol reduces the microhardness of the film to approximately 190 HV. Under an appropriate content of TiO_2 incorporation, the highly dispersed TiO_2 nanoparticles are spread in the grain boundary region, which hinders grain development and enhances fine-grain strengthening. Additionally, the highly dispersed TiO_2 nanoparticles perform the second-phase reinforcing effect that further promotes film hardness. In contrast, under an extremely high TiO_2 sol concentration, the excessive TiO_2 nanoparticle clusters cause agglomerations and reduce the films' mechanical properties.

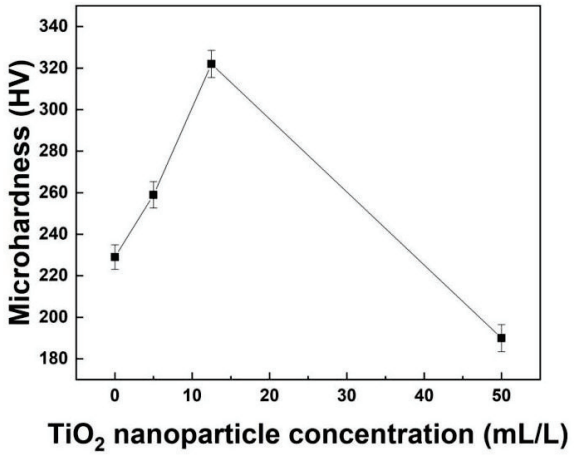


Figure 7. Microhardness tested on Co−Ni−TiO_2 films with diverse TiO_2 sol content.

Figure 8 illustrates the average friction coefficient of the Co−Ni−TiO_2 films. A Co−Ni film with no TiO_2 sol has a coefficient of 0.68, whereas a Co−Ni−12.5 mL/L TiO_2 film shows a friction coefficient of 0.42. In contrast, when the content of TiO_2 sol is 50 mL/L, the coefficient of friction increases to 0.78. The film's friction resistance will be increased using the proper TiO_2 sol (12.5 mL/L) content of the electrodeposition solution.

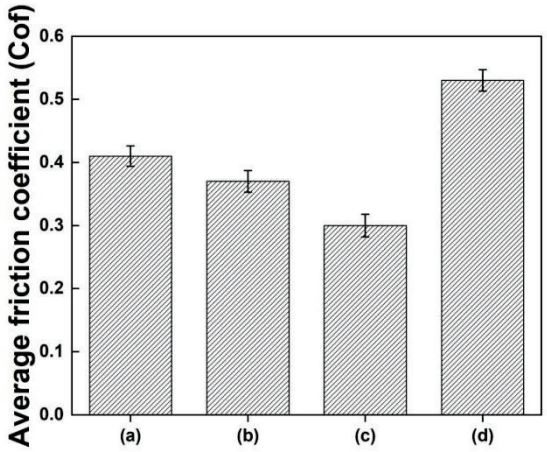


Figure 8. The friction coefficient of Co−Ni−TiO_2 films prepared with diverse content of TiO_2 sol: (**a**) 0 mL/L; (**b**) 5 mL/L; (**c**) 12.5 mL/L; (**d**) 50 mL/L.

Figure 9 illustrates the after-wear sample morphologies of Co−Ni films, Co−Ni−5 mL/L TiO_2, Co−Ni−12.5 mL/L TiO_2, and Co−Ni−50 mL/L TiO_2 films, respectively. Under the rising concentration of TiO_2 sol, the film's wear track width reduces first and then rises. A suitable content of TiO_2 sol added to the electrolytes decreases the wear track width of Co−Ni−12.5 mL/L TiO_2 to 281 mL, while the wear track width of Co−Ni−50 mL/L TiO_2 increases to about 417 μm under a higher sol concentration. The same trend is proposed: the wear resistance improves at a proper TiO_2 concentration, whereas it reduces by adding excessive TiO_2 sol.

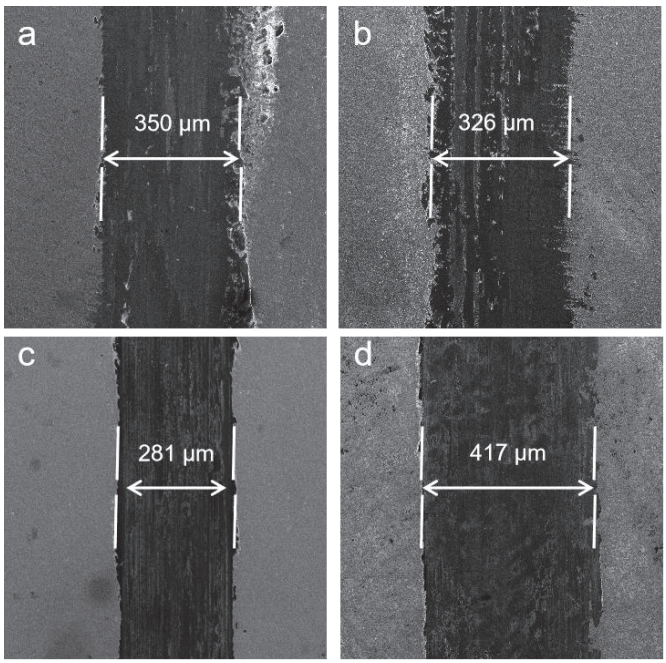


Figure 9. Wear track of Co−Ni−TiO_2 films prepared with different concentrations of TiO_2 sol: (**a**) 0 mL/L; (**b**) 5 mL/L; (**c**) 12.5 mL/L; (**d**) 50 mL/L.

3.4. Corrosion Resistance of Co−Ni−TiO_2 Films

The corrosion performance of the produced Co−Ni−TiO_2 films was investigated by measuring potentiodynamic polarization, as depicted in Figure 10. The greater the corrosion potential (E_{corr}) value of the material and the smaller the corrosion current density, the better the corrosion resistance of the film material. When the concentration of the TiO_2 sol rises, the corrosion potential of the film gradually increases. Under a 12.5 mL/L TiO_2 sol addition, the corrosion potential is the largest, showing that the film has the most excellent corrosion resistance. It is evident that the film has a worsened corrosion resistance when TiO_2 sol content reaches 50 mL/L.

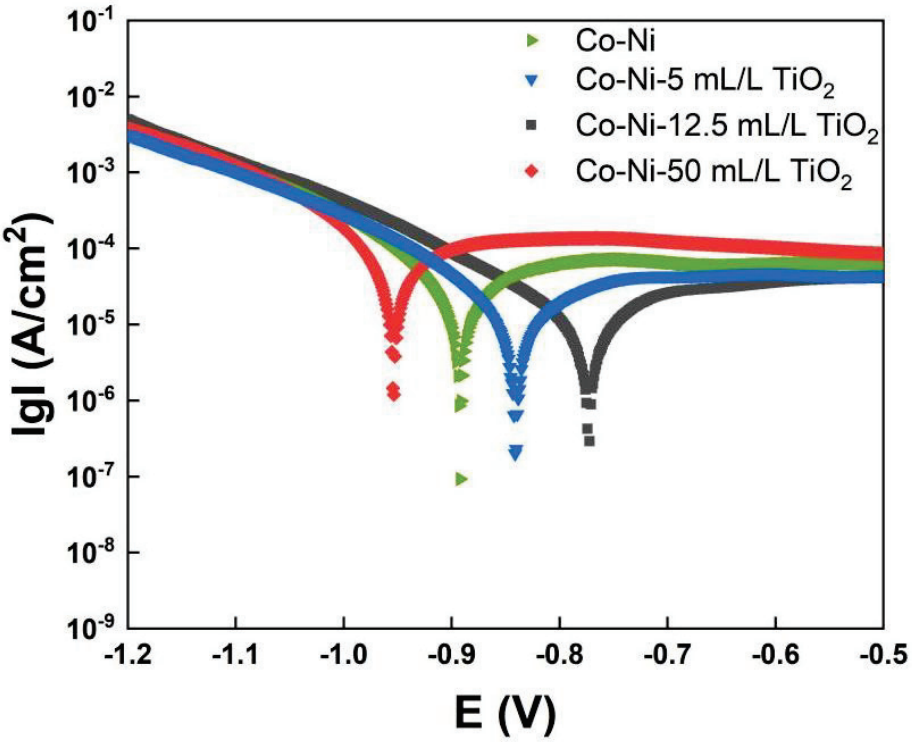


Figure 10. Potentiodynamic polarization curves of different Co−Ni−TiO_2 films.

Table 1 below shows the electrochemical parameters by fitting the polarization curves. The corrosion speed of the Co−Ni film is 0.074 mm/a, and the corrosion speed of the Co−Ni−12.5 mL/L TiO_2 film is only 0.036 mm/a. According to the findings, the corrosion resistance of the Co−Ni film is improved when the film has 12.5 mL/L TiO_2 sol. The corrosion rate for the Co−Ni−50 mL/L TiO_2 film is 0.171 mm/a, indicating that the film's corrosion resistance significantly decreases. Adding appropriate content of TiO_2 sol can form a denser film surface with refined crystals, as suggested above, which explains the enhanced corrosion performance. Nevertheless, an excessive concentration of TiO_2 sol will cause TiO_2 nanoparticles to agglomerate in the coating, impairing the coating's uniformity and decreasing the corrosion resistance.

Table 1. Potential polarization data of Co−Ni−TiO_2 films.

Sample	E_{corr} (V)	I_{corr} (μA/cm^2)	Corrosion Rate (mm/a)
Co−Ni	−0.88	6.28	0.074
Co−Ni−5 mL/L TiO_2	−0.84	3.69	0.054
Co−Ni−12.5 mL/L TiO_2	−0.76	3.09	0.036
Co−Ni−50 mL/L TiO_2	−0.99	14.6	0.171

4. Conclusions

This study utilized chemical synthesis to create TiO_2 sols with high dispersion and chemical stability. Mechanical and corrosion-resistant Co−Ni−TiO_2 films were prepared by adding a suitable amount of TiO_2 sol (12.5 mL/L) to the electrolytes during electrodeposition. The addition of TiO_2 sol controls the nucleation process and the properties of the composite films by generating TiO_2 nanoparticles in situ in the electrodeposition process. By producing TiO_2 nanoparticles in situ in electrolytes with sizes below 100 nm, nanoparticle agglomeration is largely avoided. The mechanical property testing results reveal that the Co−Ni−12.5 mL/L TiO_2 film has the highest hardness of 323 HV, an increase of 41% over the undoped samples. Electrochemical tests demonstrate a 51% reduction in the corrosion rate for the Co−Ni−12.5 mL/L TiO_2 film compared to the undoped Co−Ni film sample. Increased nucleation sites can result from the appropriate amount of TiO_2 sol, enhancing coating quality through fine-grain and dispersion-strengthening effects. Nevertheless, coarse grains and pores will result from the agglomeration of excessive TiO_2 nanoparticles under high TiO_2 sol concentration, which will have a detrimental impact on the film's performance.

Author Contributions: Conceptualization, Y.W. and Z.H.; methodology, Z.M. and J.C.; validation, Z.H. and Z.M.; formal analysis, Z.H.; investigation, Z.M.; writing—original draft preparation, Y.W.; writing—review and editing, Z.H.; visualization, S.Z.; supervision, J.C. and Z.H.; funding acquisition, Z.H. All authors have read and agreed to the published version of the manuscript.

Funding: This work was supported by the Natural Science Foundation of Jiangsu Province by grant BK20201008.

Institutional Review Board Statement: Not applicable.

Informed Consent Statement: Not applicable.

Data Availability Statement: Not applicable.

Conflicts of Interest: The authors declare no conflict of interest.

References

1. Bouzit, F.Z.; Nemamcha, A.; Moumeni, H.; Rehspringer, J.L. Morphology and Rietveld analysis of nanostructured Co-Ni electrodeposited thin films obtained at different current densities. *Surf. Coat. Technol.* **2017**, *315*, 172–180. [CrossRef]
2. Olvera, S.; Arce Estrada, E.M.; Sanchez-Marcos, J.; Palomares, F.J.; Vazquez, L.; Herrasti, P. Effect of the low magnetic field on the electrodeposition of Co_xNi_{100-x} alloys. *Mater. Charact.* **2015**, *105*, 136–143. [CrossRef]
3. Li, D.; Levesque, A.; Franczak, A.; Wang, Q.; He, J.; Chopart, J.P. Evolution of morphology in electrodeposited nanocrystalline Co-Ni films by in-situ high magnetic field application. *Talanta* **2013**, *110*, 66–70. [CrossRef] [PubMed]
4. Karpuz, A.; Kockar, H.; Alper, M. Electrodeposited Co–Ni Films: Electrolyte pH—Property Relationships. *J. Supercond. Nov. Magn.* **2012**, *26*, 651–655. [CrossRef]
5. Yu, M.M.; Li, H.Y.; Wang, Y. Study on Present Situation and New Trends of the Electrodeposition of Nickel-Cobalt Alloy. *Adv. Mater. Res.* **2012**, *535–537*, 973–976. [CrossRef]
6. Sun, L.F.; Mao, J.M.; Pan, Z.W.; Chang, B.H.; Zhou, W.Y.; Wang, G.; Qian, L.X.; Xie, S.S. Growth of straight nanotubes with a cobalt–nickel catalyst by chemical vapor deposition. *Appl. Phys. Lett.* **1999**, *74*, 644–646. [CrossRef]
7. Li, Y.; Xie, Y.; Huang, L.; Liu, X.; Zheng, X. Effect of physical vapor deposited Al_2O_3 film on TGO growth in YSZ/CoNiCrAlY coatings. *Ceram. Int.* **2012**, *38*, 5113–5121. [CrossRef]
8. Cuglietta, M.; Kuhn, J.; Kesler, O. A Novel Hybrid Axial-Radial Atmospheric Plasma Spraying Technique for the Fabrication of Solid Oxide Fuel Cell Anodes Containing Cu, Co, Ni, and Samaria-Doped Ceria. *J. Therm. Spray Technol.* **2013**, *22*, 609–621. [CrossRef]
9. Liu, C.; Su, F.; Liang, J. Nanocrystalline Co-Ni alloy coating produced with supercritical carbon dioxide assisted electrodeposition with excellent wear and corrosion resistance. *Surf. Coat. Technol.* **2016**, *292*, 37–43. [CrossRef]
10. Hu, H.; Tan, M.; Liu, L. Anomalous codeposition mechanism of Co-Ni alloy nanowires. *J. Alloys Compd.* **2017**, *715*, 384–389. [CrossRef]
11. Barzegar, M.; Allahkaram, S.R.; Naderi, R.; Ghavidel, N. Effect of phosphorous content and heat treatment on the structure, hardness and wear behavior of Co-P coatings. *Wear* **2019**, *422–423*, 35–43. [CrossRef]
12. Tebbakh, S.; Messaoudi, Y.; Azizi, A.; Fenineche, N.; Schmerber, G.; Dinia, A. The influence of saccharin on the electrodeposition and properties of Co–Ni alloy thin films. *Trans. IMF* **2015**, *93*, 196–204. [CrossRef]

13. Altamirano-Garcia, L.; Vazquez-Arenas, J.; Pritzker, M.; Luna-Sánchez, R.; Cabrera-Sierra, R. Effects of saccharin and anions (SO_4^{2-}, Cl^-) on the electrodeposition of Co–Ni alloys. *J. Solid State Electrochem.* **2014**, *19*, 423–433. [CrossRef]
14. Vazquez-Arenas, J.; Treeratanaphitak, T.; Pritzker, M. Formation of Co–Ni alloy coatings under direct current, pulse current and pulse-reverse plating conditions. *Electrochim. Acta* **2012**, *62*, 63–72. [CrossRef]
15. Wang, S. Influence of 2-butyne-1, 4-diol on the structure and performance of the Co-Ni alloy plated by electrodeposition. *Acta Metall. Sin.* **2008**, *21*, 50–56. [CrossRef]
16. Bu, A.; Zhang, Y.; Zhang, Y.; Chen, W.; Cheng, H.; Wang, L.; Wang, Y. A Novel Electrolytic Plasma Spraying Preparation SiO_2/SiC Coating on Carbon Fiber Fabric. *Coatings* **2018**, *8*, 344. [CrossRef]
17. Xiong, C.; Xiao, J.; Zhao, Y.; Wang, Y.; Tay, S.L.; Xu, W. Properties of Ni–ZrO_2 nanocomposite coatings by electroplating. *Int. J. Mod. Phys. B* **2019**, *33*, 1940024. [CrossRef]
18. Zhang, W.; Du, S.; Li, B.; Mei, T.; Miao, Y.; Chu, H.; Wang, J. Synthesis and characterization of TiN nanoparticle reinforced binary Ni-Co alloy coatings. *J. Alloys Compd.* **2021**, *865*, 158722. [CrossRef]
19. Elkhoshkhany, N.; Hafnway, A.; Khaled, A. Electrodeposition and corrosion behavior of nano-structured Ni-WC and Ni-Co-WC composite coating. *J. Alloys Compd.* **2017**, *695*, 1505–1514. [CrossRef]
20. Wang, Y.; Hu, B.; Tay, S.L.; Hou, F.; Gao, W.; Xiong, C. The microstructure and properties of sol-enhanced Sn–TiO_2 nanocomposite coatings. *Int. J. Mod. Phys. B* **2017**, *31*, 1744025. [CrossRef]
21. He, Z.; Cao, D.; Wang, Y.; Yin, L.; Hayat, M.D.; Singh, H. Preparation of Co–P–TiO_2 nanocomposite coatings via a pulsed electrodeposition process. *Surf. Eng.* **2019**, *36*, 975–981. [CrossRef]
22. Zhang, W.; Cao, D.; Qiao, Y.; He, Z.; Wang, Y.; Li, X.; Gao, W. Microstructure and Properties of Duplex Ni-P-TiO_2/Ni-P Nanocomposite Coatings. *Mater. Res.* **2019**, *22* (Suppl. 2), e20180478. [CrossRef]
23. Liu, Y.; Li, L.; Lu, G.-L.; Han, Z.-W.; Liu, J.-D.; Yu, S.-R. Fractal characteristics and wettability of Nano-Al_2O_3/Ni-Co composite coating prepared by electrodeposition. *Trans. Nonferrous Met. Soc. China* **2011**, *21*, s380–s383. [CrossRef]
24. Rasooli, A.; Safavi, M.S.; Kasbkar Hokmabad, M. Cr_2O_3 nanoparticles: A promising candidate to improve the mechanical properties and corrosion resistance of Ni-Co alloy coatings. *Ceram. Int.* **2018**, *44*, 6466–6473. [CrossRef]
25. Bakhit, B.; Akbari, A.; Nasirpouri, F.; Hosseini, M.G. Corrosion resistance of Ni–Co alloy and Ni–Co/SiC nanocomposite coatings electrodeposited by sediment codeposition technique. *Appl. Surf. Sci.* **2014**, *307*, 351–359. [CrossRef]
26. Gómez, E.; Pané, S.; Alcobe, X.; Vallés, E. Influence of a cationic surfactant in the properties of cobalt–nickel electrodeposits. *Electrochim. Acta* **2006**, *51*, 5703–5709. [CrossRef]

Disclaimer/Publisher's Note: The statements, opinions and data contained in all publications are solely those of the individual author(s) and contributor(s) and not of MDPI and/or the editor(s). MDPI and/or the editor(s) disclaim responsibility for any injury to people or property resulting from any ideas, methods, instructions or products referred to in the content.

metals

MDPI

Article

Acoustic Source Localization in Metal Plates Using BP Neural Network

Yingqi Huang [1], Can Tang [2,*], Wenfeng Hao [3] and Guoqi Zhao [1,*]

[1] Faculty of Civil Engineering and Mechanics, Jiangsu University, Zhenjiang 212013, China; yqhuang2022vip@126.com
[2] College of Civil Science and Engineering, Yangzhou University, Yangzhou 225127, China
[3] College of Mechanical Engineering, Yangzhou University, Yangzhou 225127, China; hwf@yzu.edu
* Correspondence: tangcanvip@126.com (C.T.); flagzhao@163.com (G.Z.)

Abstract: This study introduces a methodology for detecting the location of signal sources within a metal plate using machine learning. In particular, the Back Propagation (BP) neural network is used. This uses the time of arrival of the first wave packets in the signal captured by the sensor to locate their source. Specifically, we divide the aluminum plate into several areas, design eight receiving points for receiving the excitation signal, and determine the location of each sound source. In order to train and test the machine learning network, the aluminum plate model was established using the COMSOL numerical simulation platform and the propagation of five peak waves was simulated. Correspondingly, experimental verification was carried out and a scanning laser Doppler vibrometer (SLDV) was used to build an experimental platform to collect the corresponding wave field information to obtain a data set for machine learning. The results show that the trained BP neural network can classify the sound source region in both environments.

Keywords: acoustic source localization; BP neural network; metal plates; wavefield; time of arrival

1. Introduction

Plate-like structures are widely utilized in large-scale high-end equipment, such as aircraft fuselage and wings, high-speed rail wagons, and liquid fuel storage tanks. Such structures are directly exposed to the external environment and bear loads and vibrations for a long time, which reduce their structural resistance. In extreme cases, sudden disasters occur. Many studies on Structural Health Monitoring (SHM) of sheet metal structures exist in the literature [1–5]. Several industrial fields use Non-Destructive Testing (NDT) based on ultrasonic guided waves in these studies [6–10].

Lamb waves are caused by sound sources within plate-like structures. Damage detection based on Lamb wave is usually based on physical model, through the analysis and processing of the signal obtained by the sensor, and then uses various methods to identify the damage. Therefore, signal processing of guided waves is critical for establishing structural health monitoring. Tobias [11] proposed a general method for computing two dimensional defect locations from the time of arrival at the sensor for isotropic metal sheets. Based on the guided wave theory to study the propagation characteristics of acoustic signals, He et al. [12] tried to introduce a near-field acoustic emission beamforming method to estimate the position of the sound source by using a small sensor array close to the local area. Focusing on the localization of excitation sources, Kundu et al. [13] exploited an optimization-based methodology for source localization for boards with known material information and applied it to carbon/epoxy composite laminates [14,15]. Nucera et al. [16] identified the impact source on an anisotropic composite plate. Dubuc et al. [17] proposed an inversion algorithm to build the relationship between focal depth and amplitude ratio to characterize crack propagation in plates. Nakatani et al. [18] used a sensor cluster-based beamforming technique to calculate the time difference to locate sound sources in

anisotropic panels. Ciampa and Meo [19] combined continuous wavelet transform and local Newton iteration method to realize real-time monitoring of shock source location and wave velocity. The damage identification algorithm based on the physical model theory often needs to use an analytical calculation to invert and estimate the whole process of the guided wavefield propagating in the structure. For the complex boundary conditions of high-end equipment, its damage identification and evaluation effects are limited. Various signal analysis methods can interpret the damage information in the signal from different angles. However, the complexity of the guided wave propagation in the structure and its multi-modal and dispersion characteristics make fast and accurate signal analysis difficult.

Sun et al. [20] proposed a near-field source location algorithm based on a uniform linear array and verified the performance of the proposed method using numerical simulation. Tian et al. [21] used numerical simulations to verify a mixed source localization method using MUSIC and sparse signal reconstruction. Ernst et al. [22] used the finite element method to locate the wave source by back-propagating the waveform captured by the laser Doppler vibrometer. Through a series of numerical simulations, Sikdar et al. [23] proposed an impact source localization strategy based on time difference of arrival calculations to locate the impact regions in composite sandwich structures. Introducing a numerical calculation model can deal with complex boundary problems to a certain extent. Still, it is not easy to achieve an accurate evaluation due to the extensive computing resources and time required for numerical calculation.

The rapid increase in computing power in recent years has brought an abundance of available data, opening up more possibilities for data-driven approaches. To make up for the deficiencies of the above-mentioned damage detection methodologies and meet the intelligent requirements of damage detection, it is necessary to consider combining the physical model with the data model, and establish a novel methodology to process the collected signals to improve detection performance.

A novel method for multi-class classification and uncertainty quantification of impact events on composite panels using Bayesian neural networks (BNN) was proposed by Yu et al. [24]. In their study, diagnostic uncertainty due to variations in impact position, angle, and energy under actual operating conditions was considered. Karmakov et al. [25] used Transformer neural network architecture to improve the speed and robustness of impact detection on composite panels, and compared the detection effect with commonly used convolutional neural networks. Seno et al. proposed a series of data-driven methods for structural health detection in composite structures. They used a new data-driven stochastic Kriging-based method for impact localization and maximum force estimation [26], gaining more information by quantifying the uncertainty of reliably localizing impact locations and estimating severity. They also proposed a new gradient method to evaluate the impact force of composite structures under simulated environmental and operating conditions [27]. For the time-of-arrival extraction problem, they developed a novel artificial neural network (ANN)-based feature extraction method for impact localization in sensing composite structures affected by environmental and operational conditions [28]. The research of the above scholars focuses on reducing the impact of environmental factors on detection accuracy, while considering the quantification of uncertainty and the importance of position and force in the detection algorithm. In contrast to composite plate structures, metal structures will sag but not delaminate when subjected to impact loads, and the fact of sag is easily detected.

Ebrahimkhanlou et al. [29] used deep learning to develop a source localization method applied to plate-like structures with stiffeners and rivets. Ebrahimkhanlou and Salamone [30] also studied a stacked autoencoder-based methodology that relies on only one sensor to locate the source of the sound in the layer structure. Hesser [31] considered three machine-learning architectures to distinguish different sound sources in aluminum panels. The above methods all use convolutional neural networks to transform the damage recognition problem into an image classification problem, and often need to perform wavelet transform on the initial time domain signal to obtain a time-frequency scale map.

This paper employs a data-driven methodology based on BP neural networks for further developing the utilization of machine learning methods in damage recognition, hoping to obtain higher computational efficiency and accuracy. First, the wave field of the five-peak narrow-band modulated sine signal applied to a thin aluminum plate was obtained by establishing a numerical simulation model and a physical experimental platform and then using the time of arrival of the first wave packet in the waveform received by different sensors to train the Back Propagation neural network, set up different test sets to verify the prediction results and test the robustness. This paper aims to find the source of the sound generated inside a thin aluminum plate using eight sensors in both simulated and experimental environments. Although the traditional Time Difference of Arrival (TDOA) localization methods can also achieve this goal, most require prior knowledge of materials. They are computationally complex, rely on analytical models, and cannot be fast and accurate, which is very different from data-driven methodologies combined with computing intelligence.

2. Algorithm Theory of BP Neural Networks and Signal Preprocessing

2.1. The Operation Mechanism of the BP Neural Network

A typical BP neural network consists of three parts: the input layer, the hidden layer, and the output layer. There are nodes in each layer, and weights connect the nodes in adjacent layers. Theoretically, with one hidden layer, the BP neural network can approach any nonlinear function according to the predetermined accuracy requirements [32]. The core idea of the BP neural network algorithm is that the training process is mainly divided into two parts: signal forward propagation and error backpropagation. When the input layer receives the signal, it will pass it to the hidden layer. The hidden layer processes the signal according to the connection weight threshold and activation function and then passes it to the output layer. After the output layer receives the signal, it will compare the result with the actual value. The actual value is compared, and the error is obtained according to the connection weights and thresholds between the layers. Then the error is back-propagated [33], as shown in Figure 1.

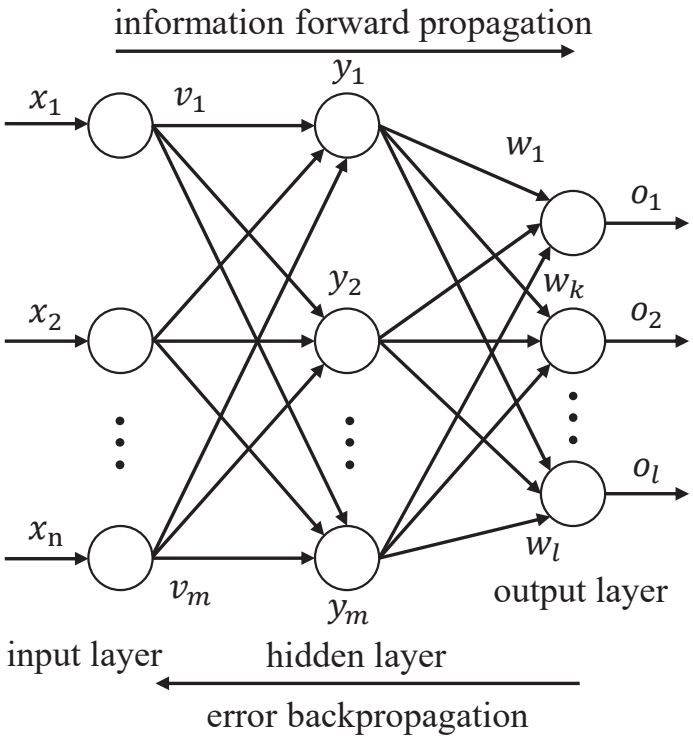


Figure 1. Schematic diagram of a typical BP neural network.

A standard BP neural network modifies the weights along the reverse of the error-performance function gradient [34]. For the transfer function, if the function is defined and differentiable at a point, the function descends fastest along the reverse of the gradient. Therefore, when using the gradient descent method, the function's gradient at a certain point should be calculated first. Then the value of the independent variable should be adjusted in a certain step along the opposite direction of the gradient. An output error E is when the network output is not equal to the expected output.

$$E = \frac{1}{2}(d - O)^2 = \frac{1}{2}\sum_{k=1}^{l}(d_k - O_k)^2 \tag{1}$$

Expanding the above error values to the hidden layer has

$$E = \frac{1}{2}\sum_{k=1}^{l}[d_k - f(net_k)]^2 = \frac{1}{2}\sum_{k=1}^{l}\left[d_k - f\left(\sum_{j=0}^{m} w_{jk}y_j\right)\right]^2 \tag{2}$$

Expand further to the input layer

$$E = \frac{1}{2}\sum_{k=1}^{l}\left\{d_k - f\left[\sum_{j=0}^{m} w_{jk}f\left(net_j\right)\right]\right\}^2 = \frac{1}{2}\sum_{k=1}^{l}\left\{d_k - f\left[\sum_{j=0}^{m} w_{jk}f\left(\sum_{i=0}^{n} v_{ij}x_i\right)\right]\right\}^2 \tag{3}$$

It can be seen from the above formula that the network error is a function of the weights w_{jk} and v_{ij} of each layer, so adjusting the weights can change the error E. The principle of adjusting the weights is to reduce the error continuously, so the adjustment amount of the weights should be proportional to the gradient descent of the error, that is

$$\Delta w_{jk} = -\eta\frac{\partial E}{\partial w_{jk}} \qquad \Delta v_{ij} = -\eta\frac{\partial E}{\partial v_{ij}} \tag{4}$$

The negative sign represents gradient descent in the formula, and the constant $\eta \in (0, 1)$ represents the scale coefficient, reflecting the learning rate during training.

The forward propagation process of the signal: the output of the input layer is equal to the input signal of the entire neural network

$$v_M^m(n) = x(n) \tag{5}$$

The input of the i-th neuron in the hidden layer is equal to the weighted sum of Equation (1)

$$u_I^i(n) = \sum_{m=1}^{M}\omega_{mi}(n)v_M^m(n) \tag{6}$$

Assuming $f(\cdot)$ is a sigmoid function, the output of the i-th neuron in the hidden layer is

$$v_I^i(n) = f\left(u_I^i(n)\right) \tag{7}$$

The input of the j-th neuron in the output layer is equal to the weighted sum of $v_I^i(n)$

$$u_J^j(n) = \sum_{i=1}^{I}\omega_{ij}(n)v_I^i(n) \tag{8}$$

The output of the j-th neuron in the output layer is

$$v_J^j(n) = g\left(\left(u_J^j(n)\right)\right) \tag{9}$$

The error of the j-th neuron in the output layer is

$$e_j(n) = d_j(n) - v_J^j(n) \tag{10}$$

The total error of the network is

$$e(n) = \frac{1}{2}\sum_{j=1}^{J} e_j^2(n) \tag{11}$$

Error signal backpropagation: First, the error backpropagation passes through the output layer, so the weight ω_{mi} is adjusted between the hidden layer and the output layer. According to the gradient descent method, the gradient $\frac{\partial e(n)}{\partial \omega_{ij}(n)}$ of the error to ω_{mi} should be calculated, and then adjusted in a reverse direction

$$\Delta\omega_{ij}(n) = -\eta\frac{\partial e(n)}{\partial \omega_{ij}(n)} \tag{12}$$

$$\omega_{ij}(n+1) = \Delta\omega_{ij}(n) + \omega_{ij}(n) \tag{13}$$

The gradient can be obtained by taking partial derivatives. According to the chain rule of differentiation, we have

$$\frac{\partial e(n)}{\partial \omega_{ij}(n)} = \frac{\partial e(n)}{\partial e_j(n)} \cdot \frac{\partial e_j(n)}{\partial v_J^j(n)} \cdot \frac{\partial v_J^j(n)}{\partial u_J^j(n)} \cdot \frac{\partial u_J^j(n)}{\partial \omega_{ij}(n)} \tag{14}$$

Since $e(n)$ is a quadratic function of $e_j(n)$, its differential is a linear function, so $\frac{\partial e(n)}{\partial e_j(n)} = e_j(n)$, $\frac{\partial e_j(n)}{\partial v_J^j(n)} = -1$.

Derivative of output layer transfer function

$$\frac{\partial v_J^j(n)}{\partial u_J^j(n)} = g' u_J^j(n), \frac{\partial u_J^j(n)}{\partial \omega_{ij}(n)} = v_I^i(n) \tag{15}$$

Therefore, the gradient value is

$$\frac{\partial e(n)}{\partial \omega_{ij}(n)} = -e_j(n) g'\left(u_J^j(n)\right) v_I^i(n) \tag{16}$$

The weight correction is

$$\Delta\omega_{ij}(n) = \eta e_j(n) g'\left(u_J^j(n)\right) v_I^i(n) \tag{17}$$

Introduce the definition of local gradient

$$\delta_J^j = -\frac{\partial e(n)}{\partial u_J^j(n)} = -\frac{\partial e(n)}{\partial e_j(n)} \cdot \frac{\partial e_j(n)}{\partial v_J^j(n)} \cdot \frac{\partial v_J^j(n)}{\partial u_J^j(n)} = e_j(n) g'\left(u_J^j(n)\right) \tag{18}$$

Therefore, the weight correction amount can be expressed as

$$\Delta\omega_{ij}(n) = \eta\delta_J^j v_I^i(n) \tag{19}$$

In the output layer, the transfer function is linear, so $g'\left(u_J^j(n)\right) = 1$.

Substitute in and obtain: $\Delta\omega_{ij}(n) = \eta e_j(n) v_I^i(n)$.

The error signal propagates forward to adjust the weight ω_{mi} between the input and hidden layers. Similar to the previous step, there should be $\Delta\omega_{mi}(n) = \eta\delta_I^i v_M^m(n)$, where $v_M^m(n)$ is the output of the input neuron, and $v_M^m(n) = x^m(n)$. δ_I^i is the local gradient, defined as

$$\delta_I^i = -\frac{\partial e(n)}{\partial u_I^i(n)} = -\frac{\partial e(n)}{\partial v_I^i(n)} \cdot \frac{\partial v_I^i(n)}{\partial u_I^i(n)} = -\frac{\partial e(n)}{\partial v_I^i(n)} f'\left(u_I^i(n)\right) \tag{20}$$

$f(g)$ is the sigmoid function. Since the hidden layer is invisible, the partial derivative of the error $\frac{\partial e(n)}{\partial v_I^i(n)}$ cannot be directly solved for the output value of this layer. Here it is necessary to use the local gradient of the output layer node obtained in the previous calculation:

$$\frac{\partial e(n)}{\partial v_I^i(n)} = \sum_{j=1}^{J} \delta_J^j \omega_{ij} \tag{21}$$

So have

$$\delta_I^i = f'\left(u_I^i(n)\right) \sum_{j=1}^{J} \delta_J^j \omega_{ij} \tag{22}$$

In this paper, the tangent Sigmoid function is used as the activation function in the training of neural networks. The function is continuously differentiable for the input of the range [–1, 1], and the derivative value changes significantly, which can meet the requirements of gradient sensitivity in the process of error backpropagation. Therefore, it is necessary to normalize the sample data before training, and map it to between -1 and 1, to avoid the saturation of neurons in each layer during the training process and, simultaneously, make the model converge more quickly. This paper uses MATLAB software's mapminmax function to perform the normalization operation. The BP neural network model used subsequently is shown in Figure 2, which is the most typical three-layer structure, including one layer of an input layer, a hidden layer, and an output layer.

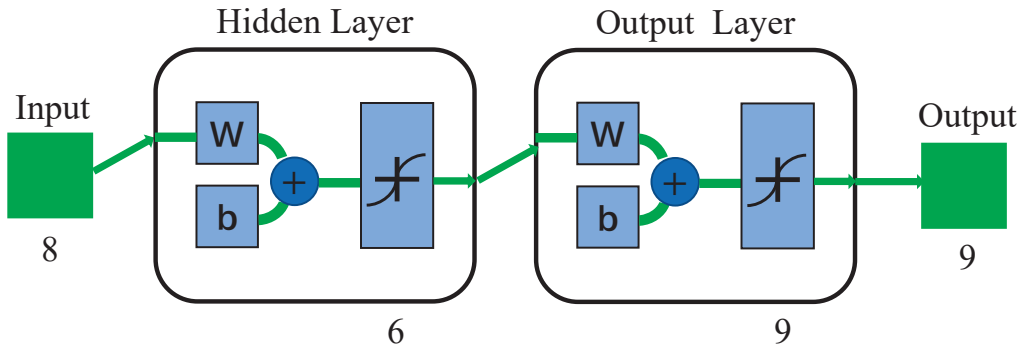


Figure 2. Schematic diagram of BP neural network structure.

After pre-processing the data, use the MATLAB platform for programming to set the parameters of the BP neural network. The training algorithm chooses the Levenberg-Marquardt algorithm, which is suitable for medium-sized feedforward networks and is one of the fastest. Since the BP algorithm is based on the principle of gradient descent, the learning rate is a critical factor in determining the size of the weight adjustment. If the learning rate is too high, the adjustment amount of each weight will be huge, which will quickly lead to the optimal extreme point in the training process, and the network will not converge. On the other hand, if the learning rate is too low, the adjustment amount of each weight will be too small, and the model will converge slowly. Considering the three-layer BP neural network model chosen in this work, the learning rate is 0.0001, the maximum training times are 50,000, and the minimum error goal is 0.0000001. So far, there is no systematic method for determining the number of hidden layer nodes in the BP neural network. This work uses the empirical formula: the number = $\sqrt{(m+n)+a}$ of hidden nodes to determine the initial number of hidden nodes, where m is the amount of input neurons, n is the amount of output neurons, and a is a random number between one and 10. Finally, the initial number of hidden nodes is determined to be six, and the increase and decrease methods are utilized to adjust the optimal number of nodes in the subsequent training.

2.2. Processing of the Captured Signals and Data Augmentation

The BP neural network's training process requires using time-domain signals constructed in the form of vectors or matrices. In this paper, the parameter of the time of

arrival of the first wave packet in the time domain signal is selected, and the eight times of arrival obtained from all receivers are collected to construct the input. In the numerical simulation, according to the set integration time step and total duration, the length of each received signal is 1500 samples. It should be pointed out that the low amount of data and lack of variability obtained in a numerical simulation environment is not sufficient to train a neural network. Therefore, it is necessary to enhance the data of the samples to improve the quantity and quality of the samples, thereby improving the model's generalization ability. Data enhancement is achieved by adding white noise to the initial time-domain signal, and the robustness of the model may also be promoted. As shown in Figure 3, four different white noises are added to the time domain signal: white Gaussian noise, white Uniform noise, white Rayleigh noise, and white Gamma noise. In a wide frequency range, the noise power spectral densities in each band of equal bandwidth are equal, and the amplitudes obey different probability distribution functions. As an example, consider white Gaussian noise to compare the influence of noise with different signal-to-noise ratios on the waveform. As shown in Figure 4, when the signal-to-noise ratio of white Gaussian noise is greater than 35 dB, it has little effect on the time of arrival of the first wave packet, which cannot achieve our purpose of expanding the dataset. While the signal-noise ratio is lowered to 30 dB, the times of arrival start to differ within a specific range. When it is reduced to 25 dB, the white noise severely impacts the initial signal. Moreover, it is hard to distinguish each wave packet. When it is further reduced, to less than 20 dB, it is no longer possible to distinguish between noise and signal. Based on the above comparison, it is proposed to add four kinds of 35 dB white noise to the initial time domain signal for data enhancement.

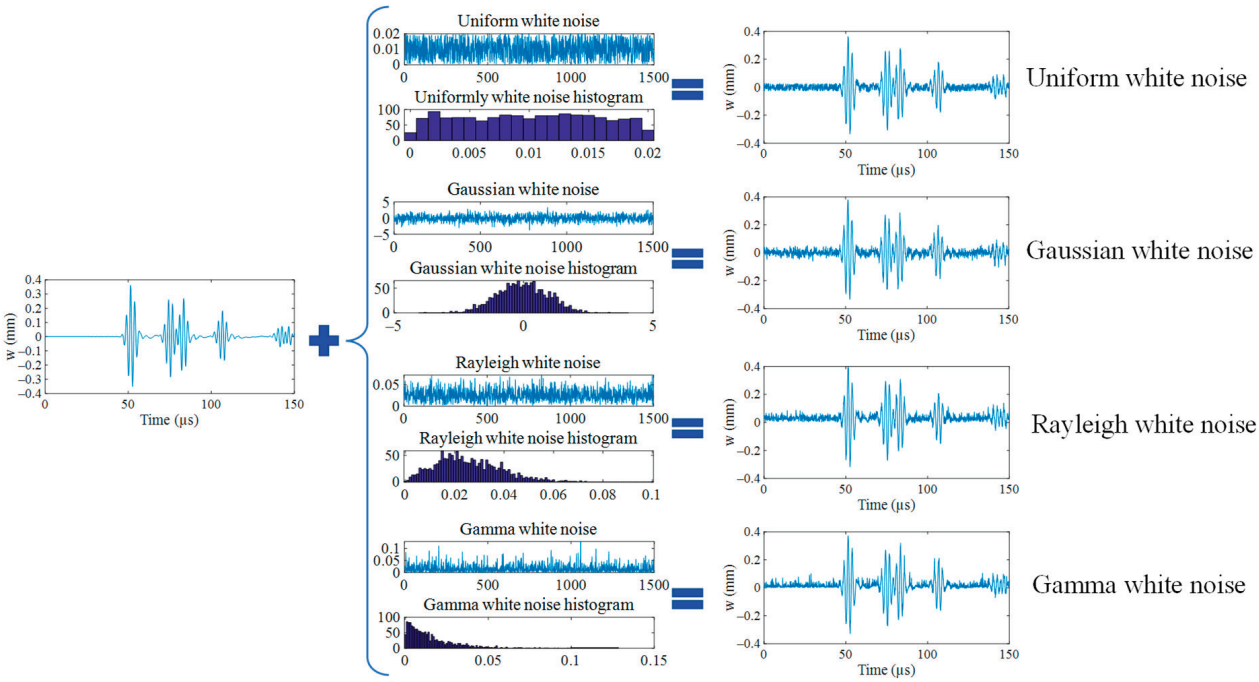


Figure 3. Adding four different groups of noise for data enhancement.

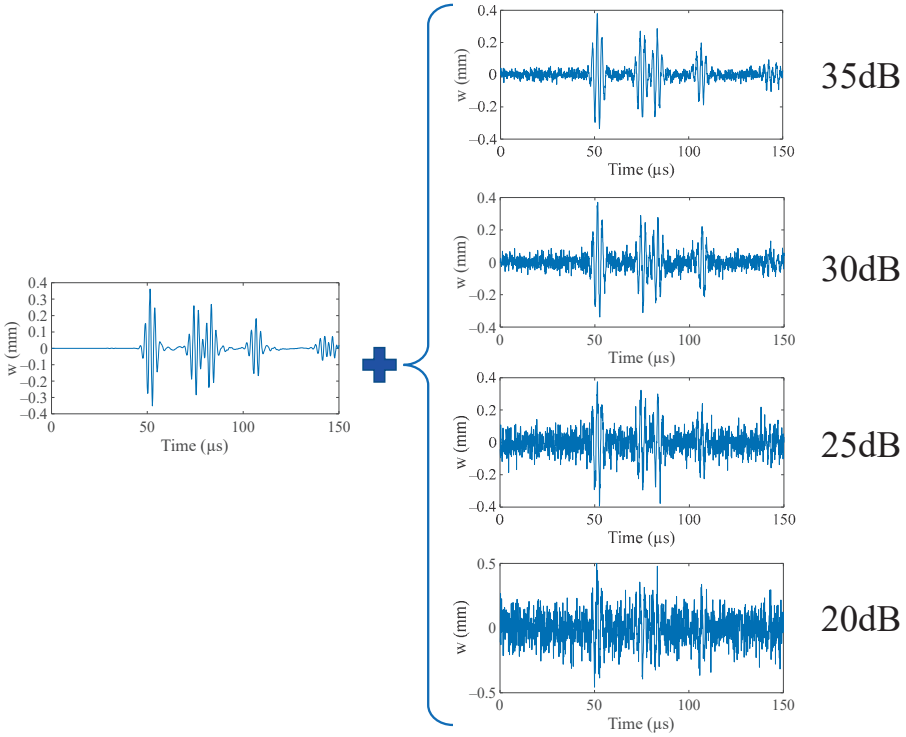


Figure 4. Effect of Gaussian white noise at different decibels on the initial signal.

Four kinds of white noise are added ten times, respectively into the signal received by each receiving point. Therefore, 40 specimens can be acquired by one operation for each area, and in the nine areas shown in Figure 5, a total of 360 specimens can be obtained. The time of arrival of the first wave packet is extracted for all samples, in this way we can obtain training set data with large variability. We use the time of arrival corresponding to the eight receiving points as the input of the neural network, and the corresponding area number as the output of the model.

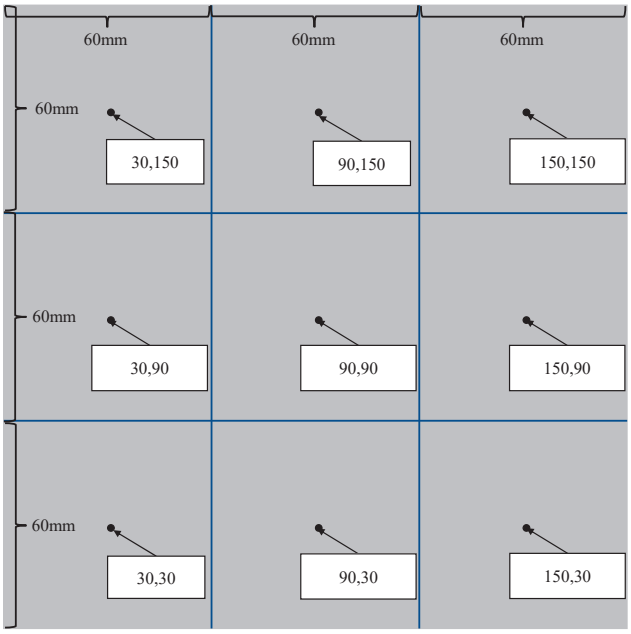


Figure 5. Schematic diagram of aluminum plate.

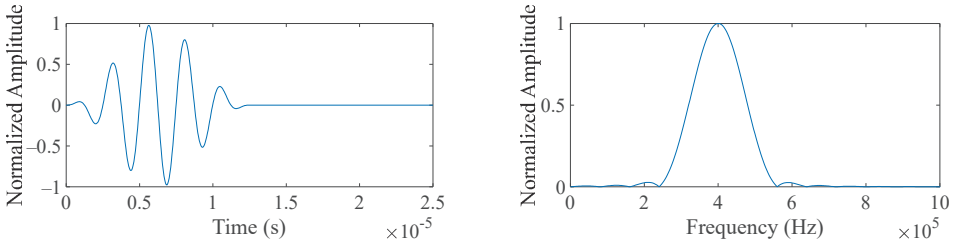
3. Establishment of the Finite Element Model

3.1. Choice of Model Arguments

COMSOL numerical software has a powerful multi-physics coupling analysis module, which is suitable for simulating the propagation of ultrasonic-guided waves in plates. A three-dimensional finite element model of the isotropic aluminum plate was established in the solid mechanic's module. Aluminum has a density of 2700 kg/m^3, a Poisson's ratio of 0.33, and Young's modulus of 70 GPa. As shown in Figure 5, the size of the aluminum plate model is 180 × 180 × 1 mm, divided into nine areas equally. Each area is a square of 60 mm × 60 mm. The training data actuate point is set at every region's center, which is (30, 150), (90, 150), (150, 150), (30, 90), (90, 90), (150, 90), (30, 30), (90, 30), (150, 30), corresponding to the coordinates of the central point of region one to region nine in Figure 5.

3.2. Choice of Actuating Loads and Location of Receivers

Because of the multi-mode and dispersion characteristics of Lamb waves in the propagation process, the signal captured by the sensor is very complex. In this paper, to compare and test the robustness of the neural network, five-peak signals with two central frequencies of 200 kHz and 400 kHz are selected, respectively. They are applied to the plate as point loads. Taking 400 kHz as an example, Figure 6 shows the input signal in this model.



(**a**). Time domain (**b**). Frequency domain

Figure 6. Excitation Signal Centered at 400 kHz.

In order to enable the model to precisely study the discrepancy in time of arrival of each input signal to the receiving point, eight receivers are set on the surface of the aluminum. As shown in Figure 7, the positions of the eight receiving points are (40, 175), (5, 140), (5, 40), (40, 5), (140, 5), (175, 40), (175, 140), (140, 175).

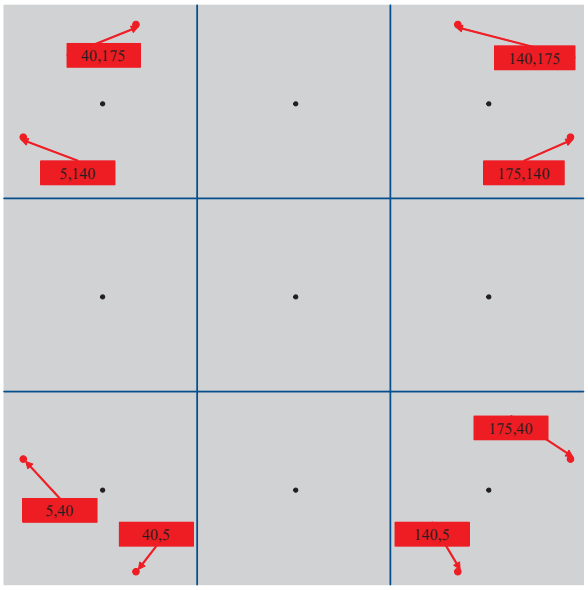


Figure 7. The location of the receiving point on the surface of the aluminum plate.

3.3. Model Accuracy and Stability

When using the finite element method to simulate Lamb waves, the size of the model grid and the integration time step will have a great impact on the accuracy and stability of the calculation results, so the two need to meet certain conditions. When setting the integration time step, it must be ensured that there are at least 20 times increments in one cycle of the Lamb wave propagating in the plate.

Usually, the mesh size is divided as acceptably as possible under the allowable conditions to upgrade the precision of the simulation outcomes. However, if the mesh is too fine, it will easily affect the computational efficiency. Therefore, it is necessary to consider the simulation model's calculation accuracy and solution efficiency. The maximum size when meshing should not be larger than one-tenth of the smallest wavelength.

There are mainly two central frequencies of the five-peak signals employed in this study, which are 200 kHz and 400 kHz, respectively. The maximum frequency of the spectrum is 550 kHz, the wavelength corresponding to the S0 mode is 9.6 mm, and the wavelength corresponding to the A0 mode is 3.56 mm. It can be seen from the above that the mesh size should not be greater than 0.356 mm, and the time step should not be more significant than 90.9 ns. Combined with the actual situation, the mesh size in this study is set to 0.35 mm, and the time step is 50 ns.

After setting up according to the above three sections, the Lamb wave propagation process is obtained when the central point of area 3 is excited once as shown in Figure 8. The rest of the regions are excited in the same way. Figure 9 shows the time domain signals captured at the eight receivers at the boundary at this time. It can be observed that there is a significant difference in the time of arrival of the first wave packet due to the different positions of the receiving point from the excitation point. This is precisely the feature that the neural network needs to study in order to map this feature value to its source.

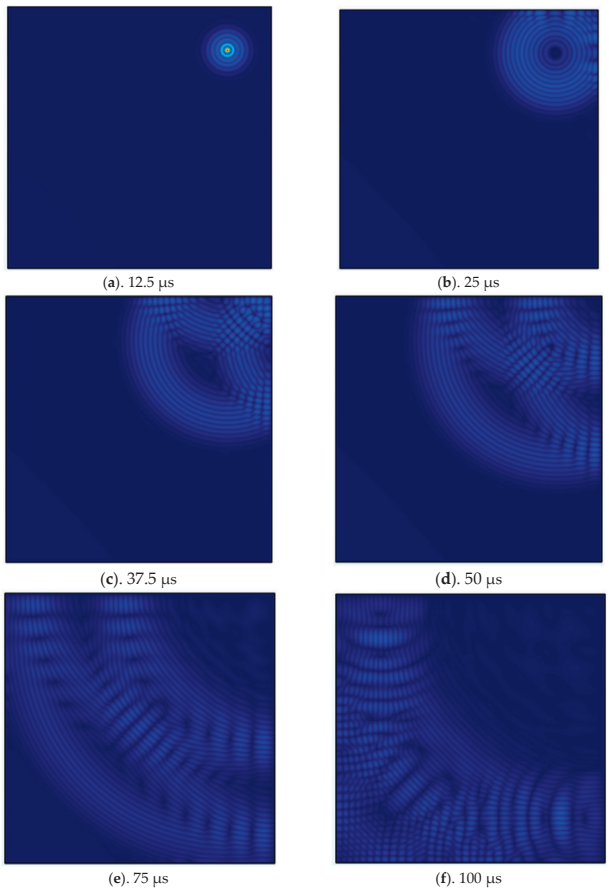


Figure 8. Wavefield diagrams at different times.

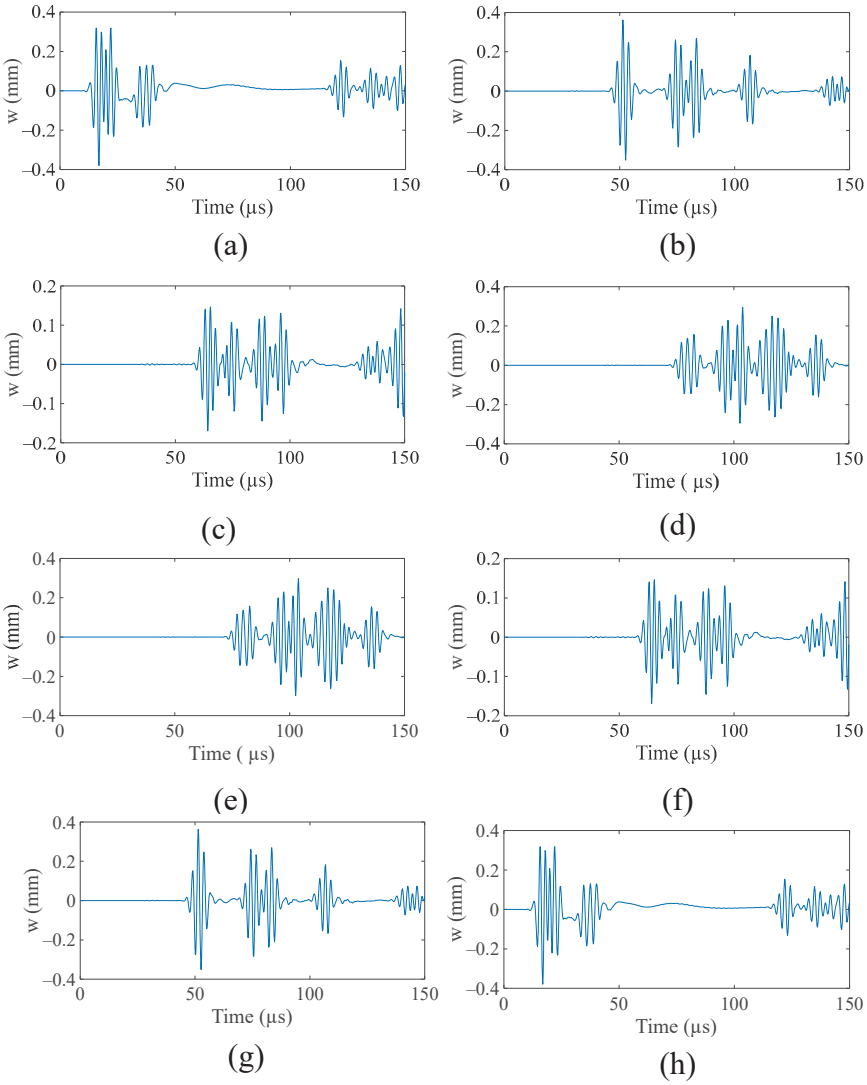


Figure 9. The initial time domain signals received by the eight receivers after one actuating in the center of area three. (**a**). The signal received by the receiving point (140, 175). (**b**). The signal received by the receiving point (40, 175). (**c**). The signal received by the receiving point (5, 140). (**d**). The signal received by the receiving point (5, 40). (**e**). The signal received by the receiving point (40, 5). (**f**). The signal received by the receiving point (140, 5). (**g**). The signal received by the receiving point (175, 40). (**h**). The signal received by the receiving point (175, 140).

4. Analysis of the Location Results of the Five-Peak Narrow-Band Sinusoidal Modulation Signal Actuating Source Area

4.1. Prediction Results When the Excitation Point of the Test Set Is 10 mm Away from the Center of Each Area

After preprocessing the training data set outlined in Section 2.2, arrange multiple sets of different test sets to test whether the trained BP neural network could determine the area to which the new five-peak narrow-band sinusoidal modulation signal excitation source belongs. First, take points near the center point of the area. As shown in Figure 10, the excitation point is set 10 mm from the center of each area, and the same signal with a central frequency of 400 kHz is applied to it for excitation. After the eight receiving points capture the time domain signal, also according to the methodology in Section 2.2, four different white noises are randomly mixed, so that five test samples can be acquired for every excitation. Altogether 45 samples in nine areas are used to test the training effect of the neural network.

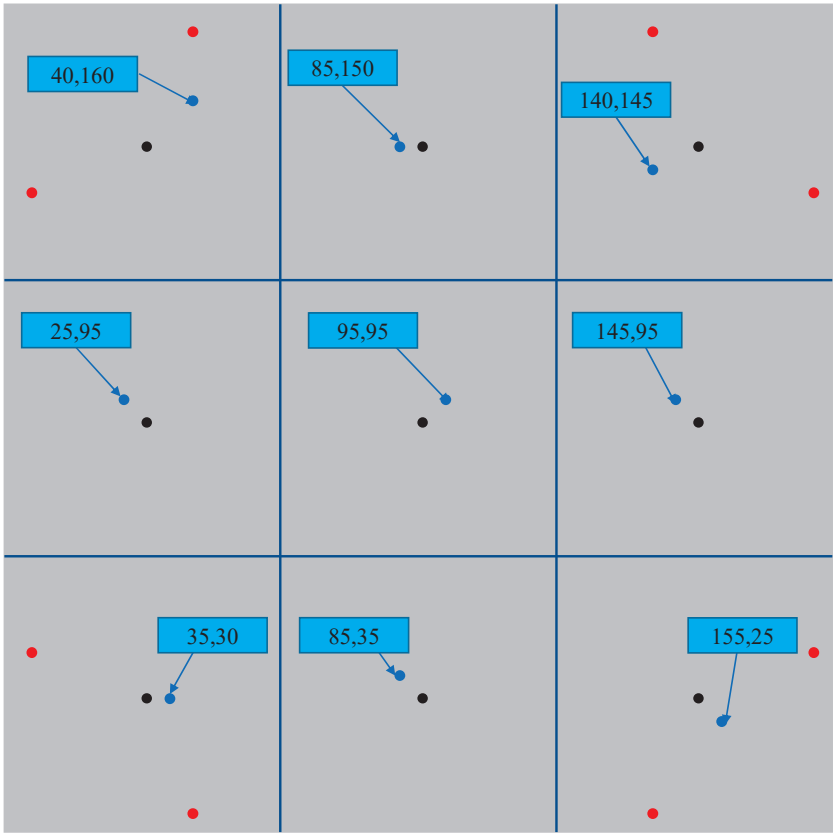


Figure 10. Test set position slightly off-center.

Having preprocessed the test data, the next step is to input the BP neural network described in Section 2.1 to make predictions. Figure 11 shows the prediction results. All 45 samples were judged correctly, and the trained model accurately predicted the region to which each wave source excitation point belonged at that moment, with a precision rate of 100%. This shows that the BP neural network model constructed in this paper can learn the regularity of the input feature values and map the excitation points to a certain extent near the central point of the training set to their sources.

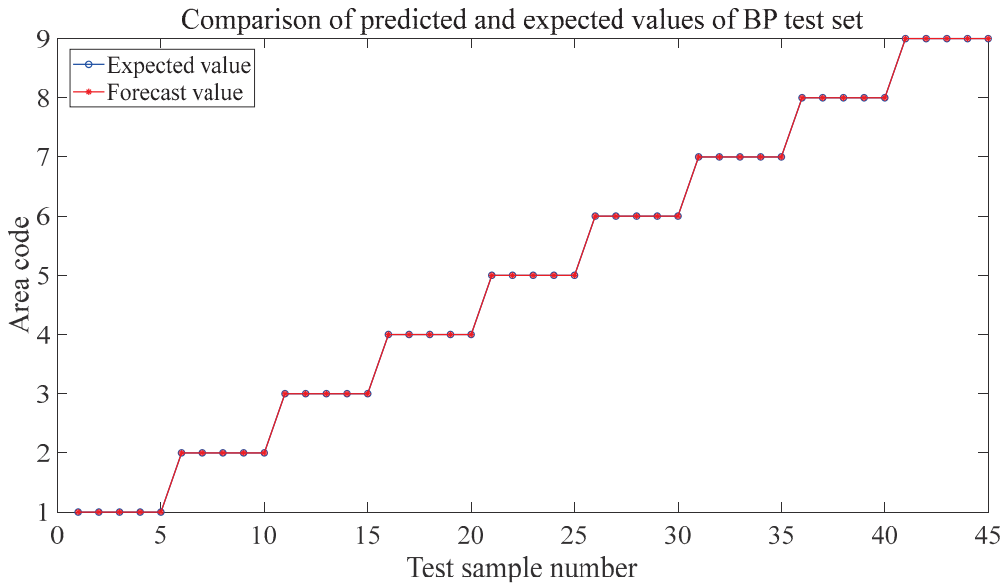


Figure 11. Prediction results when the excitation point of the test set is within 10 mm of the center.

4.2. Prediction Results When the Excitation Point of the Test Set Is 20 mm Away from the Center of Each Area

In the previous subsection, our model can predict the area where the input source is located with complete accuracy when the location of the test point is near the area's center point. In this section, we set up another set of test sets, taking points within 20 mm of the area's center point. As shown in Figure 12, compared to the test set taken in Section 4.1, the points in this test set are closer to the boundaries of adjacent regions. In this case, the signal captured by the receiving point still makes 45 samples as the test set according to the same preprocessing method.

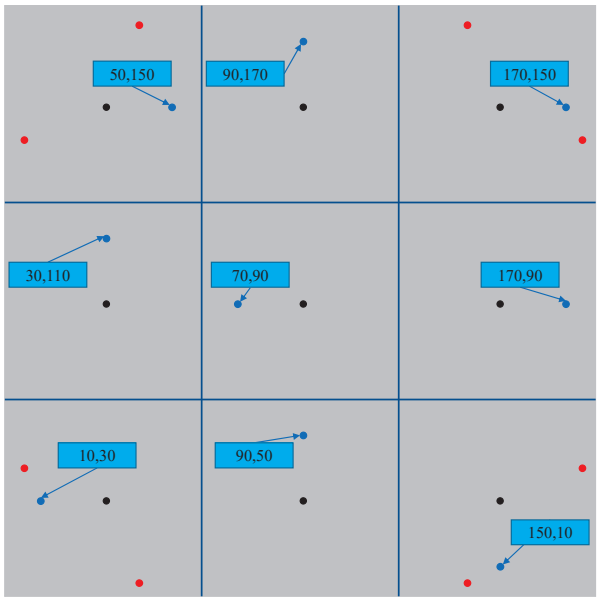


Figure 12. The test set excitation point is 20 mm away from the center.

Figure 13 shows the prediction results at this time. Although the point of the prediction set is already 20 mm away from the center of the region, which is closer to the border of the adjacent region than the point of the training set, the prediction precision of the model trained with the data set of the center of the region can still reach 100%. It can be seen that the numerical simulation environment can obtain very accurate prediction results, whether near the center or the boundary. This powerfully proves the feasibility of the methodology used in this study. The trained BP neural network could quickly and precisely determine the region where the five-peak narrow-band sinusoidal modulation signal actuating source is located in the aluminum plate.

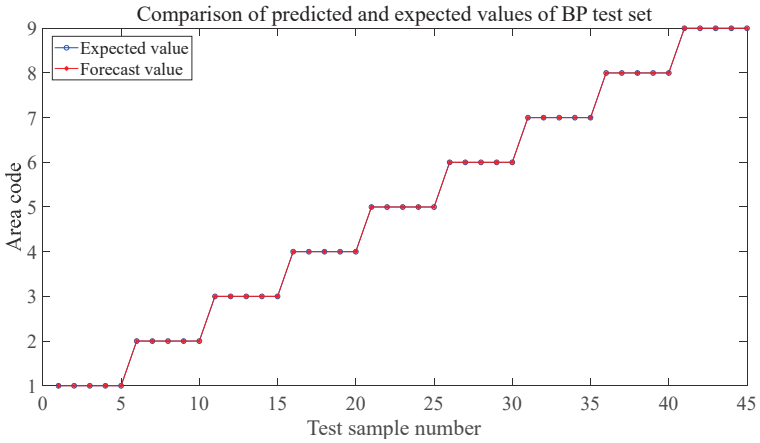
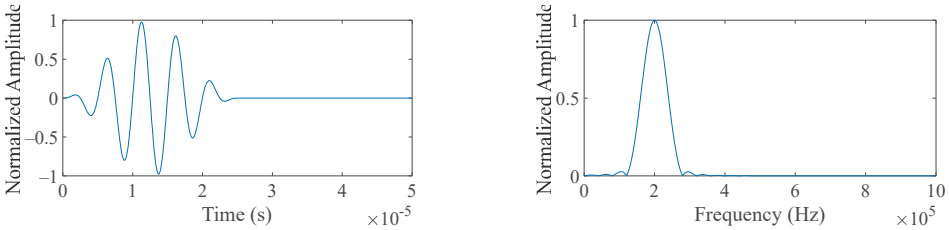


Figure 13. Prediction results when the excitation point of the test set is within 20 mm of the center.

4.3. The Effect of Different Center Frequencies on the Prediction Results

It can be seen from the above two subsections that the neural network trained in this paper can precisely determine the area where the input source is located, regardless of whether the points in the test set are near the region's center or the boundary. This section tests the robustness of the neural network by changing the five-peak narrow-band sinusoidal modulation signal input in the simulation. The source in the test set is replaced with a five-peak narrow-band sinusoidal modulation signal with a central frequency of 200 kHz. As shown in Figure 14, the loading position is not changed, and it is still in the center of the region.



(**a**). Time domain (**b**). Frequency domain

Figure 14. Excitation Signal Centered at 200 kHz.

Figure 15 shows the prediction results in this situation. When the excitation position is not changed, but only the central frequency of the input signal in the model is changed, the prediction is still accurate. The training set is still the same as before, excited by a 400 kHz five-peak narrow-band sinusoidal modulation signal in the center of every area. The only difference from the test set is that the center frequency is changed to 200 kHz. Next, we changed the data used in the training set to 200 kHz center frequency excitation and set the location of the test point in the same way as Figure 12. At this time, both the training set and the test set used a center frequency of 200 kHz.

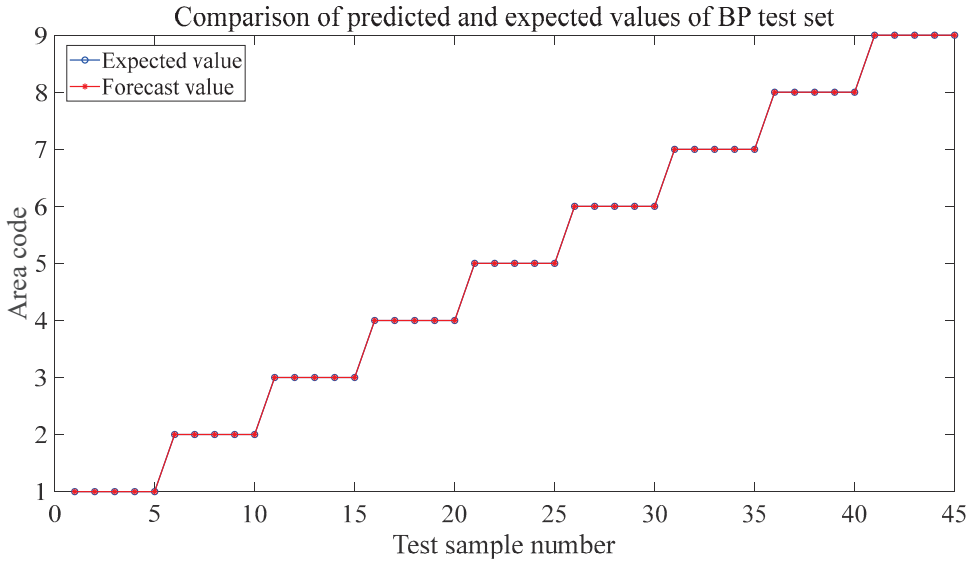


Figure 15. Predicted results when the center frequency is 200 kHz.

Figure 16 reveals the prediction results in this situation. It can be seen that after changing the central frequency, the model can still judge the position of the source accurately, regardless of whether the location of the test point is changed. This indicates that the neural network in this study is insensitive to the central frequency of excitation and has a certain robustness.

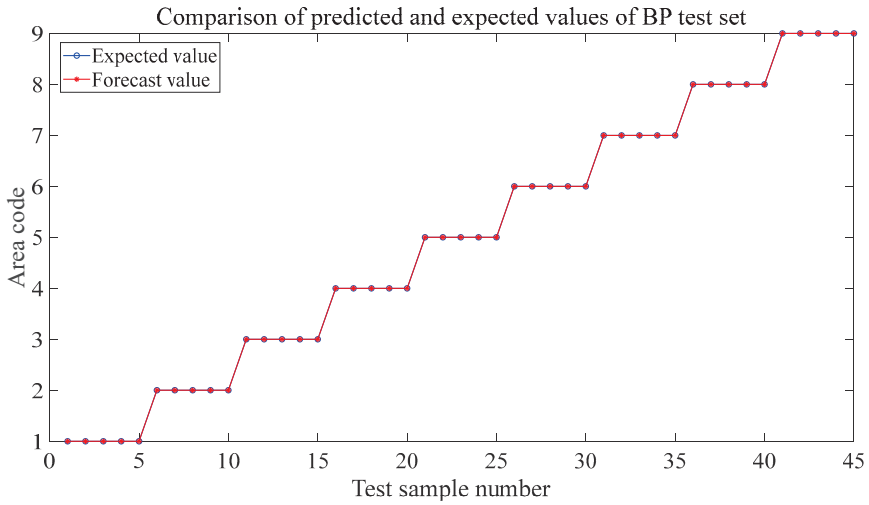


Figure 16. Prediction results when the center frequency is shifted by 20 mm at 200 kHz.

5. The Result of the Wave Source Localization in the Experiment

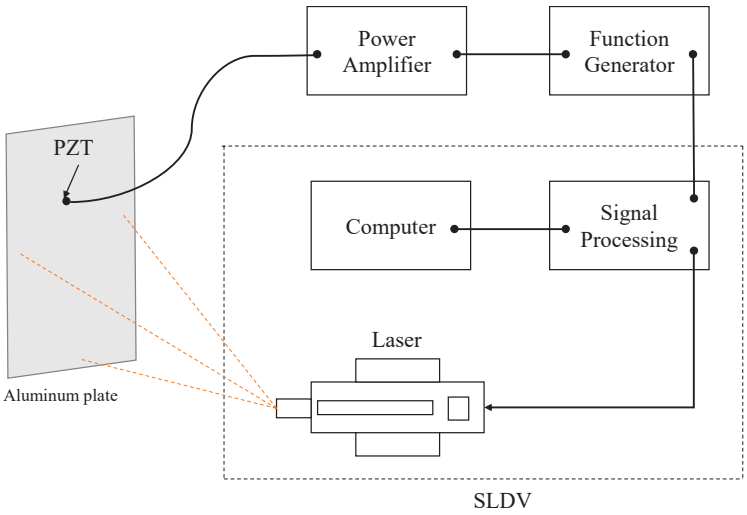
5.1. Experiment Layout of Acoustic Source Localization in the Metal Plate Structure

The prediction outcomes in the numerical simulation environment in Section 4 demonstrate that the data-driven methodology proposed in this study could efficiently identify the region where the sound source is located and offers a novel idea for the sound source localization method for isotropic metal sheets. To verify the authenticity of the simulation results, this study used a damage detection platform for sound source localization of aluminum plate structures.

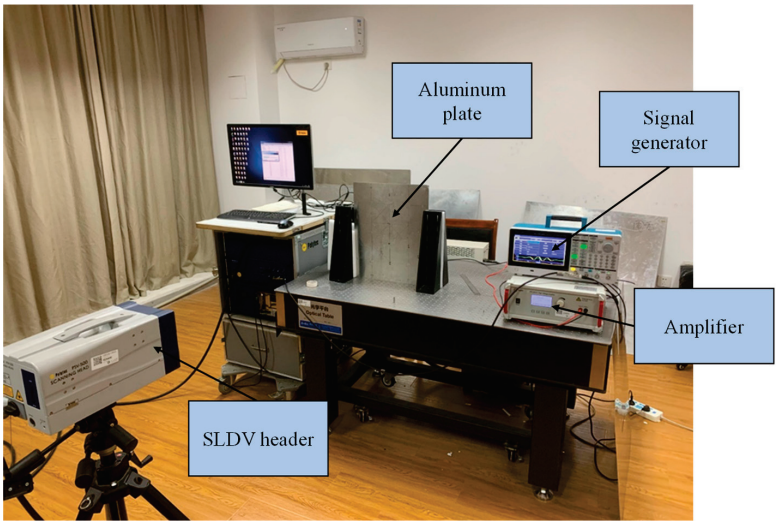
Figure 17 shows the specific arrangement of the experimental platform. First, the preset five-peak narrow-band sinusoidal modulation signal excitation signal is output through the AFG 31000 series signal generator produced by Tektronix, amplified by the Aigtek's ATA-2021H power amplifier, and then output by the piezoelectric sheet. Secondly, the PSV-500-M Laser Doppler Vibrometer (SLDV) laser head produced by Polytec is used to collect the vibration signal of the corresponding scanning point on the aluminum plate, and the collected time domain signal is sent back to the signal processor. The received signal can be seen through the display. The aim of this study is to detect the position of the sound source in the metal plate, acoustic signals are generated by vibrations, and if there is sound, there must be vibrations. A sound source in the panel generates a transient elastic wave. We want to detect the source of the sound by detecting the vibration.

This paper uses an isotropic aluminum plate consistent with the simulation as the experimental object. The size of the aluminum plate is 400 $\times$ 500 $\times$ 1 mm^3. The signal generator is used for excitation and SLDV reception. The position of the scanning point on the surface of the aluminum plate is shown in Figure 18. Eight receiving points should be set up in the same manner as in the simulation, two on each side at a distance of 10 mm from the edge. The sampling time window is set to 400 µs, and the frequency is 5120 kHz, so each received time domain signal has 2048 data points.

Figure 19 shows the area division on the back of the aluminum plate, which is divided into nine rectangular regions of 133.3 $\times$ 166.7 mm^2. Similar to Section 4, two sets of test sets with different locations are also set to check out the model's forecasting ability. The piezoelectric sheet excites the center point of each area of the aluminum plate with a five-peak narrow-band sinusoidal modulation signal with a central frequency of 200 kHz to obtain the training set data. Both red and blue markers appear in Figure 19, representing two test sets. The distance from the red mark to the center of the region is 30 mm, corresponding to the test set near the center of the region in Section 4.1; the distance from the blue mark to the center of the region is 60 mm, corresponding to the test set near the boundary of the adjacent region in Section 4.2. Set the same 200 kHz five-peak narrow-band sinusoidal modulation signal as when collecting the training set data for periodic excitation.



(**a**). Schematic diagram of the experimental platform



(**b**). Experimental setup diagram

Figure 17. Experimental platform.

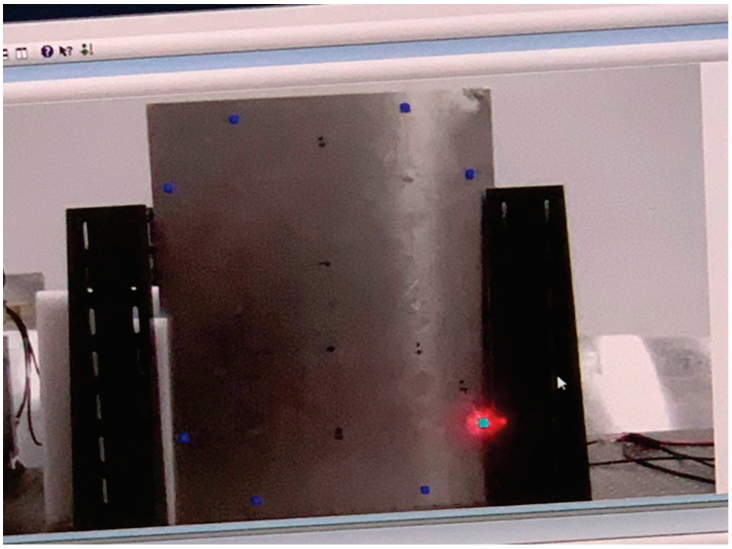


Figure 18. Scanning Laser Doppler Vibrometer scanning point location.



Figure 19. Area division of aluminum plate.

In Section 2.2, we discuss data augmentation methods for simulated data. However, the received Lamb wave signal is mixed with various environmental noises in a laboratory environment and has a high degree of variability without additional manipulation. Therefore, we omit the step of data augmentation. Figure 20 shows the time domain signals captured by eight receiving points when a five-peak narrow-band sinusoidal modulation signal is an input at the center point of area three. The signals captured by every scanning point are influenced by varying degrees of environmental noise, so we set the signal generator to perform periodic excitation at a particular time interval and collect any ten periodic time domain signals with a fixed time window, and then extract the time of arrival of all the first wave packets to make the neural network input. For the test points, three cycles of the signal were extracted for each region. We obtained 90 samples for training the neural network and 27 samples, each with offsets of 30 mm and 60 mm, as a test set.

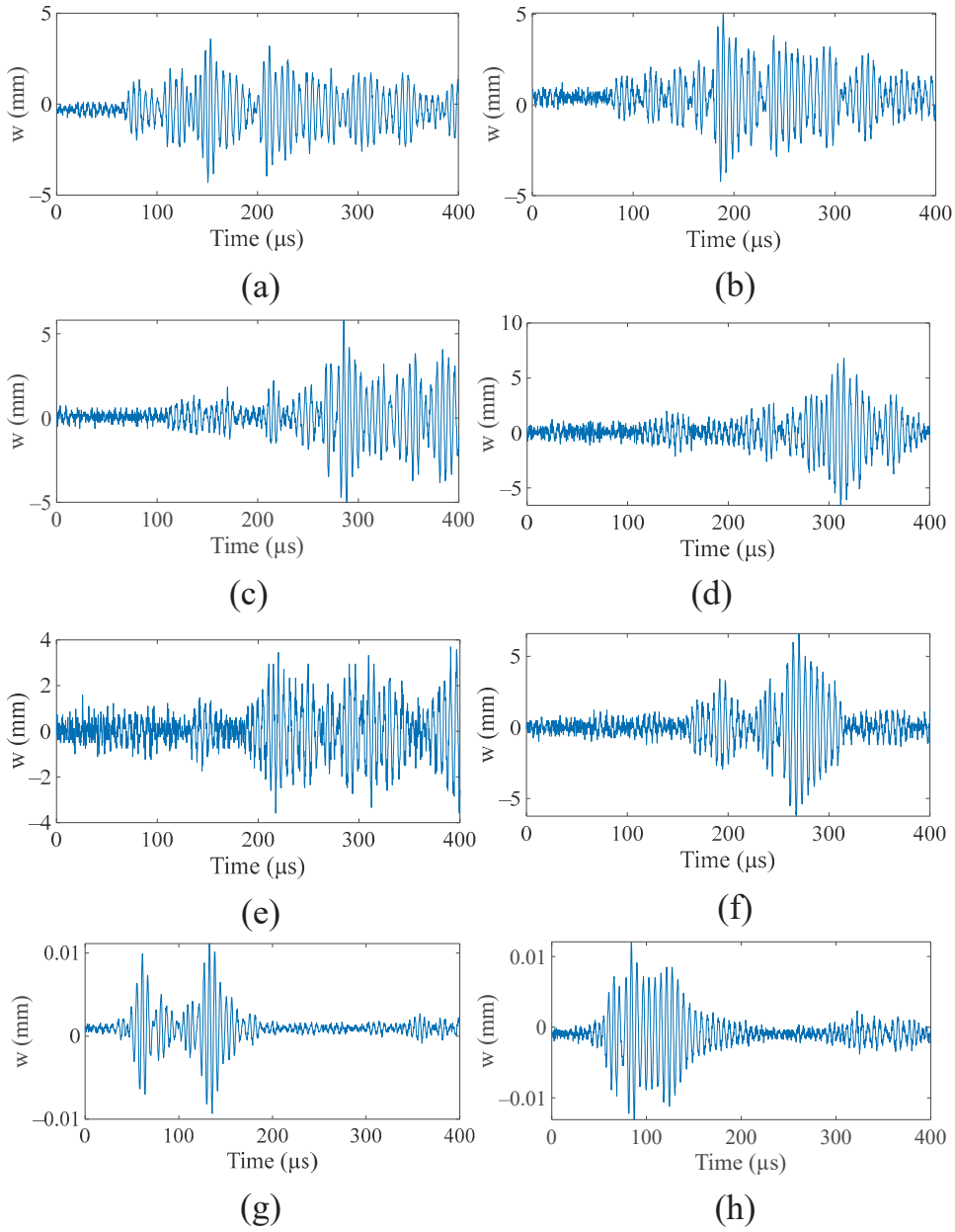


Figure 20. Signals are obtained at eight scanning points when a five-peak narrow-band sinusoidal modulation signal is input at the center of area 3. (**a**). The signal received by the receiving point (300, 490). (**b**). The signal received by the receiving point (390, 400). (**c**). The signal received by the receiving point (190, 100). (**d**). The signal received by the receiving point (300, 10). (**e**). The signal received by the receiving point (100, 10). (**f**). The signal received by the receiving point (10, 100). (**g**). The signal received by the receiving point (10, 400). (**h**). The signal received by the receiving point (100, 490).

5.2. Analysis of the Location Results of the Five-Peak Narrow-Band Sinusoidal Modulation Signal Actuating Source Area in the Experiments

After the same preprocessing, the BP neural network built in Section 2.1 predicts the region where the five-peak narrow-band sinusoidal modulation signal input source is located. After training, the fitting results of the model are shown in Figure 21. It can be seen from the iteration diagram that after the training, the fitting accuracies of training, validation, and testing are: 0.99994, 0.99789, and 0.99812, which are over 0.99 in all cases, which indicates that each dataset fits exceptionally well.

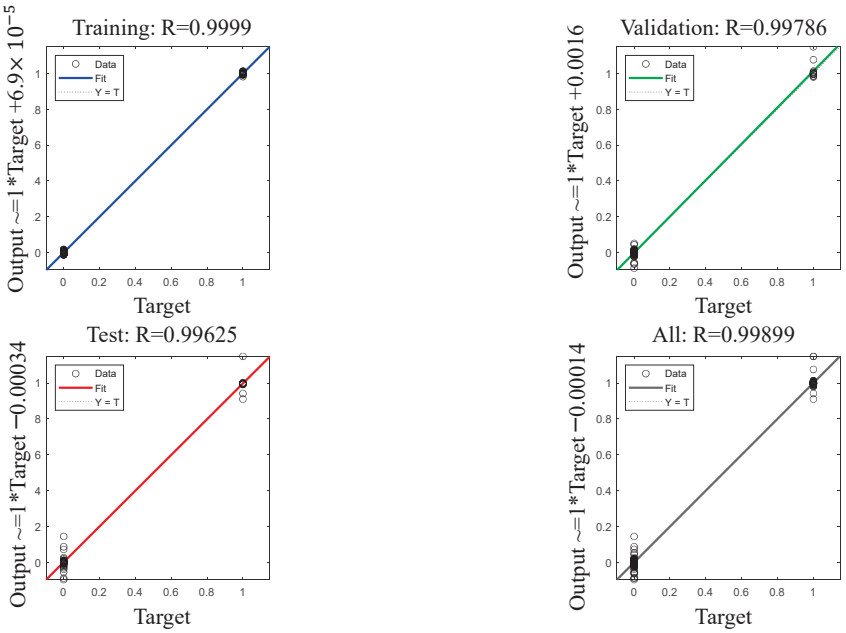


Figure 21. Regression effect of BP neural network model after training.

Figures 22 and 23 show the prediction results of input sources at different locations. Figure 22 shows that the model reaches the training target after 34 iterations. Figure 23 reveals the forecast results for each of the two test sets. Although the two sets of data are wrongly judged, the accuracy is lower than that in the numerical simulation environment in Section 4. However, for the experiment, this is a satisfactory result. In the case of a test point that is 30 mm away from the center point, that is, near the center point, only one misjudgment occurred in the 27 samples, and the accuracy rate was 96.3%—the situation in the adjacent area. As seen from the blue markings in area three in Figure 19, when offset from the center by 60 mm, the sampling points of the test set in some regions (such as region three) almost coincide with the boundary. Even so, except for the wrong judgment in region three, the other regions can still accurately predict the sound source near the boundary, with a total prediction accuracy of 88.9%. This shows that even in the experimental environment when the environment is greatly disturbed, the trained BP neural network is still capable of making exact judgments of test samples in the area, no matter where the test points are in the area.

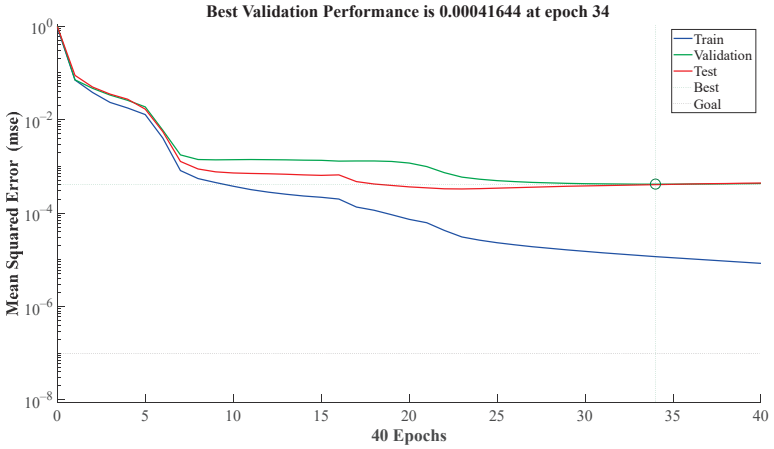
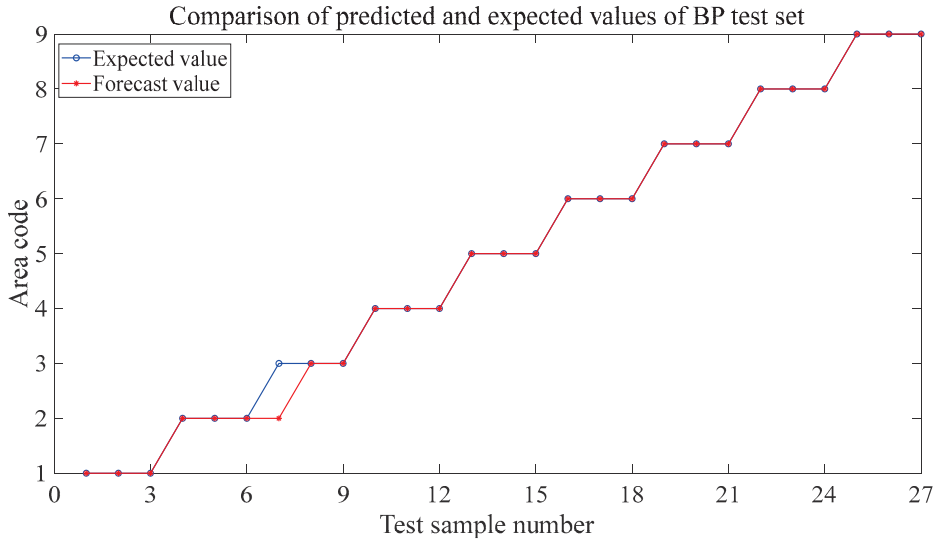
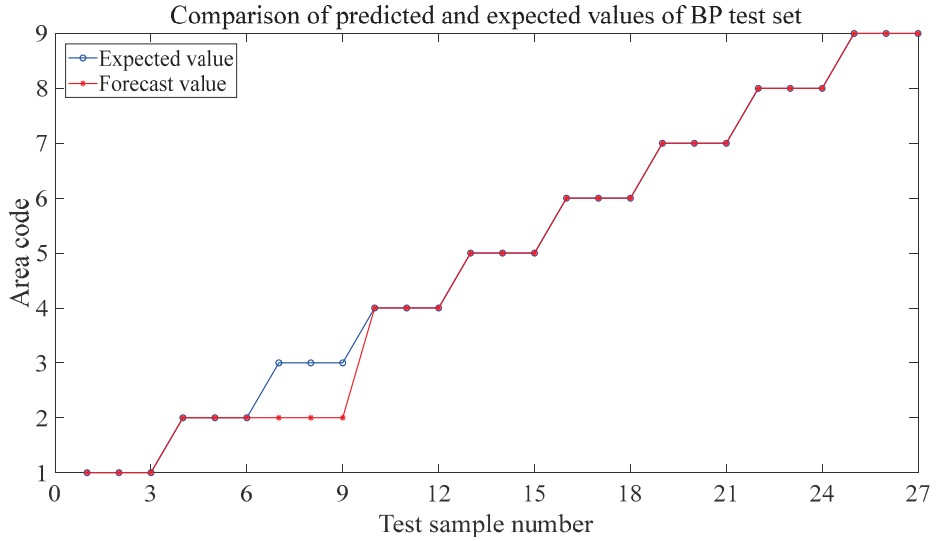


Figure 22. Graph of the number of network iterations and MSE.



(**a**). Prediction results when the excitation point of the test set is within 30 mm of the center.



(**b**). Prediction results when the excitation point of the test set is within 60 mm of the center.

Figure 23. Prediction results in a laboratory environment.

6. Conclusions

This paper utilizes a machine-learning methodology to localize the source of five-peak narrow-band sinusoidal modulation signals within an isotropic aluminum plate. In order to maximize the time of arrival of the wave packet, two receiving points are set at equal intervals on each edge of the aluminum plate. To prove the feasibility of this methodology, a database is established in two different environments: the COMSOL numerical simulation platform and PZT excitation-SLDV-receiving physical experiment platform. Because the signal obtained by the numerical simulation platform does not have variability, four different groups of noise are added for data enhancement. The prediction results of the BP neural network show that the trained model can map the time of arrival in the signal to the sound source area in both environments. Especially in the numerical simulation environment, the prediction accuracy is excellent. Whether it is near the center of the region or the border of the region, it can reach 100%. All 180 test points can accurately locate the sound source's area. In the experiments, consequently, environmental factors play a significant role and accuracy is slightly reduced. It can reach 96.3% near the regional center, and 26 of the 27 test points are correctly predicted. When the boundary is reduced to 88.9%, 24 of the 27 test points are correctly predicted. It is still possible to locate the sound source region.

Author Contributions: Conceptualization, investigation, data curation, writing- original draft preparation, Y.H.; software, data curation, validation, methodology, C.T.; conceptualization, methodology, writing- reviewing and editing, W.H. and G.Z. All authors have read and agreed to the published version of the manuscript.

Funding: The authors are grateful for the financial support provided by the National Natural Science Foundation of China (Grant No. 11872025) and the Six Talent Peaks Project in Jiangsu Province (Grant No. 2019-KTHY-059).

Data Availability Statement: No new data were created or analyzed in this study. Data sharing is not applicable to this article.

Conflicts of Interest: The authors declare no conflict of interest.

References

1. Shao, Y.; Zeng, L.; Lin, J. Damage detection of thick plates using trailing pulses at large frequency-thickness products. *Appl. Acoust.* **2021**, *174*, 107767. [CrossRef]
2. Cuadrado, M.; Pernas-Sáncheza, J.; Artero-Guerreroa, J.A.; Varas, D. Detection of barely visible multi-impact damage on carbon/epoxy composite plates using frequency response function correlation analysis. *Measurement* **2022**, *196*, 111194. [CrossRef]
3. Hu, M.; He, J.; Zhou, C.; Shu, Z.; Yang, W. Surface damage detection of steel plate with different depths based on Lamb wave. *Measurement* **2022**, *187*, 110364. [CrossRef]
4. Shi, B.; Cao, M.; Wang, Z.; Ostachowicz, W. A directional continuous wavelet transform of mode shape for line-type damage detection in plate-type structures. *Mech. Syst. Signal Process.* **2022**, *167*, 108510. [CrossRef]
5. Nicolas, M.J.; Sullivan, R.W.; Richards, W.L. Large Scale Applications Using FBG Sensors: Determination of In-Flight Loads and Shape of a Composite Aircraft Wing. *Aerospace* **2016**, *3*, 18. [CrossRef]
6. Nazeer, N.; Ratassepp, M.; Fan, Z. Damage detection in bent plates using shear horizontal guided waves. *Ultrasonics* **2017**, *75*, 155–163. [CrossRef]
7. Cui, L.; Zhao, Y.; Zhao, P.; Sun, J.; Jia, Z. Review of noncontact ultrasonic nondestructive testing for the solid materials. *Appl. Mech. Mater.* **2014**, *528*, 346–352. [CrossRef]
8. Zima, B. Determination of stepped plate thickness distribution using guided waves and compressed sensing approach. *Measurement* **2022**, *196*, 111221. [CrossRef]
9. Cho, H.; Hasanian, M.; Shan, S.; Lissenden, C.J. Nonlinear guided wave technique for localized damage detection in plates with surface-bonded sensors to receive Lamb waves generated by shear-horizontal wave mixing. *NDT E Int.* **2019**, *102*, 35–46. [CrossRef]
10. Mahajan, H.; Banerjee, H. A machine learning framework for guided wave-based damage detection of rail head using surface-bonded piezo-electric wafer transducers. *Mach. Learn Appl.* **2022**, *7*, 100216. [CrossRef]
11. Tobias, A. Acoustic-emission source location in two dimensions by an array of three sensors. *Non-Destr. Test.* **1976**, *9*, 9–12. [CrossRef]
12. He, T.; Pan, Q.; Liu, Y.; Liu, X.; Hu, D. Near-field beamforming analysis for acoustic emission source localization. *Ultrasonics* **2012**, *52*, 587–592. [CrossRef] [PubMed]
13. Kundu, T.; Das, S.; Jata, K.T. Point of impact prediction in isotropic and anisotropic plates from the acoustic emission data. *J. Acoust. Soc. Am.* **2007**, *122*, 2057. [CrossRef] [PubMed]
14. Kundu, T.; Yang, X.; Nakatani, H.; Takeda, N. A two-step hybrid technique for accurately localizing acoustic source in anisotropic structures without knowing their material properties. *Ultrasonics* **2015**, *56*, 271–278. [CrossRef]
15. Sen, N.; Kundu, T. A new wave front shape-based approach for acoustic source localization in an anisotropic plate without knowing its material properties. *Ultrasonics* **2018**, *87*, 20–32. [CrossRef]
16. Nucera, C.; White, S.; Chen, Z.M.; Kim, H.; di Scalea, F.L. Impact monitoring in stiffened composite aerospace panels by wave propagation. *Struct. Health Monit.* **2015**, *14*, 547–557. [CrossRef]
17. Dubuc, B.; Ebrahimkhanlou, A.; Livadiotis, S.; Salamone, S. Inversion algorithm for Lamb-wave-based depth characterization of acoustic emission sources in plate-like structures. *Ultrasonics* **2019**, *99*, 105975. [CrossRef] [PubMed]
18. Nakatani, H.; Kundu, T.; Takeda, N. Improving accuracy of acoustic source localization in anisotropic plates. *Ultrasonics* **2014**, *54*, 1776–1788. [CrossRef]
19. Ciampa, F.; Meo, M. Acoustic emission source localization and velocity determination of the fundamental mode A0using wavelet analysis and a Newton-based optimization technique. *Smart Mater. Struct.* **2010**, *19*, 045027. [CrossRef]
20. Sun, J.; Hao, C.; Zheng, Z. Passive Localization of Near-Field Sources Based on Overlapped Subarrays. *Circuits Syst. Signal Process.* **2020**, *39*, 502–512. [CrossRef]
21. Tian, Y.; Sun, X. Passive localization of mixed sources jointly using MUSIC and sparse signal reconstruction. *Int. J. Electron. Commun.* **2014**, *68*, 534–539. [CrossRef]
22. Ernst, R.; Zwimpfer, F.; Dual, J. One sensor acoustic emission localization in plates. *Ultrasonics* **2016**, *64*, 139–150. [CrossRef] [PubMed]

23. Sikdar, S.; Mirgal, P.; Banerjee, S. Low-velocity impact source localization in a composite sandwich structure using a broadband piezoelectric sensor network. *Compos. Struct.* **2022**, *291*, 115619. [CrossRef]
24. Yu, H.; Seno, A.H.; Khodaei, Z.S.; Aliabadi, M.H.F. Structural health monitoring impact classification method based on Bayesian neural network. *Polymers* **2022**, *14*, 3947. [CrossRef] [PubMed]
25. Karmakov, S.; Aliabadi, M.H.F. Deep learning approach to impact classification in sensorized panels using Self-Attention. *Sensors* **2022**, *22*, 4370. [CrossRef] [PubMed]
26. Seno, A.H.; Aliabadi, M.H.F. Uncertainty quantification for impact location and force estimation in composite structures. *Struct. Health Monit.* **2022**, *21*, 1061–1075. [CrossRef]
27. Seno, A.H.; Aliabadi, M.H.F. A novel method for impact force estimation in composite plates under simulated environmental and operational conditions. *Smart Mater. Struct.* **2020**, *29*, 115029. [CrossRef]
28. Seno, A.H.; Khodaei, Z.S.; Aliabadi, M.H.F. Passive sensing method for impact localisation in composite plates under simulated environmental and operational conditions. *Mech. Syst. Signal Process.* **2019**, *129*, 20–36. [CrossRef]
29. Ebrahimkhanlou, A.; Dubuc, B.; Salamone, S. A generalizable deep learning framework for localizing and characterizing acoustic emission sources in riveted metallic panels. *Mech. Syst. Signal Process.* **2019**, *130*, 248–272. [CrossRef]
30. Ebrahimkhanlou, A.; Salamone, S. Single-Sensor Acoustic Emission Source Localization in Plate-Like Structures Using Deep Learning. *Aerospace* **2018**, *5*, 50. [CrossRef]
31. Hesser, D.F.; Mostafavi, S.; Kocur, G.K.; Markert, B. Identification of acoustic emission sources for structural health monitoring applications based on convolutional neural networks and deep transfer learning. *Neurocomputing* **2021**, *453*, 1–12. [CrossRef]
32. Zhang, L.; Wang, F.; Xu, B.; Chi, W.; Wang, Q.; Sun, T. Prediction of stock prices based on LM-BP neural network and the estimation of overfitting point by RDCI. *Neural. Comput. Appl.* **2018**, *30*, 1425–1444. [CrossRef]
33. Lian-Suo, W.; Hua, L.; Di, W.; Yuan, G. Clock synchronization error compensation algorithm based on BP neural network model. *Acta Phys. Sin.* **2021**, *70*, 114203.
34. Song, S.; Xiong, X.; Wu, X.; Xue, Z. Modeling the SOFC by BP neural network algorithm. *Int. J. Hydro. Energy* **2021**, *46*, 20065–20077. [CrossRef]

Disclaimer/Publisher's Note: The statements, opinions and data contained in all publications are solely those of the individual author(s) and contributor(s) and not of MDPI and/or the editor(s). MDPI and/or the editor(s) disclaim responsibility for any injury to people or property resulting from any ideas, methods, instructions or products referred to in the content.

materials

MDPI

Article

Material Recycling for Manufacturing Aggregates Using Melting Slag of Automobile Shredder Residues

Soo-Jin Cho [1], Ha-Na Jang [2], Sung-Jin Cho [3], Young-Sam Yoon [1] and Heung-Min Yoo [1,*]

[1] Resource Recirculation Research Division, National Institute of Environmental Research, Incheon 22689, Republic of Korea
[2] Department of Environmental Finance, Yonsei University, Wonju 26493, Republic of Korea
[3] Corporate R&D Institute in Doosan Enerbility, Changwon 51711, Republic of Korea
* Correspondence: yoohm@korea.kr

Abstract: The quantity of waste from end-of-life vehicles is increasing with an increase in the number of scrapped internal combustion engine vehicles owing to international trends such as carbon neutrality and particulate matter reduction. The recycling rate must be ≥95%; however, the average recycling rate remains at approximately 89%. Therefore, the improvement of the recycling of automobile shredder residues (ASR) is gaining attention. In this study, four types of products (interlocking, clay, and lightweight swelled ceramic (LSC) bricks, and asphalt paving aggregate (APA)) were manufactured using ASR melting slag (ASRMS). Environmental performance, quality standards, and technology were evaluated to assess the recyclability of the manufactured bricks. The interlocking brick substituted melting slag for sand and stone powder as an aggregate. As melting slag content increased, absorption decreased and bending strength increased. Clay brick was manufactured by replacing kaolin and feldspar with melting slag that substituted for 20%. The quality of clay bricks mixed with over 15% melting slag was not better than standard. Asphalt paving aggregate was used to investigate the optimum condition of slag content in mixed asphalt; the mixture ratio showed that 61% broken stone of 13 mm, 6% screenings, 10% melting slag, 15% sand and 8% filler was most effective. A lightweight swelled ceramic brick was manufactured by using melting slag, front glass, and so on. Specific gravity and compressive strength ranged from 0.38 to 0.51 and from 339.7 to 373.6 N/cm^2. ASRMS exhibited an environmental performance suitable for recycling and the manufactured bricks satisfied the quality standards. The recyclability of ASR was also assessed in terms of waste usage, conformance to quality standards, market size, and demand prediction. APA showed the best results followed by interlocking, clay, and LSC bricks.

Keywords: waste; material recycling; automobile shredder residue; melting slag; environmental assessment

1. Introduction

The number of vehicles produced worldwide over the past five years was approximately 92 million. South Korea ranks fifth in automobile production with approximately 3.5 million vehicles produced each year [1]. Internal combustion engine vehicles are being scrapped by government policies and there is an international trend to achieve carbon neutrality and particulate matter reduction. In addition, the use of electric vehicles has been incentivised. The rate of scrapping internal combustion engine vehicles and eliminating the resultant waste is expected to increase significantly [2]. Approximately 9.5 million vehicles are scrapped per year in Korea and the generated waste is approximately 103,000 tons, which is mostly composed of automobile shredder residues (ASR) [3,4].

Various policies have been implemented in advanced countries to efficiently recycle waste from end-of-life vehicles (ELVs). The EU's Directive 2000/53/EC

specifies that ELVs should be processed in compliance with a recycling rate of 95% and an energy recovery rate of <10%. Countries around the world have enacted legislation to introduce ELV recycling policies [5]. In Korea, there was no recycling standard for ELVs, but the Act on Resource Circulation of Electrical and Electronic Equipment and Vehicles was enacted to prepare an institutional system for ELV recycling in keeping with international environmental regulations. The act has set a mandatory recycling rate per vehicle at 95% and an energy recovery rate of <10% [6]. However, the average ELV recycling rate has only reached approximately 89% since 2015 [7]. Therefore, it is important to improve the recycling rate by recycling ASR.

ASR exhibits a high calorific value as it is composed of metals, plastics, fibres, and non-metals, such as rubber. ASR is also highly valuable as a recycling resource because it has constant waste properties with a stable generation. Yoo et al. recovered energy through the gasification of ASR [8]. Kim et al. recovered valuable metals from ASR through a melting process [9]. In this study, a method to recycle ASR as an aggregate and a road fill material was developed to improve the ELV recycling rate and establish a resource circulation economy. ASR melting slag (ASRMS) was selected as the target sample to prepare an appropriate recycling method for molten residue after energy recovery based on the results of previous studies.

The recycling of aggregate was performed by manufacturing three types of bricks using ASRMS, including interlocking, clay, and lightweight swelled ceramic (LSC) bricks. An attempt was also made to use ASRMS as asphalt paving aggregate (APA). These technologies were assessed for their applicability according to domestic laws. Therefore, analyses of the characteristics of recycled products, heavy metals, leaching, environmental performance, and quality standards were performed and conformance to the recycling standards of the Wastes Control Act were assessed.

2. Materials and Methods

2.1. Environmental Assessment of Recycling

The legal applicability of the technologies and their technical feasibilities were assessed by investigating the legal procedures and recycling standards specified in the Wastes Control Act of Korea. In the Wastes Control Act, 301 waste codes and 41 recycling types are specified. For ASR, types that can be recycled (R-3), directly recover energy (R-8), or from which energy can be recovered (R-9), and types which allow intermediate processing of waste for product manufacturing (R-10) are specified [10].

Korea has also implemented a system that allows the recycling of new types of recycling technologies that are not specified in the waste recycling principles provided but which comply with the requirements of an environmental assessment that evaluate their impact both with and without contact with the environmental medium. Recycling methods that have contact with an environmental medium may include recycling waste through contact with soil, groundwater, and surface water, such as road substratum materials, fill materials, and soil cover [11].

ASR corresponds to waste code 51-45-01 under the current law, and its recycling is allowed in types R-3, R-8, R-9, and R-10. Therefore, technologies for recycling ASR as an aggregate (R-4-2) and a road fill material (R-7) were evaluated to improve the present ELV recycling rate. Details of the classification of automobile shredder residues (ASR) and recyclable types are presented in Figure 1.

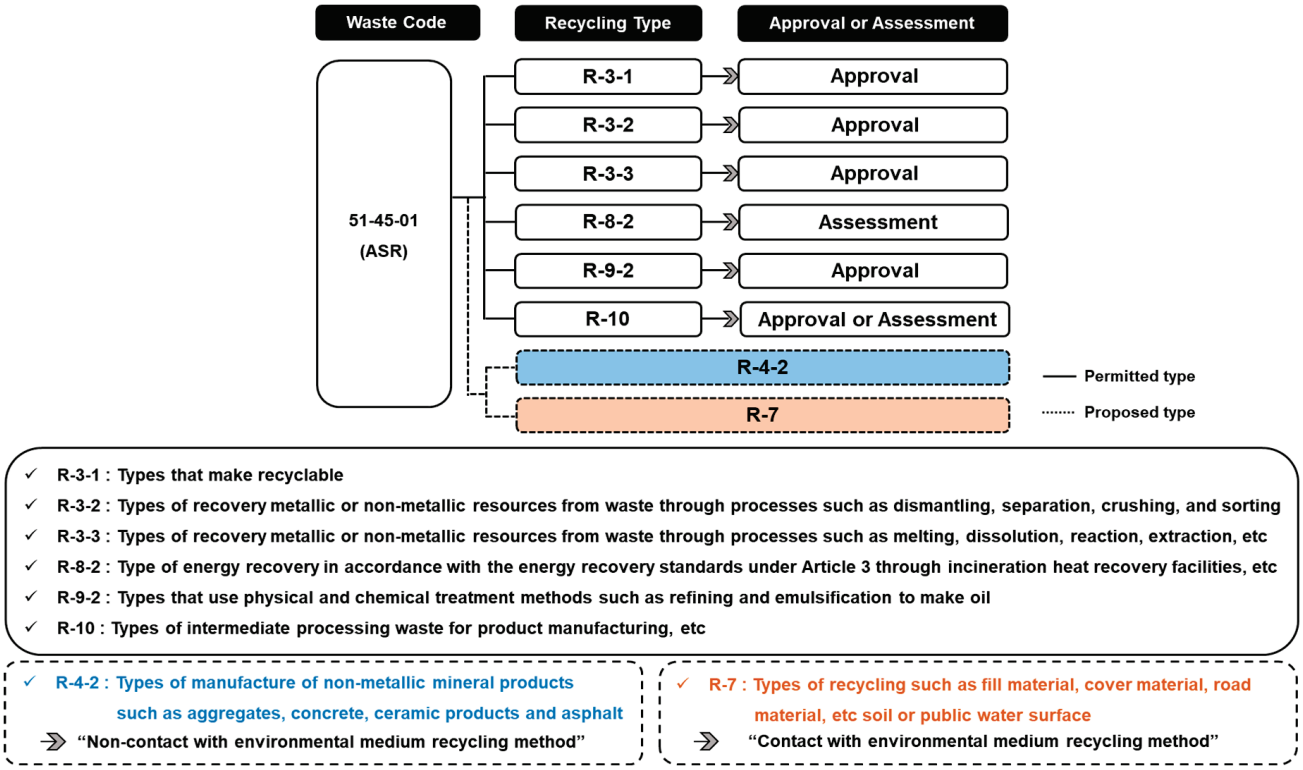


Figure 1. Classification of automobile shredder residues (ASR) and recyclable types.

2.2. Sampling and Analysis of Material Characteristics

The ASR used in this study was obtained from a shredding company in Korea, and it was composed of heavy fluff, light fluff, and glass/soil. The company compresses car bodies using a wrecker and selects materials that can be recycled. The selected materials were placed into a 660 HP pre-shredder and a 4000 HP main shredder for shredding, and light fluff (foam, dust etc.), which is a relatively light material, is separated from the materials crushed through the main shredder using a cyclone. The remaining residues are separated and recovered as iron scrap and nonferrous scrap through a separator. As for the final residue, Al, Zn, and Cu are finally discharged as heavy fluff and glass/soil through a trommel screen. Sampling was performed once per hour over three days for each ASR type.

In this study, the ASRMS generated as residue in a study by Yoo et al., 2022, which performed energy recovery by applying gasification technology to ASR, was used. The energy recovery potential of ASR was confirmed through previous studies. In connection to this, an attempt was made to examine the possibility of material recycling along with energy recovery. There is a possibility that impurities such as organic substances may be present in the ASR. Therefore, the ASR melting slag temperature condition was sufficiently reacted at 1000 °C to control the impurties and ensure the homogeneity of the melting slag. The ASRMS was generated by a melting process in a pilot plant with a capacity of 3 ton/day.

To evaluate the recyclability of the ASRMS, its physical and chemical properties and hazards were analysed. The density and water absorption ratios of the ASRMS were analysed in accordance with Korean Standard KS F 2503 [12]. In this instance, the water absorption ratio can be expressed as the ratio between the weight before drying and the weight after drying. It was measured using Equation (1):

$$\text{a } (\%) = \frac{m_1 - m_2}{m_1} \times 100 \quad (1)$$

where a: water absorption ratio (%), m_1: weight before drying (g), m_2: weight after drying (g).

In the gasification and melting system, the flow of the melt is an important factor for a reduction in the energy consumption of the melting furnace and the efficient and continuous discharge of slag. Therefore, X-ray diffraction (XRD) and X-ray fluorescence (XRF) analyses were conducted to evaluate the flow of the melt. The amorphous degree was analysed using XRD. Basicity, which affects the flow of the melt of the slag, was calculated using XRF results. Basicity is calculated using the ratio between CaO and SiO_2 (CaO/SiO_2), and when it is close to 1.0, the flow of the melt is considered excellent.

In addition, various heavy metals, such as Cd, Pb, and Hg, are used in bearing cells, indicator lamps, and batteries during automobile manufacturing. Heavy metal components in the ASRMS are not likely to be eluted because they are melted at high temperatures and are composed of stable oxides. Depending on the operating conditions, heavy metals in some of the ASRMS can be eluted because they are not completely combined with the slag and exist in the form of elements or oxides. Therefore, heavy metal contents in ASR-slag and eluate were analysed using inductively coupled plasma-optical emission spectrometry (ICP-OES) (Table 1).

Table 1. Analytical instruments and methods.

Material	Analysis	Instrument	Method
	Density	Electronics densimeter MD-300S, Alfa Mirage	KS F 2503
	XRD	X-pert Pro, PNanlytical	ASTM E 82
	XRF	EDX-720, Shimadzu	ASTM D 5381
	Heavy metal	ICP-OES 720ES, Varian	US EPA Method M-3050B
	Leaching test		ES 06150. d

2.3. Manufacturing Bricks

Four types of products (interlocking, clay and LSC bricks, and APA) were manufactured using ASRMS, and the recyclability of each product was evaluated. The interlocking brick involves a simple paving method and it can be permanently used due to its wear resistance and lack of distortion after construction. It can also be used as a flooring material for many purposes, such as roads, pavements, and squares, due to its diversity in shape, size, and colour. It is commonly used because no special technology or heavy equipment is required for installation [13]. Clay brick is commonly used as an insulation/refractory material and a paving material due to its excellent heat storage and sound absorption capabilities. Brick that is manufactured by mixing and forming various wastes, including sludge and zeolite, as main raw materials and firing the mixture at 1150 °C or higher is referred to as LSC. LSC is used in many fields, such as architecture, civil engineering, and ship building, due to its low density and high durability. Finally, the recyclability of ASRMS as APA was evaluated. In some countries, a large quantity of ASRMS has been commercialised as an aggregate for asphalt and a material for pavement blocks [14,15]. The recycling of ASRMS as an aggregate for concrete or asphalt is based on its characteristics [16]. Each type of brick was manufactured by varying the mix proportions of raw materials and ASRMS. A schematic diagram of the process of manufacturing bricks is presented in Figure 2. In addition, the particle size distribution of sand and stone powder used in general bricks is 0.6~5.0 mm, and 1.2~10.0 mm, respectively. In order to replace ASRMS with aggregates, the size of the substitute sand was specified as 0.5~5.0 mm, according to the KS standard [17].

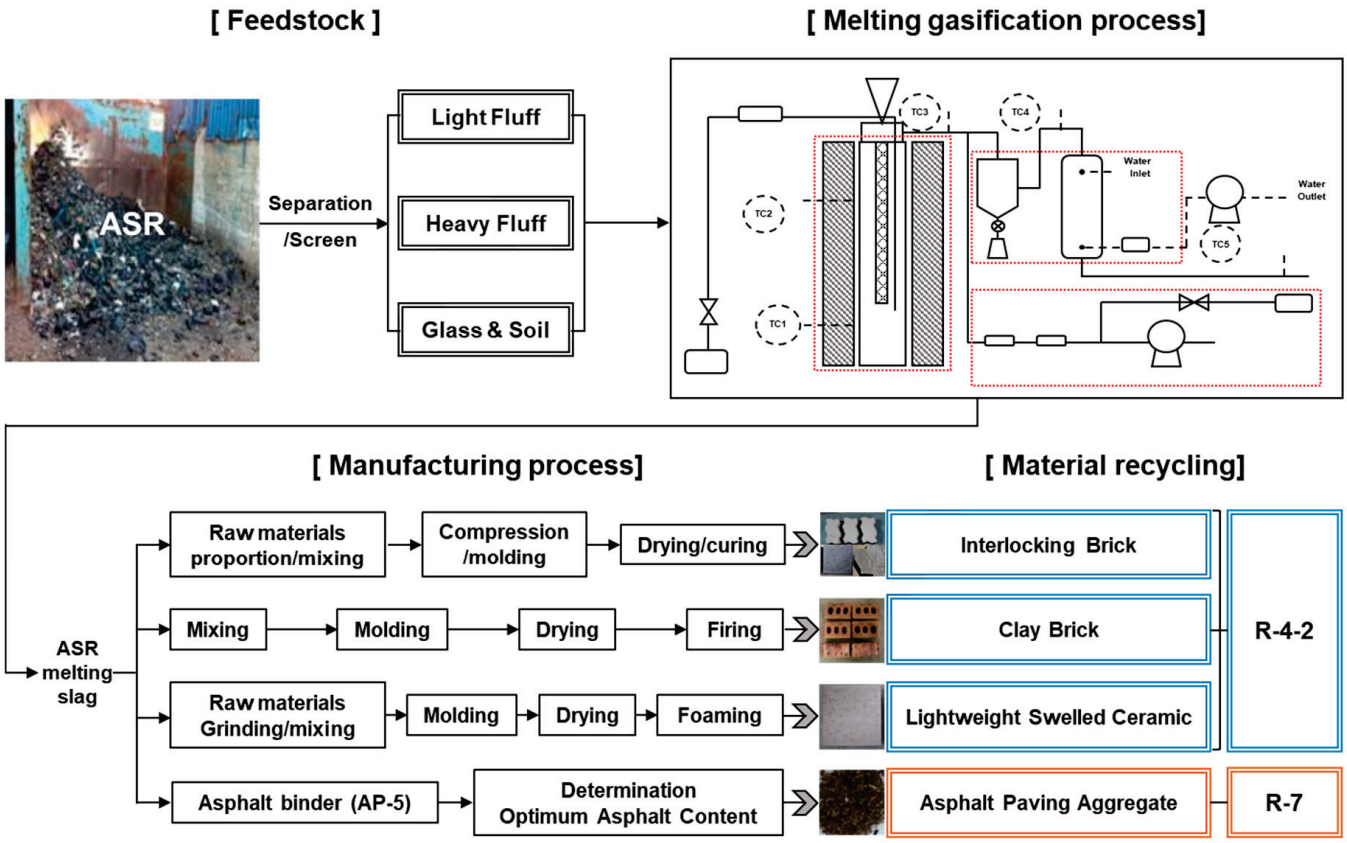


Figure 2. Manufacturing process of bricks.

2.3.1. Interlocking Brick

The interlocking brick was manufactured by proportioning raw materials, mixing, compression and moulding, and drying and curing. (Figure 3) The bricks were maintained at 20 °C in a separate drying room to maintain room temperature during the drying process. Three types (U and I types [220 L × 110 W × 60 H mm] and G type [260 L × 190 W × 80 H mm]) of bricks were manufactured. The mix proportions of ASRMS, sand, and stone powder were varied considering the size distribution of raw materials and brick type. The water/cement ratio was limited to <25%, in accordance with the Korean Standard (KS) 4419 [18]. The standard mix proportion for interlocking bricks was 50% sand and 50% stone powder. In this study, ASRMS was added to replace sand and stone powder and its proportions were 10, 20, 30, and 40%. U-type bricks were manufactured by reducing sand and stone powder by 5% each with the increase in the proportion of ASRMS. G-type bricks were manufactured by reducing stone powder from 40 to 10%, and the proportion of sand was fixed at 50% in accordance with the standard. In the case of I-type bricks, the proportion of stone powder followed the standard, and the proportion of sand was reduced from 40 to 30, 20, and 10%. Considering each factor, 12 variations of bricks were manufactured, that is, three types of bricks under four conditions, as summarised in Table 2. The appearance and size of bricks were examined. The bending strength and water absorption ratio were evaluated in accordance with KS F 4419.

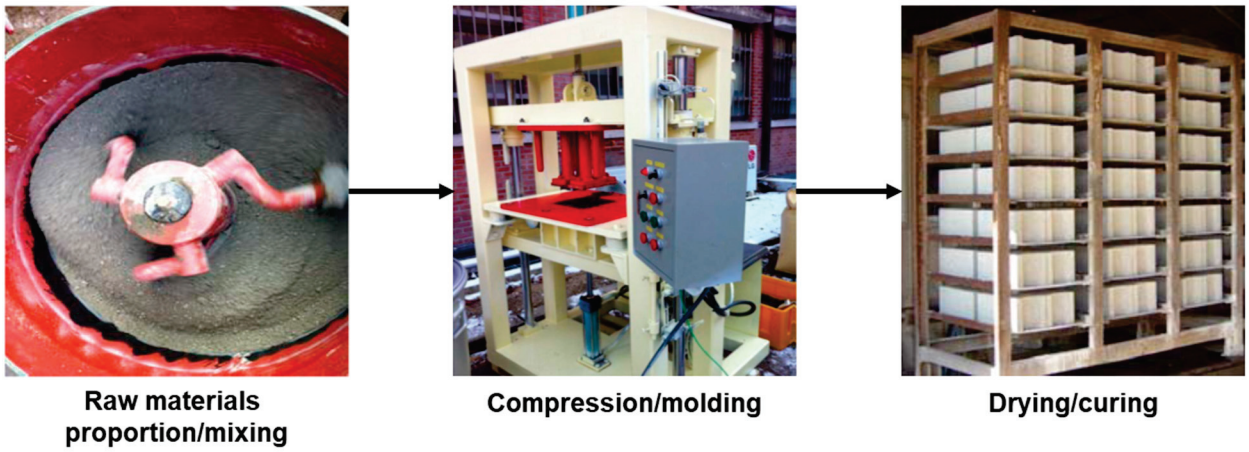


Figure 3. Manufacturing process of interlocking brick.

Table 2. Mix proportions of cement and aggregates for manufacturing interlocking bricks.

(Unit: %)

	Cement	Aggregate			Water/Cement	Standard (KS F 4419)
		ASRMS	Sand	Stone Powder		
Standard	25.0	0.0	50.0	50.0	20.0	Bending strength: ≥5 MPa Water absorption ratio: ≤10%
U-1		10.0	45.0	45.0		
U-2		20.0	40.0	40.0		
U-3		30.0	35.0	35.0		
U-4		40.0	30.0	30.0		
G-1		10.0	50.0	40.0		
G-2		20.0	50.0	30.0		
G-3		30.0	50.0	20.0		
G-4		40.0	50.0	10.0		
I-1		10.0	40.0	50.0		
I-2		20.0	30.0	50.0		
I-3		30.0	20.0	50.0		
I-4		40.0	10.0	50.0		

2.3.2. Clay Brick

The clay brick was manufactured through the process of mixing (hopper and roll mill), moulding, drying, and firing. KS L 4201 clay brick was manufactured using kaolin 50%, feldspar 20%, and clay 30% [19] (Figure 4). In this study, ASRMS was injected as a substitute for kaolin and feldspar, and clay bricks were manufactured by varying the proportions of ASRMS, kaolin, feldspar, and clay. The proportion of clay was fixed at 30%, whereas the proportion of ASRMS was increased to 5, 10, 15, and 20%. K-1 to K-4 bricks were manufactured by reducing the proportions of kaolin and feldspar by 2.5%. The F-1 to F-4 bricks were manufactured by reducing the proportion of feldspar by 5% without changing the proportion of kaolin. In the case of A-1 to A-4 bricks, the proportion of kaolin was reduced by 5% and that of feldspar was fixed at 20%. Table 3 summarises the conditions of clay brick manufacturing. Raw materials were pulverised to under 200 mesh, and 12 types of clay bricks were manufactured at a size of 190 L × 90 W × 60 H mm. The appearance and size of clay bricks were examined, and the compressive strength and water absorption ratio were evaluated in accordance with KS L 4201.

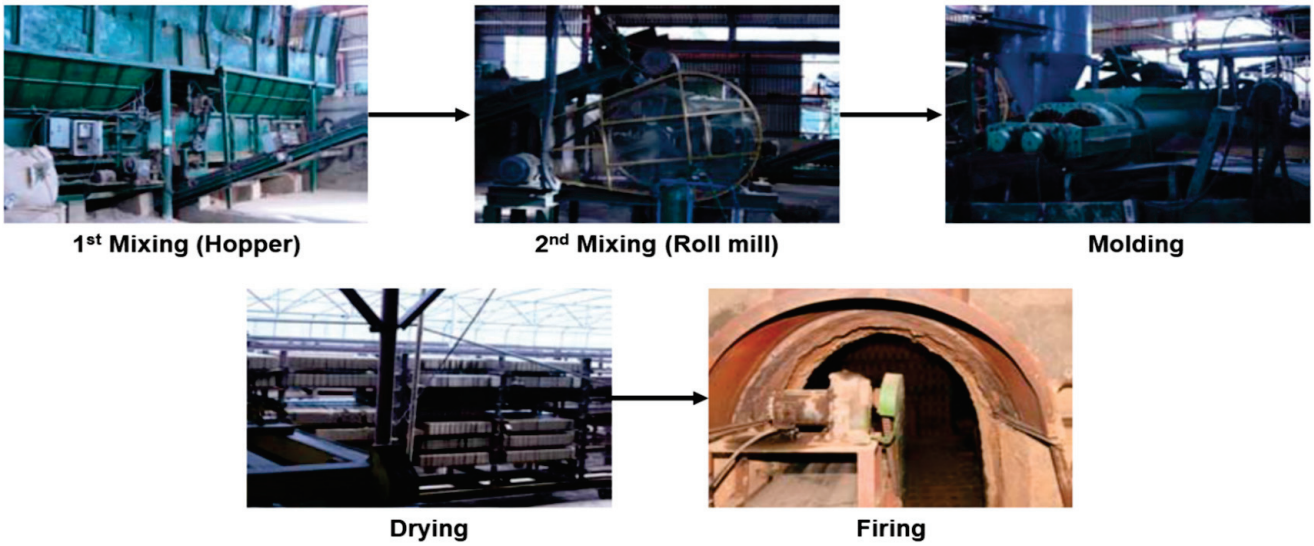


Figure 4. Manufacturing process of clay brick.

Table 3. Mix proportions of aggregates for manufacturing clay brick.

(Unit: %)

	ASRMS	Kaolin	Feldspar	Clay	Standard (KS L 4201)
Standard	0.0	50.0	20.0	30.0	Compressive strength : ≥24.50 MPa Water absorption ratio : ≤10%
K-1	5.0	47.5	17.5		
K-2	10.0	45.0	15.0		
K-3	15.0	42.5	12.5		
K-4	20.0	40.0	10.0		
F-1	5.0	50.0	15.0		
F-2	10.0	50.0	10.0		
F-3	15.0	50.0	5.0		
F-4	20.0	50.0	0.0		
A-1	5.0	45.0	20.0		
A-2	10.0	40.0	20.0		
A-3	15.0	35.0	20.0		
A-4	20.0	30.0	20.0		

2.3.3. Lightweight Swelled Ceramic Brick

LSC brick was manufactured using ASRMS (20%), automotive glass (70%), and zeolite (10%) through a process of raw material grinding and mixing, moulding, firing, and foaming at 1150 °C or higher (Figure 5). The particle sizes of automotive glass, ASRMS, and zeolite were 150, 200, and 325 mesh, respectively. In the process of manufacturing bricks, 5% NaOH solution was mixed to a level of 8% of the total raw material weight to achieve a lower firing temperature. In addition, $CaCO_3$ was mixed as the foaming agent at 1.5% of the total raw material weight to create pores to assist the escape of CO_2 generated in the firing point. A total of 500 pieces of bricks were manufactured for 25 days at a rate of 20 pieces/day with a size of 350 L × 350 W ×70 H mm. The specific gravity and compressive strength of the LSC bricks were evaluated in accordance with KS L 8551 [20]. However, in the case of LSC, an evaluation of appearance and size was not performed because the bricks were prepared in accordance with the KS specifications during the

foaming process. The mix proportions of materials used for manufacturing LSC bricks are provided in Table 4.

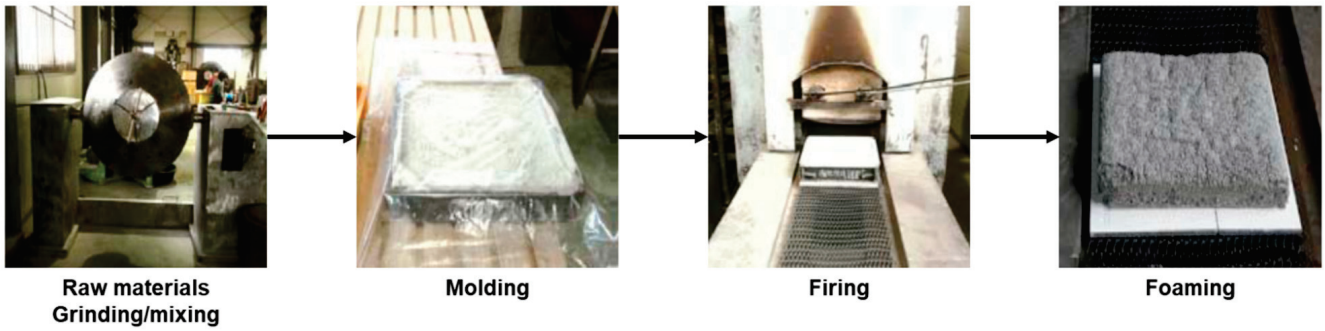


Figure 5. Manufacturing process of lightweight swelled ceramic brick.

Table 4. Mix proportions of raw materials used for manufacturing lightweight swelled ceramic bricks.

	Material	Mixing Ratio	Size	Standard (K)
Raw material	ASRMS	20%	<150 mesh	Specific gravity: 0.45–0.55 Compressive strength : 294.20 N/cm^2
	Automotive glass	70%	<200 mesh	
	Zeolite	10%	<325 mesh	
Foaming agent	$CaCO_3$	1.5% of total raw material	<200 mesh	
Mixing solution	5% NaOH solution	8% of total raw material	-	

2.3.4. Asphalt Paving Aggregate

The asphalt binder used in Korea is classified into ten types, according to the domestic market. The asphalt binder used in this study (AP-5) has excellent durability against plastic deformation with relatively low construction costs compared to AP-3, which is commonly used in Korea [21]. The quality of AP-5 was evaluated for the use of ASRMS as a road fill material. Table 5 summarises the quality evaluation items and criteria for APA.

To evaluate the recyclability of ASRMS as APA, an experiment was performed by adding ASRMS into the asphalt mixture. The asphalt mixture types were compared based on Wearing Course (WC)-1, comprising of a 13 mm grinding mixture. The mixture in which 10% ASRMS was added to WC-1 was compared with that of WC-1. After 75 double-sided compactions, specimens with 0 and 10% ASRMS were cured using a mould for one day. The Marshal test was conducted to determine the optimum asphalt content (OAC) of the heated asphalt mixture and evaluate its quality. OAC influences Marshall stability, flow value, air void, saturation, and density.

Specimens were prepared using the maximum asphalt content in the OAC range obtained through mix design, and the indirect tensile strength, recovery modulus of elasticity, and wheel tracking test were performed in accordance with ASTM D4867. The relative strength was estimated using the AASHTO TP 31-94 method by conducting the recovery modulus of an elasticity test under temperature conditions of 5, 25, and 40 °C. The properties of asphalt binder (AP-5) are shown in Table 5.

Table 5. Properties of asphalt binder (AP-5).

Quality Evaluation			Standard	Method
Properties of asphalt binder (AP-5)				
Penetration (25 °C)			60–80	KS M 2252 [22]
Flash point (25 °C)			≥260	KS M 2010 [23]
Elongation (15 °C, cm)			≥100	KS M 2254 [24]
Thin firm heating	Mass change ratio (%)		≤0.6	KS M 2258 [25]
	Penetrate index residue ratio (%)		60–80	
Toluene solubility			≥99.0	KS M 2256 [26]
Softening point (°C)			44.0–52.0	KS M 2250 [27]
Penetrate index ratio after vaporisation testing (%)			≤110	KS M 2001 [28]
Elongation after heat on thin-firm			≥100	KS M 2254 [24]
Density (15 °C, g/cm^3)			≥1.000	KS M ISO3657 [29]
Asphalt paving mixture				
Marshall test		Stability (N)	≥7500	SPS-KAI0002-F2349-5687 [30]
		Flow value	20–40	
Air void (%)			3–6	
Saturation (%)			65–80	
Indirect tensile strength test (kg$_f$/cm^2)			-	
Resilient modulus (MPs)			-	
Wheel tracking test		Dynamic stability (time/mm)	≥2500	
		Strain (mm/min)	≤0.0300	

3. Results and Discussion

3.1. Characteristics of ASRMS

Evaluation of the Quality of ASRMS as an Aggregate

Density and water absorption ratios were analysed in accordance with the Korean Standard KS F 2503 test method, and the applicability of ASRMS as an aggregate was assessed. The results satisfied the quality standard for recycled coarse aggregate with a density of 2.24 g/cm^3 and a water absorption ratio of 0.34% [31], indicating that it is appropriate to use the ASRMS obtained in this study as an aggregate for manufacturing bricks.

XRD analysis showed amorphous particles (Figure 6), indicating that during slow cooling, dense particles have adequate time to combine with each other, whereas low density particles float to the surface. Results of XRF analysis results show that the CaO and SiO_2 proportions were 31.34 and 31.09%, respectively. Based on this, the flow rate affecting the fluidity of the melt was evaluated. The fluidity of the melt is an important factor in relation to equipment operating efficiency. The flow rate is considered good as the basicity (CaO/SiO_2) gets closer to 1.0. The basicity of the ASRMS generated in this study was calculated as approximately 1.01, thereby confirming that its flow rate was excellent. Therefore, when ASR is used as feedstock, efficient equipment operation is expected, leading to continuous operation owing to the fluidity of the melt. Basicity, which affects the flow of the melts was evaluated, but pH and alkalinity were not evaluated. In addition to the operation of equipment, proportions of SiO_2 (31.09%) and Al_2O_3 (19.58%) were high (approximately 50%). The materials used as aggregates in the bricks manufactured in this study, such as sand, kaolin, and feldspar, mainly consist of SiO_2 and Al_2O_3; therefore, ASRMS is an appropriate substitute to these as an aggregate. The results of XRF analysis of ASR are presented in Table 6.

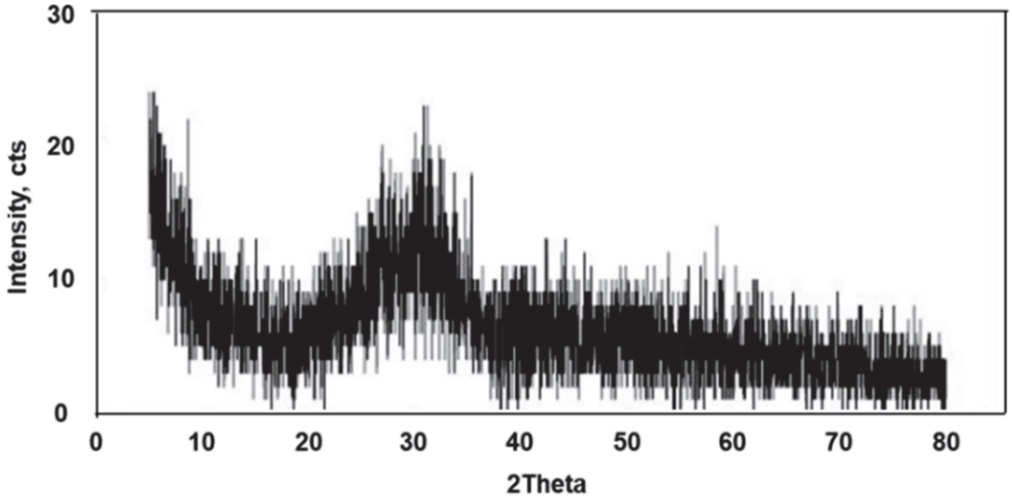


Figure 6. X-ray diffraction pattern of automobile shredder residues melting slag.

Table 6. Results of XRF analysis of automobile shredder residues.

								(Unit: %)
Analyte	CaO	SiO_2	Al_2O_3	Fe_2O_3	MgO	TiO_2	BaO	Others
	31.34	31.09	19.58	6.97	3.60	1.87	1.51	4.04

3.2. Evaluation of Environmental Performance of Raw Materials

The heavy metals contained in ASRMS were analysed in accordance with the US EPA Method M-3050B. ASRMS had high concentrations of Fe, Al and Cr and low concentrations of Hg, As, Pb, and Cd. Heavy metal concentration is managed through the Soil Environment Conservation Act in Korea [32]. Heavy metals are not likely to be released into the environment during automobile manufacturing because they are contained in ASRMS as stable oxides during the melting process; however, some heavy metals can be eluted as they exist in the form of elements or oxides. Therefore, leaching tests of ASRMS were performed to evaluate its usefulness in recycling and landfilling. Results show that all measured potential pollutants satisfied the Korean standards. Results of heavy metal analysis suggest that recycling ASRMS in the form of bricks is an eco-friendly alternative.

However, some metal components, including Fe, had high concentrations, probably because of the compositions of heavy and light fluff, which are the main components of ASR. Although results of previous studies showed that each fluff is mainly composed of organic components, it appears that metal components were concentrated in the ASRMS through the melting process. Overall, conformance to the soil contamination standard was satisfied, but concerns over unregulated substances (e.g., Mo) remain. Therefore, 'medium non-contact type' recycling that does not directly come into contact with soil, such as aggregate manufacturing and recovery processes for valuable metals, are more appropriate. In particular, in the case of valuable metal recovery, the continuity of the process, waste supply stability, and economic feasibility must be secured. Therefore, this study focused on the assessment of the applicability of product manufacturing and product quality standards rather than the recovery of raw materials during material recycling. Results of the analyses of heavy metals obtained through leaching are presented in Table 7 [33].

Table 7. Results of analyses of heavy metals obtained through leaching.

Element	Concentration (mg/kg)	Leaching Test (mg/L)	
		Korean Standard	Concentration
Pb	4.75	3.0	0.31
Cu	798.77	1.0	0.30
As	1.72	1.5	0.03
Hg	0.03	0.005	N.D.
Cd	2.98	0.3	0.02
Cr^{6+}	N.D.	1.5	N.D.
Cr	7000.98	-	0.04
Zn	20.73	-	0.43
Al	109,320.83	-	N.D.
Fe	178,234.25	-	0.10
Co	13.72	-	N.D.
Mn	1751.18	-	N.D.
Mo	14.94	-	N.D.
Ni	94.81	-	N.D.
Others *	-	-	N.D.

* Se, organic P, TCE (trichloroethylene), PCE (perchloroethylene), PCBs (polychlorinated biphenyl). N.D.: not detected.

4. Evaluation of Product Quality

4.1. Interlocking Brick

4.1.1. Appearance and Size

The thickness and size of each interlocking brick was measured in accordance with the KS F 4419 standard. Ten interlocking bricks per condition were used for the measurements. Dimensional tolerances of ± 2 mm for width and ± 3 mm for length are prescribed by the standard. The measured bricks had dimensional tolerances of ± 2 mm for width and length and -2 to -1 mm for thickness, thus satisfying the requirements of the standard. Cracks and pitting were not observed on the surface of the interlocking bricks, and they were suitable for construction.

4.1.2. Bending Strength and Water Absorption Ratio

The KS F 4419 method was used for analysis and 10 interlocking bricks per condition were tested. The bending strength was 7.8 to 8.4, 7.2 to 8.2, and 7.0 to 8.2 MPa for the U-, G-, and I-type bricks, respectively, which were above the minimum of 5 MPa specified in KS F 4419. Cement is the binder, and the bending strength of a brick increases as the cement content increases. The lower the cement content, the higher the economic feasibility. High compressive strength achieved using a small quantity of cement is an efficient brick production method. Therefore, under the same cement content, replacing sand or stone powder with ASRMS as much as possible can lead to better economic feasibility and recycling in manufacturing bricks.

The water absorption ratio was 2.2 to 2.9, 2.4 to 3.1, and 2.4 to 3.4% for the U-, G-, and I-type bricks, which satisfied the maximum permissible water absorption ratio of 10% specified in KS F 4419 (Figure 7). Because ASRMS cannot function as a binder, the experiment was conducted with a fixed ratio of cement. When the ASRMS content increased, the water absorption ratio decreased slightly, indicating that ASRMS contributes to improving the water absorption ratio. This suggests that the water absorption ratio of ASRMS is lower than that of sand and stone powder. The long-term use of interlocking bricks is possible as the lower water absorption ratio increases durability.

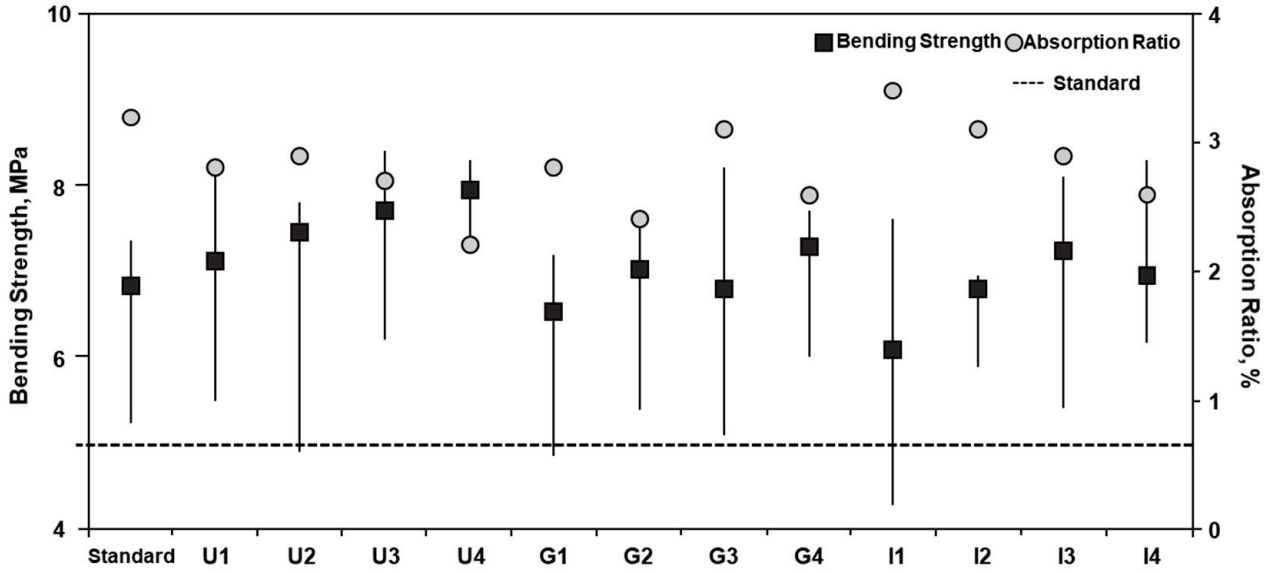


Figure 7. Bending strength and water absorption ratio of interlocking bricks.

4.2. Clay Brick

4.2.1. Appearance and Size

The quality of clay bricks was evaluated based on the KS L 4201 standard, which specifies dimensional tolerances of ±5.0, ±3.0, and ±2.5 mm for length, width, and height, respectively. In addition, the appearance must be without cracks and faults. The measured dimensional tolerances of clay bricks were 0 to +4 mm, 0 to +3 mm, and −1 to +2 mm for length, width, and height, respectively. The increase in the ASRMS content in the mix resulted in dimensions larger than that of the mould. The dimensions and appearance of all the bricks satisfied the standard.

4.2.2. Compressive Strength and Water Absorption Ratio

In order to prevent defects such as cracks that affect the strength and durability of clay brick, KS 4201 has established a standard for the compressive strength for clay bricks and evaluates their quality. Therefore, the compressive strength was evaluated along with the absorption ratio to assess the quality of the clay bricks produced in this study. The compressive strength of the clay bricks ranged from 22.8 to 46.0 MPa, which met the minimum of 22.54 MPa prescribed by the standard (Figure 8). When the contents of ASRMS in the mix were 5 and 10%, higher compressive strengths were observed and were comparable to that specified by the standard; however, when ASRMS content increased to 15 and 20%, compressive strengths were below the standard specification. It appears that the compressive strength decreased as the proportion of ASRMS increased during the firing process because the binding with other raw materials decreased. The compressive strength decreased with changes in the particle size of ASRMS. The compressive strength improved when ASRMS substituted for 10% of feldspar and kaolin rather than only feldspar. When the proportion of ASR was low and kaolin was high, the compressive strength was high. The SiO_2/Al_2O_3 ratio obtained from the XRF analysis suggests that ASR had a similar ratio (1.59) to that of kaolin (1.57) compared to feldspar (2.37) [34].

The water absorption ratio ranged from 0.224 to 2.445%, which met the criterion of the standard (Figure 8). As the density of bricks increases, the water absorption ratio decreases and compressive strength increases; however, this depends on the proportions of raw materials used.

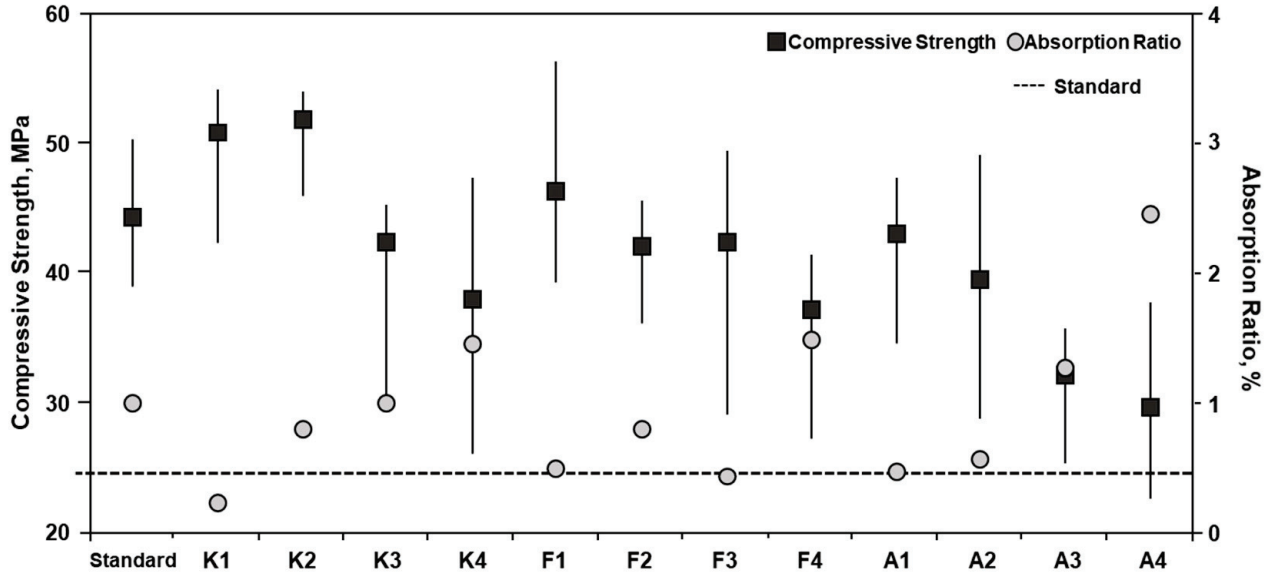


Figure 8. Compressive strength and water absorption ratio of clay bricks.

4.3. Lightweight Swelled Ceramic Brick

Specific Gravity and Compressive Strength

The qualities of ten LSC bricks manufactured using ASRMS were evaluated in accordance with KS F 8551, which specifies a specific gravity of 0.45–0.55 and a minimum compressive strength of 294.20 N/cm^2. The specific gravity of LSC bricks ranged from 0.379 to 0.504, indicating that some bricks exhibited values lower than the specified criterion. The average specific gravity of all the bricks was 0.453, which satisfied the standard requirement. The compressive strength of the LSC bricks was 339.7–373.6 N/cm^2 with an average of 364.0 N/cm^2, which satisfied the standard requirement. Compressive strength and specific gravity had the same tendency. Therefore, LSC bricks are suitable for recycling ASRMS as they are lightweight and strong (Figure 9).

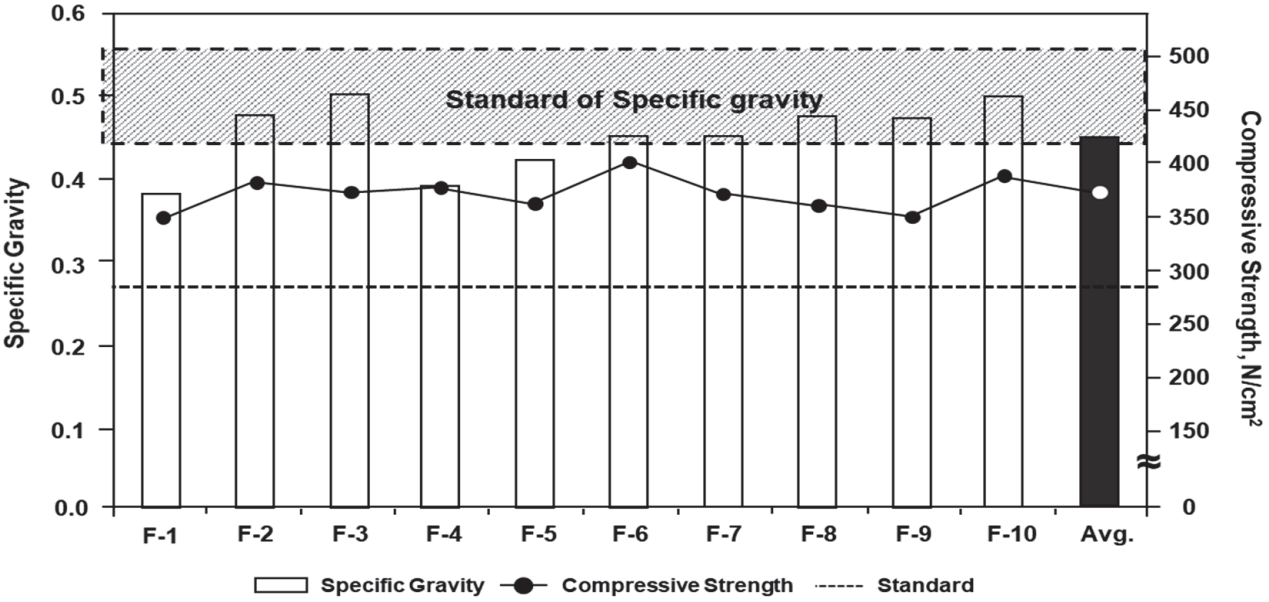


Figure 9. Compressive strength and specific gravity of lightweight swelled ceramic bricks.

4.4. Asphalt Paving Aggregate

4.4.1. Physical Characteristics of ASRMS for Use as Aggregate

After melting and gasification, the melting slag produced after cooling has a particle size of ≤5 mm. However, the ASRMS used in this study, as shown in Figure 10, had a particle size of <1.2 mm and did not satisfy the required size distribution for use as fine aggregate. Therefore, to recycle the ASRMS used in this study as fine aggregate, a pre-treatment process is required.

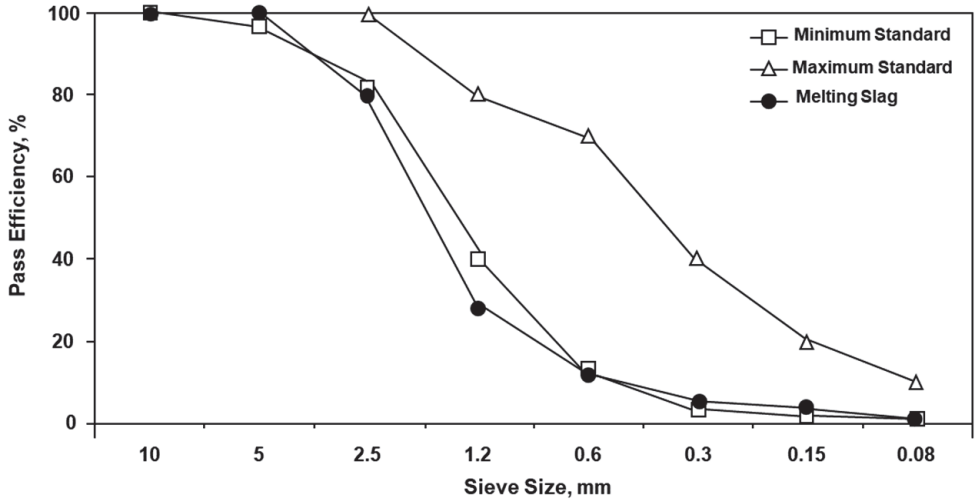


Figure 10. Size distribution of automobile shredder residues melting slag for use as fine aggregate.

The properties of aggregate were analysed after the size distribution analysis, and the results are summarised in Table 8. The asphalt binder used in this experiment satisfied all the requirements of the standard. Therefore, the ASRMS generated in this study is suitable for use as a road filling material.

Table 8. Properties of asphalt binder.

Quality Evaluation		Standard	This Study
Penetration (25 °C)		60–80	74
Flash point (25 °C)		≥260	336
Elongation (15 °C, cm)		≥100	150
Thin firm heating	Mass change ratio (%)	≤0.6	0.04
	Penetration index residue ratio (%)	60–80	77
Toluene solubility		≥99.0	99.85
Softening point (°C)		44–52	49.50
Penetration index ratio after vaporisation testing (%)		≤110	96
Elongation after heat on thin-firm		≥100	102
Density (15 °C, g/cm^3)		≥1.000	1.048

4.4.2. Optimum Asphalt Content

OAC is determined through Marshall stability, flow value, porous ratio, degree of saturation, and density tests. WC-1 must satisfy a stability of 7,500 N or higher, a flow value of 20 to 40, an air void of 3 to 6%, and a degree of saturation of 65 to 80%. Results of the Marshall stability test for the specimen mixed with 0% of ASRMS show that the stability and flow value criteria were satisfied when the asphalt content ranged from 4.0 to

6.0%. In the case of air void and saturation, the criteria were met when the asphalt content ranged from 4.5 to 6.0%. Therefore, the OAC of 0% of ASRMS ranges from 4.7 to 5.5%.

The stability and flow values of the specimen prepared by adding 10% of ASRMS met the standard criteria when the asphalt content ranged from 4.0 to 6.0%, which was similar to that of 0% ASRMS. Air void met the criterion when the asphalt content ranged from 4.5 to 5.5%, and saturation met the criterion when it ranged from 4.0 to 6.0%. Results show that the OAC of 10% ASRMS was from 4.3 to 5.0%. Compared to 0% of ASRMS, the values were reduced by approximately 0.5% when it was 10%. The factor that has the largest impact on OAC is saturation, and this tendency appears to have occurred because the saturation range of the mixture with an ASRMS content of 10% was reduced compared to the mixture with 0%. The results of the mix design with 0 and 10% ASRMS are shown in Figure 11.

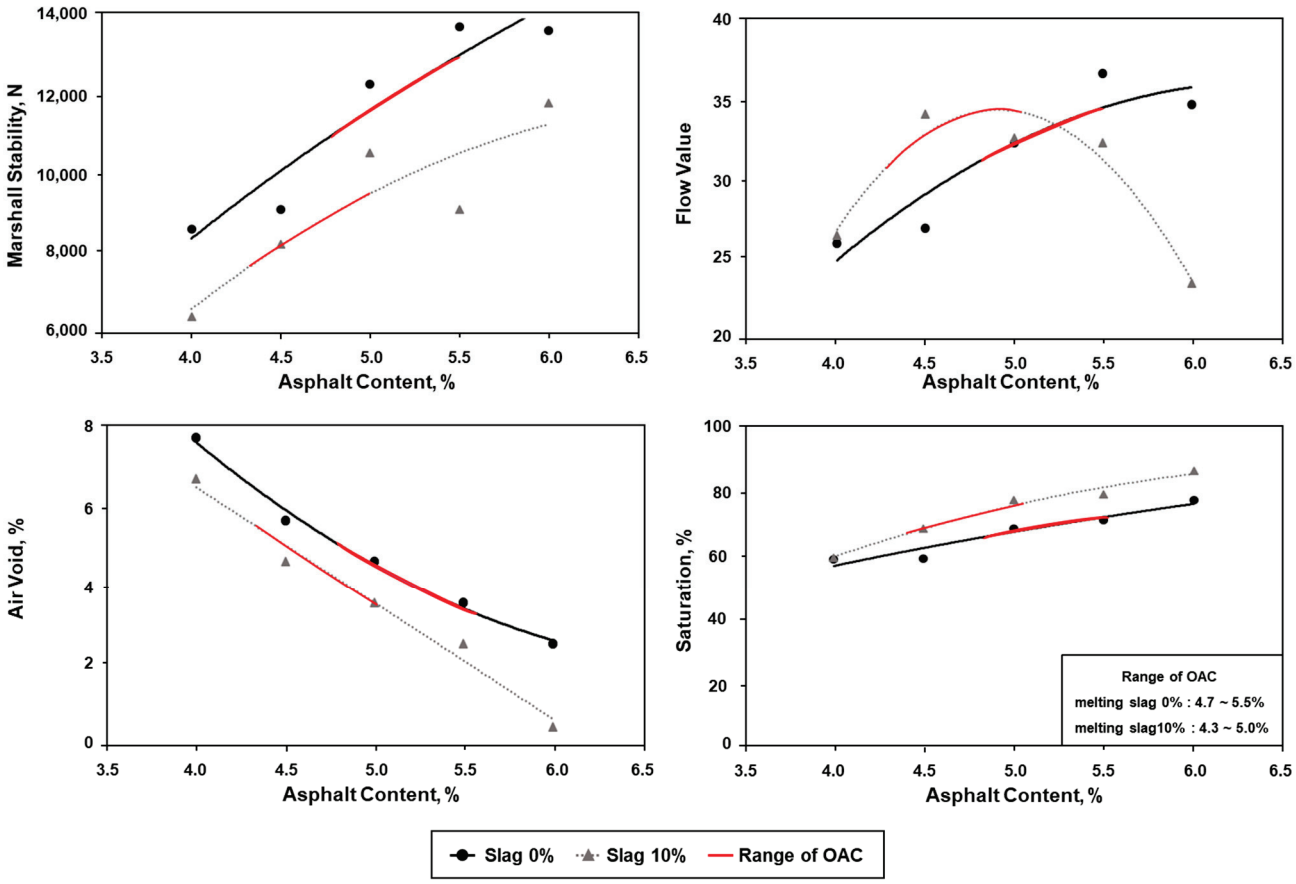


Figure 11. Results of asphalt paving mixtures and ranges of optimum asphalt content (OAC).

The specimen with an ASRMS content of 10% exhibited a high indirect tensile strength value (Table 9). This appears to be because the mixture manufactured by adding ASRMS is superior to typical asphalt mixtures in terms of low-temperature cracking. The results of the recovery modulus of the elasticity test on the 10% ASRMS specimen satisfied the values required for typical mixtures. Therefore, the domestic asphalt mixture exceeded the stability range based on the standard according to the Marshall test; however, results of the wheel tracking test confirmed that the plastic deformation was slightly weak. However, the cold cracking was excellent, especially the relative strength of the recovery modulus of elasticity, which was higher than those of general asphalt mixtures.

Table 9. Results of quality test of asphalt paving mixture with varying automobile shredder residues melting slag (ASRMS) contents.

	Indirect Tensile Strength	Resilient Modulus (MPa) 5 °C/25 °C/40 °C	Wheel Tracking Test	
			Stability (Time/mm)	Strain (mm/min)
ASRMS 0% (Asphalt content 5.5%)	8.76	11,644/1926/1144	2916.7	0.0144
ASRMS 10% (Asphalt content 5.0%)	11.35	13,944/2986/1423	2451.4	0.0171
Standard	-	-	≥2500	≤0.0300

4.5. Final Technical Evaluation for Feasibility of Material Recycling

A technical evaluation of the bricks manufactured in this study was performed by evaluating the following four items with 100 points as a perfect score: ASR waste usage (25 points), quality standard satisfaction (25 points), market size (25 points), and demand prediction (25 points). In addition, the assessment results were derived for each evaluation item based on 25 points (excellent), 20 points (good), 15 points (moderate), and 10 points (insufficient). The assessment was performed to evaluate and predict material recycling according to the technical possibility and market size, and the environmental performance and energy consumption already mentioned above were excluded.

The ASR waste usage was evaluated by calculating the quantity of ASRMS used per manufactured brick volume. The analysis results of this study were utilised for the quality standard satisfaction item, and the market size was evaluated using the production statistics of the manufacturing industry [35]. The demand prediction item was evaluated by comparing current prices with prices in 2015 under the assumption that the demand for materials that can replace the existing aggregate will increase due to an increase in brick manufacturing costs and thus an increase in demand for bricks that use ASRMS [36]. In the evaluation results, APA, which is expected to have a large market size and high demand despite a low ASR waste usage, achieved the highest score, followed by interlocking bricks, clay bricks, and LSC bricks. In particular, interlocking bricks received a high score as they are expected to be able to treat a large quantity of waste, but they received a low score for the demand prediction item because the increase in raw material cost is not significant. Overall, clay bricks showed simple results. In the case of LSC, the lowest score was given because the market size was found to be quite small despite its excellent waste usage. Table 10 summarises the results of evaluating each brick. Overall, material recycling using ASRMS is possible; however, an efficient energy recovery process is required because significant energy consumption is expected until the discharge of the ASRMS. Further research on this issue will benefit the environment and related industries.

Currently, the world is in the process of establishing a management system to avoid simple landfills and promote recycling, and Korea needs to transition to a circular-economic society that reduces waste generation and minimizes the use of natural resources and energy. A circular economy is one that can ensure that natural resources are replaced, secured and reinvested in economic activities. If inputs are efficiently utilized within production facilities, circular resources can be secured from waste products and can reduce the amount of natural resource imports. Korea is a resource- and energy-dependent country, importing over 96% of its energy and 90% its mineral resources from abroad. Therefore, the consumption of natural resources can be reduced if valuable metals or useful resources are recovered by replacing natural raw materials or appropriately recycling them as natural aggregate substitutes or concrete additives after safe treatment. In addition, the environmental impact can be significantly reduced through the reduction of greenhouse gases and the removal of harmful substances [37].

Table 10. Technical evaluation for the possibility of material recycling using automobile shredder residues melting slag (ASRMS).

(Unit: point)

Item	Interlocking Brick	Clay Brick	Lightweight Swelled Ceramic Brick	Asphalt
ASR waste usage	20	15	25	15
Quality standard satisfaction	25	15	10	25
Market size	20	15	10	25
Demand prediction	15	20	10	25
SUM	80	65	55	90
Rank	2	3	4	1

5. Conclusions

This study attempted to recycle ASRMS as an aggregate for the manufacturing of four products including interlocking, clay, and lightweight swelled ceramic bricks and asphalt paving aggregate. The eco-friendly recyclability of ASRMS was evaluated through analyses of heavy metals and leaching, and appropriate quality evaluations were performed for each product. The recycling possibility of ASRMs was confirmed based on the results of this study, and the following conclusions were drawn.

1. The ASRMS used in this study had a density of 2.24 g/cm^2, a water absorption ratio of 0.34%, and a basicity of 1.01, thereby exhibiting its applicability as an aggregate. Trace quantities of Pb, Cu, As, and Cd were detected in the leaching test, but they satisfied the leaching test criteria of Korea, indicating that the ASRMS is suitable for recycling as an aggregate.
2. ASRMS substituted for sand and stone powder as an aggregate in the manufacturing of interlocking brick. Quality evaluation of interlocking brick according to KS F 4419 in terms of appearance, size, bending strength, and water absorption ratio was satisfactory. As ASRMS content increased, absorption decreased and bending strength increased. The bending strength was $\geq$5.0 MPa. Therefore, a large quantity of ASR can be recycled in brick production with profits for the manufacturer due to a reduction in raw material costs.
3. Clay brick was manufactured by replacing kaolin and feldspar with ASRMS to an extent of 20%. The quality evaluation of clay bricks according to KS L 4201 in terms of appearance, size, compressive strength, and water absorption ratio was satisfactory. However, the quality of clay bricks manufactured with >15% ASRMS was not better than that of the standard clay brick.
4. A lightweight swelled ceramic brick was manufactured using ASRMS, zeolite, and other materials. The quality of the manufactured bricks was evaluated in accordance with KS 8551. Because all the manufactured bricks met the required criteria, manufacturing them is an appropriate recycling method for ASRMS. However, the consumption of a large quantity of ASR is unlikely for LSC because its usage is low compared to that of other bricks. It is expected that ASRMS can be utilised in many fields because it can be manufactured in various forms. Therefore, the material recycling method using ASRMS is an appropriate treatment method with many environmental benefits.
5. To utilise ASRMS as APA for road fill materials, the particle size distribution and characteristics of the aggregate were analysed, and the OAC was obtained. The standard requirements were met for most particle size ranges, indicating that the ASRMS can be used as an aggregate. Experimental results for asphalt paving mixture with ASRMS content show that the OAC was from 4.7 to 5.5% at an ASRMS content of

0% and from 4.3 to 5.0% at an ASRMS content of 10%. As a large quantity of ASRMS can be used for asphalt manufacturing, it would be an excellent eco-friendly option.

6. The products manufactured in this study were evaluated for recyclability in terms of waste usage, conformance to quality standards, market size, and demand prediction. Results show that APA achieved the highest rank, followed by interlocking, clay, and LSC bricks. Thus, the recyclability of ASRMS was confirmed. If this technology is continuously developed through further research, it would have positive effects on the environment and industries owing to its waste treatment and recycling potential accompanied by the lowering of the cost of raw materials.

Author Contributions: Writing—original draft, preparation, S.-J.C. (Soo-Jin Cho); Writing—review and editing, H.-N.J.; Formal analysis and conceptualization, S.-J.C. (Sung-Jin Cho); Methodology, Y.-S.Y.; Project administration and Validation, H.-M.Y. All authors have read and agreed to the published version of the manuscript.

Funding: This study was supported by the National Institute of Environmental Research, funded by the Ministry of Environment (NIER-2022-01-01-050).

Institutional Review Board Statement: The study was conducted in accordance with the Declaration of Korea, and approved by the Institutional Review Board of NATIONAL INSTITUTE OF ENVIRONMENTAL RESEACH (protocol code 22696 and date of approval).

Informed Consent Statement: Not applicable.

Data Availability Statement: Informed consent was obtained from all subjects involved in the study.

Conflicts of Interest: The authors declare no conflict of interest.

Abbreviations

Asphalt Paving Aggregate; APA, Automobile Shredder Residues; ASR, Automobile Shredder Residues Melting Slag; ASRMS, End-of-Life Vehicles; ELVs, Inductively coupled plasma-optical emission spectrometry; ICP-OES, Korea Standard; KS, Lightweight Swelled Ceramic; LSC, Wearing Course; WC, X-Ray Diffraction; XRD, X-Ray Fluorescence; XRF.

References

1. Korea Statistical Information Service, Automobile Production. 2021. Available online: https://kosis.kr/statHtml/statHtml.do?orgId=101&tblId=DT_2KAA511 (accessed on 3 January 2023).
2. Ministry of Environment, The Ministry of Environment to Extend Its Vehicle Scrappage—Subsidy Program to Grade 4 Diesel Vehicles from 2023. 2022. Available online: http://m.me.go.kr/eng/web/board/read.do?menuId=461&boardMasterId=522&boardId=1543110 (accessed on 3 January 2023).
3. Korea Auto Dismantlement Recycling Association, Scrapping Statistics 2021. 2022. Available online: http://www.kadra.or.kr/kadra/contents/sub02/02_01.html?idx_num=2515&pidx_num=&skin=4&mode=view&GotoPage=1&column=&keyword=&BbsId_01=&BbsId_02=&BbsId_03=&MenuNum=&BbsId=2010316112316&Tbn=&srhData1= (accessed on 3 January 2023).
4. Korea Environment Corporation, National Waste Generation and Disposal Status 2020. 2021. Available online: https://www.allbaro.or.kr (accessed on 3 January 2023).
5. EUR-Lex, Directive 2000/53/EC- End of Life Vehicles. 2000. Available online: http://data.europa.eu/eli/dir/2000/53/oj (accessed on 3 January 2023).
6. Ministry of Environment, Act on Resource Circulation of Electrical and Electronic Equipment and Vehicles. 2022. Available online: https://www.law.go.kr (accessed on 3 January 2023).
7. National Institute of Environment Research. *A Study on Life Cycle Assessment of Plastic Waste Recycling (III)—ELV and WEEE Plastic Waste*; Korean Government Report; National Institute of Environment Research: Incheon, Republic of Korea, 2021.
8. Yoo, H.M.; Lee, S.Y.; Cho, S.J.; Seo, Y.C.; Jang, H.N. Evaluation of the Melting Gasification Process for Recovery of Energy and Resources from Automobile Shredder Residues. *Energies* **2022**, *15*, 1248. [CrossRef]
9. Ministry of Environment. *Development of Intergrated System for Recovering Valuable Metals and Energy from ASR*; Korean Government Report; Ministry of Environment: Sejong, Republic of Korea, 2014.
10. Ministry of Environment, Waste Control Act. 2022. Available online: https://www.law.go.kr/%EB%B2%95%EB%A0%B9/%ED%8F%90%EA%B8%B0%EB%AC%BC%EA%B4%80%EB%A6%AC%EB%B2%95 (accessed on 3 January 2023).

11. Ministry of Environment. *Environmental Assessment Recycling Manual*; Korean Government Report; Ministry of Environment: Sejong, Republic of Korea, 2019.
12. *KS F 2503*; Testing Method for Density and 107 Absorption of Coarse Aggregate. Korea Agency for Technology and Standard: Seoul, Republic of Korea, 2019.
13. Shi, T.; Zhang, X.; Hao, H.; Chen, C. Experimental and numerical investigation on the compressive properties of interlocking blocks. *Eng. Struct.* **2021**, *228*, 111561. [CrossRef]
14. Ketov, A.; Rudakova, L.; Vaisman, I.; Ketov, I.; Haritonovs, V.; Sahmenko, G. Recycling of rice husks ash for thepreparation of resistant, lightweight and environment-friendly fired bricks. *Constr. Build. Mater.* **2021**, *302*, 124385. [CrossRef]
15. Skaf, M.; Manso, J.M.; Aragón, Á.; Fuente-Alonso, J.A. EAF slag in asphalt mixes: A brief review of its possible re-use. *Resour. Conserv. Recycl.* **2017**, *120*, 176–185. [CrossRef]
16. Cho, S.J.; Joung, H.T.; Jung, H.Y.; Yoo, H.M.; Seo, Y.C. Recyclability evaluation of melting slag as asphalt paving aggregates. *J. KSWM* **2012**, *29*, 113–120.
17. Yoo, H.M.; Lee, J.S.; Yang, W.S.; Park, J.K.; Park, S.W.; Han, B.H.; Cho, S.J.; Kim, M.H.; Seo, Y.C. Recyclability evaluation of waste CRT glass as a concrete brick aggregate. *J. KSWM* **2013**, *30*, 78–85. [CrossRef]
18. *KS F 4419*; Concrete Interlocking Block for Sidewalk and Road. Korea Agency for Technology and Standard: Maengdong-myeon, Republic of Korea, 2022. Available online: https://standard.go.kr/KSCI/standardIntro/getStandardSearchList.do (accessed on 3 January 2023).
19. *KS L 4201*; Clay Brick. Korea Agency for Technology and Standard: Maengdong-myeon, Republic of Korea, 2020. Available online: https://standard.go.kr/KSCI/standardIntro/getStandardSearchList.do (accessed on 3 January 2023).
20. *KS L 8551*; Lightweight Swelled Ceramic Block. Korea Agency for Technology and Standard: Maengdong-myeon, Republic of Korea, 2017. Available online: https://standard.go.kr/KSCI/standardIntro/getStandardSearchList.do (accessed on 3 January 2023).
21. Korea Institute of Civil Engineering and Building Technology, Guidelines for Desinging Asphalt Mixtures. 2005. Available online: https://www.codil.or.kr/viewDtlConWrkDtlSch.do?gubun=tch&pMetaCode=CIGCTG510028 (accessed on 3 January 2023).
22. *KS M 2252*; Testing Method for Penetrating of Bituminous Materials. Agency for Technology and Standard: Maengdong-myeon, Republic of Korea, 2017. Available online: https://standard.go.kr/KSCI/standardIntro/getStandardSearchList.do (accessed on 3 January 2023).
23. *KS M2010*; Testing Methods for Flash Point of Crude Oil and Petroleum Products-Determination of Flash Point-Tag Closed Cup Method. Korea Agency for Technology and Standard: Maengdong-myeon, Republic of Korea, 2017. Available online: https://standard.go.kr/KSCI/standardIntro/getStandardSearchList.do (accessed on 3 January 2023).
24. *KS M 2254*; Testing Method for Ductility of Bituminous Materials. Korea Agency for Technology and Standard: Maengdong-myeon, Republic of Korea, 2017. Available online: https://standard.go.kr/KSCI/standardIntro/getStandardSearchList.do (accessed on 3 January 2023).
25. *KS M 2258*; Testing Method for Effect of Heat on Thin-Film of Asphaltic Materials. Korea Agency for Technology and Standard: Maengdong-myeon, Republic of Korea, 2017. Available online: https://standard.go.kr/KSCI/standardIntro/getStandardSearchList.do (accessed on 3 January 2023).
26. *KS M 2256*; Testing Method for Solubility of Bituminous Materials in Trichloroethane. Korea Agency for Technology and Standard: Maengdong-myeon, Republic of Korea, 2017. Available online: https://standard.go.kr/KSCI/standardIntro/getStandardSearchList.do (accessed on 3 January 2023).
27. *KS M 2250*; Petroleum Product-Testing Method for Softening Point of Bituminous Materials (Ring and Ball Method). Korea Agency for Technology and Standard: Maengdong-myeon, Republic of Korea, 2019. Available online: https://standard.go.kr/KSCI/standardIntro/getStandardSearchList.do (accessed on 3 January 2023).
28. *KS M 2001*; Method of Sampling Crude Oil and Petroleum Products. Korea Agency for Technology and Standard: Maengdong-myeon, Republic of Korea, 2020. Available online: https://standard.go.kr/KSCI/standardIntro/getStandardSearchList.do (accessed on 3 January 2023).
29. *KS M ISO3657*; Crude Petroleum and Liquid Petroleum Product-Laboratory Determination of Density—Hydrometer Method. Korea Agency for Technology and Standard: Maengdong-myeon, Republic of Korea, 2017. Available online: https://standard.go.kr/KSCI/standardIntro/getStandardSearchList.do (accessed on 3 January 2023).
30. *SPS-KAI0002-F2349-5687*; Hot Mix Asphalt Mixture. Korea Agency for Technology and Standard: Maengdong-myeon, Republic of Korea, 2018. Available online: https://standard.go.kr/KSCI/standardIntro/getStandardSearchList.do (accessed on 3 January 2023).
31. Korea Institute of Civil Engineering and Building Technology, Quality Standard for Recycled Aggregate. 2021. Available online: https://www.law.go.kr (accessed on 3 January 2023).
32. Ministry of Environment, Soil Environment Conservation Act. 2020. Available online: https://www.law.go.kr (accessed on 3 January 2023).
33. Ministry of Environment, Enforcement Rule of Waste Control Act. 2022. Available online: https://www.law.go.kr/%EB%B2%95%EB%A0%B9/%ED%8F%90%EA%B8%B0%EB%AC%BC%EA%B4%80%EB%A6%AC%EB%B2%95%20%EC%8B%9C%ED%96%89%EA%B7%9C%EC%B9%99 (accessed on 3 January 2023).

34. Lee, J.S.; Yoo, H.M.; Yang, W.S.; Park, J.K.; Cho, S.J.; Kim, B.S.; Seo, Y.C. A study on clay brick manufacturing with powders of CRT glass waste. *J. KSWM* **2021**, *30*, 86. [CrossRef]
35. Korea Statistical Information Service, Number of Establishments, Gross Output, Value of Shipments and Year-End Invertory by Product. 2020. Available online: https://kostat.go.kr/wnsearch/search.jsp (accessed on 3 January 2023).
36. Korea Statistical Information Service, Producer Price Index. 2022. Available online: https://url.kr/3c1qhi (accessed on 3 January 2023).
37. National Institute of Environmental Research. *Study on Management of Industrial Waste for Alternative Resource of Natural Materials (III)*; Korea Government Report; National Institute of Environmental Research: Incheon, Republic of Korea, 2015.

Disclaimer/Publisher's Note: The statements, opinions and data contained in all publications are solely those of the individual author(s) and contributor(s) and not of MDPI and/or the editor(s). MDPI and/or the editor(s) disclaim responsibility for any injury to people or property resulting from any ideas, methods, instructions or products referred to in the content.

applied sciences

MDPI

Article

Vibration Performance of Steel Fiber Concrete Tunnel Lining by Adjacent Tunnel Blasting Construction

Li-Ming Wu [1,2,3], Zi-Jian Wang [3,4], Yong-Zai Chang [4,*], Feng Gao [1], Bin Zhang [4], Yi Wu [4] and Han-Xiu Fan [5]

[1] School of Civil Engineering, Chongqing Jiaotong University, Chongqing 400074, China
[2] School of Urban Construction Engineering, Chongqing Technology and Business Institute, Chongqing 400052, China
[3] Chongqing Municipal Key Laboratory of Geology and Disaster Reduction for Mountainous Highway, Waterway and Transportation, Chongqing Jiaotong University, Chongqing 400074, China
[4] School of Civil Engineering and Architecture, Chongqing University of Science & Technology, Chongqing 401331, China
[5] The 5th Engineering Ltd. of China Railway Construction Corporation 11 Group, Chongqing 400037, China
* Correspondence: changyongzai0825@163.com

Abstract: When constructing tunnels in mountainous areas, the drilling and blasting method is the most commonly used because of its economy. Ordinary reinforced concrete itself has defects such as poor crack resistance and brittleness. Therefore, when using the drilling and blasting method for ordinary reinforced concrete double-line tunnels, vibration phenomena will occur and cause cracks in the first-line tunnels, which will have adverse effects on the durability and safety of the tunnel. As a response, scholars have proposed the use of steel fiber-reinforced concrete as tunnel lining. In this paper, the LS-DYNA software is used to establish three models of plain concrete, ordinary concrete, and steel fiber-reinforced concrete, and numerical analysis is conducted with different amounts of explosives. The results show that the steel fiber-reinforced concrete tunnel lining has better performance than the other two concretes in tunnel construction.

Keywords: drilling and blasting tunneling method; double-line tunnel; steel fiber-reinforced concrete tunnel lining; vibration phenomenon; numerical analysis

1. Introduction

Western China is experiencing an increase in railways, highways and other transportation facilities with the adoption of western development policies. Due to the geographical characteristics of the region, the construction of these facilities will inevitably lead to cross tunnels and parallel tunnels with small clearance and other situations. At present, the most widely used is the New Austrian Tunneling Method (NATM), in which blasting construction will inevitably affect the safety and usability of the advance tunnel. Therefore, the research team analyzed the impact of blasting shock and vibration on the adjacent steel fiber tunnel lining through numerical simulation [1–3].

Remarkable results have been made on the blasting construction of nearby tunnels. Qi and Liu [4] studied the mechanical properties of fiber-reinforced concrete shield segments, and obtained that the bending, yield, and ultimate bending moment of the segments with fiber are significantly higher than those of ordinary segments under the same reinforcement ratio. Xu et al. [5] simulated the pure steel fiber segment of a hard rock tunnel through FLAC3D, and conducted field tests in Qingdao Metro Line 1. The result showed that the pure steel fiber concrete segment has better crack resistance, and it is feasible to replace steel. He et al. [6] also adopted FLAC3D in Hangzhou Metro Line 5 to analyze the blasting vibration in the excavation of small clear-distance tunnels to the support of the adjacent tunnel in an urban area. In the Aiminshan Tunnel in Dandong, Liaoning Province, Wang et al. [7] used ANSYS to analyze the seismic impact of blasting excavation

on the surface and concluded that the cavity effect caused the excavated surface to vibrate more quickly than the unexcavated surface. Zhang et al. [8] adopted field monitoring and software simulation to study the influence of blasting from the rear tunnel on the structural optimization of the secondary lining of the advance tunnel under soft and broken surrounding rocks in the Xinmin Tunnel. Pan et al. [9] used the numerical model to analyze the construction sequence, the time and method of secondary lining in three parallel tunnels with the middle one constructed first, as well as the impact of blasting the tunnels on both sides of the secondary lining of the middle tunnel in the parallel section of the Sunjiawan Tunnel 1 on the Yongzhou Highway and the Niupilingxia Tunnel on the Yongzhou Railway. Wang et al. [10] studied the dynamic response characteristics of the blasting from the adjacent tunnel on the lining structure at the intersection of the first tunnel in the intersection of the Wuwu high-speed railway tunnel and Xizengshan highway tunnel, and concluded that the arch shoulder and crown of the first tunnel are sensitive to blasting stress, and that close attention should be paid during construction. Wu and Ren [11] used ABAQUS to study the stress response of the first tunnel to the blasting of the rear tunnel in the small clear-distance tunnel, and concluded that the inner arch waist and the foot are most affected and deserve further observation. Guo et al. [12] used LS-DYNA and field tests to study the rule of tunnel failure under the blasting load of adjacent tunnels with different spacings, and obtained the form of the failure and the location of the crack. Mao [13] observed the on-site expansion project of the Fuzhou Mawei Tunnel, and studied the attenuation characteristics of the velocity of the vibration energy under multiple cavities. Chen et al. [14] tested on site the in situ expansion project of the Jinjishan Tunnel on the Second Ring Road in Fuzhou, Fujian Province, and concluded that in the blasting construction, the number of explosives used in the cut hole should be appropriately reduced, and increased in the wide slot hole and auxiliary hole. Ding et al. [15] studied the influence of blasting construction on the 33-story frame structure at Exit A of the Xizhen of Qingdao Metro Line 1, and the result is a reference for the protection of high-rise buildings during urban blasting construction. By employing on-site monitoring, Wu et al. [16] investigated the law of vibration in the unique stratum of the upper soft and lower hard, and confirmed the viability of numerical simulation for engineering blasting. Bao et al. [17] studied the impact of blasting on surrounding rocks in the seepage area of the tunnel ahead through on-site monitoring and numerical simulation, and concluded that the arch waist has the maximum vibration velocity, the excavation of the lower bench has greater destructive force than that of the upper bench under the same spacing, and the minimum safety clearance is D (D is the tunnel span). Guan et al. [18] first summarized the development stage of failure evolution based on the field data, then used LS-DYNA to determine the vibration response and failure mode of the temporary middle wall under different explosive amounts and blasting distances. Zhou et al. [19] studied the impact of blasting in the adjacent tunnel on the initial support and lining of the ultra-small distance tunnel based on the Jiuwuji tunnel blasting project in Guizhou Province, and the result showed that the main frequency distribution of the initial support and lining is very wide and the vibration is diverse, within 200 Hz. Zhang et al. [20], by monitoring particles on the lining of the tunnel, studied the influence of blasting on the tunnel, and concluded that the peak particle velocity generated is always caused by the cutting hole blasting. Wu et al. [21] through field monitoring and simulation by FLAC3D, analyzed the influence of blasting of a new tunnel on the operating tunnel, and concluded that the vibration velocity of the arch in the blasting surface of the existing tunnel is larger, and the blasting will have an impact on a moving train. Fang et al. [22] carried out research on the Qiandouquan Tunnel project by adopting single-layer and double-layer p blasting schemes, and found that the double-layer presplitting blasting can reduce the vibration speed better by comparison. By tracking and analyzing the field particle vibration velocity through numerical simulation in the Nanjing Metro's ultra-small clear-distance tunnel project, Zhu et al. [23] discovered that the vibration velocity of the side wall of the tunnel is greater than that of the arch foot. Moreover, the closer the blasting point, the greater the

vibration velocity. Cui et al. [24] studied the improvement of the energy performance of subway tunnels using steel fiber-reinforced concrete lining to enhance shallow geothermal energy. They found that the thermal conductivity of the steel fiber-reinforced concrete lining is better than that of ordinary concrete lining with advantages in heat exchange and cooling operation. Hosseini et al. [25] studied the use of glass fiber-reinforced polymer (GFRP) to reinforce high-strength concrete lining segments, and found that the segments with GFRP have bending and shear strength, but with little effect on the lining segments after cracking.

In summary, there is little research on the impact of small-spacing tunnel blasting construction on adjacent steel fiber tunnel linings. Some scholars have found that steel fiber-reinforced concrete lining has significant improvements in bending moment, yield moment, and ultimate moment compared with steel-reinforced concrete lining. The structural vibration velocity from blasting can be used as an indicator of the strength of the blasting vibration effect. The peak vibration velocity during blasting construction differs in tunnels, but the closer the blasting point, the greater the vibration velocity.

This paper uses LS-DYNA to establish three tunnel-lining models and simulates the impact of blasting construction on adjacent tunnel linings with different explosive amounts. The three types of tunnel linings are plain, ordinary reinforced, and steel fiber-reinforced concrete, and the explosive amounts are 14.4 kg, 18 kg, 21.6 kg, 25.2 kg, and 28.8 kg. The vibration response law of the adjacent tunnels in the three lining models under different explosive amounts is analyzed. Hopefully, the research results will provide a reference for future engineering design and tunnel construction.

2. Numerical Simulation

2.1. Tunnel Geometry

The geometric dimensions of double-track tunnels are the same: the net width of the building is 11.2 m, and the height limit is 7.94 m. The clear width of the inner contour is 9.48 m, and the clear height is 6.59 m. The excavation depth is 0.88 m. See Figure 1 for detailed layout information.

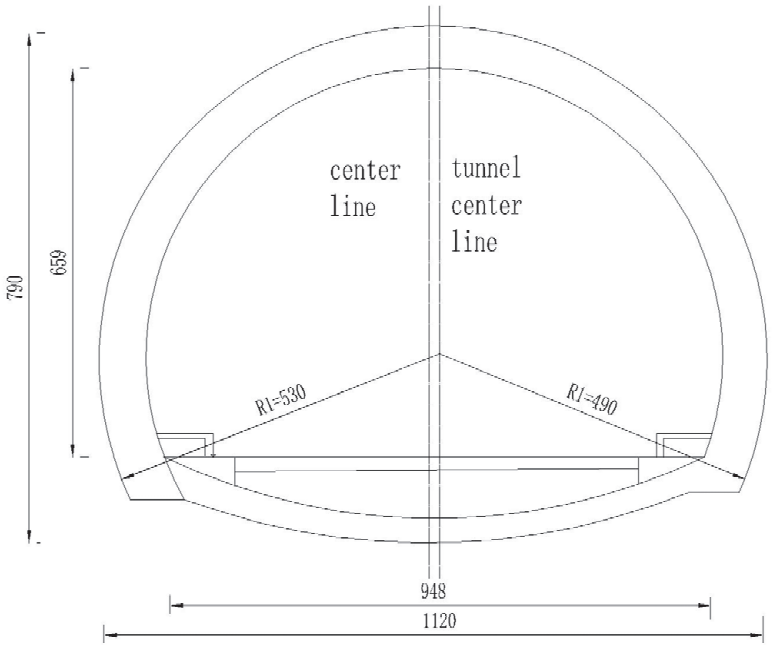


Figure 1. Layout of tunnel dimensions (unit: cm).

2.2. Establishment of Calculation Model

2.2.1. Constitutive Model of Surrounding Rock

The follow-up hardening material model is adopted for the surrounding rock, which is defined as *MAT_PLASTIC_KINEMATIC. This model describes the strengthening effect and strain rate change effect of materials, with the elastoplastic properties of the rock media considered. The yield condition is [26]:

$$\phi = \frac{1}{2}\xi_{ij}^2 - \frac{\sigma_y^2}{3} = 0 \tag{1}$$

where:

$$\xi_{ij} = s_{ij} - a_{ij} \tag{2}$$

$$\sigma_y = \left[1 + \left(\frac{\dot{\varepsilon}}{C}\right)^{\frac{1}{P}}\right]\left(\sigma_0 + \beta E_p \varepsilon_{eff}^p\right) \tag{3}$$

where: s_{ij} is the Cauchy stress tensor; P and C are input constants; σ_0 and β are initial yield stress and hardening parameter, respectively; $\dot{\varepsilon}$ is the strain rate; E_p is the plastic hardening model, where $E_p = \frac{E_r E}{E - E_r}$, E is the elastic modulus, E_r is tangent modulus; and ε_{eff}^p is the effective plastic strain.

The parameters of the surrounding rock are consistent with those tested, as shown in Table 1.

Table 1. Material parameters of tunnel surrounding rock.

Material	Uniaxial Compressive Strength (MPa)	Elasticity Modulus Ec (MPa)	Poisson's Ratio	Density ρ kg/m^3
Tunnel surrounding rock	22.2	4684	0.19	2450

2.2.2. Lining Strength Parameters

The strength parameters of the model are C30 concrete. When establishing the reinforced concrete lining model, plain and reinforced concrete are modeled, respectively. The parameters are shown in Tables 2–4.

Table 2. Strength parameters of plain concrete lining.

Material	Elasticity Modulus Ec (MPa)	Poisson's Ratio	Density ρ kg/m^3
Concrete lining	30,000	0.2	2360

Table 3. Strength parameters of reinforced concrete lining.

Material	Elasticity Modulus Ec (MPa)	Poisson's Ratio	Density ρ kg/m^3
Concrete lining	30,000	0.2	2360 kg/m^3
Rebar	210,000	0.3	1.58 kg/m

Table 4. Strength parameters of steel fiber-reinforced concrete lining.

Material	Elasticity Modulus Ec (MPa)	Poisson's Ratio	Density ρ kg/m^3
Steel fiber + concrete	34,900	0.15	2510

2.2.3. Explosive Material Model and Equation of State

Under detonation conditions, high-temperature and high-pressure gases will be generated in the structures. The composition of explosive products and various thermodynamic parameters at certain times are required to build the required equation of state through the mixing rule, but these required parameters are difficult to measure experimentally at present. Therefore, the semi-empirical equation of state (JWL) determined by experimental methods is used to describe the relationship between pressure P, volume V and temperature T. The JWL equation is shown in the following Formula [26].

$$\mathrm{p} = A(1 - \frac{\omega}{R_1 V})e^{-R_1 V} + B(1 - \frac{\omega}{R_2 V})e^{-R_2 V} + \frac{\omega E}{V} \tag{4}$$

$$\mathrm{p} = A(1 - \frac{\omega}{R_1 V})e^{-R_1 V} + B(1 - \frac{\omega}{R_2 V})e^{-R_2 V} + \frac{\omega E}{V} \tag{5}$$

Its isentropic equation is:

$$P_\mathrm{s} = A\exp(-R_1 V) + B\exp(-R_2 V) + CV^{-(\omega'+1)} \tag{6}$$

$$e_s = \frac{A}{R_1}\exp(-R_1 V) + \frac{B}{R_2}\exp(-R_2 V) + \frac{C}{\omega' V^{\omega'}} \tag{7}$$

where P is the pressure of the detonation product, V is the relative volume $V = \widetilde{v}/\widetilde{v}_0$, E is the initial internal energy of explosive per unit volume, A, B, R_1, R_2, ω are parameters of the JWL equation; and the subscript s represents an isentropic process. The specific values of each parameter of the JWL equation are shown in Table 5.

Table 5. Parameters of the JWL equation of state.

Explosive	Detonation Velocity/ms^{-1}	A/GPa	B/GPa	R_1	R_2	ω	E/GJm^{-3}
TNT	6930	3.737	3.747	4.15	0.95	0.35	6.0

The parameters above are based on TNT explosive.

2.2.4. Airy Material Model and Equation of State

The NULL model and the LINEAR_POLYNOMIAL equation are adopted, and the equation of state is:

$$P = C_0 + C_1\mu + C_2\mu^2 + C_3\mu^3 + (C_4 + C_5\mu + C_6\mu^2)E \tag{8}$$

$$\mu = \frac{1}{V} - 1 \tag{9}$$

where P is detonation pressure; E is internal energy per unit volume; and V is the relative volume. For the air model, the parameters of the polynomial equation of state are:

$$\begin{gathered} C_0 = C_1 = C_2 = C_3 = C_6 = 0 \\ C_4 = C_5 = 0.4 \end{gathered} \tag{10}$$

The air density is 1.225 kg/m^3, and the initial relative volume V_0 is 1.0.

2.3. Calculation Model

LS-DYNA is adopted for dynamic numerical simulation and calculation, and single-hole blasting is also adopted in consistency with the experiment [27–29]. The blasting point is located in the center of the tunnel face for simulation. Since the boundary size is small, in order to reduce the boundary effect and the impact caused by reflected waves, and ensure the accuracy of the calculation, the keyword *BOUNDARY_NON_REFLECTING is used to apply a non-reflective boundary at the lateral boundary of the calculation area to simulate the semi-infinite boundary of the site. The top surface is a free boundary, and the ground and all sides are normal constraints. Figure 2 depicts the 3D finite element model.

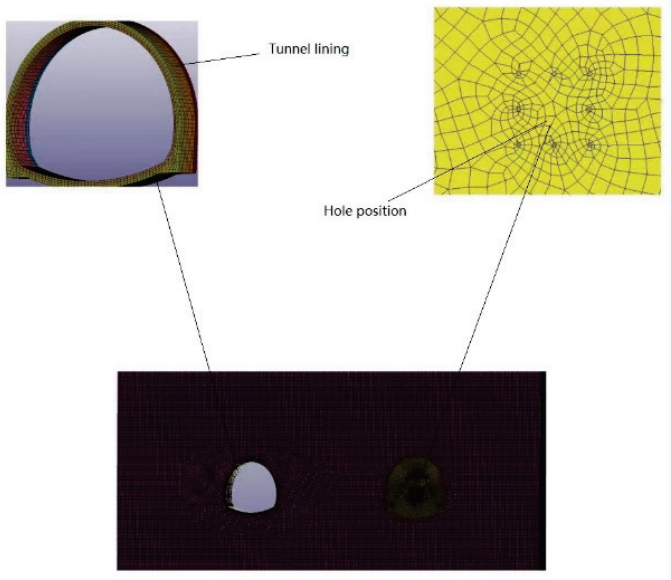


Figure 2. Three-dimensional finite element model.

3. Calculation Model Analysis

When mining tunnels, the impact on the neighboring tunnel is strongest when the highest amount of explosive is used in the cut hole [30–32]. Therefore, analysis is conducted on the impact of the cut hole blasting on the adjacent tunnel. In the three models, the length of each cutting hole is 1 m long, and the explosive amount is 1.8 kg. In each model, 8, 10, 12, 14 and 16 cutting holes are selected, respectively, so the explosive amount is 14.4 kg, 18 kg, 21.6 kg, 25.2 kg and 28.8 kg, accordingly. The monitoring points are at the left line, right arch waist, right wall, and right arch shoulder (lower). The layout of monitoring points is shown in Figure 3.

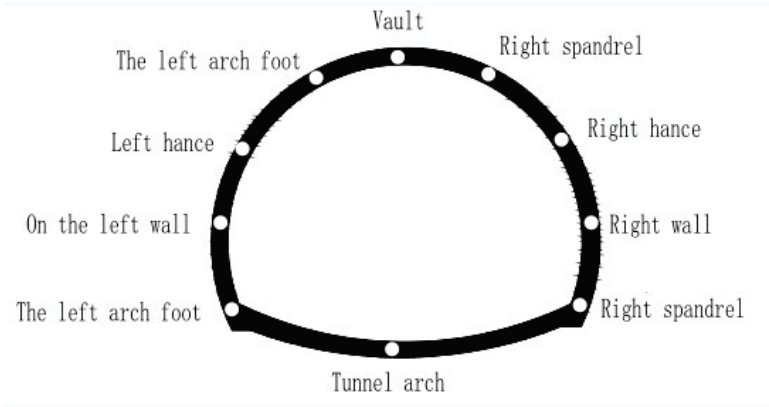


Figure 3. Layout of monitoring points on the left line.

3.1. Vibration Velocity Analysis of Plain Concrete Tunnel Lining

The analysis at each monitoring point is the comprehensive vibration velocity (the unit of vibration velocity is m/s, and the unit of time is s).

It can be seen from Figures 4–6 and Table 6 that: (1) In plain concrete lining, the peak values at each monitoring point increase with the explosive quantity, and the maximum peak values of the right wall, the right arch spandrel and the right arch waist all appear to be at the explosive amount of 28.8 kg, which are 0.00256 m/s, 0.00681 m/s and 0.0023 m/s, respectively, and the peak values all around 0.03 s. (2) Under different explosive quantities, each monitoring point's vibration law is relatively consistent. No matter how much explosive is used in the monitoring point, the right arch waist has the minimum peak, and the radius of the right arch spandrel is small. The right arch spandrel with the largest peak stress concentration suggests that it is relatively weak during the blasting excavation operation, and has to be watched.

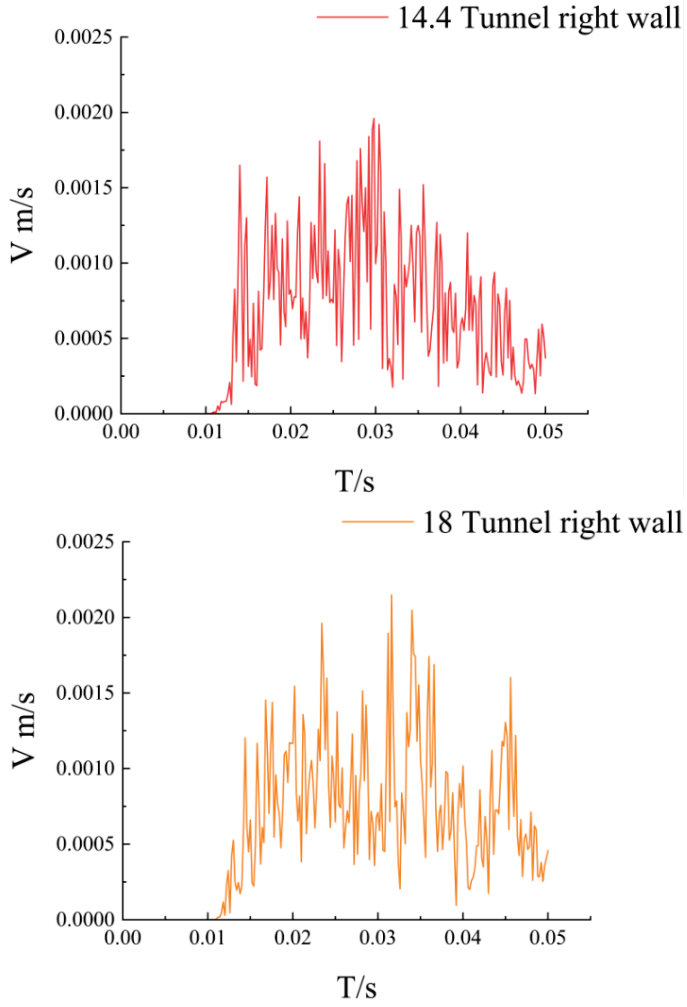


Figure 4. *Cont.*

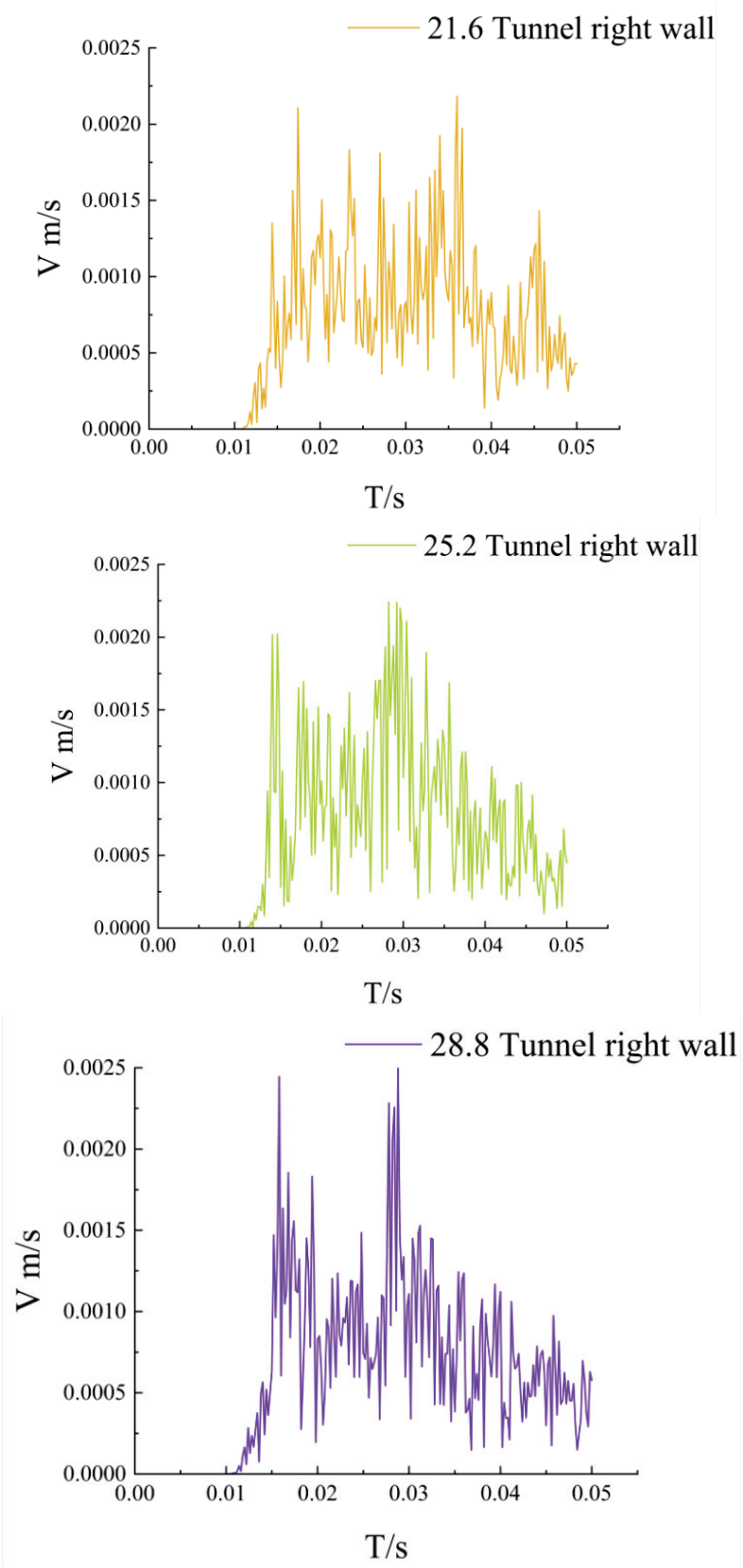
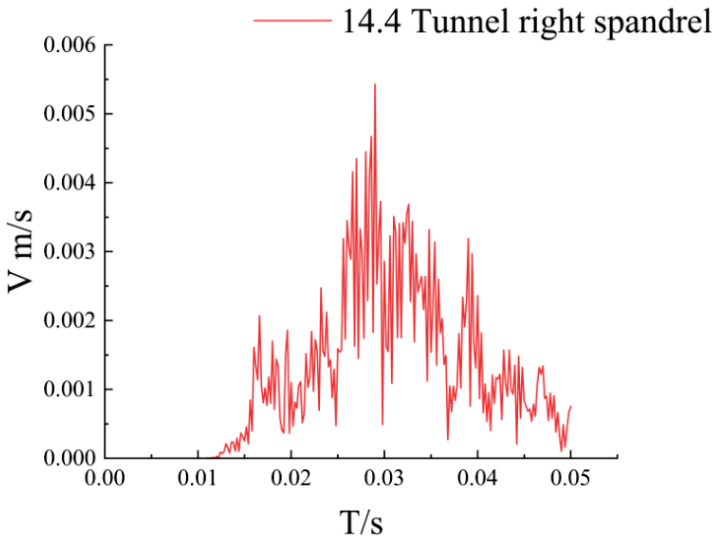
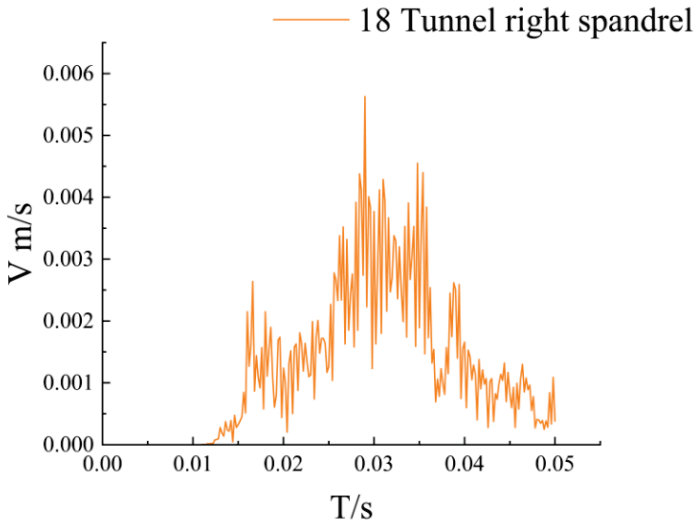


Figure 4. Vibrational velocity curve of the right wall of the plain concrete tunnel.





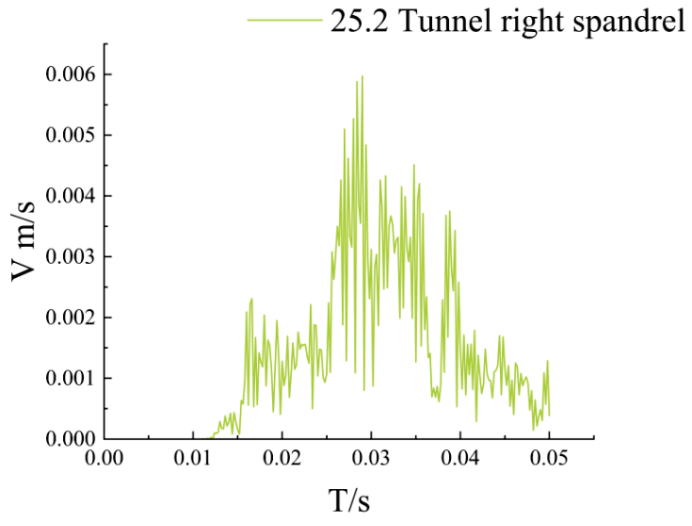


Figure 5. *Cont.*

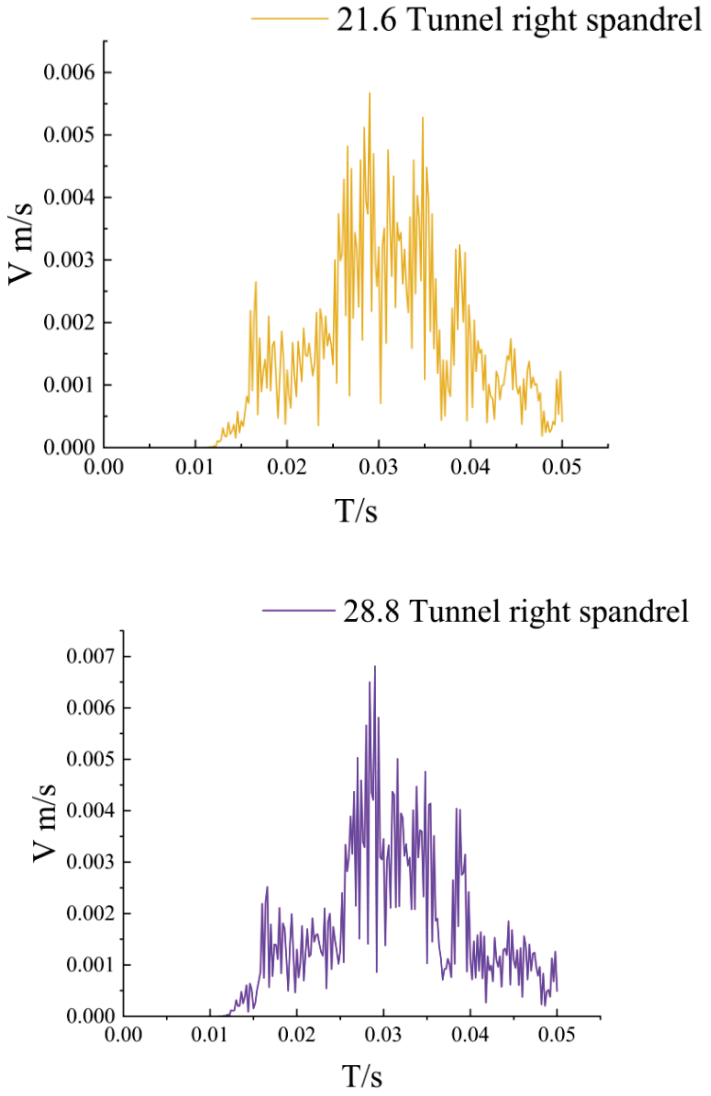


Figure 5. Vibrational velocity curve of the right arch shoulder of the plain concrete tunnel.

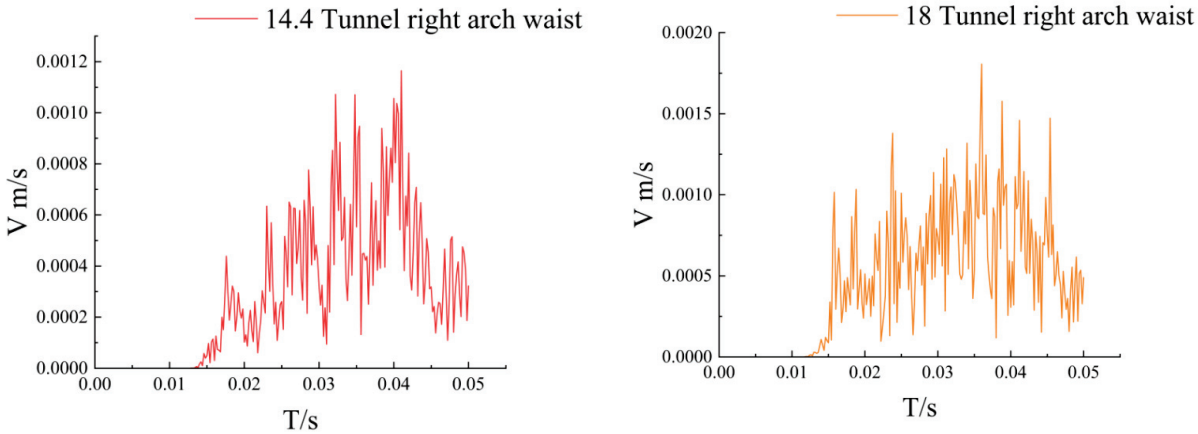


Figure 6. *Cont.*

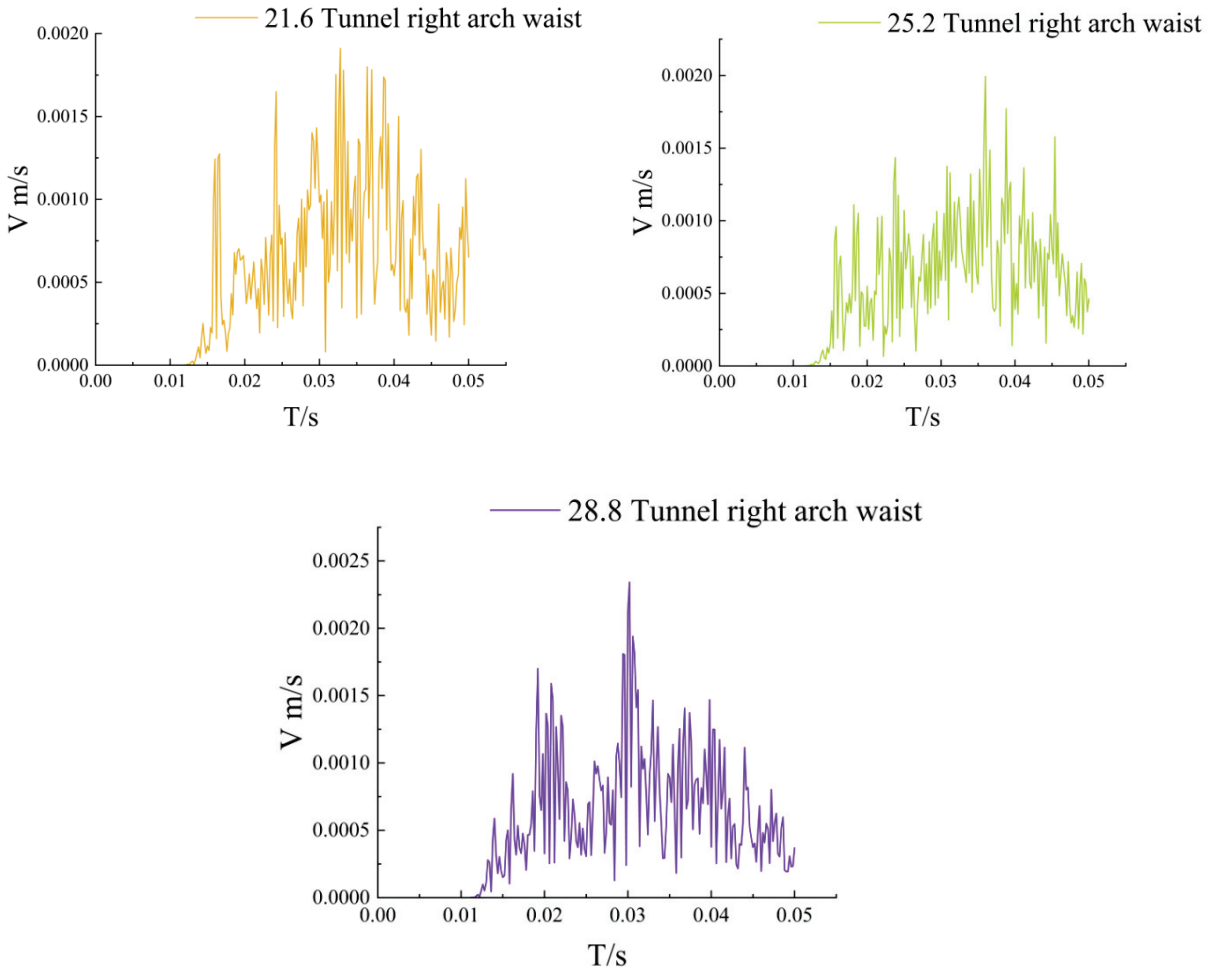


Figure 6. Vibrational velocity curve of the right arch waist of the plain concrete tunnel.

Table 6. Peak particle velocity and location with different explosive quantities.

Location	Quantity of Explosive (kg)	14.4	18	21.6	25.2	28.8
Right side wall	Peak (m/s)	0.00196	0.00215	0.00218	0.00224	0.00256
Right spandrel	Peak (m/s)	0.00543	0.00563	0.00567	0.00597	0.00681
Right hance	Peak (m/s)	0.00116	0.0018	0.0019	0.0020	0.0023

3.2. Vibration Velocity Analysis of Ordinary Concrete Tunnel Lining

The analysis at each monitoring point is the comprehensive vibration velocity (the unit of vibration velocity is m/s, and the unit of time is s).

It can be seen from Figures 7–9 and Table 7 that: (1) In ordinary reinforced concrete lining, the peak values at each monitoring point increase with the amount of explosives, and the maximum peak values of the right wall, the right arch spandrel and right arch waist are at the explosive amount of 28.8 kg, which are 0.00231 m/s, 0.00594 m/s and 0.00182 m/s, respectively, and the peak values all appear near 0.03 s. (2) The vibration law of each monitoring point is relatively consistent under different explosive quantities. No matter how much explosive is used in the monitoring point, the minimum peak value is at the right arch waist; the radius of the right arch spandrel is small, and the maximum peak value of the stress concentration is at the right arch spandrel, indicating that the right arch shoulder is relatively weak during the blasting excavation and needs to be observed. (3) Compared with plain concrete, the vibration velocity at the right wall, the right spandrel

and right arch waist is generally larger as a result of good integrity from the addition of reinforcement.

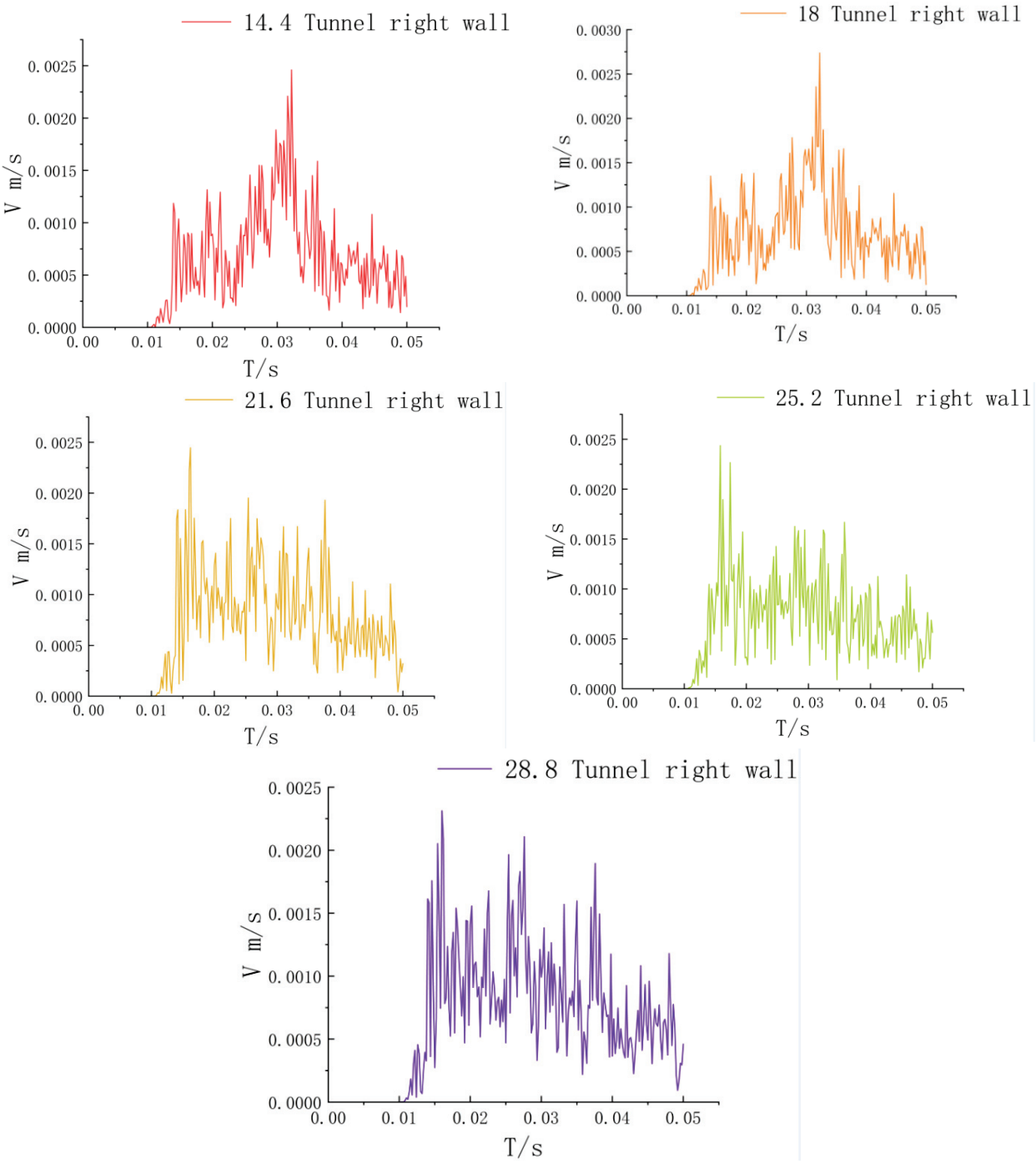


Figure 7. Reinforced concrete tunnel right wall vibration speed curve.

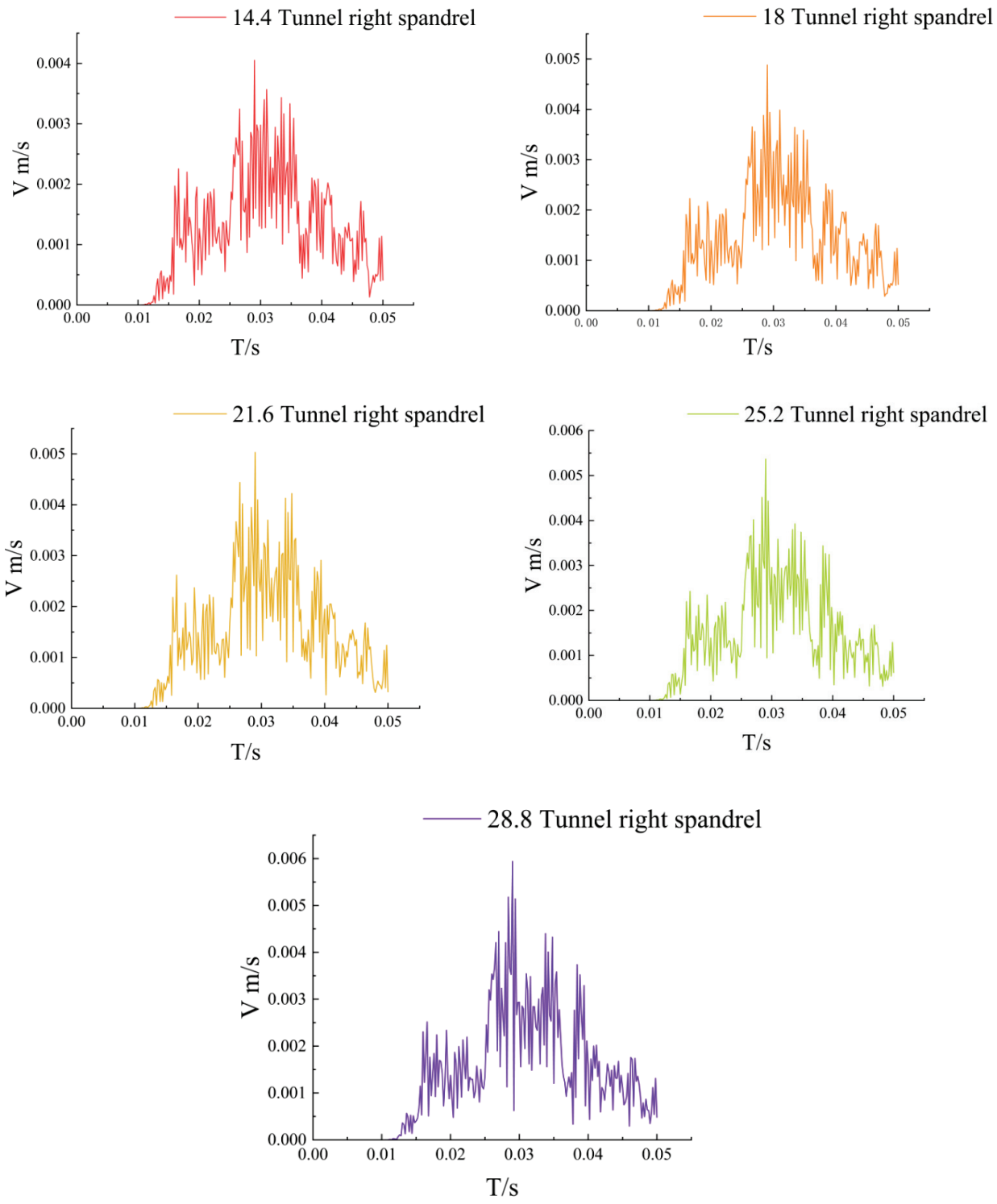


Figure 8. Vibration velocity curve of right arch shoulder of reinforced concrete tunnel.

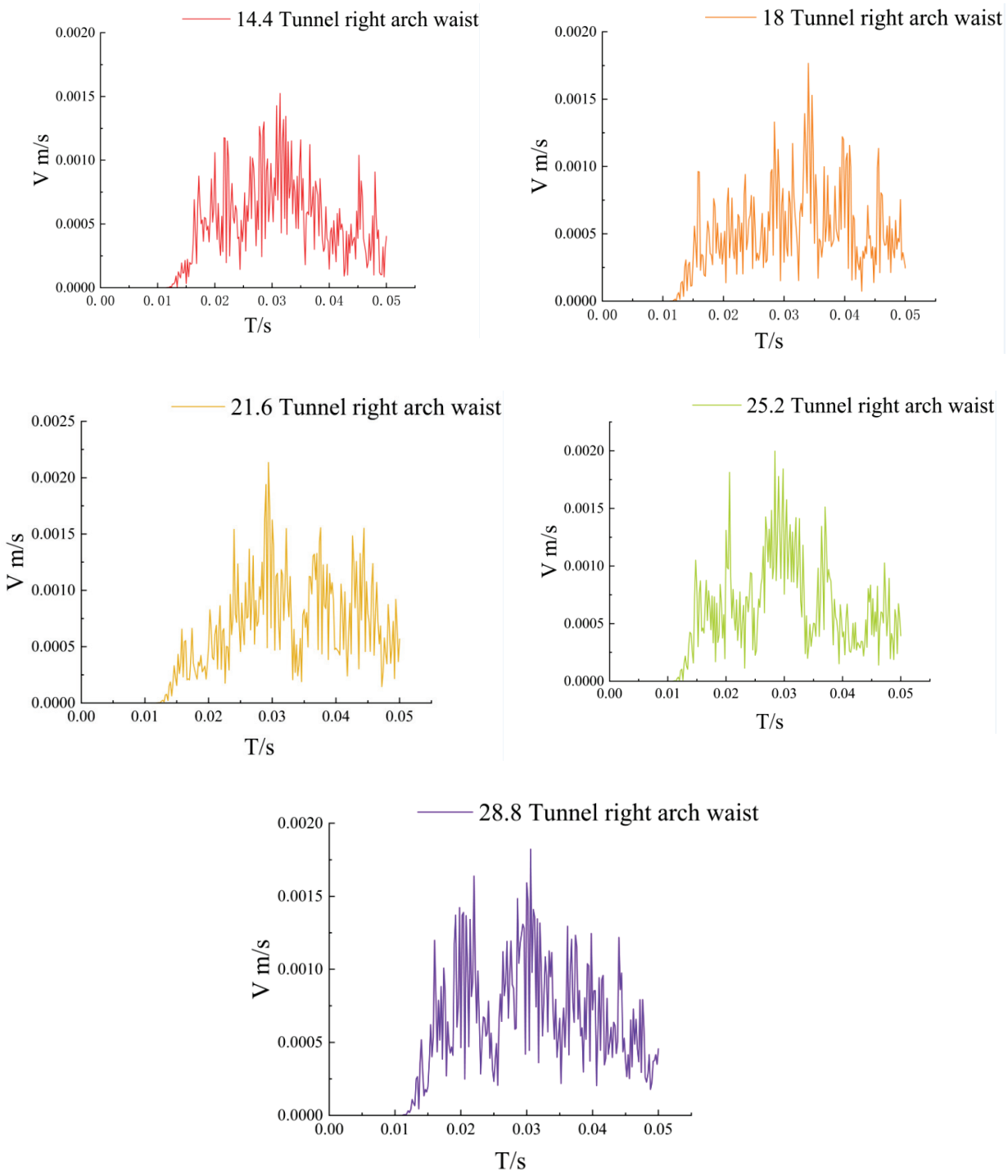


Figure 9. Reinforced concrete tunnel right arch waist vibration speed curve.

Table 7. Peak particle velocity and location with different explosive quantities.

Location	Quantity of Explosive (kg)	14.4	18	21.6	25.2	28.8
Right side wall	Peak (m/s)	0.00246	0.00274	0.00245	0.002444	0.00231
Right spandrel	Peak (m/s)	0.00405	0.00488	0.00503	0.00537	0.00594
Right arch waist	Peak (m/s)	0.00152	0.00177	0.00213	0.00200	0.00182

3.3. Vibration Velocity Analysis of Steel Fiber-Reinforced Concrete Tunnel Lining

The analysis at each monitoring point is the comprehensive vibration velocity (the unit of vibration velocity is m/s, and the unit of time is s).

It can be observed from Figures 10–12 and Table 8 that: (1) In the ordinary reinforced concrete lining, the peak values at each monitoring point increase with the explosive quantity. The maximum peak values of the right wall and the right arch spandrel occur at the explosive amount of 28.8 kg, which are 0.00301 m/s and 0.00832 m/s, respectively. The maximum peak of the right arch waist occur at the explosive amount of 21.6 kg, which is 0.00232 m/s, and the peak values appear at around 0.03 s. (2) The vibration law of the monitoring points on the right wall and the right arch spandrel is relatively consistent and increase all the time under different explosive quantities. However, the vibration speed of the monitoring points on the right arch waist increases first and then falls as the explosive quantity increases, which results from the biggest radius, where the vibration speed is propagated to further sites as the explosive quantity increases.

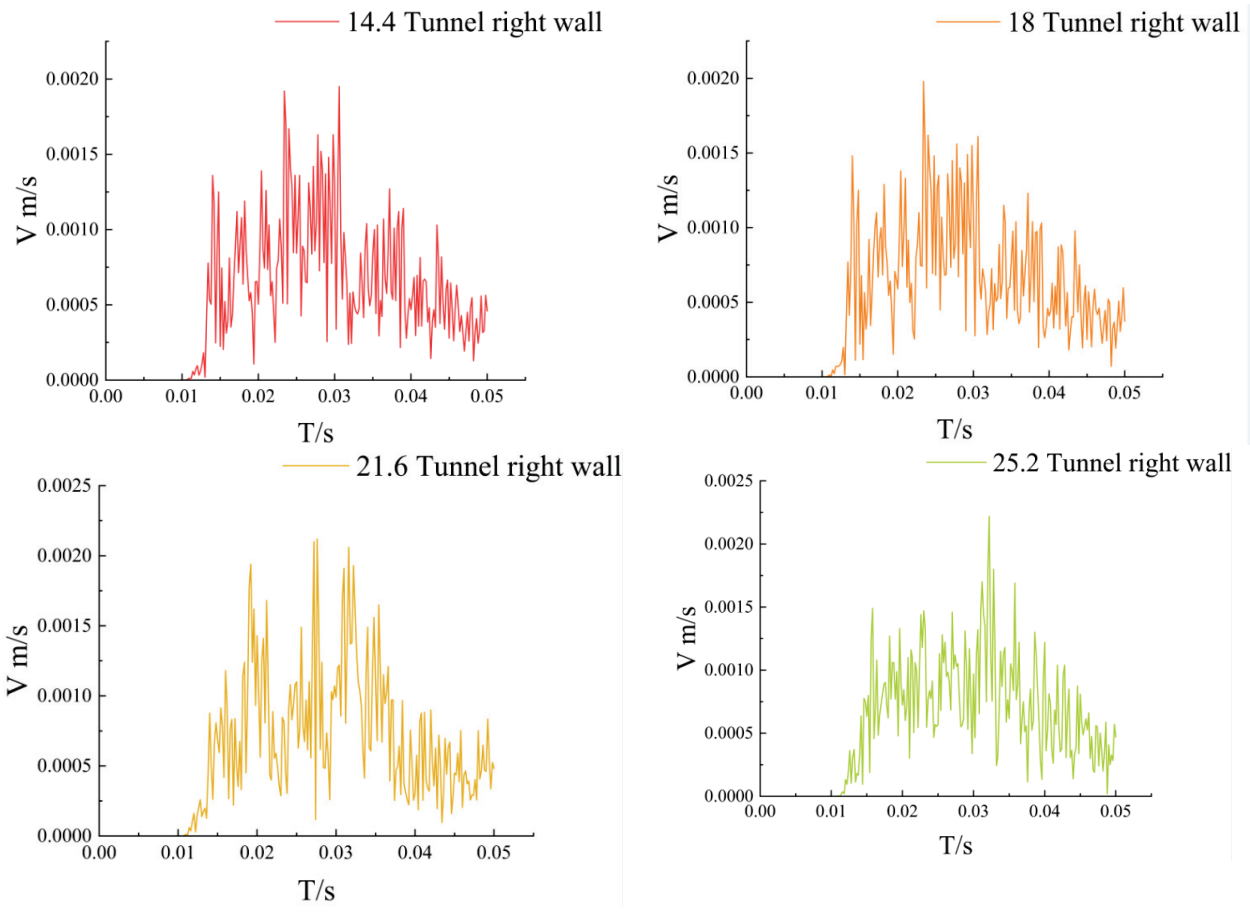


Figure 10. *Cont.*

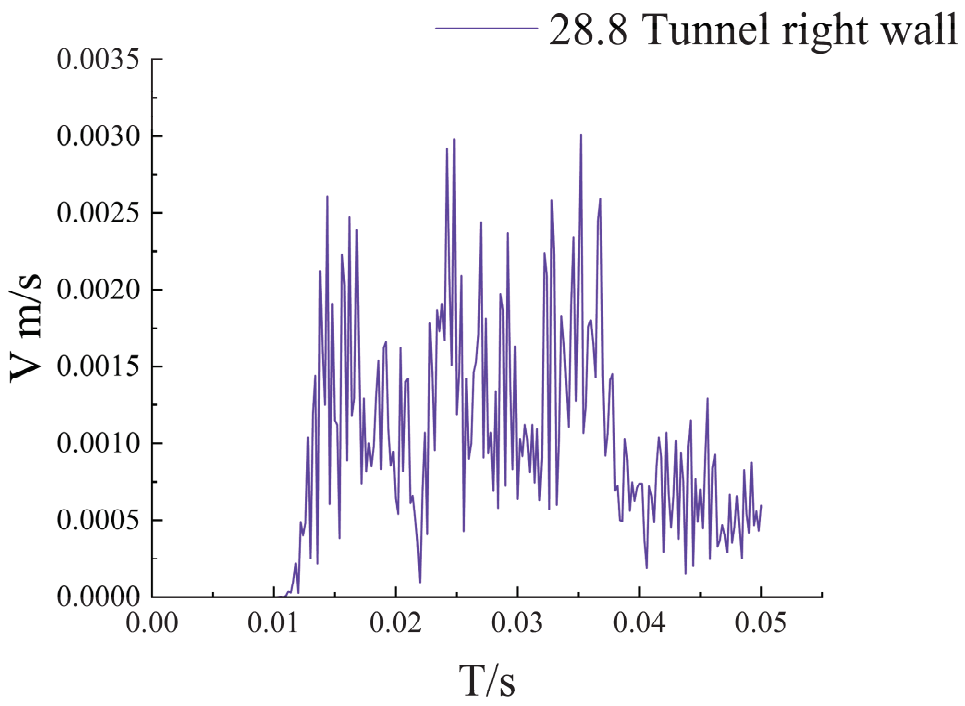


Figure 10. Steel fiber concrete tunnel right wall vibration speed curve.

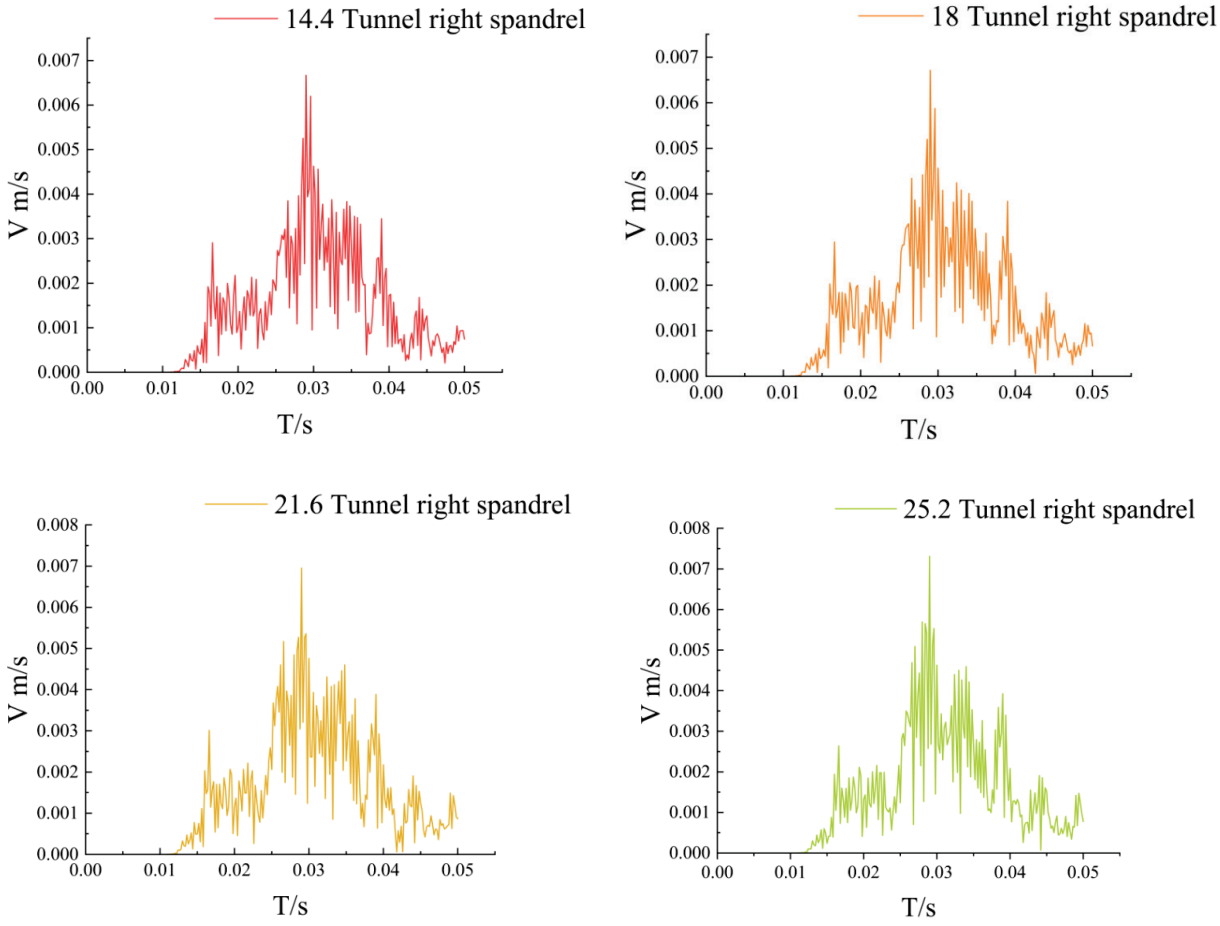


Figure 11. *Cont.*

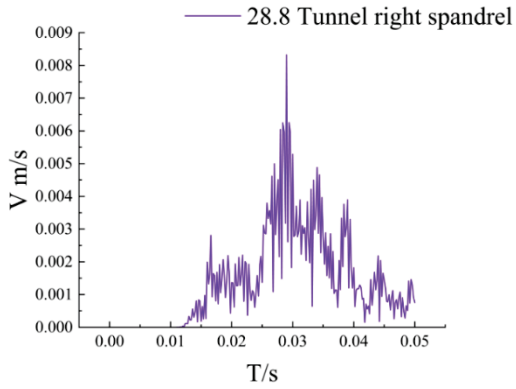


Figure 11. Vibration velocity curve of right arch shoulder of steel fiber concrete tunnel.

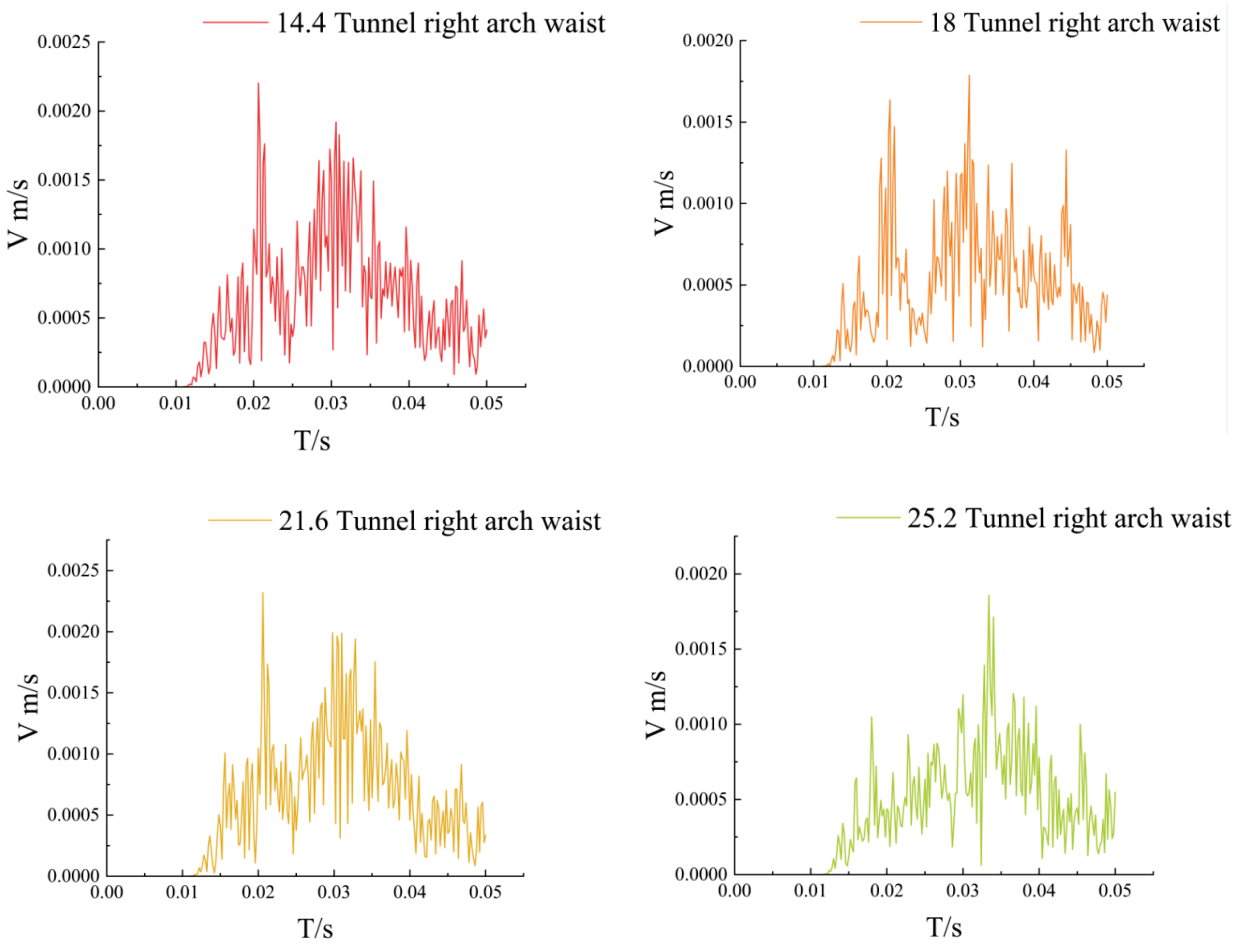


Figure 12. *Cont.*

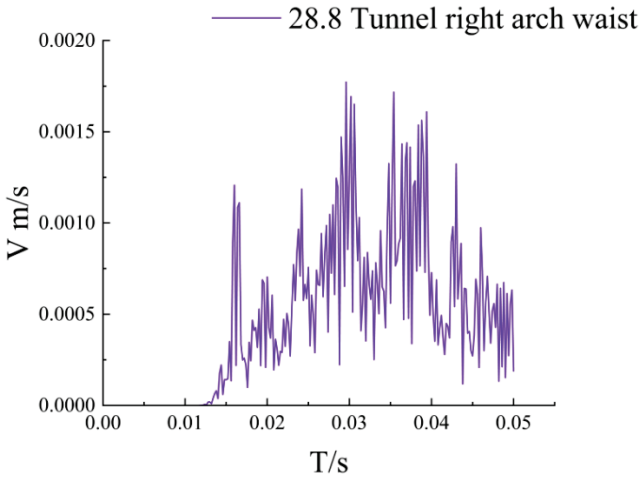


Figure 12. Steel fiber concrete tunnel right arch waist vibration speed curve.

Table 8. Peak particle velocity and position of vibration velocity with the same explosive quantity.

Location	Quantity of Explosive (kg)	14.4	18	21.6	25.2	28.8
Right side wall	Peak (m/s)	0.00195	0.00198	0.00212	0.00222	0.00301
Right spandrel	Peak (m/s)	0.00667	0.00671	0.00695	0.00731	0.00832
Right arch waist	Peak (m/s)	0.00220	0.00179	0.00232	0.00186	0.00177

4. Summary

In this paper, ANSYS/LS-DYNA are used to study the impact of blasting the subsequent tunnel on a steel fiber tunnel lining in advance. By establishing three tunnel models of plain concrete, ordinary reinforced concrete, and steel fiber, and comparing the explosive quantities in the blasting of the subsequent tunnel, the following conclusions are drawn:

1. With plain concrete lining, the peak value of the vibration velocity at each monitoring point appears to be around 0.03 s and increases with the explosive quantity. With the velocity curve basically symmetrical around 0.03 s, it demonstrates consistency in the vibration law.
2. With ordinary reinforced concrete lining, the overall vibration speed is basically the same as that of plain concrete, but increases as a result of the integrity after adding reinforcement.
3. The biggest difference between the steel fiber and the plain concrete tunnel lining is at the right arch waist. The vibration velocity at the right waist increases with the number of explosives, but in the steel fiber tunnel, the vibration velocity at the right arch waist increases and then decreases, with the vibration trend consistent with the other two monitoring points.
4. By comparing the peak values of the vibration velocity at each monitoring point of the three kinds of tunnel lining, it can be concluded that the ordinary reinforced concrete lining at the right wall has the largest vibration velocity; the maximum vibration velocity of the steel fiber tunnel lining occurs at the right arch spandrel, and the gap is large; the maximum vibration velocity of steel fiber tunnel lining is at the right arch waist. Therefore, the integrity of steel fiber tunnel lining is better than the other tunnel linings, with a relatively larger vibration velocity.
5. In conclusion, the steel fiber-reinforced concrete tunnel lining has better integrity compared to plain concrete and reinforced concrete tunnel linings. Therefore, the use of steel fiber-reinforced concrete lining in blasting construction is feasible and can effectively reduce the adverse impact on adjacent tunnels. However, there is

a limitation in data on steel fiber-reinforced concrete as tunnel lining in practical engineering.

Author Contributions: Conceptualization, L.-M.W.; formal analysis, Z.-J.W.; investigation, Y.-Z.C. and Y.W.; methodology, L.-M.W.; software, H.-X.F.; supervision, B.Z.; validation, F.G.; writing—original draft, L.-M.W.; writing—review and editing, Y.-Z.C. All authors have read and agreed to the published version of the manuscript.

Funding: This work was sponsored by the Natural Science Foundation of Chongqing, China (Grant No. CSTB2022NSCQ-MSX0975), Key Laboratory of Geological Hazards Mitigation for Mountainous Highway and Waterway, Chongqing Municipal Education Commission Chongqing Jiaotong University (Grant No. kfxm2018-06), Science and Technology Research Program of Chongqing Municipal Education Commission (Grant No. KJQN20210156 and KJZD202204001), Key Scientific Research Projects of Chongqing Technology and Business Institute (Grant No. NDZD2021-03), Steering Science and Technology Plan Project of Civil Engineering Architectural Network of University Chongqing (Grant No. 2022A04, 2022B05, 2022B09, 2023A03, 2023B03, 2023B04 and 2023B05).

Institutional Review Board Statement: Not applicable.

Informed Consent Statement: Not applicable.

Data Availability Statement: Not applicable.

Conflicts of Interest: The authors declare no conflict of interest.

References

1. Zhang, W.; Kang, S.; Huang, Y.; Liu, X. Behavior of Reinforced Concrete Beams without Stirrups and Strengthened with Basalt Fiber–Reinforced Polymer Sheets. *J. Compos. Constr.* **2023**, *27*, 04023007. [CrossRef]
2. Huang, H.; Yao, Y.; Liang, C.; Ye, Y. Experimental study on cyclic performance of steel-hollow core partially encased composite spliced frame beam. *Soil Dyn. Earthq. Eng.* **2022**, *163*, 107499. [CrossRef]
3. Huang, H.; Li, M.; Yuan, Y.; Bai, H. Experimental Research on the Seismic Performance of Precast Concrete Frame with Replaceable Artificial Controllable Plastic Hinges. *J. Struct. Eng.* **2023**, *149*, 04022222. [CrossRef]
4. Qi, M.S.; Liu, X. A full-scale experimental study on bearing capacity of fiber reinforced concrete segments. *Chin. J. Undergr. Space Eng.* **2019**, *15 (Supp. 1)*, 55–60.
5. Xu, Z.; Li, D.M.; Wang, B.; Zhan, G.Y.; Zhang, S.J.; Shi, J. Application of pure steel fiber concrete segment in hard rock tunnel. *J. Shandong Univ.* **2020**, *50*, 44–49+55.
6. He, J.; Zhu, Y.C.; Shen, M.W.; Yu, F.P. Small clearance blasting in MTR tunnels on adjacent tunnels support vibration response study. *Subgrade Eng.* **2022**, *1*, 171–176.
7. Wang, H.J.; Li, Y.W.; Zhao, X.Q.; Wei, H. Numerical simulation of ground vibration effect caused by tunnel blasting excavation. *J. Shenyang Univ. Technol.* **2022**, *44*, 461–466.
8. Zhang, W.; Wang, S.F.; Yu, J.B. Study on Optimization of Blasting Scheme for Back Tunnel of Double Arch Tunnel without Pilot Tunnel: Take Xinmin Tunnel as an Example. Tunnel Construction. 2022. Available online: http://kns.cnki.net/kcms/detail/44.1745.u.20220721.1502.004.html (accessed on 29 August 2022).
9. Pan, W.T.; He, C.; Wu, F.Y.; Xu, Y.J.; Yao, R.J.; Yan, Q.X. Research on the influence of approaching excavation and blasting vibration of small interval three-hole parallel highway tunnels and railway tunnels. *Railw. Stand. Des.* **2022**. [CrossRef]
10. Wang, H.C.; Wang, X.W.; Zhang, Y.B. Analysis of the impact of blasting construction of new tunnels on cross sections of existing tunnels. *Sichuan Archit.* **2022**, *42*, 182–184.
11. Wu, W.Q.; Ren, X.F. Study on the Effect of Small Clear Distance Tunnel Blasting Excavation on Adjacent Caverns. *Highway* **2011**, *12*, 204–208.
12. Guo, D.M.; Liu, K.; Zhang, W.; Yang, J.; Fan, L.; Xue, L. Research on failure rule and dynamic response of tunnel under adjacent blasting loads of different spacing. *J. Beijing Inst. Technol.* **2018**, *38*, 1000–1005.
13. Mao, Z.C. Field test and wavelet analysis of blasting vibration from in-situ tunnel expansion. *Eng. Blasting* **2022**, *28*, 103–110.
14. Chen, L.B.; Li, Y.S.; Ling, X.; Liao, C.H. Blast vibration test analysis of in-situ expansion by drill-and-blast method for tunnels with very large cross-sections. *Subgrade Eng.* **2017**, *3*, 196–200.
15. Ding, X.; Ji, X.; Gao, S.; Sun, Z.; Wang, H. Vibration response law of high-rise building to tunnel blasting. *IOP Conf. Ser. Earth Environ. Sci.* **2021**, *768*, 012165. [CrossRef]
16. Wu, B.; Lan, Y.; Huang, W.; Yang, S. Study on Vibration of Tunnel Blasting Construction in Upper Soft and Lower Hard Ground. *IOP Conf. Ser. Earth Environ. Sci.* **2019**, *242*, 062004. [CrossRef]
17. Bao, X.; Zhang, W.; Zhao, S.; Yu, C.; Lü, Y.; Wang, S.; Wu, N. Study on the Influence of the Blasting of Preceding Tunnel on the Pre-Penetration Surrounding Rock in Succeeding Tunnel with Small Clear Distance. *Shock Vib.* **2022**, *2022*, 5181154. [CrossRef]

18. Guan, X.; Yang, N.; Zhang, W.; Li, M.; Liu, Z.; Wang, X.; Zhang, S. Vibration response and failure modes analysis of the temporary support structure under blasting excavation of tunnels. *Eng. Fail. Anal.* **2022**, *136*, 106188. [CrossRef]
19. Zhou, X.; Zhang, X.; Feng, H.; Zhang, S.; Yang, J.; Mu, J.; Hu, T. Study on Dominant Frequency Attenuation of Blasting Vibration for Ultra-Small-Spacing Tunnel. *Appl. Sci.* **2022**, *12*, 1058. [CrossRef]
20. Zhang, Q.; Zhang, Z.; Wu, C.; Yang, J.; Wang, Z. Characteristics of Vibration Waves Measured in Concrete Lining of Excavated Tunnel during Blasting in Adjacent Tunnel. *Coatings* **2022**, *12*, 954. [CrossRef]
21. Wu, B.; Lan, Y.B.; Yang, J.X.; Han, Y.L.; Pang, X.Y. Influence of new tunnel blasting on vibration characteristics of adjacent existing tunnel. *China Saf. Sci. J.* **2019**, *29*, 89–95.
22. Fang, N.; Yang, C.H.; Sun, J.P.; Ma, Y.Q.; Miao, Y.S. Study on vibration of single double layer pre-cracking blasting in ultra-small clearances tunnels. *Railw. Eng.* **2015**, *7*, 58–60.
23. Zhu, Z.G.; Sun, M.L.; Zhu, Y.Q.; Sun, X.L. Field monitoring on blasting vibration and dynamic response of ultra-small spacing tunnels. *Rock Soil Mech.* **2012**, *33*, 3747–3752.
24. Cui, H.; Li, Y.; Bao, X.; Tang, W.; Wang, S.; Chen, X. Thermal performance and parameter study of steel fiber-reinforced concrete segment lining in energy subway tunnels. *Tunn. Undergr. Space Technol.* **2022**, *128*, 104647. [CrossRef]
25. Hosseini, S.M.; Mousa, S.; Mohamed, H.M.; Eslami, A.; Benmokrane, B. Experimental and Analytical Study on Precast High-Strength Concrete Tunnel Lining Segments Reinforced with GFRP Bars. *J. Compos. Constr.* **2022**, *26*, 04022062. [CrossRef]
26. Bai, J.Z. *LS-DYNA3D Theoretical Basis and Example Analysis*; Science Press: Beijing, China, 2005.
27. Huang, Y.; Huang, J.; Zhang, W.; Liu, X. Experimental and numerical study of hooked-end steel fiber-reinforced concrete based on the meso- and macro-models. *Compos. Struct.* **2023**, *309*, 116750. [CrossRef]
28. Dong, Z.; Quan, W.; Ma, X.; Li, X.; Zhou, J. Asymptotic homogenization of effective thermal-elastic properties of concrete con-sidering its three-dimensional mesostructure. *Comput. Struct.* **2023**, *279*, 106970. [CrossRef]
29. Liu, H.; Yue, Y.; Liu, C.; Spencer, B.; Cui, J. Automatic recognition and localization of underground pipelines in GPR B-scans using a deep learning model. *Tunn. Undergr. Space Technol.* **2023**, *134*, 104861. [CrossRef]
30. Zhang, Z.; Liang, G.; Niu, Q.; Wang, F.; Chen, J.; Zhao, B.; Ke, L. A Wiener degradation process with drift-based approach of determining target reliability index of concrete structures. *Qual. Reliab. Eng. Int.* **2022**, *38*, 3710–3725. [CrossRef]
31. Wu, M.; Ba, Z.; Liang, J. A procedure for 3D simulation of seismic wave propagation considering source-path-site effects: Theory, verification and application. *Earthq. Eng. Struct. Dyn.* **2022**, *51*, 2925–2955. [CrossRef]
32. Lu, Z.-Q.; Liu, W.-H.; Ding, H.; Chen, L.-Q. Energy Transfer of an Axially Loaded Beam with a Parallel-Coupled Nonlinear Vibration Isolator. *J. Vib. Acoust.* **2022**, *144*, 4054324. [CrossRef]

Disclaimer/Publisher's Note: The statements, opinions and data contained in all publications are solely those of the individual author(s) and contributor(s) and not of MDPI and/or the editor(s). MDPI and/or the editor(s) disclaim responsibility for any injury to people or property resulting from any ideas, methods, instructions or products referred to in the content.

coatings

MDPI

Article

Failure Analysis of Printed Circuit Board Solder Joint under Thermal Shock

Zhidai Zhou [1], Jiahuan Chen [1], Chen Yu [1], Yuxin Wang [1,*] and Yu Zhang [2,*]

[1] School of Materials Science and Engineering, Jiangsu University of Science and Technology, Zhenjiang 212003, China
[2] Shanghai Motor Vehicle Inspection Certification and Tech Innovation Center Co., Ltd., Shanghai 201805, China
* Correspondence: ywan943@163.com (Y.W.); yuz@smvic.com.cn (Y.Z.); Tel.: +86-15262916598 (Y.W.); +86-15905287016 (Y.Z.)

Abstract: Investigating the failure mechanism of solder joints under different temperature conditions is significant to ensure the service life of a printed circuit board (PCB). In this research, the stress and strain distribution of a PCB solder joint was evaluated by high- and low-temperature thermal shock tests. The cross-section of the solder joint after thermal shock testing was measured using a 3D stereoscopic microscope and SEM equipped with EDS. The microstructure of the lead-free solder joint and the phase of the intermetallic compound (IMC) layer were studied by XRD. The working state of the PCB solder joint under thermal shock was simulated and analyzed by the finite element method. The results show that thermal shock has a great effect on the reliability of solder joints. The location of the actual crack is consistent with the maximum stress–strain concentration area of the simulated solder joint. The brittle Cu_6Sn_5 and Cu_3Sn phases at the interface accelerate the failure of solder joints. Limiting the growth of Cu_6Sn_5 and Cu_3Sn phases can improve the reliability of solder joints to a certain extent.

Keywords: finite element modelling; lead-free soldering; PCB solder joint; failure mechanism

1. Introduction

Printed circuit boards (PCB) [1–4] can provide necessary mechanical support for various components in the circuit, and have become an important part of electronic products. In addition, PCBs have the characteristics of high set neutrality, and high reliability, which is also convenient for daily production, design and maintenance. Using PCBs can greatly improve the level of mechanical automation and product production efficiency. Based on the above, PCBs have been extensively employed in computers, automotive, aerospace, and other industries.

At present, the solder used in PCB manufacture is mainly lead-free solder [5–10]. The most commonly used lead-free solders mainly include Sn-Ag [11–14], Sn-Cu [15–18], Sn-Zn [19–22], and Sn-Ag-Cu (SAC) [23–25]. SAC305 solder [26] is widely used because of its high performance and low cost. The reliability of solder joints is one of the important research directions in the field of electronic packaging. The reliability of a PCB board usually depends on the life of its solder joints. The PCB solder joint is a weak part of the entire electronic product. It is prone to crack initiation, propagation, and even fractures in harsh environments such as high-temperature, low-temperature, and violent vibration environments [27]. Voids and cracks cause damage to the pins of electronic components, adversely affecting the reliability of their solder joints and even seriously reducing the service life of the PCB board [28–30]. According to existing research, solder joint failure is responsible for nearly 60% of electronic product failures [31]. The PCB industry has developed towards high precision, high density, and high reliability in recent years, which

further puts higher demands on PCB process reliability. Therefore, it is crucial to study the reliability of PCB solder joints.

In this research, the stress and strain distributions of PCB solder joints under high- and low-temperature thermal shock tests were evaluated by experiments and finite element simulation, respectively. The failure mechanism of PCB solder joints was discussed based on the comparative study between finite element simulation and experimental research. ANSYS simulation and specific experiments were combined to analyze PCB board failure. Micromorphology observation and phase analysis of PCB solder failure parts were performed. The failure mechanisms of SAC305, a commonly used joint solder in the industry, under thermal shock are summarized. This study can provide a basis for the analysis of possible failures in PCB board manufacturing and use.

2. Methods

2.1. Research Object

The PCB pin components included copper parts with excellent electronic properties. The solder used in this experiment was a lead-free silver solder, SAC305 solder [26], which consisted of 96.5% tin, 3% silver, and 0.5% copper. The components studied in this paper were 0603 resistors of the square flat package (QFP) [32], which were installed on a 2 mm thick PCB made of epoxy resin board (FR4) [33].

2.2. Thermal Shock Test

The thermal shock test was carried out in a self-made device equipped with a muffle furnace (Sante, Luoyang, China) and a freezer (Haier, Qingdao, China). The test conditions were based on the standards specified in GB2423.22. The temperature range of the test was set to −18–155 °C. The time of temperature change was set at 2 min, and the temperature was kept at −18 and 155 °C for 2 h (10 cycles), respectively. The thermal shock test was loaded for 10 cycles. The temperature loading curve used in the thermal shock test is shown in Figure 1.

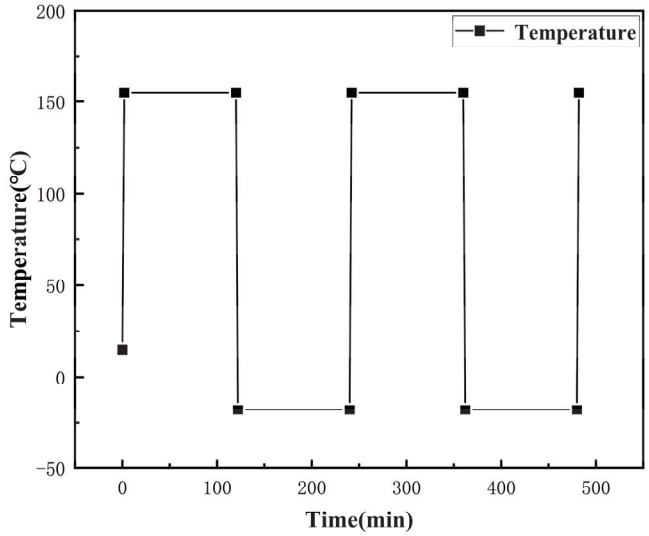


Figure 1. Temperature loading curve of the thermal shock test.

2.3. Finite Element Analysis

ANSYS is a commonly used simulation software [34–38]. In order to simulate finite elements, the coarse and fine mesh method was utilized. The finite element analysis of the model was carried out in a global and local manner. SolidWorks software (version 2022) was used to model the entire component and solder joint after establishing the overall temperature impact model. The analysis simulation was conducted using ANSYS analysis software (ANSYS 14.5).

As shown in Figure 2a, the PCB single-component graphic was created using SolidWorks software (version 2022) based on dimensional criteria. Figure 2b shows the single-component finite element mesh model created using ANSYS software. The specific thermodynamic parameters are listed in Table 1.

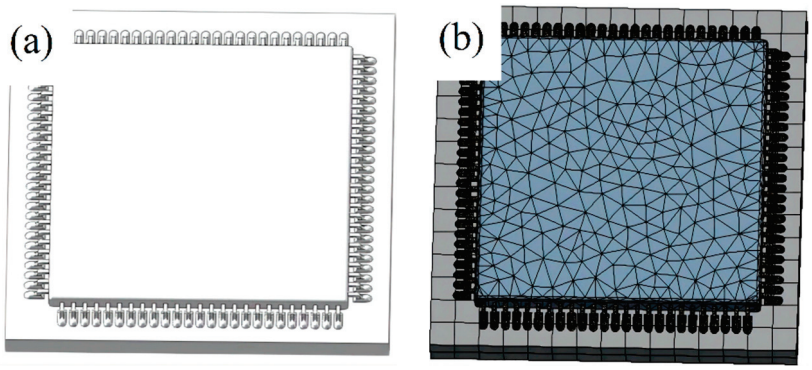


Figure 2. Simulation diagrams of the PCB board sample: (**a**) SolidWorks drawing; (**b**) PCB finite element mesh model.

Table 1. Solder thermodynamic parameters.

Solder	Poisson Ratio V	Elastic Modulus E (GPa)	Coefficient of Expansion (ppm/°C)
SAC305	0.35	45	24.5

The model was simulated and the stress–strain diagram of the solder joints in the corresponding temperature range was obtained. Mises criterion was used to analyze the thermal shock stress–strain behavior of the solder joints. The equivalent stress and equivalent strain were used to analyze the internal stress–strain distribution.

The relationship between the equivalent force and the stress tensor is shown in the following equation [39].

$$\sigma = \frac{\sqrt{2}}{2}\left[(\sigma_x - \sigma_y) + (\sigma_y - \sigma_z) + (\sigma_x - \sigma_z) + 6\left(\tau_{xy}^2 + \tau_{yz}^2 + \tau_{xz}^2\right)\right]^{\frac{1}{2}} \quad (1)$$

σ is the equivalent force, Pa (Pascal); σ_x, σ_y, σ_z are the positive stresses in the X, Y, and Z directions, respectively; τ_{xy} is the shear stress in the Y-axis direction perpendicular to the X-axis plane, Pa; τ_{yz} is the shear stress perpendicular to the Z-axis plane of the Y-axis, Pa; τ_{xz} is the shear stress perpendicular to the Z-axis plane of the X-axis, Pa.

The relationship between the equivalent variation effect and the strain tensor components is shown in the following equation.

$$\varepsilon = \frac{\sqrt{2}}{3}\left[(\varepsilon_x - \varepsilon_y)^2 + (\varepsilon_y - \varepsilon_z)^2 + (\varepsilon_x - \varepsilon_z)^2 + \frac{3}{2}\left(\gamma_{xy}^2 + \gamma_{yz}^2 + \gamma_{xz}^2\right)\right]^{\frac{1}{2}} \quad (2)$$

Among them, ε is the equivalent value; ε_x, ε_y, ε_z are positive strains in the X, Y, and Z directions, respectively; γ_{xy} is the shear strain in the Y-axis direction perpendicular to the X-axis plane; γ_{yz} is the shear strain in the Z-direction perpendicular to the Y-plane plane; γ_{xz} is the shear strain perpendicular to the Z-axis plane in the X-axis plane.

2.4. Characterization

Observation of the internal topography was achieved by industrial CT (YXLON FF35CT) at the operating power of 320 W. The microstructure and elemental composition were characterized by scanning electron microscopy (SEM, Regulus-8100, Hitachi, Tokyo,

Japan) and energy dispersive spectroscopy (EDS, Pro X, Phenom, Eindhoven, The Netherlands). An X-ray diffractometer (Bruker D2 phaser, Bruker, Karlsruhe, Germany) was used to test the phase composition at cross-section cracks. The diffraction angle 2θ ranged from 30° to 100°. DIFFRAC (SUITE) and Jade6.0 software were used to calibrate the phase of the solder cracks.

3. Results and Discussion

3.1. Morphology of Solder Joints

Figure 3 shows the industrial computed tomography (CT) images of the PCB board sample. The solder joints of the PCB are well-formed and neatly arranged. Moreover, the solder joints have no obvious damage marks and are spread in a streamlined pattern. The processor generates a significant amount of heat when operating under high loads. This extreme environment can easily cause solder joint failure [40]. To ensure the functional reliability of PCBs under harsh environmental conditions, thermal shock experiments are designed and studied to explore the failure mechanism of PCB solder joints in harsh environments.

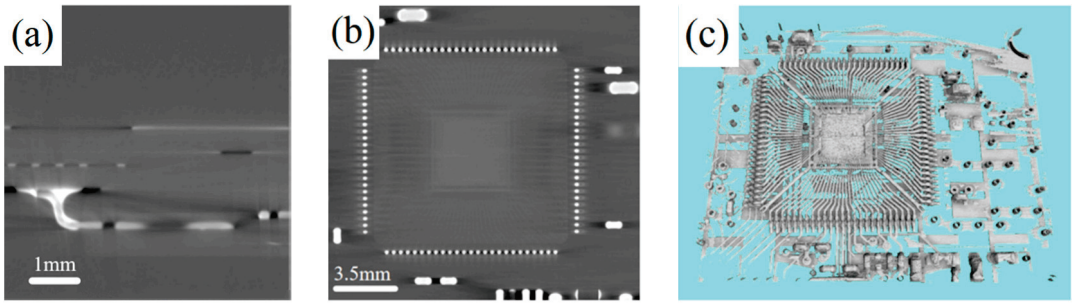


Figure 3. Industrial CT images of the PCB board sample: (**a**) cross-sectional morphology, (**b**) distribution of solder joint positions and (**c**) overall internal structure of the component.

3.2. Finite Element Analysis

Specific dimensions of the PCB resistance components were measured and the finite element analysis model was established using ANSYS. Finite element analysis was accomplished according to the thermodynamic parameters of the substrate, components, Cu lead, and solder. Nephograms of stress and strain were obtained, and the distribution of stress and strain at different temperatures was analyzed. The 3D solid model was then divided into 3D solid meshes. The model contains 69,108 nodes and 30,993 cells after meshing. The solder of the model was identified as linear material, and the linear unit Solid 45 was used. The physical parameters were considered to be isotropic. It was assumed that the structure of the material was uniform without segregation, the welding interface was in good contact, and there were no defects such as pores and holes. The temperature of each area of the model was the same, and the influence of partial temperature non-uniformity caused by the difference in the convective heat transfer coefficient of each material was ignored.

In the process of thermal shock, the three-dimensional structural stress distribution of the solder joint is multi-axial. The equivalent stress profile of each component is shown in Figure 4. The stress distribution of the left and right solder joints is roughly the same. The stress generated at the interface of each component is greater than that generated in the component. The connection between the components and Cu lead, the connection between the solder joint and Cu plate, and the interface between the solder and Cu lead represent typical locations where defects can easily occur.

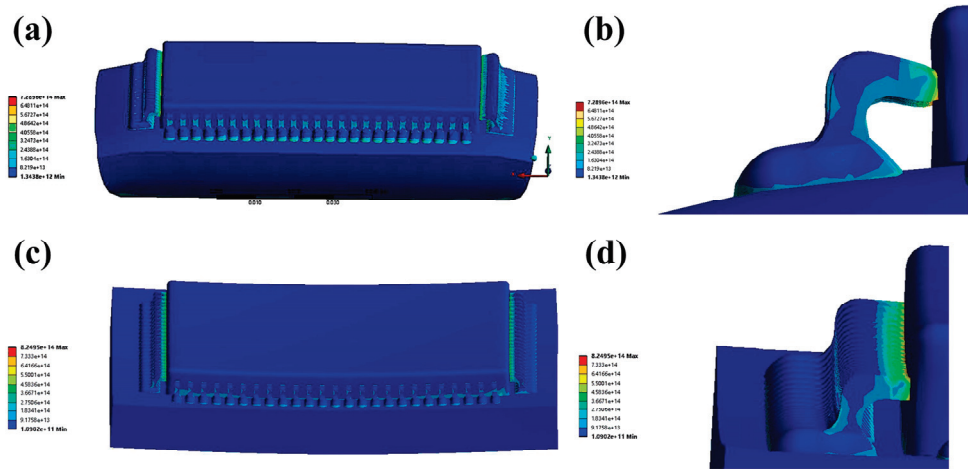


Figure 4. Stress distribution at extreme temperatures: (**a**) element (155 °C), (**b**) solder joint (155 °C), (**c**) element (−18 °C) and (**d**) solder joint (−18 °C).

Figure 5 shows the grid segmentation analysis diagram of solder joints at high and low temperatures. In Figure 5, it is evident that a single solder joint is prone to failure at the junction of the solder and copper plate and the junction of the Cu wire and solder. After being subjected to obvious thermal expansion and contraction, the interface between the solder, Cu lead and Cu bottom disk is prone to generate a high stress value and increase the risk of failure. The stress distribution in the solder joint is uneven. The contact surface between the solder joint and the components is subjected to the maximum stress value, which is close to the junction of the solder, components, and pads. There is a certain area of high stress at the top when the temperature is −18 °C, as shown in Figure 5b. This area becomes smaller and smaller as the temperature increases. When the temperature reaches 80 °C, the high-stress concentration decreases and the stress tends to average out, as shown in Figure 5e. In addition, the stress concentration begins to slowly increase at the edge, and the area grows larger as the temperature increases. It can be predicted that the top of the joint between the solder and the components is also a position prone to defects. Fractures are more likely to develop and cause solder joint failure when the joint is in use at low temperatures. Defects between the solder and components on either side of the joint may also occur during service at high temperatures, reducing the reliability of the solder joint.

The temperature of zero stress is set at 22 °C, and the stress value decreases first and then increases with the increase in temperature. The maximum and minimum stress values at each temperature are shown in Table 2. Under actual working conditions, plastic deformation occurs in the solder joint. The greater the cyclic stress, the higher the plastic deformation, and the easier the solder joint will fail. The stress distribution diagram shows that the more extreme the difference in temperature between high and low temperatures, the more likely it is that failure will occur.

The maximum and minimum strain values at each temperature are shown in Table 3. As the temperature increases, the solder joint strain decreases first and then increases. The solder joint demonstrates different types of deformation under different temperature impact conditions. At high temperatures, the solder joint expands when heated, and the solder joint exerts "extrusion pressure" on the components and pads. At low temperatures, the solder joint contracts when it is cold, and the solder joint exerts tensile stress on the components and pads. Since solder is defined as an elastic material, the strain diagram of the solder joint is almost the same as the stress diagram. The internal strain distribution is uneven. The interface between the component and the Cu pad is the maximum strain area, which is consistent with the stress diagram. As the temperature increases, the high strain zone gradually moves to both sides and the strain distribution gradually becomes uniform.

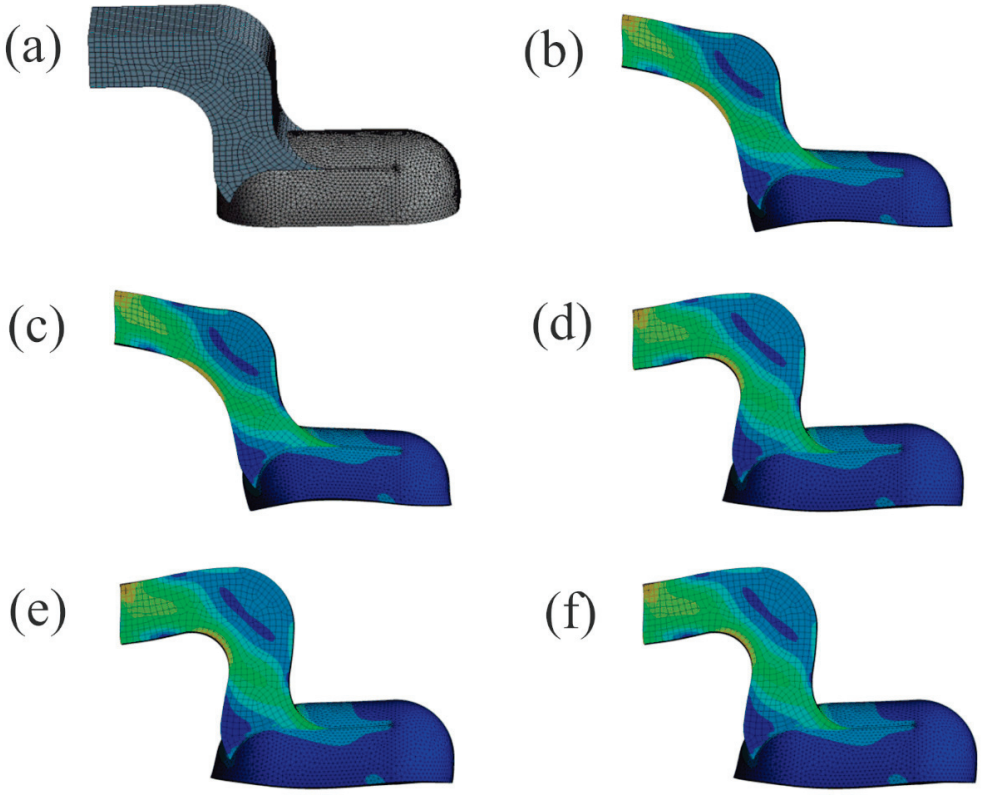


Figure 5. Finite element analysis of weld joints at different temperatures: (**a**) mesh generation, (**b**) −18 °C, (**c**) 10 °C, (**d**) 40 °C, (**e**) 80 °C and (**f**) 155 °C.

Table 2. Maximum and minimum stress values at different temperatures.

Temperature (°C)	−18	10	22	40	80	155
Maximum stress value	1.8	0.72	0	1.08	3.51	8.05
Minimum stress value	0.24	0.055	0	0.083	0.27	0.62

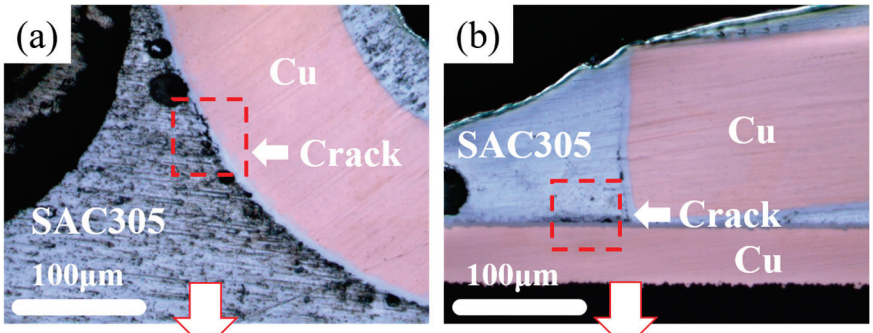
Table 3. Maximum and minimum strain values at different temperatures.

Temperature (°C)	−18	10	22	40	80	155
Maximum strain value	0.98	0.29	0	0.44	1.42	3.25
Minimum strain value	0.68	0.20	0	0.31	0.98	2.26

3.3. Thermal Shock Analysis

After the thermal shock, the cross-section of the solder joint can be observed in Figure 6. It can be observed that the crack occurs at the interface between the filler metal and the Cu lead wire and the joint between the filler metal and the Cu bottom plate. In the process of thermal shock, cyclic tensile and compressive stresses are generated between the solder joint and the copper plate, due to the different thermal expansion coefficients between the solder joint and the copper plate. This will also lead to uneven shrinkage or expansion of each component, resulting in a large concentration of stress at the interface, causing cracks and accelerating material failure. Meanwhile, the increase in intermetallic compound (IMC) layer thickness will also affect the joint strength between the solder joint and the copper plate. According to the EDS analysis in Figure 6c,d, Cu and Sn elements appear in the area of points a and d (IMC layer) [41]. The mass ratio of Cu to Sn at point a is about 1:3. Correspondingly, the mass ratio of Cu to Sn at point d is about 1:4. There is a mixture of Cu and Sn in this area. The solder is affected by the accumulated residual stress during the thermal shock. Stress shows an increasing trend at the heating stage.

The maximum stress concentration occurred at the 155 °C insulation stage. Due to stress relaxation during the cooling process, stress on the pin and interface is released. Under the impact load of temperature, the internal stress of the solder joint changes periodically. When the temperature sharply drops, the stress of the solder joint sharpy increases due to the increase in the thermal expansion ratio. During the insulation process at −18 °C, the stress minimally changes and there is no obvious stress relaxation. The stress change caused by thermal expansion and contraction is the main reason for solder joint failure.



sample	Cu(wt%)	Ag(wt%)	Sn(wt%)
a	23.96	0	76.04
b	0.25	1.13	98.62
c	100	0	0

sample	Cu(wt%)	Ag(wt%)	Sn(wt%)
d	20.25	0	79.75
e	0.78	3.06	96.16
f	100	0	0

Figure 6. Cross section images of solder joints under different thermal shock times: (**a**) analyzed twice and (**b**) 10 times by metallurgical microscope; (**c**) analyzed twice and (**d**) 10 times by SEM and EDS analysis.

Figure 7 shows the XRD analysis at the cross-section of the solder joint. Cu_6Sn_5 (6Cu + 5Sn → Cu_6Sn_5) [42] was formed on an IMC layer during thermal shock. During the heat preservation process, the Cu_6Sn_5 phase gradually grows with the extension of the reaction time. The Cu substrate reacts with Cu_6Sn_5 in the IMC layer to generate Cu_3Sn (Cu_6Sn_5 + 9Cu → $5Cu_3Sn$) [42], which is very thin and accounts for a small proportion overall. As the reaction continues, the fusion of Sn and Cu substrates intensifies, and Cu_6Sn_5 accounts for a much higher proportion in the IMC layer compared to Cu_3Sn [43]. Cu_6Sn_5 and Cu_3Sn easily cause cracks in the stress concentration process due to their hardness and fragility, which is detrimental to the bond strength of solder joints.

Figure 8 shows the failure mechanism of the PCB solder joint. The solder joint is affected by stress and small cracks are first produced in the IMC layer during the thermal shock process. With continuous thermal shock, cracks grow along the IMC layer, and eventually form larger cracks. These cracks are the main source of solder joint failure.

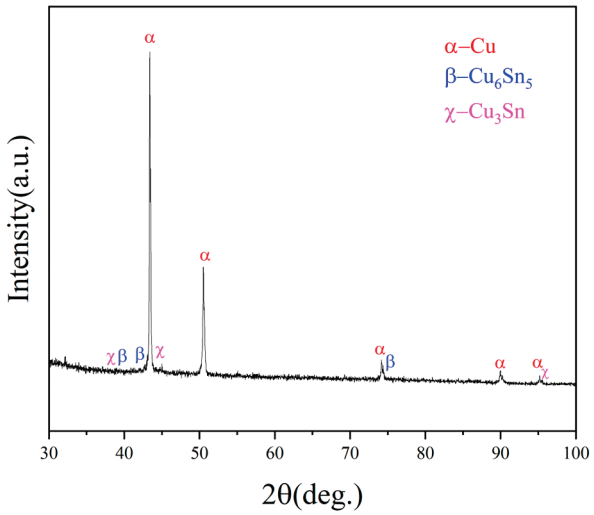


Figure 7. XRD pattern at the cross section of the solder joint.

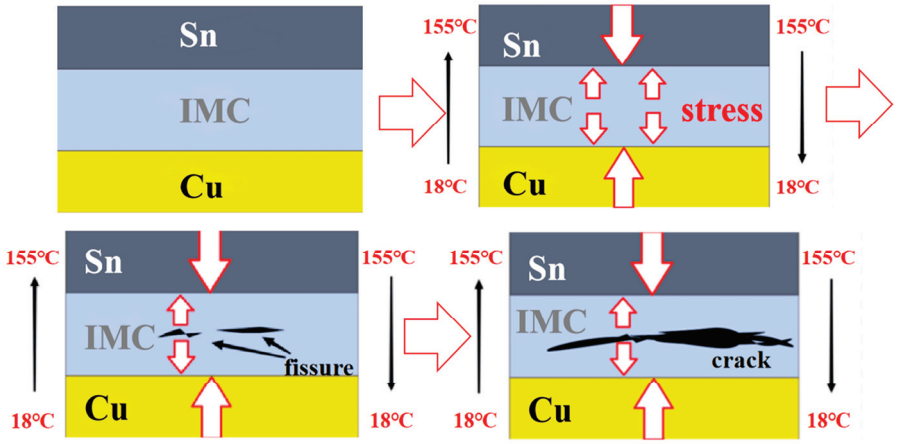


Figure 8. Schematic diagram of PCB solder joint failure.

4. Conclusions

In this study, the failure mechanism of SAC305 joint solder under thermal shock was analyzed by combining an ANSYS simulation and experiment. Improvement measures were put forward according to the problems of solder joints under thermal shock conditions.

- When a PCB board is subjected to thermal shock, the difference in the thermal expansion coefficient between Cu and solder will lead to a high stress concentration.
- Cracks at the solder/Cu lead interface and the solder/Cu bottom plate joint are the main reasons for solder joint failure.
- The simulation results show that the crack location is consistent with the position of the maximum stress and strain of the simulated solder joint.
- The formation and growth of brittle Cu_6Sn_5 and Cu_3Sn phases at the interface accelerated the failure of solder joints.
- Reducing the use of PCBs in −18 to 155 °C thermal shock environments effectively avoids solder joint failure caused by Cu_6Sn_5 and Cu_3Sn phase precipitation.

Author Contributions: Conceptualization, Z.Z. and Y.W.; methodology, Z.Z.; software, C.Y.; validation, Z.Z., C.Y., and Y.W.; formal analysis, C.Y.; investigation, Z.Z.; resources, Y.Z.; data curation, Z.Z.; writing—original draft preparation, Z.Z.; writing—review and editing, Z.Z.; visualization, J.C.; supervision, Y.Z.; project administration, Y.W.; funding acquisition, Y.W. All authors have read and agreed to the published version of the manuscript.

Funding: The authors are grateful for the financial support provided by the Shanghai Motor Vehicle Inspection Certification & Tech Innovation Center Co., Ltd., Jiangsu Provincial Natural Science Fund Research Project (grant number BK20211344), Jiangsu Provincial Six Talent Peaks (grant number 2018XCL-028) and Jiangsu Provincial Postgraduate Research & Practice Innovation Program (grant number KYCX21_3451).

Institutional Review Board Statement: Not applicable.

Informed Consent Statement: Not applicable.

Data Availability Statement: Not applicable.

Conflicts of Interest: The authors declare no conflict of interest.

References

1. Alshihmani, H.; Maghrebi, M.-J.; Sardarabadi, M. Thermal performance prediction of a phase change material based heat-sink cooling system for a printed circuit board, using response surface method. *J. Energy Storage* **2022**, *55*, 105499. [CrossRef]
2. Atintoh, A.; Kpobie, W.; Bonfoh, N.; Fendler, M.; Addiego, F.; Lipinski, P. Multiscale characterization of the mechanical behavior of a printed circuit board (PCB). *Mater. Today Commun.* **2023**, *34*, 104968. [CrossRef]
3. Kumar, V.; Gupta, M. Comparative study of different natural fibre printed circuit board (PCB) composites. *Mater. Today Proc.* **2021**, *44*, 2097–2101. [CrossRef]
4. Tang, J.; Wan, X.; Zhang, L. A sustainable printed circuit board derived hierarchically porous carbon/polyaniline composites for supercapacitors. *Ceram. Int.* **2022**. [CrossRef]
5. Kumar, N.; Maurya, A. Development of lead free solder for electronic components based on thermal analysis. *Mater. Today Proc.* **2022**, *62*, 2163–2167. [CrossRef]
6. Li, Q.; Zhao, M.; Lin, J.; Lu, S. Effect of temperature on the corrosion behavior of lead-free solders under polyvinyl chloride fire smoke atmosphere. *J. Mater. Res. Technol.* **2021**, *15*, 3088–3098. [CrossRef]
7. Xiao, J.; Tong, X.; Liang, J.; Chen, Q.; Tang, Q. Microstructure and morphology of the soldering interface of Sn–2.0Ag–1.5Zn low Ag content lead-free solder ball and different substrates. *Heliyon* **2023**, *9*, e12952. [CrossRef]
8. Yahaya, M.Z.; Nazeri, M.F.M.; Salleh, N.A.; Kurt, A.; Kheawhom, S.; Illés, B.; Skwarek, A.; Abdullah, A.M.; Mohamad, A.A. Selective etching of lead-free solder alloys: A brief review. *Mater. Today Commun.* **2022**, *33*, 104520. [CrossRef]
9. Chen, J.; He, Z.; Liu, J.; Wang, Y.; Hodgson, M.; Gao, W. Antibacterial anodic aluminium oxide-copper coatings on aluminium alloys: Preparation and long-term antibacterial performance. *Chem. Eng. J.* **2023**, *461*, 141873. [CrossRef]
10. Wang, D.; Chen, G.; Wang, A.; Wang, Y.; Qiao, Y.; Liu, Z.; Qi, Z.; Liu, C.T. Corrosion behavior of single- and poly-crystalline dual-phase TiAl-Ti_3Al alloy in NaCl solution. *Int. J. Miner. Metall. Mater.* **2023**, *30*, 689–696. [CrossRef]
11. Amagai, M. A study of nanoparticles in Sn–Ag based lead free solders. *Microelectron. Reliab.* **2008**, *48*, 1–16. [CrossRef]
12. Niranjani, V.; Rao, B.C.; Sarkar, R.; Kamat, S. The influence of addition of nanosized molybdenum and nickel particles on creep behavior of Sn–Ag lead free solder alloy. *J. Alloys Compd.* **2012**, *542*, 136–141. [CrossRef]
13. Tunthawiroon, P.; Kanlayasiri, K. Effects of Ag contents in Sn–xAg lead-free solders on microstructure, corrosion behavior and interfacial reaction with Cu substrate. *Trans. Nonferrous Met. Soc. China* **2019**, *29*, 1696–1704. [CrossRef]
14. Wang, Y.; Hu, B.; Tay, S.L.; Hou, F.; Gao, W.; Xiong, C. The microstructure and properties of sol-enhanced Sn–TiO_2 nanocomposite coatings. *Int. J. Mod. Phys. B* **2017**, *31*, 1744025. [CrossRef]
15. Freitas, E.S.; Osório, W.R.; Spinelli, J.E.; Garcia, A. Mechanical and corrosion resistances of a Sn–0.7wt.%Cu lead-free solder alloy. *Microelectron. Reliab.* **2014**, *54*, 1392–1400. [CrossRef]
16. Kanlayasiri, K.; Mookam, N. Influence of Cu content on microstructure, grain orientation and mechanical properties of Sn–xCu lead-free solders. *Trans. Nonferrous Met. Soc. China* **2022**, *32*, 1226–1241. [CrossRef]
17. Qu, D.; Li, C.; Bao, L.; Kong, Z.; Duan, Y. Structural, electronic, and elastic properties of orthorhombic, hexagonal, and cubic Cu_3Sn intermetallic compounds in Sn–Cu lead-free solder. *J. Phys. Chem. Solids* **2020**, *138*, 109253. [CrossRef]
18. Gao, W.; Cao, D.; Jin, Y.; Zhou, X.; Cheng, G.; Wang, Y. Microstructure and properties of Cu-Sn-Zn-TiO_2 nano-composite coatings on mild steel. *Surf. Coat. Technol.* **2018**, *350*, 801–806. [CrossRef]
19. El-Daly, A.; Hammad, A. Elastic properties and thermal behavior of Sn–Zn based lead-free solder alloys. *J. Alloys Compd.* **2010**, *505*, 793–800. [CrossRef]
20. Mayappan, R.; Ahmad, Z.A. Effect of Bi addition on the activation energy for the growth of Cu_5Zn_8 intermetallic in the Sn–Zn lead-free solder. *Intermetallics* **2010**, *18*, 730–735. [CrossRef]
21. Nazeri, M.F.M.; Mohamad, A.A. Corrosion measurement of Sn–Zn lead-free solders in 6M KOH solution. *Measurement* **2014**, *47*, 820–826. [CrossRef]
22. Wang, Y.; Gao, W.; He, Z.; Jin, Y.; Qiao, Y.; Cheng, G.; Gao, W.; Zhi, Z. Cu–Sn–Zn nanocomposite coatings prepared by TiO_2 sol-enhanced electrodeposition. *J. Appl. Electrochem.* **2020**, *50*, 875–885. [CrossRef]
23. Ben Romdhane, E.; Roumanille, P.; Guédon-Gracia, A.; Pin, S.; Nguyen, P.; Frémont, H. From early microstructural evolution to intergranular crack propagation in SAC solders under thermomechanical fatigue. *Microelectron. Reliab.* **2021**, *126*, 114288. [CrossRef]

24. Gan, G.-S.; Huang, T.; Chen, S.-Q.; Jiang, L.-J.; Cheng, D.-Y.; Zhang, S.-Y. Low-temperature interconnection and strengthening mechanism of Cu/Cu joint with SAC particles solders. *Mem.-Mater. Devices Circuits Syst.* **2023**, *4*, 100026. [CrossRef]
25. Wu, M.-L.; Lan, J.-S. Reliability and failure analysis of SAC 105 and SAC 1205N lead-free solder alloys during drop test events. *Microelectron. Reliab.* **2018**, *80*, 213–222. [CrossRef]
26. Cheng, S.; Huang, C.-M.; Pecht, M. A review of lead-free solders for electronics applications. *Microelectron. Reliab.* **2017**, *75*, 77–95. [CrossRef]
27. Muhammad, N.; Fang, Z.; Shoaib, M. Remaining useful life (RUL) estimation of electronic solder joints in rugged environment under random vibration. *Microelectron. Reliab.* **2020**, *107*, 113614. [CrossRef]
28. Dalton, E.; Ren, G.; Punch, J.; Collins, M.N. Accelerated temperature cycling induced strain and failure behaviour for BGA assemblies of third generation high Ag content Pb-free solder alloys. *Mater. Des.* **2018**, *154*, 184–191. [CrossRef]
29. Shnawah, D.A.; Sabri, M.F.M.; Badruddin, I.A. A review on thermal cycling and drop impact reliability of SAC solder joint in portable electronic products. *Microelectron. Reliab.* **2012**, *52*, 90–99. [CrossRef]
30. Matin, M.; Vellinga, W.; Geers, M. Thermomechanical fatigue damage evolution in SAC solder joints. *Mater. Sci. Eng. A* **2007**, *445–446*, 73–85. [CrossRef]
31. Jiang, N.; Zhang, L.; Liu, Z.-Q.; Sun, L.; Long, W.-M.; He, P.; Xiong, M.-Y.; Zhao, M. Reliability issues of lead-free solder joints in electronic devices. *Sci. Technol. Adv. Mater.* **2019**, *20*, 876–901. [CrossRef] [PubMed]
32. Han, Z.-J.; Xue, S.-B.; Wang, J.-X.; Zhang, X.; Zhang, L.; Yu, S.-L.; Wang, H. Mechanical properties of QFP micro-joints soldered with lead-free solders using diode laser soldering technology. *Trans. Nonferrous Met. Soc. China* **2008**, *18*, 814–818. [CrossRef]
33. Harikirubha, S.; Baranidharan, V.; Saranya, S.; Keerthana, K.; Nandhini, M. Different shapes of microstrip line design using FR4 substrate materials—A comprehensive review. *Mater. Today Proc.* **2021**, *45*, 3404–3408. [CrossRef]
34. Ananthavel, S.; Padmanaban, S.; Shanmugham, S.; Blaabjerg, F.; Ertas, A.H.; Fedak, V. Analysis of enhancement in available power transfer capacity by STATCOM integrated SMES by numerical simulation studies. *Eng. Sci. Technol. Int. J.* **2016**, *19*, 671–675. [CrossRef]
35. Jain, S.; Ramulu, C.; Padmanaban, S.; Ojo, J.O.; Ertas, A.H. Dual MPPT algorithm for dual PV source fed Open-End Winding Induction Motor Drive for pumping application. *Eng. Sci. Technol. Int. J.* **2016**, *19*, 1771–1780. [CrossRef]
36. Sundaram, E.; Gunasekaran, M.; Krishnan, R.; Padmanaban, S.; Chenniappan, S.; Ertas, A.H. Genetic algorithm based reference current control extraction based shunt active power filter. *Int. Trans. Electr. Energy Syst.* **2021**, *31*, e12623. [CrossRef]
37. Padmanaban, S.; Blaabjerg, F.; Wheeler, P.; Ojo, J.O.; Ertas, A.H. High-Voltage DC-DC Converter Topology for PV Energy Utilization—Investigation and Implementation. *Electr. Power Compon. Syst.* **2017**, *45*, 221–232. [CrossRef]
38. Padmanaban, S.; Daya, F.J.; Blaabjerg, F.; Wheeler, P.W.; Szcześniak, P.; Oleschuk, V.; H.Ertas, A. Wavelet-fuzzy speed indirect field oriented controller for three-phase AC motor drive—Investigation and implementation. *Eng. Sci. Technol. Int. J.* **2016**, *19*, 1099–1107. [CrossRef]
39. Mises, R.V. Mechanik der festen Körper im plastisch-deformablen Zustand. In *Nachrichten von der Gesellschaft der Wissenschaften zu Göttingen, Mathematisch-Physikalische Klasse*; Göttinger Digitalisierungszentrum: Göttingen, Germany, 1913; Volume 1913, pp. 582–592.
40. Zhang, Y.; Wu, K.; Li, H.; Shen, S.; Cao, W.; Li, F.; Han, J. Thermal fatigue analysis of gold wire bonding solder joints in MEMS pressure sensors by thermal cycling tests. *Microelectron. Reliab.* **2022**, *139*, 114829. [CrossRef]
41. Teja, M.B.K.; Sharma, A.; Das, S.; Das, K. A review on nanodispersed lead-free solders in electronics: Synthesis, microstructure and intermetallic growth characteristics. *J. Mater. Sci.* **2022**, *57*, 8597–8633. [CrossRef]
42. Billah, M.; Aad, A.R.; Das, S.; Motalab, M.; Paul, R. Dependence of mechanical and thermal deformation behaviors on crystal size and direction of Cu_3Sn intermetallic: A molecular dynamics study. *Alex. Eng. J.* **2023**, *66*, 79–96. [CrossRef]
43. Wang, K.-K.; Gan, D.; Hsieh, K.-C. The orientation relationships of the Cu_3Sn/Cu interfaces and a discussion of the formation sequence of Cu_3Sn and Cu_6Sn_5. *Thin Solid Films* **2014**, *562*, 398–404. [CrossRef]

Disclaimer/Publisher's Note: The statements, opinions and data contained in all publications are solely those of the individual author(s) and contributor(s) and not of MDPI and/or the editor(s). MDPI and/or the editor(s) disclaim responsibility for any injury to people or property resulting from any ideas, methods, instructions or products referred to in the content.

applied sciences

MDPI

Article

Study on Shock Initiation Randomness of Energetic Materials on a Macroscopic Scale

Lan Liu [1,*], Weidong Chen [1,*], Shengzhuo Lu [1,*], Yanchun Yu [2], Shibo Wu [1] and Peiwen Wu [1]

[1] College of Aerospace and Civil Engineering, Harbin Engineering University, Harbin 150001, China
[2] School of Water Conservancy and Civil Engineering, Northeast Agricultural University, Harbin 150030, China
* Correspondence: wangyi_liulan@163.com (L.L.); chenweidong@hrbeu.edu.cn (W.C.); lusz@hrbeu.edu.cn (S.L.)

Abstract: The shock initiation randomness problem of energetic materials (SIREM) is an important problem in the research field of energetic material safety. With the purposes of solving SIREM on a macroscopic scale and obtaining the statistics, such as the initiation probabilities of energetic materials and the statistical characteristics of the detonation pressure, this paper considers the effect of the randomness of the parameters of the Lee–Tarver equation of reaction rate and the JWL equation of state of energetic materials and the randomness of load intensity parameters—such as fragment shock velocity—on the randomness of the shock initiations of energetic materials. It then decomposes SIREM into an initiation probability problem (IP) and a detonation pressure randomness problem (DPR). Further, with the Back Propagation Neural Networks optimized by the Genetic Algorithm (GABPNN) as the surrogate models of the numerical models of two-phase reactive flow, this paper proposes the approach of solving IP and DPR in turn, adopting Monte Carlo Simulations, which use the calculations of GABPNNs as repeated sampling tests (GABP-MCSs). Finally, by taking the shock initiation randomness problem of Composition B as an applied example, this paper adopts GABP-MCS under the randomness conditions that the means of fragment shock velocities are 1050 m/s and 1000 m/s and that the coefficients of variation (CVs) of BRVs are 0.005, 0.01, 0.015, and 0.02 in order to obtain the initiation probabilities of Composition B and the statistical characteristics, such as the means and CVs of the detonation pressure. It further observes the variation tendencies that these statistics show under various randomness conditions, so as to prove the effectiveness of GABP-MCS in solving SIREM. Therefore, this paper investigates SIREM on a macroscopic scale and proposes a universal technique for solving SIREM by GABP-MCS, in the hope of shedding some light on the SIREM study.

Keywords: energetic material; shock initiation randomness; initiation probability; detonation pressure randomness; Back Propagation Neural Network (BPNN); Genetic Algorithm (GA); surrogate model; Monte Carlo Simulation (MCS)

1. Introduction

Energetic materials, with randomly distributed micro-sized grains and many voids and cracks among them, are heterogeneous on a mesoscopic scale and show stochastic detonation characteristics on a macroscopic scale. Thus, the macro responses of energetic materials are generally stochastic under the action of shock loads. This explains why the shock load indexes of the initiation probability 50% (such as the fragment shock velocity, drop hammer height, shock pressure, or shock energy) are always the important characteristic indexes of the impact sensitivity tests of energetic materials [1–4]. Gresshoff [5] earlier recognized the importance of solving the shock initiation randomness problem of energetic materials (SIREM) and established the Probabilistic Shock Threshold Criterion based on the James Initiation Criterion and the assumption of initiation probability distribution, but they also contended that these empirical criterions, such as the James Initiation Criterion,

were more crude than the numerical simulations using reactive flow models in determining the impact responses of energetic materials. Similarly, Rashkovskii [6] constructed a probabilistic model of the shock initiation of heterogeneous explosive materials based on the critical initiation stress of explosive grains and the assumption of initiation probability distribution. In recent years, with the continuously improved mesoscale numerical simulation techniques, many research teams have begun to apply the numerical models of multiphase reactive flow in the SIREM study at mesoscale. Baer [7] took the initiative and adopted the mesoscale numerical model of multiphase reactive flow to solve SIREM, and they developed a universal method to describe the ignition randomness of energetic materials at mesoscale. After that, the research team of Zhou also carried out in-depth and comprehensive studies on SIREM by adopting the mesoscale numerical models of multiphase reactive flow. Zhou [8,9] developed an approach to computationally predict and quantify the stochasticity of the ignition process in condensed explosives under shock loads and studied the effect of the microstructure randomness on the shock response randomness of condensed explosives. Zhou [10–12] also developed an approach to calculate the probabilistic ignition threshold of condensed explosives based on mesoscale numerical simulation techniques and empirical ignition criterions. Zhou [13] also used this approach and the newly developed probabilistic formulation to calculate the probabilistic ignition thresholds of the HMXs with four microstructural forms. Zhou [14] also used three-dimensional, mesoscale, numerical simulation techniques to calculate the run-to-detonation distances of condensed explosives and led to the probabilistic formulations for the run-to-detonation distances as the shock pressure functions. In addition to Zhou's team, other research teams also used the mesoscale numerical models of multiphase reactive flow to solve SIREM. Kittell [15] believed that the microstructure randomness of heterogeneous energetic materials could lead to the randomness of heat release rates from a chemical reaction, and that the heat release fluctuations of heterogeneous energetic materials could be coupled to the reactive Euler equations, which could then be solved via the Riemann problem. Based on the study results in the literature [15], Kittell [16] drew the conclusion that the randomness of the heat release, yield strength, and material impedance could also lead to the reaction rate randomness of heterogeneous solid explosives, and constructed the stochastic burn model of heterogeneous solid explosives by using Langevin-type equations. Lee [17] considered the randomness of the specific heat, Grüneisen parameter, bulk modulus, yield strength, thermal expansion coefficient, and thermal conductivity of HMXs at mesoscale and established the probability density function of the run-to-detonation distances of HMXs by applying the Meso-informed Ignition and Growth model. Bakarjia [18] treated the initial porosity in the microstructure of energetic materials as a random field and adopted the Monte Carlo Simulations of a two-phase, five-equation, dynamic compaction model to calculate the probability of hotspot initiation. Mi [19] investigated the influence of the randomness of four microbubble distributions on the impact sensitivity randomness of liquid nitromethane by the mesoscale numerical simulation technique. Liu [20] researched the mechanical–thermal–chemical response of PBXs under low-velocity impact, obtained the influence of the density number and the statistical distribution of microcracks on the impact ignition of PBXs, and described the ignition probability of PBXs based on the Weibull distribution. Miller [21] proposed a simplified shock initiation criterion, classified the initiation responses of HMXs under different test conditions by using mesoscale numerical simulations, and obtained the probabilistic responses of the HMX samples to the variations in the mean porosity and chemical kinetics rate.

It can be seen from the researches above that SIREM is a common problem in the research field of energetic material safety, which has been solved, under the assumption of initiation probability distribution, by applying various techniques, such as empirical initiation criterions and mesoscale numerical simulations of multiphase reactive flow, with substantial achievements. However, none of the research has used the numerical models of multiphase reactive flow in solving SIREM on a macroscopic scale. Therefore, the initiation probabilities of energetic materials with standard specifications under standard

test conditions and, thus, their probabilistic initiation thresholds can be obtained through the previous research results. So is the effect of the microstructure randomness on the shock sensitivity randomness of the energetic material specimens. Yet, unknown remain the initiation probabilities of the energetic materials under complex working conditions (such as complex structural shielding, shock loads, and geometrical shapes) and the randomness of the detonation pressure in different positions inside these energetic materials after they are initiated. This means that the existing research has conducted only a preliminary theoretical study on SIREM and that it is difficult to be widely applied to engineering practices, such as assessments of the shock safety randomness of ammo and rocket motors. In this sense, it is necessary to analyze SIREM on a macroscopic scale and to apply the macroscale numerical models of multiphase reactive flow and their surrogate models in the SIREM study in the hope of better meeting the needs of engineering practices.

Some research has provided reference to analyzing SIREM on a macroscopic scale. Gresshoff [5] argued that the Lee–Tarver equation of reaction rate was tuned to an idealized 50% threshold and, thus, could not directly provide the analyst with a sense of "margin to initiation"; Gresshoff [5] also pointed out that uncertainties from experimental conditions and random heterogeneities in the specimens could lead to the randomness of the shock initiation test results of energetic materials. Landerville [22] showed that the parameters vary to a large degree among experiments due to the inherent noise of experiments and the inconsistencies in fitting ranges and schemes. In addition, in studying the randomness of underwater explosions, the research team of Chen contended that the parameters of the Jones–Wilkins–Lee (JWL) equation of state of energetic materials, obtained from parametric measurement tests, demonstrated a random nature, which led to the randomness of the detonation pressure of energetic materials [23]. In their study of the stochastic dynamics of structures under explosive loads, they also argued that the parameters of the Mie–Gruneisen equation of state, the Johnson–Cook constitutive equation, and the Johnson–Cook failure model of metal structures showed randomness, which led to the randomness of the normal stress and deviatoric stress of metal structures under explosive loads, and further led to the randomness of the dynamic responses of metal structures [24,25]. Enlightened by these researches, it is natural to hold that the parameters of the Lee–Tarver equation of reaction rate and the JWL equation of state will probably show random errors in parametric measurement tests. Since, in the numerical models of two-phase reactive flow, the Lee–Tarver equation of reaction rate describes the reaction rates of energetic materials, and the JWL equation of state describes the Pressure–Volume–Energy (P-V-E) relationships of energetic materials, the parameters of these two equations can fully describe the detonation characteristics of energetic materials. Therefore, when solving SIREM on a macroscopic scale by adopting the numerical models of two-phase reactive flow and their surrogate models, they should attribute the randomness of SIREM to the randomness of the parameters of these two equations and the randomness of the physical quantities, such as the fragment shock velocity that affects shock load intensity, which should be taken as the starting point to further study the initiation probabilities of energetic materials under random shock loads and the randomness of the detonation pressure after energetic materials are initiated. In fact, the randomness of the parameters of these two equations is the macroscopic manifestation of the randomness of the microstructure of energetic materials considered in the literature [7–21]; hence, these two kinds of randomness are equivalent and can both represent the randomness of the detonation characteristics of energetic materials, which will be also mentioned in Discussion 5.

In addition, since the numerical models of two-phase reactive flow involve the processes in which the unreacted energetic materials of the condensed phase are transformed into the reaction products of gas phase, a very complicated relationship appears between the parameter randomness of the Lee–Tarver equation of reaction rate and the JWL equation of state and the shock response randomness of energetic materials, and also marked differences appear in the random response values between the initiation and non-initiation states of energetic materials. This means that the common stochastic analysis methods,

such as semi-analytical methods and surrogate model methods of response surfaces, may not be used to solve SIREM on a macroscopic scale. Therefore, what should be adopted are the methods of combining the Artificial Neural Networks (ANNs), which are more powerful in nonlinear mapping, with Monte Carlo Simulations (MCSs) to solve SIREM on a macroscopic scale. Since the Back Propagation Neural Network optimized by the Genetic Algorithm (GABPNN) is an ANN with strong nonlinear mapping ability [26–29], this paper adopts GABPNNs as the surrogate models of the numerical models of two-phase reactive flow, and it adopts the MCSs, which use the calculations of GABPNNs as repeated sampling tests (GABP-MCS) to solve SIREM. The specific reasons for selecting GABP-MCS will be given in Discussion 5.

In a nutshell, in order to develop a universal technique for calculating the initiation probabilities of energetic materials under complex working conditions and the statistical characteristics of detonation pressure, so as to make the study on SIREM better meet the needs of engineering practices, this paper investigates SIREM on a macroscopic scale, decomposes SIREM into an initiation probability problem (IP) and a detonation pressure randomness problem (DPR), and identifies the basic random variables (BRVs) and random responses (RRs) of IP and DPR. Then, this paper proposes the approaches of adopting GABP-MCS to solve IP and DPR in turn. Finally, by taking the shock initiation randomness problem of Composition B as an example, this paper demonstrates the specific process of adopting GABP-MCS to solve SIREM and verifies the effectiveness of this integrated method, in the hope of providing a technical reference for further study on SIREM.

2. Problem Analysis

2.1. Problem Decomposition

Under the effects of both the detonation characteristic randomness of energetic materials and the shock load randomness, it is a random problem whether energetic materials can be initiated. So is the detonation pressure after energetic materials are initiated. Therefore, the SIREM study on a macroscopic scale should process the initiation probabilities of energetic materials and the randomness of detonation pressure after energetic materials are initiated in turn. It is necessary to decompose SIREM into an initiation probability problem (IP) and a detonation pressure randomness problem (DPR).

2.2. BRVs of the Problem

Since the randomness of the shock initiation of energetic materials is caused by the randomness of the detonation characteristics of energetic materials and the randomness of shock load conditions, the BRVs of SIREM should also be divided into the BRVs on the detonation characteristics of energetic materials and the BRVs on shock load conditions. The following is the identification of these two kinds of BRVs.

(1) BRVs on detonation characteristics of energetic materials

In the numerical models of two-phase reactive flow of the shock initiation problem of energetic materials, the equations of reaction rate, showing the shock initiation reaction rate of energetic materials, generally adopt the Lee–Tarver equation of reaction rate, and the equations of state of the unreacted energetic materials of the condensed phase and the reaction products of the gas phase generally adopt the JWL equation of state. See the two in Equations (1) and (2) [30–32].

$$\frac{d\lambda}{dt} = I(1-\lambda)^b(\mu-a)^x + G_1(1-\lambda)^c\lambda^d p^y + G_2(1-\lambda)^e\lambda^g p^z \quad (1)$$

where λ is the fraction of an energetic material that has reacted, t is the time, $\frac{d\lambda}{dt}$ is the reaction rate, μ is the current compression degree, a is the critical compression degree, and I, b, x, G_1, c, d, y, G_2, e, g, and z are the parameters.

$$p = A\left(1-\frac{w}{R_1V}\right)\exp(-R_1V) + B\left(1-\frac{w}{R_2V}\right)\exp(-R_2V) + \frac{wE}{V} \quad (2)$$

where p is the pressure, V is the relative volume, E is the energy in per unit volume, and A, B, R_1, R_2, and w are the parameters. The five parameters of unreacted energetic materials and reaction products are respectively marked as A_c, B_c, R_{c1}, R_{c2}, w_c, and A_g, B_g, R_{g1}, R_{g2}, w_g in order to distinguish between the two types.

The literature [32] has pointed out that the three terms in the Lee–Tarver equation of reaction rate are the ignition term, growth term, and completion term. For the parameters of these three terms, a controls the critical compression degrees of energetic materials, and when μ is less than a, energetic materials cannot be initiated; I, G_1, and G_2 are the coefficients of these three terms; b, c, d, e, and g are the burnup indices of these three terms; y and z are the pressure indices of the growth term and completion term; I and x control the number of hot spots; b and c control the combustion of inward spherical particles; G_1 and d control the reaction growth duration at the early stage of hot spots; and G_2 and z control the reaction rate at high pressure. For the parameters of the JWL equation of state, A_c, B_c, A_g, and B_g are the parameters of the linear relationship between the detonation pressure and the isentropic expansion pressure, and R_{c1}, R_{c2}, w_c, R_{g1}, R_{g2}, and w_g are the parameters related to energetic materials. Therefore, the parameters of these two equations can fully describe the detonation characteristics of energetic materials, and the effect of the changes of the factors, such as the density, temperature, and humidity, on the detonation characteristics of energetic materials can also be expressed by the numerical changes of these parameters. In addition, the parameters of the Lee–Tarver equation of reaction rate are fitted by the shock initiation tests and numerical simulations [33–35], and the parameters of the JWL equation of state are fitted by the cylinder tests and numerical simulations [36–38]. The literature [5,22–25] suggests that such parametric measurement tests and corresponding numerical simulations generally have random errors, and so do the parameters obtained. Based on the previous achievements, this paper holds that the parameters of these two equations also have randomness, and the randomness of the detonation characteristics of energetic materials can also be described by the randomness of these parameters. Therefore, the main BRVs on the detonation characteristics of energetic materials can be selected from these parameters, and the randomness of the factors, such as the density, temperature, and humidity of energetic materials, can also be expressed by the randomness of these parameters. In addition, the relationship between the randomness of these parameters and the randomness of the microstructure of energetic materials considered in the literature [7–21] will be discussed in Discussion 5.

(2) BRVs on shock load conditions

Since the mass m, shock velocity v, and shock angle θ of a fragment are the important physical quantities that directly affect the intensity of shock loads, the randomness of shock load conditions can be represented by the randomness of these physical quantities. Therefore, the main BRVs on shock load conditions can be selected from these physical quantities.

2.3. RRs of the Problem

Since SIREM is decomposed into IP and DPR, the RRs of IP and DPR should be identified respectively.

(1) RR of IP

In IP, the initiation-recognizing coefficient δ as a new physical quantity is introduced to recognize whether energetic materials are initiated under the combined action of the above two kinds of BRVs; that is, if energetic materials are initiated, δ will be recognized to be 1, and if not, δ will be recognized to be 0. So, under the action of BRVs, the randomness of the shock initiation of energetic materials can be represented by the randomness of the 0–1 recognition results of δ. In this sense, δ should be defined as the RR of IP, and IP can be summarized as the problem of calculating the initiation probabilities R's of energetic materials under the action of BRVs, according to the statistical analysis results of δ.

(2) RR of DPR

In DPR, the detonation pressure P of energetic materials should be defined as the RR of DPR, and DPR can be summarized as the problem of calculating the statistical analysis results of P under the combined action of the above two kinds of BRVs.

Above is the analysis of SIREM on a macroscopic scale. Figure 1 below is the corresponding flow chart.

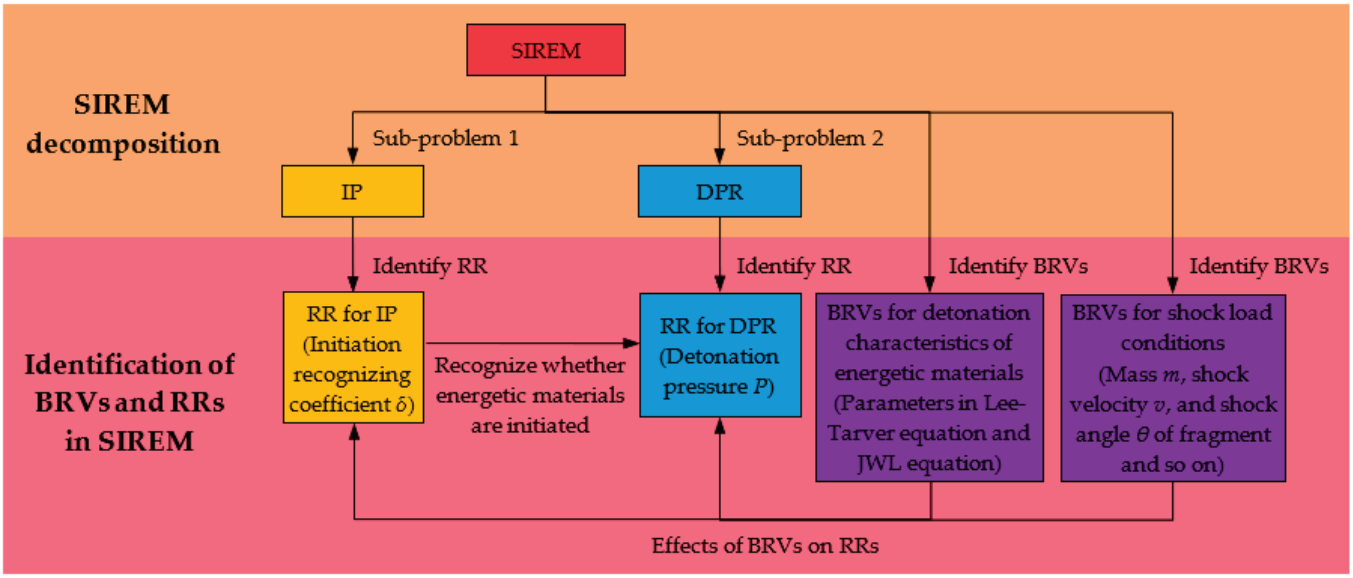


Figure 1. The schema for SIREM.

It should be noted that the above BRVs are just those that may be involved in SIREM on a macroscopic scale. Yet, in studies, it is necessary to take real factors into account in order to identify with caution the main BRVs involved and to obtain their actual statistical distributions.

3. Methodology

Since the principles of GABPNN have been discussed in a lot of literature [26–29], the following will present directly the main processes of using GABP-MCS to solve SIREM on a macroscopic scale, and the reasons for selecting this method will be given in Discussion 5.

(1) Constructing training sample sets and test sample sets

Firstly, BRV sample points are randomly generated according to the statistical distributions of BRVs, and the repeated numerical simulations are conducted based on the numerical models of two-phase reactive flow, so as to obtain the 0–1 recognition result of δ and the P of each gauge in numerical models that correspond to each BRV sample point. Then, these data are standardized, and the standardized BRV sample points are taken as the input data, and the 0–1 recognition results of δ are taken as the expected output data, so as to construct the training sample sets and test sample sets of the GABPNN of IP. Finally, the standardized BRV sample points that can lead energetic materials to be initiated are selected from all the standardized BRV sample points and are taken as the input data, and the standardized values of the P of each gauge are taken as the expected output data, so as to construct the training sample sets and test sample sets of the GABPNN of DPR.

In addition, it should be pointed out that, in the repeated numerical simulations, whether detonation waves are generated inside energetic materials under shock loads can be taken as the shock initiation criterion of energetic materials. That is, if detonation waves are generated, it means energetic materials are initiated, and δ is assigned as 1. If no detonation wave is generated, it means energetic material are not initiated, and δ is assigned as 0.

(2) Constructing surrogate models of IP and DPR

Two GABPNNs are trained and tested by the training sample sets and test sample sets of IP and DPR, respectively, so as to construct the surrogate models of IP and DPR. Furthermore, IP is a problem of pattern classification, and there is a very complicated mapping between BRVs and δ, so the double-hidden-layer GABPNN should be chosen as the surrogate model of IP. DPR is a function approximation problem. Cotter [39] and Castro [40] have proven that the forward artificial neural networks of a 3-layer structure can address most function approximation problems, so the single-hidden-layer GABPNN can be taken as the surrogate model of DPR.

(3) Addressing IP and DPR by GABP-MCSs

Firstly, new BRV sample points are generated, which conform to the corresponding statistical distribution and whose sampling ranges and densities meet statistical needs, and these BRV sample points are standardized, so as to construct the prediction sample sets of IP. Then, all the standardized BRV sample points of the prediction sample sets of IP, as input data, are inputted in turn into the surrogate model (GABPNN) of IP, so as to quickly calculate the 0–1 recognition results of δ corresponding to these sample points. Then, these 0–1 recognition results of δ are statistically analyzed, so as to obtain the estimates of the R's of energetic materials, thus solving IP.

After that, according to the above 0–1 recognition results of δ, the standardized BRV sample points that can lead energetic materials to be initiated are selected from the prediction sample sets of IP, so as to constitute the prediction sample sets of DPR. Then, all the standardized BRV sample points of the prediction sample sets of DPR, as input data, are inputted in turn into the surrogate model (GABPNN) of DPR, so as to quickly calculate the output results corresponding to these sample points. Then, these output results are inversely standardized, so as to obtain the predicted values of the P of each gauge in numerical models corresponding to these sample points. Finally, the predicted values of the P of each gauge are statistically analyzed, so as to obtain the estimates of the statistical characteristics, such as the mean and coefficient of variation (CV) of the P of each gauge, thus solving DPR.

The above processes are shown in the global technical route in Figure 2.

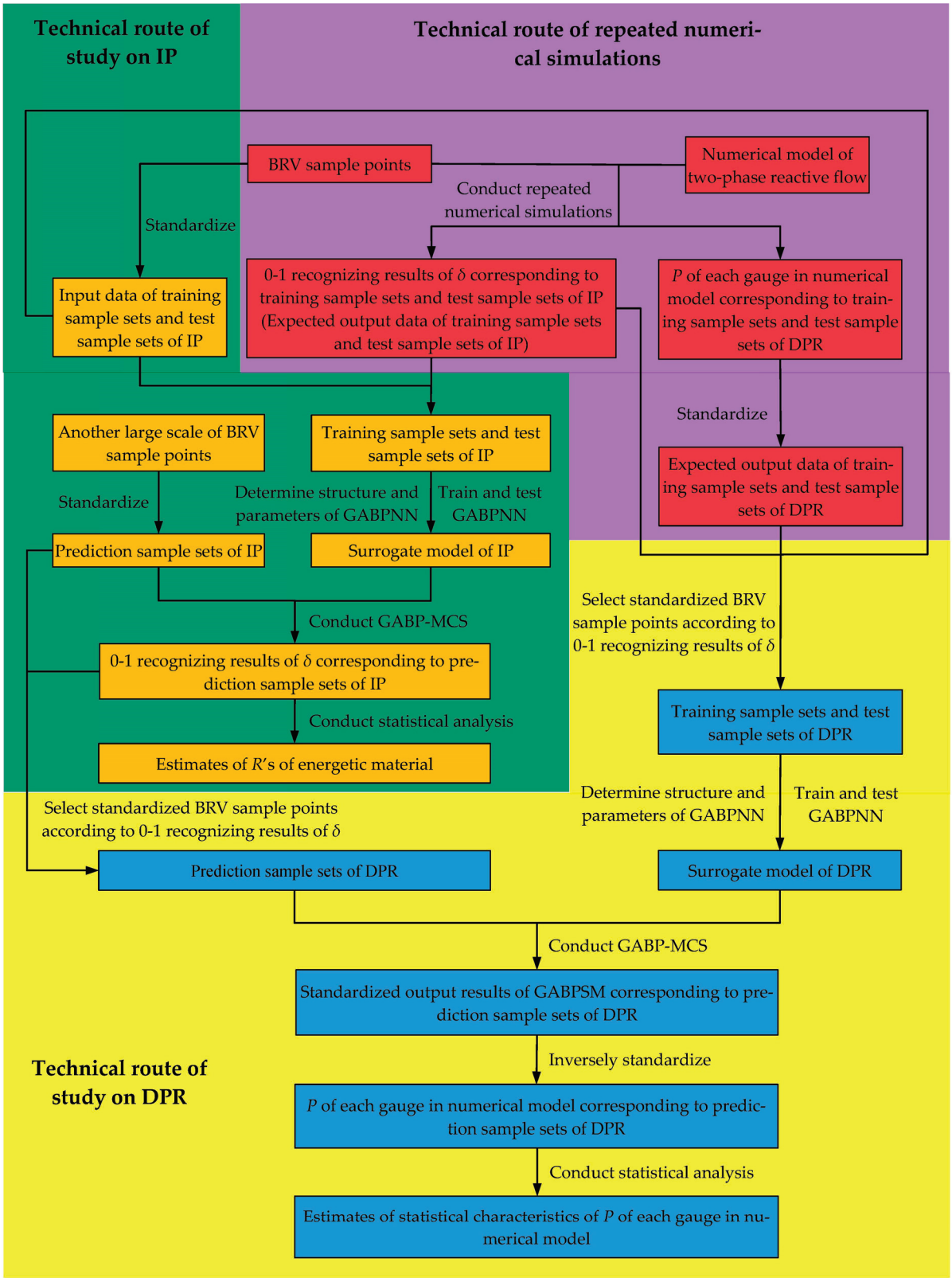


Figure 2. The global technical route to addressing SIREM.

4. Applied Example

Composition B, composed of TNT and RDX in fixed proportions, which are typical energetic materials, and they are widely used as military explosives. Similar to most energetic materials, the shock initiation of Composition B can also be simulated by the

numerical models of two-phase reactive flow, and the shock initiation reaction rate and P-V-E relationship of Composition B can also be described by the Lee–Tarver equation of reaction rate and the JWL equation of state, respectively. Therefore, Composition B is representative among various kinds of energetic materials. It can also be used as an example of solving SIREM on a macroscopic scale with the specific processes of adopting GABP-MCS to solve the shock initiation randomness problem of Composition B. Therefore, the shock initiation test of Composition B with shield plate recorded in the literature [41] is taken as the applied example in this paper, and the exploration of the randomness in this example will be expressed in detail to demonstrate the specific processes of solving SIREM by GABP-MCS and to verify the effectiveness of this integrated method. In addition, as the Back Propagation Neural Networks (BPNN) and Radial Basis Function Neural Network (RBFNN) are two very classical ANNs, they are usually used as the comparisons of other ANNs. Therefore, in this example, these two ANNs are also used as the comparisons of GABPNN, so as to investigate the advantages of GABPNN as the surrogate model of the numerical model of two-phase reactive flow.

4.1. Numerical Model

The example [41] took Composition B as the test explosives, the 5 mm-thick steel plates as the shield plates, and the 20 mm-long cylindrical steel with a diameter of 10 mm as the fragments. The test results showed that, with a shock velocity of fragments lower than 1003.5 m/s, Composition B was not initiated, while with a shock velocity of fragments higher than 1049.8 m/s, Composition B was initiated. It can, thus, be seen that the critical shock initiation velocity of Composition B should be between 1000 m/s and 1050 m/s under the above working conditions.

In the repeated numerical simulations of the randomness study on this example, the numerical model of two-phase reactive flow worked as the theoretical model, the generalized interpolation material point method (GIMPM) [42] worked as the numerical simulation method, and the calculation program was the self-compiled GIMPM program in the Fortran language. The numerical model constructed by this GIMPM program is shown in Figure 3, and the coordinates of the three gauges in this model are shown in Table 1. In addition, the deterministic parameter values of Composition B in the Lee–Tarver equation of reaction rate and the JWL equation of state were taken from the literature [43], and these deterministic parameter values are shown in Tables 2 and 3.

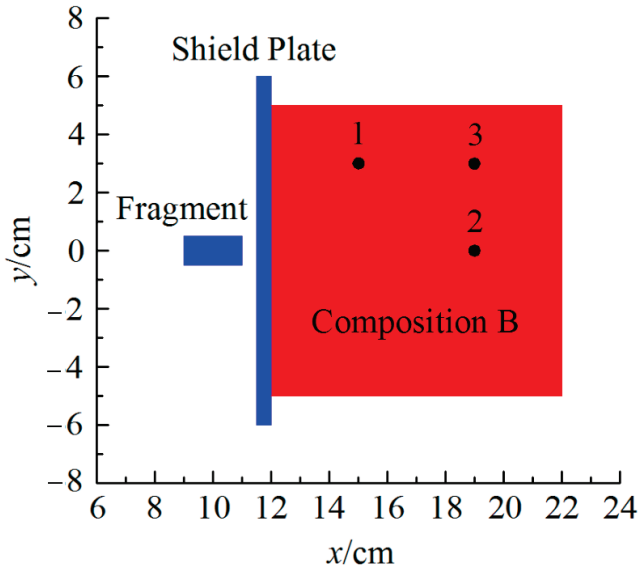


Figure 3. The numerical model of the example.

Table 1. The coordinates of the gauges.

Gauge Number	1	2	3
x coordinate (cm)	15.0	19.0	19.0
y coordinate (cm)	3.0	0.0	3.0

Table 2. The deterministic parameter values of Composition B in the Lee–Tarver equation of reaction rate.

Parameter	a	I (μs^{-1})	b	x	G_1 ($Mbar^{-y}\mu s^{-1}$)	c	d	y	G_2 ($Mbar^{-z}\mu s^{-1}$)	e	g	z
Value	0.01	44.0	2/9	4.0	414.0	2/9	2/3	2.0	0.0	0.0	0.0	0.0

Table 3. The deterministic parameter values of Composition B in the JWL equation of state.

Parameter	A_c (Mbar)	B_c (Mbar)	R_{c1}	R_{c2}	w_c	A_g (Mbar)	B_g (Mbar)	R_{g1}	R_{g2}	w_g
Value	778.1	−0.05031	11.3	1.13	0.8938	5.242	0.07678	4.2	1.1	0.34

For the accuracy of the training sample sets and the test sample sets constructed by the GIMPM program, it is necessary to verify in advance the accuracy of the test result simulations of this example under this program. To this end, this program simulates the shock response results of Composition B under the shock load conditions that the fragment impact velocities are 1003.5 m/s and 1049.8 m/s, respectively. The pressure curves of the three gauges are shown in Figure 4 and the color contour plots of the pressure in Figure 5.

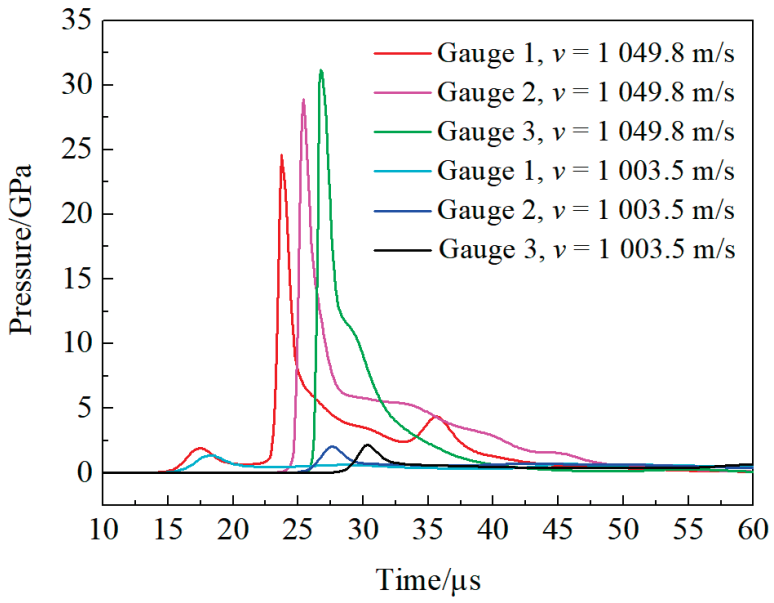


Figure 4. The pressure curves of the three gauges of the numerical model when the v's are 1003.5 m/s and 1049.8 m/s, respectively.

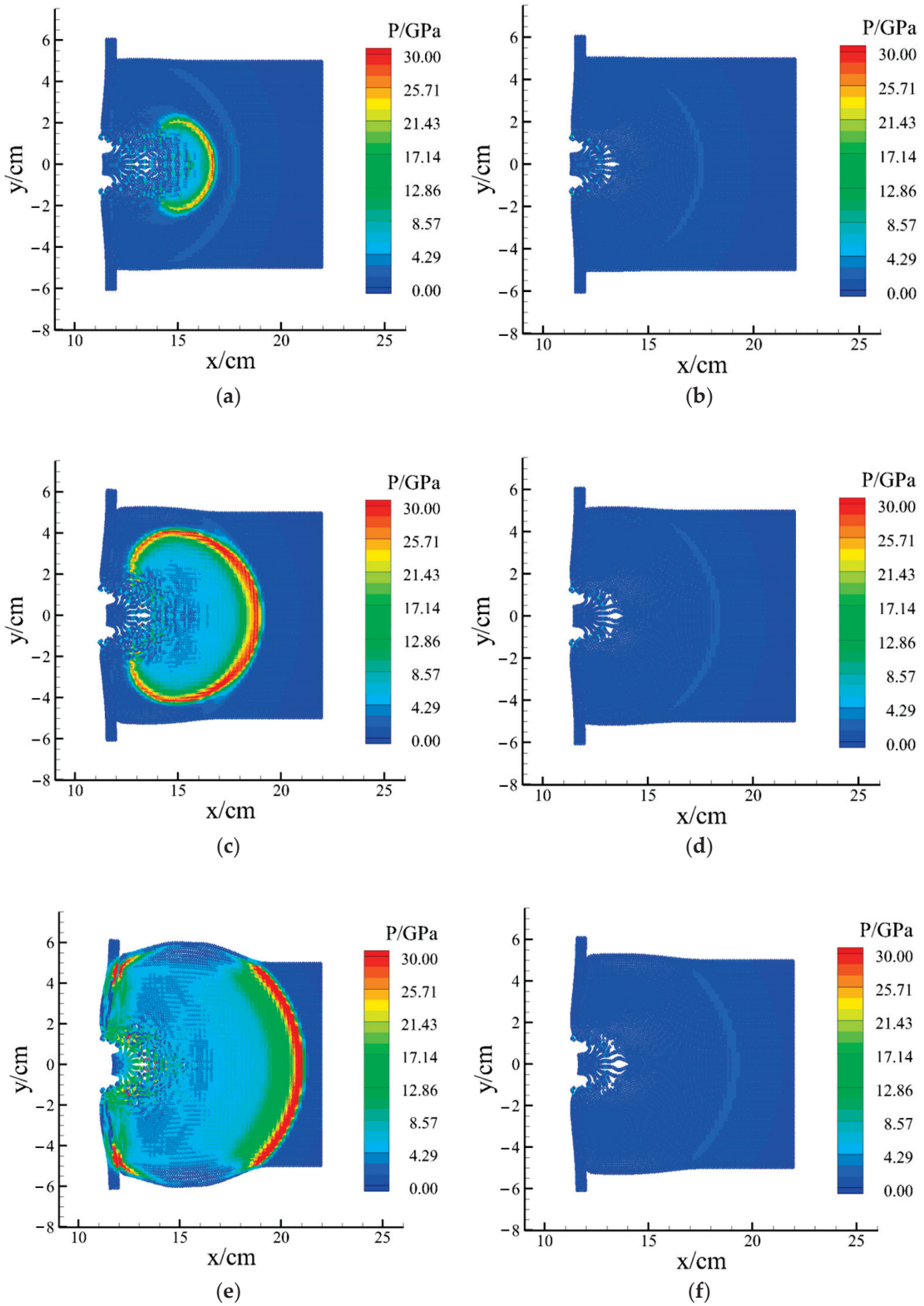


Figure 5. The color contour plots of the pressure when the v's are 1003.5 m/s and 1049.8 m/s, respectively. (**a**) The contour plot when t = 22 μs, v = 1049.8 m/s. (**b**) The contour plot when t = 22 μs, v = 1003.5 m/s. (**c**) The contour plot when t = 25 μs, v = 1049.8 m/s. (**d**) The contour plot when t = 25 μs, v = 1003.5 m/s. (**e**) The contour plot when t = 28 μs, v = 1049.8 m/s. (**f**) The contour plot when t = 28 μs, v = 1003.5 m/s.

Figures 4 and 5 show that when the fragment shock velocity is 1049.8 m/s, all the pressure peaks of the three gauges are over 20 GPa, and detonation waves are also generated inside Composition B, suggesting that Composition B has been initiated by the shock load. What can also be concluded is that when the fragment shock velocity is 1003.5 m/s, the pressure curves of the three gauges are all gentle, with a pressure peak lower than 2.5 GPa, and stress waves with low pressure, not detonation waves, are generated inside Composition B, suggesting that Composition B has not been initiated by the shock load. These numerical simulation results are consistent with the test results. Thus, this program can accurately simulate the shock initiation of Composition B, and the training sample sets and test sample sets constructed by the repeated numerical simulations via this program can also be identified as accurate and qualified to meet the needs of training and testing the GABPNNs.

4.2. Identification of BRVs and RRs

In this example, each test used cylindrical steel fragments of the same size, and the ballistic trajectories of all the fragments were horizontal straight lines; so, the randomness of the masses m and the shock angles θ of these fragments could be ignored. However, due to the significant influence of the charge errors of the fragment shooting gun and the fragment shock velocity recording errors of the recording equipment, the fragment shock velocity v recorded in each test had obvious randomness. In addition, according to Table 2, the values of all 4 parameters, G_2, e, g, and z, are 0.0, which indicates that the Lee–Tarver equation of reaction rate of Composition B does not have the completion term. So, in this example, there are 19 main BRVs, namely, the 8 parameters a, I, b, x, G_1, c, d, and y in the ignition and the growth terms of the Lee–Tarver equation of reaction rate, and the 10 parameters A_c, B_c, R_{c1}, R_{c2}, w_c, A_g, B_g, R_{g1}, R_{g2}, and w_g in the JWL equation of state, and the v in the shock load conditions. The RRs in the IP and DPR are, respectively, the δ and the P's of the three gauges in the numerical model shown in Figure 3 and Table 1.

4.3. Randomness Study

For conciseness and brevity of expression, the shock initiation randomness problem of Composition B is also abbreviated to SIREM in this example. According to what has been discussed in Section 4.1, when the mean $\overline{v}$ of the v is 1050 m/s or 1000 m/s, Composition B approaches the critical shock initiation state, with obvious randomness in the shock initiation, so the SIREM was solved under the two shock load conditions where the values of the $\overline{v}$ were, respectively, 1050 m/s and 1000 m/s. Moreover, in order to reveal the common and universal aspects of the SIREM study, it is assumed that the 19 main BRVs in this example are all independent of each other and subject to the normal distribution, and the 4 randomness conditions, in which the CVs of these BRVs were, respectively, 0.005, 0.01, 0.015, and 0.02, were considered under these 2 shock load conditions.

4.3.1. Shock Load Condition Where $\overline{v}$ Is 1050 m/s

(1) Study on IP

(i) Constructing training sample set and test sample sets

In addressing the IP when the $\overline{v}$ is 1050 m/s, in order to guarantee the excellent generalization ability of the ANNs, 2000 sample points were generated for the BRVs with the CV of 0.02, and 500 sample points were generated for the BRVs with the CV of 0.005, so as to construct the training sample set with 2500 sample points. Then, a test sample set of 1000 sample points was constructed for the BRVs with each of the CVs of 0.005, 0.01, 0.015, and 0.02. The four test sample sets tested whether the ANNs could accurately calculate the RRs under these randomness conditions. The statistical results of the initiation and non-initiation frequencies of Composition B in these training sample set and test sample sets are shown in Table 4.

Table 4. The statistical results of the initiation and non-initiation frequencies of Composition B in the training sample set and test sample sets under the shock load condition where $\overline{v}$ is 1050 m/s.

Sample Set		Sample Size q	Initiation Frequency	Non-Initiation Frequency
Training sample set		2500	1554	946
Test sample set	CV of BRVs being 0.005	1000	768	232
	CV of BRVs being 0.01	1000	685	315
	CV of BRVs being 0.015	1000	612	388
	CV of BRVs being 0.02	1000	585	415

(ii) Determining the structure and important parameters of ANNs

In this example, according to the numbers of the BRVs and RR in the IP, the neuron numbers of the input layer, first hidden layer, second hidden layer, and output layer of the GABPNN for the IP were, respectively, set as 19, 25, 15, and 1. So, the structure of this GABPNN was $19 \times 25 \times 15 \times 1$. In addition, the network maximum training time $T_{\max}$ was set as 20,000, the network training rate R_t was set as 0.05, the network training allowable error E_a was set as 0.001, the population size M_p was set as 20, the maximum generation $G_{\max}$ was set as 30, the chromosome crossover probability P_c was set as 0.75, the chromosome mutation probability P_m was set as 0.1, and the fitness coefficient C was set as 20.0.

In addition, the structure and corresponding parameters of the BPNN were the same as the corresponding ones of the GABPNN. The neuron numbers of the input layer and output layer of the RBFNN were the same as the corresponding ones of the GABPNN, and the neuron number of the hidden layer of the RBFNN was equal to the sample size q of the training sample set.

(iii) Performance comparison of ANNs

Firstly, the GABPNN, BPNN, and RBFNN were trained by the above training sample set. Then, these three trained ANNs were tested by each of the above four test sample sets, with the test results shown in Table 5 and Figure 6. In Table 5, the δ_T stands for the calculation results of these three ANNs (the actual output results of the δ), and the δ_E the expected output results of the δ.

Table 5. The comparison of the test results of the ANNs in the IP study under the shock load condition where $\overline{v}$ is 1050 m/s.

Test Sample Set		ANN Being Tested	δ_T Being the Same as δ_E		δ_T Being Different from δ_E		Accuracy of Testing (%)
CV of BRVs	Test Number		Both δ_T and δ_E Being 1	Both δ_T and δ_E Being 0	δ_T Being 1 and δ_E Being 0	δ_T Being 0 and δ_E Being 1	
0.005	1000	GABPNN	723	180	52	45	90.3
		BPNN	697	145	87	71	84.2
		RBFNN	746	102	130	22	84.8
0.01	1000	GABPNN	627	275	40	58	90.2
		BPNN	611	269	46	74	88.0
		RBFNN	663	238	77	22	90.1
0.015	1000	GABPNN	564	358	30	48	92.2
		BPNN	548	349	39	64	89.7
		RBFNN	589	331	57	23	92.0
0.02	1000	GABPNN	553	379	36	32	93.2
		BPNN	536	375	40	49	91.1
		RBFNN	561	359	56	24	92.0

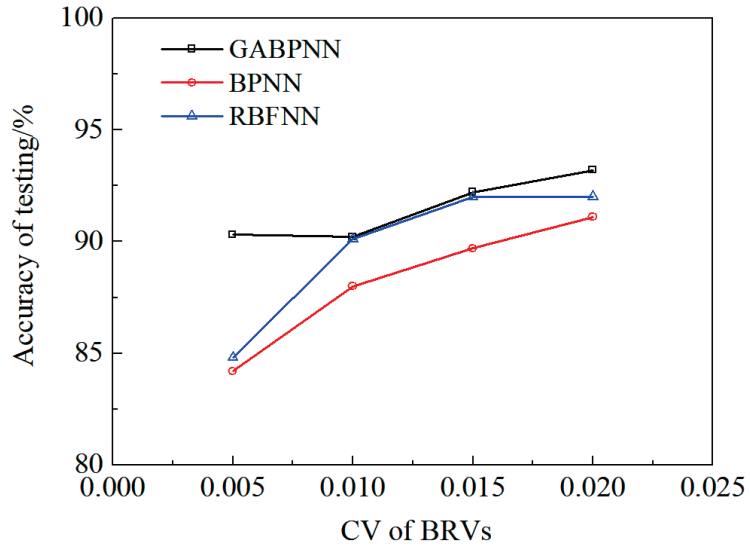


Figure 6. The comparison of the testing accuracy of the ANNs in the IP study under the shock load condition where $\overline{v}$ is 1050 m/s.

According to the test results shown in Table 5 and Figure 6, all the test accuracy results with which the GABPNN calculated the 0–1 recognition results of the δ corresponding to these 4 test sample sets were above 90%, and these test results were also better than the test results of BPNN and RBFNN. It is proved that the GABPNN has stronger nonlinear mapping ability than the BPNN and RBFNN, and the GABPNN can accurately calculate the 0–1 recognition results of the δ corresponding to the BRV sample points. Therefore, the GABPNN can be used as the surrogate model of the IP, and the GABP-MCS can also be used to estimate the R's of Composition B.

(iv) Estimation of R based on GABP-MCS

A prediction sample set with 100,000 sample points was constructed under each of the above 4 randomness conditions, and the 0–1 recognition results of the δ corresponding to these 4 prediction sample sets were obtained by the GABP-MCS, so as to obtain accurate estimates of the actual R's of Composition B under these 4 randomness conditions. The results are shown in Table 6 and Figure 7.

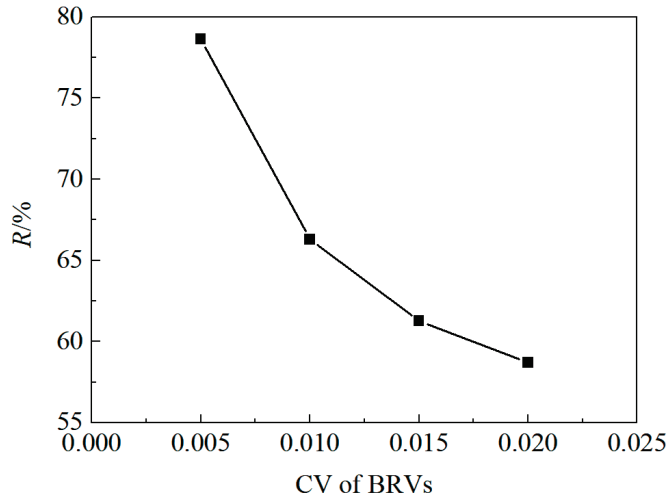


Figure 7. The correlation curve between the R of Composition B and the CV of the BRVs under the shock load condition where $\overline{v}$ is 1050 m/s.

Table 6. The calculation results of the GABP-MCS in the IP study under the shock load condition where $\overline{v}$ is 1050 m/s.

CV of BRVs	Simulation Number	Initiation Frequency	Non-Initiation Frequency	*R* (%)
0.005	100,000	78,654	21,346	78.65
0.01	100,000	66,291	33,709	66.29
0.015	100,000	61,281	38,719	61.28
0.02	100,000	58,711	41,289	58.71

According to the statistical data in Table 6 and the correlation curve in Figure 7, it can be concluded that when the $\overline{v}$ is 1050 m/s, the *R* of Composition B is negatively correlated with the CV of the BRVs; that is, the smaller the CV of the BRVs, the higher the *R* of Composition B. This is because the smaller the CV of the BRVs, the more concentrated the distribution of the BRV sample points in the corresponding prediction sample sets, the more BRV sample points there are that can lead Composition B to be initiated, the lower the randomness of the SIREM, and the more likely this SIREM is a deterministic problem; thus, the randomness calculation results of this SIREM will be closer to the deterministic results described in Section 4.1. So, it can be further deduced that, if the CV of the BRVs dropped to 0, this SIREM would become a deterministic problem, so Composition B would definitely be initiated (the *R* would increase to 1) under the shock load condition where $\overline{v}$ was 1050 m/s, which would be exactly the same as the deterministic results presented in Section 4.1.

(2) Study on DPR

(i) Constructing the training sample set and test sample sets

The sample points that could lead Composition B to be initiated were selected again from the training sample set and test sample sets of the IP, so as to construct the training sample set and test sample sets of the DPR. Therefore, according to the statistical data in Table 4, in addressing the DPR, the training sample set had 1554 sample points, and the 4 test sample sets, with the CVs of the BRVs being respectively 0.005, 0.01, 0.015, and 0.02, had 768, 685, 612, and 585 sample points respectively.

(ii) Determining the structure and important parameters of ANNs

According to the numbers of the BRVs and RRs in the DPR, the neuron numbers of the input layer, hidden layer, and output layer of the GABPNN for the DPR were, respectively, set as 19, 25, and 3. So, the structure of this GABPNN was $19 \times 25 \times 3$. In addition, the $T_{\max}$ was set as 20,000, the R_t was set as 0.05, the E_a was set as 0.001, the M_p was set as 20, the $G_{\max}$ was set as 30, the P_c was set as 0.75, the P_m was set as 0.1, and the *C* was set as 0.5.

In addition, the structure and corresponding parameters of the BPNN were the same as the corresponding ones of the GABPNN. The neuron numbers of the input layer and output layer of the RBFNN were the same as the corresponding ones of the GABPNN, and the neuron number of the hidden layer of the RBFNN was equal to the sample size *q* of the training sample set.

(iii) Performance comparison of ANNs

Firstly, the GABPNN, BPNN, and RBFNN were trained by the above training sample set. Then, these three trained ANNs were tested by each of the above four test sample sets, and the test results are shown in Table 7 and Figure 8.

Table 7. The comparison of the test results of the ANNs in the DPR study under the shock load condition where $\overline{v}$ is 1050 m/s.

Gauge Number		1				2				3			
CV of BRVs		0.005	0.01	0.015	0.02	0.005	0.01	0.015	0.02	0.005	0.01	0.015	0.02
MAPE of *P* (%)	GABPNN	2.16	1.75	1.49	1.25	1.46	1.25	1.10	1.19	0.91	0.75	0.82	0.83
	BPNN	2.45	2.00	1.63	1.53	1.75	1.43	1.20	1.37	1.25	0.92	0.95	0.94
	RBFNN	3.17	2.81	2.41	3.12	1.54	1.36	1.23	1.45	1.06	0.70	0.68	0.84

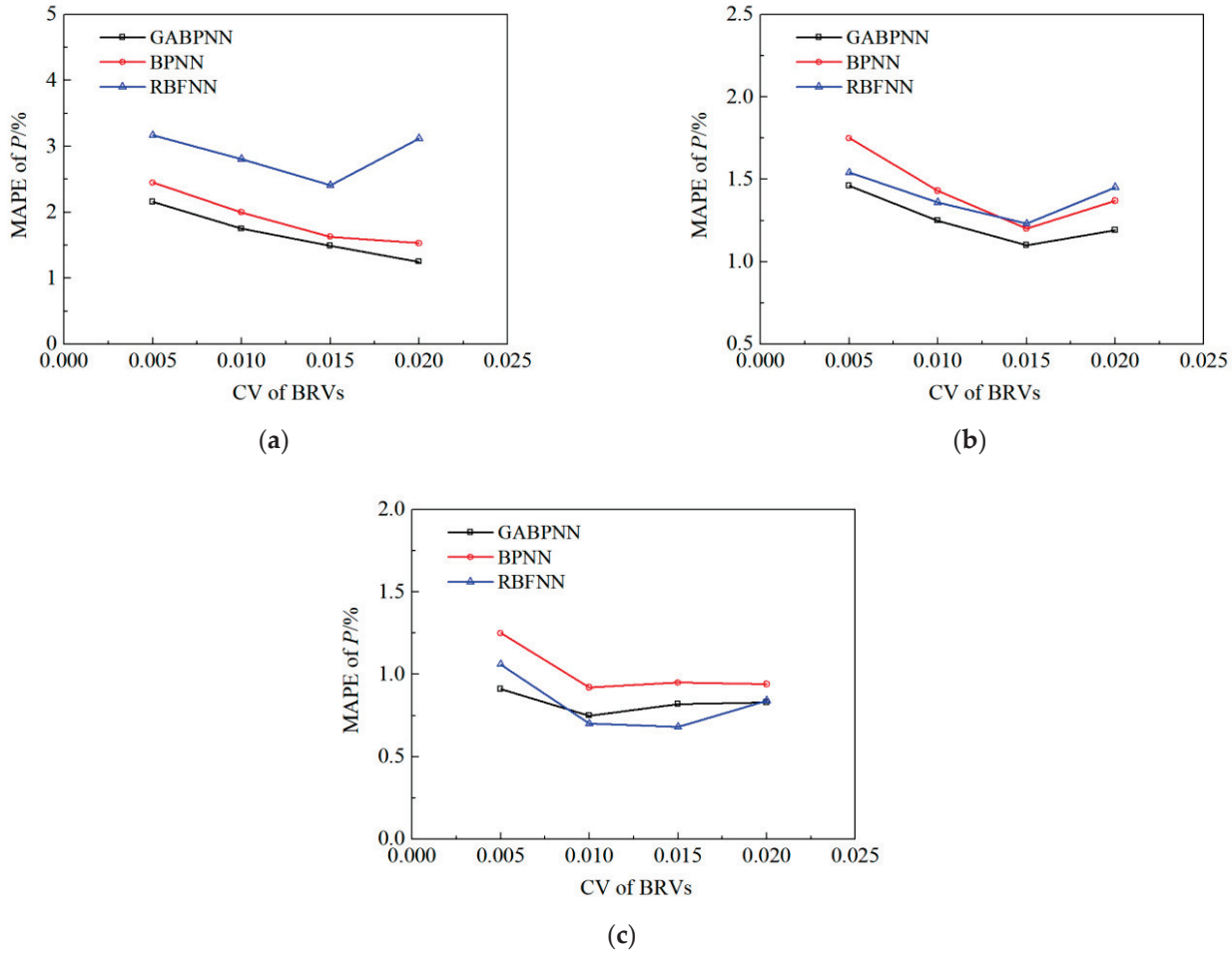


Figure 8. The comparisons of the MAPEs that the ANNs calculate the P's of the three gauges in the numerical mode in the DPR study under the shock load condition where $\overline{v}$ is 1050 m/s. (**a**) Gauge 1. (**b**) Gauge 2. (**c**) Gauge 3.

The test results in Table 7 and Figure 8 show that the GABPNN consistently had a Mean Absolute Percentage Errors (MAPE) lower than 2.2% in calculating the P of each gauge in the numerical model corresponding to these 4 test sample sets, and the MAPEs of the GABPNN were slightly higher than the corresponding ones of the RBFNN only when calculating the P of the gauge 3 corresponding to the test sample sets where the CVs of BRVs were respectively 0.01 and 0.015, and the MAPEs of the GABPNN were lower than the corresponding ones of the RBFNN and BPNN when calculating the P of each gauge under other conditions. It is proved that the GABPNN has stronger nonlinear mapping ability than the BPNN and RBFNN, and the GABPNN can accurately calculate the P of each gauge corresponding to the BRV sample points. Therefore, the GABPNN can be used as the surrogate model of the DPR, and the GABP-MCS can also be used to estimate the statistical characteristics of the P of each gauge of Composition B.

(iv) Estimation of the statistical characteristics of P based on GABP-MCS

The sample points that could lead Composition B to be initiated were selected from the prediction sample sets of the IP, so as to construct the prediction sample sets of the DPR. According to Table 6, in addressing the DPR, the 4 prediction sample sets, with the CVs of the BRVs being, respectively, 0.005, 0.01, 0.015, and 0.02, had 78,654, 66,291, 61,281, and 58,711 sample points, respectively. The calculation results of the P's of the three gauges in the numerical model corresponding to these four prediction sample sets were obtained by the GABP-MCS, so as to obtain the accurate estimates of the actual statistical characteristics

of the P's of these three gauges under the above four randomness conditions, as shown in Table 8 and Figure 9.

Table 8. The calculation results of the GABP-MCS in the DPR study under the shock load condition where $\overline{v}$ is 1050 m/s.

Gauge Number		1				2				3			
CV of BRVs		0.005	0.01	0.015	0.02	0.005	0.01	0.015	0.02	0.005	0.01	0.015	0.02
Statistical characteristic of P	Mean of P (GPa)	26.55	27.30	27.91	28.30	29.18	29.58	29.96	30.30	31.61	31.88	32.22	32.54
	CV of P	0.0618	0.0736	0.0824	0.0965	0.0271	0.0423	0.0567	0.0736	0.0228	0.0364	0.0509	0.0664

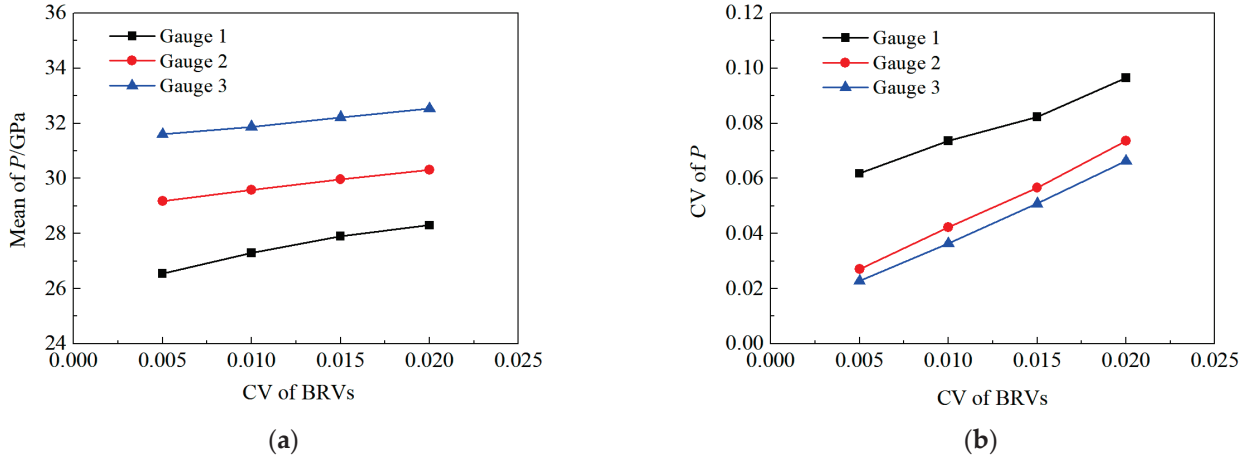


Figure 9. The correlation curves between the statistical characteristics of the P and the CVs of the BRVs under the shock load condition where $\overline{v}$ is 1050 m/s. (**a**) The correlation curves between the means of the P and the CVs of the BRVs. (**b**) The correlation curves between the CVs of the P and the CVs of the BRVs.

The following are the three observations from Table 8 and Figure 9 and their interpretation. First, for each gauge, the mean of its P is positively correlated with the CV of the BRVs; that is, the mean of its P can increase gradually with the CV of the BRVs. This is because the more likely the BRV sample points result in the initiation of Composition B, the greater P Composition B tends to generate in subsequent detonations. Furthermore, the larger the CV of the BRVs, the more scattered the distribution of the BRV sample points in the corresponding prediction sample sets, and the more BRV sample points that can result in lower values of the P will be eliminated in addressing the DPR for the initiation failure of Composition B. In this case, a higher proportion of the BRV sample points, which result in the higher values of the P in the prediction sample sets, suggests the higher estimated means of the P. What is also observed is that, under these four randomness conditions, the CVs of the P's of the three gauges in the numerical model are all significantly larger than the CVs of the BRVs, which indicates that the randomness of the BRVs can magnify the randomness of the P. The third observation is that, for each gauge, the CV of its P is also positively correlated with the CV of the BRVs; that is, the CV of its P can decrease with the CV of the BRVs. This is because the smaller the CV of the BRVs, the lower the randomness of the SIREM and the lower the randomness of the P, which suggests the smaller the CV of the P. So, it can be further deduced that, if the CV of the BRVs dropped to 0, the SIREM would become a deterministic problem, the CVs of the P would also drop to 0, and the P would also become a deterministic variable accordingly.

4.3.2. Shock Load Condition Where $\overline{v}$ Is 1000 m/s

(1) Study on IP

(i) Constructing training sample set and test sample sets

In addressing the IP when the $\overline{v}$ is 1000 m/s, in order to guarantee the excellent generalization ability of the ANNs and sufficient training sample points for the DPR, 3000 sample points were generated for the BRVs with the CV of 0.02, and 1000 sample points were generated for the BRVs with the CV of 0.005, so as to construct the training sample set with 4000 sample points. Then, a test sample set with 1000 sample points was constructed for the BRVs with each of the CVs of 0.005, 0.01, 0.015, and 0.02. Table 9 shows the statistical results of the initiation and non-initiation frequencies of Composition B in these training sample set and test sample sets.

Table 9. The statistical results of the initiation and non-initiation frequencies of Composition B in the training sample set and test sample sets under the shock load condition where $\overline{v}$ is 1000 m/s.

Sample Set		Sample Size q	Initiation Frequency	Non-Initiation Frequency
Training sample set		4000	1580	2420
Test sample set	CV of BRVs being 0.005	1000	258	742
	CV of BRVs being 0.01	1000	367	633
	CV of BRVs being 0.015	1000	398	602
	CV of BRVs being 0.02	1000	454	546

(ii) Determining the structure and important parameters of ANNs

In this stage, under the shock load condition that the $\overline{v}$ is 1000 m/s, the setting of the structure and important parameters of the GABPNN, BPNN, and RBFNN is the same as the corresponding operation under the shock load condition where the $\overline{v}$ is 1050 m/s; see Section 4.3.1.

(iii) Performance comparison of ANNs

Firstly, the GABPNN, BPNN, and RBFNN were trained by the above training sample set. Then, these three trained ANNs were tested by each of the above four test sample sets, and the test results shown in Table 10 and Figure 10 were obtained.

Table 10. The comparison of the test results of the ANNs in the IP study under the shock load condition where $\overline{v}$ is 1000 m/s.

Test Sample Set		ANN Being Tested	δ_T Being the Same as δ_E		δ_T Being Different from δ_E		Accuracy of Testing (%)
CV of BRVs	Test Number		Both δ_T and δ_E Being 1	Both δ_T and δ_E Being 0	δ_T Being 1 and δ_E Being 0	δ_T Being 0 and δ_E Being 1	
0.005	1000	GABPNN	196	684	58	62	88.0
		BPNN	198	667	75	60	86.5
		RBFNN	115	688	54	143	80.3
0.01	1000	GABPNN	311	572	61	56	88.3
		BPNN	309	567	66	58	87.6
		RBFNN	275	596	37	92	87.1
0.015	1000	GABPNN	341	553	49	57	89.4
		BPNN	334	542	60	64	87.6
		RBFNN	321	561	41	77	88.2
0.02	1000	GABPNN	405	504	42	49	90.9
		BPNN	390	503	43	64	89.3
		RBFNN	398	520	26	56	91.8

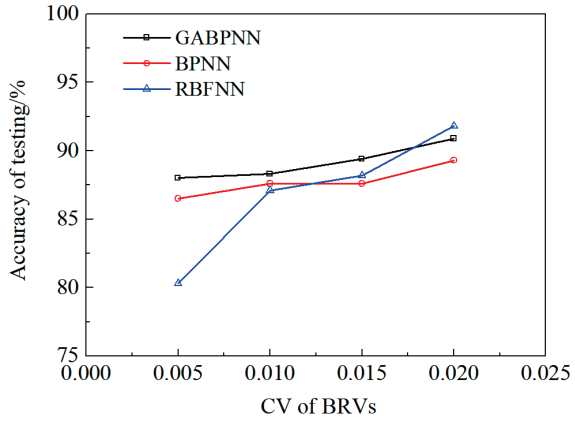


Figure 10. The comparison of the testing accuracy of the ANNs in the IP study under the shock load condition where $\overline{v}$ is 1000 m/s.

According to the test results shown in Table 10 and Figure 10, the test accuracy when the GABPNN calculated the 0–1 recognition results of the δ corresponding to these 4 test sample sets was consistently higher than 87%, and the testing accuracy of the GABPNN was slightly lower than the corresponding one of the RBFNN only when calculating the 0–1 recognition results of the δ corresponding to the test sample set with the CV of BRVs as 0.02, and the testing accuracies of the GABPNN were higher than the corresponding ones of the RBFNN and BPNN when calculating the 0–1 recognition results of the δ under other conditions. It is proved that the GABPNN has stronger nonlinear mapping ability than the BPNN and RBFNN, and the GABPNN can accurately calculate the 0–1 recognition results of the δ corresponding to the BRV sample points. Therefore, the GABPNN can be used as the surrogate model of the IP, and the GABP-MCS can also be used to estimate the R's of Composition B.

(iv) Estimation of R based on GABP-MCS

A prediction sample set with 100,000 sample points was constructed under each of the above 4 randomness conditions, and the 0–1 recognition results of the δ corresponding to these 4 prediction sample sets were obtained by the GABP-MCS, so as to obtain the accurate estimates of the actual R's of Composition B under these 4 randomness conditions. Table 11 and Figure 11 show the results.

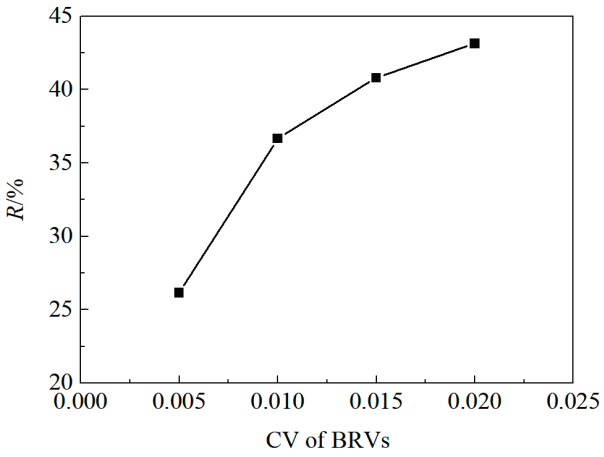


Figure 11. The correlation curve between the R of Composition B and the CV of the BRVs under the shock load condition where $\overline{v}$ is 1000 m/s.

Table 11. The calculation results of the GABP-MCS in the IP study under the shock load condition where $\overline{v}$ is 1000 m/s.

CV of BRVs	Simulation Number	Initiation Frequency	Non-Initiation Frequency	*R* (%)
0.005	100,000	26,151	73,849	26.15
0.01	100,000	36,677	63,323	36.68
0.015	100,000	40,812	59,188	40.81
0.02	100,000	43,155	56,845	43.16

According to the statistical data in Table 11 and the correlation curve in Figure 11, it can be concluded that, when the $\overline{v}$ is 1000 m/s, the *R* of Composition B is positively correlated with the CV of the BRVs; that is, the smaller the CV of the BRVs, the lower the *R* of Composition B. This is because the smaller the CV of the BRVs, the more concentrated the distribution of the BRV sample points in the corresponding prediction sample sets, the less BRV sample points there are that can lead Composition B to be initiated, and the lower the randomness of the SIREM. If the CV of the BRVs dropped to 0, this SIREM would become a deterministic problem, so Composition B would not be initiated (the *R* would drop to 0) under the shock load condition where $\overline{v}$ was 1000 m/s, which would be exactly the same as the deterministic results described in Section 4.1.

(2) Study on DPR

(i) Constructing training sample set and test sample sets

The same method discussed in Section 4.3.1 was adopted to construct the training sample set and test sample sets of the DPR. Table 9 shows that in addressing the DPR, the training sample set had 1580 sample points and the 4 test sample sets with 258, 367, 398, and 454 sample points, which correspond, respectively, to the CVs of the BRVs at 0.005, 0.01, 0.015, and 0.02.

(ii) Determining the structure and important parameters of ANNs

When the $\overline{v}$ is 1000 m/s, the setting of the structure and important parameters of the GABPNN, BPNN, and RBFNN is the same as the corresponding operation when the $\overline{v}$ is 1050 m/s; see Section 4.3.1 for the setting process.

(iii) Performance comparison of ANNs

Firstly, the GABPNN, BPNN, and RBFNN were trained by the above training sample set. Then, these three trained ANNs were tested by each of the above four test sample sets, and the test results shown in Table 12 and Figure 12 were obtained.

Table 12. The comparison of the test results of the ANNs in the DPR study under the shock load condition where $\overline{v}$ is 1000 m/s.

Gauge Number		1				2				3			
CV of BRVs		0.005	0.01	0.015	0.02	0.005	0.01	0.015	0.02	0.005	0.01	0.015	0.02
MAPE of *P* (%)	GABPNN	2.48	1.86	1.66	1.72	2.51	1.86	1.92	2.38	2.46	1.11	1.23	1.28
	BPNN	3.25	2.22	1.86	1.76	3.89	2.47	2.26	2.48	2.62	1.23	1.29	1.42
	RBFNN	3.06	3.16	2.87	3.34	4.03	2.90	2.83	3.68	2.74	1.54	1.61	2.04

According to the test results shown in Table 12 and Figure 12, the GABPNN consistently had MAPEs lower than 2.6% in calculating the *P* of each gauge in the numerical model corresponding to these 4 test sample sets, and these test results were also better than the test results of BPNN and RBFNN. It is proved that the GABPNN has stronger nonlinear mapping ability than the BPNN and RBFNN, and the GABPNN can accurately calculate the *P* of each gauge corresponding to the BRV sample points. Therefore, the GABPNN can be used as the surrogate model of the DPR, and the GABP-MCS can also be used to estimate the statistical characteristics of the *P* of each gauge of Composition B.

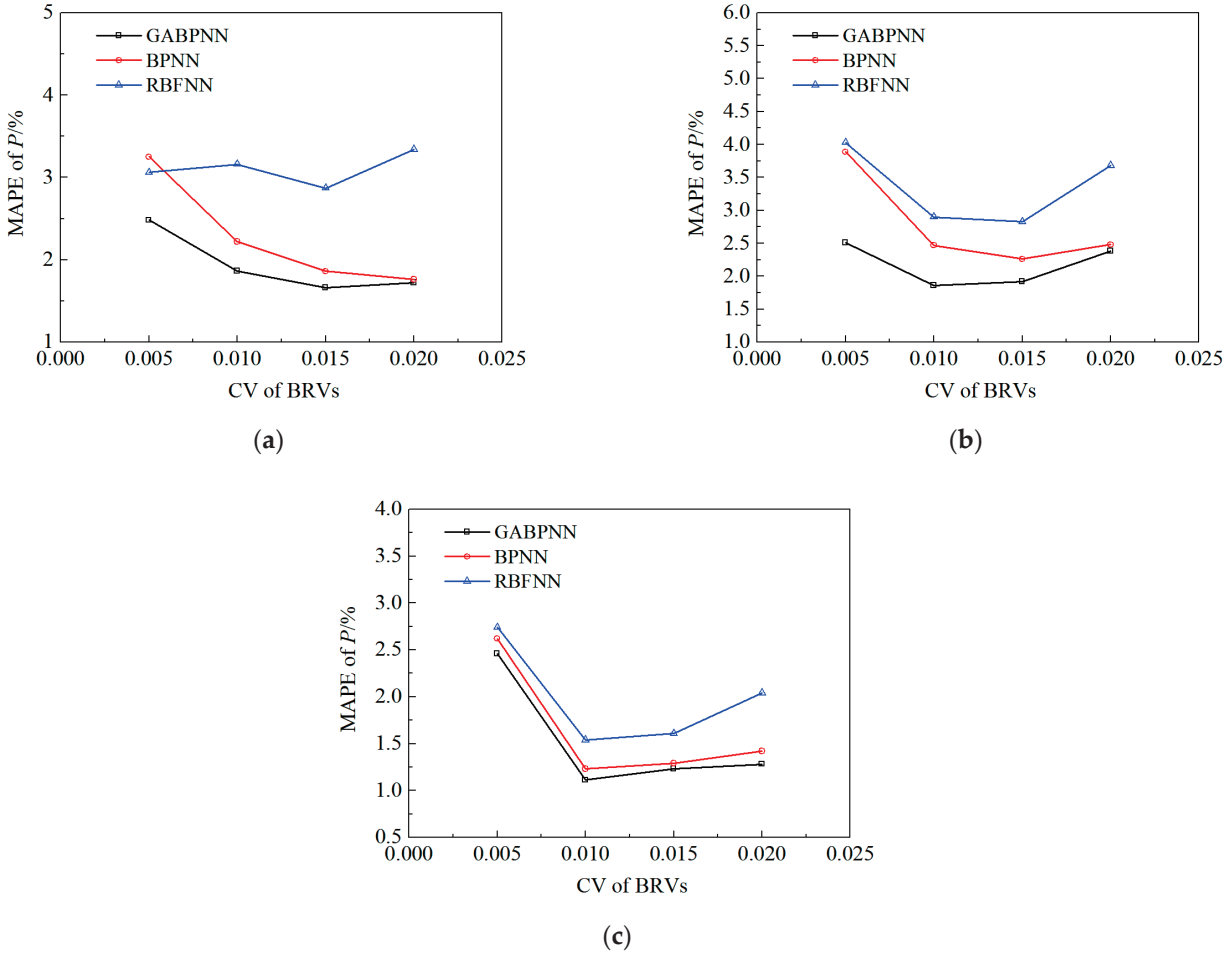


Figure 12. The comparisons of the MAPEs that the ANNs calculate the P's of the three gauges in the numerical mode in the DPR study under the shock load condition where $\overline{v}$ is 1000 m/s. (**a**) Gauge 1. (**b**) Gauge 2. (**c**) Gauge 3.

(iv) Estimation of the statistical characteristics of P based on GABP-MCS

The sample points that could lead Composition B to be initiated were selected from the prediction sample sets of the IP, so as to construct the prediction sample sets of the DPR. According to Table 11, in addressing the DPR, the 4 prediction sample sets, with the CVs of the BRVs being, respectively, 0.005, 0.01, 0.015, and 0.02, had 26,151, 36,677, 40,812, and 43,155 sample points, respectively. The calculation results of the P's of the three gauges in the numerical model corresponding to these four prediction sample sets were obtained by the GABP-MCS, so as to obtain the accurate estimates of the actual statistical characteristics of the P's of these three gauges under the above four randomness conditions, as shown in Table 13 and Figure 13.

Table 13. The calculation results of the GABP-MCS in the DPR study under the shock load condition where $\overline{v}$ is 1000 m/s.

Gauge Number		**1**				**2**				**3**			
CV of BRVs		0.005	0.01	0.015	0.02	0.005	0.01	0.015	0.02	0.005	0.01	0.015	0.02
Statistical characteristic of P	Mean of P (GPa)	24.96	26.61	27.44	28.06	28.33	29.34	29.90	30.38	31.25	32.05	32.45	32.80
	CV of P	0.0613	0.0804	0.0900	0.0991	0.0441	0.0552	0.0676	0.0829	0.0317	0.0406	0.0533	0.0674

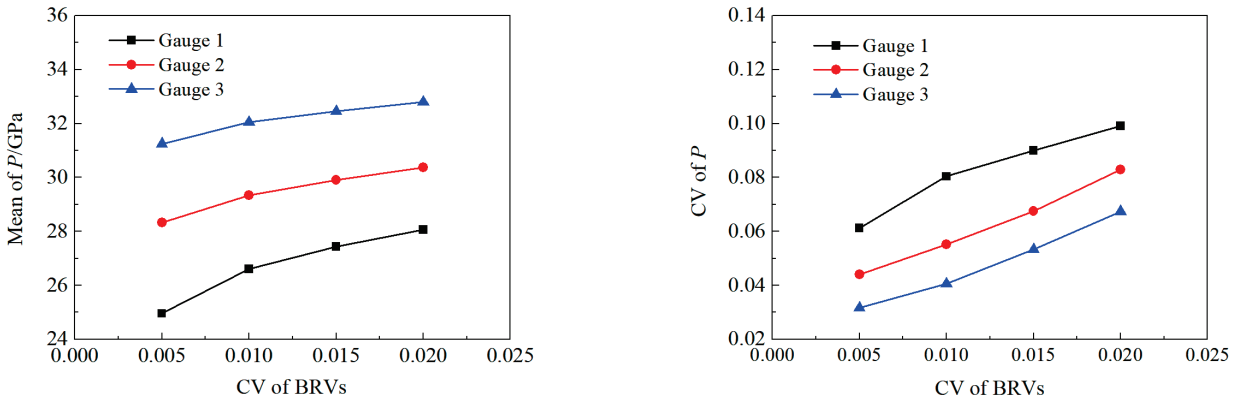


Figure 13. The correlation curves between the statistical characteristics of the P and the CVs of the BRVs under the shock load condition where $\overline{v}$ is 1000 m/s. (**a**) The correlation curves between the means of the P and the CVs of the BRVs. (**b**) The correlation curves between the CVs of the P and the CVs of the BRVs.

The following are the three observations from Table 13 and Figure 13 and their interpretation. First, for each gauge, the mean of its P is positively correlated with the CV of the BRVs; that is, the mean of its P can increase with the CV of the BRVs. This is because the more likely the BRV sample points result in the initiation of Composition B, the greater P Composition B tends to generate in subsequent detonations. Furthermore, the larger the CV of the BRVs, the more scattered the distribution of the BRV sample points in the corresponding prediction sample sets, and the more BRV sample points that can result in higher values of the P will be reserved in addressing the DPR, for they can lead to the initiation of Composition B. This suggests the higher estimates of the means of the P. What is also observed is that, under these four randomness conditions, the CVs of the P's of the three gauges in the numerical model are all significantly larger than the CVs of the BRVs, which indicates that the randomness of the BRVs can magnify the randomness of the P. The third observation is that, for any gauge, the CV of its P is also positively correlated with the CV of the BRVs; that is, the CV of its P can increase with the CV of the BRVs. This is because the larger the CV of the BRVs, the higher the randomness of the SIREM, and the higher the randomness of the P, which suggests the larger the CV of the P.

The above are the details of this applied example. The study results show that the shock response of Composition B has obvious randomness under the action of the main BRVs, and that the GABP-MCS can be adopted to solve the SIREM to obtain satisfactory randomness study results. Moreover, since Composition B is representative among various kinds of energetic materials, this example can also prove the universality of GABP-MCS in the study on SIREM.

5. Discussion

(1) Selection of study methods of SIREM on a macroscopic scale

With many well-established stochastic analysis methods and the uniqueness of SIREM on a macroscopic scale, it is necessary to discuss the selection of the study methods of SIREM.

The common stochastic analysis methods available may fall into three broad types. The first type is semi-analytical methods, including such typical methods as the center point method [44,45], checking point method [46,47], and perturbation method [48,49]. In applying this type of method between BRVs and RRs, they must form a definite performance function, which must be continuously differentiable to BRVs so as to obtain the statistical analysis results of RRs through the derivative of the performance function to BRVs. The next type is MCS and its improved versions. This type, on the basis of the law

of large numbers, conducts repeated sampling tests by selecting a large number of BRV sample points to obtain the corresponding statistical analysis results of RRs. The last type refers to surrogate model methods, represented by the response surface method [50,51], Kriging method [52–54], and artificial neural network (ANN) method. The philosophy of this type is that a substitute surrogate model for original calculation ones is constructed, together with the first two types of method, to obtain the statistical analysis results of RRs.

In the studies on SIREM on a macroscopic scale, semi-analytical methods may not apply, for it is nearly impossible to construct a definite performance function due to the quite complex nonlinear mapping between BRVs and RRs. It is impractical to adopt MCS or its improved versions, which directly use the numerical simulations of the shock initiation of energetic materials as repeated sampling tests, because the great amount of time required by these numerical simulations renders this type of method quite time- and effort-consuming. In addition, common surrogate model methods, such as the response surface method and Kriging method, may not fit the SIREM study either. This is because the marked differences in the RR values between the initiation and non-initiation states of energetic materials suggest the impossibility of forming an approximate continuous limit state surface between BRVs and RRs. Therefore, what can be adopted are the methods of combining the ANNs, which are more powerful in nonlinear mapping and quick enough in calculating, with MCSs in the SIREM study.

As GABPNN is an ANN with strong nonlinear mapping ability and high computational efficiency, the GABP-MCS with GABPNN as the surrogate model is adopted to solve SIREM in this paper. Yet, what should be noticed is that with the rapid development of machine learning and artificial intelligence, new ANNs with greater nonlinear mapping ability have been developed one after another, so it is necessary to try to apply other new ANNs to solve SIREM in future work.

(2) Correlation between mesoscopic and macroscopic studies on SIREM

Although the mesoscopic studies on SIREM recorded in the literature [7–21] are limited to preliminary theoretical exploration under standard test conditions to obtain the initiation probabilities and probabilistic initiation thresholds of energetic materials, the effect of the indeterminacy of the microstructure of energetic materials on the impact sensitivity of energetic materials has been investigated. This can better explore the source of the impact sensitivity randomness of energetic materials; that is, the random distribution of the micro-sized energetic grains, binder grains, voids, and cracks inside the energetic materials is among the root causes of the impact sensitivity randomness of energetic materials, which may further the perceptions of the nature of this issue. On the other hand, although the macroscopic study on SIREM in this paper can obtain the initiation probabilities of energetic materials under more complex working conditions and the statistical characteristics of the detonation pressure in different positions inside these energetic materials after they are initiated, so as to better meet the needs of engineering practices, the source of the impact sensitivity randomness of energetic materials cannot be directly addressed by taking the parameters of the Lee–Tarver equation of reaction rate and the JWL equation of state as the BRVs of the detonation characteristics. This forms the limitations of solving SIREM on a macroscopic scale. In fact, our research team believes that the randomness of these parameters is the macroscopic manifestation of the randomness of the microstructure of energetic materials. Hence, these two kinds of randomness are equivalent and can both represent the randomness of the detonation characteristics of energetic materials, with the former being the macroscopic phenomenological representation of the randomness of the detonation characteristics of energetic materials, and the latter being the mesoscale source.

Therefore, due to the complementary relationship between the mesoscopic and macroscopic SIREM studies, it is suggested that researchers should conduct studies from both perspectives to make the fullest use of them. In addition, no well-established theoretical methods are now available to conduct a quantitative study of the effects of the microstructure randomness of energetic materials on the parameter randomness of the Lee–Tarver equation of reaction rate and the JWL equation of state. This indicates the absence of a

unified research system that involves the detonation characteristic randomness of energetic materials, as well as its phenomenological representation and natural representation, which requires further study in the future.

6. Conclusions

The macroscopic SIREM study should explore in turn the R's of energetic materials and the randomness of P after energetic materials are initiated, so it is natural to decompose SIREM into IP and DPR. The main BRVs on the detonation characteristics of energetic materials can be selected from the parameters a, I, b, x, G_1, c, d, y, G_2, e, g, and z in the Lee–Tarver equation of reaction rate and the parameters A_c, B_c, R_{c1}, R_{c2}, w_c, A_g, B_g, R_{g1}, R_{g2}, and w_g in the JWL equation of state. The main BRVs on shock load conditions can be selected from the physical quantities, such as the mass m, shock velocity v, and shock angle θ of a fragment. In IP, δ should be introduced as RR. In DPR, the P of energetic materials should be defined as RR.

The macroscopic SIREM study should adopt the method of combining ANN surrogate models with MCSs due to the quite complex nonlinear mapping between RRs and BRVs. Therefore, this paper uses GABPNNs as the surrogate models of the numerical models of two-phase reactive flow, adopts GABP-MCS to solve SIREM, and develops the approaches.

To verify the effectiveness of GABP-MCS in solving SIREM and to provide the specific solving processes, the shock initiation randomness problem of Composition B is taken as an applied example in this paper. Under the randomness conditions that the $\overline{v}$'s are 1050 m/s and 1000 m/s and that the CVs of the BRVs are 0.005, 0.01, 0.015, and 0.02, the R's of Composition B and the statistical characteristics, such as the means and CVs of the P of Composition B, are obtained, and the variation tendencies that these statistics show under various randomness conditions are further observed.

In a nutshell, this paper analyzes SIREM on a macroscopic scale and proposes the approach of adopting GABP-MCS to solve SIREM, so as to develop a universal technique for calculating the initiation probabilities of energetic materials under complex working conditions and the statistical characteristics of detonation pressure. This technique can be widely applied to engineering practices, such as assessments of the shock safety randomness of energetic materials.

In addition, as mentioned in Discussion 5, GABPNN is just a mature ANN, and it is necessary to try to apply other new ANNs to solve SIREM in future work. Moreover, no well-established theoretical methods are now available to conduct a quantitative study of the effects of the microstructure randomness of energetic materials on the parameter randomness of the Lee–Tarver equation of reaction rate and the JWL equation of state, which requires further study in the future.

Author Contributions: Conceptualization, L.L. and W.C.; methodology, L.L., W.C. and S.L.; software, Y.Y.; validation, L.L. and Y.Y.; formal analysis, L.L.; investigation, L.L., S.L., S.W. and P.W.; data curation, L.L., S.L., S.W. and P.W.; writing—original draft preparation, L.L.; writing—review and editing, W.C. and S.L.; supervision, W.C. and S.L. All authors have read and agreed to the published version of the manuscript.

Funding: This research received no external funding.

Institutional Review Board Statement: Not applicable.

Informed Consent Statement: Not applicable.

Data Availability Statement: Not applicable.

Acknowledgments: We would like to extend our deep gratitude to Xiquan Song, Xiande Wu, and Jiangtao Xu for their insightful discussions and valuable suggestions on the study. We must also express our appreciation to Guang Chen, Rongzheng Song, Mingwu Sun, and Bo Sun on our research team for their kind help in the study, and we hope to further our research cooperation with them in the future.

Conflicts of Interest: The authors declare no conflict of interest.

References

1. Zeman, S.; Krupka, M. New aspects of impact reactivity of polynitro compounds, Part III. Impact Sensitivity as a Function of the Imtermolecular Interactions. *Propellants Explos. Pyrotech.* **2003**, *28*, 301–307. [CrossRef]
2. Wang, G.J.; Sun, C.W.; Chen, J.; Liu, C.L.; Zhao, M.H.; Tan, F.L.; Ning, Z. Large area and short-pulse shock initiation of a TATB/HMX mixed explosive. In Proceedings of the American-Physical-Society-Topical-Group on Shock Compression of Condensed Matter, Waikoloa, HI, USA, 24–29 June 2007.
3. Preston, D.N.; Brown, G.W.; Skidmore, C.B.; Reardon, B.L.; Parkinson, D.A. Small-scale explosives sensitivity safety testing: A Departure From Bruceton. In Proceedings of the 7th Biennial Conference of the American-Physical-Society-Topical-Group on Shock Compression of Condensed Matter, Chicago, IL, USA, 26 June–1 July 2011.
4. Xie, W.; Zhao, Y.; Zhang, W.; Liu, Y.; Fan, X.; Wang, B.; He, W.; Yan, Q. Sensitivity and stability improvements of NEPE propellants by inclusion of FOX-7. *Propellants Explos. Pyrotech.* **2018**, *43*, 308–314. [CrossRef]
5. Gresshoff, M.; Hrousis, C.A. Probabilistic shock threshold criterion. In Proceedings of the 14th International Detonation Symposium, Coeur d'Alene, ID, USA, 11–16 April 2010.
6. Rashkovskii, S.A.; Savenkov, G.G. Probabilistic model of the shock initiation of heterogeneous explosive materials. *Tech. Phys. Lett.* **2014**, *40*, 485–487. [CrossRef]
7. Baer, M.R.; Gartling, D.K.; DesJardin, P.E. Probabilistic models for reactive behaviour in heterogeneous condensed phase media. *Combust. Theory Model.* **2012**, *16*, 75–106. [CrossRef]
8. Barua, A.; Kim, S.; Horie, Y.; Zhou, M. Prediction of probabilistic ignition behavior of polymer-bonded explosives from microstructural stochasticity. *J. Appl. Phys.* **2013**, *113*, 184907. [CrossRef]
9. Kim, S.; Barua, A.; Horie, Y.; Zhou, M. Ignition probability of polymer-bonded explosives accounting for multiple sources of material stochasticity. *J. Appl. Phys.* **2014**, *115*, 174902. [CrossRef]
10. Kim, S.; Miller, C.; Horie, Y.; Molek, C.; Welle, E.; Zhou, M. Computational prediction of probabilistic ignition threshold of pressed granular octahydro-1,3,5,7-tetranitro-1,2,3,5-tetrazocine (HMX) under shock loading. *J. Appl. Phys.* **2016**, *120*, 115902. [CrossRef]
11. Kim, S.; Wei, Y.C.; Horie, Y.; Zhou, M. Prediction of shock initiation thresholds and ignition probability of polymer-bonded explosives using mesoscale simulations. *J. Mech. Phys. Solids* **2018**, *114*, 97–116. [CrossRef]
12. Wei, Y.C.; Kim, S.; Horie, Y.; Zhou, M. Quantification of probabilistic ignition thresholds of polymer-bonded explosives with microstructure defects. *J. Appl. Phys.* **2018**, *124*, 165110. [CrossRef]
13. Miller, C.; Kittell, D.; Yarrington, C.; Zhou, M. Prediction of probabilistic detonation threshold via millimeter-Scale microstructure-explicit and void-explicit simulations. *Propellants Explos. Pyrotech.* **2019**, *45*, 254–269. [CrossRef]
14. Coffelt, C.; Olsen, D.; Miller, C.; Zhou, M. Effect of void positioning on the detonation sensitivity of a heterogeneous energetic material. *J. Appl. Phys.* **2022**, *131*, 065101. [CrossRef]
15. Kittell, D.E.; Yarrington, C.D.; Lechman, J.B.; Baer, M.R. Letter: Modeling reactive shock waves in heterogeneous solids at the continuum level with stochastic differential equations. *Phys. Fluids* **2018**, *30*, 051701. [CrossRef]
16. Kittell, D.E.; Yarrington, C.D.; Lechman, J.B.; Damm, D.L.; Baer, M.R. Modelling the fluctuations of reactive shock waves in heterogeneous solid explosives as stochastic processes. *Propellants Explos. Pyrotech.* **2019**, *45*, 295–315. [CrossRef]
17. Lee, S.; Sen, O.; Rai, N.K.; Gaul, N.J.; Choi, K.K.; Udaykumar, H.S. Effects of parametric uncertainty on multi-scale model predictions of shock response of a pressed energetic material. *J. Appl. Phys.* **2019**, *125*, 235104. [CrossRef]
18. Bakarji, J.; Tartakovsky, D.M. Microstructural heterogeneity drives reaction initiation in granular materials. *Appl. Phys. Lett.* **2019**, *114*, 254101. [CrossRef]
19. Mi, X.C.; Michael, L.; Nikiforakis, N.; Higgins, A.J. Effect of spatial distribution of mesoscale heterogeneities on the shock-to-detonation transition in liquid nitromethane. *Combust. Flame* **2020**, *222*, 392–410. [CrossRef]
20. Liu, R.; Wang, X.J.; Chen, P.W.; Kang, G.; Zhu, S.P.; Guo, Y.S. The role of tension–compression asymmetrical microcrack evolution in the ignition of polymer-bonded explosives under low-velocity impact. *J. Appl. Phys.* **2021**, *129*, 175108. [CrossRef]
21. Miller, C.M.; Springer, H.K. Probabilistic effects of porosity and chemical kinetics on the shock initiation of an octahydro-1,3,5,7-tetranitro-1,3,5,7-tetrazocine (HMX) based explosive. *J. Appl. Phys.* **2021**, *129*, 215104. [CrossRef]
22. Landerville, A.C.; Conroy, M.W.; Budzevich, M.M.; Lin, Y.; White, C.T.; Oleynik, I.I. Equations of state for energetic materials from density functional theory with van der Waals, thermal, and zero-point energy corrections. *Appl. Phys. Lett.* **2010**, *97*, 251908. [CrossRef]
23. Xu, X. Research on Random of Underwater Explosion Problem Based on Material Point Method. Master's Thesis, Harbin Engineering University, Harbin, China, 2018.
24. Chen, W.D.; Shi, Y.Q.; Ma, J.X.; Xu, C.L.; Lu, S.Z.; Xu, X. Stochastic material point method for analysis in non-Linear dynamics of metals. *Metals* **2019**, *9*, 107. [CrossRef]
25. Chen, W.D.; Shi, Y.Q.; Yan, H.; Ma, J.X.; Yang, Y.Z.; Xu, C.L. A stochastic material point method for probabilistic dynamics and reliability. *Comput. Mech.* **2019**, *63*, 1069–1082. [CrossRef]
26. Zheng, B.H. Material procedure quality forecast based on genetic BP neural network. *Mod. Phys. Lett. B* **2017**, *31*, 19–21. [CrossRef]
27. Li, H.X.; Li, G.; Huang, Z.Y.; Chen, M. Application of BP neural network based on genetic algorithm optimization. In Proceedings of the 4th International Conference on Intelligent Information Processing (ICIIP 2019), Guilin, China, 16–17 November 2019.

28. Tan, T.J.; Yang, Z.; Chang, F.; Zhao, K. Prediction of the first weighting from the working face roof in a coal mine based on a GA-BP Neural Network. *Appl. Sci.* **2019**, *9*, 4159. [CrossRef]
29. Qian, K.; Hou, Z.C.; Sun, D.K. Sound quality estimation of electric vehicles based on GA-BP artifificial neural networks. *Appl. Sci.* **2020**, *10*, 5567. [CrossRef]
30. Lee, E.L.; Tarver, C.M. Phenomenological model of shock initiation in heterogeneous explosives. *Phys. Fluids* **1980**, *23*, 2362–2372. [CrossRef]
31. Li, Y.H.; Yang, X.Y.; Wen, Y.Q.; Xiong, S.H.; Li, X.G. Determination of Lee-Tarver Model Parameters of JO-11C Explosive. *Propellants Explos. Pyrotech.* **2018**, *43*, 1032–1040. [CrossRef]
32. Liu, Y.K.; Yin, J.P.; Wang, Z.J. Study on the overdriven detonation wave propagation in double-layer shaped charge. *Phys. Fluids* **2019**, *31*, 092110.
33. Hussain, T.; Liu, Y.; Huang, F.L.; Duan, Z.P. Ignition and growth modeling of shock initiation of different particle size formulations of PBXC03 explosive. *J. Energetic Mater.* **2016**, *34*, 38–48. [CrossRef]
34. Vandersall, K.S.; Garcia, F.; Tarver, C.M. Shock initiation experiments with ignition and growth modeling on low density Composition B. In Proceedings of the 19th Biennial American-Physical-Society (APS) Conference on Shock Compression of Condensed Matter (SCCM), Tampa, FL, USA, 14–19 June 2015.
35. Vandersall, K.S.; DeHaven, M.R.; Strickland, S.L.; Tarver, C.M.; Springer, H.K.; Cowan, M.R. Shock initiation experiments with ignition and growth modeling on the HMX-based explosive LX-14. In Proceedings of the 20th Biennial Conference of the Topical-Group of the American-Physical-Society (APS) on Shock Compression of Condensed Matter (SCCM), St. Louis, MO, USA, 9–14 July 2017.
36. Duan, Y.L.; Han, Y.; Lu, X.J.; Tan, K.Y.; Song, Q.G. Driving ability of HMX based aluminized explosive affected by the reaction degree of aluminum powder. In Proceedings of the 20th Biennial Conference of the Topical-Group of the American-Physical-Society (APS) on Shock Compression of Condensed Matter (SCCM), St. Louis, MO, USA, 9–14 July 2017.
37. Castedo, R.; Natale, M.; López, L.; Sanchidrian, J.; Santos, A.; Navarro, J.; Segarra, P. Estimation of Jones-Wilkins-Lee parameters of emulsion explosives using cylinder tests and their numerical validation. *Int. J. Rock Mech. Min. Sci.* **2018**, *112*, 290–301. [CrossRef]
38. Anastacio, A.C.; Selesovsky, J.; Kunzel, M.; Kucera, J.; Pachman, J. Detonation parameters of PlSEM plastic explosive. *Cent. Eur. J. Condens. Explos.* **2019**, *16*, 487–503. [CrossRef]
39. Cotter, N.E. The Stone-Weierstrass Theorem and Its Application to Neural Networks. *IEEE Trans. Neural Netw.* **1990**, *1*, 290–295. [CrossRef]
40. Castro, J.L.; Mantas, C.J.; Benitez, J.M. Neural networks with a continuous squashing function in the output are universal approximators. *Neural Netw.* **2000**, *13*, 561–563. [CrossRef]
41. Dong, X.R.; Sui, S.Y. Research on the Response of Fragment Impact of Explosive with Shell. *J. North China Inst. Technol.* **1999**, *20*, 236–238.
42. Bardenhagen, S.G.; Kober, E.M. The generalized interpolation material point method. *CMES Comput. Model. Eng. Sci.* **2004**, *5*, 477–495.
43. Murphy, M.J.; Lee, E.L.; Weston, A.M.; Williams, A.E. Modeling shock initiation in Composition B. In Proceedings of the 10th International Detonation Symposium, Boston, MA, USA, 12–16 July 1993.
44. Kong, X.G.; Liu, J.Q. Reliability analysis of plate on elastic foundation. In Proceedings of the 4th International Conference on Technology of Architecture and Structure (ICTAS 2011), Xi'an, China, 22–24 September 2011.
45. Liu, Y.; Meng, L.L.; Liu, K.; Zhang, Y.M. Chatter reliability of milling system based on first-order second-moment method. *Int. J. Adv. Manuf. Technol.* **2016**, *87*, 801–809. [CrossRef]
46. Wu, E.J.; Ni, Y.H. Parametric statistics of building lifting-up engineering and reliability evaluation of lifting support. In Proceedings of the International Conference on Civil Engineering and Transportation (ICCET 2011), Jinan, China, 14–16 October 2011.
47. Tao, Y.R.; Cao, L.; Cheng, G.Q.; Huang, Z.H. Safety analysis of structures with probability and evidence theory. *Int. J. Steel Struct.* **2016**, *16*, 289–298. [CrossRef]
48. Chen, W.D.; Yu, Y.C.; Jia, P.; Wu, X.D.; Zhang, F.C. Application of finite volume method to structural stochastic dynamics. *Adv. Mech. Eng.* **2013**, *5*, 391704. [CrossRef]
49. Han, S.K.; Guo, R.; Cai, Y. Reliability design for automobile rear axle by perturbation method. In Proceedings of the International Conference on Design, Manufacturing and Mechatronics (ICDMM), Changsha, China, 21–24 March 2014.
50. Goswami, S.; Ghosh, S.; Chakraborty, S. Reliability analysis of structures by iterative improved response surface method. *Struct. Saf.* **2016**, *60*, 56–66. [CrossRef]
51. Yang, Q.; Ma, H.K.; Ma, J.C.; Sun, Z.L.; Li, C.L. Sensitivity analysis of reliability of low-mobility parallel mechanisms based on a response surface method. *Appl. Sci.* **2021**, *11*, 9002. [CrossRef]
52. Chen, W.D.; Xu, C.L.; Shi, Y.Q.; Ma, J.X.; Lu, S.Z. A hybrid Kriging-based reliability method for small failure probabilities. *Reliab. Eng. Syst. Saf.* **2019**, *189*, 31–41. [CrossRef]

53. Xu, C.L.; Chen, W.D.; Ma, J.X.; Shi, Y.Q.; Lu, S.Z. AK-MSS: An adaptation of the AK-MCS method for small failure probabilities. *Struct. Saf.* **2020**, *86*, 101971. [CrossRef]
54. Niu, L.; Liu, Y.; Wang, J.C.; Tu, H.M.; Dong, H.P.; Yan, N. Reliability analysis of pyrotechnic igniter for hydrogen-oxygen rocket engine with low temperature combustion instability failure mode. *Appl. Sci.* **2022**, *12*, 3414. [CrossRef]

Disclaimer/Publisher's Note: The statements, opinions and data contained in all publications are solely those of the individual author(s) and contributor(s) and not of MDPI and/or the editor(s). MDPI and/or the editor(s) disclaim responsibility for any injury to people or property resulting from any ideas, methods, instructions or products referred to in the content.

coatings

MDPI

Article

Investigation of the Microstructure, Thermal Properties, and Mechanical Properties of Sn-Bi-Ag and Sn-Bi-Ag-Si Low Temperature Lead-Free Solder Alloys

Sheng Chen [1,†], Xinbao Wang [1,†], Zhiqiu Guo [2,*], Changjun Wu [1], Yongxiong Liu [3], Ya Liu [1,*] and Xuping Su [1]

[1] Jiangsu Key Laboratory of Material Surface Science and Technology, Changzhou University, Changzhou 213164, China
[2] Jinko Solar Co., Ltd., Haining 314416, China
[3] School of Materials Science and Engineering, Xiangtan University, Xiangtan 411105, China
* Correspondence: zhiqiu.guo@jinkosolar.com (Z.G.); yliu@cczu.edu.cn (Y.L.)
† These authors contributed equally to this work.

Abstract: In this study, we investigated the microstructure, mechanical properties, and thermal performance of Sn-xBi-1Ag (x = 35, 37, 45, and 47 wt.%) solders, with a particular focus on the effect of adding trace Si atoms. The impact of different Ag concentrations on the properties of Sn-xBi-Ag-0.5Si solders was also studied. The results indicated that as the amount of Bi added to Sn-xBi-1Ag solder alloys increased, the tensile strength, microhardness, melting temperature, and melting range decreased somewhat, but the wettability improved. The Cu_6Sn_5 layer between the soldering alloy and the Cu substrate became thinner upon increasing the Bi content. Adding microcrystalline Si atoms to the Sn-Bi-1Ag alloy improved the tensile strength and microhardness, but the melting point and melting range were not significantly changed. The wettability was optimized, and the diffusion layer formed with the Cu matrix was significantly thinner. By increasing the Ag content in the Sn-Bi-(1,3)Ag-0.5Si alloy, the tensile strength of the alloy was continuously strengthened, while the hardness decreased slightly and the melting point and melting range increased slightly. The wettability was greatly improved, and the Cu_6Sn_5 layer became thinner.

Keywords: lead-free low-temperature solder; Sn-Bi-Ag-Si; melting point; wettability; tensile strength

1. Introduction

Sn-Pb alloys have been the primary solder alloys due to their excellent wettability, mechanical properties, and appropriate price [1–5]. However, Sn-Pb solders can no longer satisfy the demands of current industrial development due to increased environmental consciousness and the introduction of Restriction of Hazardous Substances (RoHS) and Waste Electrical and Electronic Equipment (WEEE) standards [6–8]. As a result, various types of lead-free solders, such as Sn-Zn and Sn-Ag, have been suggested as replacements [9–14]. Sn-Bi alloys are ideal lead-free solders because of their non-toxicity and lower melting point [15–17]. However, the inherent brittleness after adding Bi atoms results in poor solder reliability [18–20]. The wettability of Sn-Bi solder alloys is much lower than that of conventional Sn-40Pb solders, and the bias of Bi at the solder/Cu interface causes joint embrittlement, which greatly reduces the strength of the solder joint [21–25].

Because of its excellent conductivity and wettability, Ag is often added to Sn-Bi solders to enhance their properties [26–28]. Yang et al. [29] added Ag to a Sn-58Bi solder and found that the Ag_3Sn phase was formed in the alloy, which had fine-grain strengthening and second-phase strengthening effects that improved the solder's tensile strength. A modest quantity of Ag added to the Sn-58Bi solder also enhanced its microhardness [30]. Dong et al. [31] found that the addition of Ag accelerated the wetting reaction's speed and enhanced the Sn-58Bi solder's wettability. Wang et al. [32] further investigated the impact

of Ag on the wetting of a Sn-58Bi solder. As a result, the addition of Ag not only optimized the wettability but also restrained the development of the IMC layer (intermetallic layer) at the interface and enhanced the shear strength of the joint. Furthermore, low-eutectic Sn-Bi solders have better mechanical properties than eutectic Sn-Bi solders [33–36].

Currently, research on Sn-Bi-Ag solders has predominantly focused on the eutectic part (Sn-58Bi) and the hypoeutectic part (Sn-10Bi), but eutectic solders have weak mechanical properties, while hypoeutectic solders have a high melting point. There is little systematic data on Sn-xBi-Ag (x = 30–50) solders. In addition, during the hot-dipping of Zn-Al alloys, the addition of an appropriate amount of Si to the molten pool repressed the development of the intermetallic layer at the coating/steel interface [37,38]. However, there is limited information about the effect of Si on the properties of Sn-Bi-Ag solder alloys.

The purpose of this work was to study the microstructure, melting point, mechanical properties, wetting, and interface interactions of Sn-xBi-1Ag (x = 35, 37, 45, and 47 wt.%). The impact of the Si content on the characteristics of the Sn-Bi-Ag solder alloy and the IMC layer formed at the solder/Cu interface, as well as the effect of the Ag content on the properties of Sn-Bi-Ag-Si alloy solder, were also investigated.

2. Experimental Procedure

Sn particles, Bi blocks, Ag particles, and Si pieces with a purity of 99.99% were utilized in this experiment. Appropriate amounts of pure elements were weighed based on their nominal constituents. An aggregate mixture weighing 100 g for each solder was measured. The mixture was sealed in a vacuum quartz tube under an argon environment, melted at 300 °C for 12 h, and finally quenched in cold water. To promote reactions between components while heating, the quartz tube was shaken upside down for 2 min every 30 min during melting. To verify the sample's composition uniformity, the quenched sample was repeatedly melted three times according to the above heat treatment process.

For the Sn-Bi-Ag-Si solders, due to a huge difference between the melting points of Ag (961.3 °C), Si (1410 °C), Sn (231.89 °C), and Bi (271.5 °C), the Ag-0.5Si master alloy was initially synthesized by arc-melting in a high Ti-gettered argon atmosphere with a non-consumable tungsten electrode and a water-cooled Cu case. The prepared Ag-0.5Si master alloy sample was sealed in a vacuum quartz tube under an argon atmosphere, annealed at 1000 °C for 7 days, and finally water quenched. Then, an appropriate amount of Sn particles, Bi particles, and Ag-0.5Si alloy were sealed in a vacuum quartz tube under an argon atmosphere, melted at 480 °C for 12 h, and quenched in water. All samples were homogenized by melting three times. A schematic diagram of the samples' preparation is shown in Figure 1.

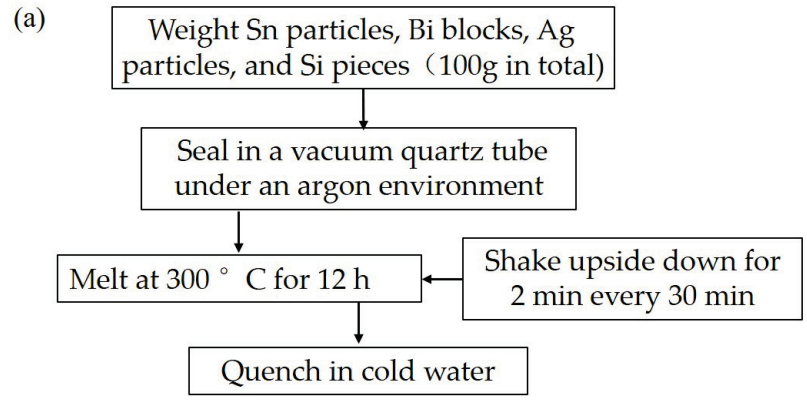


Figure 1. *Cont.*

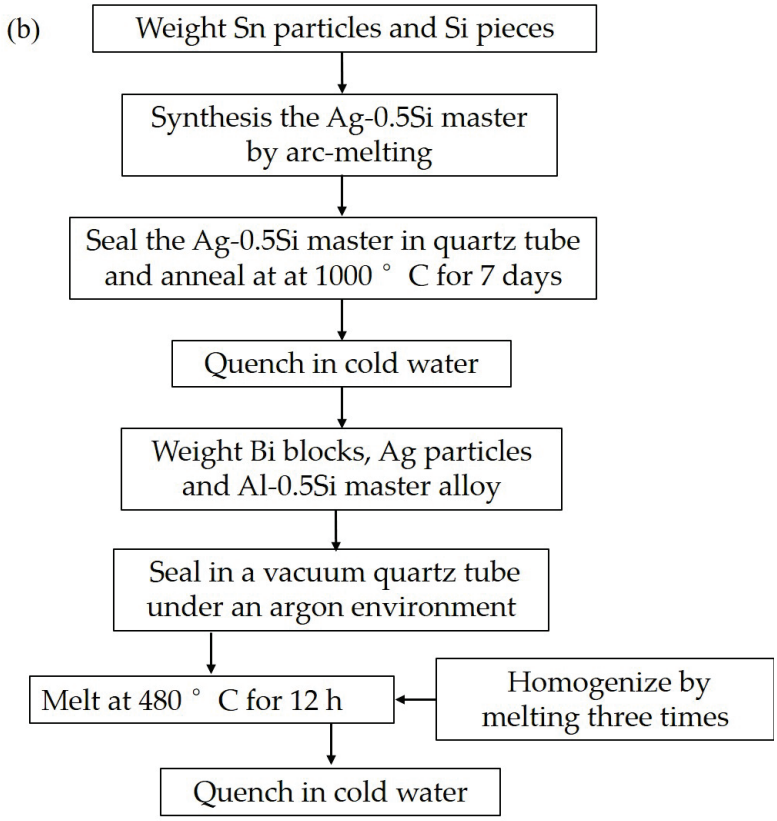


Figure 1. Schematic diagram of the samples' preparation: (**a**) Sn-Bi-Ag alloy and (**b**) Sn-Bi-Ag-Si alloy.

Prior to observing the alloy's microstructure, all samples were polished with 0.3 μm Al_2O_3 suspension. Scanning electron microscopy (JSM-6510, JEOL, Tokyo, Japan) combined with an energy-dispersive X-ray spectrometer (Oxford, UK) (SEM-EDS) was utilized to observe the microstructure. The probe diameter was 1 mm, and the acceleration voltage was 20 kV. The data in this work are the average of at least three measurements. Phase identification was performed by using a D/max 2500 PC X-ray diffractometer (Rigaku, Tokyo, Japan) and Cu Kα radiation for X-ray diffraction (XRD) measurements. Data in the 2θ range of 10–90° were collected, and the XRD patterns were indexed and calculated by the Jade 5.0 software.

A WDT-3030KN universal tensile tester was used to measure both the tensile strength and elongation of solders. A schematic diagram of the tensile test specimens in this work is shown in Figure 2. Tensile tests were performed with a loading speed of 1 mm/min at room temperature. The data in this work were the mean of at least five different measures. The microhardness of alloys was tested with a Vickers hardness tester (HXD-1000TMCLCD, XTZ, Shanghai, China) under a load of 0.245 N and a residence time of 5 s at room temperature.

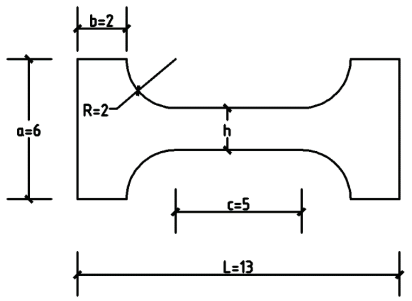


Figure 2. Schematic of tensile specimen dimensions.

To estimate the phase transition point of solder alloys, a NETZSCH DSC 404 F3 (METZSCH, Selb, Germany) differential scanning calorimeter was used at a heating rate of 10 °C/min. Wettability tests were carried out by using the hanging drop high-temperature wettability angle measuring instrument, during which drops of solder alloy liquid from a dropper fell onto a Cu plate on a platform. Interfacial reactions between the solder alloy and Cu plate were investigated by analyzing the cross-sectional microstructure of Cu sheets that were hot-dipped in a Sn-Bi-Ag-based alloy bath at 190 °C for 1 min.

3. Results and Discussion

3.1. Microstructure of Solder Alloys

Figure 3a shows an SEM image of the Sn-35Bi-1Ag solder alloy. Based on the differences in shape and brightness in the grayscale images, there were three different phases in the alloy. The composition of each typical region marked "P", "Q", and "N" in Figure 3a is shown in Figure 3b–d, respectively. Combined with the EDS analysis, the bright phase was (Bi), the grey matrix was (Sn), and there was a small amount of dark grey Ag_3Sn phase distributed throughout the (Sn) matrix. Most of the (Bi) phase existed as large granules, only a few of which were embedded in the (Sn) matrix. The characteristic peaks of the (Sn) and (Bi) phases were evident from the XRD patterns in Figure 4a,b. The Ag_3Sn phase was not observed, perhaps due to the small amount of Ag added.

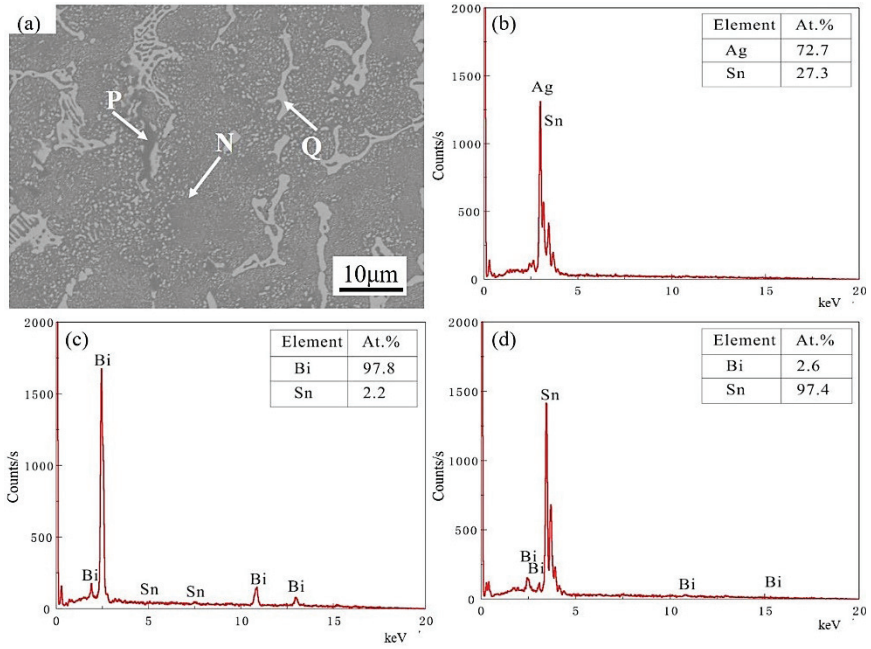


Figure 3. (**a**) SEM images of the Sn-35Bi-1Ag alloy, and (**b**–**d**) EDS profiles of regions marked "P", "Q", and "N", respectively.

Figure 5 shows the SEM images of the Sn-xBi-1Ag solder alloys with different Bi contents. More (Bi) precipitated as the Bi content increased. Figure 5 shows the SEM images of the Sn-xBi-1Ag-0.5Si solder alloys with different Bi contents. Similarly, the (Bi) phase grew as the Bi concentration rose. By comparing the SEM images in Figures 5 and 6, it can be seen that adding a small amount of Si refined the structure, and the (Bi) phase changed from large blocks to a smaller network. The amount of needle-like (Bi) phase embedded in the (Sn) matrix increased. A plausible explanation for this fine structure was that after adding particles, undercooling of the Sn-rich solder was reduced, thereby inhibiting the growth of intermetallic compounds and further refining the microstructure [39,40].

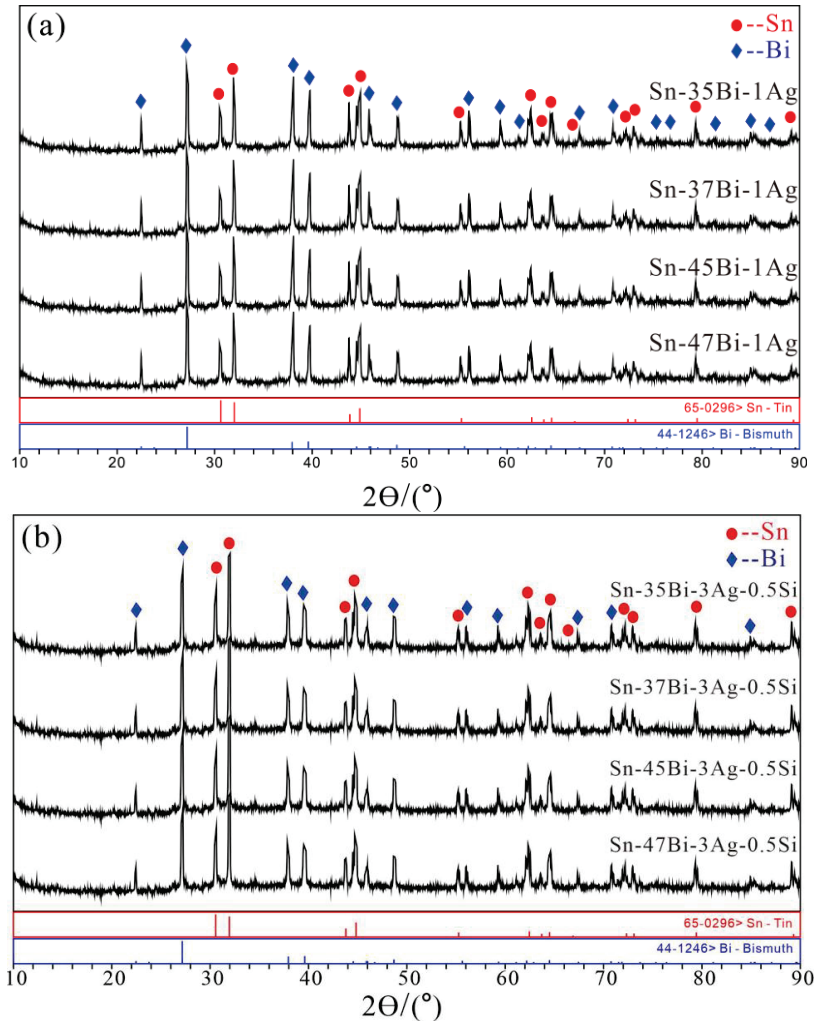


Figure 4. XRD patterns of (**a**) Sn-xBi-1Ag and (**b**) Sn-xBi-3Ag-0.5Si alloys.

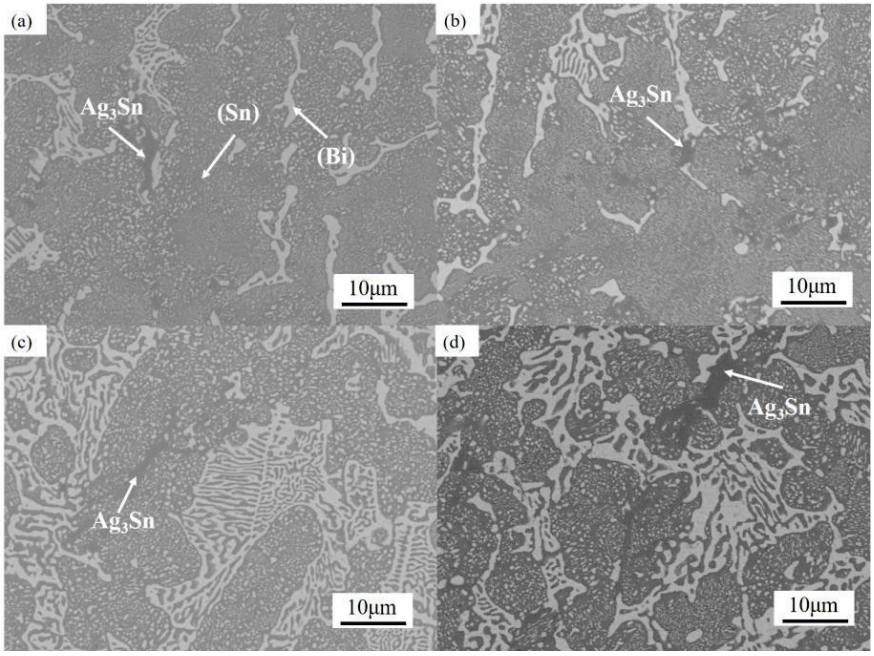


Figure 5. SEM images of the Sn-xBi-1Ag solder alloys: (**a**) x = 35, (**b**) x = 37, (**c**) x = 45, and (**d**) x = 47.

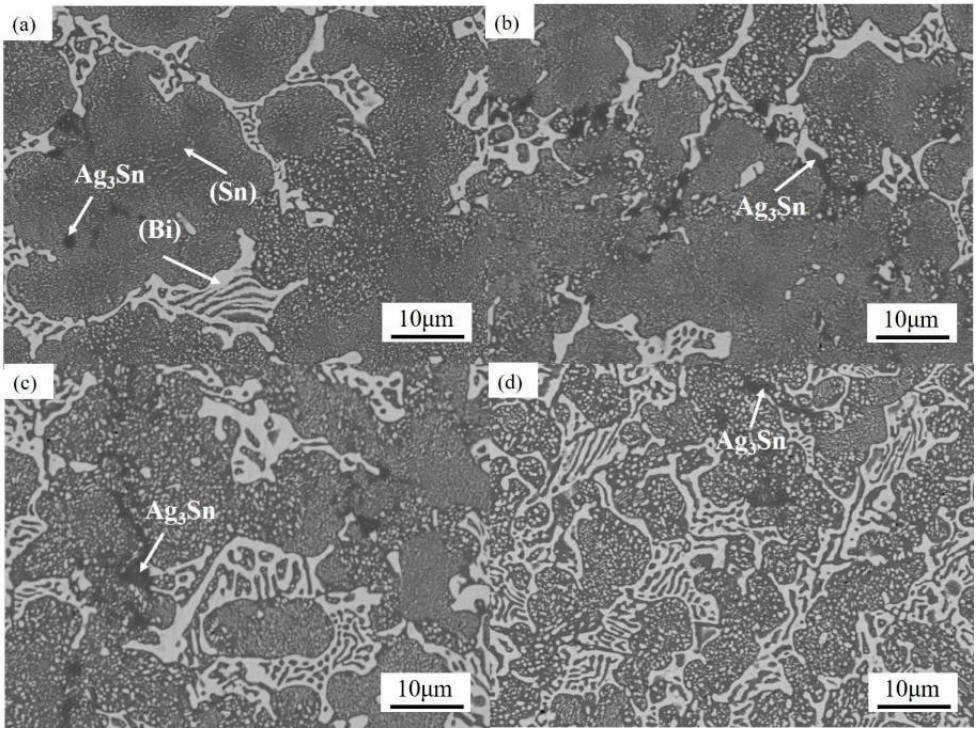


Figure 6. SEM images of the Sn-xBi-1Ag-0.5Si alloys: (**a**) x = 35, (**b**) x = 37, (**c**) x = 45, and (**d**) x = 47.

Figure 7 shows the SEM images of Sn-xBi-3Ag-0.5Si alloys with different Bi contents. Compared with Figure 5, the content of the dark black Ag_3Sn phase increased significantly upon increasing the Ag content. However, the Ag_3Sn phase was still not detected in the XRD patterns shown in Figure 4b as its content was still below the detection limit.

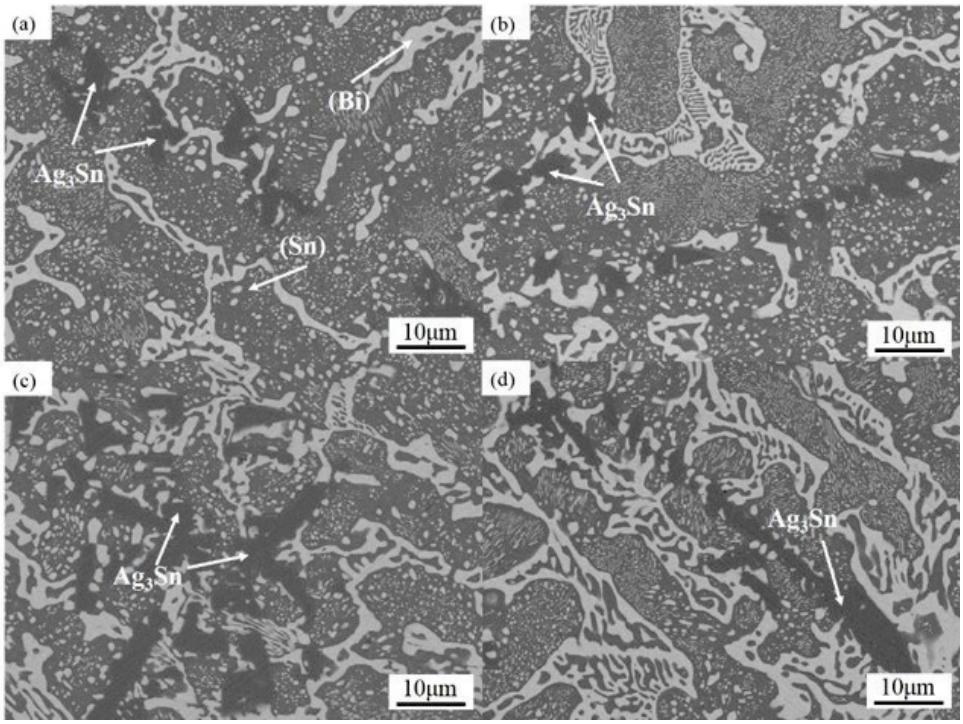


Figure 7. SEM images of the Sn-xBi-3Ag-0.5Si alloys: (**a**) x = 35, (**b**) x = 37, (**c**) x = 45, and (**d**) x = 47.

3.2. Mechanical Properties of the Solder Alloys

3.2.1. Tensile Strength

Solder alloys with a high tensile strength can help increase the solder's stability. Figure 8 shows the tensile strength of 12 kinds of solder alloys in this experiment. For Sn-xBi-1Ag solder alloys, when the Ag content remained unchanged, a higher Bi content decreased the tensile strength of the alloy. According to the microstructure shown in Figures 5–7, the (Bi) phase increased as the Bi concentration rose and segregation became more visible. The solid solution and precipitation of Bi in the Sn matrix improved the strength and hardness of the alloy, but this also reduced its plasticity and toughness. Therefore, the tensile strength of Sn-xBi-1Ag solder alloys declined as the Bi content increased.

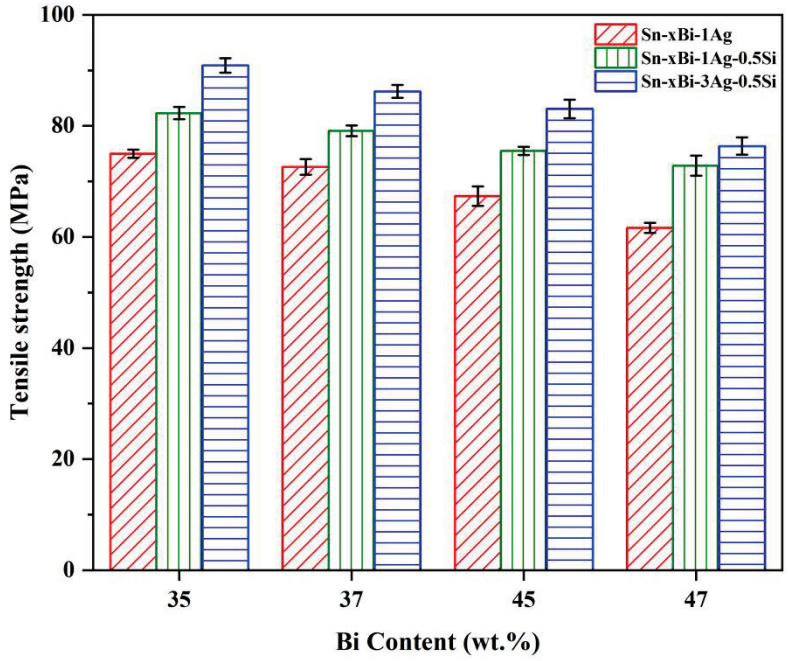


Figure 8. Tensile strength of solder alloys.

When the concentrations of Ag and Bi were identical, adding trace Si greatly increased the alloy's tensile strength, as shown in Figure 8. After adding a small amount of Si atoms to the Sn-45Bi-1Ag solder alloy, the tensile strength improved by 18.2%. The addition of trace Si might refine the eutectic phase, inhibiting the segregation of the coarse brittle (Bi) phase and reducing the alloy's brittleness. As a second-phase strengthening mechanism, the addition of Si enhanced the tensile strength of the solder alloy. When the Ag content of the Sn-xBi-yAg-0.5Si solder alloy increased, the alloy's tensile strength might have been further improved. The Sn-45Bi-3Ag-0.5Si alloy's tensile strength even exceeded that of the Sn-35Bi-1Ag-0.5Si alloy. The tensile strength of the Sn-35Bi-3Ag-0.5Si alloy reached 90.87 MPa. A plausible explanation is that as the Ag content increased, more Ag_3Sn phase precipitated in the alloy's microstructure. The Ag_3Sn phase in the solder alloy tended to be coarse, which prevented dislocation movement. Slip was hampered during deformation, resulting in unequal plastic deformation throughout the matrix. Finally, the local plastic constraint of the solder was strengthened, so that the solder alloy's tensile strength was greatly increased. When adding 2 wt.% Ag to the Sn-0.7Cu eutectic alloy, El-Daly and Hammad [41] also found that the Ag_3Sn phase formed in the microstructure enhanced the solder's tensile strength and elongation at break.

3.2.2. Microhardness

Figure 9 compares the microhardness of Sn-Bi-1Ag, Sn-Bi-1Ag-0.5Si, and Sn-Bi-3Ag-0.5Si series solder alloys. Compared with the microhardness of the Sn-Bi-1Ag alloy, these alloys showed a higher microhardness after adding 0.5 wt.% Si, an increase of about 4.5%.

The reason for this phenomenon was that Si inhibited the formation and segregation of coarse and brittle Bi in the alloy, which refined the microstructure. Figure 9 illustrates that the microhardness values of the Sn-Bi-3Ag-0.5Si solder alloys were all lower than those of the Sn-Bi-1Ag-0.5Si solder alloys. By comparing the microstructures shown in Figures 6 and 7, the excessive addition of Ag in the Sn-Bi-3Ag-0.5Si solder alloys led to a more coarse Ag_3Sn phase precipitating in the alloy, and the Bi content in the substrate was relatively higher than that in Sn-Bi-1Ag-0.5Si solder alloys, so more white tiny (Bi) were precipitated, resulting in a decrease in the microhardness of the alloys [42]. The size of the Ag_3Sn phase may also play a key role in limiting lamellae formation and microstructure refinement [29].

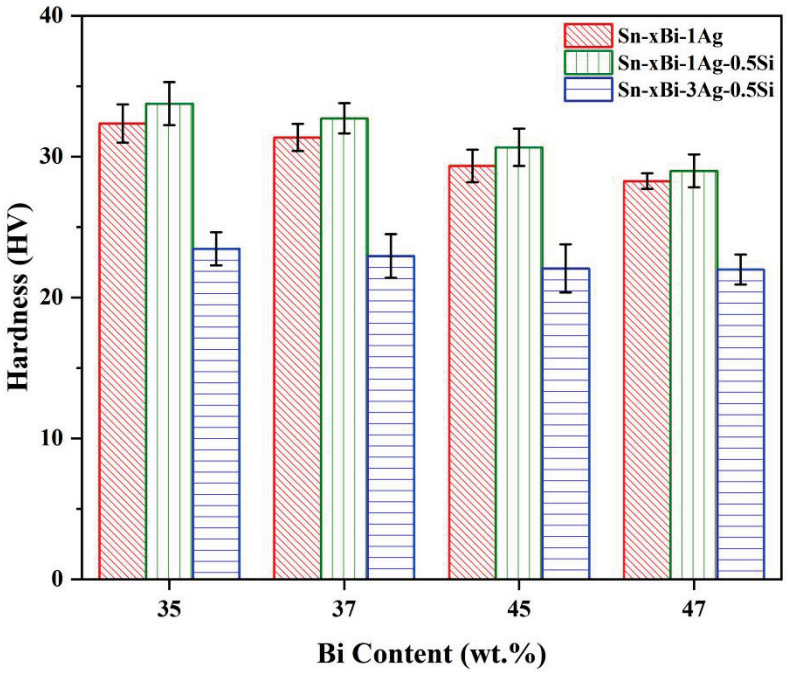


Figure 9. Microhardness of solder alloys.

For the Sn-Bi-1Ag series solders, the alloys' hardness and tensile strength both steadily declined as the Bi content increased. After adding a small amount of Si, the alloy's microhardness and tensile strength were both enhanced. The hardness of the Sn-Bi-Ag-0.5Si solder alloy decreased as the Ag percentage rose, while the tensile strength increased.

3.3. Melting Properties of the Solder Alloys

Figures 10–12 show the DSC curves of Sn-Bi-1Ag, Sn-Bi-1Ag-0.5Si, and Sn-Bi-3Ag-0.5Si series solder alloys. Here, the intersection of the tangent line at the maximum slope of the leading edge of the heat absorption peak in the DSC curve with the front baseline extension is T_m. In addition, the intersection of the tangent at the maximum slope of the trailing edge of the endothermic peak and the extension line of the back baseline is T_n. The difference between T_n and T_m is regarded as the melting range of the solder alloy. The values of T_m, T_n, and the melting ranges of the 12 solder alloys were collected in Tables 1–3.

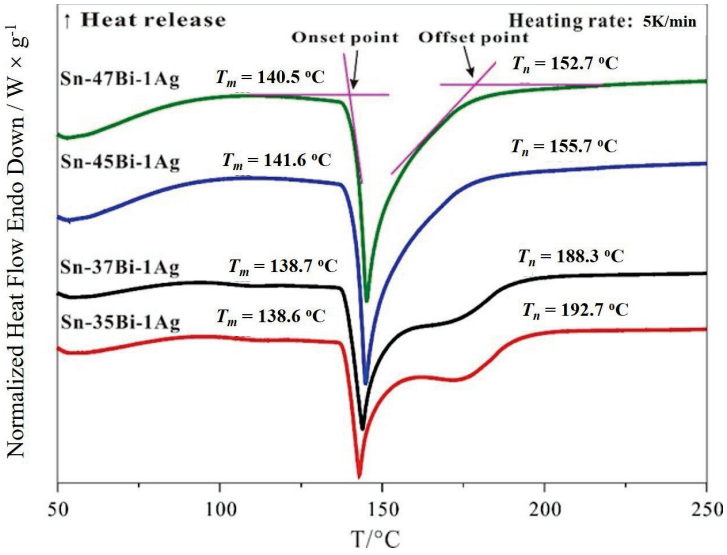


Figure 10. DSC curves of the Sn-xBi-Ag solder alloys.

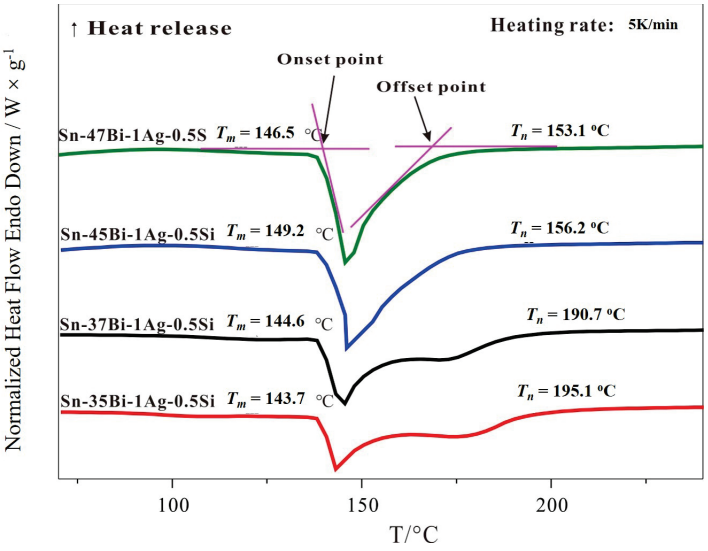


Figure 11. DSC curves of the Sn-xBi-1Ag-0.5Si solder alloys.

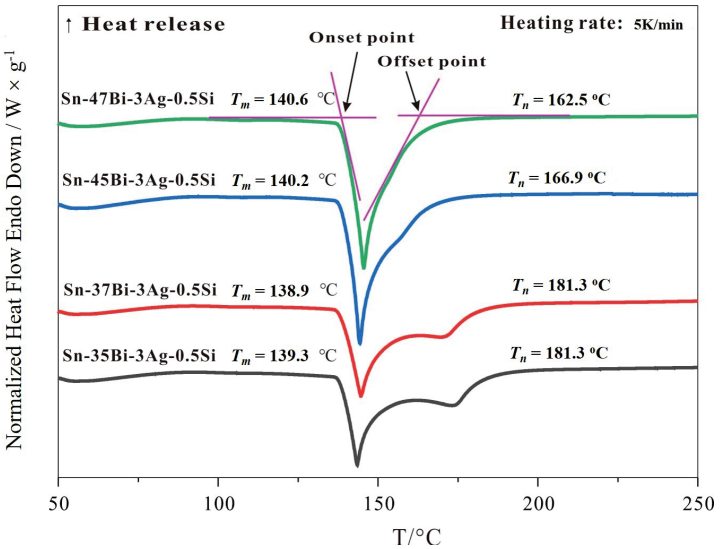


Figure 12. DSC curves of Sn-xBi-3Ag-0.5Si solder alloys.

Table 1. Phase transition temperature and melting range of the Sn-xBi-1Ag solder alloys.

Alloys	T_m/°C	T_n/°C	Melting Range/°C
Sn-35Bi-1Ag	138.6	192.7	54.1
Sn-37Bi-1Ag	138.7	188.3	49.6
Sn-45Bi-1Ag	141.6	155.7	14.1
Sn-47Bi-1Ag	140.5	152.7	12.2

Table 2. Phase transition temperature and melting range of the Sn-xBi-1Ag-0.5Si solder alloys.

Alloys	T_m/°C	T_n/°C	Melting Range/°C
Sn-35Bi-1Ag-0.5Si	139.5	195.1	55.6
Sn-37Bi-1Ag-0.5Si	139.6	190.7	51.1
Sn-45Bi-1Ag-0.5Si	142.2	156.2	14
Sn-47Bi-1Ag-0.5Si	141.3	153.1	11.8

Table 3. Phase transition temperature and melting range of the Sn-xBi-3Ag-0.5Si solder alloys.

Alloys	T_m/°C	T_n/°C	Melting Range/°C
Sn-35Bi-3Ag-0.5Si	139.3	183.3	44
Sn-37Bi-3Ag-0.5Si	138.9	181.3	42.4
Sn-45Bi-3Ag-0.5Si	140.2	166.9	26.7
Sn-47Bi-3Ag-0.5Si	140.6	162.5	21.9

Figure 10 shows that the DSC curves of the Sn-45Bi-1Ag and Sn-47Bi-1Ag solder alloys had only one main peak, while those of the Sn-35Bi-1Ag and Sn-37Bi-1Ag solder alloys also had a secondary peak near 165 °C. The secondary peak appeared because the alloy was incompletely melted after the eutectic reaction, and there were still primary phases that continued to melt. For the Sn-Bi-1Ag series solder alloys, as the Bi content increased from 35 wt.% to 47 wt.%, the starting temperature of the solder alloy did not change much. The difference was within 2 °C, and the main peak temperature was also basically the same. The termination point varied greatly, so changes in the Bi content affected the initial phase crystallization temperature of the alloy, i.e., the liquidus temperature. When there was only one main peak in the curve, the melting range was within 15 °C. When a secondary peak appeared, the melting range of the alloy broadened significantly to 50 °C. The melting range of the alloy steadily widened as the Bi concentration decreased and the secondary peak value increased. The termination point temperature gradually decreased as the Bi concentration rose, i.e., the temperature required to completely melt the solder alloy decreased continuously. Billah et al. [43] suggested that the temperature required for complete melting gradually decreased as the Bi content increased and approached the eutectic point of the Sn-Bi binary alloy.

The DSC curves of Sn-Bi-Ag-0.5Si solder alloys with different Bi contents are shown in Figure 11. Comparing Figures 10 and 11, as well as Tables 1 and 2, shows that the starting melting temperature of the solder alloy remained almost unchanged after adding 0.5 wt.% Si to the Sn-Bi-Ag series solder alloys, which have a maximum difference of only 0.9 °C. The main peak temperature and the secondary peak temperature were basically the same. In addition, the termination point did not significantly change, showing that the Bi content had no discernible influence on the solder alloy's melting range.

Figure 12 shows the DSC curves of the Sn-xBi-3Ag-0.5Si series solder alloys with different Ag contents. Table 3 shows the starting melting temperature of the Sn-xBi-3Ag-0.5Si solder alloy. Increasing the Ag content in the Sn-Bi-Ag-0.5Si series solder alloys produced essentially no change in the onset point of the Sn-Bi-Ag-Si solder alloy and had no significant effect on the primary and secondary peak temperatures. Nevertheless, when the Bi content was low ($\leq$37 wt.%), the termination temperature of the alloys diminished marginally, and the maximum difference reached 11.8 °C. When the Bi content exceeded

45 wt.%, the termination temperature of the solder alloy increased, and the maximum difference reached 10.7 °C. When the Bi content was less than 40 wt.%, the inclusion of Ag limited the alloy's melting range due to interactions between Ag and Sn, which produced the intermetallic complex Ag_3Sn. The melting point of the eutectic compound was lower than that of Sn, and Sn was consumed during the generation of the compound. As more Ag was added, more Sn was consumed, which resulted in little change in the liquid phase line temperature and a decrease in the solid phase line temperature. This led to a reduction in the solder alloy's melting range. When the Bi content was too high (≥45 wt.%), as more Ag was added, the solidus temperature increased while the liquidus temperature did not change much, thus increasing the alloy's melting range.

3.4. Wettability of the Solder Alloys

Wettability is a crucial metric for determining the solderability of an alloy. Generally, wettability is reflected by the contact angle of the solder alloy on a Cu substrate, which may be affected by many factors, such as surface roughness and operating parameters [44]. To evaluate the wettability of solder alloys, we measured the contact angle of molten solder alloy droplets on a Cu plate. In general, a smaller contact angle indicates better wettability of the solder alloy toward the Cu sheet.

Figures 13–15 show the wetting spreading diagrams of Sn-xBi-1Ag, Sn-xBi-1Ag-0.5Si, and Sn-xBi-1Ag-0.5Si solders on a Cu sheet, respectively. The contact angle curves of all solder alloys are shown in Figure 16. The contact angle of Sn-Bi-Ag series solder alloys on Cu substrates decreased upon increasing the Bi content. Bismuth improved the alloy's wettability because it is a surface-active element that can depress the interfacial tension of welding materials. Although the wettability of the alloys was better, the contact angle remained high. Furthermore, the contact angle of the Sn-35Bi-1Ag-0.5Si solder alloy on the Cu sheet was 65°, which was approximately 35% lower than that of the Sn-35Bi-1Ag solder alloy. When the Bi content reached 45 wt.%, the contact angle was approximately 33.5°.

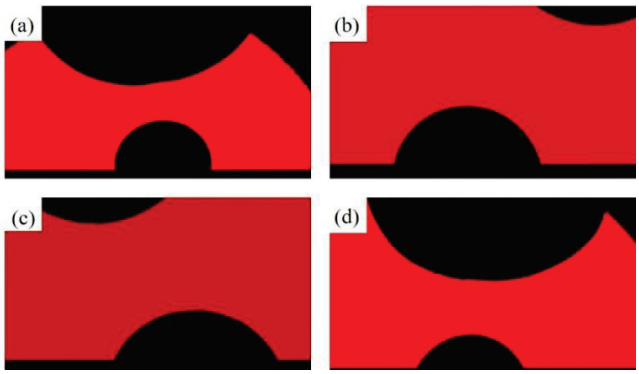


Figure 13. The spreading diagram of Sn-xBi-1Ag solder alloys dropped on a Cu substrate: (**a**) x = 35, (**b**) x = 37, (**c**) x = 45, and (**d**) x = 47.

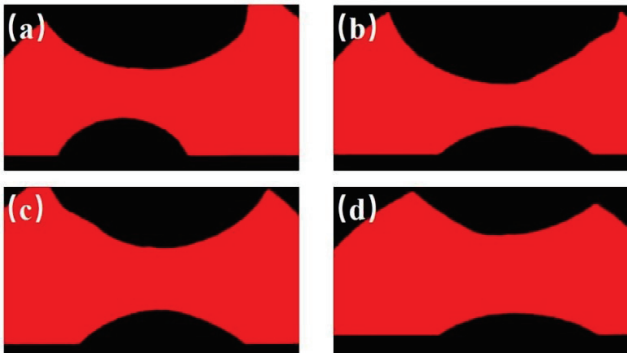


Figure 14. The spreading diagram of Sn-xBi-1Ag-0.5Si solder alloys dropped on a Cu substrate: (**a**) x = 35, (**b**) x = 37, (**c**) x = 45, and (**d**) x = 47.

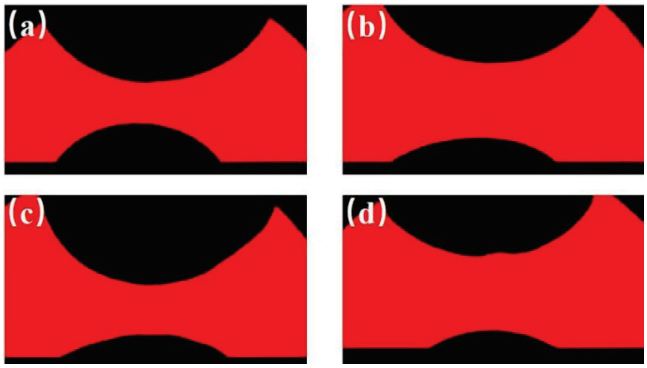


Figure 15. The spreading diagram of Sn-xBi-3Ag-0.5Si solder alloys dropped on a Cu substrate: (**a**) x = 35, (**b**) x = 37, (**c**) x = 45, and (**d**) x = 47.

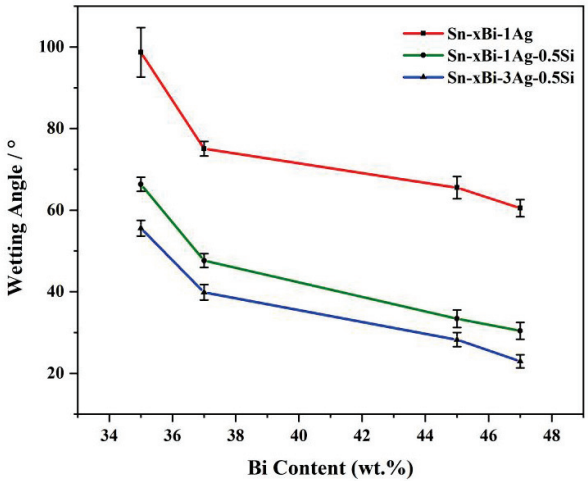


Figure 16. Comparison of the wetting angles of the Sn-xBi-1Ag, Sn-xBi-1Ag-0.5Si, and Sn-xBi-3Ag-0.5Si solder solutions on a Cu substrate.

When the contact angle was greater than 0 and less than 20°, the wettability was excellent, but when the contact angle was higher than 40°, the wettability was poor [45]. As shown in Figure 16, the contact angles of Sn-Bi-3Ag-0.5Si series solders on Cu sheets were usually small, and the contact angle of Sn-47Bi-3Ag-0.5Si solder was even close to 20°. Since the surface tension of Ag is very low (0.03 N/m), the addition of Ag reduced the surface tension of the Sn-Bi-Ag-Si series solder alloys, thereby reducing their contact angle on the Cu sheet and increasing their wettability, which was consistent with the results of this experiment. In addition, due to the wetting and diffusion of molten solder on the Cu substrate, an intermetallic compound layer formed at the interface. This thin intermetallic compound layer helped ensure a strong metal bonding between the molten solder and Cu. However, an excessively thick compound layer increased the surface tension. Silver atoms reduced the surface tension of Sn on the compound layer, thereby reducing the surface tension of the solder on the Cu substrate. Therefore, upon increasing the Ag content, the wettability of the Sn-Bi-Ag-Si solder alloy was improved. In summary, the wettability of the Sn-45Bi-1Ag-0.5Si, Sn-47Bi-1Ag-0.5Si, Sn-45Bi-3Ag-0.5Si, and Sn-47Bi-3Ag-0.5Si solders were all superior to that of the traditional $Sn_{60}Pb_{40}$ solder.

3.5. Interfacial Reactions of the Solder Alloys with Cu Sheet

The formation of a thin and continuous intermetallic compound layer during welding is necessary for good wetting and connections and improves the mechanical properties of solder joints [46]. However, since intermetallic compounds are brittle, an excessively thick compound layer will significantly reduce the reliability of solder joints.

Figure 17 shows the SEM images of the interface between the Sn-xBi-1Ag solder and Cu substrate after reacting at 190 °C for 1 min. The EDS analysis showed that the IMC layer was Cu_6Sn_5 phase. In addition, (Sn), (Bi), and Ag_3Sn phases were observed close to the Cu_6Sn_5 IMC layer. This indicated that Sn in the solder solution preferentially diffused throughout the Cu matrix, while Bi and Ag atoms did not react with the Cu matrix. The formation and growth of the Cu_6Sn_5 layer were mainly controlled by diffusion. Cu atoms were dissolved in a molten Sn-based solder and reacted with Sn atoms. The relationship between the thickness of the Cu_6Sn_5 IMC layer and the Bi content is shown in Figure 18. A higher Bi content decreased the thickness of the IMC layer, probably because of the content of Sn atoms in the solder. As shown in Figure 16, the wetting angles of the Sn-xBi-Ag solder solutions on the Cu substrate decreased with increasing Bi content, which facilitated the interfacial reaction between Cu and Sn. When the Cu substrate was covered with Cu-Sn IMC, the interfacial reaction would be inhibited and the thickness of Cu-Sn IMC would be limited. So, a higher Bi content restricted the development of the IMC layer.

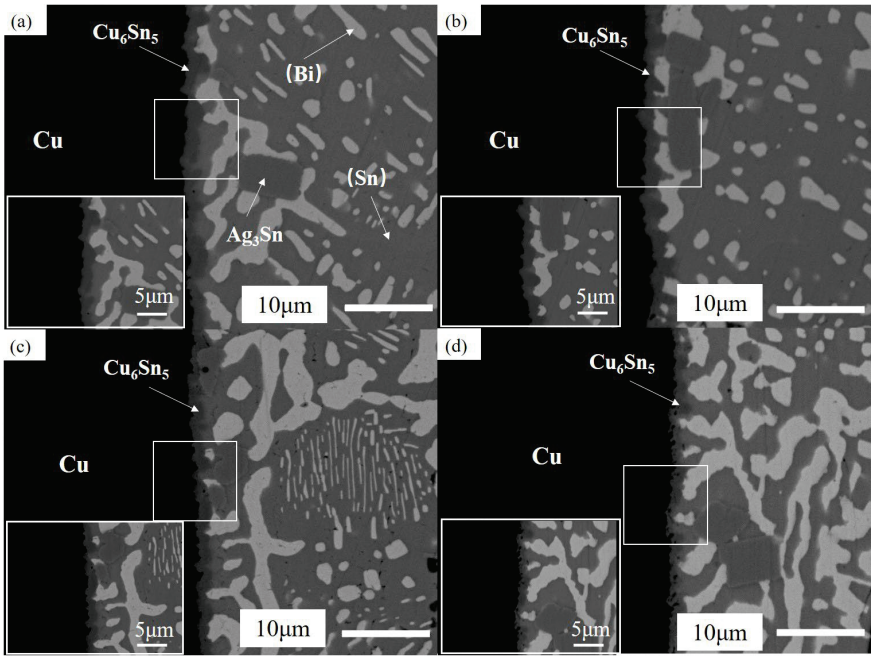


Figure 17. SEM images showing the interfacial morphology of Sn-xBi-1Ag/Cu at 190 °C: (**a**) x = 35, (**b**) x = 37, (**c**) x = 45, and (**d**) x = 47.

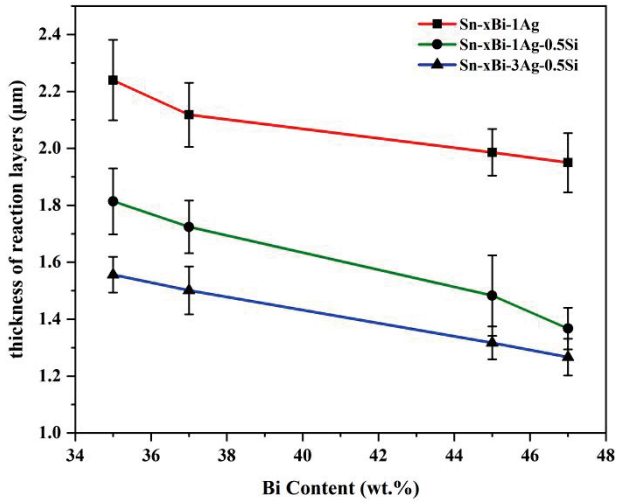


Figure 18. Thickness of solder/Cu reaction layers.

Figure 19 shows the SEM images of the interface between the Sn-xBi-1Ag-0.5Si solder and Cu substrate after reacting at 190 °C for 1 min. The IMC's thickness decreased due to the addition of Si. In particular, when the Bi content was 45 wt.%, the thickness of the interfacial reaction layer decreased by nearly 42% after adding Si. The addition of Si did not result in the formation of intermetallic compounds but only formed Si particles, which hindered the diffusion of Cu atoms into the molten solder. Figure 20 shows the SEM images of the interface between the Sn-xBi-3Ag-0.5Si alloy and Cu substrate after reacting at 190 °C for 1 min. The IMC layer's thicknesses of Sn-35Bi-3Ag-0.5Si/Cu and Sn-37Bi-3Ag-0.5Si/Cu were much thinner than those of Sn-35Bi-1Ag-0.5Si/Cu and Sn-37Bi-1Ag-0.5Si/Cu. Upon increasing the Ag content, the Ag_3Sn phase content greatly increased and coarsened, which hindered interfacial passage during atomic diffusion and reduced the interface growth rate. Therefore, the formation and growth of an IMC layer at the interface were inhibited. The Ag_3Sn phase helped improve the strength of the matrix at the front of the IMC layer, which helped inhibit the fracture of Sn-Bi-Ag-Si/Cu joints in the matrix and made them more likely to occur at the intersection between the matrix and IMC layer.

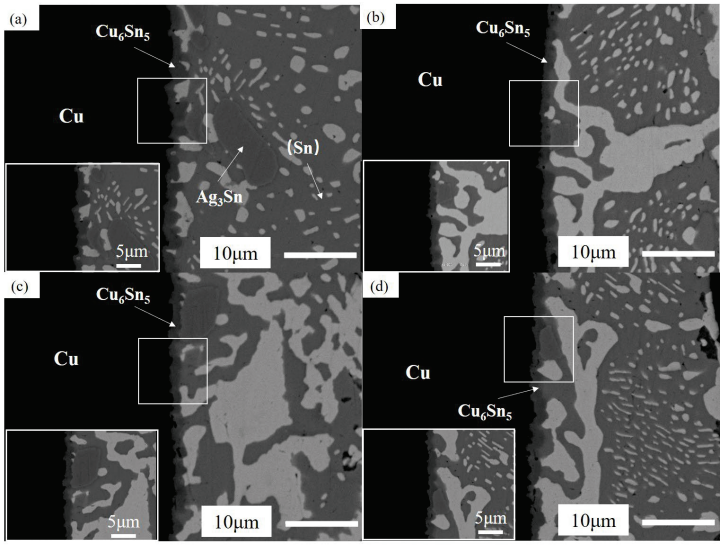


Figure 19. SEM images showing the interfacial morphology of Sn-xBi-1Ag-0.5Si/Cu at 190 °C: (**a**) x = 35, (**b**) x = 37, (**c**) x = 45, and (**d**) x = 47.

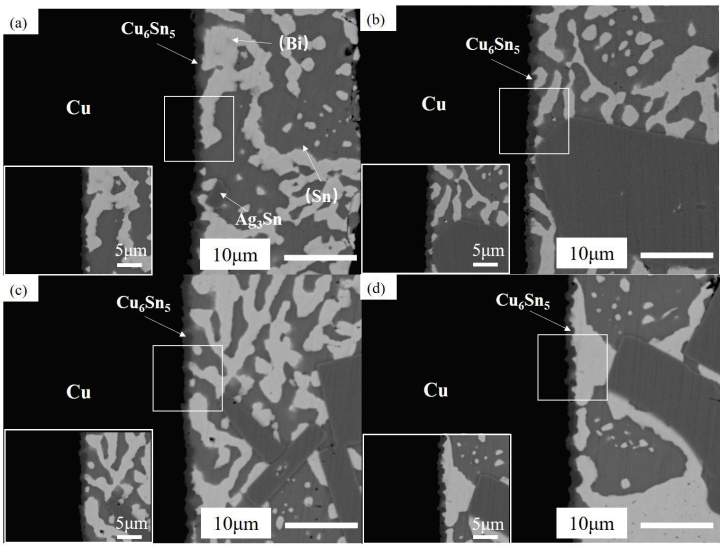


Figure 20. SEM images showing the interfacial morphology of Sn-xBi-3Ag-0.5Si/Cu at 190 °C: (**a**) x = 35, (**b**) x = 37, (**c**) x = 45, and (**d**) x = 47.

4. Conclusions

The main conclusions of this experiment were as follows:

(1) For Sn-x (x = 35, 37, 45, and 47) Bi-1Ag solder alloys, the segregation of Bi became more obvious, and bright, irregular-shaped areas continued to increase upon increasing the Bi content. The mechanical properties of the alloy decreased upon increasing the Bi content, and the melting point and melting range were slightly reduced, but the wettability was improved. The thickness of the Cu_6Sn_5 IMC layer decreased upon increasing the Bi content.

(2) After adding Si to the Sn-xBi-1Ag alloy, the structure was refined. In particular, the size of the Bi phase decreased from the large blocks into a network shape. The amount of needle-like Bi phase embedded in the Sn matrix increased. After adding trace Si, the melting point and melting range of the alloys did not markedly change, while tensile strength and hardness were improved, the wettability was optimized, and the thickness of the diffusion layer formed with the Cu substrate was significantly reduced.

(3) Upon increasing the Ag content in the Sn-Bi-Ag-0.5Si alloy, the dark black Ag_3Sn phase increased significantly. The tensile strength of the Sn-Bi-Ag-0.5Si solder continued to increase, while its hardness decreased slightly. The melting point and melting range increased slightly. Moreover, the wettability of the Sn-Bi-3Ag-0.5Si series solder alloys improved greatly, and the width of the Cu_6Sn_5 layer decreased.

Author Contributions: Conceptualization, Y.L. (Ya Liu) and Z.G.; methodology, S.C., X.W. and X.S.; validation, S.C., X.W. and C.W.; formal analysis, S.C. and X.W.; investigation, S.C., X.W. and Y.L. (Yongxiong Liu); resources, S.C. and X.W.; data curation, S.C. and X.W.; writing—original draft preparation, S.C. and X.W.; writing—review and editing, Y.L. (Ya Liu); visualization, S.C. and X.W.; supervision, Z.G. and Y.L. (Ya Liu). All authors have read and agreed to the published version of the manuscript.

Funding: We would like to express our gratitude for financial supports from the National Science Foundation of China (Grant Nos. 52271005 and 52171003) and the Jiangsu Provincial Higher Education Key Discipline Construction Grant Program.

Institutional Review Board Statement: Not applicable.

Informed Consent Statement: Not applicable.

Data Availability Statement: Not applicable.

Conflicts of Interest: The authors declare no conflict of interest.

References

1. Garcia, L.R.; Osório, W.R.; Peixoto, L.C.; Garcia, A. Wetting Behavior and Mechanical Properties of Sn-Zn and Sn-Pb Solder Alloys. *J. Electron. Mater.* **2009**, *38*, 2405–2414. [CrossRef]
2. Qiu, H.; Hu, X.; Li, S.; Wan, Y.; Li, Q. Shear strength and fracture surface analysis of lead-free solder joints with high fraction of IMCs. *Vacuum* **2020**, *180*, 109611. [CrossRef]
3. Chen, G.; Liu, L.; Silberschmidt, V.V.; Liu, C.; Wu, F.; Chan, Y.C. Microstructural evolution of 96.5Sn–3Ag–0.5Cu lead free solder reinforced with nickel-coated graphene reinforcements under large temperature gradient. *J. Mater. Sci. Mater. Electron.* **2018**, *29*, 5253–5263. [CrossRef]
4. Dias, M.; Costa, T.A.; Soares, T.; Silva, B.L.; Cheung, N.; Spinelli, J.E.; Garcia, A. Tailoring Morphology and Size of Microstructure and Tensile Properties of Sn-5.5 wt.%Sb-1 wt.%(Cu,Ag) Solder Alloys. *J. Electron. Mater.* **2018**, *47*, 1647–1657. [CrossRef]
5. Mahmudi, R.; Mahin-Shirazi, S. Effect of Sb addition on the tensile deformation behavior of lead-free Sn–3.5Ag solder alloy. *Mater. Des.* **2011**, *32*, 5027–5032. [CrossRef]
6. George, E.; Pecht, M. RoHS compliance in safety and reliability critical electronics. *Microelectron. Reliab.* **2016**, *65*, 1–7. [CrossRef]
7. Yuan, Y.; Chen, X.; Zhou, Z.; Li, Y.; Xu, B.; Liu, D.; Yang, B. Theoretical study on Sn–Sb-based lead-free solder by ab initio molecular dynamics simulation. *J. Mater. Res.* **2019**, *34*, 2543–2553. [CrossRef]
8. Ren, G.; Collins, M.N. The effects of antimony additions on microstructures, thermal and mechanical properties of Sn-8Zn-3Bi alloys. *Mater. Des.* **2017**, *119*, 133–140. [CrossRef]
9. Han, Y.; Gao, Y.; Jing, H.; Wei, J.; Zhao, L.; Xu, L. A modified constitutive model of Ag nanoparticle-modified graphene/Sn–Ag–Cu/Cu solder joints. *Mater. Sci. Eng. A* **2020**, *777*, 139080. [CrossRef]

10. Shen, Y.-A.; Chen, S.-W.; Chen, H.-Z.; Chang, C.-M.; Ouyang, Y.-H. Extremely thin interlayer of multi-element intermetallic compound between Sn-based solders and FeCoNiMn high-entropy alloy. *Appl. Surf. Sci.* **2021**, *558*, 149945. [CrossRef]
11. Wei, Y.; Liu, Y.; Zhao, X.; Tan, C.; Dong, Y.; Zhang, J. Effects of minor alloying with Ge and In on the interfacial microstructure between Zn–Sn solder alloy and Cu substrate. *J. Alloys Compd.* **2020**, *831*, 154812. [CrossRef]
12. Zhou, S.; Yang, C.-H.; Shen, Y.-A.; Lin, S.-K.; Nishikawa, H. The newly developed Sn–Bi–Zn alloy with a low melting point, improved ductility, and high ultimate tensile strength. *Materialia* **2019**, *6*, 100300. [CrossRef]
13. Wang, Y.; Zhao, X.-C.; Liu, Y.; Wang, Y.; Li, D.-M. Microstructure, wetting property of Sn–Ag–Cu–Bi–xCe solder and IMC growth at solder/Cu interface during thermal cycling. *Rare Met.* **2021**, *40*, 714–719. [CrossRef]
14. Durga, A.; Wollants, P.; Moelans, N. Phase-field study of IMC growth in Sn–Cu/Cu solder joints including elastoplastic effects. *Acta Mater.* **2020**, *188*, 241–258. [CrossRef]
15. Yang, J.; Zhang, Q.; Song, Z. Influences of Ag and In Alloying on Microstructure and Mechanical Properties of Sn-58Bi Solder. *J. Electron. Mater.* **2021**, *50*, 283–290. [CrossRef]
16. Shen, Y.-A.; Chen, H.-Z.; Chen, S.-W.; Chiu, S.-K.; Guo, X.-Y.; Hsieh, Y.-P. Graphene as a diffusion barrier at the interface of Liquid–State low-melting Sn–58Bi alloy and copper foil. *Appl. Surf. Sci.* **2022**, *578*, 152108. [CrossRef]
17. Miao, H.-W.; Duh, J.-G. Microstructure evolution in Sn–Bi and Sn–Bi–Cu solder joints under thermal aging. *Mater. Chem. Phys.* **2001**, *71*, 255–271. [CrossRef]
18. Hirata, Y.; Yang, C.-H.; Lin, S.-K.; Nishikawa, H. Improvements in mechanical properties of Sn–Bi alloys with addition of Zn and In. *Mater. Sci. Eng. A* **2021**, *813*, 141131. [CrossRef]
19. Wu, X.; Wu, J.; Wang, X.; Yang, J.; Xia, M.; Liu, B. Effect of In addition on microstructure and mechanical properties of Sn–40Bi alloys. *J. Mater. Sci.* **2020**, *55*, 3092–3106. [CrossRef]
20. Chen, X.; Xue, F.; Zhou, J.; Yao, Y. Effect of In on microstructure, thermodynamic characteristic and mechanical properties of Sn–Bi based lead-free solder. *J. Alloys Compd.* **2015**, *633*, 377–383. [CrossRef]
21. Li, C.; Yan, Y.; Gao, T.; Xu, G. The influence of Ag on the microstructure, thermal properties and mechanical behavior of Sn–25Sb-xAg high temperature lead-free solder. *Vacuum* **2021**, *185*, 110015. [CrossRef]
22. Jiang, N.; Zhang, L.; Gao, L.-L.; Song, X.-G.; He, P. Recent advances on SnBi low-temperature solder for electronic interconnections. *J. Mater. Sci. Mater. Electron.* **2021**, *32*, 22731–22759. [CrossRef]
23. Xu, K.-K.; Zhang, L.; Gao, L.-L.; Jiang, N.; Zhang, L.; Zhong, S.-J. Review of microstructure and properties of low temperature lead-free solder in electronic packaging. *Sci. Technol. Adv. Mater.* **2020**, *21*, 689–711. [CrossRef]
24. Hu, F.; Zhang, Q.; Jiang, J.; Song, Z. Influences of Ag addition to Sn-58Bi solder on SnBi/Cu interfacial reaction. *Mater. Lett.* **2018**, *214*, 142–145. [CrossRef]
25. Mei, Z.; Morris, J.W. Characterization of eutectic Sn-Bi solder joints. *J. Electron. Mater.* **1992**, *21*, 599–607. [CrossRef]
26. Myung, W.-R.; Ko, M.-K.; Kim, Y.; Jung, S.-B. Effects of Ag content on the reliability of LED package component with Sn–Bi–Ag solder. *J. Mater. Sci. Mater. Electron.* **2015**, *26*, 8707–8713. [CrossRef]
27. Silva, B.L.; Garcia, A.; Spinelli, J.E. Complex eutectic growth and Bi precipitation in ternary Sn-Bi-Cu and Sn-Bi-Ag alloys. *J. Alloys Compd.* **2017**, *691*, 600–605. [CrossRef]
28. Gain, A.K.; Zhang, L. Effect of Ag nanoparticles on microstructure, damping property and hardness of low melting point eutectic tin–bismuth solder. *J. Mater. Sci. Mater. Electron.* **2017**, *28*, 15718–15730. [CrossRef]
29. Yang, T.; Zhao, X.; Xiong, Z.; Tan, W.; Wei, Y.; Tan, C.; Yu, X.; Wang, Y. Improvement of microstructure and tensile properties of Sn–Bi–Ag alloy by heterogeneous nucleation of β-Sn on Ag3Sn. *Mater. Sci. Eng. A* **2020**, *785*, 139372. [CrossRef]
30. Li, Y.; Chan, Y. Effect of silver (Ag) nanoparticle size on the microstructure and mechanical properties of Sn58Bi–Ag composite solders. *J. Alloys Compd.* **2015**, *645*, 566–576. [CrossRef]
31. Dong, W.; Shi, Y.; Xia, Z.; Lei, Y.; Guo, F. Effects of Trace Amounts of Rare Earth Additions on Microstructure and Properties of Sn-Bi-Based Solder Alloy. *J. Electron. Mater.* **2008**, *37*, 982–991. [CrossRef]
32. Wang, Z.; Zhang, Q.K.; Chen, Y.X.; Song, Z.L. Influences of Ag and In alloying on Sn-Bi eutectic solder and SnBi/Cu solder joints. *J. Mater. Sci. Mater. Electron.* **2019**, *30*, 18524–18538. [CrossRef]
33. Qin, W.; Li, J.; Zhang, Q.; Jiang, S.; Feng, J.; Yang, W.; Zhan, Y. Effect of addition of Al and Cu on the properties of Sn–20Bi solder alloy. *J. Mater. Sci. Mater. Electron.* **2022**, *33*, 177–189. [CrossRef]
34. Guo, Q.; Zhao, Z.; Shen, C. Comparison study on microstructure and mechanical properties of Sn-10Bi and Sn-Ag-Cu solder alloys and joints. *Microelectron. Reliab.* **2017**, *78*, 72–79. [CrossRef]
35. Ye, D.; Du, C.; Wu, M.; Lai, Z. Microstructure and mechanical properties of Sn–xBi solder alloy. *J. Mater. Sci. Mater. Electron.* **2015**, *26*, 3629–3637. [CrossRef]
36. Lai, Z.; Ye, D. Microstructure and fracture behavior of non eutectic Sn–Bi solder alloys. *J. Mater. Sci. Mater. Electron.* **2016**, *27*, 3182–3192. [CrossRef]
37. Karim, M.R.A.; Daniel, S.; Ul Haq, E.; Ahmad, A.; Khan, K.I.; Raza, S.A. Raza. Improving the Corrosion Resistance of API X56 and API X70 Pipeline Steels by Hot Dip Aluminization. In *Key Engineering Materials*; Trans Tech Publications Ltd.: Bäch, Switzerland, 2021; Volume 875, p. 315. [CrossRef]
38. Kab, M.; Mendil, S.; Taibi, K. Evolution of the Microstructure of Intermetallic Compounds Formed on Mild Steel During Hot Dipping in Molten Aluminum Alloy Baths. *Met. Microstruct. Anal.* **2020**, *9*, 476–483. [CrossRef]

39. Silva, B.L.; Garcia, A.; Spinelli, J.E. Cooling thermal parameters and microstructure features of directionally solidified ternary Sn–Bi–(Cu,Ag) solder alloys. *Mater. Charact.* **2016**, *114*, 30–42. [CrossRef]
40. Dias, M.; Costa, T.; Rocha, O.; Spinelli, J.E.; Cheung, N.; Garcia, A. Interconnection of thermal parameters, microstructure and mechanical properties in directionally solidified Sn–Sb lead-free solder alloys. *Mater. Charact.* **2015**, *106*, 52–61. [CrossRef]
41. El-Daly, A.; Hammad, A. Development of high strength Sn–0.7Cu solders with the addition of small amount of Ag and In. *J. Alloys Compd.* **2011**, *509*, 8554–8560. [CrossRef]
42. Kim, K.; Huh, S.; Suganuma, K. Effects of cooling speed on microstructure and tensile properties of Sn–Ag–Cu alloys. *Mater. Sci. Eng. A* **2002**, *333*, 106–114. [CrossRef]
43. Billah, M.; Shorowordi, K.M.; Sharif, A. Effect of micron size Ni particle addition in Sn–8Zn–3Bi lead-free solder alloy on the microstructure, thermal and mechanical properties. *J. Alloys Compd.* **2014**, *585*, 32–39. [CrossRef]
44. Gain, A.K.; Zhang, L. Interfacial microstructure, wettability and material properties of nickel (Ni) nanoparticle doped tin–bismuth–silver (Sn–Bi–Ag) solder on copper (Cu) substrate. *J. Mater. Sci. Mater. Electron.* **2015**, *26*, 3982–3994. [CrossRef]
45. Kripesh, V.; Teo, P.-S.; Tai, C.; Vishwanadam, G.; Mui, Y.C. Development of a Lead Free Chip Scale Package for Wireless Applications. In *51st Electronic Components and Technology Conference Proceedings*; IEEE: Piscataway, NJ, USA, 2001. [CrossRef]
46. Cheng, J.; Hu, X.; Jiang, X. Interfacial reaction and IMC growth between Sn-37 Pb and heterogeneous dual-phase substrate. *Vacuum* **2019**, *159*, 112–124. [CrossRef]

Disclaimer/Publisher's Note: The statements, opinions and data contained in all publications are solely those of the individual author(s) and contributor(s) and not of MDPI and/or the editor(s). MDPI and/or the editor(s) disclaim responsibility for any injury to people or property resulting from any ideas, methods, instructions or products referred to in the content.

coatings

MDPI

Article

Effect of Cold Deformation on the Hydrogen Permeation Behavior of X65 Pipeline Steel

Chan Yao [1,2], Hongliang Ming [2,*], Jian Chen [2,*], Jianqiu Wang [2] and En-Hou Han [2]

[1] National Center for Materials Service Safety, University of Science and Technology Beijing, Beijing 100083, China
[2] CAS Key Laboratory of Nuclear Materials and Safety Assessment, Institute of Metal Research, Chinese Academy of Sciences, Shenyang 110016, China
* Correspondence: hlming12s@imr.ac.cn (H.M.); jchen@imr.ac.cn (J.C.)

Abstract: In this study, an electrochemical hydrogen permeation experiment was used to determine the diffusion parameters, and a hydrogen microprint test was used to visualize the distribution of hydrogen in X65 pipeline steel with different levels of cold deformation. The hydrogen permeation curves show that both hydrogen permeation current density and effective hydrogen diffusion coefficient decrease with increasing cold deformation. The density of reversible and irreversible hydrogen traps is calculated from the permeation parameters, and it is found that the amount of both traps increases with increasing deformation, especially a significant increase in reversible hydrogen traps, which is in agreement with the results measured by thermal desorption spectroscopy. Hydrogen microprint test results indicate that the degree of hydrogen aggregation on the specimen surface increases with increasing cold deformation, especially at phase and grain boundaries. In addition, the dislocation configuration after cold deformation was further investigated by transmission electron microscopy.

Keywords: pipeline steel; hydrogen permeation; hydrogen microprint test

1. Introduction

With the rapid development of the global population, economy, and industry, human demand for energy is rising. Transporting crude oil and natural gas at higher working pressure to increase the capacity is now an important requirement [1,2]. Due to the advantages of low investment cost, large scale, high transport efficiency, safety, and reliability, pipeline transportation has become the main way for oil and gas transportation [3–6].

However, during the service of pipeline steel, hydrogen atoms can enter into the material due to not only the cathodic protection but also the influence of the transport medium and other issues. In general, the entrance of hydrogen into the metals is a prerequisite for hydrogen-related failure. There are usually three sources of hydrogen entering the interior of metals [7]. One is the hydrogen atoms introduced directly into the steel in certain amounts during the production process, e.g., during smelting, pickling, electroplating, etc. This hydrogen existing internally before the usage of a material is called internal hydrogen. The second one is the hydrogen absorbed directly from the gases containing H atoms in the service environment, e.g., the H in the lattice by collision, adsorption, dissociation, and the reaction of gases such as H_2 on the material surface during the service of pipeline steel. The third one is the absorption of hydrogen atoms from the liquid phase in the service environment of the steel. When the corrosion potential in the service environment is below the hydrogen evolution line, hydrogen atoms will be generated and adsorbed on the surface of the steel and then enter into the steel.

In addition, the large plastic strain may present during the production, construction, and usage of pipeline steels, and it will have a significant effect on hydrogen permeation behaviors [8]. Previous studies have found that the effect of plastic strain on hydrogen permeation is mainly due to the alteration of dislocations [9,10]. Dislocations are generally

considered to be important reversible hydrogen traps in materials [11,12]. Therefore, dislocation proliferation caused by plastic deformation is expected to affect hydrogen permeation. For cold-rolled iron and ferritic steels, the effect of dislocations on the hydrogen diffusion behaviors was often investigated by electrochemical permeation tests [13–17]. In these tests, the number of hydrogen atoms diffused from the charging side of a Devanathan–Stachurski cell through a metal specimen would be measured by the oxidation current density on the detection side. Kim and Lee investigated the relationship between plastic deformation and hydrogen transport behavior of quenched and partitioned (Q&P) steels by electrochemical hydrogen permeation tests and thermal desorption spectroscopy (TDS). They concluded that the trapped hydrogen content increased with increasing deformation level [10]. The increase in hydrogen traps in Q&P steels could be attributed to the increase in dislocation density in the ferrite and martensite from the substable austenite phase transformation. Cabrini et al. studied the hydrogen transport behavior of low alloy steels under cyclic loading conditions by electrochemical permeation techniques [18]. The results showed that the decrease in the apparent diffusion coefficient was also related to the increase in dislocation density with increasing deformation or the change in trap binding energy. Wang and Hui et al. studied the hydrogen permeation process in low alloy steels after pre-deformation and obtained the same results, where plastic pre-deformation promoted the absorption and permeation of hydrogen in the material, leading to an increase in hydrogen content [19]. In conclusion, it is found that hydrogen permeation behavior is sensitive to the dislocation density caused by plastic deformation [20]. In addition, the hydrogen diffusion kinetic parameters obtained by hydrogen permeation tests are crucial.

X65 is one of the most important kinds of pipeline steels used for natural gas transportation domestically, and it is now considered to be one of the potential materials for the transport of natural gas doped with hydrogen. Large residual strain may exceed 20%, usually present adjacent to the welds. Hence, the purpose of this study is to clarify the effect of strain level on the hydrogen permeation behavior of X65 pipeline steel, and the mechanism of hydrogen permeation is explored. This study used double hydrogen permeation tests to determine the hydrogen permeation parameters with different cold deformation levels. The parameters include the hydrogen diffusion flux (N_∞), effective hydrogen diffusion coefficient (D_{eff}), apparent solubility (c_0), and hydrogen trap density (N_T). A hydrogen microprint test (HMT) was used to characterize the hydrogen distribution on the surface of the material after cold deformation. The mechanism of the effect of cold deformation on hydrogen permeation was also investigated by TDS and transmission electron microscopy (TEM).

2. Materials and Methods

2.1. Materials

X65 pipeline steel was used in this study and its chemical compositions are listed in Table 1. The content of all main elements of X65 pipeline steel meets the requirements of API 5L. The optical microstructure of X65 pipeline steel was observed with an optical microscope (OM, Axio Observer Z1, Zeiss, Oberkochen, Germany), as shown in Figure 1. It can be found that the material is composed of polygonal ferrite (PF) and a small amount of pearlite (P).

Table 1. Chemical compositions of API X65 steel (wt.%).

Steel	C	Si	P	S	Cr	Mn	Ni	Cu	Mo	Fe
X65	0.081	0.190	0.014	<0.001	0.050	1.320	<0.030	<0.030	<0.030	Bal.

Plate tensile specimens were taken from the direction perpendicular to the diameter of the pipe, with the dimensions of 150 mm × 25 mm × 2 mm, as shown in Figure 2a. Tensile tests were carried out by using a universal testing machine (Zwick Z150, Zwick, North Rhine-Westphalia, Germany) at room temperature with a stretching rate of 0.75 mm/min to simulate different cold deformations. A certain deformation was

applied to the specimens and the actual deformation after unloading was measured to obtain the real cold deformation level. Three kinds of specimens were prepared, 0.00% for undeformed specimens, 4.25% and 7.25% for deformed ones, respectively, as shown in Figure 2b. Hydrogen permeation specimens were cut from the parallel sections of the tensile specimens, as shown in Figure 2a.

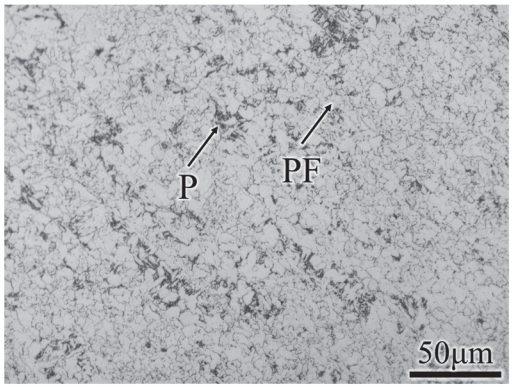


Figure 1. Optical microstructure of X65 pipeline steel.

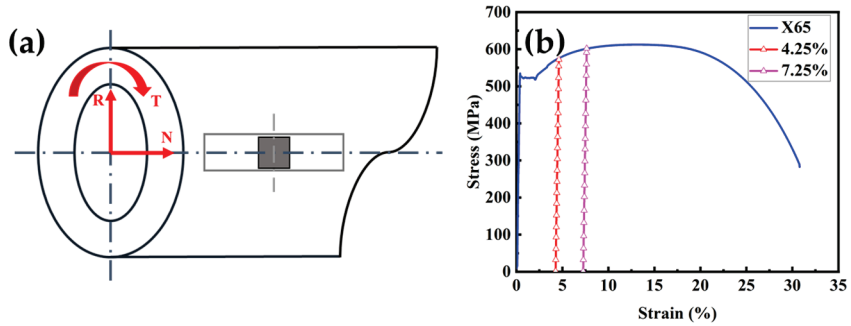


Figure 2. (**a**) Hydrogen permeation specimen sampling diagram, (**b**) engineering strain curves in the cold deformation loaded–unloaded condition.

The dislocation configuration after cold deformation was further investigated using TEM (TEM, JEM-2100F, JEOL, Tokyo Metropolis, Japan) with an accelerating voltage of 200 kV. The specimens used for TEM observation were first mechanically ground to a thickness of 60 μm and then were electrolytically double sprayed with a 10% perchloric acid ethanol solution at a voltage of 30 V below −20 °C.

2.2. Hydrogen Permeation Experiment

A modified Devanthan–Stachurski dual cell (Figure 3) was used for electrochemical hydrogen permeation tests in this study. The apparatus consists of two electrolytic cells that are not in contact with each other. The two cells are separated by a specimen. The cathode cell is on one side of the specimen. A constant cathodic current is applied to the specimen and hence the hydrogen ions in solution will be transformed into hydrogen atoms by gaining electrons on the surface of the specimen. Some of the hydrogen atoms produced by the reaction will combine on the specimen surface to form hydrogen molecules and then escape to the atmosphere, while others will diffuse to the other side of the specimen driven by the hydrogen concentration gradient. On the other side of the specimen is the anode cell, where an electrochemical workstation applies a constant anodic potential to the specimen, and then the hydrogen atoms penetrating from the cathode chamber will be oxidized into hydrogen ions again.

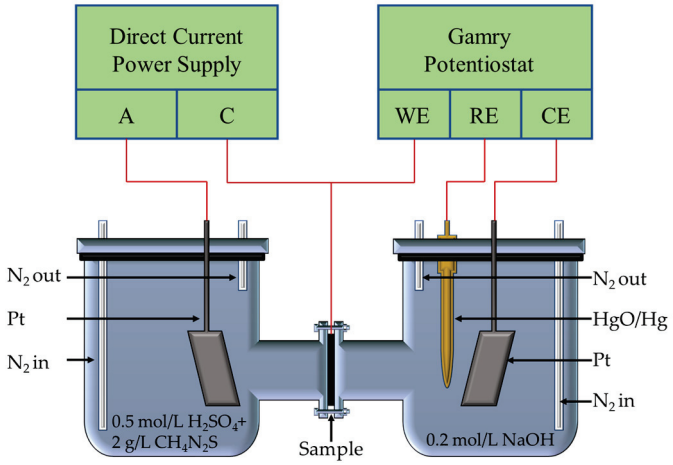


Figure 3. Schematic diagram of the electrochemical hydrogen permeation cell.

The specimen dimensions were 20 mm × 20 mm × 1 mm, with a diameter of 16 mm exposed to the solution. The specimens were first polished and then nickel-plated on one side. The nickel-plating solution was 300 g/L $NiSO_4 \cdot 6H_2O$, 30 g/L $NiCl_2 \cdot 6H_2O$, 40 g/L H_3BO_3, and 0.1 g/L $C_{12}H_{25}$-OSO_3Na; the plating was performed at a current density of 5 mA/cm^2 and with a duration of 5 min. After the specimen was connected to the wire and tested for conductivity, it was mounted in the middle of the electrolytic cells, with the nickel-plated side facing the anode cell and the other side facing the cathode cell. After adding 0.2 mol/L NaOH solution into the anode cell, a constant potential of 0.3 V (vs. Hg/HgO) would be applied to the specimen via a Gamry 600 electrochemical workstation. Until the background current was less than 0.1 μA/cm^2, 0.5 mol/L H_2SO_4 + 2 g/L CH_4N_2S solution would be added to the cathode cell and a constant cathodic current of 5 mA/cm^2 then be applied to the specimen via a constant current source. The change in current of the anode cell should be detected during the whole test until the current reached a steady state. In this study, the same specimen was subjected to a double hydrogen permeation test to investigate the effect of reversible and irreversible hydrogen traps on the changes in the hydrogen permeation behavior of pipeline steel.

2.3. Hydrogen Microprint Test

The specimen with dimensions of 20 mm × 20 mm × 1 mm was polished and then hydrogen was charged on one side with a current density of 5 mA/cm^2 for 5 h. After that, a microstamping solution (5 g AgBr + 10 mL 1.4 mol/L $NaNO_2$) was applied to the uncharged side and held for 30 min. Then immediately, the specimen was placed in a fixing solution (0.6 mol/L $Na_2S_2O_3$ + 1.4 mol/L $NaNO_2$) and soaked for 30 min. The specimen was then carefully cleaned with ethanol and dried in air. Afterward, the coated side was slightly etched with a 4% nitric acid ethanol solution to present the microstructure of the material. The whole process should be carried out in a light-proof environment. In the end, scanning electron microscope (SEM, XL30-FEG, FEI, Hillsboro, OR, USA) was used to observe the distribution of the silver particles. Silvery particles represent the distribution of hydrogen atoms.

2.4. Hydrogen Desorption Spectroscopy

The specimen with a diameter of 20 mm and a thickness of 1 mm was polished to 2000# to remove the surface oxide layer on both sides, followed by rinsing it with distilled water and ethanol before hydrogen charging. The specimen was charged within a 0.5 mol/L H_2SO_4 + 2 g/L CH_4N_2S solution for 12 h at a current density of 5 mA/cm^2. After that, the specimen was immediately placed in liquid nitrogen and quickly transferred to the quartz tube of the thermal desorber. The rate of hydrogen desorption from the steel was

measured by a quadrupole mass spectrometer and set at a ramp-up rate of 300 °C/h from room temperature to 800 °C.

3. Results and Discussion

3.1. Hydrogen Permeation

The hydrogen permeation curves for X65 pipeline steel with different cold deformation levels after a double test are shown in Figure 4. The trends of the hydrogen permeation curves are consistent and can be roughly divided into three stages, which are the permeation current incubation stage, the permeation current rise stage, and the permeation current stabilization stage. However, it is obvious that the cold deformation not only slightly delays the current incubation time but also affects the steady current density (J_∞). The J_∞ slightly decreases with increasing the cold deformation levels for both the first and second hydrogen permeation tests, especially for the second test, and this is consistent with the findings in Refs. [21,22]. The J_∞ responds to the magnitude of hydrogen diffusion flux (N_∞) and is also related to D_{eff} and c_0. D_{eff} is the quantity of hydrogen that diffuses through a unit cross-sectional area of the specimen in unit time due to the different H concentration between two surfaces, and c_0 corresponds to the hydrogen concentration in the lattice, reversible and irreversible traps [23]. Researchers commonly use the time lag method to calculate the hydrogen permeation parameters by using the following equations [24–26]:

$$N_\infty = \frac{J_\infty}{F} \tag{1}$$

$$D_{eff} = \frac{d^2}{6t_L} \tag{2}$$

$$c_0 = \frac{N_\infty \times d}{D_{eff}} \tag{3}$$

where N_∞ is the hydrogen diffusion flux (mol/(cm^2·s)), J_∞ is the steady-state current density (A/cm^2), F is Faraday's constant(96,500 Coulombs/mol) [27], D_{eff} is the effective hydrogen diffusion coefficient (cm^2/s), d is the specimen thickness (0.8 mm in this study), t_L is the lag time, i.e., the time corresponding to $J/J_\infty = 0.63$, and c_0 is the apparent solubility (mol/cm^3). See Appendix A Table A1 for parameters and the corresponding abbreviations.

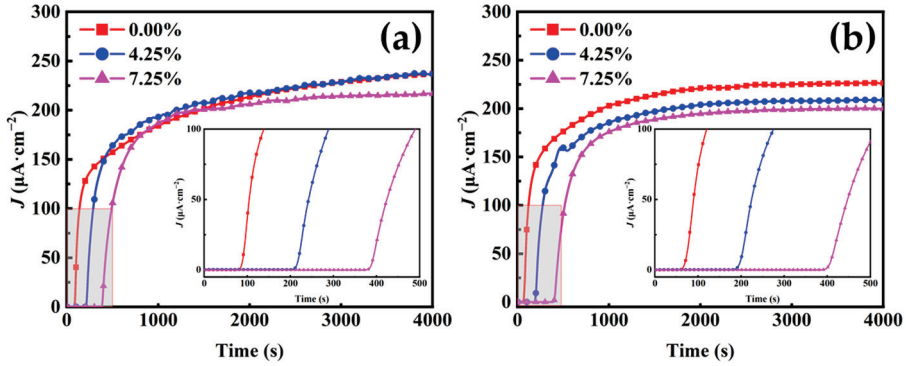


Figure 4. Hydrogen permeation curves of X65 steel with different cold deformation levels: (**a**) the first hydrogen permeation curves, (**b**) the second hydrogen permeation curves.

The electrochemical hydrogen permeation parameters are derived from the measured hydrogen permeation curves and the results are listed in Tables 2 and 3, respectively. In order to visually compare the effect of cold deformation on the N_∞, D_{eff}, and c_0 for the first and second hydrogen permeation, the calculated parameters are plotted against the cold deformation levels in Figure 5. It can be found that N_∞ fluctuates within a very small range and remains almost constant. When comparing the results, it can be seen that the D_{eff} of the second hydrogen permeation test

is greater than that of the first test. The analysis concluded that X65 pipeline steel contains both reversible and irreversible hydrogen traps. During the first hydrogen permeation test, the hydrogen entering the specimen is trapped by both the reversible and irreversible hydrogen traps during diffusion, while during the second test, the irreversible hydrogen traps have been already filled. Hence, the second hydrogen permeation curve only reflects the capture of hydrogen in the reversible traps [28]. Therefore, the D_{eff} for the second test is higher. Moreover, the D_{eff} decreases from 3.553×10^{-6} to 1.775×10^{-6} cm^2/s for the first hydrogen permeation test and from 4.265×10^{-6} to 1.903×10^{-6} cm^2/s for the second one as the cold deformation level increases from 0.00% to 7.25%, while the c_0 shows an opposite trend. From the above results, it is found that cold deformation inhibits the hydrogen permeation behavior for X65 pipeline steel, and this should be related to the microstructure changes caused by cold deformation.

Table 2. Parameters from the first hydrogen permeation curves of X65 pipeline steel with different cold deformation levels.

Cold Deformation (%)	$N_\infty \times 10^{-9}$ (mol/(cm^2·s))	$D_{eff} \times 10^{-6}$ (cm^2/s)	$c_0 \times 10^{-5}$ (mol/cm^3)
0.00	2.451 ± 0.052	3.553 ± 0.311	5.551 ± 0.368
4.25	2.473 ± 0.026	2.717 ± 0.090	7.288 ± 0.163
7.25	2.342 ± 0.022	1.775 ± 0.006	10.557 ± 0.133

Table 3. Parameters from the second hydrogen permeation curves of X65 pipeline steel with different cold deformation levels.

Cold Deformation (%)	$N_\infty \times 10^{-9}$ (mol/(cm^2·s))	$D_{eff} \times 10^{-6}$ (cm^2/s)	$c_0 \times 10^{-5}$ (mol/cm^3)
0.00	2.331 ± 0.022	4.265 ± 0.455	4.418 ± 0.431
4.25	2.137 ± 0.013	2.947 ± 0.024	5.801 ± 0.013
7.25	2.122 ± 0.062	1.903 ± 0.058	8.922 ± 0.010

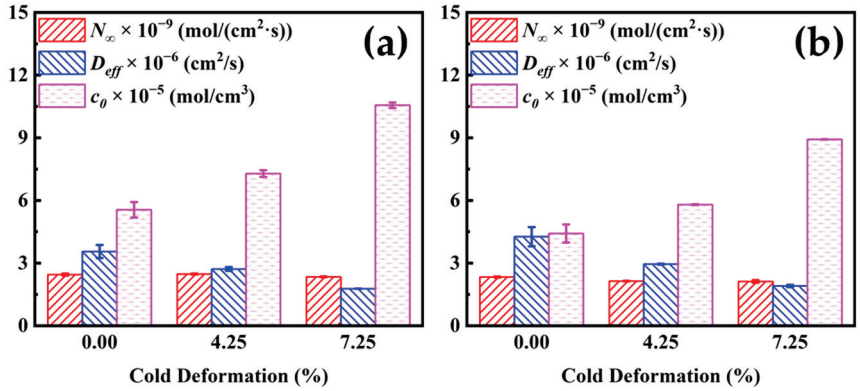


Figure 5. Effect of cold deformation on hydrogen permeation behavior: (**a**) hydrogen permeation parameters from the first permeation curves, (**b**) hydrogen permeation parameters from the second permeation curves.

3.2. Hydrogen Microprinting

The purpose of using the HMT is to understand more clearly the effect of cold deformation on the hydrogen permeation behavior, as it can visually indicate the distribution of hydrogen atoms. In this study, the hydrogen atoms diffuse from one side of the specimen to the other side and are oxidized by the Ag^+, allowing us to observe the distribution of hydrogen by Ag particles. The hydrogen content is higher in areas with a higher density of Ag particles. HMT was performed on specimens with 0.00% and 7.25% deformation

(Figure 6). Figure 6a,c shows the low magnification images of the silver particle distribution on the surface of the specimens with 0.00% and 7.25% cold deformation, respectively. It can be clearly seen that the silver particles are relatively uniformly distributed on the surface of the specimens, with a greater enrichment on the surface with higher cold deformation levels. The explanation for this is that the N_∞ remains almost constant after cold deformation, while the D_{eff} decreases. The reason for the decrease in the permeability coefficient is the increase in hydrogen traps, which will be clearly explained in the next section. The increase in trapped hydrogen leads to an increase in the enrichment of the silver particles. Figure 6b,d shows higher magnification images of Figure 6a,c, respectively, the silver particles are more likely to be distributed at the grain boundaries and phase boundaries than in other regions. Grain boundaries and phase boundaries act as hydrogen trapping points and have a higher capacity for hydrogen enrichment than interstitial positions [29,30].

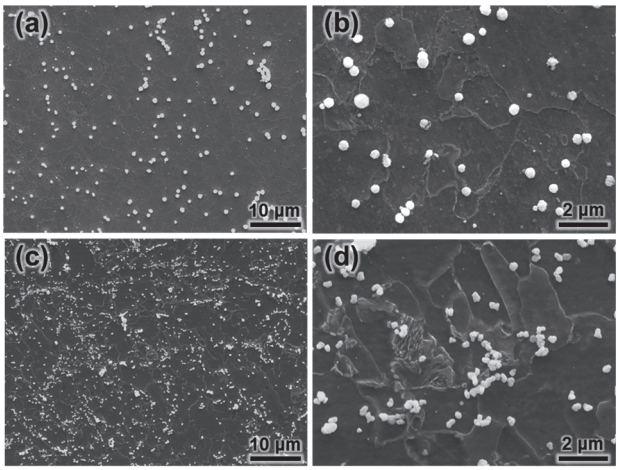


Figure 6. SEM images of X65 steel with different cold deformation levels after hydrogen microprinting: (**a**,**b**) without cold deformation (0.00%), (**c**,**d**) with 7.25% cold deformation.

3.3. Effect of Cold Deformation on Hydrogen Permeation

Exploring the potential mechanisms and the underlying causes of the hydrogen permeation behavior of X65 pipeline steel requires an in-depth understanding of the interactions between hydrogen and microstructural features. In a previous study [31], hydrogen diffusivity in various sheets of steel exhibited unique behavior, mainly due to the presence of various hydrogen traps. Hydrogen atoms in steel not only occupy interstitial sites but also can be captured by defects, such as vacancies, dislocations, grain boundaries, voids, interstitial atoms, second phases, and nonmetallic inclusions, etc. These defects are usually referred to as hydrogen traps. According to the binding energy of hydrogen with traps, traps can be divided into reversible and irreversible ones. Reversible traps are low energy traps that will not permanently trap hydrogen, such as dislocations, small angle grain boundaries, voids, etc. Irreversible traps are high-binding energy traps at ambient temperatures, which include nonmetallic inclusion, second phases, interstitial atoms, vacancies, etc. [32,33].

The D_{eff} for two hydrogen permeations decreases with increasing cold deformation because of the increasing N_T. Some researchers have suggested that the N_T in the material can be calculated from the following equation [34]:

$$N_T = \frac{c_0}{3}\left(\frac{D_L}{D_{eff}} - 1\right) \tag{4}$$

where the value of the lattice diffusion coefficient in trap-free bcc iron is supposed as $D_L = 1.28 \times 10^{-4}$ cm^2/s. The results of the second hydrogen permeation test reflect the reversible hydrogen trap density (N_{RT}). The N_T of the first hydrogen permeation test

minus the N_T of the second test should then be the irreversible hydrogen trap density (N_{IRT}) [34]. The calculated results are shown in Figure 7a, and it can be found that both N_{RT} and N_{IRT} increase with increasing cold deformation, especially the N_{RT}. The N_{RT} increases significantly from 1.93×10^{20} to 1.19×10^{21} cm^{-3}, an increase of approximately six times. A comparison of D_{eff} and c_0 reveals that N_T is positively proportional to c_0 and inversely proportional to D_{eff}. This is consistent with the results from previous studies [34]. The researchers found that reduced permeability and diffusivity, as well as increased solubility, led to more hydrogen being trapped in the steel. This also explains the greater abundance and density of silver particles with increasing cold deformation in 3.2. Figure 7b demonstrates the effect of cold deformation on the TDS results of X65, showing a similar trend as in Figure 7a. The TDS curves show two types of desorption peaks, peak 1 and peak 2, for both the specimen without deformation and the specimen with 7.25% deformation. Peak 1 is the low-temperature peak where hydrogen is desorbed from the reversible hydrogen traps while peak 2 is the high-temperature peak where hydrogen is desorbed from the irreversible hydrogen traps. Peak 1 appears at around 130 °C and peak 2 at around 400 °C when without deformation. However, when deformation reaches 7.25%, peak 1 shifts to around 165 °C and peak 2 to 600 °C. It can be found that after deformation, both the two peaks shift to potions with higher temperatures. In addition, the intensity of both peaks increases after deformation. It is generally believed that peak 1 corresponds to reversible hydrogen traps (mainly dislocations) and the increase in the intensity of peak 1 indicates an increase in dislocation density [9,35]. TEM micrographs of specimens with cold deformation of 4.25% and 7.25% are shown in Figure 7c,d. From Figure 7c, it is found that after 4.25% cold deformation, clearly visible dislocation lines are found in the material, with slight dislocation entanglement in the middle of the dislocation. For 7.25% cold deformation material (Figure 7d), a significant increase in dislocation density is observed, accompanied by dislocation build-up and entanglement. The increase in dislocation density confirms that the density of reversible hydrogen traps increases with increasing cold deformation, and this is the main reason for the different hydrogen permeation behavior after cold deformation.

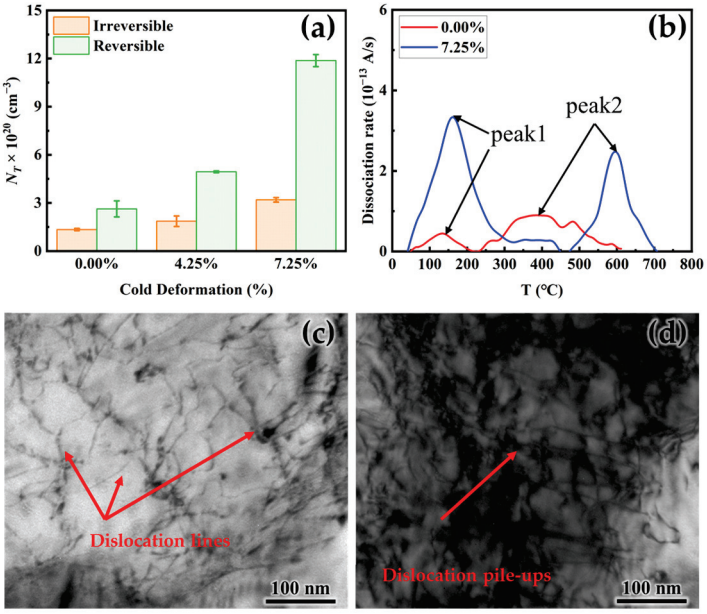


Figure 7. (**a**) Hydrogen trap density diagram for X65 pipeline steel from the electrochemical hydrogen permeation test, (**b**) TDS curves for X65 pipeline steel with different cold deformation levels, (**c**) TEM micrographs of X65 steel with 4.25% cold deformation, (**d**) TEM micrographs of X65 steel with 7.25% cold deformation.

4. Conclusions

The effect of cold deformation on the hydrogen permeation behavior of X65 pipeline steel is investigated in combination with electrochemical hydrogen permeation tests, TDS, TEM, and HMT, and the following conclusions can be drawn:

(1) The D_{eff} decreases with increasing cold deformation (from 0.00% to 7.25%), from 3.553×10^{-6} to 1.775×10^{-6} cm^2/s for the first penetration test and from 4.265×10^{-6} to 1.903×10^{-6} cm^2/s for the second one, while c_0 increases with increasing cold deformation. The increase in cold deformation level inhibits hydrogen permeation.

(2) In the HMT tests, the enrichment of silver particles on the surface increases with the cold deformation level and particles are more likely to be enriched at the grain boundaries and phase boundaries.

(3) Both N_T and N_{RT} increase with increasing cold deformation which is proved by hydrogen penetration tests as well as by TDS. The dislocation density increases significantly after cold deformation and is accompanied by dislocation entanglement.

The current method for studying hydrogen permeation behavior is still the traditional electrochemical hydrogen permeation test. However, with a large number of applications of hydrogen-doped natural gas pipelines and pure hydrogen pipelines, studying the hydrogen permeation behavior in gaseous hydrogen environments will be more valuable for engineering. We will modify the cathode cell of the Devanthan–Stachurski dual cell so that the cathode cell can hold high pressure gaseous hydrogen. This will enable hydrogen permeation study in high-pressure hydrogen environments and compare the effect of liquid and gas phase hydrogen charging on the hydrogen permeation behavior.

Author Contributions: Conceptualization, C.Y. and H.M.; methodology, H.M.; validation, J.C., H.M. and J.W.; investigation, C.Y. and J.C.; resources, J.W.; data curation, C.Y.; writing—original draft preparation, C.Y.; writing—review and editing, H.M.; visualization, E.-H.H.; supervision, J.W.; project administration, H.M.; funding acquisition, J.W. All authors have read and agreed to the published version of the manuscript.

Funding: This work is jointly supported by the National Key R&D Program of China (2021YFB4001601) and Youth Innovation Promotion Assessment CAS (2022187).

Institutional Review Board Statement: Not applicable.

Informed Consent Statement: Not applicable.

Data Availability Statement: Not applicable.

Conflicts of Interest: The authors declare no conflict of interest.

Appendix A

Table A1. Parameters and the corresponding abbreviations in this study.

Parameters	Abbreviations
Hydrogen diffusion flux	N_∞
Steady current density	J_∞
Effective hydrogen diffusion coefficient	D_{eff}
Apparent solubility	c_0
Specimen thickness	d
Lag time	t_L
Faraday constant	F
Trap free bcc iron	D_L
Hydrogen trap density	N_T
Reversible hydrogen trap density	N_{RT}
Irreversible hydrogen trap density	N_{IRT}

References

1. Khalaj, G.; Azimzadegan, T.; Khoeini, M.; Etaat, M. Artificial neural networks application to predict the ultimate tensile strength of X70 pipeline steels. *Neural Comput. Appl.* **2013**, *23*, 2301–2308. [CrossRef]
2. Khalaj, G.; Pouraliakbar, H.; Arab, N.; Nazerfakhari, M. Correlation of passivation current density and potential by using chemical composition and corrosion cell characteristics in HSLA steels. *Measurement* **2015**, *75*, 5–11. [CrossRef]
3. Gholamreza, K.; Ali, N.; Hesam, P. Prediction of martensite fraction of microalloyed steel by artificial neural networks. *Artif. Neural Netw.* **2013**, *23*, 117–130.
4. Huang, F.; Cheng, P.; Zhao, X.Y.; Liu, J.; Hu, Q.; Cheng, Y.F. Effect of sulfide films formed on X65 steel surface on hydrogen permeation in H2S environments. *Int. J. Hydrogen Energy* **2017**, *42*, 4561–4570. [CrossRef]
5. Khalaj, G.; Pouraliakbar, H.; Mamaghani, K.R.; Khalaj, M.-J. Modeling the correlation between heat treatment, chemical composition and bainite and bainite fraction of pipelines steels by means of artificial neural networks. *Artif. Neural Netw.* **2013**, *23*, 351–367. [CrossRef]
6. You, Y.; Shang, C.; Wenjin, N.; Subramanian, S. Investigation on the microstructure and toughness of coarse grained heat affected zone in X-100 multi-phase pipeline steel with high Nb content. *Mater. Sci. Eng. A* **2012**, *558*, 692–701. [CrossRef]
7. Tiwari, G.P.; Bose, A.; Chakravartty, J.K.; Wadekar, S.L.; Totlani, M.K.; Arya, R.N.; Fotedar, R.K. A study of internal hydrogen embrittlement of steels. *Mater. Sci. Eng. A* **2000**, *286*, 269–281. [CrossRef]
8. Zheng, C.B.; Jiang, H.K.; Huang, Y.L. Hydrogen permeation behaviour of X56 steel in simulated atmospheric environment under loading. *Corros. Eng. Sci. Technol.* **2013**, *46*, 365–367. [CrossRef]
9. Chen, L.; Xiong, X.; Tao, X.; Su, Y.; Qiao, L. Effect of dislocation cell walls on hydrogen adsorption, hydrogen trapping and hydrogen embrittlement resistance. *Corrosion Sci.* **2020**, *166*, 108428. [CrossRef]
10. Kim, H.-J.; Lee, M.-G. Analysis of hydrogen trapping behaviour in plastically deformed quenching and partitioning steel in relation to microstructure evolution by phase transformation. *J. Alloys Compd.* **2022**, *904*, 164018. [CrossRef]
11. Hutchings, R.B.; Turnbull, A. The effect of prior mechanical deformation on hydrogen transport through 13% chromium martensitic stainless steel. *Corros. Sci.* **1992**, *33*, 713–728. [CrossRef]
12. Turnbull, A. Perspectives on hydrogen uptake, diffusion and trapping. *Int. J. Hydrogen Energy* **2015**, *40*, 16961–16970. [CrossRef]
13. Xiukui, S.; Xu, X.J. Permeation of hydrogen in 21-6-9 austenitic stainless steel. *J. Chin. Soc. Corros. Prot.* **1987**, *7*, 274–280.
14. Jian, X.; Xiukui, S. Hydrogen permeation and diffusion in low-carbon steels and 16Mn steel. *J. Mater. Sci. Technol.* **1994**, *10*, 92–96.
15. Xu, J.; Xiukui, S.; Qingquan, L.; Wenxiu, X. Characteristics of hydrogen permeation in GH718 alloy. *J. Chin. Soc. Corros. Prot.* **1994**, *14*, 151–155.
16. Stachurski, M. The adsorption and diffusion of electrolytic hydrogen in palladium. *Proc. R. Soc. Ser. A-Math. Phys. Eng. Sci.* **1962**, *270*, 90–102.
17. Brass, A.M.; Chêne, J. Influence of tensile straining on the permeation of hydrogen in low alloy Cr–Mo steels. *Corros. Sci.* **2006**, *48*, 481–497. [CrossRef]
18. Cabrini, M.; Coppola, L.; Lorenzi, S.; Testa, C.; Carugo, F.; Bucella, D.P.; Pastore, T. Hydrogen Permeation in X65 Steel under Cyclic Loading. *Materials* **2020**, *13*, 2309. [CrossRef] [PubMed]
19. Wang, J.J.; Hui, W.; Xie, Z.; Wang, Z.; Zhao, X. Hydrogen embrittlement of a cold-rolled Al-containing medium-Mn steel: Effect of pre-strain. *Int. J. Hydrogen Energy* **2020**, *45*, 22080–22093. [CrossRef]
20. Zhao, W.; Zhang, T.; He, Z.; Sun, J.; Wang, Y. Determination of the critical plastic strain-induced stress of X80 steel through an electrochemical hydrogen permeation method. *Electrochim. Acta* **2016**, *214*, 336–344. [CrossRef]
21. Sun, Y.; Cheng, Y.F. Hydrogen permeation and distribution at a high-strength X80 steel weld under stressing conditions and the implication on pipeline failure. *Int. J. Hydrog. Energy* **2021**, *46*, 23100–23112. [CrossRef]
22. Li, H.; Venezuela, J.; Zhou, Q.; Shi, Z.; Dong, F.; Yan, M.; Knibbe, R.; Zhang, M.; Atrens, A. Effect of cold deformation on the hydrogen permeation in a dual-phase advanced high-strength steel. *Electrochim. Acta* **2022**, *424*, 140619. [CrossRef]
23. Zhang, T.; Zhao, W.; Li, T.; Zhao, Y.; Deng, Q.; Wang, Y.; Jiang, W. Comparison of hydrogen embrittlement susceptibility of three cathodic protected subsea pipeline steels from a point of view of hydrogen permeation. *Corros. Sci.* **2018**, *131*, 104–115. [CrossRef]
24. Zhang, S.; Li, J.; An, T.; Zheng, S.; Yang, K.; Lv, L.; Xie, C.; Chen, L.; Zhang, L. Investigating the influence mechanism of hydrogen partial pressure on fracture toughness and fatigue life by in-situ hydrogen permeation. *Int. J. Hydrogen Energy* **2021**, *46*, 20621–20629. [CrossRef]
25. Jack, T.A.; Pourazizi, R.; Ohaeri, E.; Szpunar, J.; Zhang, J.; Qu, J. Investigation of the hydrogen induced cracking behaviour of API 5L X65 pipeline steel. *Int. J. Hydrogen Energy* **2020**, *45*, 17671–17684. [CrossRef]
26. Xue, H.B.; Cheng, Y.F. Characterization of inclusions of X80 pipeline steel and its correlation with hydrogen-induced cracking. *Corros. Sci.* **2011**, *53*, 1201–1208. [CrossRef]
27. Cheng, Y. Analysis of electrochemical hydrogen permeation through X-65 pipeline steel and its implications on pipeline stress corrosion cracking. *Int. J. Hydrogen Energy* **2007**, *32*, 1269–1276. [CrossRef]
28. Zhao, W.; Zhang, T.; Zhao, Y.; Sun, J.; Wang, Y. Hydrogen permeation and embrittlement susceptibility of X80 welded joint under high-pressure coal gas environment. *Corros. Sci.* **2016**, *111*, 84–97. [CrossRef]
29. Momotani, Y.; Shibata, A.; Terada, D.; Tsuji, N. Hydrogen embrittlement behavior at different strain rates in low-carbon martensitic steel. *Mater. Today Proc.* **2015**, *2*, S735–S738. [CrossRef]

30. Koyama, M.; Yamasaki, D.; Nagashima, T.; Tasan, C.C.; Tsuzaki, K. In situ observations of silver-decoration evolution under hydrogen permeation: Effects of grain boundary misorientation on hydrogen flux in pure iron. *Scr. Mater.* **2017**, *129*, 48–51. [CrossRef]
31. Liu, M.A.; Rivera-Diaz-del-Castillo, P.E.J.; Barraza-Fierro, J.I.; Castaneda, H.; Srivastava, A. Microstructural influence on hydrogen permeation and trapping in steels. *Mater. Des.* **2019**, *167*, 107605. [CrossRef]
32. Ghosh, G.; Rostron, P.; Garg, R.; Panday, A. Hydrogen induced cracking of pipeline and pressure vessel steels: A review. *Eng. Fract. Mech.* **2018**, *199*, 609–618. [CrossRef]
33. Sun, Y.; Frank Cheng, Y. Hydrogen-induced degradation of high-strength steel pipeline welds: A critical review. *Eng. Fail. Anal.* **2022**, *133*, 105985. [CrossRef]
34. Mohtadi-Bonab, M.A.; Szpunar, J.A.; Razavi-Tousi, S.S. Hydrogen induced cracking susceptibility in different layers of a hot rolled X70 pipeline steel. *Int. J. Hydrogen Energy* **2013**, *38*, 13831–13841. [CrossRef]
35. Yu, S.-H.; Lee, S.-M.; Lee, S.; Nam, J.-H.; Lee, J.-S.; Bae, C.-M.; Lee, Y.-K. Effects of lamellar structure on tensile properties and resistance to hydrogen embrittlement of pearlitic steel. *Acta Mater.* **2019**, *172*, 92–101. [CrossRef]

Disclaimer/Publisher's Note: The statements, opinions and data contained in all publications are solely those of the individual author(s) and contributor(s) and not of MDPI and/or the editor(s). MDPI and/or the editor(s) disclaim responsibility for any injury to people or property resulting from any ideas, methods, instructions or products referred to in the content.

materials

MDPI

Article

Effect of Different Temperatures on the Hydration Kinetics of Urea-Doped Cement Pastes

Hui Su [1,2], Yawei Luan [1,2], Qiujuan Ma [1,2], Baowen Hu [1,2,*], Shaoxing Liu [1,2] and Yanjie Bai [1,3]

[1] School of Water Conservancy and Hydroelectric Power, Hebei University of Engineering, Handan 056038, China
[2] Hebei Provincial Key Laboratory of Intelligent Water Resources, Handan 056038, China
[3] Nanjing Hydraulic Research Institute, State Key Laboratory of Hydrology-Water Resources and Hydraulic Engineering, Nanjing 210029, China
* Correspondence: hubaowen1984@gmail.com; Tel.: +86-152-0117-1749

Abstract: Urea can solve the problem of concrete cracking due to temperature stress. However, its effect is affected by temperature. The influencing mechanism of temperature on urea-doped cement pastes is still unclear. This paper explores the effect of different temperatures on the hydration kinetics of urea-doped cement pastes. The isothermal calorimeter (TAM Air) was used to test hydration at three constant temperatures (20 °C, 40 °C, and 60 °C). The effects of the urea admixture and temperature on the hydration process and hydration kinetics parameters were investigated. The hydration mechanism was analyzed, and the changes in macroscopic mechanical compressive strength and porosity were tested. The results show that, as the urea content (UC) increases, the rate of hydration gradually decreases, and the increase in temperature promotes the inhibitory effect of urea. At 60 °C, UC of 8% can be reduced by 23.5% compared with the pure cement (PC) group's hydration rate. As the temperature increases from 20 °C to 60 °C, the Krstulovic–Dabic model changes from the NG-I-D process to the NG-D process. The effect of urea on the compressive strength of the cement is mainly shown in the early stage, and its effect on later strength is not obvious. In addition, urea will increase its early porosity. The porosity will gradually decrease in the later stage. The results of the study clarify the effect of temperature on urea-doped cement pastes. The optimal content of urea in cement is about 8%, which will provide theoretical guidance for solving the cracking problem of large-volume concrete due to temperature stress.

Keywords: temperature; urea; hydration kinetics; Krstulovic–Dabic model; compressive strength; porosity; hydration mechanism; temperature stress; crack development

1. Introduction

Cement is a commonly used material in hydraulic buildings [1–5]; however, the phenomenon of cracking concrete due to temperature stress occurs from time to time. The temperature around the environment of a hydraulic building can seriously affect cement hydration [6,7], and reducing the hydration rate of cement to avoid concentrated exotherm is one way to deal with this problem [8]. However, most scholars have mainly focused on reducing the hydration rate of cement under ambient temperature conditions by adding traditional mineral admixtures such as fly ash [9], silica fume [10], and slag [11], etc. Under ambient conditions [12], He et al. [13] mixed fly ash into the cement and tested its 72 h heat of hydration at 20 °C and found that fly ash was able to reduce the total amount of hydration heat from cement hydration for 72 h. The fly ash inhibition is mainly able to bind nucleation. Briki et al. [14] replaced cement with limestone powder and found that limestone powder can promote cement hydration. The mechanism of the influence of traditional mineral admixtures is becoming gradually clear. However, there is less research on the mechanism of the influence of urea [15,16], a common material in daily life, on cement hydration. Urea can reduce the hydration rate in the early stage of curing, thereby

reducing temperature stress and avoiding cracks in concrete in the early stage of curing. Park et al. [17] explored the effect of urea on hydration at the normal temperature, noting that the amount of admixture should not exceed 10%. Kim et al. [18] found that, when urea was mixed with concrete, it significantly reduced the ambient temperature around the concrete at the moment of its dissolution.

The Krstulovic–Dabic model of hydration kinetics is one way to understand the hydration process [19–21]. Meng et al. [22] used the Krstulovic–Dabic model to study the effect of nano-SiO_2 on cement hydration and analyzed its mechanism. Changes in cement hydration also cause changes in the microscopic morphology and porosity of the cement pastes [23–27]. Dong et al. [28] observed the morphology of the hydration products through the Electron Microscopy, demonstrating that the nano-silica can make the structure of C-S-H gel more compact. In summary, current scholars studying the hydration effect of urea on cement usually carry out their experiments at 20 °C, and the influence of temperature is rarely taken into account. The effects of urea on cement hydration at different temperatures using the Krstulovic–Dabic model have yet to be further studied.

In this paper, therefore, by testing the hydration rate and the total accumulated hydration heat amount of the cement pastes for 120 h at three constant temperatures (20 °C, 40 °C, and 60 °C), and with urea content (UC) of 0% (PC), 2%, 5%, and 8%, respectively, to replace cement, a comparative analysis was conducted. The Krstulovic–Dabic hydration kinetics model was used to further explore the effects of different urea admixtures on cement hydration under different temperature environments. The effect of urea on the compressive strength of cement paste at different temperatures was analyzed. Finally, according to the pore changes of cement paste, the effect of urea on cement pores under the influence of temperature is further analyzed. This study can provide some theoretical guidance to solve the problem of cement cracking due to temperature stress.

2. Materials and Methods

2.1. Materials

The cement used was P●O 42.5R ordinary Portland cement produced by Handan Jinyu Taihang Cement Co., Ltd. (Handan, China), and its chemical composition is shown in Table 1. Urea adopts Xilong Science Co., Ltd. (Shantou, China) to produce urea. Its morphology is a white crystalline powder. The physical properties are shown in Table 2. The sand used was the standard sand produced by Xiamen Esio Standard Sand Co., Ltd. (Xiamen, China), and its particle size was 0.08–2.0 mm. The water was deionized water. Table 3 shows the mix proportions of this experiment [29].

Table 1. Chemical compositions of cement/wt%.

CaO	SiO_2	Al_2O_3	Fe_2O_3	SO_3	MgO	K_2O	P_2O_5	Na_2O	Loss
64.95	18.31	4.21	2.95	4.22	0.64	0.788	-	-	3.21

Table 2. Physical properties of urea.

Molecular Formula	Melting Point/°C	Density g/cm^3	Water Soluble g/L	Relative Molecular Mass	Crystallization Heat J/g
CH_4N_2O	131–135	1.335	1080	60.06	224

Table 3. Mix proportion of three groups of 40 mm × 40 mm × 160 mm concrete test pieces.

Components	Cement/g	Water/g	Standard Sand/g	Urea/g
PC	450	225	1350	0
UC = 2%	441	225	1350	9
UC = 5%	427.5	225	1350	22.5
UC = 8%	414	225	1350	36

2.2. Test Method

2.2.1. TAM Air Installation

TAM Air is an isothermal heat conduction calorimeter that operates in the milliwatt range. All calorimetric channels are mounted together to form a calorimeter block that is mounted in a temperature-controlled air thermostat. The TAM Air used in this article is a three-channel version. Each calorimetric channel is constructed in a dual configuration, with a sample on one side and another sample on the other. During the measurement, the sample and reference material are kept in a 100 mL Abe bottle. Measurement data includes hydration rate and total hydration heat release. This data can be continuously recorded in real-time by a computer. In addition, TAM Air thermostats have an operating temperature range of 5 °C to 90 °C and stability of ±0.02 °C.

2.2.2. Test Process

According to the Chinese Standard GB/T17671-2021 test method of cement mortar, sand specimens of 40 mm × 40 mm × 160 mm are required for a suitable strength. We used a WDW-200E microcomputer-controlled electronic universal testing machine to test compressive strength at 3 different temperatures and 4 different dosages for 3, 7, and 28 days. Each working condition casted three groups of specimens, and three groups of specimens were first subjected to a flexural test to obtain six groups of compressive strength test specimens. Then, the average value of the compressive strength of the six groups of specimens for each of these conditions' compressive strength values was obtained. Obtaining the heat of hydration test included weighing 28 g of cement–urea coagulation mixed into a paper cup and 14 g of deionized water, which was poured it into the paper cup and stirred quickly with a stirring bar for 120 s. Next, we weighed 21 g of cement paste into the TAM Air microcalorimeter special ampoule as the sample group, and used 9.8 g of deionized water into the ampoule as the reference group before placing the ampoule with a lid sealed into the TAM Air microcalorimeter, which was made in the United States. Then, we started the test to assess its hydration rate and the total accumulated hydration heat under three constant temperatures for 120 h. For the microscopic pore test, the test pieces under the completed curing conditions were soaked in anhydrous ethanol, dried, and cracked to select the flatter test pieces from the center of the test pieces. Then, the microscopic morphology and pore changes were monitored using a three-dimensional, ultra-deep field microscope; then, six test pieces were randomly selected for each group of working conditions, and the average value was taken.

2.3. Hydration Kinetics Model

The Krstulovic–Dabic model [19–22] divides the whole process of cement hydration into three basic processes: the nucleation and crystal growth process (NG), phase boundary reaction process (I), and diffusion process (D). The three processes can be carried out simultaneously or sequentially but are mainly determined by the slowest reaction among the three processes [22].

The equations controlling the hydration reaction process for NG, I, and D, respectively, are:

$$\mathrm{NG}: [-\ln(1-\alpha)]^{1/n} = K_1'(t-t_0) \quad (1)$$

$$\mathrm{I}: [1-(1-\alpha)^{1/3}] = K_2'(t-t_0) \quad (2)$$

$$\mathrm{D}: [1-(1-\alpha)^{1/3}]^2 = K_3'(t-t_0) \quad (3)$$

where α is the degree of hydration, t_0 indicates the moment when the acceleration period begins, K_1', K_2', and K_3' are the rate constants for the NG, I, and D phases, respectively, n is

the number of reaction stages, representing the growth of geometric crystals. Differentiating the above Equations (1)–(3), the dynamic differential equation is obtained as:

$$\text{NG}: \frac{d\alpha}{dt} = K_3'n(1-\alpha)[-\ln(1-\alpha)]^{(n-1)/n} \tag{4}$$

$$\text{I}: \frac{d\alpha}{dt} = 3K_2'(1-\alpha)^{2/3} \tag{5}$$

$$\text{D}: \frac{d\alpha}{dt} = \frac{3K_3'(1-\alpha)^{2/3}}{2-2(1-\alpha)^{1/3}} \tag{6}$$

where $\frac{d\alpha}{dt}$ is the reaction rate.

Degree of hydration α in the following equation was used for the calculation:

$$\frac{d\alpha}{dt} = \frac{dQ}{dt} \cdot \frac{1}{Q_{\max}} \tag{7}$$

$$\frac{1}{Q} = \frac{1}{Q_{\max}} + \frac{t_{50}}{Q_{\max} \cdot (t - t_0)} \tag{8}$$

$$\alpha = \frac{Q}{Q_{\max}} \tag{9}$$

where Q is the heat release at the beginning of the acceleration period at moment t, J•g^{-1}; $Q_{\max}$ is the total heat release of hydration when the cement paste terminates hydration, J•g^{-1}; t_{50} is the time when the total heat release of hydration reaches 50%, h.

3. Results and Discussion

3.1. Analysis of Hydration Process

3.1.1. Heat of Hydration Analysis

According to Figure 1, the hydration process consists of five stages: preinduction, induction, acceleration, deceleration, and stabilization [30].

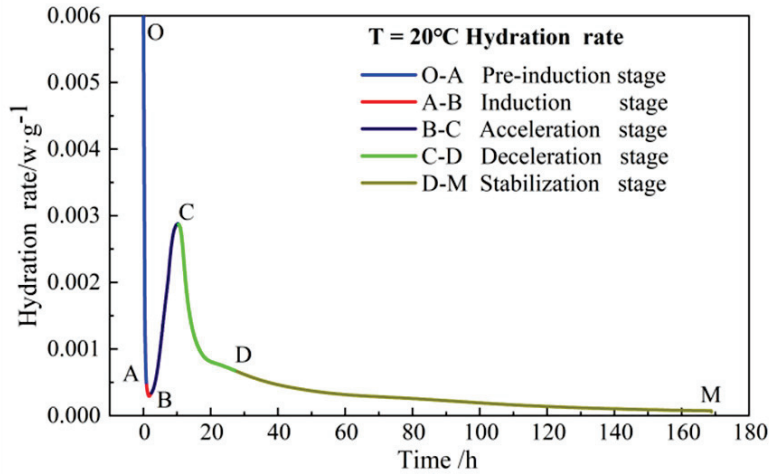


Figure 1. Cement hydration stage division.

The O–A section is the preinduction period, mainly C_3A in cement hydration. The A–B section is the induction section. The B–C section is the acceleration stage. The C–D section is the deceleration phase; at this time, it is the hydration reaction rate with the growth of time and constantly. The last section, D–M, is the stabilization period, and the reaction rate does not change much regarding the growth of time and tends to stabilize, and the structure of this stage becomes denser [31,32].

The rate of hydration and cumulative heat release diagrams at different temperatures with different urea blending conditions are shown in Figure 2.

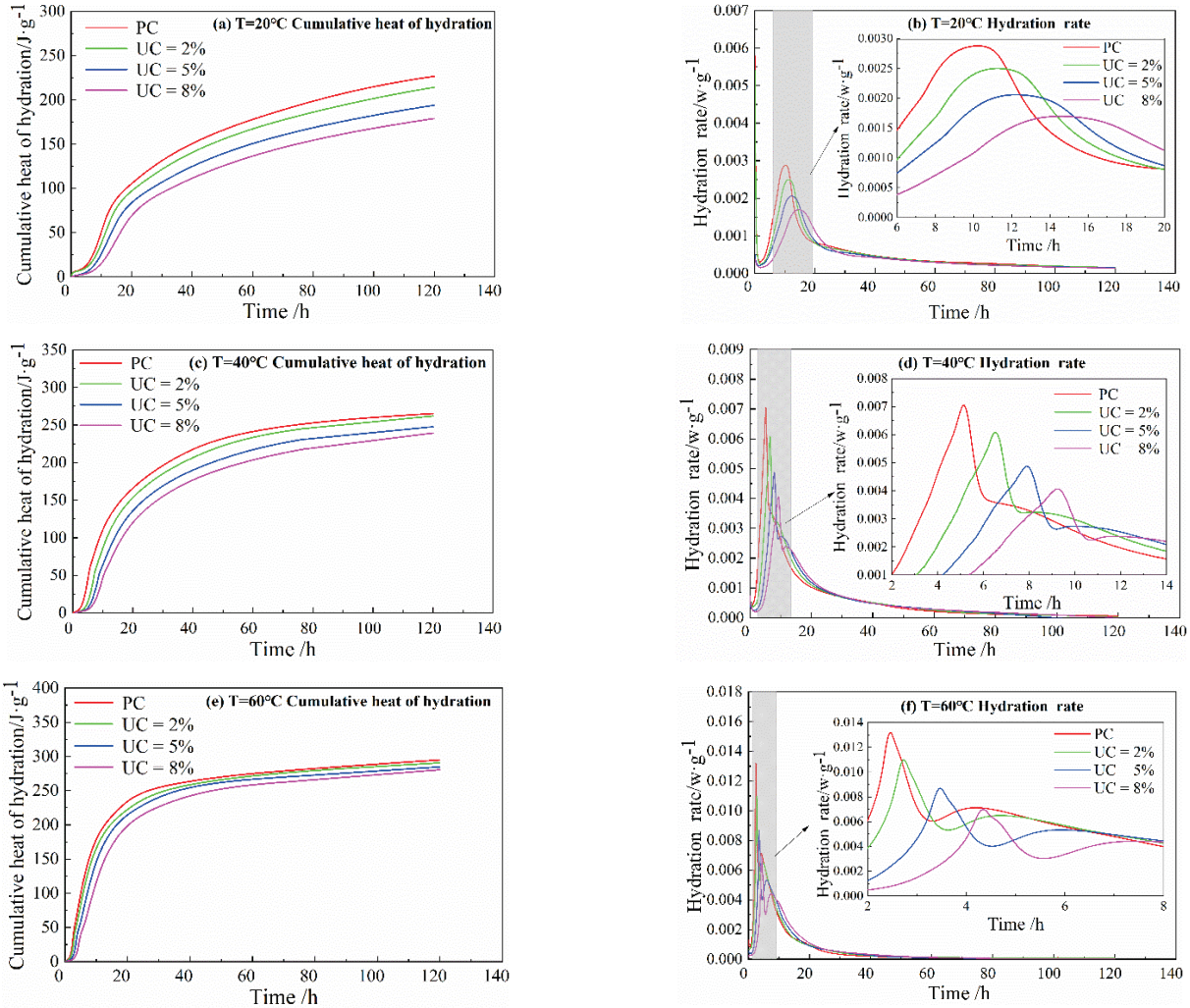


Figure 2. Hydration rate and cumulative heat release graph.

Their values are shown in Table 4.

Table 4. Rate of hydration and total cumulative heat release of hydration.

Temperature (°C)	Urea Content	Peak Hydration Rate Time of Occurrence (h)	Peak Hydration Rate ($w \cdot g^{-1}$)	Total Heat Release ($J \cdot g^{-1}$)
20	0%	10.24	0.00287	226.665
	2%	11.29	0.00249	214.154
	5%	12.23	0.00206	193.948
	8%	14.55	0.00169	178.907
40	0%	5.13	0.00704	265.088
	2%	6.52	0.00608	262.071
	5%	7.89	0.00487	247.783
	8%	9.25	0.00407	239.476
60	0%	2.46	0.01319	294.855
	2%	3.74	0.01097	290.586
	5%	5.92	0.00533	284.637
	8%	7.45	0.00442	280.451

When the UC is the same, the peak hydration rate gradually increases with the increase in temperature from 20 °C to 60 °C, the time of peak appearance gradually advances, and the total accumulated hydration heat amount increases. UC of 2% at 60 °C increases the hydration rate by 4.4 times compared with 2% of UC at 20 °C. The peak appearance time advances by 7.55 h, and the total accumulated hydration amount increases by 76.432 $J \cdot g^{-1}$, which is because the increase in temperature increases the number of activated molecules in the cement for the reaction, increases the effective collision, promotes the hydration rate of the cement, shortens its induction period, and makes the peak of hydration rate appear earlier.

Under the same temperature condition, an increase in UC reduces the peak rate of the hydration heat, delays peak occurrences, and further reduces this cumulative release heat. Under the condition of 20 °C and UC of 8% compared with PC, the peak hydration rate is reduced by 41%, the peak appearance time is delayed by 4.31 h, and the total cumulative heat release of 120 h is reduced by 47.76 $J \bullet g^{-1}$. While under the condition of 60 °C, with UC of 8% compared with PC, the peak hydration rate is reduced by 66%, and the peak time is delayed by 4.99 h, which shows that urea will inhibit the hydration rate of cement. The reason for this phenomenon is the chemical reaction between urea and water, as shown in Equation (10). This reaction is a heat absorption process, which absorbs the heat around it, inhibiting the hydration of cement. In addition, the addition of urea reduces the content of cement in the cement paste, which reduces the rate of cement hydration to a certain extent.

$$CO(NH_2)_2 + H_2O = CO_2 + 2NH_3 \quad (10)$$

It can be concluded from the analysis of heat of hydration that the increase in curing temperature will shorten the induction period and make the peak of the hydration rate appear earlier. Urea can inhibit the cement hydration reaction under certain parameters. The inhibition effect is more obvious under the higher curing temperature.

In summary, with an increase in urea content, the peak hydration rate gradually decreases, and the time of peak occurrence is postponed. This indicates that the addition of urea avoids the concentrated heat release of cement. In this way, it can effectively avoid the problem of cracking concrete due to temperature stress in the early stage.

3.1.2. Analysis of Hydration Kinetics

Since the preinduction and induction periods last as short as 0–0.5 h, in the actual project pouring, the preinduction and induction periods are often over [30]. Therefore, the hydration kinetics model is simulated from the acceleration period. The hydration kinetics model under different temperatures and different urea admixtures is shown in Figure 3.

The paste under the conditions of 20 °C and 40 °C has experienced three processes of NG, I, and D, indicating that its reaction process is more moderate. Hydration-generated hydration products make a smooth shift in the control mechanism of the hydration kinetics model. In the whole hydration reaction process, in different stages, the main control factors are different. In the early stage of hydration, when the hydration products just began to generate, crystallization nucleation and the crystal growth process (NG) play the main control role. This time is often during the acceleration period. As the generated hydration products gradually increase, the ion migration rate becomes slow. The phase boundary reaction process (I) plays a primary control role at this time in the acceleration and deceleration period, followed by smooth changes in the structure of the paste. Finally, when turned to the diffusion process, (D) plays a primary control role at this time in the deceleration and stabilization period. The whole reaction process rate shows that the phenomenon of the prehydration reaction is intense and affects late reaction stability.

As can be seen from Figure 3, the hydration kinetics model NG, I, and D processes can simulate the actual hydration rate $d\alpha/dt$ curve in a better segment. The process (NG) and the process (D) are better simulated, while the phase boundary reaction process (I) simulation effect has a certain error, which is similar to the conclusion of Zhang et al. [33]. This is because the hydration rate at the peak occurs at this stage, which increases the

simulation error. The addition of urea makes K_1' decrease compared to the PC group. This phenomenon arises mainly because the addition of urea suppresses the cement hydration rate. Urea affects the transition process between the acceleration and deceleration phases, changing the duration of the main control process of the model, but not fundamentally changing the hydration kinetics process.

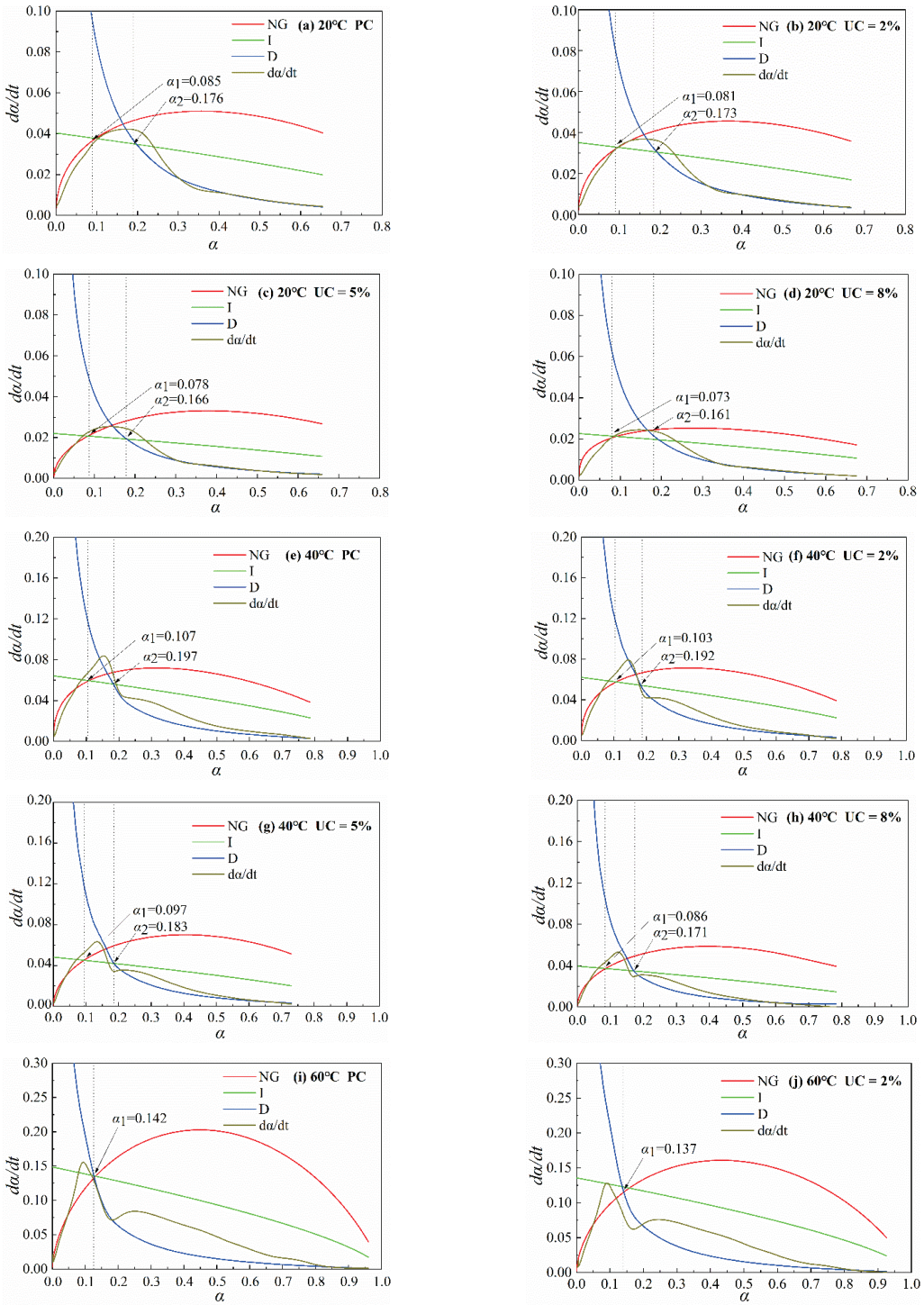


Figure 3. *Cont.*

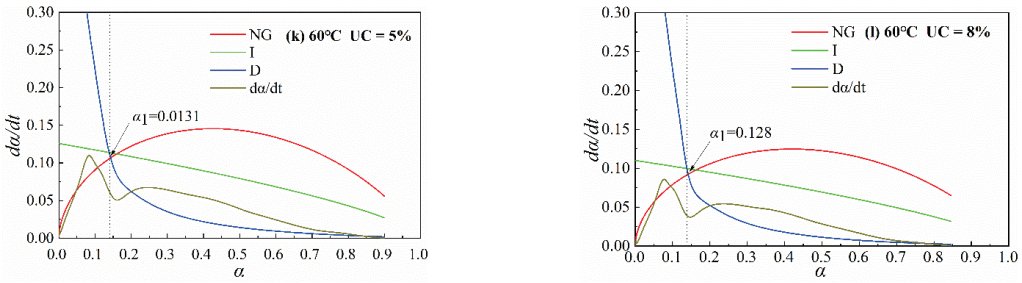


Figure 3. Hydration kinetic model diagram.

As the temperature increases, it makes K_1' increase, so that the NG process begins to shift to the I process at a higher degree of hydration. Even when the temperature increases to 60 °C, the reaction no longer goes through the I process, but directly shifts from the NG process to the D process, which is because the rise in temperature increases the hydration rate of cement, leading to a large number of hydration products in a relatively short period, which accelerates the transformation of the hydration reaction. Thus, it can be seen that the temperature will fundamentally change the hydration kinetics process.

Table 5 shows the kinetics parameters; α_1 and α_2 represent the turning point of the NG-to-I process and the turning point of the I-to-D phase, respectively.

Table 5. Hydration kinetics parameters.

Temperature (°C)	Urea Content	n	K_1'	K_2'	K_3'	α_1	α_2	α_2-α_1	Model Phase
20	0%	1.79	0.0530	0.0120	0.00165	0.085	0.176	0.094	NG-I-D
	2%	1.84	0.0466	0.0117	0.00136	0.081	0.173	0.092	NG-I-D
	5%	1.89	0.0333	0.0073	0.00081	0.078	0.166	0.088	NG-I-D
	8%	1.92	0.0323	0.0075	0.00088	0.073	0.161	0.088	NG-I-D
40	0%	1.61	0.1107	0.0214	0.00214	0.107	0.197	0.090	NG-I-D
	2%	1.66	0.0923	0.0188	0.00228	0.103	0.192	0.890	NG-I-D
	5%	1.72	0.0797	0.0150	0.00179	0.097	0.183	0.086	NG-I-D
	8%	1.85	0.0682	0.0131	0.00130	0.086	0.171	0.085	NG-I-D
60	0%	1.46	0.2022	0.0330	0.00315	0.142	-	-	NG-D
	2%	1.52	0.1691	0.0323	0.00322	0.137	-	-	NG-D
	5%	1.63	0.1564	0.0279	0.00289	0.131	-	-	NG-D
	8%	1.69	0.1135	0.0229	0.00224	0.128	-	-	NG-D

As can be seen from Table 5, K_1' is about 3–5 times as much as K_2' and about 15–30 times as much as K_3'. The NG process in the three stages is the fastest reaction rate in the whole hydration process, and the D process is the slowest. The reaction rate is relatively fast, and the hydration products grow rapidly. As the reaction proceeds, the hydration process enters the D stage, in which the hydration products make the cement paste pore structure denser. The less permeable C-S-H gel adsorbs on the surface of the unhydrated particles and increases the resistance to further hydrate the unhydrated particles. Therefore, the reaction rate is lowest in the D stage.

The effect of urea's addition on the K-value was limited: at a temperature of 20 °C, there was a 2% increase in urea admixture, and K_1', K_2', and K_3' values decreased by 12%, 2.5%, and 17.6%, respectively. Moreover, the temperature had a greater effect on K values. The temperature raised from 20 °C to 60 °C, and the K_1', K_2', and K_3' values improved by 2.8, 1.75, and 1.2 times, respectively.

After the replacement of cement with urea, the value of n gradually increased, and the values of K_1', K_2', and K_3' all decreased. At the same temperature, the values of K_1', K_2', and K_3' were the highest for the pure cement system, followed by the 2% UC system. The lowest values of K_1', K_2', and K_3' were also found in the 8% UC system. This indicates

that different levels of urea have different effects on the growth process of the hydration products and, consequently, on their kinetic parameters. The varying patterns of reaction rates K_1', K_2', and K_3' with urea are consistent with the various patterns of hydration rates with urea, which is consistent with the experimentally measured hydration data, indicating that this model applies to the cement paste in the paper.

The values of K_1', K_2', and K_3' of the cement paste increase as the n value decreases with increasing temperature under the condition of the same urea dosage. The hydration of cement is autocatalytic at the beginning. Many soluble compounds are dissolved from the cement, and the pore solution reaches supersaturation after a few hours. Then, many stable nuclei are formed and start to grow, and temperature increases the rate of dissolution. The supersaturation arrival time is shortened, thus increasing the reaction rate.

3.2. Compressive Strength Analysis

The compressive strength of the cement paste at different temperatures and different urea admixtures is shown in Figure 4.

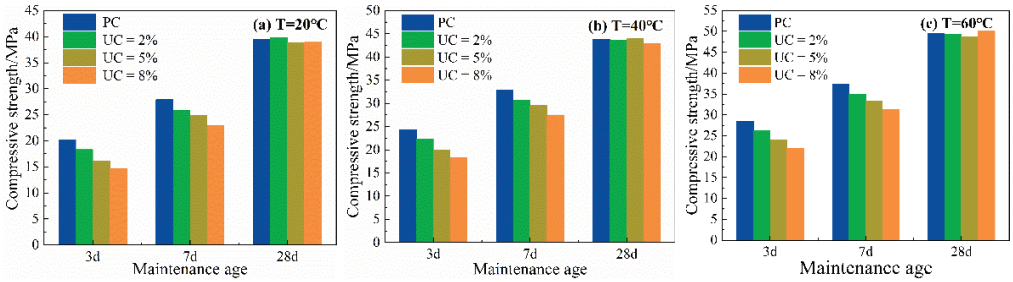


Figure 4. Compressive strength of cement mortar at different temperatures.

At the same temperature, the compressive strength of the cement paste gradually decreases with an increase in UC at 3 days and 7 days. According to the results of the previous heat of hydration test, it can be assumed that urea inhibits the hydration rate at the early stage of hydration so that the amount of hydration products generated is lower. This is mainly because, with the prolongation of the maintenance period, the amount of $Ca(OH)_2$ generated by hydration products gradually increases. The CO_2 produced by the reaction reacts with the water in the cement paste to produce unstable H_2CO_3, as in Equation (11). H_2CO_3 reacts with the hydration product $Ca(OH)_2$ to generate the stable $CaCO_3$ as in Equation (12), which compensates for the large pores generated in the early stage and reduces the porosity, making the cement paste structure denser, and thus increasing the compressive strength in the later stage [17]. Among them, at 20 °C, the compressive strength of the cement paste with 2% UC decreased by 9.5% at 3 days and 8% at 7 days compared to the PC paste, while the compressive strength increased by 1% at after 28 days.

$$CO_2 + H_2O = H_2CO_3 \quad (11)$$

$$H_2CO_3 + Ca(OH)_2 = CaCO_3 + 2H_2O \quad (12)$$

The temperature increases the hydration rate of cement, so that it produces more hydration products at higher temperatures, leading to the higher mechanical strength of the cement paste. Therefore, the negative effect of incorporating a certain content of urea on its mechanics occurs mainly in the early stage. The mechanical properties will recover to a comparable level with the growth of the period age.

3.3. Microscopic Morphology and Pore Analysis

Since cement hydration mainly occurred in the first 3 days [34–39], super depth-of-field microscopy was used to observe the apparent morphology and pore distribution of the cement net paste specimens under different conditions and analyze the evolution mechanism of their microstructure [40–42]. Figure 5 shows the microscopic images of the

cement net paste (Zoom in 50×) and the pore distribution images after image segmentation processing (The red color represents the pores).

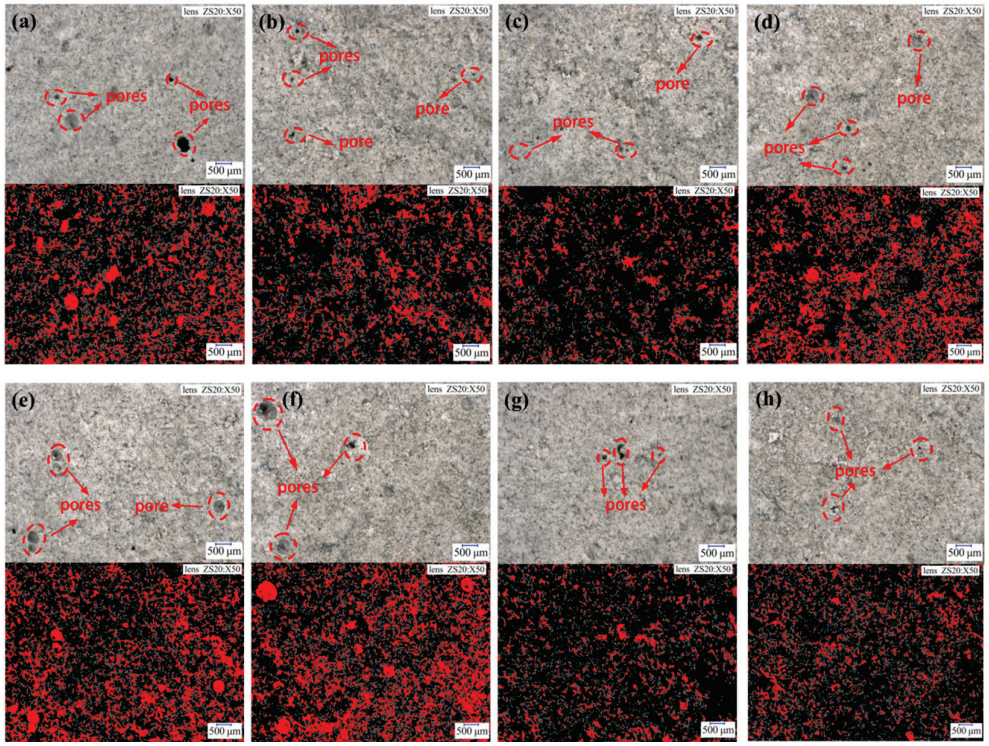


Figure 5. Microscopic morphology and pore distribution of net cement paste under different conditions: (**a**) 20 °C 1d PC; (**b**) 20 °C 2d PC; (**c**) 20 °C 3d PC; (**d**) 20 °C 1d UC = 2%; (**e**) 20 °C 1d UC = 5%; (**f**) 20 °C 1d UC = 8%; (**g**) 40 °C 1d PC; (**h**) 60 °C 1d PC.

Table 6 shows the porosity and average pore size under different conditions.

Table 6. Porosity and average pore size of net cement paste under different conditions.

Temperature (°C)	Maintenance Period of Age (d)	Urea Content	Porosity	Average Pore Size (μm)
20	1	0%	36%	28.32
	2	0%	28%	27.74
	3	0%	21%	26.21
	1	2%	38%	29.33
	1	5%	40%	30.06
	1	8%	43%	31.45
40	1	0%	25%	27.01
60	1	0%	20%	25.33

Figure 5 and Table 6 show that, at the same temperature and the same curing age, the lower the urea reference amount, the more uniform and denser the specimen. Moreover, the higher the urea reference amount, the more pore distribution, and mostly the distribution of large pores. The UC increases by 8% and the porosity increases by 7% under the condition of 20 °C at after 1 day. This is because urea itself has strong hygroscopicity and can absorb water molecules around the environment at the early stage of hydration, so that, if there is excess water in the paste, this excess water does not participate in the preliminary hydration reaction, thus resulting in a larger porosity value at the early stage [43–45]. In addition, urea inhibits the hydration rate, resulting in the hydration products not being able to fill the pores in time and thus inhibiting the further reduction of the pores.

While the temperature increased from 20 °C to 60 °C and porosity decreased by 16%, the curing period age was extended to 3 days, and the porosity decreased by 14%, which means that the increase in curing time and temperature will promote the generation of hydration products and will compensate for early porosity, so that the pore area is further reduced. In summary, the microscopic pore changes are consistent with the previous thermal and mechanical changes of hydration.

4. Conclusions

This paper studied the effects of urea on cement hydration, compressive strength, and microscopic porosity at three constant temperatures. The conclusion is as follows.

1. Urea can reduce the hydration rate, delay the appearance of the peak hydration rate, and avoid the concentration of cement hydration. As the temperature increases, the inhibition effect of urea is better, which can effectively reduce the risk of the cracking of cement due to temperature stress;
2. The hydration kinetics model can effectively simulate the cement hydration process. Urea will make the hydration kinetics model parameters K_1', K_2', and K_3' decrease. The temperature will make it increase. At 60 °C, the Krstulovic–Dabic model reaction no longer goes through process I. Moreover, 60 °C will fundamentally change the kinetics process of hydration;
3. Urea has an effect on the early reduction in compressive strength. However, with the extension of the age of the curing period, its compressive strength will gradually recover to the same level as the compressive strength of PC and has little effect on the later strength; moreover, the higher the temperature, the better its mechanical strength recovery effect;
4. Urea increases the early porosity of cement pastes. The increase in curing time and temperature will gradually reduce the porosity and average pore size.

Author Contributions: Conceptualization, H.S. and Y.L.; Data curation, Y.L.; Formal analysis, Y.B.; Investigation, Y.L.; Methodology, Q.M.; Project administration, H.S.; Resources, Y.B.; Software, Y.L.; Validation, Q.M. and S.L.; Writing—original draft, B.H.; Writing—review and editing, S.L. All authors have read and agreed to the published version of the manuscript.

Funding: This research was funded by the National Key Research and Development Project of China (Grant no. 2018YFE0101100), the Hebei Provincial Natural Science Foundation of China (Grant no. E2020402087, E2019402256), and the Foshan Science and Technology Innovation Special Fund Funding Project (Grant Nos. BK20BE008, BK21BE014).

Institutional Review Board Statement: Not applicable for studies not involving humans or animals.

Informed Consent Statement: Not applicable.

Data Availability Statement: The data presented in this study are available on request the corresponding author.

Acknowledgments: We are very grateful to all the people who gave us valuable advice in the process of writing this paper. We are especially grateful to An Li for his help in the test process part of this paper.

Conflicts of Interest: The authors declare no conflict of interest.

References

1. Wei, B.; Liu, B.; Yuan, D.; Mao, Y.; Yao, S. Spatiotemporal hybrid model for concrete arch dam deformation monitoring considering chaotic effect of residualseries. *Eng. Struct.* **2021**, *228*, 111488. [CrossRef]
2. Pirooznia, A.; Moradloo, A.J. Investigation of size effect and smeared crack models in ordinary and dam concrete fracture tests. *Eng. Fract. Mech.* **2020**, *226*, 106863. [CrossRef]
3. Yang, D.; Gu, C.; Zhu, Y.; Dai, B.; Li, B. A concrete dam deformation prediction method based on LSTM with attention mechanism. *IEEE Access* **2020**, *8*, 185177–185186. [CrossRef]
4. Singh, V.P.; Kumar, M.; Srivastava, R.S.; Vaish, R. Thermoelectric energy harvesting using cement-based composites: A review. *Mater. Today Energy* **2021**, *21*, 3–4. [CrossRef]

5. Kong, X.J.; Zhang, Y.; Zou, D.G.; Qu, Y.Q.; Yu, X. Seismic cracking analyses of two types of face slab for concrete-faced rockfill dams. *Sci. China Technol. Sci.* **2017**, *60*, 510–522. [CrossRef]
6. Qiu, J.; Li, Y.; Xu, Y.; Wu, A.; Macdonald, D.D. Effect of Temperature on Corrosion of Carbon Steel in Simulated Concrete Pore Solution under Anoxic Conditions. *Corros. Sci.* **2020**, *175*, 108886. [CrossRef]
7. Valipour, M.; Khayat, K.H. Robustness of Ultra-High-Performance concrete to changes in material temperature. *ACI Mater. J.* **2020**, *117*, 4. [CrossRef]
8. Qin, C.; Gong, J.; Xie, G. Modeling hydration kinetics of the Portland-Cement-Based cementitious systems with mortar blends by Non-Assumptive projection pursuit regression. *Thermochim. Acta* **2021**, *705*, 179035. [CrossRef]
9. He, J.; Long, G.; Ma, K.; Xie, Y.; Cheng, Z. Improvement of the hydration of a fly ash–cement system by the synergic action of triethanolamine and C-S-H Seeding. *ACS Sustain. Chem. Eng.* **2021**, *9*, 7. [CrossRef]
10. Yang, M.; Paudel, S.R.; Asa, E. Comparison of pore structure in alkali activated fly ash geopolymer and ordinary concrete due to alkali-silica reaction using micro-computed tomography. *Constr. Build. Mater.* **2020**, *236*, 117524. [CrossRef]
11. He, Y.; Liu., S.; Hooton, R.D.; Zhang, X.; He, S. Effects of TEA on rheological property and hydration performance of lithium slag-cement composite binder. *Constr. Build. Mater.* **2022**, *318*, 125757. [CrossRef]
12. Liu, S.; Wang, L.; Gao, Y.; Yu, B.; Tang, W. Influence of fineness on hydration kinetics of supersulfated cement. *Thermochim. Acta* **2015**, *605*, 37–42. [CrossRef]
13. He, J.; Long, G.; Ma, K.; Xie, Y. Influence of fly ash or slag on nucleation and growth of early hydration of cement. *Thermochim. Acta* **2021**, *701*, 178964. [CrossRef]
14. Briki, Y.; Maciej, Z.; Haha, M.B.; Scrivener, K.L. Impact of limestone fineness on cement hydration at early age. *Cem. Concr. Res.* **2021**, *147*, 106515. [CrossRef]
15. Gong, C.; Zhou, X.; Dai, W.; Liu, Y.; Lu, L.; Cheng, X. Effects of carbamide on fluidity and setting time of sulphoaluminate cement and properties of planting concrete from sulphoaluminate cement. *Constr. Build. Mater.* **2018**, *182*, 290–297. [CrossRef]
16. Kim, H.Y. On the Feasibility of Using Industrial Urea to Mitigate Thermal and Shrinkage Cracking in Concrete. *Appl. Sci.* **2021**, *11*, 2483. [CrossRef]
17. Park, J.K.; Sang, H.H.; Hong, K.N.; Yong, I.C.; Chai, Y. Influence on Compressive Strength and Drying Shrinkage of Concrete with Urea-Water Soluble Sulfur Admixture. *J. Korean Soc. Saf.* **2016**, *31*, 74–81. [CrossRef]
18. Kim, H.Y. Urea additives for reduction of hydration heat in cement composites. *Constr. Build. Mater.* **2017**, *156*, 790–798. [CrossRef]
19. Miao, M.; Liu, Q.; Zhou, J.; Feng, J. Early hydration kinetics of expansive cementitious binders. *Materials* **2019**, *12*, 1900. [CrossRef] [PubMed]
20. Li, Z.; Gao, X.; Lu, D.; Dong, J. Early hydration properties and reaction kinetics of multi-composite cement pastes with supplementary cementitious materials (SCMs). *Thermochim. Acta* **2022**, *709*, 179157. [CrossRef]
21. Liu, L.; Yang, P.; Qi, C.; Zhang, B.; Guo, L.; Song, K.I. An experimental study on the early-age hydration kinetics of cemented paste backfill. *Constr. Build. Mater.* **2019**, *212*, 283–294. [CrossRef]
22. Meng, T.; Hong, Y.; Wei, H.; Xu, Q. Effect of Nano-SiO2 with Different Particle Size on the Hydration Kinetics of Cement. *Thermochim. Acta* **2019**, *675*, 127–133. [CrossRef]
23. Qin, J.; Qin, Q.; Li, X.; Xue, J.; Wang, R.; Zhang, Q.; Wang, P.; Guo, Z.; Gong, Y. Urea supply control in microbial carbonate precipitation to effectively fill pores of concrete. *Constr. Build. Mater.* **2021**, *310*, 125123. [CrossRef]
24. Zhang, X.; Yang, Z.J.; Huang, Y.J.; Wang, Z.Y.; Chen, X.W. Micro CT Image-based simulations of concrete under high strain rate impact using a Continuum-Discrete coupled model. *Int. J. Impact Eng.* **2021**, *149*, 103775. [CrossRef]
25. Trofimov, A.; Mishurova, T.; Lanzoni, L.; Radi, E.; Bruno, G.; Sevostianov, I. Microstructural analysis and mechanical properties of concrete reinforced with polymer short fibers. *Int. J. Eng. Sci.* **2018**, *133*, 210–218. [CrossRef]
26. Liu, S.; Diederik, J. Coupled reactive transport model study of pore size effects on solubility during cement-bicarbonate water interaction. *Chem. Geol.* **2017**, *466*, 588–599. [CrossRef]
27. Wang, L.G.; Ju, S.Y.; Chu, H.Y.; Liu, Z.Y.; Yang, Z.Q.; Wang, F.J.; Jing, J.Y. Hydration process and microstructure evolution of low exothermic concrete produced with urea. *Constr. Build. Mater.* **2020**, *248*, 118640. [CrossRef]
28. Dong, P.; Allahverdi, A.; Andrei, C.; Basim, N. Liquid cell transmission electron microscopy reveals the role of Nano-silica in cement hydration reactions. *Microsc. Microanal.* **2020**, *26*, 2414–2416. [CrossRef]
29. *GB/T17671-2021*; Test Method of Cement Mortar Strength (ISO Method). Standards Press of China: Beijing, China, 2021. (In Chinese)
30. Ridi, F.; Fratini, E.; Luciani, P.; Winnefeid, F.; Baglioni, P. Hydration kinetics of tricalcium silicate by calorimetric methods. *J. Colloid Interface Sci.* **2011**, *364*, 118–124. [CrossRef]
31. Liu, K.; Cheng, X.; Gao, X.; Zhang, X.; Zhuang, J. Effect of the hydration rate and microstructure of Portland cement slurry on hydrostatic pressure transfer. *Powder Technol.* **2019**, *352*, 251–261. [CrossRef]
32. Ding, W.; Xu, W.; Dong, Z.; Liu, Y.; Shiotani, T. Influence of hydration capacity for cement matrix on the piezoelectric properties and microstructure of cement-based piezoelectric ceramic composites. *Mater. Charact.* **2021**, *179*, 111390. [CrossRef]
33. Zhang, H.; Yang, Z.; Su, Y. Hydration kinetics of cement-quicklime system at different temperatures. *Thermochim. Acta* **2019**, *673*, 1–11. [CrossRef]
34. Kopec, M.; Ranachowski, P.; Ranachowski, Z.; Dbowski, T.; Schabowicz, K. Mechanical and Non-Destructive testing of plasterboards subjected to a hydration process. *Materials* **2020**, *13*, 2405. [CrossRef]

35. Stroh, J.; Schlegel, M.C.; Schmidt, W.; Nguyen, T.Y.; Meng, B.; Emmerling, F. Time-resolved in situ investigation of Portland cement hydration influenced by chemical admixtures. *Constr. Build. Mater.* **2016**, *106*, 106. [CrossRef]
36. Lin, C.; Wei, W.; Hu, Y.H. Catalytic behavior of graphene oxide for cement hydration process. *J. Phys. Chem. Solids* **2016**, *89*, 128–133. [CrossRef]
37. Tan, L.; Xiao, J.; Zhu, C. Hydration process modeling of ITZ between new and old cement paste. *Constr. Build. Mater.* **2016**, *109*, 120–127. [CrossRef]
38. Choobbasti, A.J.; Kutanaei, S.S. Microstructure characteristics of cement-stabilized sandy soil using nanosilica. *J. Rock Mech. Geotech. Eng.* **2017**, *5*, 203–210. [CrossRef]
39. Asgari, H.; Ramezanianpour, A.; Butt, H.J. Effect of water and nano-silica solution on the early stages cement hydration. *Constr. Build. Mater.* **2016**, *129*, 11–24. [CrossRef]
40. Kupwade-Patil, K.; Al-Aibani, A.F.; Abdulsalam, M.F.; Mao, C.; Bumajdad, A.; Palkovic, S.D.; Buyukozturk, O. Microstructure of cement paste with natural pozzolanic volcanic ash and Portland cement at different stages of curing. *Constr. Build. Mater.* **2016**, *113*, 423–441. [CrossRef]
41. Pu, L.; Unluer, C. Investigation of carbonation depth and its influence on the performance and microstructure of MgO cement and PC mixes. *Constr. Build. Mater.* **2016**, *120*, 349–363. [CrossRef]
42. Pang, B.; Zhang, Y.; Liu, G. Study on the effect of waterborne epoxy resins on the performance and microstructure of cement paste. *Constr. Build. Mater.* **2018**, *167*, 831–845. [CrossRef]
43. Jiang, J.; Lu, Z.; Niu, Y.; Li, J.; Zhang, Y. Investigation of the properties of high-porosity cement foams based on ternary portland cement–metakaolin–silica fume blends. *Constr. Build. Mater.* **2016**, *107*, 181–190. [CrossRef]
44. Gao, Z.; Wang, L.; Yang, H. Investigation of the residual mechanical and porosity properties of cement mortar under axial stress during heating. *Materials* **2021**, *14*, 1944. [CrossRef] [PubMed]
45. Baleani, M.; Fognani, R.; Toni, A. The influence of stem insertion rate on the porosity of the cement mantle of hip joint replacements. *Proc. Inst. Mech. Eng. H—J. Eng. Med.* **2016**, *217*, 199–205. [CrossRef] [PubMed]

metals

MDPI

Article

Removal of Pb(II) from Water by FeSiB Amorphous Materials

Xiang-Yun Zhang [1,2,*], Liang-Liang He [1], Jin-Ying Du [1] and Zi-Zhou Yuan [1]

[1] State Key Laboratory of Advanced Processing and Recycling of Nonferrous Metals, Lanzhou University of Technology, Lanzhou 730050, China
[2] Wenzhou Engineering Institute of Pump & Valve, Lanzhou University of Technology, Wenzhou 325105, China
* Correspondence: zhangxiangyun86@163.com; Tel.: +86-13109322559

Abstract: Amorphous materials have shown great potential in removing azo dyes in wastewaters. In this study, the performance of FeSiB amorphous materials, including FeSiB amorphous ribbons ($FeSiB^{AR}$), and FeSiB amorphous powders prepared by argon gas atomization ($FeSiB^{AP}$) and ball-milling ($FeSiB^{BP}$), in removing toxic Pb(II) from aqueous solution was compared with the widely used zero valent iron (ZVI) powders (Fe^{CP}). The results showed that the removal efficiency of all the amorphous materials in removing Pb(II) from aqueous solution are much better than Fe^{CP}. Pb(II) was removed from aqueous solution by amorphous materials through the combined effect of absorption, (co)precipitation and reduction. Furthermore, $FeSiB^{AP}$ and $FeSiB^{BP}$ have relatively higher removal efficiencies than $FeSiB^{AR}$ due to a high specific surface area. Although the $FeSiB^{BP}$ has the highest removal efficiency up to the first 20 min, the removal process then nearly stopped due to aggregation.

Keywords: amorphous alloys; heavy metal; Pb(II) solution

1. Introduction

The rapid development of the modern industry brings more and more threat to our environment. For example, a great deal of lead-containing sewage is produced by smelting, manufacturing, and the oil industry. Excessive lead intake may cause neurological, hematological, and immunological disease. Therefore, these lead ions in the sewage must be removed before it is discharged into the environment. In previous decades, ZVI was widely used to remove various heavy metal ions in water, but it can be easily oxidized, which causes the degradation capability to decay rapidly [1]. In order to improve its degradation capability, various methods have been proposed, including nanotechnology [2,3] and bimetallic technology [4,5], but new limitations such as high production costs, physiological toxicity, and aggregation restrict their application.

Recent reports show that Fe-based amorphous materials in ribbon state or powder state can not only degrade azo dyes from the aqueous solution more efficiently than the wildly used Fe^{CP} but also exhibit relatively stable reusability due to their homogeneous microstructure, thermodynamically metastable nature, and the existence of metalloid elements [6–10]. Furthermore, researchers found that ball-milled amorphous powders can further improve the degradation capacity in degrading azo dyes due to the uneven topography and the stored deformation energy induced by ball milling [11–15]. In view of this, Fe-based amorphous materials in various states may also be able to efficiently remove lead ions in the wastewater.

In this paper, the removal capability and mechanism of lead ion (Pb(II)) from aqueous solution by FeSiB amorphous ribbons were investigated and compared with those of the widely used Fe^{CP}. Furthermore, considering that a more specific surface area always leads to a higher reaction efficiency, the removal capacity and mechanism of FeSiB amorphous powders prepared by argon gas-atomization and ball-milling were also studied.

2. Materials and Methods

The amorphous ribbons and argon gas-atomized amorphous powders with a composition of $Fe_{78}Si_9B_{13}$ (atomic ratio) were provided by Jiangsu Chuangling Technology Co. and Haoxi Nano technology Co. of China, respectively. The Fe^{CP} was provided by Tianjin Chemical Reagent Research Institute. The amorphous ribbons were cut into pieces of 3 mm × 3 mm × 0.03 mm. Of these, part of the ribbons were used directly as removal material for Pb(II), and the rest were annealed at 653 K (below the crystallization temperature) for 1 h in an argon atmosphere and then ground by a high-energy ball mill under an argon atmosphere for 4 h at 200 r/min, with a ball-to-powder mass ratio of 10:1. Afterwards, the pulverized fine powders were filtered by mesh screens of 300 meshes per inch and used as removal material for Pb(II).

Pb(II) solutions were prepared by dissolving $Pb(NO_3)_2$ salt in ultra-pure water. The reaction tests were conducted in 1000 mL beakers placed in a temperature-controlled water-bath device and continuously stirred at 200 r/min. All tests were conducted with removal materials of 1 g/L and Pb(II) solutions of 500 mL, with a concentration of 100 mg/L at pH 5. About 5 mL of solution was extracted at fixed time intervals by a syringe and filtered through a 0.2 μm membrane. Then, they were tested by Inductively Coupled Plasma Optical Emission Spectrometer (ICP-OES, ICAP-7000, Thermo Fisher Scientific, Waltham, MA, USA) to determine their concentration. Cycling experiments were carried out one after another with the same ribbons.

Structure and morphology of the materials were investigated by X-ray diffraction (XRD, D/MAX-2400, monochromated Cu-Kα radiation) (Rigaku Ltd., Tokyo, Japan) equipped with an Ni filter and a graphite crystal monochromator, and by scanning electron microscopy (SEM, QUANTA FEG 450, FEI Ltd., Hillsborough, Atlanta, GA, USA) equipped with an Energy Dispersive X-ray Spectrometer (EDS). Specific surface areas of materials were recorded on the Brunauer–Emmett–Teller (BET, ASAP2020, Micromeritics Ltd., Atlanta, GA, USA) using the nitrogen method. Surface elemental information of the materials was determined by X-ray photoelectron spectroscopy (XPS, AXIS SUPRA, Shimadzu Ltd., Manchester, UK).

3. Results and Discussion

3.1. Removal Capacity of the Materials

Figure 1 shows the XRD spectrum of the four kinds of removal materials. Sharp crystalline peaks of a single α-Fe phase are observed on the spectrum of Fe^{CP}. The spectra of the other materials present a broad hump in the 2θ range of 40–50°, indicating their amorphous structure. Furthermore, there are tiny crystalline peaks superimposed on the broad humps, indicating that a small part of the samples may crystallize during the preparation process of the amorphous materials.

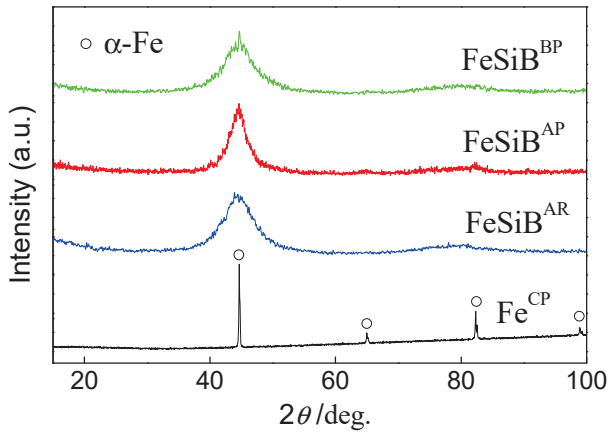


Figure 1. XRD spectrum of the removal materials.

Figure 2 shows SEM images of the materials. The morphologies of Fe^{CP}, $FeSiB^{AR}$, $FeSiB^{AP}$, and $FeSiB^{BP}$ are shown in Figure 2a–d. All the particles are well-dispersed with no aggregation. The particle size of Fe^{CP} is about 20–50 μm. Grain boundaries can be obviously seen from the enlarged surface morphology in Figure 2a, indicating that these particles are polycrystalline, composed of crystal grains with a size of about 2–5 μm, whereas the thickness of $FeSiB^{AR}$ is about 30 μm (Figure 2b). SEM images of both the top and bottom sides of the ribbon are shown in the inset of Figure 2b. It can be seen that both sides of the ribbon are generally smooth, even if ripples are shown on the roll-contact surface. Compared with the round and ellipsoid morphology of the 10–20 μm sized $FeSiB^{AP}$ particles (Figure 2c), the morphology of the $FeSiB^{BP}$ appears to be rather irregular (Figure 2d). Furthermore, compared with the as-quenched ribbon, thickness of the $FeSiB^{BP}$ reduced to between 5 and 15 μm due to severe mechanical deformation during the ball-milling process, as shown in Figure 2e. Additionally, the surfaces of $FeSiB^{AP}$ are smooth, but the surfaces of $FeSiB^{BP}$ are full of protrusions and microcracks, as shown in the high-magnitude image of Figure 2f.

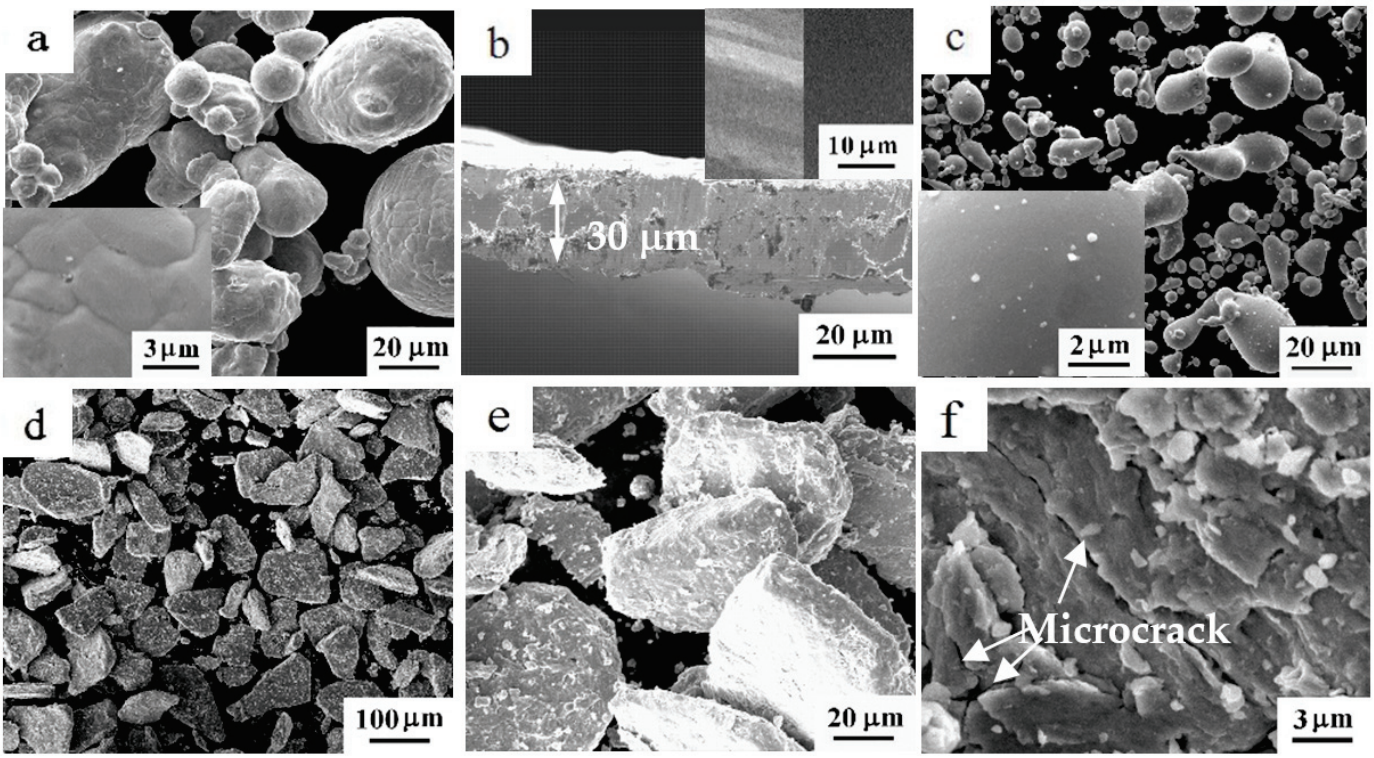


Figure 2. SEM images of the removal materials: (**a**) Fe^{CP}, (**b**) $FeSiB^{AR}$, (**c**) $FeSiB^{AP}$, and (**d**) $FeSiB^{BP}$. (**e**) and (**f**) are enlarged images of the particles in (**d**). The insets highlight surface details of the materials.

The removal effects of the four materials on Pb(II) solutions at room temperature were investigated. Figure 3 compares the removal performance, dependent on reaction time, for the four materials. C_t is the concentration of Pb(II) at a reaction time of t, and C_0 is the initial concentration of Pb(II). It can be seen obviously that the removal efficiency of all the amorphous materials are much better than that of Fe^{CP}, among which $FeSiB^{BP}$ has the highest removal efficiency up to the first 20 min. Wang et al. [15] also found that the dye degradation capability of Fe-based amorphous ribbons could be enhanced by ball-milling. However, different from Wang's reported results, the removal process seems to stop working and increasing the reaction time cannot effectively reduce the Pb(II) when the Pb(II) concentration is reduced to about 89% at 20 min. Considering the high residual Pb(II) concentration, despite its high removal rate, $FeSiB^{BP}$ is not an optimal removal material

for Pb(II) from aqueous solution. Furthermore, except for $FeSiB^{BP}$, the removal process by other materials can be well-fitted by the first-order reaction equation (Equation (1)) [16]:

$$C_t/C_0 = \exp(-kt) \quad (1)$$

where k denotes the reaction rate constant, which is estimated to be 0.026, 0.079, and 0.116 min^{-1} for the removal processes by Fe^{CP}, $FeSiB^{AR}$, and $FeSiB^{AP}$ by nonlinear regression analysis, respectively. Therefore, the removal rates of $FeSiB^{AR}$ and $FeSiB^{AP}$ are approximately 21 and 87 times as fast as the widely used Fe^{CP}.

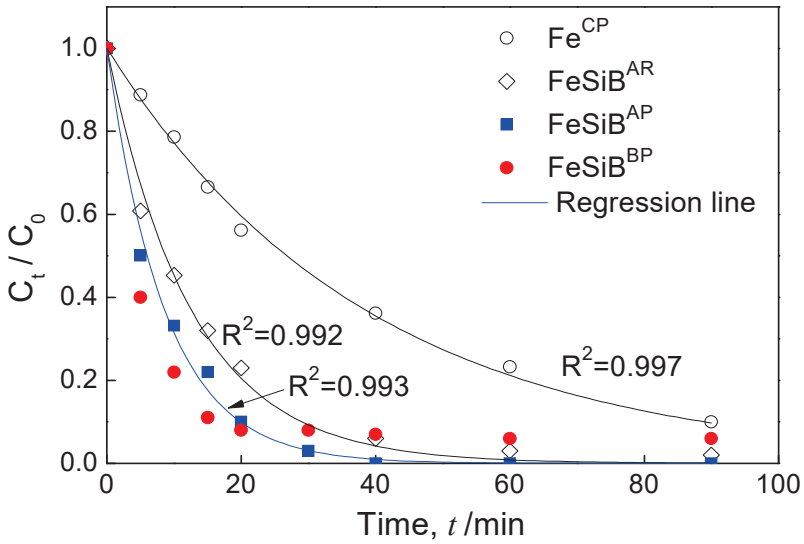


Figure 3. The normalized concentration of Pb^{2+} ions dependence on the reaction time.

Considering that the particle size of $FeSiB^{AP}$ is much smaller than that of Fe^{CP}, specific surface areas of Fe^{CP} and $FeSiB^{AP}$ are measured to be 0.339 and 0.329 m^2/g by a BET analysis, respectively. Thus, the surface area normalized rate constants k_{SA} of Fe^{CP} and $FeSiB^{AP}$ are calculated to be 0.07 and 0.353 $L/(m^2 \cdot min)$ by the equation: $k_{SA} = k/\rho_a$, where ρ_a is the surface area concentration of the sample [17]. Therefore, the reaction rate of per-unit surface area of $FeSiB^{AP}$ is about 99 times that of Fe^{CP}.

3.2. Removal Mechanism of the Amorphous Ribbons

Reaction active energy (ΔE) is an effective parameter for exploring the removal mechanism of various reactions. Figure 4 shows the dependence of normalized concentration of Pb(II) on reaction time at different temperatures for Fe^{CP} and $FeSiB^{AR}$. Based on the calculated reaction rate constants at different temperatures, the reaction active energy ΔE can be derived using the Arrhenius-type equation, $\ln k = -\Delta E/RT + \ln A$, where R is the gas constant, and A is a constant [16]. ΔE is calculated to be 31.2 and 22.4 kJ/mol for Fe^{CP} and $FeSiB^{AR}$, indicating that the reaction between $FeSiB^{AR}$ and the Pb(II) solution is easier. According to the perspective of thermodynamics, diffusion-controlled reactions in solution have relatively lower activation energies (~8–21 kJ/mol), whereas the surface-controlled chemical reactions have larger activation energies (>29 kJ/mol) [18,19]. Consequently, the reaction between Fe^{CP} and the Pb(II) solution is surface-controlled, whereas interface resistance in the reaction between $FeSiB^{AR}$ and the Pb(II) solution has been greatly reduced. The results are consistent with the report that ZVI removes Pb(II) from solution, mainly by absorption and coprecipitation [20].

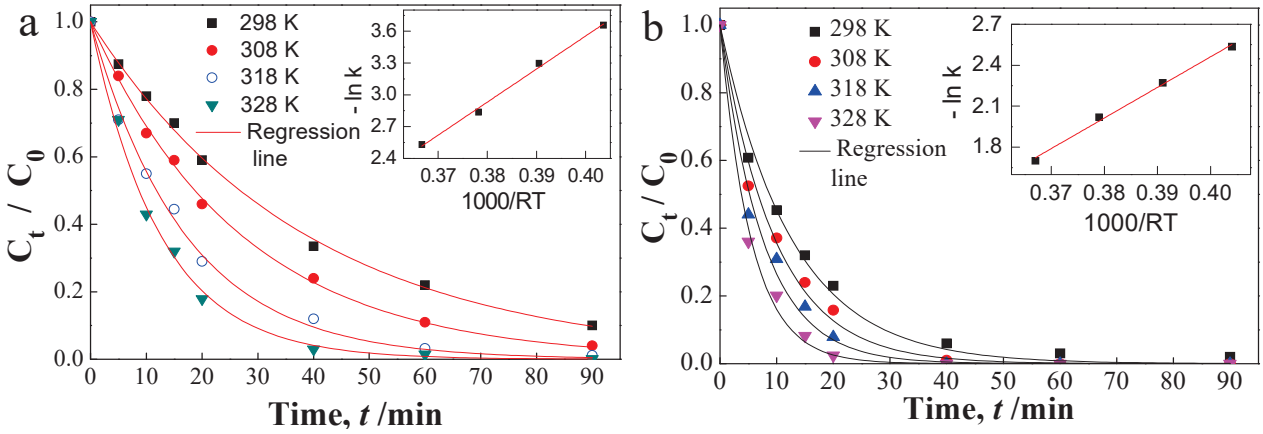


Figure 4. Effect of temperature on reaction process of (**a**) Fe^{CP} and (**b**) $FeSiB^{AR}$ in the Pb(II) solution. Insert: Arrhenius plots of $-\ln k$ versus $1000/RT$ for the two kinds of materials, respectively.

In order to investigate the removal mechanism of the amorphous ribbon, XRD patterns of the reacted $FeSiB^{AR}$ are compared with the reacted Fe^{CP}. Figure 5 shows XRD patterns of the $FeSiB^{AR}$ and Fe^{CP} after reaction with the aqueous solution for 40 min at room temperature. Diffraction peaks of FeO(OH) appear on both the XRD patterns of the reacted $FeSiB^{AR}$ and Fe^{CP}. According to the studies of treatment on Pb(II)-contaminated solution by ZVI, the FeO(OH) complexes with strong flocculation coprecipitate with Pb(II) during the reaction process (Equation (2)) [19]. Therefore, a small part of Pb(II) in aqueous solution was also removed by $FeSiB^{AR}$ by absorption and coprecipitating with Pb(II). Furthermore, compared with Fe^{CP}, a large number of diffraction peaks of Pb are found on XRD patterns of the reacted $FeSiB^{AR}$ and the precipitate of $FeSiB^{AR}$, indicating that reduction (Equation (3)) played an important role in the removal process of Pb(II) by $FeSiB^{AR}$. In addition, there are some tiny unknown diffraction peaks found on the XRD patterns of the reacted $FeSiB^{AR}$ and the precipitate. Combined with XRD patterns of the reacted $FeSiB^{AP}$ and $FeSiB^{BP}$, which will be discussed later, these tiny diffraction peaks may represent SiO_2 and PbO.

$$\text{Absorption}: \equiv Fe - OOH + Pb^{2+} \rightarrow \equiv Fe - OOPb + 2H^{+} \quad (2)$$

$$\text{Reduction}: \ Fe^{0} + Pb^{2+} \rightarrow Fe^{2+} + Pb^{0} \quad (3)$$

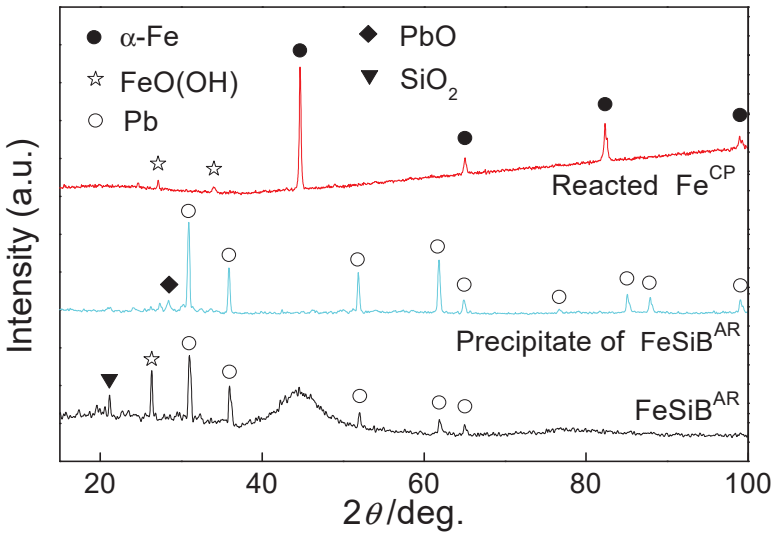


Figure 5. XRD patterns of the reacted $FeSiB^{AR}$ and Fe^{CP}, and XRD pattern of the precipitate from the aqueous solution reacted with $FeSiB^{AR}$.

In addition, it was reported that hydroxide ions (OH^-) were generated by the reaction of Fe^0 with H_2O (Equations (4) and (5)) at a pH above 4.5 [21], leading to the increase in the pH of the solution. Then, oxides and hydroxides of iron and lead cover the ZVI particles or form precipitates (Equations (6)–(11)) [2,22,23]. However, some of the reactions cannot be observed by the XRD patterns.

$$Fe^0 + O_2 + 2H_2O - 2e^- \rightarrow Fe^{2+} + 4OH^- + H_2 \uparrow \quad (4)$$

$$Fe^{2+} + O_2 + H_2O + 3e^- \rightarrow Fe^{3+} + O^{2-} + 2OH^- \quad (5)$$

$$Fe^{2+} + 2OH^- \rightarrow Fe(OH)_2 \downarrow \quad (6)$$

$$Fe^{3+} + OH^- \rightarrow Fe(OH)_3 \downarrow \quad (7)$$

$$Fe(OH)_3 \rightarrow FeOOH + H_2O \quad (8)$$

$$FeOOH \rightarrow Fe_2O_3 + H_2O \quad (9)$$

$$(Co)precipitation: \ Pb^{2+} + OH^- \rightarrow Pb(OH)_2 \downarrow + PbO \cdot xH_2O \quad (10)$$

$$Re - dissolution: \ Pb(OH)_2 + OH^- \rightarrow Pb(OH)_4^{2-} \quad (11)$$

In view of the limited resolution of XRD, XPS is used to further investigate the surface chemical composition of $FeSiB^{AR}$ and Fe^{CP}. Figure 6 shows Pb $4f_{7/2}$ spectra of the reacted $FeSiB^{AR}$ and Fe^{CP}. It can be observed that only Pb(II) (138.7 eV) can be found on the surface of the reacted Fe^{CP}. However, both Pb(II) (138.5 eV) and Pb(136.7 eV) [24] are found on the surface of the reacted $FeSiB^{AR}$. This discovery further confirms the XRD results showing that the removal of Pb(II) by Fe^{CP} is mainly through absorption and (co)precipitation, while the removal mechanism of Pb(II) by $FeSiB^{AR}$ involves absorption, (co)precipitation, and reduction.

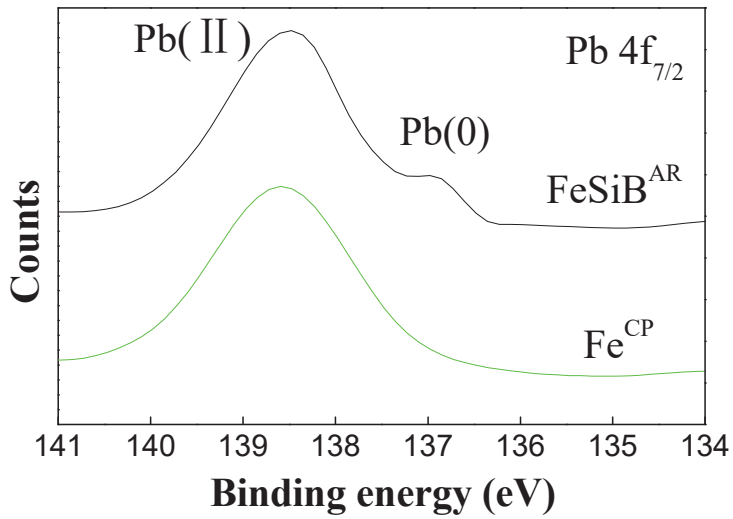


Figure 6. Pb $4f_{7/2}$ spectra of the reacted $FeSiB^{AR}$ and Fe^{CP}.

Furthermore, the XPS spectra of $FeSiB^{AR}$ before and after reaction are compared in Figure 7. The surface of the as-received $FeSiB^{AR}$ was surrounded by oxide and hydroxide of iron, silicon oxide, and boron oxide. However, the XPS peak of O 1s disappeared after Ar^+ sputtered at 0.4 nm/s for 20 s, suggesting that the thickness of the oxidation layer on the surface of the $FeSiB^{AR}$ produced in the atmosphere is about 8 nm. Furthermore, compared with the nominal composition of $Fe_{78}Si_9B_{13}$ amorphous ribbon, the atomic ratios of Fe:Si:B on the surface of the as-received $FeSiB^{AR}$ is 47:37:16, indicating that Si and B atoms are enriched on the surface due to a lower binding energy and the larger diffusion coefficient of Si and B elements [25]. The enrichment of Si and B element may leave an incompact

Fe layer on the surface, which may provide an incompact deposition site for chemical reaction. The possible compositions of the surface layer for the as-received $FeSiB^{AR}$ are ascribed to be Fe_2O_3(713.45 eV), FeOOH (711.02, 724.35 eV), Fe^{2+} (710.4 eV), Fe^0 (706.65 eV), and oxides of boron and silicon [26–28]. After reaction, there are a few changes in the chemical compositions on the surface of the Fe-Si-B^{AR}. It contains Fe_2O_3(713.6, 726.61 eV); FeOOH (711.21, 724.25 eV); Fe^{2+} (710.51 eV); and oxides of boron, silicon, and lead [26–28], indicating the reactions of Equations (4)–(11) involved in the Pb(II) removal process by $FeSiB^{AR}$. Therefore, the combined effect of absorption, (co)precipitation, and reduction lead to the high removal efficiency of $FeSiB^{AR}$, which is similar to the removal mechanism of Pb(II) by nano ZVI [29].

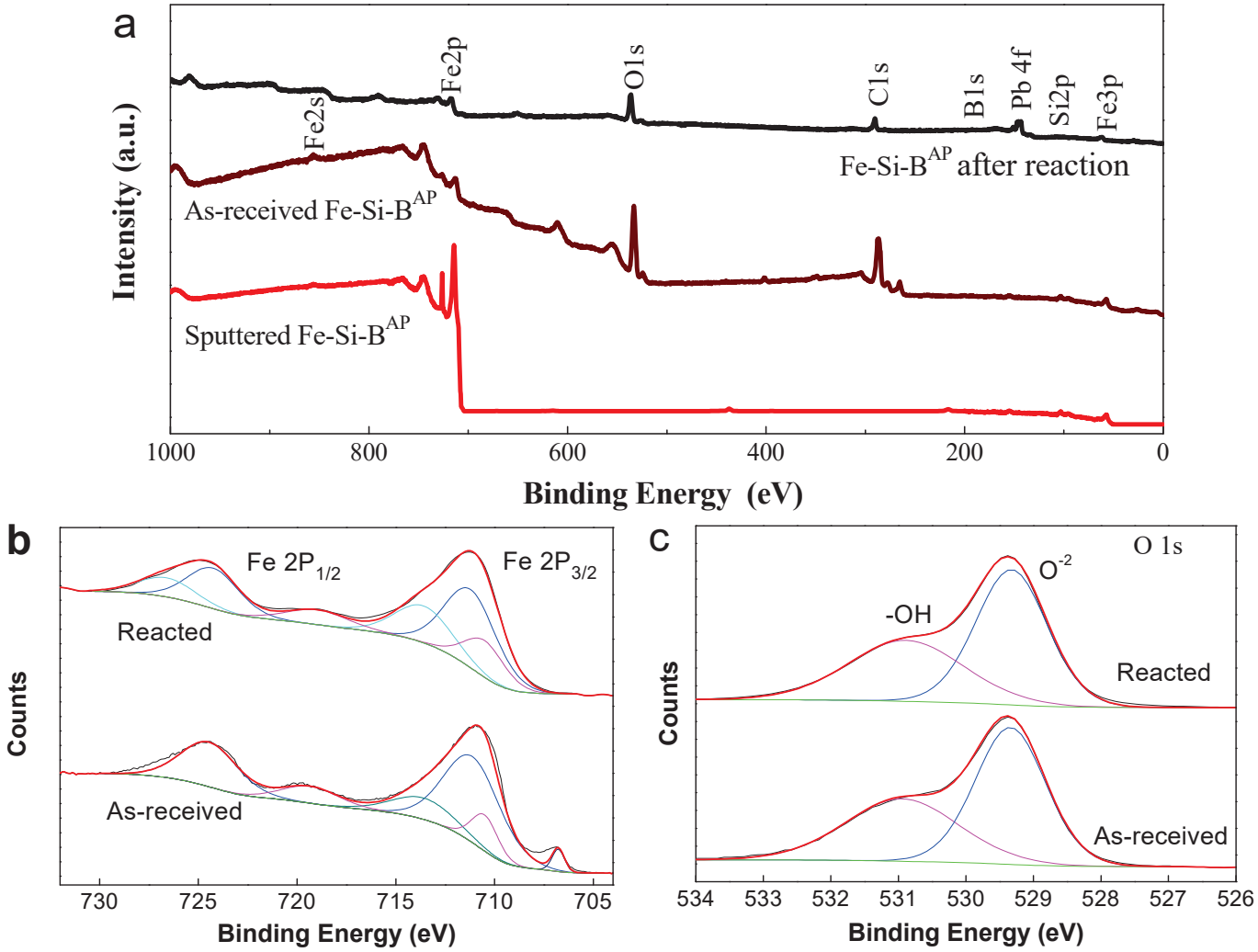


Figure 7. XPS spectra of $FeSiB^{AR}$ before and after reaction: (**a**) whole XPS, (**b**) Fe 2p, (**c**) O 1s.

SEM images of the precipitate and reacted $FeSiB^{AR}$ were also observed. Figure 8 shows microscopic morphology of the precipitate. The main features observed are a large number of particles with a size of about 5 μm surrounded by a thin layer of reaction product. It can be seen from the enlarged image in Figure 8b that the particles are surrounded by a villous product layer. EDS elemental analyses in Figure 8d show that the particles are mainly Pb crystallines. This result is in accordance with the XRD analyses that show that the precipitates are mainly Pb. The irregular multi-prism morphology of crystal Pb can be clearly seen from the backscattered electron image of the particles in Figure 8c due to the large difference in atomic number between Pb and the other elements.

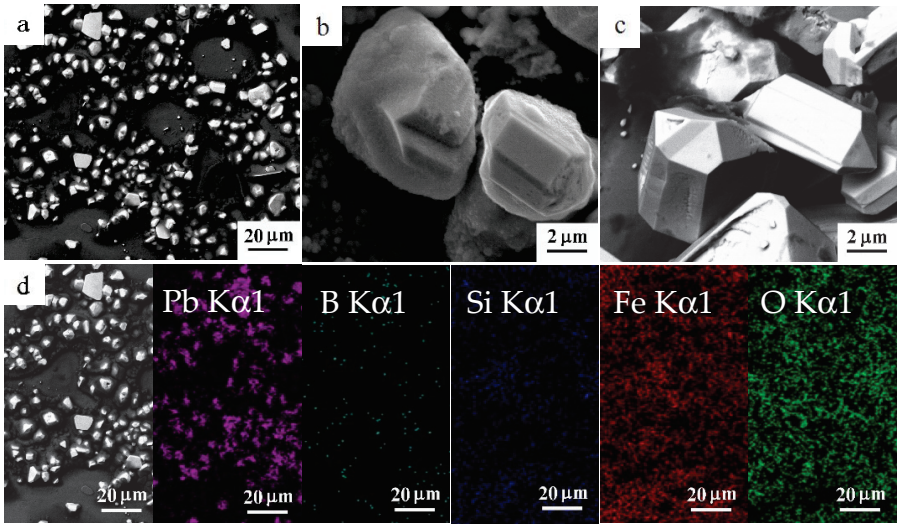


Figure 8. (**a**) SEM images of the precipitate after FeSiB^{AR} reacted with the Pb(II) solution. (**b**) Enlarged secondary electron image and (**c**) backscattered electron image of the particles in (**a**). (**d**) EDS elemental mapping images of the precipitate.

Figure 9 shows SEM images of the reacted FeSiB^{AR}. Parts of the product layer have peeled off the ribbon (region B) and have formed bright and dark regions on the surface of the FeSiB^{AR}, as shown in Figure 9a. The micrograph of region A and B are shown in high resolution in Figure 9b,c, respectively. Cracks have emerged on the surface of the residual product layer, as shown in Figure 9b. Following this, pieces of product layer tear along the cracks due to agitation and expose a fresh amorphous matrix. Then, a new product layer generates, as shown in Figure 9c. It can be seen that lamellar PbO, irregular multi-prism Pb, and worm-like iron oxide or silicon oxide have covered the fresh amorphous matrix. Furthermore, the high-magnitude image of region C in Figure 9d shows that the new product layer is a loose porous structure. The easily detached and loose porous product layer not only helps the elements exchange and accelerates the reaction process but also contributes to the reuse and durability performance of the FeSiB^{AR}.

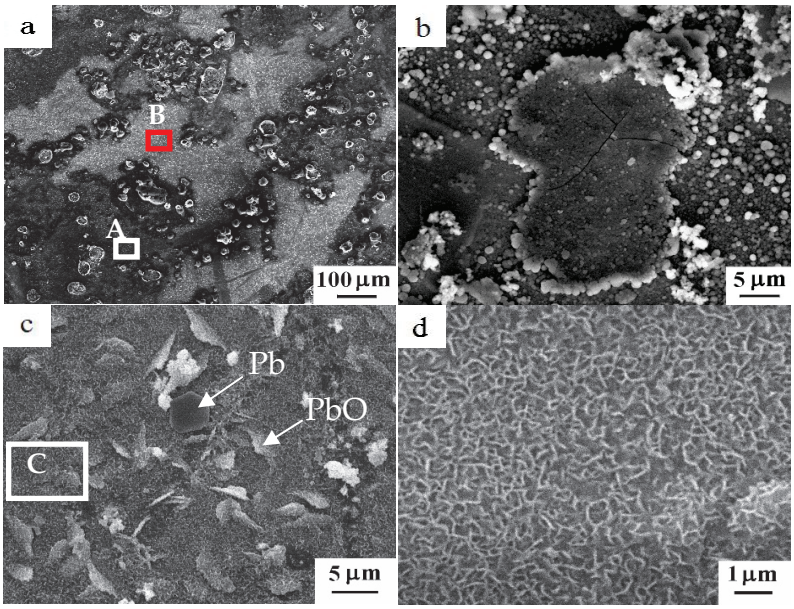


Figure 9. (**a**) Surface layer of the reacted FeSiB^{AR} and (**b**,**c**) enlarged views of the corresponding region A and B in (**a**), respectively. (**d**) Enlarged view of the corresponding region C in (**c**).

ZVI is the typical material for water purification, but fast corrosion always leads to rapid decay of its efficiency [28]. To verify the reusability of $FeSiB^{AR}$, repeated removal experiments were carried out for six 90 min cycles. Figure 10 shows the removal efficiency of $FeSiB^{AR}$ for six cycles. Although the removal efficiency gradually decreases after every cycle, removal efficiency up to 54% is still present until the sixth cycle, indicating that $FeSiB^{AR}$ can be reused conveniently for a few times without any treatment.

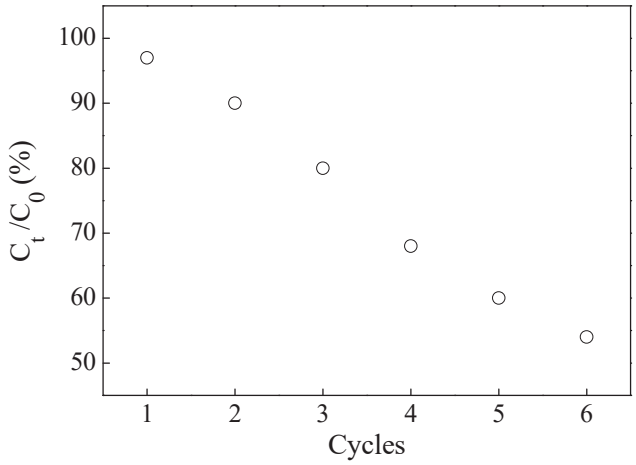


Figure 10. Removal efficiency of $FeSiB^{AR}$ reacting with Pb(II) solutions for six 90 min cycles.

The summarized removal mechanism of $FeSiB^{AR}$ is illustrated in Figure 11. $FeSiB^{AR}$ can be rapidly covered by oxidations of Fe, Si, and B in the atmosphere. However, in an oxygenated solution environment, Fe^{2+} and B^{3+} preferentially dissolved into the solution, leaving a porous and incompact layer of Si oxide on the surface of $FeSiB^{AR}$. This not only provides an incompact transport channel for element exchange, but also makes the product layer easy to be peeled off from the ribbon and keeps the ribbon having a relatively stable reusability. Furthermore, the Fe^0 beneath the oxide layer acts as an electron donor through the anodic reaction, $Fe \rightarrow Fe^{2+} + 2e^-$, and releases a steady stream of Fe^{2+} ions into the solution. At the same time, Pb^{2+} is adsorbed on the oxidation layer of $FeSiB^{AR}$ and reduced by Fe^0. In addition, the reaction of Fe^0 with H_2O generates hydroxide ions (OH^-) and increases the pH of the solution. Then, oxides and hydroxides of iron and lead may cover the $FeSiB^{AR}$ or form precipitates. In this process, the hydroxides of iron can form surface complexes with Pb(II) and act as an adsorbent of Pb(II), while the precipitate of lead oxide can separate Pb(II) from the solution.

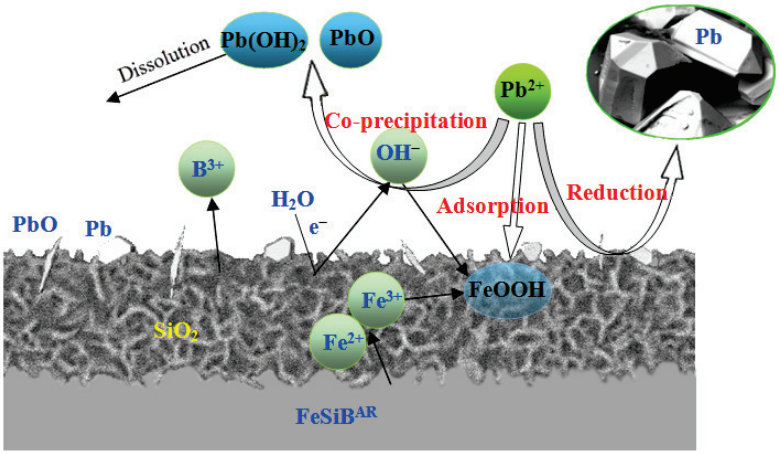


Figure 11. Removal mechanism of $FeSiB^{AR}$ in Pb(II) aqueous solution.

In conclusion, the removal of Pb(II) by Fe^{CP} is a surface-controlled process and is mainly controlled by absorption and coprecipitation, but the results suggest that, because of the special amorphous structure, $FeSiB^{AR}$ not only removes Pb(II) in solution by absorption, (co)precipitation, and reduction, but also produces a loose porous product layer. The combination of these effects leads to the high removal efficiency of $FeSiB^{AR}$.

3.3. Removal Mechanism of the Amorphous Powders

Figure 12 shows XRD patterns of the $FeSiB^{AP}$ and $FeSiB^{BP}$ after a reaction with the aqueous solution for 40 min at room temperature. The particles are too small to be distinguished from the precipitate, so the samples used for the XRD tests, included the reacted particles and the precipitate. XRD patterns of the $FeSiB^{AP}$ and $FeSiB^{BP}$ show nearly the same diffraction peaks that Pb, PbO, FeO(OH), and SiO_2 are superimposing on the broad hump of amorphous particles. The reaction product is consistent with the reaction product of $FeSiB^{AR}$.

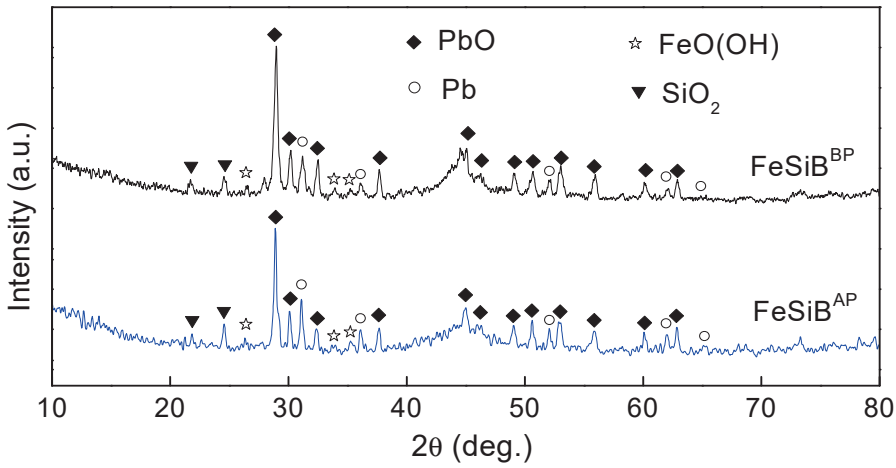


Figure 12. XRD patterns of the reacted $FeSiB^{AP}$ and $FeSiB^{BP}$.

Figure 13 shows SEM images of the $FeSiB^{AP}$ after reaction with the aqueous solution for 20 min at room temperature. The reacted $FeSiB^{AP}$ maintains its round or ellipsoid morphology and is covered with heterogeneous phases. It can be seen from Figure 13b that the phases appear to have the same morphologies as the product layers of the reacted $FeSiB^{AR}$. Minor amounts of irregular multi-prism Pb are also present on surface of the reacted $FeSiB^{AP}$, as shown in high resolution in Figure 13c. However, the sizes of the Pb particles are much smaller than those produced by the reaction between $FeSiB^{AR}$ and the Pb(II) solution, which may be related to the short reaction time and relatively dispersed Pb crystalline due to the large specific surface area of the $FeSiB^{AP}$. Additionally, it can be seen from region B that pieces of product layer have peeled off and a new product layer composed of worm-like oxides has generated, as shown in high resolution in Figure 13d. The same phenomenon also appears on the surface of the reacted $FeSiB^{AR}$. Therefore, it can be concluded that $FeSiB^{AR}$ and $FeSiB^{AP}$ have nearly the same reaction mechanism. Compared with $FeSiB^{AR}$, it is the high specific surface area that leads to the higher removal efficiency of $FeSiB^{AP}$.

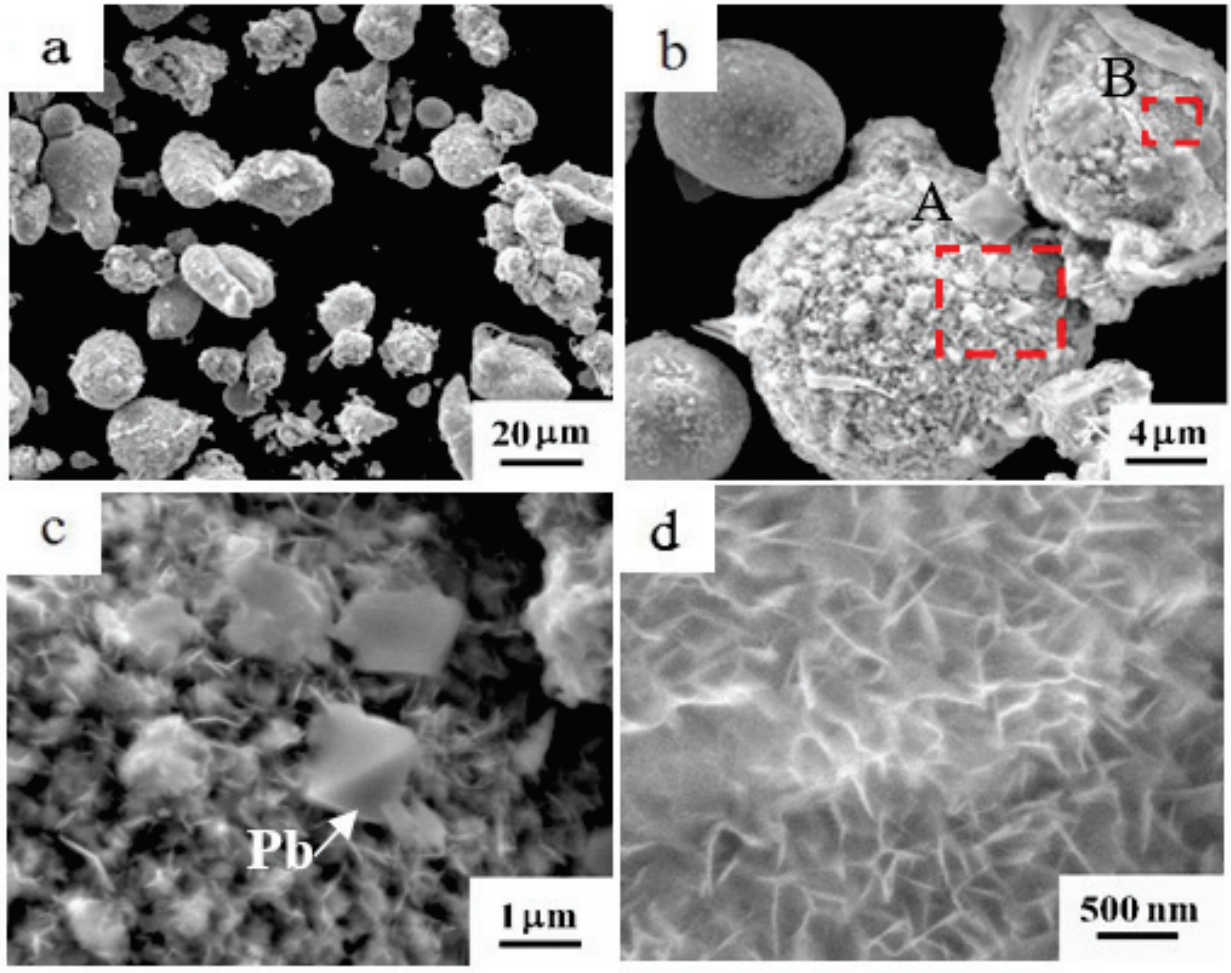


Figure 13. (**a**,**b**) SEM images with different magnifications of the reacted $FeSiB^{AP}$ and (**c**,**d**) enlarged views of the corresponding regions A and B, respectively.

It is interesting that the specific surface area of $FeSiB^{BP}$ is measured to be 0.0649 m^2/g, corresponding to one fifth of the specific surface area of $FeSiB^{AP}$, but $FeSiB^{BP}$ has the highest removal efficiency after the first 20 min. This phenomenon must be related to the special microstructure induced by the ball-milling process. According to Wang [11], huge residual stress and plastic deformation energy are stored in the $FeSiB^{BP}$ due to intense plastic deformation during the ball-milling process, which may facilitate the reaction activity and contribute to the low reaction active energy. Figure 14 shows SEM images of the $FeSiB^{BP}$ after reaction for 20 min at room temperature. Compared with $FeSiB^{AP}$, the reacted $FeSiB^{BP}$ and the reaction products gather together, as shown in Figure 14a, which may be responsible for the slowing of the removal process after reacting for 20 min.

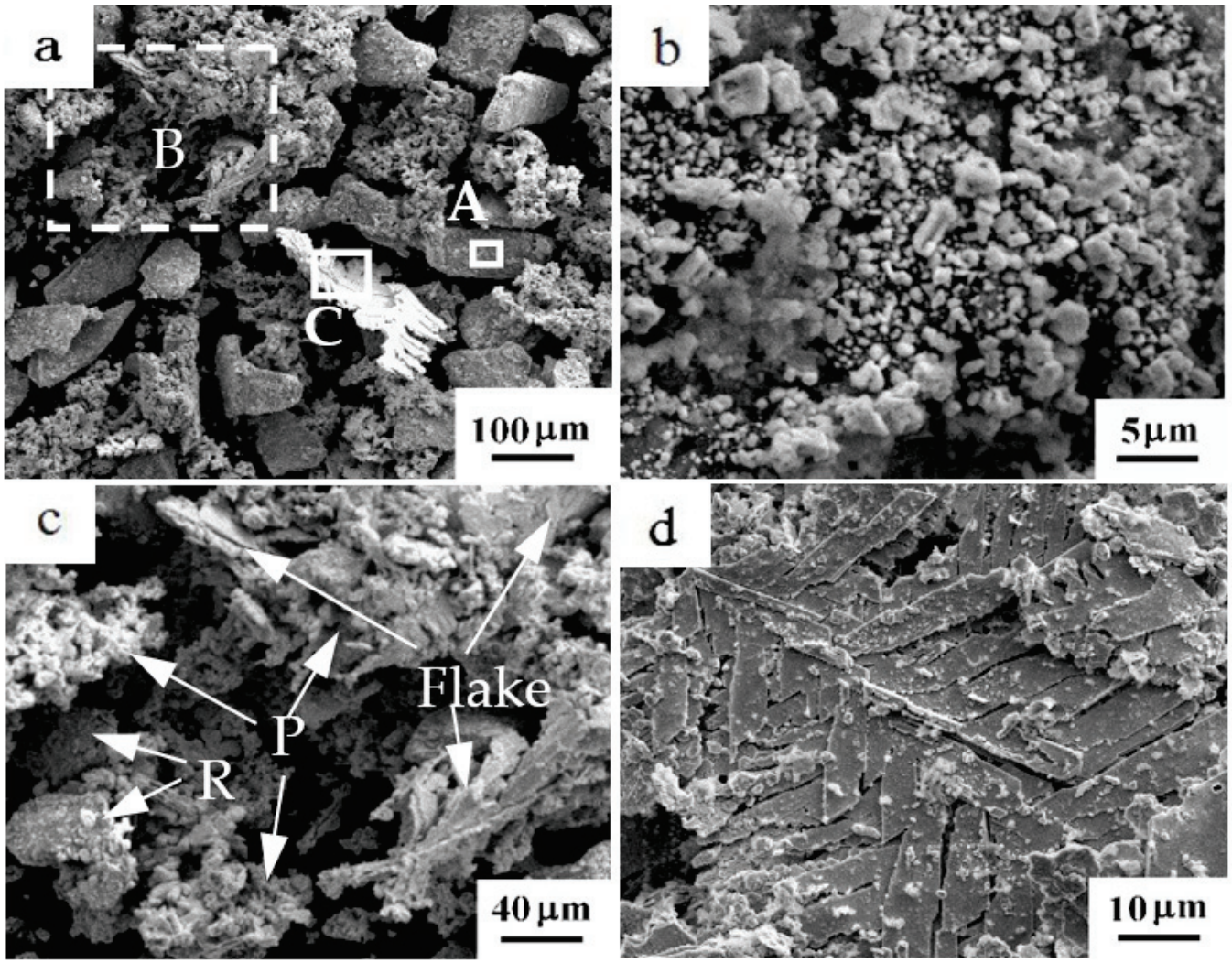


Figure 14. (**a**) SEM images with different magnifications of the reacted $FeSiB^{BP}$ and (**b**–**d**) enlarged views of the corresponding regions A, B, and C, respectively.

It can be seen from the enlarged image of region B in Figure 14c that the aggregation is composed of reaction product particles (marked as P), flakes, and the $FeSiB^{BP}$ residue (marked as R).

The EDS elemental analysis of the reaction product particles in Figure 15 shows that the particles are mainly Pb crystalline, according with the reaction precipitates of $FeSiB^{AR}$. Additionally, there are more Pb particles found on the surface layer of $FeSiB^{BP}$ than on surface of $FeSiB^{AP}$, as shown in Figure 14b. It can be deduced from so large a number of reaction products of Pb crystalline that the reduction is enhanced and plays a main role in the removal process of Pb(II) by $FeSiB^{BP}$, which may be induced by the high deformation energy stored in the $FeSiB^{BP}$.

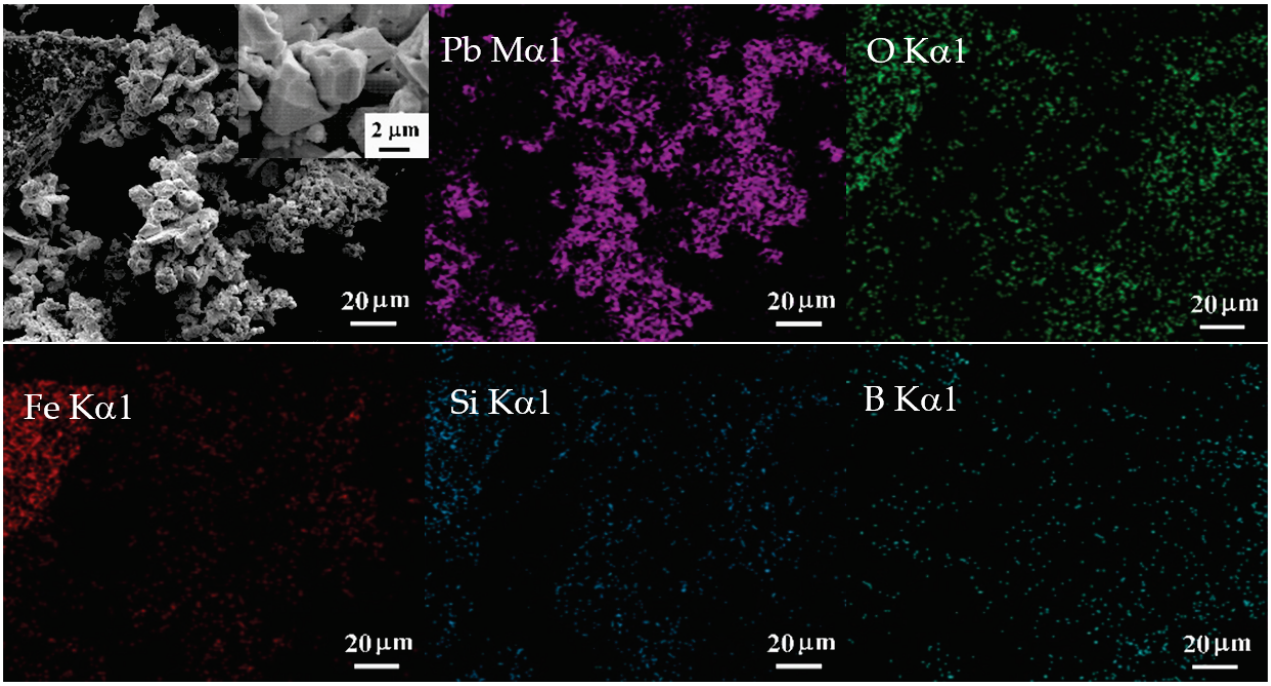


Figure 15. SEM image of the reaction products for $FeSiB^{BP}$ and the corresponding EDS elemental mapping images. The insets highlight the details of the particles.

Furthermore, microcracks formed in the ball-milling process on the original $FeSiB^{BP}$ also affect the reaction process. These microcracks may grow and propagate due to the crevice corrosion effect and the huge residual stress in the agitated Pb(II) solution, especially when the $FeSiB^{BP}$ is very thin. The thinner the $FeSiB^{BP}$, the easier it is for the cracks to penetrate the $FeSiB^{BP}$ and break it into small pieces. Figure 14d shows surface details of the flake. It is obvious that the flake would have broken into many small pieces if it had been further agitated. The flakes in Figure 14c have a similar morphology. The increased specific surface areas induced by the breaking of the $FeSiB^{BP}$ may also contribute to the reaction process.

Therefore, even though the original specific surface areas of $FeSiB^{BP}$ are low, the combined effect of high deformation energy stored in the $FeSiB^{BP}$ and increased specific surface areas make them the most reactive material. However, the aggregation of the reaction product and the $FeSiB^{BP}$ residue leads to the rapid decay of its efficiency after reaction for 20 min.

4. Conclusions

In summary, the removal efficiency of all the amorphous materials, including $FeSiB^{AR}$, $FeSiB^{AP}$, and $FeSiB^{BP}$, in removing Pb(II) from aqueous solution are much better than the widely used Fe^{CP}. Furthermore, it is interesting to find that $FeSiB^{BP}$ has the highest removal efficiency after the first 20 min, but the removal process stops at 20 min, when the Pb(II) concentration is reduced to about 89%.

The removal mechanism of $FeSiB^{AR}$ was discussed, and the results show that, different from the surface-controlled chemical reaction of Fe^{CP}, Pb(II) was removed from aqueous solution by $FeSiB^{AR}$ through the combined effect of absorption, (co)precipitation, and reduction. In addition, the product layer on the surface of $FeSiB^{AR}$ is easily detached and is a loose porous structure, which not only accelerates the reaction process but also makes $FeSiB^{AR}$ maintain a relatively stable reusability.

$FeSiB^{AP}$ and $FeSiB^{BP}$ have nearly the same reaction mechanism as $FeSiB^{AR}$, but they have a relatively higher removal efficiency than $FeSiB^{AR}$, due to high specific surface areas. Although $FeSiB^{BP}$ has the highest removal efficiency up to the first 20 min, aggregation of

reaction product and the $FeSiB^{BP}$ residue makes the reaction process nearly halt after the first 20 min of reaction.

This study suggests that all the amorphous materials have great application potential in removal of Pb(II) from wastewater. Despite this, the long-term use of $FeSiB^{BP}$ for Pb(II) removal may need further treatment due to the rapid decay of its efficiency.

Author Contributions: Original draft preparation and Funding Acquisition, X.-Y.Z.; supervision, Z.-Z.Y.; investigation, J.-Y.D.; formal analysis, L.-L.H. All authors have read and agreed to the published version of the manuscript.

Funding: This work was financially supported by the National Natural Science Foundation of China (NSFC) (No. 52061024 and No. 52161027), the Natural Science Foundation of Zhejiang Province (No. LQ20E010002), the Natural Science Foundation of Gansu Province (No. 21JR7RA260) and the Hongliu Research Funds of Lanzhou University of Technology for Distinguished Young Scholars.

Institutional Review Board Statement: Not applicable.

Informed Consent Statement: Not applicable.

Data Availability Statement: Data sharing not applicable.

Acknowledgments: The authors acknowledge all the authors, editors, and reviewers who contributed to this article.

Conflicts of Interest: The authors declare no conflict of interest.

References

1. Lv, Z.W.; Yan, Y.Q.; Yuan, C.C.; Huang, B.; Yang, C.; Ma, J.; Wang, J.Q.; Huo, L.S.; Cui, Z.Q.; Wang, X.L.; et al. Making Fe-Si-B amorphous powders as an effective catalyst for dye degradation by high-energy ultrasonic vibration. *Mater. Des.* **2020**, *194*, 108876. [CrossRef]
2. Wang, J.; Liu, G.; Li, T.; Zhou, C.; Qi, C. Zero-Valent Iron Nanoparticles (NZVI) Supported by Kaolinite for CuII and NiII Ion Removal by Adsorption: Kinetics. *Aust. J. Chem.* **2015**, *68*, 1305–1315. [CrossRef]
3. Wang, W.; Hua, Y.L.; Li, S.L.; Yan, W.L.; Zhang, W.X. Removal of Pb(II) and Zn(II) using lime and nanoscale zero-valent iron (nZVI): A comparative study. *Chem. Eng. J.* **2016**, *304*, 79–88. [CrossRef]
4. Ma, H.; Huang, Y.; Shen, M.; Hu, D.; Yang, H.; Zhu, M.; Yang, S.; Shi, X. Enhanced decoloration efficacy of electrospun polymer nanofibers immobilized with Fe/Ni bimetallic nanoparticles. *RSC Adv.* **2013**, *3*, 6455–6465. [CrossRef]
5. Pooja; Goel, A. A Highly Ultrafine Core–Shell Ir–Cu Bimetallic Nanoparticles and Their Application in Catalytic Oxidation of Textile Dye, Congo Red, by Hexacyanoferrate(III) Ions: A Kinetic Approach. *Kinet. Catal.* **2021**, *62*, 592–603. [CrossRef]
6. Wang, F.; Wang, H.; Zhang, H.F.; Dan, Z.H.; Weng, N.; Tang, W.Y.; Qin, F.X. Superior azo-dye degradation of Fe-Si-B-P amorphous powders with graphene oxide addition. *J. Non-Cryst. Solids* **2018**, *491*, 34–42. [CrossRef]
7. Zhang, L.C.; Jia, Z.; Lyu, F.; Liang, S.X.; Lu, J. A review of catalytic performance of metallic glasses in wastewater treatment: Recent progress and prospects. *Prog. Mater. Sci.* **2019**, *105*, 100576. [CrossRef]
8. Liu, P.; Zhang, J.L.; Zha, M.Q.; Shek, C.H. Synthesis of an Fe rich amorphous structure with a catalytic effect to rapidly decolorize Azo dye at room temperature. *ACS Appl. Mater. Inter.* **2014**, *6*, 5500–5505. [CrossRef]
9. Qin, X.D.; Li, Z.K.; Zhu, Z.W.; Fang, D.W.; Zhang, H.F. Fenton-like degradation of coke wastewater using Fe78Si8B14 and $Fe_{73.5}Nb_3Cu_1Si_{13.5}B_9$ metallic glasses. *J. Phys. Chem. Solids* **2019**, *133*, 85–91. [CrossRef]
10. Qin, X.D.; Li, Z.K.; Zhu, Z.W.; Fu, H.M.; Li, H.; Wang, A.M.; Zhang, H.W.; Zhang, H.F. Mechanism and kinetics of treatment of acid orange II by aged Fe-Si-B metallic glass powders. *J. Mater. Sci. Technol.* **2017**, *33*, 1147–1152. [CrossRef]
11. Wang, J.Q.; Liu, Y.H.; Chen, M.W.; Xie, G.Q.; Louzguine-Luzgin, D.V.; Inoue, A.; Perepezko, J.H. Rapid Degradation of Azo Dye by Fe-Based Metallic Glass Powder. *Adv. Funct. Mater.* **2012**, *22*, 2567–2570. [CrossRef]
12. Wang, J.Q.; Liu, Y.H.; Chen, M.W.; Louzguine-Luzgin, D.V.; Inoue, A.; Perepezko, J.H. Excellent capability in degrading azo dyes by MgZn-based metallic glass powders. *Sci. Rep.* **2012**, *2*, 418. [CrossRef]
13. Qin, X.D.; Zhu, Z.W.; Liu, G.; Fu, H.M.; Zhang, H.W.; Wang, A.M.; Li, H.; Zhang, H.F. Ultrafast degradation of azo dyes catalyzed by cobalt-based metallic glass. *Sci. Rep.* **2015**, *5*, 18226. [CrossRef]
14. Xie, S.H.; Huang, P.; Kruzic, J.J.; Zeng, X.R.; Qian, H.X. A highly efficient degradation mechanism of methyl orange using Fe-based metallic glass powders. *Sci. Rep.* **2016**, *6*, 21947. [CrossRef] [PubMed]
15. Miao, F.; Wang, Q.Q.; Di, S.Y.; Yun, L.; Zhou, J.; Shen, B.L. Enhanced dye degradation capability and reusability of Fe-based amorphous ribbons by surface activation. *J. Mater. Sci. Technol.* **2020**, *53*, 163–173. [CrossRef]
16. Jia, Z.; Kang, J.; Zhang, W.C.; Wang, W.M.; Yang, C.; Sun, H.; Habibi, D.; Zhang, L.C. Surface aging behaviour of Fe-based amorphous alloys as catalysts during heterogeneous photo Fenton-like process for water treatment. *Appl. Catal. B Environ.* **2017**, *204*, 537–547. [CrossRef]

17. Zhang, X.Y.; Liu, J.K.; Li, J.Q.; Li, C.Y.; Yuan, Z.Z. Excellent capability in remediating Cu^{2+} from aqueous solution by Fe–Si–B amorphous alloys. *Appl. Phys. A* **2020**, *126*, 291. [CrossRef]
18. Tang, Y.; Shao, Y.; Chen, N.; Liu, X.; Chen, S.Q.; Yao, K.F. Insight into the high reactivity of commercial Fe-Si-B amorphous zero-valent iron in degrading azo dye solutions. *RSC Adv.* **2015**, *5*, 34032–34039. [CrossRef]
19. Zhang, C.Q.; Zhu, Z.W.; Zhang, H.F. Effects of the addition of Co, Ni or Cr on the decolorization properties of Fe-Si-B amorphous alloys. *J. Phys. Chem. Solids* **2017**, *110*, 152–160. [CrossRef]
20. Sun, J.F.; Tian, A.R.; Feng, Z.Y.; Zhang, Y.; Jiang, F.Y.; Tang, Q. Evaluation of Zero-Valent Iron for Pb(II) Contaminated Soil Remediation: From the Analysis of Experimental Mechanism Hybird with Carbon Emission Assessment. *Sustainability* **2021**, *13*, 452. [CrossRef]
21. Liu, X.J.; Lai, D.G.; Wang, Y. Performance of Pb(II) Removal by an Activated Carbon Supported Nanoscale Zero-Valent Iron Composite at Ultralow Iron Content. *J. Hazard. Mater.* **2019**, *361*, 37–48. [CrossRef]
22. Scott, T.B.; Popescu, I.C.; Crane, R.A.; Noubactep, C. Nano-scale metallic iron for the treatment of solutions containing multiple inorganic contaminants. *J. Hazard. Mater.* **2011**, *186*, 280–287. [CrossRef] [PubMed]
23. Cheng, Y.; Jiao, C.; Fan, W.J. Synthesis and characterization of coated zero-valent iron nanoparticles and their application for the removal of aqueous Pb^{2+} ions. *Desalin Water Treat.* **2015**, *54*, 502–510. [CrossRef]
24. Liu, M.H.; Wang, Y.H.; Chen, L.T.; Zhang, Y.; Lin, Z. $Mg(OH)_2$ Supported Nanoscale Zero Valent Iron Enhancing the Removal of Pb(II) from Aqueous Solution. *ACS Appl. Mater. Interfaces* **2015**, *7*, 7961–7969. [CrossRef] [PubMed]
25. Zhang, S.L.; Liu, H.P.; Fu, X.T. Oxidation Behavior of Fe-based Amorphous Ribbons. *J. Iron Steel Res. Int.* **2016**, *23*, 1219–1225. [CrossRef]
26. Dai, M.Y.; Liu, Y.G.; Zeng, G.M.; Liu, S.B.; Ning, Q.M. Adsorption studies of 17β-dstradiol from aqueous solution using a novel stabilized Fe-Mn binary oxide nanocomposite. *Environ. Sci. Pollut. Res.* **2019**, *26*, 7614–7626. [CrossRef]
27. Miao, S.; An, H.L.; Zhao, X.Q.; Wang, Y.J. Preparation of highly selective and stable Cu-Mg-Fe catalyst and its catalytic performance for one-step synthesis of 2-ethylhexanol from n-butyraldehyde. *React. Kinet. Mech. Catal.* **2019**, *128*, 395–412. [CrossRef]
28. Houda, J.; Joaquin, M.-O.; Imne, M.; Mourad, M.; Teresa, B.; Grard, D. On the performance of Fe-Cu-ZSM-5 catalyst for the selective catalytic reduction of NO with NH3: The influence of preparation method. *Res. Chem. Intermed.* **2019**, *45*, 1057–1072. [CrossRef]
29. Tarekegn, M.M.; Hiruy, A.M.; Dekebo, A.H. Nano zero valent iron (nZVI) particles for the removal of heavy metals (Cd^{2+}, Cu^{2+} and Pb^{2+}) from aqueous solutions. *RSC Adv.* **2021**, *11*, 18539. [CrossRef] [PubMed]

applied sciences

MDPI

Article

Influence of Effective Microorganisms, Colloidal Nanosilver and Silver Compounds on Water Content in New and Used Engine Oil: A Preliminary Study

Rafał Krakowski

Department of Marine Propulsion Plants, Faculty of Marine Engineering, Gdynia Maritime University, Morska Street 81-87, 81-225 Gdynia, Poland; r.krakowski@wm.umg.edu.pl

Abstract: This paper presents research upon the impact of ecological measures on the water content of new and used oil. Water and microorganisms are major factors of contamination for engine oils and fuels, and they lead to a significant reduction in the lifetime and performance of engines. The microorganisms occur naturally in the environment, from which they enter into the oil and fuel. Despite various preventive measures, it is not possible to completely remove water from petrochemical products. That is why the protection against and prevention of the various types of contamination of petroleum products, especially microbiological contamination, is very important. Biocides are one example of the agents used for the prevention of contamination; biocides belong to a group of pesticides that are used to eliminate microbial contamination. Due to the fact that currently available methods are ineffective and often have a detrimental effect on the natural environment, research is underway to discover modern and ecological measures to combat the phenomenon of the microbiological contamination of petroleum products. This paper shows the effects of environmentally friendly additives on the water content in lubricating oil, i.e., whether these additives cause the release of water bound in the oil, and whether their composition increases the water content of the oil. Samples of new and used oil were utilized for the tests. Effective microorganisms (EM), in both liquid form and within ceramic tubes, were added to the new and used oil samples. In addition, silver solution and silver compounds were added in the same amounts as the liquid effective microorganisms. In order to confirm and compare the obtained test results, the dynamic viscosity, flash point, acid number, base number, and water content were measured, and these are presented in this study. These measurements were followed by the analysis of the influence of the additives on the water content. It was found that the adding of effective microorganisms to fresh oil in liquid form caused a significant increase in the water content of the oil; in the case of a smaller amount (2.5 mL), the water content more than doubled, and in the case of a larger amount, the water content exceeded the measuring range of the device. Next, an evaluation of the impact of these environmental measures on the water content was carried out. It was found that the adding of liquid effective microorganisms to new oil caused a significant increase in the water content of the oil; the water content more than doubled for the addition of 2.5 mL, while for a larger addition (5 mL), the water content exceeded the measuring range of the device. The same was true for the addition of silver compounds, regardless of their type and amount. The best results were obtained with ceramic effective microorganisms, but the results for silver cannot be presented due to the over-titration of the device (the amount of water exceeded the measuring range). For used oil, the liquid effective microorganism was found to give the best result.

Keywords: engine oil; water content; oil properties; effective microorganisms; silver compounds

1. Introduction

The microbial contamination of both fuels and engine oils has been the subject of many past studies. At the same time, this problem is still valid and has become more and

more popular as an area of research. Studies have shown that microbial activity can be detrimental to the operation of various modes of transport [1–5]. It is important to prevent microbial contamination that can occur in petroleum products. Microbial contamination can be prevented through proper cleansing, decontamination, or by chemical methods. Another method of protection against microbial contamination is the use of specialized coatings on fuel tanks [6].

One means of combating harmful organisms are commonly used synthetic or natural compounds, i.e., biocides. Cleaning agents are also used during fuel storage to help reduce the amount of water in the tank. Currently, for the sake of environmental protection, it is necessary to develop new methods to prevent the growth of harmful microorganisms in engine oil. When developing methods of eliminating the phenomenon of the microbiological contamination of petrochemical products with the use of ecological measures, it is necessary to take into account both the structure and the phenomena occurring in the supply systems and the lubrication of machine elements [7–9].

Ecological methods of improving the performance parameters of engine oils may include the addition of effective microorganisms [10–14], i.e., a set of cultures of naturally occurring, non-genetically modified microorganisms; these are specially selected, microscopic organisms found on Earth. These microorganisms are used, among others, in industry, medicine, horticulture, and also in environmental protection. Another environmentally friendly measure involves the use of silver [15]. This element has long been used for protective and healing purposes. It is also applied in filters, and to clean the air of microorganisms and water in closed spaces, e.g., on airplanes. The method of silver ionization contributed to the enhancement of the disinfecting effect of this element. Silver ionization, as with copper ionization, has found application in the qualifying selection of some bacteria [16–20]. Silver is also used in the form of nanosilver. This article presents a study of the influence of additives commonly recognized as environmentally friendly on the water content in new and used oil.

2. Oil Contamination with Water

One of the tasks of engine oils is the reduction of friction between the surfaces of two moving and interacting elements of mechanical devices. Lubricating oils consist of a base oil and an active ingredient. The base oil gives typical characteristics to the lubricating oil, and the actual performance is determined by the active substances that improve the base oils in terms of resistance to oxidation, corrosion protection, wear protection, as well as wetting and emulsifying ability [21–31].

The problem is water bound in the lubricating oil. Water in oil comes in three forms: dissolved water, emulsified water, and free water. The point at which the oil cannot absorb more dissolved water is called the oil saturation point [32]. If more water enters the oil, the excess water will appear as separated water or an emulsion. Generally, if the saturation point is exceeded, the oil changes to a milky appearance. The water amount in the oil depends mainly on the additive package, operating temperature, pressure, and the quality of the base oil. For example, a highly refined oil with few additives will withstand a small amount of water before being saturated, around 100 ppm at 21 °C. On the other hand, an ester-based oil can withstand 3000 ppm of water at 21 °C and above [31–33]. Water contained in oil systems deteriorates the rheological properties of the working fluid used, reducing its lubricating and insulating abilities. Water in oil reduces the possibility of the transference of bearing loads, accelerates the processes of oil oxidation, rinses out improvers, increases the amount of deposits, and causes corrosion.

Water promotes the aeration of oil, which causes a foaming problem and has a negative effect on oil improvers, causing them to undergo the process of hydrolysis or be washed out [34–36].

3. Materials and Methodology

3.1. Materials Used in the Research

For the tests, 5W30 synthetic oil was used. It is ESP (emission system protection) formula fully synthetic oil manufactured by Mobil. This oil changes its viscosity slightly during temperature changes. As a result, it perfectly lubricates engine parts, while protecting against carbon deposits, sludge, and other harmful impurities that can accelerate wear.

The described oil retains its optimal viscosity from −30 °C and its fluidity at −35 °C; 5W30 oil has high pumpability, thanks to which it is highly effective in cleaning the most important engine components, while also contributing to their efficient cooling [37].

A 5W30 automotive oil, according to the SAE J300 standard of 2015, must meet the following criteria [38]:

- Maximum dynamic viscosity of 6600 cP at −30 °C;
- Maximum pumpability temperature of 60,000 cP at the temperature of −35 °C;
- Kinematic viscosity at temperature 100 °C min, 3.8 mm^2/s to 9.3–12.5 mm^2/s;
- Viscosity HTHS in 150 °C min, 2.9 cP.

The used oil is of the same type as the new oil, and is sourced from a compression ignition internal combustion engine. Its mileage is approximately 1000 km, having been in operation for a year in various real conditions on mixed routes (city and motorway routes).

Effective microorganisms and silver were added to the oil about 4 weeks prior to beginning the research.

The effective microorganisms used comprised 81 different strains of aerobic and anaerobic microorganisms, including lactic bacteria (*Lactobacillus casei, Streptococcus lactis*), yeasts (*Saccharom–yces* spp., *Candida utilis*), photosynthetic bacteria (*Rhodopseudomonas palustrus*, *Rhodobacter spae*), molds (*Aspergillus oryzae*, *Mucom hiemalis*), and actinomycetes (*Streptomyces*, *Streptomyces griseus*) [39].

Photosynthetic bacteria under certain conditions, for example, CO_2 or property temperature, produce useful biochemical active substances from organic matter or toxic gases. Lactic acid bacteria also slow down the growth of harmful bacteria. Another important component of the mixture is yeast. Mushroom fermentation breaks down organic matter and neutralizes unpleasant odors.

The action of EMs includes natural processes, and furthermore, as these microorganisms are not genetically modified, they are therefore environmentally friendly [40]. Effective microorganisms in the form of ceramic tubes are a special type of clay inoculated with beneficial microflora (fermented clay), which mature in natural conditions for several months, before being fired under high temperatures in anaerobic conditions; they include compositions of beneficial microorganisms, sugar cane molasses, and restructured water. Clays inoculated with microbes mature for many weeks in appropriate humidity and temperature levels, and then, depending on their intended use, they are fired at high temperatures (gray) of 1200–1300 °C. When fired, they become a viscous liquid, and when cooled to ambient temperature, they bind strongly and are extremely hard. Ceramics fired using this method are less porous, denser, and less brittle. The raw materials used in traditional ceramics include minerals such as clay, silica stone, and feldspar. Ceramics are inorganic and contain no metals. The ceramic tubes used were shaped and then hardened by firing at high temperatures. Ceramics do not react chemically, do not burn, and are harder than steel. The shapes of the fired elements or dishes are adjusted in accordance to their future use, and the content of effective microorganisms is 3% in each ceramic tube [41].

Effective microorganisms in the commercial forms presented in Figure 1 were used for the research with the following composition: water: 94%; Effective Microorganisms® (lactic acid bacteria, photosynthetic bacteria, saprophytic bacteria, yeast, fungi, and actinomycetes): 3%; molasses: 3%.



Figure 1. The commercial forms of effective microorganisms [42,43].

An EM product manufactured by Greenland Technologia was used in the research. The company deals with the production and sale of products based on the technology of Effective Microorganisms®, which are widely used in agriculture and horticulture, animal husbandry, or in biological environmental treatment (municipal and home sewage treatment plants, regeneration of soil and water reservoirs).

Greenland Technologia EM Ltd. is the sole licensee of EM Research Organization Inc. (EMRO) for Poland and Central and Eastern Europe. The Japanese company EMRO is also a licensor for producers and distributors of products in several dozen countries on all continents.

The second additive used in the research is colloidal silver, also known as nanosilver and silver solution.

Ion silver is as transparent as water, is stored in glass bottles, and consists of 90% silver ions and only about 10% silver particles. This type of silver is called "silver solution". After entering the body, silver ions immediately combine with it, creating an insoluble salt–silver chloride. Such a property is not exhibited by electrically neutral silver particles. This salt does not have any properties that are attributed to colloidal silver.

Nanosilver consists of microscopic particles and silver ions that can only be observed through an electron microscope. Due to the high concentration of silver nanoparticles, colloidal silver does not resemble water. Its characteristic feature is a clear color, which can range from yellow to amber. Colloidal silver has a darker color because the silver particles dispersed in the water block the light passing through them with a specific wavelength, which is approximately 400 nm. Additionally, colloidal silver can be stored in plastic bottles because silver nanoparticles are chemically insensitive and completely resistant to the damaging effects of UV radiation.

Colloidal silver with silver nanoparticles is the least common type of silver commercially available due to its complicated production process and high production costs. However, it is the only effective silver with scientifically proven properties. Real colloidal silver consists of 80% silver particles, with the remaining 20% made up of silver ions. The decisive factors for the quality of real colloidal silver are the content of silver particles and their very active total surface. In colloidal silver, nanometer-sized particles form a colloid, so it is not necessary to use a protein substrate to suspend them in water. Due to their electrokinetic potential, nanoparticles repel each other, keeping the colloid stable.

Silver suppressed to the form of nanoparticles has a large active surface, and enormous biocidal potential. The productive value of nanosilver includes the eradication of over 99.99% of bacteria, viruses, mold, and fungi. Good carriers for nanosilver are activated carbon fibers (ACFs), commonly used in sewage treatment plants for removing various types of contamination [44].

Experimental data from studies [45] show that silver nanoparticles at a concentration of 4 mg/mL completely inhibit the growth of *Staphylococcus aureus* bacteria. The results of transmission electron microscopy confirmed the damage to the cell walls caused by silver nanoparticles and the accumulation of these particles in the bacterial cell membrane [46,47].

Silver solution and colloidal nanosilver was used for the tests in the commercial form shown in Figure 2. Silver solution (transparent), sold as Silver Klar Ag+, was created on the basis of demineralized water and ionic silver (25 ppm), and was produced by the Naoliwieni company located in Rosanów (Poland). Colloidal silver (amber), sold as ARGENTUM200, was created on the basis of demineralized water with a colloidal non-ionic silver content of 25 ppm, and was manufactured by Aura Herbals Ltd in Sopot (Poland).



Figure 2. The commercial forms of colloidal nanosilver and silver solution [48,49].

3.2. Methodology

The water content of new and used oil with and without any additives was tested using the Cou-Lo AquaMax KF automatic titrator for water content determination in accordance with the Karl Fischer method. This device (Figure 3) uses the coulometric titration technique to ensure the repeatable and reliable measurement of the water content from 1 ppm upwards. It uses the technique of the precise generation of iodine into the system as a result of electrolysis, taking place in a very tight measuring vessel with the lowest level of moisture penetration from the outside, i.e., the so-called "drift". The selected parameters of the Cou-Lo AquaMax KF automatic titrator are shown in Table 1.



Figure 3. Tested oil with solvent and iodine on Automatic Cou-Lo AquaMax KF titrator.

Table 1. Selected parameters of the Cou-Lo AquaMax KF automatic titrator.

Parameters	Cou-Lo Aquamax KF Moisture Meter
Titration method	Coulometric Karl Fischer titration
Endpoint detection	AC polarity
Measurement range	1 μg–10 mg of water, max 200 mg of water
Moisture range	1 ppm–100% water
Maximum titration rate	2.24 mg per minute
Maximum electrolysis current	400 mA
Drift Compensation	Controlled automatically
Minimum titration time	0–30 min, user programmable
Precision	10–100 μg ± 3 μg, 100 μg–1 mg ± 3 μg (ppm), over 1 mg ± 0.3%
Display format	μg, mg/kg, ppm, %

New and used oils with liquid and ceramic effective microorganisms, silver solution, and colloidal nanosilver, were used for the research, wherein 2.5 mL and 5 mL of additives per 100 mL of oil, and three or six pieces of ceramic tube with diameters of 9 mm and heights of 11 mm were added to the samples.

In order to obtain the results of the water content of the oil itself and of the oil with additives:

1. The Aquagent Coulometric solvent (100 mL) was poured into the measuring vessel;
2. An ampoule of iodine in the amount of 5 mL was added;
3. The parts were twisted together and the device was placed on the stand;
4. The "G" generation electrode and the "D" detection electrode were connected;
5. It was then possible to start conditioning, i.e., to begin removing the moisture from the measuring system in order for the obtained measurement to correspond to the tested sample;
6. It was necessary to fill the glass syringe with test oil and weigh the oil-filled syringe, then the sample itself, to obtain the weight of the test sample;
7. After completing the measurement of the water content, the previously measured mass of the tested oil was fed into the device in order to obtain the water content as a percentage.

There is a platinum charge-generating electrode in the measurement system, which is responsible for the release of stoichiometric amounts of iodine into the system (with a ceramic diaphragm), precisely, optimally, and according to the following relationship: the 10.71 coulomb charge generated in the system releases the amount of iodine that balances the content of 1 mg of water. The AquaMAX KF device works according to the rules of coulometry and determines the water content of the sample by coulometric titration until the end point is reached. The end point means that free iodine appears in the system. Stoichiometric: 1 mole of water reacts with 1 mole of iodine. This means that 1 mg of water (0.001 g) is equivalent to 10.71 electric coulombs (1C = 1A × 1s). The device determines the water content in the tested sample by measuring the total amount of charges generated as the sum of the electrolysis current needed to produce the required amount of iodine in the system to bind the water contained in the tested material [50].

4. Results and Discussion

The research results are presented in the form of graphs in Figures below. These charts demonstrate the analysis of the influence of each of the additives on the amount of water in the oil samples. Each sample of pure oil and oil with additives was tested three times. However, this article presents the average result for each case.

Analyzing the obtained outcomes, it can be noted that in Figure 4, the water content of fresh oil with no EMs is 0.096%. The addition of 2.5 mL of microorganisms to the oil causes a considerable increase in the amount of water in the oil, because it is more than twice as high compared to oil without such an additive and amounts to 0.21% of the water content. With the addition of more microorganism solution, i.e., 5 mL, it was not possible

to determine the water content due to over-titration. It follows that this amount of water in oil was above 1%, i.e., above the measuring range of the device.

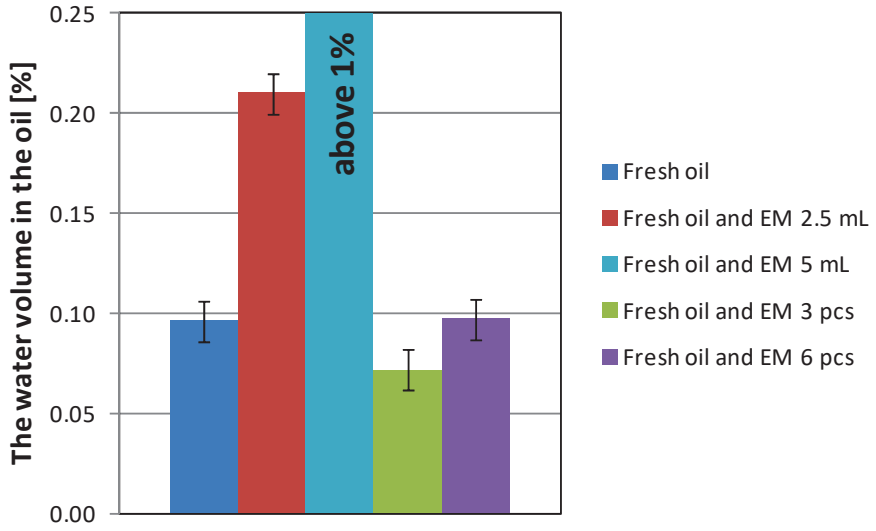


Figure 4. Water content in fresh oil and fresh oil with EMs in liquid form and ceramic tube form.

The situation was different with the addition of ceramic tubes, wherein the microorganisms are bound and do not mix with the oil as in their liquid form. In Figure 4, we can see that the addition of microorganisms, especially in a smaller amount (3 pcs), reduced the water content in the oil, which is positive from an oil exploitation point of view, while the greater number of tubes does not affect the water content of the oil in any significant way.

Figure 5 shows the color of the samples, and demonstrates that after adding microorganisms in a liquid form to the new oil, they became an oil–water emulsion and in this form were not suitable for use as a lubricating oil (there is probably some decomposition and release of water bound in the oil or a chemical reaction that resulted in the formation of such a large amount of water, which is related to the composition of the liquid additive of effective microorganisms).

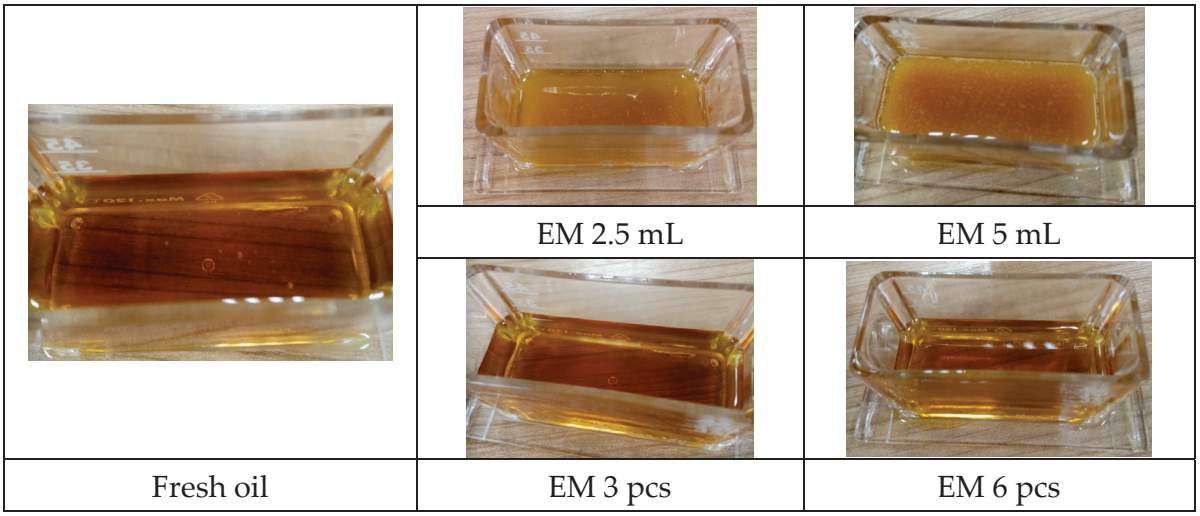


Figure 5. Coloring of fresh oil, with the addition of effective microorganisms in liquid form and ceramic tube form.

Silver compounds were also added to the new oil in amounts of 2.5 mL and 5 mL. In this case, it was not possible to read the results of the water content in the oil with the addition of both the first and the second type of silver for each amount, because after

prolonged operation, the titrator showed over-titration, i.e., the water content in the oil exceeded the measuring range of the device. The mixtures of oil with the addition of silver solution and colloidal nanosilver are presented in Figure 6.

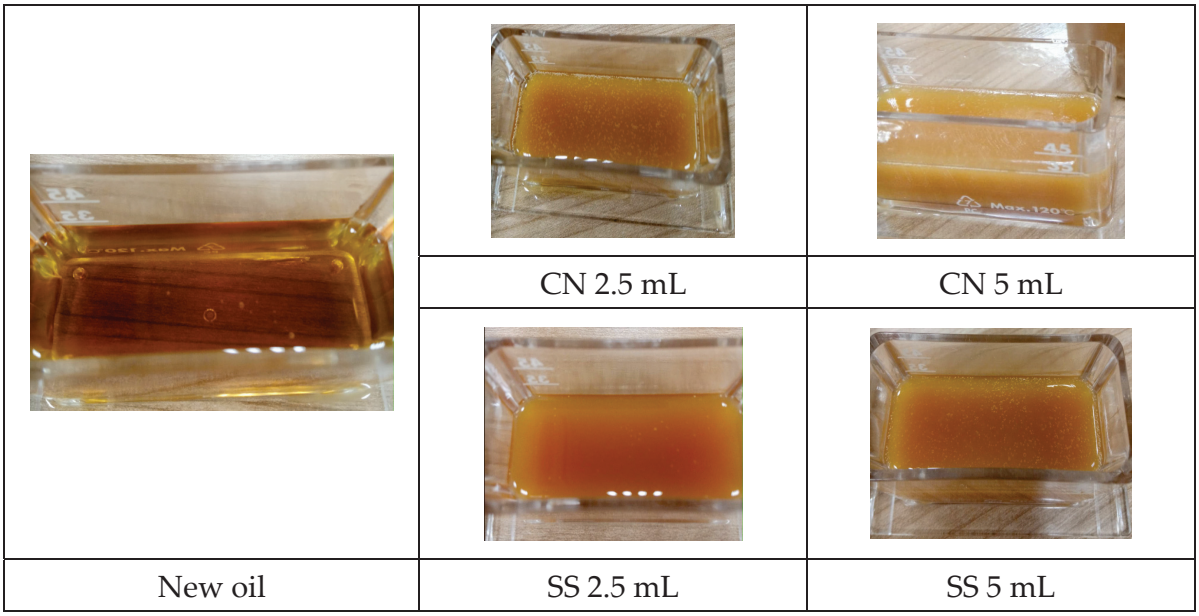


Figure 6. Coloring of new oil, with the addition of silver solution (SS) and colloidal nanosilver (CN) in liquid form.

These photos show that additives caused the formation of a water–oil emulsion. In this form, the lubricating oil will not properly perform the tasks for which it was intended. The milky appearance may be the outcome of Pickering emulsification [51–53], in which the bacteria and colloidal silver accumulate at the water–oil interface and prevent the water-in-oil droplets from coalescing. In the case of EMs, emulsification may also be caused by biosurfactants [54].

Figure 7 shows the flash point of fresh oil with the same additives as for the water content test. As in the case of the water content results, the best value of the flash point was obtained for three picks of ceramic-based effective microorganisms. The flash point was similar to new oil without additives. The remaining samples achieve results in a similar range of approximately 200 °C, which disqualifies them; due to safety reasons, the flash point should have the highest possible value.

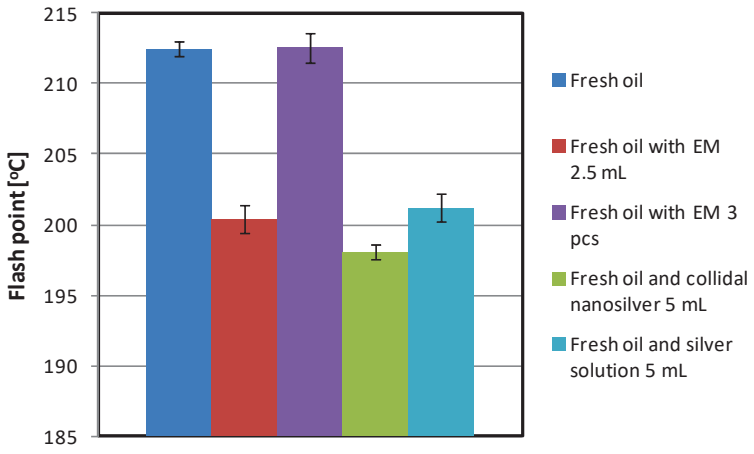


Figure 7. Flash point for oil with effective microorganisms (EM), colloidal nanosilver (CN), and silver solution (SS).

Statistical analysis was performed for a significance level of 95%. The obtained results for the water content and the flash point for the new oil and the new oil with additives for this significance level do not show any significant errors, because they fall within the lower and upper confidence intervals.

In order to confirm the obtained results, the article also presents a graph of viscosity versus temperature (Figure 8). In this diagram we can see that the curve of viscosity versus temperature for oil with the ceramic tubes is very similar to the curve for new oil without additives. On the other hand, the highest viscosity, which differs significantly from the viscosity of the oil without any additives, is of the oil with 2.5 mL of EM. Viscosity is 720 mPa·s at approximately 2 °C, which is similar to that of used oil 6, for which the viscosity at this temperature is 719 mPa·s. Other additives, including silver compounds, also increase the viscosity of the oil, but not as much as liquid effective microorganisms.

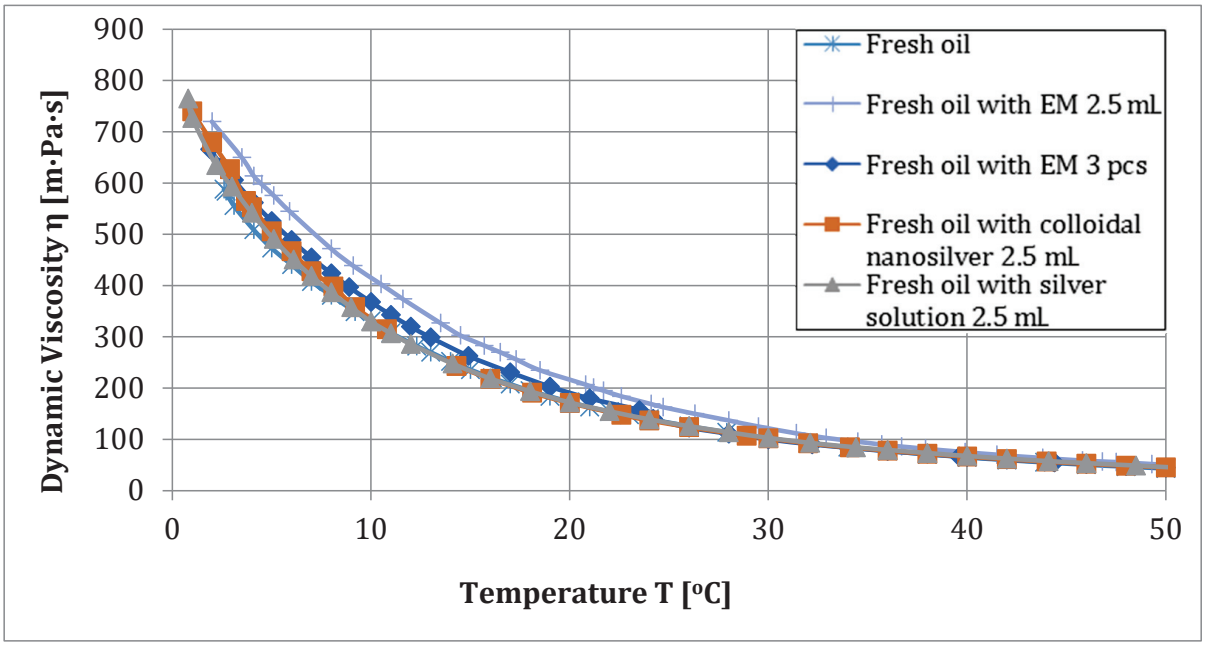


Figure 8. Viscosity for oil samples with the addition of effective microorganisms (EM), colloidal nanosilver (CN), and silver solution (SS).

Although effective microorganisms contain molasses, which is rich in sugar, no adverse effects on the rheology of the engine oil have been observed. At this stage, the dynamic viscosity was measured with a vibration viscometer. The obtained results demonstrate that the addition of ceramic effective microorganisms is more effective in new oil, whereas their liquid form is more effective in used oil. This should be confirmed by future research, and the effect of additives on the elemental composition of the oil and investigation into whether rheological shear thinning is evident are other potential areas of research. These tests will check whether molasses has a negative effect on the performance of the engine oil.

Figure 9 shows the water content in used oil (additives were added after using the oil). The chart compares the water content of oil without additives with that of oil that has been mixed with effective microorganisms and silver compounds. For a better illustration, the graph also shows the result for new oil. From this figure, we can see that for used oil the water content is approximately 0.17%, while for liquid microorganisms in a quantity of 2.5 mL, this amount is 0.6%, and for 5 mL, the result was not obtained due to over-titration, as was the case with new oil. This means that the water content was above the measuring range. As for new oil, the situation was different for microorganisms in a ceramic tube form. The water content for three ceramic tubes was about 0.02%, for six tubes it was 0.05%, while for new oil the water content was 0.09%. The addition of silver, regardless its

type and amount, is also not possible to present on the graph due to over-titration, i.e., the amount of water with these additives was above 1%.

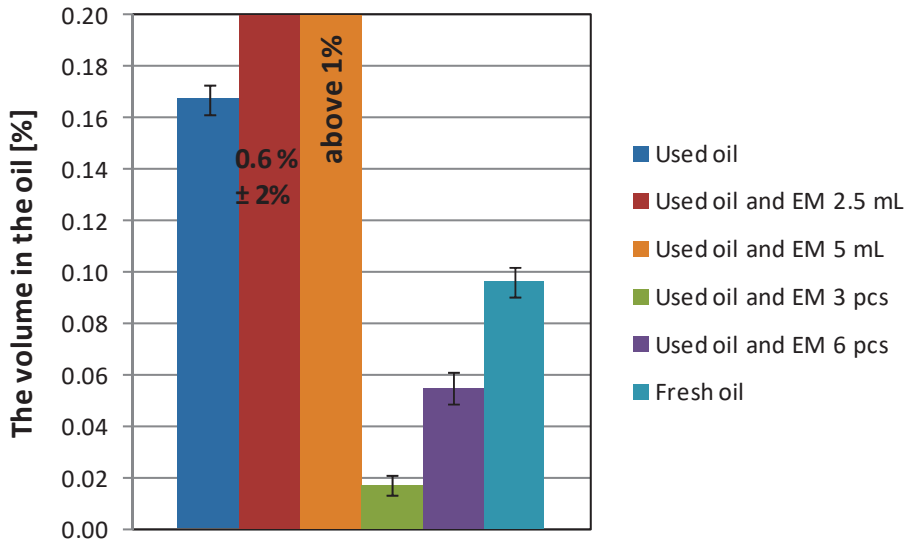


Figure 9. Water content in used oil and used oil with effective organisms in liquid form and ceramic tubes.

Similarly to new oil, in this case the lowest water content was obtained with the addition of EMs in the form of ceramic tubes, in a smaller quantity. Previous research [55–57] also shows that better parameters for used oil are obtained by adding EMs in liquid form. An example is the flash point shown in Figure 9. Moreover, Tables 2–5 show a comparison between the parameters of fresh and used oil without additives, and those in which the additives of effective microorganisms and silver compounds were added. Furthermore, analyzing the data from the tables, it can be concluded that the best additive for new oil is the ceramic tube form of effective microorganisms, and for waste oil, the addition of liquid effective microorganisms works best. As for the silver solutions, they adversely affect the parameters of both new and used oil. All the presented results confirm the obtained results, which show that microorganisms in the shape of ceramic tubes fulfill their role better in new oil, compared to in liquid form in used oil. Colloidal silver deteriorates the properties of both new and used oil, regardless of its type.

Table 2. Comparison of the parameters of new oil with and without effective microorganisms.

	Dynamic Viscosity in 2 °C	Flash Point	Acid Number	Base Number	Water Content
	[m·Pa·s]	[°C]	[mgKOH/g]	[mgKOH/g]	[%]
Fresh oil	596	212.4	2.560	3.907	0.096
Fresh oil and EM 2.5 mL	720	200.4	3.021	3.606	0.210
Fresh oil and EM 5 mL	713	199.6	2.497	3.444	above 1
Fresh oil with EM 3 pcs	667	212.5	3.113	3.962	0.072
Fresh oil with EM 6 pcs	696	213.5	2.366	3.894	0.097

In regards to the flash point shown in Figure 10, better results were also obtained for used oil with effective microorganisms than for those with additional silver compounds. The higher flash point of approximately 202 °C was obtained for effective microorganisms in the liquid form. The remaining additives have a flash point temperature below that of used oil, i.e., approximately 199 °C.

Table 3. Comparison of the parameters of fresh oil without additives with fresh oil with the addition of colloidal nanosilver and silver solution.

	Dynamic Viscosity in 2 °C	Flash Point	Acid Number	Base Number	Water Content
	[m·Pa·s]	[°C]	[mgKOH/g]	[mgKOH/g]	[%]
Fresh oil	596	212.4	2560	3.907	0.096
Fresh oil and colloidal nanosilver 2.5 mL	686	200.4	2.668	3.604	above 1
Fresh oil and colloidal nanosilver 5 mL	742	198.4	2.659	3.751	above 1
Fresh oil and silver solution 2.5 mL	698	206.9	2.682	3.479	above 1
Fresh oil and silver solution 5 mL	736	201.2	2.660	3.731	above 1

Table 4. Comparison of the parameters of used oil without additives with waste oil with effective microorganisms.

	Dynamic Viscosity in 2 °C	Flash Point	Acid Number	Base Number	Water Content
	[m·Pa·s]	[°C]	[mgKOH/g]	[mgKOH/g]	[%]
Used oil	719	198.8	4.027	1.358	0.167
Used oil and EM 2.5 mL	580	202.4	4.373	0.937	0.606
Used oil and EM 5 mL	758	202.1	5.411	0.844	above 1
Used oil with EM 3 pcs	732	197.5	6.027	1.250	0.017
Used oil with EM 6 pcs	652	198.1	5.499	0.749	0.054

Table 5. Comparison of the parameters of waste oil without additives and waste oil with the colloidal nanosilver and silver solution.

	Dynamic Viscosity in 2 °C	Flash Point	Acid Number	Base Number	Water Content
	[m·Pa·s]	[°C]	[mgKOH/g]	[mgKOH/g]	[%]
Used oil	719	198.8	4.027	1.358	0.167
Used oil and colloidal nanosilver 2.5 mL	712	186.2	2.668	1.350	above 1
Used oil and colloidal nanosilver 5 mL	758	194.0	2.659	1.402	above 1
Used oil and silver solution 2.5 mL	796	191.6	2.682	1.037	above 1
Used oil and silver solution 5 mL	806	197.6	2.660	1.199	above 1

In regards to the fresh oil, statistical analysis was performed with a 95% significance level for used oil. The obtained results for water content and flash point for used oil and used oil with additives for this significance level also showed no significant errors and fell within the lower and upper confidence interval.

Similarly, from the graph of viscosity versus temperature (Figure 11), it can be seen that better results are obtained for effective microorganisms, also in liquid, because at the 2.5 mL for 2 °C, the viscosity is 588 mPa·s. This means that this value was lowered to a level similar to that of new oil, for which the viscosity is 596 mPa·s at the same temperature. For example, for colloidal nanosilver in a quantity of 2.5 mL, a viscosity of 1050 at 3.5 °C

was obtained, while the viscosity of the oil used at this temperature was 645 mPa·s. This means that the best additive to improve the properties of used oil is microorganisms in liquid form.

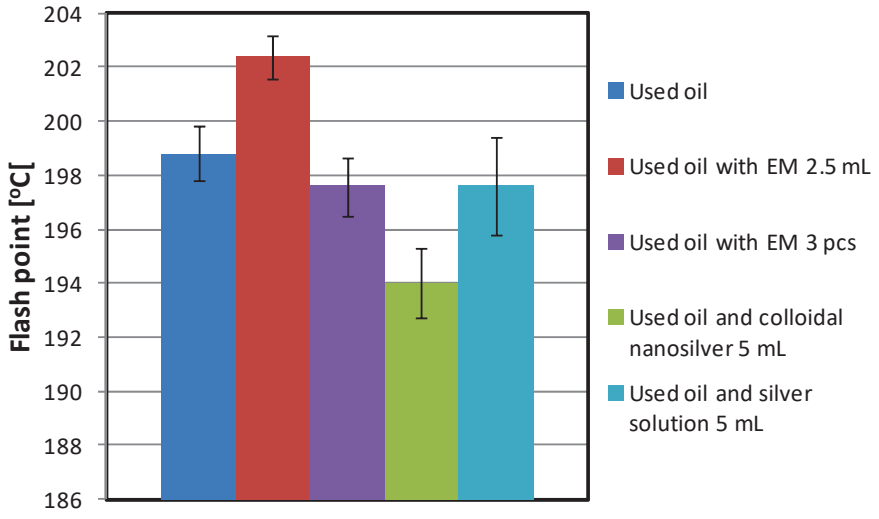


Figure 10. Oil flash point of waste oil and waste oil with effective microorganisms (EM), colloidal nanosilver (CN), and silver solution (SS).

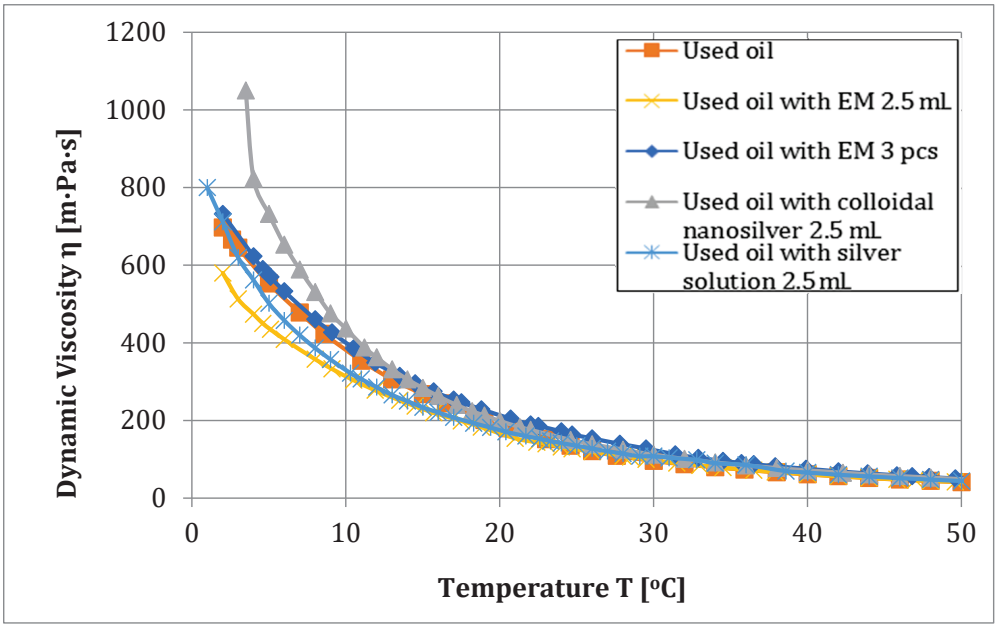


Figure 11. Comparison of viscosity of samples of used oil with and without the addition of effective microorganisms (EM), colloidal nanosilver (CN), and silver solution (SS).

5. Conclusions

In this paper, the influence of various environmentally friendly additives on the water content of lubricating oil was presented.

For fresh oil, the water content was 0.096%. Liquid effective microorganisms in a quantity of 2.5 mL, taken from a 1 L package, resulted in a more than twofold increase in the water content in the oil, while 5 mL of the solution of effective microorganisms resulted in the over-titration of the device, i.e., the water content exceeded 1%.

Silver solution and colloidal nanosilver in amounts of 2.5 mL and 5 mL were also added to the fresh oil. In this case, it was not possible to read the result of the water content in the oil for both the first and the second type of silver and for each amount, because after

prolonged operation the titrator showed over-titration, i.e., the water content in the oil exceeded the measuring range of the device. The reason for this is also too much water in the additive itself, which is a silver solution.

The situation is different for the addition of EM ceramic tubes, wherein which the microorganisms are bound in the clay and there is no water in the composition of the ceramic tube. Ceramic tubes in an amount of three pieces reduced the water content in the new oil, which may have a good effect on the parameters of the oil, as it will cause the subsequent deterioration of the properties of the oil operating in the internal combustion engine. As can be seen from the charts obtained, an increase in the number of ceramic tubes did not result in a further reduction of the water content, so in further research it is worth examining what parameters would be obtained with fewer than three tubes.

The analysis of the water content graphs for used oil with and without the addition of effective microorganisms, colloidal nanosilver, and silver solution show that the effect of additives presents similar results to those of new oil.

In the used oil, the water content was about 0.17%, while for microorganisms in liquid form added to the oil in an amount of 2.5 mL, the water content was 0.6%; for 5 mL the result was not obtained due to excessive titration. The same was the case with fresh oil. This means that the water amount was above the measuring range. The water content for three ceramic tubes was about 0.02%, for six tubes it was 0.05%, and for fresh oil the water content was 0.09%. The addition of silver, regardless of its type and amount, resulted in an amount of water greater than 1%.

To conclude, in practice the most effective and recommended type of engine oil treatment is the use of effective microorganisms in the form of ceramic tubes. In future research, the influence on the parameters of the oil will be investigated with a smaller number of ceramic tubes, which will then be used within the internal combustion engine, in conditions similar to real ones. This will make it possible to verify the current research and more precisely determine which additives may be better used to ameliorate the parameters of the engine oil.

Funding: This research received no external funding.

Institutional Review Board Statement: Not applicable.

Informed Consent Statement: Not applicable.

Data Availability Statement: The data used to support the finding of this study are available from the corresponding author upon request.

Conflicts of Interest: The author declares no conflict of interest.

Nomenclature

ACE	Automatic Error Compensation
ACF	Activated Carbon Fiber
DNA	Deoxyribonucleic Acid
EM	Effective Microorganisms
HTHS	High Temperature High Shear Rate
SAE	Society of Automotive Engineers
SS	Silver solution
CN	Colloidal nanosilver

References

1. Duda, A. Problems of microbial contamination in the distribution and storage of petroleum fuels. *Oil-Gas* **2002**, *58*, 160–167. (In Polish)
2. Janda, K. Microbiological contamination of fuels. *Adv. Microbiol.* **2005**, *44*, 157–169. (In Polish)
3. Du, Y.; Wu, T.; Gong, R. Properties of water-contaminated lubricating oil: Variation with temperature and small water content. *Tribol.-Mater. Surf. Interfaces* **2017**, *11*, 1–6. Available online: https://www.tandfonline.com/doi/abs/10.1080/17515831.2017.1279845 (accessed on 12 July 2022). [CrossRef]

4. Fass, R.; Ben-Asher, J.; Shavit, A.B. Effects of microbial contamination in storage tanks on the long-term stability of jet fuel. In Proceedings of the 2nd International Conference on Long-Term Storage Stabilities of Liquid Fuels, San Antonio, TX, USA, 29 July–1 August 1986; pp. 253–263.
5. Vidal-Verdú, À.; Gómez-Martínez, D.; Latorre-Pérez, A.; Peretó, J.; Porcar, M. The car tank lid bacteriome: A reservoir of bacteria with potential in bioremediation of fuel. *NPJ Biofilms Microbiomes* **2022**, *8*, 32. [CrossRef]
6. Zhang, J.; Luo, H.; Yin, X.; Shi, Y.; Zhang, Y.; Tan, L. Surface coating on aluminum substrate with polymeric guanidine derivative to protect jet fuel tanks from microbial contamination. *Surf. Coat. Technol.* **2021**, *422*, 127521. [CrossRef]
7. Gaylarde, C.C.; Bento, F.; Kelley, J. Microbial contamination of stored hydrocarbon fuels and its control. *Rev. Microbiol.* **1999**, *30*, 1–10. Available online: https://www.scielo.br/j/rm/a/YTvpcRy9YY8V5WgzHjBTnhP/?format=pdf&lang=en (accessed on 12 July 2022). [CrossRef]
8. Turkiewicz, A. The Role of Microorganisms in the Oil and Gas Industry. *Ochr. Środowiska* **2011**, *13*, 227–240.
9. Passman, F.J. Microbial contamination and its control in fuels and fuel systems since 1980—A review. *Int. Biodeterior. Biodegrad.* **2013**, *81*, 88–104. Available online: https://www.sciencedirect.com/science/article/pii/S0964830512002120 (accessed on 12 July 2022). [CrossRef]
10. Higa, T. Effective microorganisms—Technology of the 21st century. In Proceedings of the Effective Microorganisms in the World, London, UK, 23 July 2005.
11. Higa, T. *A Revolution in Protecting Our Planet*; Foundation for Development of the Warsaw University of Life Sciences: Warsaw, Poland, 2003. (In Polish)
12. Kolasa-Więcek, A. Will effective microorganisms revolutionize the world? *Adv. Food Process. Technol.* **2010**, *1*, 66–69. Available online: http://yadda.icm.edu.pl/baztech/element/bwmeta1.element.baztech-article-BPL2-0021-0030 (accessed on 30 August 2022). (In Polish)
13. Mayer, J.; Scheid, S.; Widmer, F.; Fließbach, A.; Oberholzer, H.-R. How effective are 'Effective microorganisms® (EM)'? Results from a field study in temperate climate. *Appl. Soil Ecol.* **2010**, *46*, 230–239. [CrossRef]
14. Rizwan, S.A.; Khan, H.; Bier, T.A.; Adnan, F. Use of Effective Micro-organisms (EM) technology and self-compacting concrete (SCC) technology improved the response of cementitious systems. *Constr. Build. Mater.* **2017**, *152*, 642–650. [CrossRef]
15. Morones-Ramirez, J.R.; Winkler, J.A.; Spina, C.S.; Collins, J.J. Silver enhances antibiotic activity against Gram-negative bacteria. *Sci. Transl. Med.* **2013**, *5*, 190ra81. [CrossRef]
16. Dzikowska, A.; Gościańska, J.; Nowak, I. Synthesis, physicochemical properties and applications of silver nanoparticles in cosmetics. In *Cosmetics—Chemicals for the Body*; Cursiva Publisher: Kostrzyń, Poland, 2011; pp. 163–182. (In Polish)
17. Available online: https://www.mydelkoznanosrebrem.pl/nanosrebro.php (accessed on 12 July 2022). (In Polish)
18. Aluyor, E.O.; Ori-jesu, M. Biodegradation of mineral oils—A review. *Afr. J. Biotechnol.* **2009**, *8*, 915–920. Available online: http://www.academicjournals.org/AJB (accessed on 12 July 2022).
19. Feyisayo, V.A. Crude Oil Contaminated Water Treatment: Development of Water Filter from Locally Sourced Materials. *Procedia Manuf.* **2017**, *7*, 465–471. Available online: https://www.sciencedirect.com/science/article/pii/S2351978916302025 (accessed on 12 July 2022).
20. Demello, J.A.; Carmichael, C.A.; Peacook, E.E. Biodegradation and environmental behavior of biodiesel mixtures in the sea: An initial study. *Mar. Pollut. Bull.* **2007**, *54*, 894–904. Available online: https://pubmed.ncbi.nlm.nih.gov/17481669/ (accessed on 12 July 2022). [CrossRef] [PubMed]
21. Farah, M.A.; Oliveira, R.C.; Caldas, J.N.; Rajagopal, K. Viscosity of water-in-oil emulsions: Variation with temperature and water volume fraction. *J. Pet. Sci. Eng.* **2005**, *48*, 169–184. Available online: https://www.sciencedirect.com/science/article/abs/pii/S0920410505001129 (accessed on 12 July 2022). [CrossRef]
22. Niewczas, A.; Wrona, J.; Wrona, R. Contamination of the lubricating oil and their influence on the durability of the internal combustion engine. *Buses Technol. Oper. Transp. Syst.* **2010**, *11*, 6. Available online: http://yadda.icm.edu.pl/baztech/element/bwmeta1.element.baztech-article-BWAK-0037-0042 (accessed on 12 July 2022). (In Polish)
23. Nowak, P.; Kucharska, K.; Kaminski, M. Ecological and Health Effects of Lubricant Oils Emitted into the Environment. *Int. J. Environ. Res. Public Health* **2019**, *16*, 3002. Available online: https://www.ncbi.nlm.nih.gov/pmc/articles/PMC6720566/ (accessed on 12 July 2022). [CrossRef] [PubMed]
24. Available online: https://www.ecol.com.pl/pl/zanieczyszczenie-oleju-woda-i-metody-jej-usuwania-artykul/ (accessed on 12 July 2022). (In Polish)
25. Das, N.; Chandran, P. Microbial Degradation of Petroleum Hydrocarbon Contaminants: An overview. *Biotechnol. Res. Int.* **2011**, *2011*, 13. Available online: https://pubmed.ncbi.nlm.nih.gov/21350672/ (accessed on 12 July 2022). [CrossRef] [PubMed]
26. Lasocki, J.; Karwowska, E. The impact of microorganisms in the environment of diesel oil and biodiesel on the fuel system of vehicles powered by self-ignition engines. *Automot. Arch.* **2010**, *3*, 167–183. Available online: http://yadda.icm.edu.pl/baztech/element/bwmeta1.element.baztech-article-BGPK-3062-2091 (accessed on 12 July 2022). (In Polish)
27. Robbins, J.A.; Levy, R. A review of the microbiological degradation of fuel. *Dir. Microbicides Prot. Mater.* **2005**, 177–201. Available online: https://link.springer.com/content/pdf/10.1007%2F1-4020-2818-0_11.pdf (accessed on 12 July 2022).
28. Zyska, B. Microbiological Decomposition and Corrosion of Technical Materials. Technical Microbiology. conference materials. Lodz University of Technology, Lodz, Polish, 2000. (In Polish)
29. Available online: https://badania-olejow.pl/zanieczyszczenie-oleju-woda/ (accessed on 12 July 2022). (In Polish)

30. Available online: https://dieselship.com/marine-technical-articles/motor-engineering-knowledge/microbial-degradation-of-lubricating-oils-onboard/ (accessed on 12 July 2022).
31. Maduka, C.M.; Okpokwasili, G.C. Microbial growth in brake fluids. *Int. Biodeterior. Biodegrad.* **2016**, *114*, 31–38. [CrossRef]
32. Fregolente, P.B.L.; Fregolente, L.V.; Wolf-Maciel, M.R. Water Content in Biodiesel, Diesel, and Biodiesel–Diesel Blends. *J. Chem. Eng. Data* **2012**, *57*, 1817–1821. [CrossRef]
33. Dealtry, S.; Ghizelinib, A.M.; Mendonça-Hagler, L.C.S.; Chaloubd, R.M.; Reinert, F.; de Campos, T.M.P.; Gomes, N.C.M.; Smallag, K. Petroleum contamination and bioaugmentation in bacterial rhizosphere communities from Avicennia schaueriana. *Environ. Microbiol.* **2018**, *49*, 757–769. Available online: https://www.ncbi.nlm.nih.gov/pmc/articles/PMC6175736/ (accessed on 12 July 2022). [CrossRef]
34. Kulkarni, S.J. Biological treatment of petroleum wastewater: A review on research and studies. *Int. J. Pet. Petrochem. Eng.* **2016**, *2*, 17–21. Available online: https://www.arcjournals.org/ijppe/volume-2-issue-2/4 (accessed on 12 July 2022).
35. Kvenvolden, K.A.; Cooper, C.K. Natural seepage of crude oil into the marine environment. *Geo-Mar. Lett.* **2003**, *23*, 140–146. Available online: https://link.springer.com/article/10.1007/s00367-003-0135-0 (accessed on 12 July 2022). [CrossRef]
36. Sander, J. *Water Contamination: Management of Water during the Lubricant Life Cycle*; Lubrication Engineers Corp.: Wichita, KS, USA, 2009. Available online: https://docplayer.net/21508315-Water-contamination-management-of-water-during-the-lubricant-life-cycle.html (accessed on 12 July 2022).
37. Available online: https://www.ucando.pl/blog/olej-samochodowy-5w30-cos-dla-kierowcow-z-lekka-noga-ceniacych-sobie-ekonomike-jazdy-oraz-jej-wplyw-na-ochrone-srodowiska/ (accessed on 12 July 2022). (In Polish)
38. Available online: https://incar.pl/baza-wiedzy/olej-silnikowy-5w30-czym-sie-charakteryzuje,ranking.html (accessed on 12 July 2022). (In Polish)
39. Available online: https://www.aptekarzpolski.pl/2015/01/01-2015-technologia-efektywnych-mikroorganizmow/ (accessed on 12 July 2022). (In Polish)
40. Schicht, M.L. To understand EM. *EMECHO* **2008**, *8*, 3.
41. Available online: https://emsustains.co.uk/EM-ceramics.html (accessed on 12 July 2022).
42. Available online: https://falaem.pl/rurki-ceramiczne-uzdatnianie-wody (accessed on 12 July 2022). (In Polish)
43. Available online: https://www.ecoshop.com.pl/mikroorganizmy/3556-greenland-em-melasa-1l-5907738935220.html (accessed on 12 July 2022). (In Polish)
44. Kim, J.S.; Kuk, E.; Yu, K.N.; Kim, J.H.; Park, S.J.; Lee, H.J.; Kim, S.H.; Park, Y.K.; Park, Y.H.; Hwang, C.Y.; et al. Antimicrobial effects of silver nanoparticles. *Nanomed. Nanotechnol. Biol. Med.* **2007**, *3*, 95–101. Available online: https://www.sciencedirect.com/science/article/pii/S1549963406003467?casa_token=J6KTF9cUdVIAAAAA:xFmuaoDImoQCz6K3_fJyRoRWNKrLKwo8paA-s2seeKTkHO1I33Ah2nXcHHK_TCot3a3SzW526iCO (accessed on 12 July 2022). [CrossRef]
45. Available online: https://cen.acs.org/articles/93/web/2015/07/Antimicrobial-Silver-Nanoparticles-Strengthen-Bacterial.html (accessed on 12 July 2022).
46. Mirzajani, F.; Ghassempour, A.; Aliahmadi, A.; Esmaeili, M.A. Antibacterial effect of silver nanoparticles on Staphylococcus aureus. *Res. Microbiol.* **2011**, *162*, 542–549. [CrossRef]
47. Available online: https://auraherbals.pl/blog/srebro-koloidalne-jak-wybrac-prawdziwe-i-nie-dac-sie-oszukac/ (accessed on 12 July 2022).
48. Available online: https://allegro.pl/oferta/srebro-koloidalne-jonowe-ag-500ml-9929512556 (accessed on 12 July 2022).
49. Available online: https://enaturalnie.pl/argentum200-niejonowe-srebro-100-ppm-plyn-tonik-500-ml-aura-herbals_2838.html (accessed on 12 July 2022).
50. Available online: https://archive-resources.coleparmer.com/Manual_pdfs/94101-00.pdf (accessed on 12 July 2022).
51. Binks, B.P. Particles as surfactants—Similarities and differences. *Curr. Opin. Colloid Interface Sci.* **2002**, *7*, 21–41. [CrossRef]
52. Kapellos, G.E. Microbial strategies for oil biodegradation. In *Modeling of Microscale Transport in Biological Processes*; Academic Press: Cambridge, MA, USA, 2017; pp. 19–39. [CrossRef]
53. Valdivia-Rivera, S.; Ayora-Talavera, T.; Lizardi-Jiménez, M.A.; García-Cruz, U.; Cuevas-Bernardino, J.C.; Pacheco, N. Encapsulation of microorganisms for bioremediation: Techniques and carriers. *Rev. Environ. Sci. Bio/Technol.* **2021**, *20*, 815–838. [CrossRef]
54. Geetha, S.J.; Banat, I.M.; Joshi, S.J. Biosurfactants: Production and potential applications in microbial enhanced oil recovery (MEOR). *Biocatal. Agric. Biotechnol.* **2018**, *14*, 23–32. [CrossRef]
55. Krakowski, R. Research on the effect of the effective microorganisms, silver solution and colloidal nanosilver addition on the engine oil acid number (TAN). *Combust. Engines* **2021**, *186*, 59–63. Available online: http://www.combustion-engines.eu/Research-on-the-effect-of-the-effective-microorganisms-silver-solution-and-colloidal,140730,0,2.html (accessed on 12 July 2022). [CrossRef]

56. Krakowski, R. Research on the effect of the effective microorganisms, silver solution and colloidal nanosilver addition on the engine oil base number (TBN). *Combust. Engines* **2021**, *187*, 8–11. Available online: http://www.combustion-engines.eu/Research-on-the-effect-of-the-effective-microorganisms-silver-solution-and-colloidal,140112,0,2.html (accessed on 12 July 2022). [CrossRef]
57. Krakowski, R. Research into the effects of the effective microorganisms addition on the engine oil viscosity. *J. KONES* **2019**, *26*, 105–112. Available online: https://kones.eu/ep/2019/vol26/no3/105-112_JOK_2019_NO.3_VOL.26_ISSN_1231-4005-KRAKOWSKI.pdf (accessed on 12 July 2022). [CrossRef]

coatings

MDPI

Article

Experimental Study on Performance of Local Bond-Slip Test of Steel Strand Tendons and Concrete

Rihua Yang [1,2], Yiming Yang [1,*], Xuhui Zhang [3,*] and Xinzhong Wang [1]

[1] School of Civil Engineering, Hunan City University, Yiyang 413000, China
[2] Hunan Engineering Research Center of Structural Safety and Disaster Prevention for Urban Underground Infrastructure, Hunan City University, Yiyang 413000, China
[3] School of Civil Engineering and Mechanics, Xiangtan University, Xiangtan 411105, China
* Correspondence: yangyiming@hncu.edu.cn (Y.Y.); xuhui.zhang@xtu.edu.cn (X.Z.)

Abstract: In order to study the bond-slip constitutive model between prestressed tendons and concrete, the pull-out tests of single-strand and multi-strands specimens are carried out. The effect of the number of prestressed tendons on the failure mode, slip characteristics and concrete strain of the pull-out specimens are analyzed, and the constitutive models of bond-slip between for single- strand and multi-strand tendons are also proposed. The results show that the bond mechanism between steel strand and concrete is basically similar to that of deformed steel bar, but the slip process of steel strand along the axis direction is accompanied by rotation phenomenon because it is twisted. Moreover, compared with the single-strand prestressed tendon, the average ultimate bond stress of each tendon of the three-strand prestressed tendons decreases by 13.2%. In addition, the calculated result of the pull-out limit load for the single-strand prestressed tendon is only 2% higher than the experimental value, while the corresponding value of three-strand prestressed tendon is only 3.74% lower than the experimental value. This means that the proposed bond-slip models for single- strand and multi-strand tendons have high reliability.

Keywords: prestressed concrete beam; steel strands; bond slip; experimental study;constructive model

1. Introduction

The effective bond between strand and concrete is the basis for the work of bonded prestressed concrete beams [1]. With the increase of service time of post-tensioned prestressed concrete (PTPC) structures, the long-term erosion of concrete by carbon dioxide and chlorine elements, as well as construction defects such as insufficient grouting, can lead to strand corrosion or even local fracture. For PTPC beams after local fracture of the strand, an effective bond between the strand and the concrete is the primary factor that allows it to continue to work properly. The prestressing tendons achieve secondary anchorage through the bond between them and the concrete [2,3]. Therefore, under the premise of the end anchorage failure of PTPC beam or the local prestressed tendon fracture, it is important to study the bond performance of multiple tendons in the prestressing tendon to accurately estimate the bearing capacity of the structure.

Some scholars have conducted experimental studies on the bonding performance of single strands and proposed a model for bonding performance measurement of single strands. Mohandoss [4] emphasized that the existing test methods to determine the bond strength in rebar-concrete systems cannot be used for strand-concrete systems, and the failure of strand-concrete depend on the failure of concrete keys, which is a function of shear strength of concrete and interlocking effects due to the helical shape of the strands. Franceschini [5] proposed a new constitutive law (CPS-model) to predict the mechanical behavior of prestressing strands induced by pitting corrosion. Wang [6] investigated the bond-slip property of high-strength stainless steel strand in engineered cementitious

composites (ECC) with tensile strength, steel strand diameter and relative anchorage length, and established the bond-slip relationship model between steel strand and ECC according to the improved BPE model. Dai [7] predicted the transfer length in pre-tensioned concrete beams according with corrosive cracking. Dyba [8,9] developed a finite element analysis method for bond stresses in prestressing tendons. However, most of the above research only focused on single prestressed reinforcement. The bond mechanism between multi-bar prestressed steel strands and concrete is not clear, and the corresponding bond-slip model has not been proposed.

It is different from the single prestressing tendon that the bond performance at the interface between the prestressing bundle and the compression slurry is inevitably influenced by the interaction of the individual tendon. As a result, the bonding behavior of prestressing bundles as a combination of multiple prestressing tendons is more complex. In view of the above problems, some scholars have gradually paid attention to the effect of the number of prestressed steel strands on the bond-slip performance. Zghayar [10] found that the bond performance between the prestressing bundle and the compression slurry is greatly influenced by the number of prestressing forces as well as the arrangement density. For prestressing FRP tendons, Zhang [11] found a non-uniform bonding force problem between the interface of multiple force tendons and the compression slurry. Wu [12] investigated the effect of temperature on bond strength and found that the bond strength deteriorated with a rise in temperature and the degradation of bond strength was more severe than that of other mechanical properties. Zhu [13] studied the influence laws of spacing between transverse stainless-steel strand, diameter of longitudinal stainless-steel strand and relative anchorage length on the bond properties of steel strand in ECC. The test results show that the bond failure can be transformed from brittle failure to ductile failure by adding the transverse steel strands. Mei [14] studied the bond-slip behavior of CFRP tendons inside anchors and multiaxial stresses of the steel sleeve, and the test results shown that bond-slip relationship of CFRP tendon inside anchor is nonlinear. Most of the above studies focus on prestressed steel tendons not used for bridges, which leads to doubts about the applicability of existing conclusions in ordinary PC structures. Therefore, it is urgent to study the bond performance between multi-bar prestressed steel strands and concrete.

The main purpose of this paper is to study the bonding performance between multi-bar prestressed tendons and concrete. First, the pull-out test of single-strand and multi-strands specimens are carried out. Next, the effect of the number of prestressed tendons on the damage mode, specimen slip characteristics and concrete strain is analyzed, and the bond mechanism of multi strand tendons is also revealed. Finally, the local bond-slip constructive model for single-bar and multi-strand tendons are further established, and the effectiveness of the above model is also verified. Among them, studying the bond mechanism of multi-bar prestressed tendons and proposing a bond-slip constructive model for multi-bar prestressed tendons are the novelties of this paper.

2. Test Introduction

2.1. Specimen Design

Two pull-out specimens, numbered as PLS1 and PLS2, are designed in this test according to the specification of JTG 3362-2018 [15]. The section forms of the above specimens are set as rectangle to match the actual rectangular beam. To avoid splitting failure of the two specimens, the lengths of specimens are designed as 1000 mm, and the ratio between the concrete cover and the diameter of steel strand are set to be greater than 5. In addition, the cross-sectional dimensions of the two specimens are set as 300 mm $\times$ 500 mm according to the commonly used size range of rectangular section. PLS1 is a single-bar specimen for comparison and its prestressed bar is a single 7-wire twisted steel strand of Φ15.2. PLS2's prestressed bars are three 7-wire twisted steel strands of Φ15.2. Eight HRB400 deformed bars with Φ12 mm is configured longitudinally as erection bars, and the HPB235 plain round bars with Φ8 mm is selected as stirrups with a spacing of 100 mm. The steel strands

are placed in the center of the specimen section. The detailed dimension and reinforcement layout of these specimens are as shown in Figures 1 and 2.

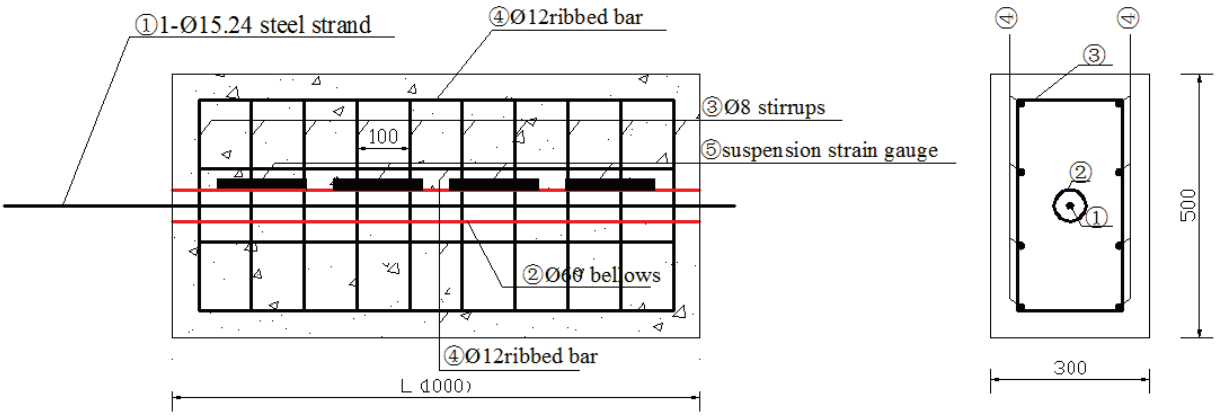


Figure 1. Dimension and reinforcement of specimen PLS1.

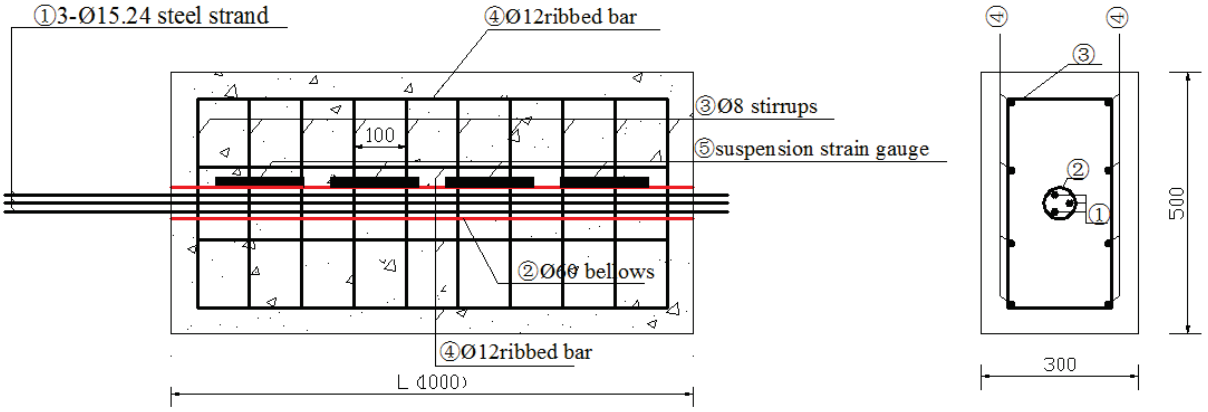


Figure 2. Dimension and reinforcement of specimen PLS2.

The HRB 400-grade ribbed bars with a diameter of 16mm and 10mm are arranged in the tension area and compression area, respectively. The HPB235 plain round bars with a diameter of 8 mm is selected as stirrups. The 1860-grade 7-wire steel stands with a diameter of 15.2 mm is adopted as the prestressed steel bars. The yield strength, limit strength, elasticity modulus, and elongation of the above reinforcement and steel strand have been tested according to the specification of GB/T228.1-2021 [16] and the test method used in Wang et al. [17], and the test results are shown in Table 1.

Table 1. Mechanical properties of steel bars.

Diameter (mm)	Yield Strength (MPa)	Limit Strength (MPa)	Elasticity Modulus (GPa)	Elongation (%)
15.2	1830	1915	190	14.3
12	475.6	611.6	200	14.5
8	265.8	365.9	210	15.3

The concrete specimens are manufactured using C425 ordinary silicate cement. The natural river sand is used as fine aggregate, the graded gravel is used as coarse aggregate with a maximum nominal particle size of 25 mm, and the tap water mixed from the laboratory is used. The mix proportion of specimens is cement: sand: gravel: water = 1:1.62:2.73:0.44. The mortar is the commercial cement paste of the same grade as concrete, and the tension stress of sand-steel strand is 1395 MPa. Material properties of the steel strands and the ordinary

steel bars are shown in Table 1. The two test components are cast with the same batch of concrete at one time, so the concrete compression strength of each specimen is the same. The standard cube specimen is made of the same batch of concrete and cured together with the test components. The average compressive strength of concrete in 28 days is 56.5 MPa.

2.2. Test Devices and Monitoring Point Arrangement

According to the test rules of the bond stress between concrete and steel strands, draw-off gear is self-designed. After the test components are completed, a center hole jack with a range of 150 tons is used for tensioning and the pull-out force is measured by rope meter.

Since the steel strands in the test are made by twisting seven wires, the axis of the steel strands cannot be slotted, or strain gauge cannot be pasted on their surface to monitor the strain of the steel strands because of the twisting angle. Therefore, suspension strain gauges are placed at the outer wall of the corrugated pipes with a spacing of 17.5 cm in order to monitor the strain of concrete and calculate strain distribution and real-time bond length of the steel strands. In the test, free end and loading end of the specimens are both installed with a dial indicator to record the relative slippage between steel strands and concrete. Distribution of the strain gauges and the devices for the pull-out test are shown in Figure 3.



Figure 3. Devices for the pull-out test.

Pre-tensioning is carried out before formal tensioning to eliminate inelastic deformation between test devices, and the pre-tensioning force is set as 5 kN. After that, a step-by-step loading method is adopted here. The initial loading is 5kN for each stage, and the load for each stage is adjusted to 15 kN after reaching 15 kN. When the steel strand is pulled out or broken, as well as the slip at the loading end is large and the load cannot continue to increase or the increment is very small, the specimen is considered as bond slip failure. That is, the pull-out test has been completed.

3. Test Results and Analysis

3.1. Damage Mode

In the test process, PLS1 and PLS2 are both strand fractures, and when the two specimens reached 1000 mm, they both have sufficient bond lengths. The maximum bond strength of the steel strands provided by concrete is larger than the ultimate tensile strength of the strands.

For PLS1 steel strand, its slippage at the free end is close to zero, almost nonexistent. All steel wires of PLS1 steel strand are basically broken at the same time, and there is no splitting failure of concrete or overall pull-out of steel strand. However, the increase rate of the slippage at the tension end of PLS2 steel strand is much faster than that of PLS1 steel strand, and the slippage at the free end also increased rapidly. Finally, the steel strand is necked and then pulled to failure, as shown in Figure 4. Neither of the two specimens has splitting failure, so it can be considered that the specimens have sufficient thickness of protective layer.



Figure 4. Steel strand pull-off damage.

3.2. Slip Performance under Load

In the pull-out test, the steel strands slipped in a way that is not consistent with that of ordinary deformed steel bars and twisted along the steel strands. This is similar to the screw-out mode of a long stud, namely, the spiral slippage. The reason should be related to the fact that the steel strands are formed in a twisted way, so the strands slipped not only in a linear way but also a rotary way, which is similar to long studs and the pitch should be the distance of twist. This proves that the twisted steel strands slipped through the concrete in a way such as removing a stud along the nut. However, different from the greater ductility of the real nuts are made of metal materials, concrete nuts are made of fragile materials and their threads are easier to break, which results in the weakened rotational confinement effect and further the direct slippage between the steel strands and concrete. Meanwhile, with the increase of load, after each rotary slippage, the load will decrease to a certain extent. As the load continues to be increased, the undamaged concrete threads will work again, and then the load will continue to be increased, resulting in a sawtooth shape on the load-slip curve. The concrete that occurred and worked as nuts was of fragile material, and its thread is easily damaged by twisted wires of the steel strands. The total slippage of the steel strands is composed of linear slippage and rotary slippage. The linear slippage means the slippage of the steel strands in their direct pull-out along the axis, while rotary slippage means the slippage at an end during the strand rotation. Therefore, the bond and cementation effect are gradually destroyed, and after the loss of cementation, the bonding force is mainly composed of the friction force between the concrete and the steel strands and the bite force between the steel wires in the twisting direction.

Figure 4 shows the load-slip curves of loading and free ends of PLS1 and PLS2. For specimen PLS1, when the drawing force gradually increases, the slip increases. When the drawing force is less than 90 kN, the slip value has a linear relation with the increase of the drawing force, then there is a nonlinear relation between the value of the drawing force and the slip of the loading end. The increasing speed of the slip is obviously greater than that of the drawing force. Finally, the drawing force increases slowly, while the slip value increases rapidly, and the steel strands are broken. At the same time, almost no slip at the free end is measured during the whole drawing process. Since the steel strands are broken and their maximum load corresponds to their ultimate tensile strength, and the cementation of the concrete and the steel strands at the free end is not damaged yet, the maximum bonding force provided by the specimens is inevitably greater than the ultimate tensile strength of the steel strands.

As indicated in Figure 5, the load-slip curve of a single-wire steel strand is not consistent with that of a three-wire steel strand, specimen PSL2 slips at the free end and has a

sawtooth shape at the loading end. Therefore, the effective bond length of PLS2 is obviously larger than that of PLS1. Meanwhile, from the load-slip curves of PLS1 and PLS2, it can be drawn that their ultimate drawing loads are, respectively, 262 kN and 776 kN. These two specimens have effective bond performance, and the effective bond length is less than the designed length. The reason is that for the tendons, the concrete cracking areas around each wrapped steel strand overlap each other due to the small spacing of the multiple steel strands, and the micro-cracks become wider, and the cracking range is obviously larger than that of a single-strand component. According to the thick cylinder theory, the concrete with multi-strand components cracked in a single tendon cannot provide the wall thickness of a single strand in a single tendon and thus cannot provide enough binding force to the steel tendon, resulting in the reduction of mechanical interaction and friction force, and the bonding stiffness and strength smaller than those of a single-strand component, so a longer bonding length is needed.

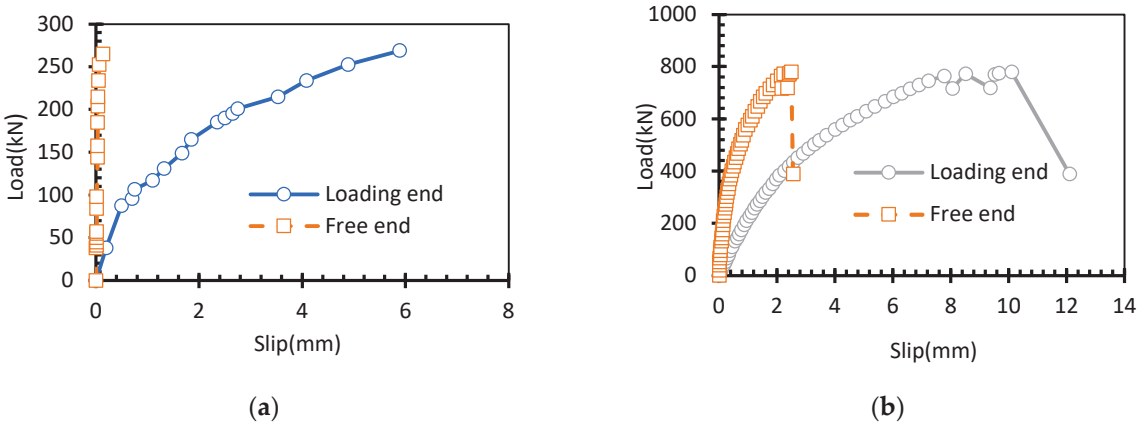


Figure 5. Load-slip curves of the drawing specimens. (**a**) PLS1; (**b**) PLS2.

3.3. Concrete Strain Distribution

By recording the strains of the suspension strain gauge for each specimen under different drawing load and drawing lines according to their distribution, the concrete strains at different distances from the loading end are obtained, as shown in Figure 6. In the test, the strain is assumed to be uniformly distributed along the whole cross section, without considering the influence of its uneven distribution at the same cross section. It can be seen from Figure 6 that with the pull-out force, the strain distribution of concrete is non-uniform and nonlinear along the specimen length, the line slope between two adjacent strains under a same load and the slope between two identical points under different pull-out forces are both different. When the pull-out force is small, the value of the concrete strain near the loading end is very big, and with the increase of the pull-out force, concrete strain is gradually transferred to the free end and the strain becomes smaller gradually from the loading end to the free end. These two specimens suffer significantly different drawing loads when the initial strain occurs at the free end. For PLS1, its strain at the free end is zero under ultimate load, and for PLS2, when the drawing load increases to 200 kN, some negative strains at the free end and even the concrete turn into tiny positive strains. From Figure 5, it may be concluded that the effective length of PLS1 under the ultimate load is 88 cm and that of PLS2 is 100 cm.

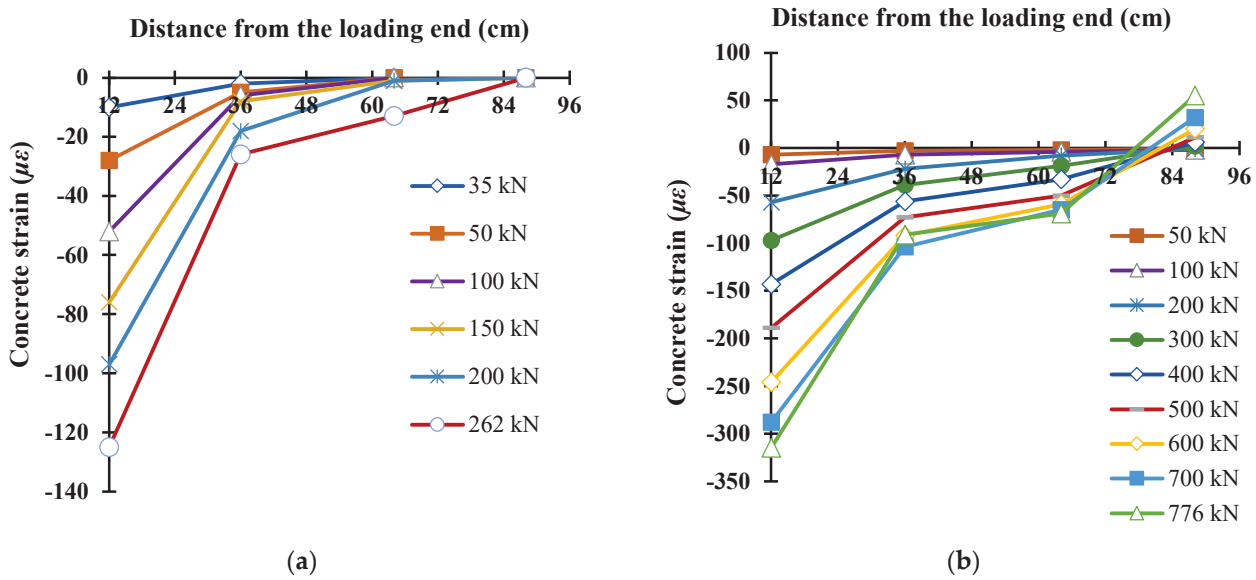


Figure 6. Concrete strain distribution under pull-out load. (**a**) PLS1; (**b**) PLS2.

3.4. Average Bond Stress

It can be inferred from Figure 6 that the distribution of bond stress is not uniform along the length of the specimen. In order to discuss the influence of the number of steel strands on the bond stress, it can be assumed that the bond stress is consistent in the range of the bond length. Therefore, the average bond stress may be calculated through Equation (1)

$$\overline{\tau} = \frac{P}{l_e \sum s} \tag{1}$$

where: $\overline{\tau}$ is average bond stress, P is pull-out force, l_e is effective bond length, and $\sum s$ is total circumference of steel strands.

According to Equation (1), the average bond stress of PLS1 under the ultimate pull-out force is 6.23 MPa, and that of PLS2 is 5.41 MPa, reduced by 13.2%. It can be drawn that both stiffness and average bond strength of the three-strand specimen decrease significantly, compared with those of single-strand specimen.

4. Local Bond-Slip Model of Steel Strand Tendons

4.1. Local Bond-Slip Model of Steel Strands

For the local bond-slip performance of deformed bars, many scholars in the world have developed lots of bond-slip curve models, which are generally simplified as multi-segment broken-line or curvilinear model. The most used one is four-segment local bond-slip model recommended by the CEB-FIP Code [18], which, as shown in Figure 7, is divided into four segments including nonlinear increase, linear segment, linear decrease, and constant residual bond. In Figure 7, τ_{cr} is splitting bond stress, τ_{max} is ultimate bond stress and τ_f is residual bond stress. s_1, s_2, and s_3 are the slip values corresponding to τ_{cr}, τ_{max} and τ_f.

In order to simplify the calculation, many scholars [19,20] have ignored this part in model building. Considering that the bond stiffness and strength of steel strands are composed of adhesive force, mechanical friction force and biting force and so are those of the deformed steel bars, in the calculation of this paper, the CEB-FIP Model may be

improved by removing the linear segment, and the local bond-slip model may be used in the calculation of PLS1, which can be expressed as Figure 8 and Equation (2).

$$\tau = \begin{cases} \tau_{max}\left(\frac{s}{x_1}\right)^{0.4} & 0 \le s \le x_1 \\ \tau_{max} - \left(\tau_{max} - \tau_f\right)\left(\frac{s-x_1}{x_2-x_1}\right) & x_1 \le s \le x_2 \\ \tau_f & s \ge x_2 \end{cases} \quad (2)$$

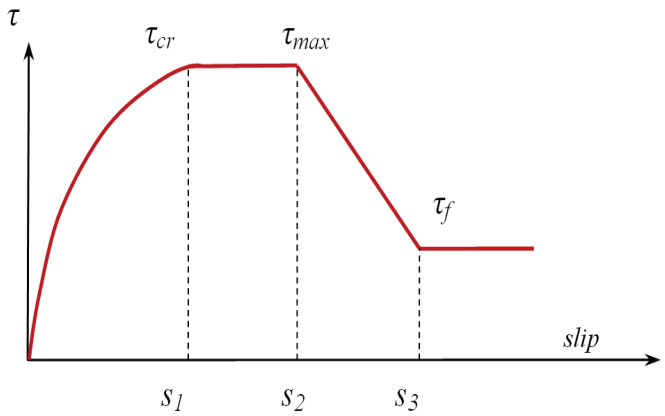


Figure 7. Local bond-slop model under CEB-FIP Code.

where τ_{max} is maximum bond stress, and f_c is compressive strength of concrete. τ_f is residual bond strength, and its value is set as $0.4\tau_{max}$. x_1 is local slip under the maximum bond stress, x_2 is local slip under the residual friction and bond stress. According to the calculation method proposed by Haskett [21] and Zhang [19], x_1 is taken as 3 mm and x_2 is taken as 12 mm. α is a constant parameter and is taken as 0.4.

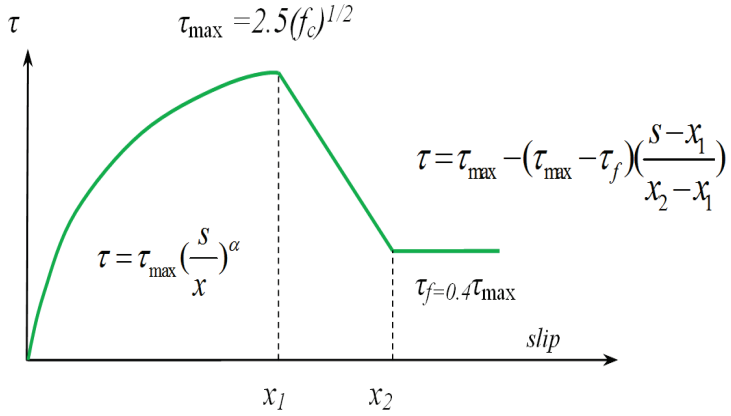


Figure 8. Local bond-slip model for PLS1.

4.2. Analysis Method of Local Bond-Slip Model for a Single Steel Strand

According to Equation (1), if x_1 and x_2 are determined, the local bond-slip relation between a single strand of a single strand tendon and concrete can be determined if the maximum bond stress is determined. The bond-slip relation is calculated by assuming the value of the maximum bond stress τ_{max}. The calculated curve and the test value are compared with each other repeatedly in order to correct the maximum bond stress τ_{max}, until the difference between the two curves meet the accuracy requirements.

Divide specimen PLS1 into n pieces of girder elements and number them as $1, \ldots i \ldots n$ consecutively. For a simple calculation, set all elements with a same length of 10mm. In addition, considering the very minimal girder length, assume that all girder

elements have the same force and slip. With τ_{max}, calculate the local bond-slip relation between steel strands and concrete according to Equation (1) and then acquire s_p, the slip value at the loading end under pull-out force P. Collect strain gauge readings and determine the effective transfer length in the girders, that is, both concrete strain and steel strand slip at the end of the effective length are zero, see Figure 9 for the calculation diagram. The specific calculation process is as follows:

(1) Set the slip value at the loading end under the pull-out force P as s_p, and calculate s_1, the slip value of element 1 of the bond segment of the specimen according to load and deformation relation.
(2) Set pull-out force as $P = F_1$ and the slip value of 1 of element 1 as $s_1 = s_p$, and repeatedly calculate the local bond stress of this element $\tau_1 = f(s_1)$ with prepared bond-slip constructive model according to the amount of slip, and calculate local load increment according to equation $\Delta F_1 = L_s l_1 \tau_1$ (L_s is the sum of the circumference of the cross section of steel strand).
(3) Since all elements are very short, it can be assumed that all elements are subject to the same force. Calculate the strand strain of element 1# ($\varepsilon_{s1} = F_1 / A_s E_s$) and concrete strain ($\varepsilon_{c1} = -F_1 / A_c E_c$), in which A_s and A_c are, respectively, the sectional area of steel strands and concrete of specimen PLS1, E_s and E_c are, respectively, the elasticity modulus of steel strands and concrete of specimen PLS1.
(4) Calculate the relative slip of steel strands and concrete of element 1 $\Delta s_1 = (\varepsilon_{s1} - \varepsilon_{c1}) l_1$.
(5) Calculate the stress of steel strands of element 2 ($F_2 = F_1 - \Delta F_1, F_1 = F$).
(6) Calculate the amount of slip of element 2 ($s_2 = s_1 - \Delta s_1$).

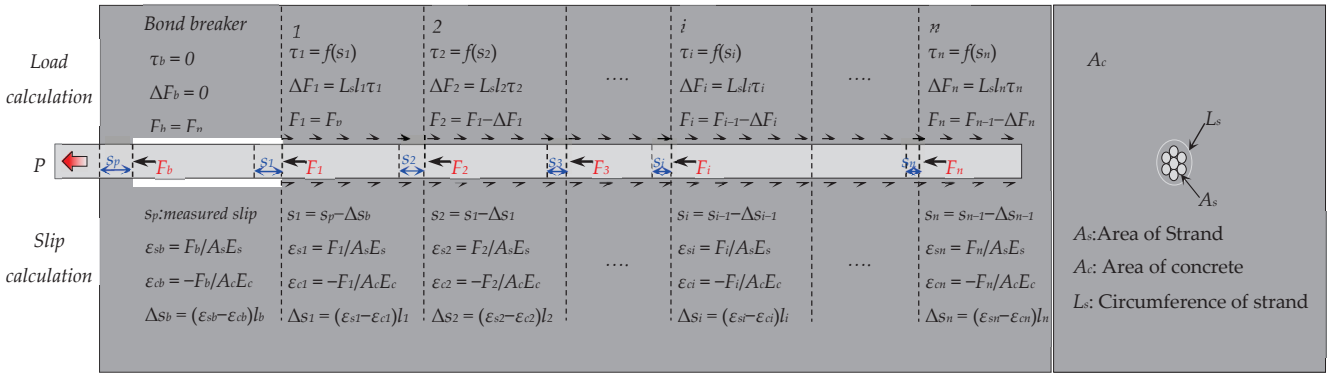


Figure 9. Calculation diagram of specimen PLS1.

In the same way, the pull-out force F_i and slip s_i of the steel strands of any ith element can be calculated. Since the slip at the free end of PLS1 is zero, its boundary conditions may be set that if both the pull-out force and slip of an element in the specimen meet the accuracy requirements, the assumed τ_{max} is considered correct, otherwise, τ_{max} should be reset, until the boundary condition error is within the allowable range.

Based on results of the pull-out test, the boundary conditions may be divided into two types. The first one is that when the load is relatively small, no slip occurs at the free end, the length of bond transfer is less than the length of the entire specimen and the boundary condition is that the pull-out force F_i and slip s_i of the steel strands of a certain element in the specimen are both 0. The second one is that when the drawing load is relatively great, the pull-out force exists along the whole specimen length and slip occurs at the free end, the boundary condition is that the pull-out force F_n of the steel strands at element n at the free end is 0.

And according to the test results, the failure of the specimens is the fracture of steel strands, so elastoplastic deformation should be considered for the strand strain, namely

$$\varepsilon_{si} = \begin{cases} \frac{F_i}{A_s E_s} & F_i \le A_s f_{sy} \\ \varepsilon_{sy} + \frac{F_i}{A_s E_{sp}} - \frac{f_{sy}}{E_{sp}} & F_i \ge A_s f_{sy} \end{cases} \quad (3)$$

where f_{sy} is yield strength of the steel strands, ε_{sy} is corresponding yield strain, E_{sp} is strain-hardening modulus after yield, ε_{si} is strain of the steel strands at ith element, and F_i is pull-out force of the steel strands at ith element.

In view of compressive property of concrete, some scholars have pointed out that when the pressure stress is within 40% of the compressive strength, concrete may be regarded as linear elastic material, without considering nonlinear effect of the material. The maximum pull-out force F withstood by the steel strands in the test is about 262 kN, so the maximum pressure stress withstood by corresponding concrete is about 3 MPa. The standard value of axial compressive strength of concrete (f_{ck}) can be calculated according to the conversion relationship between it and the concrete cubic compressive strength (f_{cu} = 56.5 MPa) provided by the code of GB 50010-2020 [22], and its value is 36.7 MPa.

4.3. Validation of Constitutive Model of a Single-Strand Specimen

According to the calculation and analysis method stated in Section 4.2, calculate the load-slip curve of the loading end of specimen PLS1 of a single-strand prestressed tendon. By calculation, τ_{max} is set as $2.1\sqrt{f_{ck}}$.

The load-slip calculation curve of loading end is calculated based on Equation (3) and τ_{max} (which is set as $2.1\sqrt{f_{ck}}$), as shown in Figure 10. As indicated, the calculated value of pull-out limit load is 262 kN, which is only 2% higher than the experimental value of 257 kN. That is, the calculation results are in good agreement with the experimental result. By calculation, the boundary condition is determined as the first type and it can be confirmed that the failure mode of the steel strand is consistent with the actual test results, namely, tensile failure. Therefore, it may be concluded that the local bond-slip model amended according to CEB-FIP code as proposed in Equation (3) has relatively high calculation accuracy.

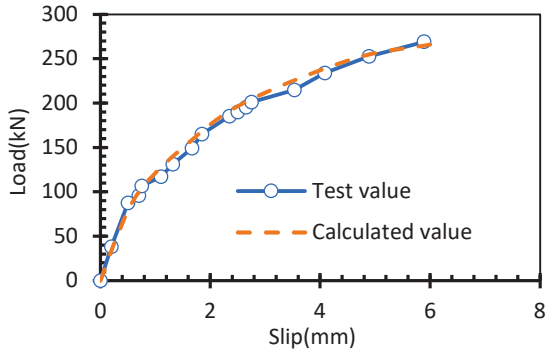


Figure 10. Comparison of the measured and calculated load-slip curves of the loading end of specimen PLS1.

4.4. Local Bond-Slip Model of Three-Strand Prestressed Specimen

According to the CEB-FIP Code [17], the three-strand prestressed specimen should have similar local bond-slip model of concrete and steel strands as the single-strand prestressed specimen. Based on the bond mechanism, the interaction between the multi-strand tendons and concrete is much complex and the bond between the multi-strand tendons and grouting interface is inevitably affected by the interaction of all bars. When the spacing of each strand is small, the extent of micro-cracks in some concrete around the steel strand increases and the constraint on the steel strands decreases, so the interaction of multiple steel strands may not only affect the bond strength between steel strands and

concrete, but also affect the bond stiffness, which is in inverse proportion to the number of strands. From Equation (1), it can be seen that τ_{max} may affect both the bond stiffness and strength, therefore, the bond-slip model of the steel strands can be adjusted simply by correcting the value of τ_{max}. For this purpose, this paper explored the local bond characteristics of three steel strands and concrete simply by correcting the value of τ_{max}.

Similar to determining the bond-slip model of a single steel strand and concrete, a calculation was made with trial method for the bond-slip constructive model of the three-strand specimen PLS2 and a bond-slip curve of the loading end was obtained. The difference from the calculation process of PLS1 is that the first type of boundary condition is taken when no slip occurs at the free end of PLS2, or otherwise, the second type of boundary condition may be taken, that is, the pull-out force F_n of the steel strands at element n# at the free end is 0, and in specific calculation. The first step is to set the maximum bond stress τ_{max} according to the method in Section 4.2, successively calculate the pull-out force and slip value of each strand element. For Nth element, if the pull-out force meets the accuracy requirement, the setting is feasible, otherwise, the calculation should be re-made by correcting τ'_{max}. The comparison between the load-slip curve of the loading end calculated with this method and the measured curve is as shown in Figure 11. By comparison, it can be drawn that for specimen PLS2, the calculated values are all in good agreement with the test values under all grades of load by correcting τ_{max}, and coincide with actual test results, and the steel strands are broken. This shows that it is reasonable and feasible to represent the local bond characteristics of steel strands and concrete by correcting τ_{max}. See Equation (4) for the corrected bond-slip constructive model.

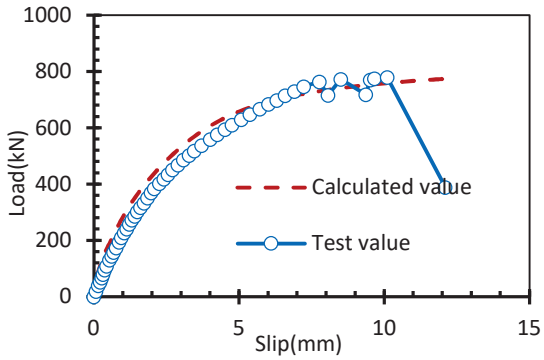


Figure 11. Comparison of measured and calculated load-slip curves of PLS2.

By calculation, see Equation (4) for the corrected bond-slip constructive model.

$$\tau = \begin{cases} \tau'_{max}\left(\frac{s}{x_1}\right)^{0.4} & 0 \le s \le 3 \text{ mm} \\ \tau'_{max} - \left(\tau'_{max} - \tau'_f\right)\left(\frac{s-x_1}{x_2-x_1}\right) & 3 \text{ mm} \le s \le 12 \text{ mm} \\ \tau'_f & s \ge 12 \text{ mm} \end{cases} \quad (4)$$

where τ'_{max} is set as $2.1 \times \sqrt{f_c}/n^{0.64}$, $\tau'_f = 0.4\tau'_{max}$, n is the number of steel strands.

According to Equation (4), the load-slip curve of the loading end of PLS2 was calculated by setting n as 3. The calculated curve and the measured curve are as shown in Figure 11. As indicated, the calculated value of pull-out limit load is 747 kN, which is 3.74% lower than the test value of 776 kN. The prediction deviation fully meets the engineering prediction requirements. Moreover, the failure mode of the drawing specimens obtained after calculation was the fracture of steel strands, in agreement with test results. Therefore, it can be drawn that by introducing the number of the steel strands as a parameter, the corrected local bond-slip model of the concrete and steel strands has relatively high calculation accuracy.

5. Conclusions

In this paper, the effect of the number of prestressed tendons on the failure mode, slip characteristics and concrete strain of the pull-out specimens are analyzed, and the constitutive models of bond-slip between for single-bar and multi-strand tendons are also proposed. The conclusions are summarized as follows:

(1) The bond mechanism between steel strands and concrete is basically similar to that of deformed steel bars, but the slip process of steel strand along the axis direction is accompanied by rotation phenomenon because it is twisted.
(2) Three-strand prestressed tendons have a smaller bond stress than those of single-strand prestressed tendons. In this test, the mean ultimate bond stress of three-strand prestressed tendons is about 13.2% smaller than that of single-strand prestressed tendons.
(3) Based on load-slip data of the loading end of single-strand prestressed tendons, the maximum bond strength can be determined by a trial calculation with the model suggested by CEB-FIP code.
(4) A simplified bond-slip constructive model between three strand prestressing tendons and concrete is proposed. The bond force is degraded exponentially according to the number of strands that make up the prestressing tendon. The validity of the proposed model is verified by comparing the experimental results with the predicted values.

The limitation of this study is that only two kinds of strand quantities are considered, and the effect of more types of strand quantities on the bond performance needs to be further studied. Moreover, the effect of tendon configurations with different numbers but the same total area on the bond performance is also the focus of future research.

Author Contributions: Conceptualization, R.Y.; methodology, R.Y.; X.Z. and X.W.; validation, R.Y. and Y.Y.; writing—original draft preparation, R.Y. and Y.Y.; writing—review and editing, R.Y., Y.Y., X.Z. and X.W.; supervision, X.Z. and X.W.; funding acquisition, R.Y. and X.W.; All authors have read and agreed to the published version of the manuscript.

Funding: This research was funded by the Hunan Provincial Natural Science Foundation of China (grant no. 2021JJ50156 and 2021JJ50153), and the Research Foundation of Education Bureau of Hunan Province (grant no. 18A401 and 19C0343).

Institutional Review Board Statement: Not applicable.

Informed Consent Statement: Not applicable.

Data Availability Statement: Not applicable.

Conflicts of Interest: The authors declare that they have no known competing financial interests or personal relationships that could have appeared to influence the work reported in this paper.

References

1. Dang, C.N.; Hale, W.M.; Martí-Vargas, J.R. Quantification of bond performance of 18-mm prestressing steel. *Constr. Build. Mater.* **2018**, *159*, 451–462. [CrossRef]
2. Dai, L.Z.; Xu, W.G.; Wang, L.; Yi, S.C.; Chen, W. Secondary transfer length and residual prestress of fractured strand in post-tensioned concrete beams. *Front. Struct. Civ. Eng.* **2022**, *16*, 388–400. [CrossRef]
3. Yang, R.H.; Zhang, J.R.; Wang, L.; Zhang, X.H. Experimental research for flexural behavior on concrete beams with local corrosion fracture of strands. *J. Cent. South Univ. (Sci. Technol.)* **2018**, *49*, 2593–2601.
4. Mohandoss, P.; Pillai, R.G.; Gettu, R. Determining bond strength of seven-wire strands in prestressed concrete. *Structures* **2021**, *33*, 2413–2423. [CrossRef]
5. Franceschini, L.; Vecchi, F.; Tondolo, F.; Belletti, B.; Sánchez Montero, J. Mechanical behaviour of corroded strands under chloride attack: A new constitutive law. *Constr. Build. Mater.* **2022**, *316*, 125872. [CrossRef]
6. Wang, X.L.; Zhao, Y.K.; Zhou, Q.W.; Zhu, J.T. Study on bond-slip property of high strength stainless steel strand and ECC. *J. Huazhong Univ. Sci. Technol. (Nat. Sci. Ed.)* **2020**, *48*, 108–113.
7. Dai, L.Z.; Chen, H.; Wang, L.; Ma, Y.F.; Zhang, J.R. Transfer length prediction in pre-tensioned concrete beams under corrosive cracking. *Structures* **2021**, *30*, 938–948. [CrossRef]

8. Dyba, M. FEM Simulations of Bond Behaviour between Concrete and Seven-Wire Prestressing Strand. *IOP Conf. Ser. Mater. Sci. Eng.* **2020**, *960*, 032076. [CrossRef]
9. Dyba, M. FEM Analysis of Bond between Concrete and Seven-Wire Prestressing Strand. *IOP Conf. Ser. Mater. Sci. Eng.* **2020**, *960*, 032077. [CrossRef]
10. Zghayar, E.E.; Mackie, K.R.; Haber, Z.B.; Potter, W. Secondary Anchorage in Post-Tensioned Bridge Systems. *ACI Struct. J.* **2013**, *110*, 629–638.
11. Zhang, K.Y.; Fang, Z.; Nanni, A. Behavior of Tendons with Multiple CFRP Rods. *J. Struct. Eng.* **2016**, *142*, 04016065. [CrossRef]
12. Wu, X.Q.; Huang, T.; Zhang, L.; Au, F.T.K. Bond performance of grouted tendons at elevated temperatures. *ICE Proc. Struct. Build.* **2021**, *174*, 791–803. [CrossRef]
13. Zhu, J.T.; Zhang, K.; Wang, X.L.; Li, K.; Li, Y. Bond-slip relational model between high-strength stainless steel wire mesh and ECC. *China Civ. Eng. J.* **2020**, *53*, 83–92.
14. Mei, K.H.; Sun, S.J.; Li, B.; Sun, Y.M.; Jin, G.Q. Experimental investigation on the mechanical properties of a bond-type anchor for carbon fiber reinforced polymer tendons. *Compos. Struct.* **2018**, *201*, 193–199. [CrossRef]
15. *JTG 3362-2018*; Specifications for Design of Highway Reinforced Concrete and Prestressed Concrete Bridges and Culverts. People's Communications Press Co., Ltd.: Beijing, China, 2018.
16. *GB/T228.1-2021*; Metallic Materials-Tensile Testing-Part 1: Method of Test at Room Temperature. China Standards Press: Beijing, China, 2021.
17. Wang, X.Z.; Yang, Y.M.; Yang, R.H.; Liu, P. Experimental Analysis of Bearing Capacity of Basalt Fiber Reinforced Concrete Short Columns under Axial Compression. *Coatings* **2022**, *12*, 654. [CrossRef]
18. CEB-FIP. *FIB Model Code for Concrete Structures*; Ernst & Sohn: Lausanne, Switzerland, 2010.
19. Zhang, X.H. Theory of Computation of Corrosion Prestressed Reinforcement and Concrete Deformation Coordination and Component Bearing Capacity. Ph.D. Thesis, Changsha University of Science and Technology, Changsha, China, 2016.
20. Yu, F.; Jia, J.Q.; Song, Y.P. Experimental study on flexural fatigue performance of partially prestressed concrete beams after steel strand corrosion. *Build. Struct.* **2012**, *42*, 97–100.
21. Haskett, M.; Oehlers, D.J.; Mohamed, A.M.S. Local and global bond characteristics of steel reinforcing bars. *Eng. Struct.* **2008**, *30*, 376–383. [CrossRef]
22. *GB 50010-2020*; Code for Design of Concrete Structures. China Architecture and Building Press: Beijing, China, 2019.

coatings

MDPI

Article

Effect of Surfactants on the Corrosion Protectability of Calcium Phosphate Conversion Coatings on Duplex Structured Mg-8Li (in Wt.%) Alloy

Jiyu Hou [1], Baojie Wang [1,*], Daokui Xu [2,3,4,*], Liji Cui [1] and Jie Sun [1]

[1] School of Environmental and Chemical Engineering, Shenyang Ligong University, Shenyang 110159, China
[2] Key Laboratory of Nuclear Materials and Safety Assessment, Institute of Metal Research, Chinese Academy of Sciences, Shenyang 110016, China
[3] Binzhou Institute of Technology, Binzhou 256606, China
[4] Shandong Key Laboratory of Advanced Aluminium Materials and Technology, Binzhou 256606, China
* Correspondence: bjwang@alum.imr.ac.cn (B.W.); dkxu@imr.ac.cn (D.X.)

Abstract: Calcium phosphate chemical conversion coatings with the additions of sodium lauryl sulfate (SLS) and dodecanesulfonic acid sodium (DSS), respectively, were prepared on the surface of the Mg-8Li alloy. The surface and cross-sectional corrosion morphologies, compositions, and corrosion behavior of the coated surfaces in 3.5 wt.% NaCl solution were respectively investigated by using a scanning electron microscope (SEM), energy dispersive spectrometer (EDS), electrochemical workstation, hydrogen evolution apparatus, and optical microscope (OM). The results demonstrated that Ca-P coatings had a petal-like structure being composed of leaf-like particles. After being respectively performed for 30 min in conversion solutions containing SLS and DSS, the corresponding average film thicknesses of surface coatings were 27 μm and 7 μm. In addition, the corrosion current densities of coated surfaces by using the conversion solutions containing SLS and DSS were 1.438×10^{-5} A·cm^{-2} and 4.719×10^{-5} A·cm^{-2}, respectively. The effect of surfactants on phosphate chemical conversion coating was discussed in detail.

Keywords: Mg-Li alloy; surfactants; coatings; corrosion resistance; pitting

1. Introduction

The especially structural relationship between magnesium and lithium was discovered in 1910 by Masing et al., which attracts a lot of attention of scholars, enabling the rapid development of Mg-Li alloys [1]. Due to low density, high specific strength, specific stiffness, ductility, good electromagnetic wave shielding capacity, and the improved preparation process [2–8], Mg-Li alloys have great application prospects. Moreover, their microstructure is closely related to the content of element Li [9–16], i.e., (1) when the content of Li is below 5.5 wt.%, the alloys are only comprised of α-Mg phase with hexagonal close packed (hcp) structure; (2) when the content of Li is more than 10.3 wt.%, the alloys are comprised of a β-Li phase with a body-centered cubic (bcc) structure; (3) when the Li content is in the range of 5.5–10.3 wt.%, the alloys have a typical dual-phase structure (α-Mg + β-Li), ensuring their higher specific strength and stiffness. However, micro galvanic corrosion easily occurs in the duplex structured Mg-Li alloys due to the potential difference at the α-Mg/β-Li interfaces, resulting in their poor corrosion resistance and limited applications [6,9]. Thus, it is quite necessary to improve the corrosion resistance of the duplex structured Mg-Li alloys. So far, there are commonly three kinds of methods for increasing corrosion resistance of Mg-Li alloys, including alloying, deformation processes, and protective coatings [6,9,15–21]. However, these methods are difficult to be carried out and have a relatively limited effect for improving the corrosion resistance of Mg-Li alloys. Therefore, the most effective method for protecting the corrosion of Mg alloys is surface treatment technology [6,18,20,22–28].

So far, the commonly applied surface protection methods for enhancing the corrosion resistance of Mg alloys include micro arc oxidized [23,29], organic coating [22,24,30], vapor phase method [28], electroless coating [25], and chemical conversion coating [26,27,31–33]. Among them, the chemical conversion coating is widely applied because it is simple for operation. In the initial development of conversion coatings, the chromate conversion coatings were put into industrial production because it exhibits excellent corrosion resistance and adhesion ability. However, the chromate conversion coatings are currently prohibited in most application fields due to the presence of severe toxicity of Cr^{6+}. Thus, the investigation on the much more environmentally friendly conversion coatings becomes the hot topic [34–36].

Due to the simplicity in operation and low prices, phosphate conversion coatings being an alternative to chromate conversion coatings are developed [31,32,37–40]. Through preparing a manganese phosphate conversion coating (MnPCC) on the Mg-10Li-1Zn alloy (in wt.%) and measuring its corrosion resistance, Zhang et al. reported that the MnPCC of Mg alloys had the better corrosion resistance than chromate conversion coatings [33]. Moreover, the additives on the surface coatings can also influence the corrosion behavior of Mg alloys. The functions of additives mainly include: (1) promoting coating formation; (2) reducing particle crystallinity; (3) controlling conversion rate; (4) increasing hydrophobicity of the metal surface and 5) enhancing the solubility of the main components of the conversion fluid in water [41–52]. Cui et al. [43] reported the influence of the added $Mn(NO_3)_2$ and Na_2MoO_4 on the phosphate conversion coatings on the surface of AZ31B alloy and found that the corrosion protectability of phosphate conversion coatings with additives was significantly improved because the particle size of phosphate conversion coatings was significantly decreased with the addition of Na_2MoO_4. Through adding the sodium lauryl sulfate (abbreviated as SLS, $C_{12}H_{25}SO_4Na$) in the calcium phosphate conversion coatings of Mg-9Li-7Al-1Sn and Mg-9Li-5Al-3Sn-1Zn alloys, Maurya et al. found that the coatings with additives were composed of dense arranged tiny petals and then ensured the higher corrosion resistance of the coated alloys [47]. However, the influence of the SLS additives on the formation mechanism of coatings is unknown. Through studying the effect of SLS on phosphate conversion coating on the AZ31 alloy and exploring its mechanisms, Amini et al. reported that the coating with the addition of SLS was more uniform and had the faster formation rate, resulting in more micro cathodes on the surface of the alloy and thereby the improvement of the coating formation process [41].

Based on the description mentioned above, it seems that the additives have a positive impact on the performance of phosphate conversion films and the surfactant of SLS can improve the corrosion resistance of Mg alloys. Thus, it is important to carry out an in-depth investigation on the corrosion process and the formation mechanism of conversion coating with the additives. At the same time, the dodecane sulfonic acid sodium (DSS, $C_{12}H_{25}SO_3Na$) is also a very commonly used surfactant, and it has a similar chemical structure to SLS. However, so far, it lacks the comparison about the effects of SLS and DSS on the corrosion behavior of Mg alloys. Moreover, the corrosion behavior of a coated dual phase structure Mg-Li alloys is seldomly investigated. In this work, the target is to investigate and compare the corrosion behavior and formation mechanism of conversion coatings respectively prepared by the addition of SLS (defined as the C_1 sample) and DSS (defined as the C_2 sample) for deepening the understanding about the effect of additives on the formation and corrosion protectability of conversion films on Mg-Li alloys. Moreover, the effect mechanism of the surfactant on the corrosion resistance of coated surfaces of dual phase Mg-Li alloys is disclosed.

2. Experimental Procedures

2.1. Preparation of Calcium Phosphate Conversion Coatings

The experimental material was an as-cast Mg-8 wt.% Li alloy ingot. The cubic samples with the dimensions of 10 mm × 10 mm × 10 mm were cut and grinded with 400# SiC papers and sealed by the epoxy resin AB glue with an exposed area of 1 cm^2. The working

area was ground gradually with 400#–2000# SiC papers. Then, ultrasonic cleaning in acetone and washing in alkaline solution (50 g/L NaOH, 10 g/L $NaNO_3$) were applied for 5 min to remove the grease impurities on the Mg-Li alloy. To remove the residual alkaline solution on the surfaces, samples were then washed in acid solution (40 wt.% H_3PO_4) for 8 s. After pre-treatment, the conversion treatment experiments were respectively conducted in phosphate conversion solutions (Solution 1: 35 g/L $Ca(NO_3)_2 \cdot 4H_2O$, 25 g/L $(NH_4)_2HPO_4$, pH = 3, 0.4 g/L SLS; Solution 2: 35 g/L $Ca(NO_3)_2 \cdot 4H_2O$, 25 g/L $(NH_4)_2HPO_4$, 0.4 g/L DSS pH = 3) at 40 °C for 30 min. Then, samples were washed with distilled water and dried with cold air. The detailed description about the processing procedures for the phosphate chemical conversion treatments on Mg-Li alloys can be referred in the literature [47].

2.2. Characterization of Calcium Phosphate Conversion Coating

The surface morphology, cross-sectional morphology, and composition of C_1 and C_2 were characterized by using a scanning electron microscope (SEM; FEI Quanta 450, Hillsboro, OR, USA) and energy dispersive X-ray spectroscopy (EDS). Electrochemical tests were carried out with the CS350 electrochemical workstation (Corrtest Co. Ltd.,Wuhan, China). The three-electrode system was applied with the coated surfaces as the working electrode, the saturated calomel electrode (SCE) as the reference electrode, and the Pt plate as the auxiliary electrode. Before the measurement, an open-circuit potentials (OCP) were tested for 600 s. Then, the potentiodynamic polarization (PP) and electrochemical impedance spectrum (EIS) were tested. EIS measurement was in the frequency range from 100 kHz to 10 mHz with the perturbation amplitude of 10 mV. The EIS measured data were analyzed and fitted by ZsimpWin software (ZSimDemo 3.30) on the basis of the proposed equivalent circuit model. Polarization curves were measured at a scanning rate of 0.166 mV/s and fitted with the mode of Tafel. The relevant methods for the determination of electrochemical parameters can be referred in the literature [6,11,18]. To analyze and compare the corrosion behavior of the two differently coated samples, the volume of hydrogen evolution was collected by the hydrogen evolution apparatus and the details can be referred in the literature [14]. The volume of hydrogen evolution was measured for up to 24 h, and the data were recorded with an interval of 1 h. To reflect and compare the evolution processes of two types of conversion coatings, their surface morphologies after immersion in corrosive media for 2 h, 4 h, 6 h, 16 h, and 24 h were observed by a stereo optical microscope (OM; VHX-900 F, Keyence International, Mechelen, Belgium). Moreover, their cross-sectional morphologies and compositions after being immersed in corrosive media for 6 h were characterized by SEM and EDS. For all electrochemical measurements, the hydrogen evolution and immersion tests were carried out in 3.5 wt.% NaCl solution.

3. Results and Discussion

3.1. Microstructure

The surface and cross-sectional morphologies of C_1 and C_2 samples are shown in Figure 1. It can be seen that C_1 and C_2 samples all exhibit a flower-like structure consisting of regularly arranged leaf-like particles. The high magnification images of C_1 sample (Figure 1a) and C_2 (Figure 1c) samples show that leaf-like particles of C_1 are much larger in size than that of C_2. Moreover, there are no obvious gaps or holes present in either C_1 or C_2 samples, indicating that the coatings would have excellent corrosion protectability. The petal-like structure of C_1 and C_2 samples not only enhances the corrosion protection of the Mg-8Li alloy, but also increases surface roughness of the substrate and improves the adhesion ability of the organic coatings on alloy surfaces [53]. To measure the thicknesses of conversion coatings on sample surfaces, their cross sections containing epoxy, film layer, and substrate matrix are perpendicularly observed by using SEM. Based on the cross-sectional morphologies of C_1 and C_2 samples (Figure 1b,d), it demonstrates that the coating layers can be clearly distinguished and outlined by the dot lines. By referring the scale bar, the average thicknesses of conversion coating layers on C_1 and C_2 sample surface are respectively measured to be 27 μm and 7 μm. Since the thickness of the coating is

proportional to its corrosion resistance, the C_1 sample has the better corrosion resistance than the C_2 sample.

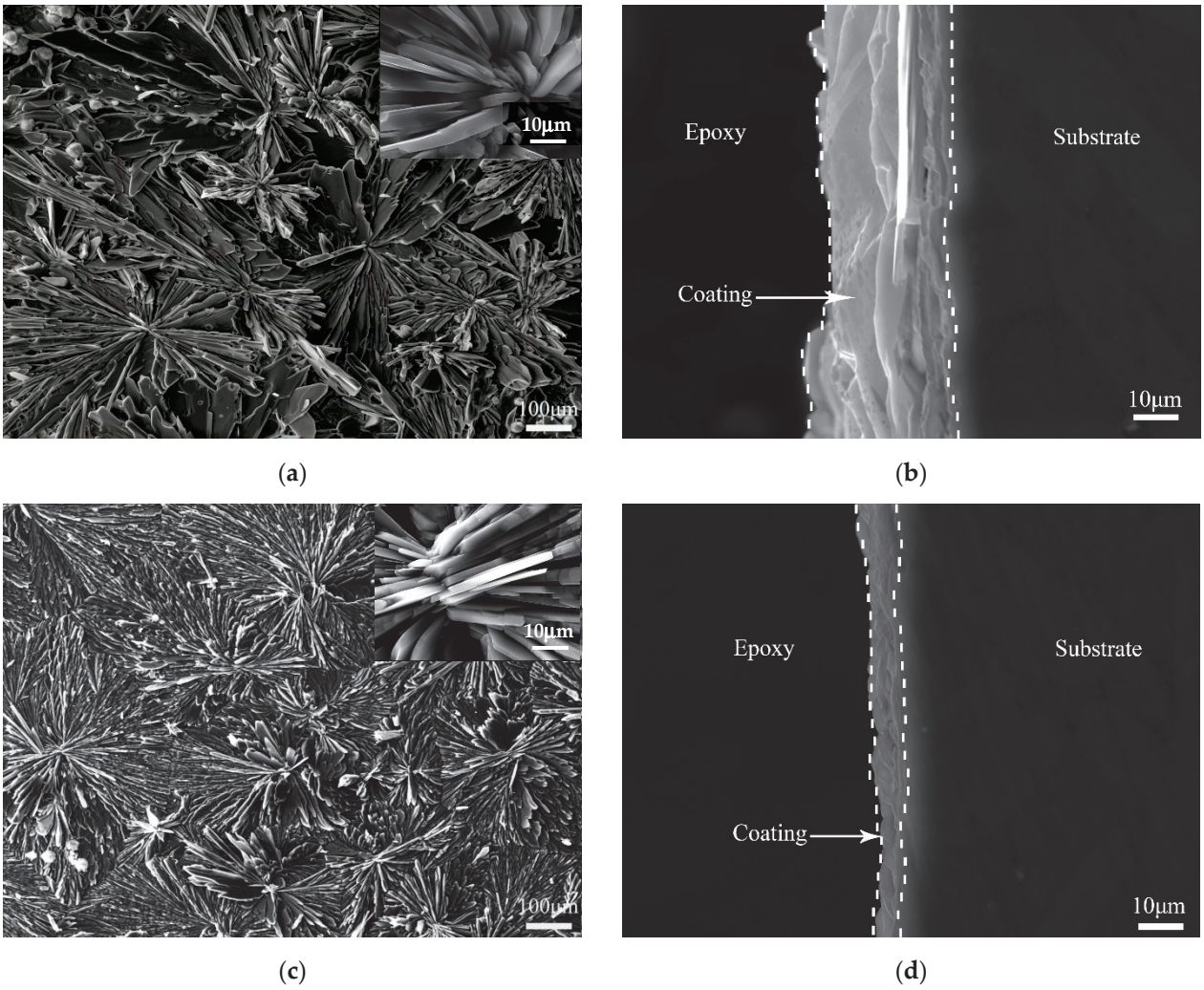


Figure 1. SEM observations: (**a**) and (**c**) surface morphologies of C_1 and C_2 samples, (**b**) and (**d**) cross-sectional morphologies of C_1 and C_2 samples.

The EDS analysis demonstrates that the surface coating of C_1 sample is composed of Ca, O, P, and C, whilst the surface coating of C_2 sample consists of Ca, O, P, C, and Mg, as shown in Figure 2. Moreover, P is the main component element in the surface coatings of C_1 and C_2 samples, suggesting that calcium phosphate is the main composition of coatings [54–58]. On the contrary, S element cannot be detected, indicating that the surfactants do not participate in the formation of the conversion coating. The specimen is rinsed with plenty of distilled water after the preparation of the coating, and the surfactant is less likely to remain due to its good solubility in water. Additionally, it can be concluded that C element is from CO_3^{2-} present in conversion solution instead of from surfactants. The related reaction is shown in Equation (1). There are two possible reasons for the existence of Mg element in the surface coating of C_2 sample, i.e., (1) Mg is involved in formation of the coating [56]; (2) the surface coating of C_2 sample is very thin and the electron beam can easily penetrate the film and detect Mg of the matrix. Since the surface coating of C_1 sample is thick and the electron beam can hardly penetrate the film, element Mg is not detected in the surface coating of C_1 sample. According to the thermodynamically stable

phase diagram for solutions containing PO_4^{3-} and Ca^{2+} [59], the existence of Ca is in the form of $Ca_3(PO_4)_2$ and $CaHPO_4 \cdot 2H_2O$ (The reaction is shown in Equations (2) and (3).).

$$CO_2 + H_2O \rightarrow CO_3^{2-} + 2H^+ \quad (1)$$

$$3Ca^{2+} + 2PO_4^{2-} \rightarrow Ca_3(PO_4)_2 \quad (2)$$

$$Ca^{2+} + H_2PO_4^- + OH^- + H_2O \rightarrow CaHPO_4 \cdot 2H_2O \quad (3)$$

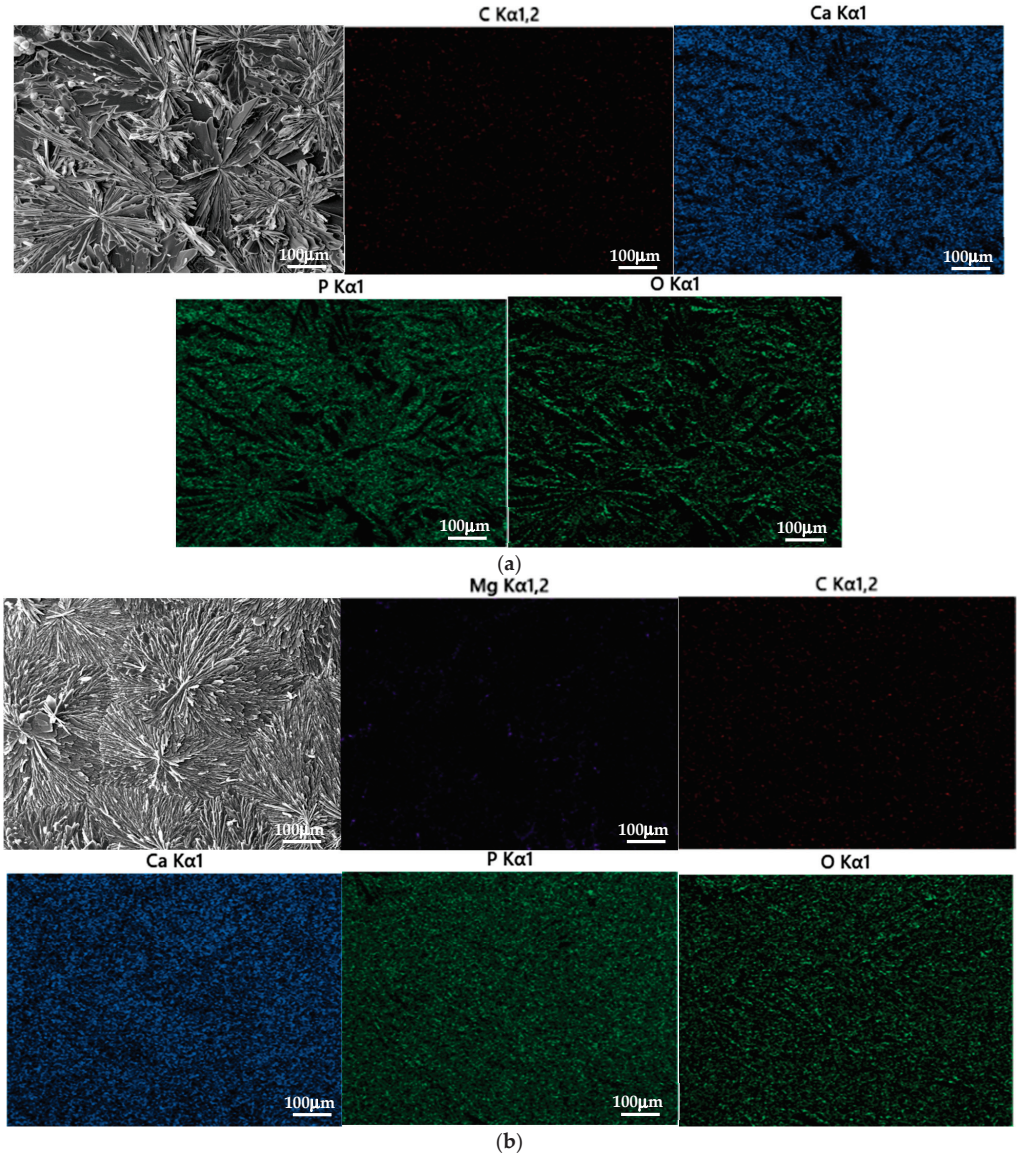


Figure 2. The EDS mappings of: (**a**) C_1 and (**b**) C_2 samples.

Mg^{2+}, Ca^{2+}, and Li^+ are present in the conversion solution and could form precipitation with CO_3^{2-}. According to the theory of dissolution equilibrium and the calculation of solubility product constant (K_{sp}) from Equation 4, the order of obtained K_{sp} values of $MgCO_3$ and $LiCO_3$ are as follows: $CaCO_3 < MgCO_3 < LiCO_3$ [60]. Therefore, it can be inferred that calcium carbonate, magnesium carbonate and lithium carbonate should be sequentially precipitated. However, there is a high concentration of PO_4^{3-} in conversion solution; Mg^{2+} and Ca^{2+} can firstly form deposition with PO_4^{3-} because $Ca_3(PO_4)_2$ and $Mg_3(PO_4)_2$ have the very low value of K_{sp} and can hardly react with CO_3^{2-}. Thus, the

carbonate precipitation in the conversion coating is dominated by Li_2CO_3 (The reaction is shown in Equations (5)–(9)):

$$K\ (A_mB_n) = K_{sp}\ (A_mB_n) = c(A^{n-})^m \cdot c(B^{m-})^n \quad (4)$$

$$Ca^{2+} + {CO_3}^{2-} \rightarrow CaCO_3 \quad (5)$$

$$Mg^{2+} + {CO_3}^{2-} \rightarrow MgCO_3 \quad (6)$$

$$2Li^{2+} + {CO_3}^{2-} \rightarrow Li_2CO_3 \quad (7)$$

$$3Mg^{2+} + 2{PO_4}^{3-} \rightarrow Mg_3(PO_4)_2 \quad (8)$$

$$Mg^{2+} + {H_2PO_4}^{-} + OH^{-} + H_2O \rightarrow MgHPO_4{\cdot}2H_2O \quad (9)$$

It is well known that DSS and SLS are both anionic surfactants and can be adsorbed on the micro anode sites due to their negative charge. Thus, their existence may increase electron density at the micro anode sites and behave as micro cathode sites. Machu put forward the hypothesis of precipitation of metal phosphates on the micro cathodic sites due to the pH gradient at the metal–electrolyte interface [61]. As a result, the rate of phosphate coating creation may be increased due to the increase number of micro cathodic sites. On the other hand, the adsorption of DSS and SLS on the micro anode sites prevent magnesium from dissolution. However, it is reported that SLS can accelerate the speed of reduction reaction [62,63]. The cathode process on the surface of alloy matrix is that the hydrogen ion obtains electrons and then generates hydrogen gas. With the progress of cathodic reaction, the pH of the solution at the interface increases, and then the cations and anions in the solution react to form precipitation, which is deposited on the surface of the sample. Thus, it is clear why the surface coating of C_1 sample is much thicker than that of the C_2 sample.

3.2. Electrochemical Testing

Figure 3 shows the potentiodynamic polarization curves, electrochemical impedance spectroscopy (EIS), and the equivalent circuit model based on EIS of the C_1 and C_2 samples. The cathode branches of C_1 and C_2 samples are basically identical, indicating that the coating is unaffected on the cathodic process. Thus, the cathodic branches are used for fitting analysis. The Tafel fitted results of potentiodynamic polarization curves (Figure 3a) are listed in Table 1. It can be seen that the corrosion current densities (I_{corr}) of C_1 and C_2 samples are 1.438×10^{-5} A·cm^{-2} and 4.719×10^{-5} A·cm^{-2}, respectively. Moreover, the corrosion potential (E_{corr}) of C_1 sample is -1.537 V_{SCE} and much higher than -1.593 V_{SCE} of the C_2 sample.

Based on the EIS curves, there exists a capacitive loop for the C_1 and C_2 samples (Figure 3b). The capacitive loop is caused by the charge transfer resistance between the coating and the solution. Corrosion resistance of samples can be compared by the radius of the capacitive loops. Thus, the C_1 sample has the better corrosion resistance than the C_2 sample due to its bigger radius. The equivalent circuit model based on EIS of the C_1 and C_2 samples is proposed (Figure 3c), and the fitted values are listed in Table 2. R_s is the solution resistance. Q_{dl} reveals the electric double layer between coating and solution and is determined by Y_{dl} and n_{dl}. R_{ct} represents charge transfer resistance, the values of which are related to the corrosion resistance of the specimen. The R_{ct} value of C_1 sample is 6289 Ω·cm^2, which is much higher than that of the C_2 sample. Therefore, it can be seen that the result of EIS curves agrees with that of potentiodynamic polarization curves.

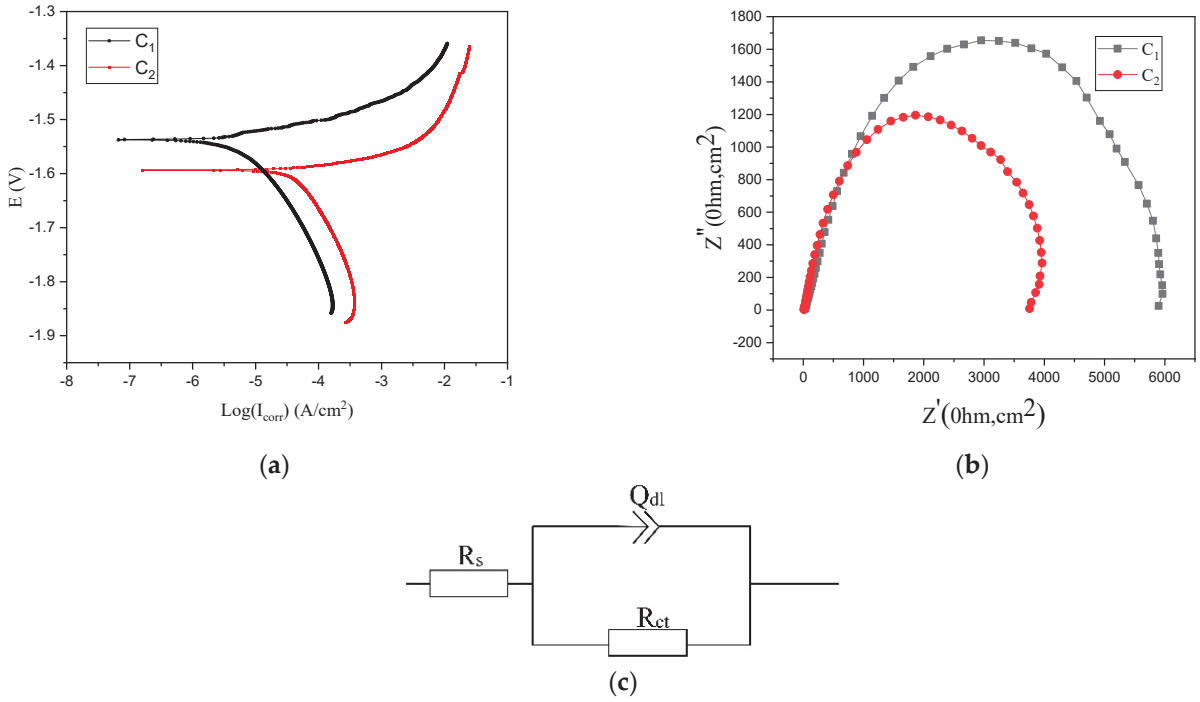


Figure 3. Electrochemical measurements: (**a**) potentiodynamic polarization curves, (**b**) electrochemical impedance spectra, (**c**) equivalent circuit models for fitting EIS.

Table 1. Fitted results of potentiodynamic polarization curves.

	C_1 Sample	C_2 Sample
I_{corr}/A·cm^{-2}	1.438×10^{-5}	4.719×10^{-5}
E_{corr}/V vs SCE	−1.53731	−1.59341

Table 2. Fitted EIS results on the basis of the equivalent circuits.

	C_1 Sample	C_2 Sample
R_s/Ω·cm^2	24.57	14.24
Y_{dL}/μΩ·cm^2·S^n	31.569	32.253
n_{dL}	0.63443	0.71218
R_{ct}/Ω·cm^2	6289	4033

3.3. Hydrogen Evolution

Figure 4 shows the volume of hydrogen evolution–time curves of C_1 and C_2 samples immersed in 3.5 wt.% NaCl solution for 24 h. Generally, the amount of volume of hydrogen evolution reflects the dissolution of the matrix. Therefore, the more hydrogen evolution, the worse corrosion resistance of the samples. It can be seen that, after 24 h immersion, the volumes of hydrogen evolution of C_1 and C_2 samples are 1.45 mL/cm^2 and 2.69 mL/cm^2, respectively. Moreover, the volume of hydrogen evolution of C_1 sample is much lower than that of the C_2 sample during the whole process of immersion.

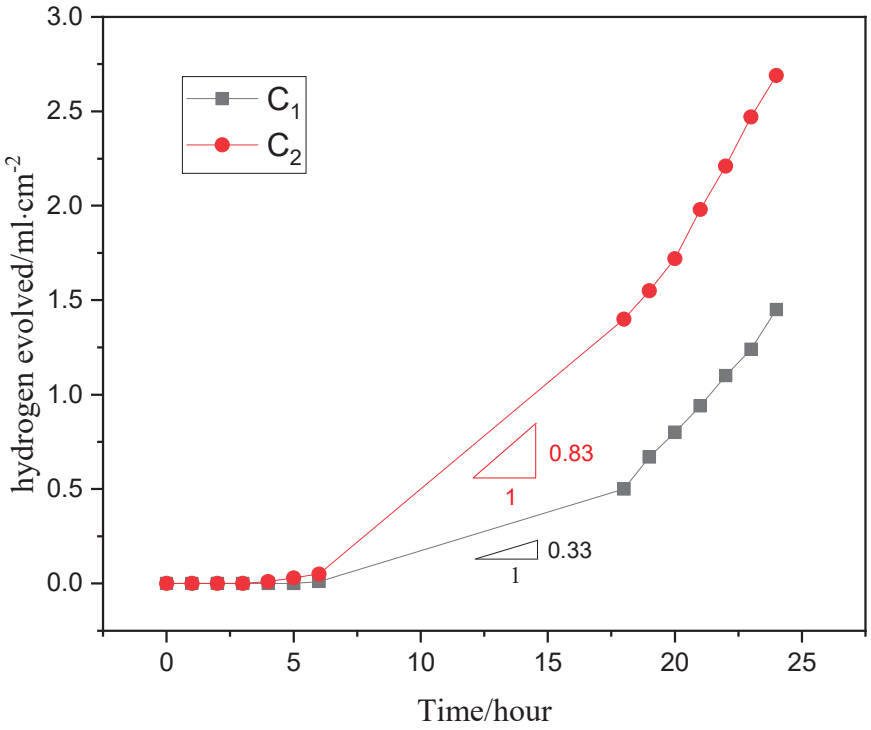


Figure 4. Volume of hydrogen evolution versus time curves of C_1 and C_2 samples measured in 3.5 wt.% NaCl solution.

At the early immersion stage of 0 h–6 h, the volumes of hydrogen evolution of C_1 and C_2 samples are relatively low, indicating that the Mg-8Li alloy samples with the conversion coatings have good corrosion resistance. At the middle immersion stage of 6 h–18 h, the rates of hydrogen evolution of C_1 and C_2 samples are increased. Moreover, the difference in the volumes of hydrogen evolution of C_1 and C_2 samples increases at the same time. Based on the slopes of the curves, the hydrogen evolution rate of C_1 sample is remarkably lower than a C_2 sample when the immersion time varies from 6 h to 18 h, indicating that C_2 sample has less corrosion resistance than the C_1 sample. Moreover, the rates of hydrogen evolution of C_1 and C_2 samples during the period of 18 h–24 h are further increased, which should be related with the integrity of films. At this stage, the coating is probably invaded by Cl^- in NaCl solution, and the corrosion protectability of films is degraded, resulting in the increased dissolution of the substrate at anodic region and a high rate of hydrogen evolution in the cathodic region.

3.4. Corrosion Morphology

3.4.1. Surface Corrosion Morphology

The surface corrosion morphology and corresponding 3D images of C_1 and C_2 samples after immersed in 3.5 wt.% NaCl solutions for 2 h, 4 h, 6 h, 16 h and 24 h are shown in Figures 5 and 6. The heights of corrosion products of C_1 and C_2 samples increase with the prolonging of immersion time. However, the corrosion pits in C_1 sample are much weaker than those in the C_2 sample. The height of the pits of the C_1 sample is 35.75 μm after immersion for 2 h and increases to 69.95 μm after immersion for 24 h. At the same time, the C_2 sample has a value of 21.59 μm for the height of the corrosion products after immersion for 2 h and then the value increases to 118.77 μm after immersion for 24 h. Thus, the height of pits in C_1 sample is smaller than that of the C_2 sample at the same immersion time. After immersion for 24 h, there are still some regions without covering corrosion products at the surface of the C_1 sample, whereas the surface of the C_2 sample is completely occupied by corrosion products. By comparing the surface corrosion morphologies and the

corresponding 3D images of C_1 and C_2 samples, it can be concluded that the C_1 sample has the better corrosion resistance than the C_2 sample.

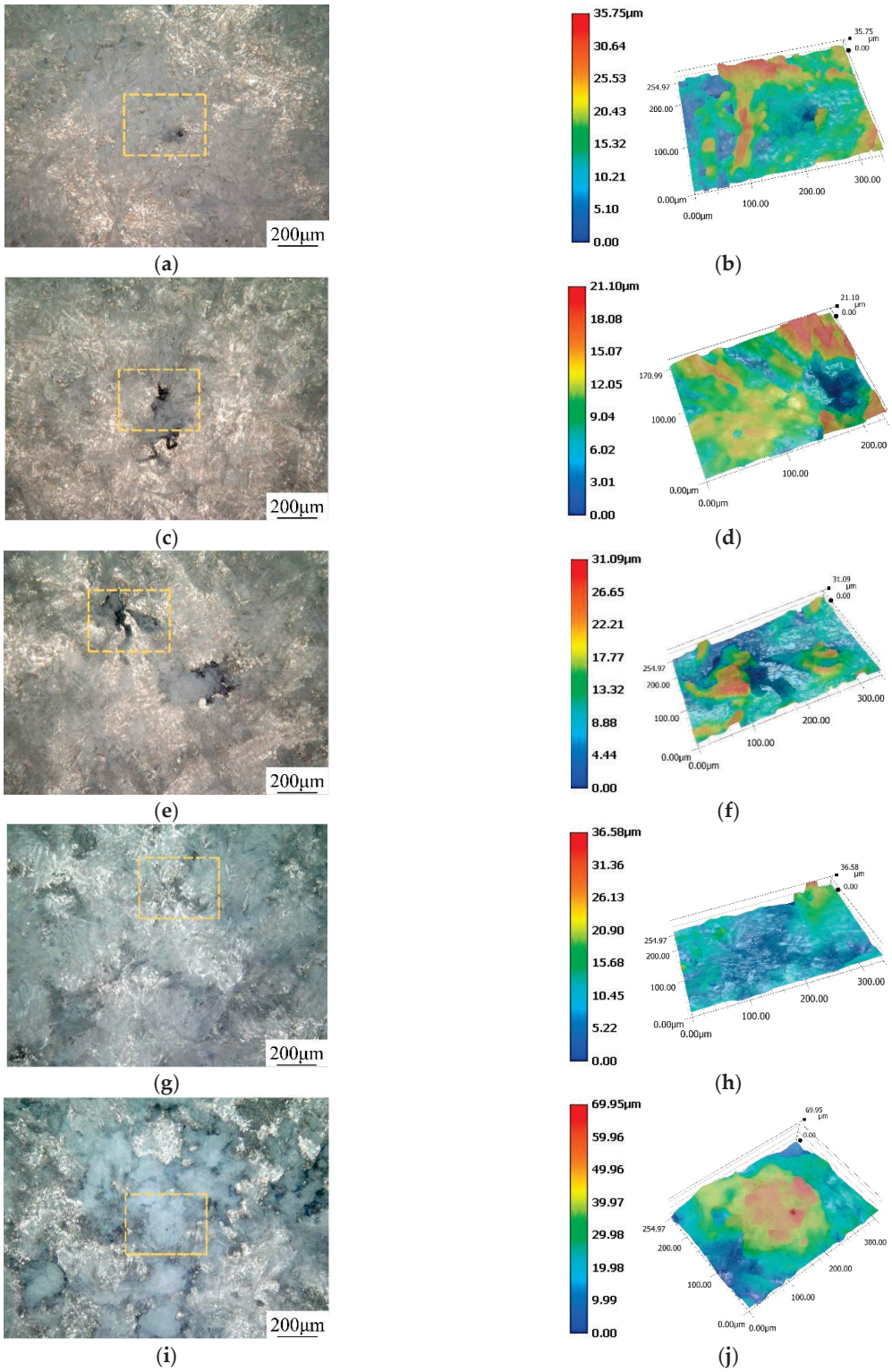


Figure 5. Surface morphologies of C_1 samples after being immersed in 3.5 wt.% NaCl solution for different immersion time: (**a**) 2 h, (**c**) 4 h, (**e**) 6 h, (**g**) 16 h, and (**i**) 24 h. Images (**b**,**d**,**f**,**h**,**j**) are the 3D images of the images (**a**,**c**,**e**,**g**,**i**), respectively.

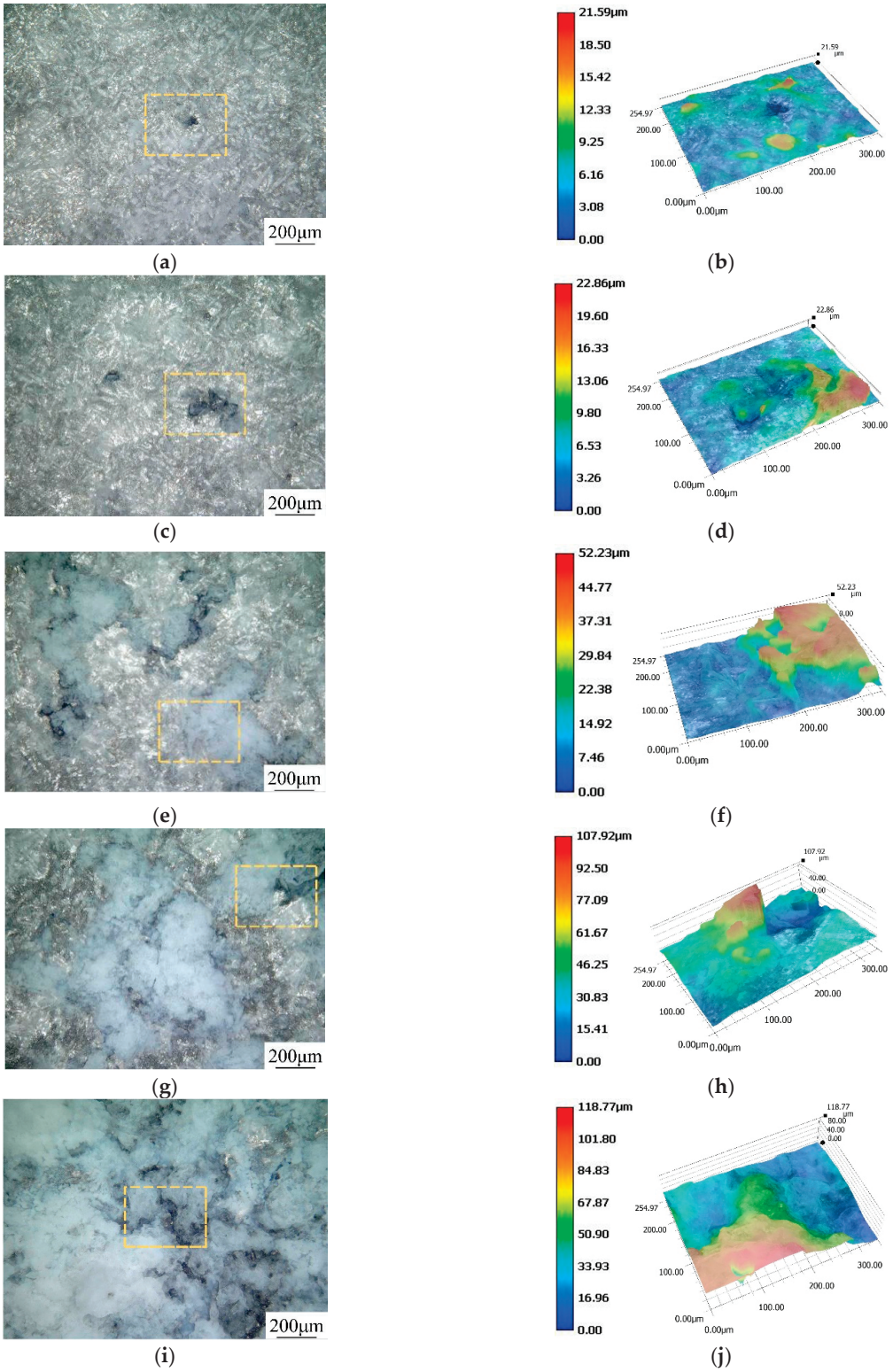
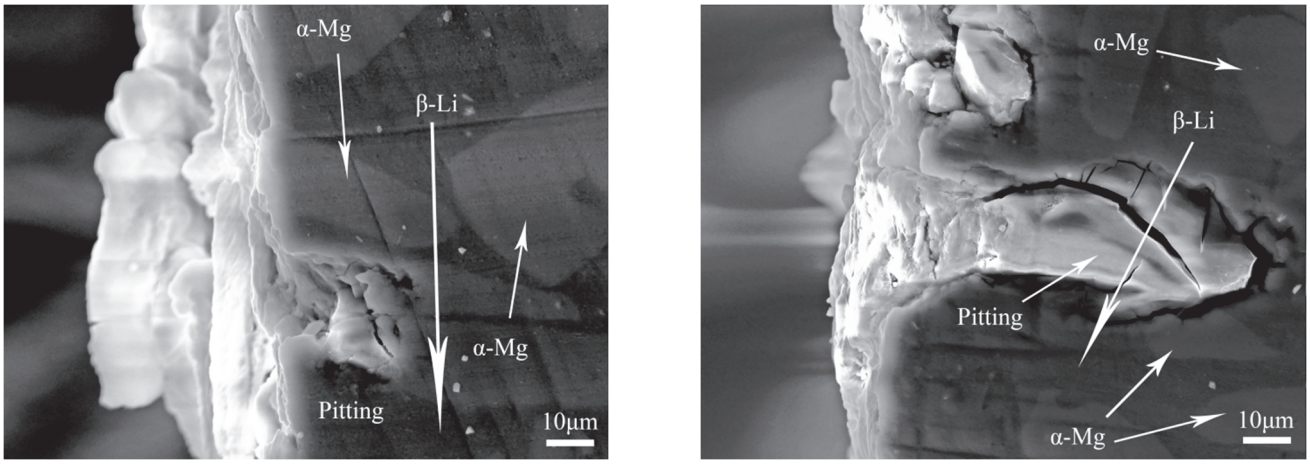


Figure 6. Surface morphologies of C_2 samples after being immersed in 3.5 wt.% NaCl solution for different immersion time: (**a**) 2 h, (**c**) 4 h, (**e**) 6 h, (**g**) 16 h, and (**i**) 24 h. Images (**b**,**d**,**f**,**h**,**j**) are the 3D images of the images (**a**,**c**,**e**,**g**,**i**), respectively.

3.4.2. Cross-Sectional Corrosion Morphology

To disclose the corrosion behavior of conversion coating of duplex structured Mg-Li alloys in detail, the cross-sectional corrosion morphologies of C_1 and C_2 samples immersed in 3.5 wt.% NaCl solution for 6 h are observed, as shown in Figure 7. It can be seen that the

localized corrosion of C_1 sample is much lighter than that of C_2 samples. The maximum depth of corrosion pits for C_1 sample is approximately 16 μm, whereas the corrosion pits on the surface exceed 40 μm in depth for the C_2 sample. It is worth noting that, for the two kinds of coated samples, corrosion pits preferentially occur in the α-Mg phase [11,64]. For the duplex structured Mg-Li alloys, the β-Li phase is preferentially corroded in the NaCl solution due to its lower potential. However, the film of Li_2CO_3 can be formed on the surface of the β-Li phase, which is dense and can provide a good corrosion protection to the underneath matrix [64]. It can be concluded that the corrosion mechanisms of calcium phosphate conversion coating on the duplex structured Mg-Li alloy are quite similar to the corrosion behavior of an uncoated alloy.



(**a**) (**b**)

Figure 7. Cross-sectional corrosion morphologies of: (**a**) C_1 and (**b**) C_2 samples after being immersed in 3.5 wt.% NaCl solution for 6 h.

4. Conclusions

(1) Since the SLS can accelerate the cathodic process of an electrode reaction, the thickness of a C_1 sample is much thicker than that of a C_2 sample and the petal-like particles of a C_1 sample have the bigger size when compared with those of a C_2 sample.
(2) The corrosion resistance of a C_1 sample is higher than a C_2 sample in 3.5 wt.% NaCl solution because it is more difficult for Cl^- to penetrate the thick coating and then can effectively weaken the corrosion attack of an Mg-8Li alloy.
(3) Corrosion pits and filiform-like corrosion can occur on the surfaces of C_1 and C_2 samples.

Author Contributions: Conceptualization, D.X. and B.W.; methodology, J.H.; software, L.C.; validation, B.W., J.H. and J.S.; formal analysis, B.W.; investigation, J.H.; resources, B.W.; data curation, J.H.; writing—original draft preparation, B.W.; writing—review and editing, L.C.; visualization, D.X. and B.W.; supervision, B.W.; project administration, D.X. and B.W.; funding acquisition, D.X. All authors have read and agreed to the published version of the manuscript.

Funding: This work was supported by the National Natural Science Foundation of China Projects under Grant Nos. 52071220, 51871211, U21A2049, 51701129, and 51971054, Liaoning Province's project of "Revitalizing Liaoning Talents" (XLYC1907062), the Doctor Startup Fund of Natural Science Foundation Program of Liaoning Province (No. 2019-BS-200), High level achievement construction project of Shenyang Ligong University (SYLUXM202105), the Strategic New Industry Development Special Foundation of Shenzhen (JCYJ20170306141749970), the funds of International Joint Laboratory for Light Alloys, the Liaoning BaiQianWan Talents Program, the Domain Foundation of Equipment Advance Research of 13th Five-year Plan (61409220118), the National Key Research and Development Program of China under Grant Nos. 2017YFB0702001 and 2016YFB0301105, the Innovation Fund of Institute of Metal Research (IMR), the Chinese Academy of Sciences (CAS), the

National Basic Research Program of China (973 Program) project under Grant No. 2013CB632205, and the Fundamental Research Fund for the Central Universities under Grant No. N2009006, and the Bintech-IMR R&D Program No. GYY-JSBU-2022-009.

Institutional Review Board Statement: Not applicable.

Informed Consent Statement: Not applicable.

Data Availability Statement: Not applicable.

Conflicts of Interest: The authors declare no conflict of interest.

References

1. Wu, R.Z.; Zhang, M.L. Reviews on the influences of alloying elements on the microstructure and mechanical properties of Mg-Li base alloys. *Rev. Adv. Mater. Sci.* **2010**, *24*, 14–34.
2. Guo, K.W. A Review of magnesium/magnesium alloys corrosion. *Recent. Pat. Corros. Sci.* **2011**, *1*, 72–90. [CrossRef]
3. Zhu, W.H.; Zheng, X.Z.; Feng, J.Z.; Hong, H.X.; Wang, Y.T.; Lu, L.L. Dynamic design method for magnesium alloys wheel of new energy vehicles. *Adv. Mat. Res.* **2010**, *961*, 930–934. [CrossRef]
4. Bolat, E.; Yanardağ, T.; Küyükoğlu, M.; Aksüt, A.A. Corrosion of magnesium modified with different compounds in chloride solution. *Prot. Met. Phys. Chem.* **2012**, *48*, 259–264. [CrossRef]
5. Haferkam, P.H.; Niemeyer, M.; Boehem, R. Development, processing and applications range of magnesium lithium alloys. *Mater. Sci. Forum.* **2000**, *350*, 31–42. [CrossRef]
6. Wang, B.J.; Xu, K.; Xu, D.K.; Cai, X.; Qiao, Y.X.; Sheng, L.Y. Anisotropic corrosion behavior of hot-rolled Mg-8 wt.% Li alloy. *J. Mater. Sci. Technol.* **2020**, *53*, 102–111. [CrossRef]
7. Aghion, E.; Bronfin, B.; Eliezer, D. The role of the magnesium industry in protecting the environment. *J. Mater. Process. Technol.* **2001**, *117*, 381–385. [CrossRef]
8. Kannan, M.B.; Raman, R.S. In vitro degradation and mechanical integrity of calcium-containing magnesium alloys in modified-simulated body fluid. *Biomaterials.* **2008**, *29*, 2306–2314. [CrossRef]
9. Cai, X.; Wang, Z.; Wang, X.Y.; Qiao, Y.X.; Xu, D.K.; Zhou, J.; Xue, F. Effect of quasicrystal I-Phase on microstructure and mechanical properties of hot-rolled diphasic Mg-8 wt.% Li alloy. *J. Mater. Eng. Perform.* **2021**, *31*, 3054–3064. [CrossRef]
10. Xu, D.K.; Wang, B.J.; Li, C.Q.; Li, C.Q.; Zu, T.T.; Han, E.H. Effect of icosahedral phase on the thermal stability and ageing response of a duplex structured Mg-Li alloy. *Mater. Des.* **2015**, *69*, 124–129. [CrossRef]
11. Li, C.Q.; Xu, D.K.; Chen, X.B.; Wang, B.J.; Wu, R.Z.; Han, E.H.; Birbilis, N. Composition and microstructure dependent corrosion behaviour of Mg-Li alloys. *Electrochim. Acta.* **2017**, *260*, 55–64. [CrossRef]
12. Li, C.Q.; Tong, Z.P.; He, Y.B.; Huang, H.P.; Dong, Y.; Zhang, P. Comparison on corrosion resistance and surface film of pure Mg and Mg14Li alloy. *T. Nonferr. Metal. Soc.* **2020**, *30*, 2413–2423. [CrossRef]
13. Wang, B.J.; Xu, D.K.; Cai, X.; Qiao, Y.X.; Sheng, L.Y. Effect of rolling ratios on the microstructural evolution and corrosion performance of an as-rolled Mg-8 wt.% Li alloy. *J. Magnes. Alloy.* **2020**, *9*, 560–568. [CrossRef]
14. Wang, B.J.; Hou, J.Y.; Luan, J.Y.; Xu, D.K.; Sun, H.J.; Sun, J. The corrosion behaviors of an as-Rolled Mg-8Li (in wt.%) alloy in two differently concentrated NaCl solutions. *Coatings.* **2022**, *12*, 406. [CrossRef]
15. Wang, B.J.; Luan, J.Y.; Xu, D.K.; Sun, J.; Li, C.Q.; Han, E.H. Research Progress on the Corrosion Behavior of Magnesium-Lithium-Based Alloys: A Review. *Acta Metall. Sin.* **2019**, *32*, 1–9. [CrossRef]
16. Xiong, X.M.; Yang, Y.; Deng, H.J.; Li, M.M.; Li, J.G.; Wei, G.B.; Peng, X.D. Effect of Ca content on the mechanical properties and corrosion behaviors of extruded Mg-7Li-3Al alloys. *Metals* **2019**, *9*, 1212. [CrossRef]
17. Xu, D.K.; Han, E.H. Effect of quasicrystalline phase on improving the corrosion resistance of a duplex structured Mg-Li alloy. *Scripta. Mater.* **2014**, *71*, 21–24. [CrossRef]
18. Zhao, Z.L.; Li, Y.H.; Zhong, Y.F.; Liu, Y.D. Corrosion performance of as-rolled Mg-8Li-xAl alloys. *Int. J. Electrochem. Sci.* **2019**, *14*, 6394–6405. [CrossRef]
19. Yao, Y. Effect of deformation and heat treatment on pitting corrosion behavior of 7050 Al alloy. *Int. J. Electrochem. Sci.* **2020**, *15*, 7531–7544. [CrossRef]
20. Perugu, C.S.; Cheksa, E.M.; Mohan, M.S.; Femi, O.E.; Padaikathan, P. Influence of cold rolling and thermal treatment on microstructure and texture evolution, and tensile behaviour of high strength Al-Co-Sc-Zr alloys. *J. Alloys Compd.* **2022**, *907*, 164427. [CrossRef]
21. Amir, M.M.; Mohammad, F.; Matin, P.; Mohammad, J.N. Effect of RE elements on the microstructural and mechanical properties of as-cast and age hardening processed Mg-4Al-2Sn alloy. *J. Magnes. Alloy.* **2018**, *6*, 309–317.
22. Xing, J.C.; Cheng, L.; Zheng, H.Z.; Zhao, M. Preparation and anticorrosion properties of polyaniline-containing coating on Mg-Li alloy. *Anti-Corros. Methods Mater.* **2012**, *59*, 7–8.
23. Fischerauer, S.F.; Kraus, T.; Wu, X.; Tangl, S.; Sorantin, E.; Hänzi, A.C.; Löffler, J.F.; Uggowitzer, P.J.; Weinberg, A.M. In vivo degradation performance of micro-arc-oxidized magnesium implants: A micro-CT study in rats. *Acta Biomater.* **2013**, *9*, 5411–5420. [CrossRef] [PubMed]

24. Hu, R.G.; Zhang, S.; Bu, J.F.; Lin, C.J.; Song, G.L. Recent progress in corrosion protection of magnesium alloys by organic coatings. *Prog. Org. Coat.* **2012**, *73*, 129–141. [CrossRef]
25. Wasserbauer, J.; Buchtík, M.; Tkacz, J.; Fintová, S.; Minda, J.; Doskočil, L. Improvement of AZ91 alloy corrosion properties by duplex Ni-P coating deposition. *Materials.* **2020**, *13*, 1357. [CrossRef] [PubMed]
26. Nakamura, A.; Oue, S.; Koga, H.; Nakano, H. Formation behavior of phosphoric acid-based chemical conversion coating containing alkaline earth metals on magnesium alloy. *J. Jpn. Inst. Met.* **2016**, *80*, 684–690. [CrossRef]
27. Thomaz, T.R.; Weber, C.R.; Pelegrini, T.; Dick, L.F.P.; Knörnschild, G. The negative difference effect of magnesium and of the AZ91 alloy in chloride and stannate-containing solutions. *Corros. Sci.* **2010**, *52*, 2235–2243. [CrossRef]
28. Ishizaki, T.; Kudo, R.; Omi, T.; Teshima, K.; Sonoda, T.; Shigematsu, I.; Sakamoto, M. Magnesium hydroxide/magnesium phosphate compounds composite coating for corrosion protection of magnesium alloy by a combination process of chemical conversion and steam curing. *Mater. Lett.* **2012**, *68*, 122–125. [CrossRef]
29. Pan, Y.K.; Chen, C.Z.; Feng, R.; Cui, H.W.; Gong, B.K.; Zheng, T.T.; Ji, Y.R. Effect of calcium on the microstructure and corrosion behavior of microarc oxidized Mg-xCa alloys. *Biointerphases* **2018**, *13*, 011003. [CrossRef]
30. Scharnagl, N.; Mueller, P. Pre-treatment and organic coating of Al free Mg alloy for controlling degradation rates. *Mater. Sci. Forum.* **2015**, *828–829*, 327–333. [CrossRef]
31. Liu, H.L.; Tong, Z.P.; Yang, Y.; Zhou, W.F.; Chen, J.A.; Pan, X.Y.; Ren, X.D. Preparation of phosphate conversion coating on laser surface textured surface to improve corrosion performance of magnesium alloy. *J. Alloys Compd.* **2021**, *865*, 158701. [CrossRef]
32. Hafeez, M.A.; Farooq, A.; Zang, A.; Saleem, A.; Deen, K.M. Phosphate chemical conversion coatings for magnesium alloys: A review. *J. Coat. Technol. Res.* **2020**, *17*, 827–849. [CrossRef]
33. Zhang, H.; Yao, G.C.; Wang, S.L.; Liu, Y.H.; Luo, H.J. A chrome-free conversion coating for magnesium–lithium alloy by a phosphate-permanganate solution. *Surf. Coat. Technol.* **2008**, *202*, 1825–1830. [CrossRef]
34. Sharma, A.K. Chromate conversion coating for magnesium-lithium alloys. *Met. Finishing.* **1989**, *87*, 73–74.
35. Sekiguchi, M.; Otani, C.; Takaya, M. Effect of conversion coatings on bond strength of magnesium alloy adhesive joints. *J. Jpn. I Light Met.* **2006**, *25*, 156–161. [CrossRef]
36. Ševčíková, B.; Fintová, S.; Wassebauer, J.; Tkacz, J. Effect of quench environment on the conversion coatings on magnesium alloy AZ91. *Acta Univ. Agric. Et Silvic. Mendel. Brun.* **2018**, *66*, 203–210. [CrossRef]
37. Zhao, H.; Cai, S.; Ding, Z.T.; Zhang, M.; Li, Y.; Xu, G.H. A simple method for the preparation of magnesium phosphate conversion coatings on a AZ31 magnesium alloy with improved corrosion resistance. *Rsc Adv.* **2015**, *5*, 24586–24590. [CrossRef]
38. Liu, F.; Shan, D.Y.; Han, E.H.; Liu, C.S. Barium phosphate conversion coating on die-cast AZ91D magnesium alloy. *Trans. Nonferrous Met. Soc.* **2008**, *18*, 344–348. [CrossRef]
39. Wu, Q.; Yu, B.X.; Zhou, P.; Zhang, T.; Wang, F.H. Fabrication of phosphate conversion coatings on rolled AZ31 magnesium alloy: Variation of corrosion resistance on different planes induced by the crystallographic texture. *Mater. Chem. Phys.* **2021**, *273*, 125121. [CrossRef]
40. Yue, J.H.; Lou, G.; Zhou, G.R.; Leng, J.F.; Feng, Y.; Teng, X.Y. Corrosion resistance of zinc phosphate conversion coatings on AZ91D surface. *Mater. Sci. Forum.* **2020**, *5930*, 1110–1117. [CrossRef]
41. Amini, R.; Sarabi, A.A. The corrosion properties of phosphate coating on AZ31 magnesium alloy: The effect of sodium dodecyl sulfate (SDS) as an eco-friendly accelerating agent. *Appl. Surf. Sci.* **2011**, *257*, 7134–7139. [CrossRef]
42. Phuong, N.V.; Lee, K.; Chang, D.; Kim, M.; Lee, S.; Moon, S. Zinc phosphate conversion coatings on magnesium alloys: A review. *Met. Mater. Int.* **2013**, *19*, 273–281. [CrossRef]
43. Cui, X.J.; Bai, C.B.; Zhu, Y.B.; Wen, H.Y.; Wang, R.; Lin, X.Z. Effect of additives $Mn(NO_3)_2$ and/or Na_2MoO_4 on micromorphology and corrosion performance of phosphate coating on AZ31B magnesium alloy. *J. Chin. Soc. Corros. Prot.* **2014**, *34*, 477–482.
44. Thomas, R.; Umapathy, M.J. Environment friendly nano silicon dioxide accelerated zinc phosphate coating on mild steel using a series of surfactants as additives. *Silicon* **2017**, *9*, 675–688. [CrossRef]
45. Lou, G.; Jia, P.; Teng, X.Y.; Zhang, J.Y.; Ye, Z.J.; Wu, H.; Leng, J.F.; Zuo, M. Nano ZnO-assisted formation of zinc phosphate conversion coating for improving corrosion protection of AZ91D magnesium alloy. *Mater. Res. Express.* **2019**, *6*, 086405. [CrossRef]
46. Phuong, N.V.; Gupta, M.; Moon, S. Enhanced corrosion performance of magnesium phosphate conversion coating on AZ31 magnesium alloy. *T. Nonferr. Metal. Soc.* **2017**, *27*, 1087–1095. [CrossRef]
47. Maurya, R.; Siddiqui, A.R.; Balani, K. An environment-friendly phosphate chemical conversion coating on novel Mg-9Li-7Al-1Sn and Mg-9Li-5Al-3Sn-1Zn alloys with remarkable corrosion protection. *Appl. Surf. Sci.* **2018**, *443*, 429–440. [CrossRef]
48. Yan, W.; Chen, Z.; Yu, Q.; Zhu, W.; Wang, H.; Du, B.Q. Effects of fatty alcohol polyoxyethylene ether AEO on PbO_2 structure and electrodeposition behavior. *J. Electrochem. Soc.* **2016**, *163*, D414–D420. [CrossRef]
49. Xu, Y.D.; Qi, S.; Wang, L.; Shi, M.; Ding, N.; Pang, Z.C.; Wang, Q.; Peng, X.D. Effects of hydroxylamine sulfate and sodium nitrite on microstructure and friction behavior of zinc phosphating coating on high carbon steel. *Chin. J. Chem. Phy.* **2015**, *28*, 197–202. [CrossRef]
50. Sankaranarayanan, T.; Subbaiyan, M. Influence of hexadecyl dithiocarbamate on phosphate surface chemical conversion coatings on mild steel. *Surf. Coat. Tech.* **1990**, *43*, 543–553. [CrossRef]
51. Niu, L.Y.; Li, G.Y.; Jiang, Z.H.; Sun, L.P.; Han, D.; Lian, J.S. Influence of sodium metanitrobenzene sulphonate on structures and surface morphologies of phosphate coating on AZ91D. *Trans. Nonferrous. Met. Soc. China.* **2006**, *16*, 567–571. [CrossRef]

52. Noh, Y.T.; Kim, H.Y.; Byoun, Y.M.; Seo, S.K.; Hyun, S.K.; Lee, C.H. Effect of surface activation agents on manganese phosphate coating of carbon steel. *J. Nanosci. Nanotechnol.* **2019**, *19*, 4188–4194. [CrossRef]
53. Sun, R.X.; Wang, P.F.; Zhao, D.D.; Sun, Z.Z.; Li, C.Q.; Chen, K.Z. An environment-friendly calcium phosphate conversion coating on AZ91D alloy and its corrosion resistance. *Mater. Corros.* **2015**, *66*, 383–386. [CrossRef]
54. Gray, J.E.; Luan, B. Protective coatings on magnesium and its alloys-A critical review. *J. Alloys Compd.* **2002**, *336*, 88–113. [CrossRef]
55. Su, Y.C.; Cuo, Y.T.; Huang, Z.L.; Zhang, Z.H.; Li, G.Y.; Lian, J.S.; Ren, L.Q. Preparation and corrosion behaviors of calcium phosphate conversion coating on magnesium alloy. *Surf. Coat. Technol.* **2016**, *16*, 21516. [CrossRef]
56. Zai, W.; Zhang, X.R.; Su, Y.C.; Man, H.C.; Li, G.Y.; Lian, J.S. Comparison of corrosion resistance and biocompatibility of magnesium phosphate (MgP), zinc phosphate (ZnP) and calcium phosphate (CaP) conversion coatings on Mg alloy. *Surf. Coat. Technol.* **2020**, *397*, 125919. [CrossRef]
57. Zhang, L.S.; Jiang, Y.; Zai, W.; Li, G.Y.; Liu, S.C.; Lian, J.S.; Jiang, Z.H. Fabrication of superhydrophobic calcium phosphate Coating on Mg-Zn-Ca alloy and its corrosion resistance. *J. Mater. Eng. Perform.* **2017**, *26*, 6117–6129. [CrossRef]
58. Chen, X.B.; Birbilis, N.; Abbott, T.B. Effect of [Ca^{2+}] and [PO_4^{3-}] levels on the formation of calcium phosphate conversion coatings on die-cast magnesium alloy AZ91D. *Corros. Sci.* **2012**, *55*, 226–232. [CrossRef]
59. Zhu, Y.H.; Zhi, Y.S.; Fan, J.W. *Industrial Water Treatment*; Tong Ji University Press: Shanghai, China, 2016.
60. Liu, Y.M.; Zhang, P.S. *Commonly Used Excipients for Pharmaceutical Preparations*; Tianjin Technology Translation Publication: Tianjin, China, 1994.
61. Machu, W. Remarks on the response of R Weiner to F Halla to my work: "The cover theory of passivity, the restrained pickling solution theory and phosphatisation". *Z. Fur Elektrochem. Und Angew. Phys. Chem.* **1943**, *49*, 137.
62. Katarzyna, M.; Marta, L. Voltametric determination of natamycin using a cathodically pretreated boron-doped diamond electrode in the presence of sodium dodecyl sulfate. *Microchem. J.* **2020**, *159*, 105570.
63. Guzel, Z.; Endzhe, Z.; Herman, B. Electrochemical reduction and quantification of menadione in sodium dodecyl sulfate micellar media. *J. Solid. State. Electrochem.* **2013**, *17*, 2679–2685.
64. Xu, W.Q.; Birbilis, N.; Sha, G.; Wang, Y.; Daniels, J.E.; Xiao, Y.; Ferry, M. A high-specific-strength and corrosion-resistant magnesium alloy. *Nat. Mater.* **2015**, *14*, 1229–1235. [CrossRef] [PubMed]

coatings

MDPI

Article

Improvement of Monitoring Technology for Corrosive Pollution of Marine Environment under Cloud Computing Platform

Yongzeng Jiang [1,*], Jing Dong [2], Xiaoyu Qi [2] and Fazhi Wang [2]

[1] College of Computer and Control Engineering, Qiqihar University, Qiqihar 161000, China
[2] College of Communication and Electronic Engineering, Qiqihar University, Qiqihar 161000, China; darkblue_312@163.com (J.D.); dongjing_1979@126.com (X.Q.); fazhiwang2021@126.com (F.W.)
* Correspondence: qdrsch@126.com

Abstract: In view of the increasingly serious problem of marine ecological environmental pollution, the traditional marine environmental corrosive pollution monitoring technology has poor monitoring accuracy and poor monitoring timeliness, and the improvement of the marine environmental corrosive pollution monitoring technology under the cloud computing platform is proposed. The research significance and corrosion influence factors of steel corrosion in the marine environment are described, and the research progress of corrosion mechanism in five different zones of the marine environment is reviewed. Cloud computing parallelizes the processing of corrosive pollution data in the marine environment through virtualization and distributed technology, which greatly improves the efficiency of the algorithm. This paper studies the existing cloud computing platform and ocean monitoring system architecture, uses the distributed architecture to design a cloud computing-oriented ocean monitoring system and meets the design requirements in data collection and data processing. The experimental results show that the precision of marine environmental corrosion pollution monitoring technology proposed in this paper is 96% on average, and the completion rate of monitoring images is 82% on average, which can effectively realize marine environmental corrosion pollution monitoring.

Keywords: cloud computing; marine environment; corrosive pollution; environmental monitoring

1. Introduction

The global marine environmental problems endanger the safety of marine ecosystems and human health. Online, real-time, sensitive, and safe implementation of marine environmental monitoring, providing a scientific basis for marine environmental planning, environmental management (especially pollutant total control, environmental law enforcement), environmental governance, etc., has become a major social demand and a key scientific issue. The ocean contains huge resource wealth and has extremely broad development prospects: the development and utilization of ocean resources cannot be separated from the construction of offshore infrastructure. Because the marine environment is very corrosive to the steel structure, it is easy to form corrosive water film on the steel surface due to the influence of the atmospheric environment with far higher relative humidity. Moreover, seawater contains a high concentration of salt, forming an electrolyte solution that is easy to conduct electricity, and has extremely high corrosiveness [1]. At the same time, waves, tides, and currents will produce low-frequency reciprocating stress and impact metal components. In addition, marine microorganisms, attached organisms, and their metabolites will directly or indirectly accelerate the corrosion process. Therefore, engineering materials such as steel structures widely used in many engineering fields are prone to various catastrophic corrosion damage. This not only involves the waste of materials but more serious is the cause of catastrophic accidents, causing oil and gas leakage, causing environmental pollution, casualties, etc., resulting in huge economic losses. As an industrial material, steel materials are widely used in marine environments due to

their high toughness, high strength, and low price. However, the harsh marine corrosive environment makes the corrosion of steel structures inevitable. Therefore, steel corrosion and protection in the marine environment is a major issue as a research subject [2,3]. Therefore, monitoring technologies for corrosive pollution in the marine environment is of great significance for extending the service life of marine steel facilities, ensuring the normal operation and safe use of marine steel structures, and promoting the development of the marine economy.

The development of the ocean by mankind has put more and more pressure on the marine environment; at the same time, marine pollution sources are diversified, such as industrial chemical pollution, marine noise pollution, and biological pollution. The accuracy and timeliness of real-time monitoring of pollution sources is the key to the entire marine environmental protection system [4,5].

Wu and Liao (2019) propose a laser-induced fluorescence marine pollution detection method [6]. According to the law of ultraviolet radiation energy distribution given by Beer's law, a large number of laser-induced fluorescence detection of the influence of ultraviolet radiation on marine oil pollution are eliminated, and the wavelength is 360 nm. The laser raises the Raman scattering peak, reduces the overlap of Raman scattering and fluorescence, and reduces the detection error; Qin et al. established a hazardous chemical marine environment emergency monitoring information card, which includes classification, index number, and inclusion in the list, physical and chemical judgment of nature and behavior characteristics, health hazards and protection requirements, detection methods and evaluation standards, and four other types of information [7]. It is recommended to further screen the typical or high-risk chemicals involved in marine pollution accidents, refine the SEBC system, and strengthen rapid detection technology research.

The traditional marine environment monitoring system is based on single-center information processing. With more and more types of pollution sources monitored, the single-center processing structure has become increasingly unable to adapt to the timeliness requirements of modern monitoring systems [8–12]. With the development of network technology, data collection is moving towards large concurrency and broadband development. The later data transmission and processing capabilities need to match the front-end concurrency and rate requirements. The cloud computing platform is based on a new generation of computing and storage architecture. It uses virtualization technology and distributed technology to uniformly logically divide the hardware of different protocols in the network; at the software level, it uses MPI technology to parallelize multiple algorithms, and the divided logical subprograms are dispatched to each logical computing unit to realize the parallelization of the program. This paper proposes an improved technology for monitoring corrosive pollution in the marine environment under a cloud computing platform.

2. Corrosive Pollution of the Marine Environment

2.1. Influencing Factors of Steel Corrosion in Marine Environment

Seawater is not only constituted of salinity between 32% and 37%. Other important factors affecting corrosion are the pH value between 8 and 8.2, such as the sky value, the flow velocity, marine organisms, and other environmental elements [13–15]. They are also often interrelated.

(1) Dissolved oxygen: Oxygen is a depolarizer for the seawater corrosion of steel. If there is no dissolved oxygen in the seawater, steel will not corrode. Therefore, dissolved oxygen in seawater is one of the important factors affecting the corrosion of steel in the sea. It continuously reacts in the cathode area of the microbattery corroded by steel and produces strong cathode depolarization. The metal in the anode area of the microbattery continuously dissolves to form ferrous hydroxide, which causes the metal to be corroded. On the other hand, for those metals that rely on surface passivation film to improve corrosion resistance, such as stainless steel, the formation, and repair of the metal surface oxide film can inhibit the corrosion reaction to a certain extent.

(2) Salinity: A large number of neutral salts such as NaCI, KCI, and Na_2SO_4 are dissolved in seawater, of which NaCl accounts for 78%. The concentration of NaCl in seawater is generally about 3%. The corrosion rate is at its maximum near this concentration. When the salt concentration is low, the corrosion rate increases rapidly as the salt content increases. This is mainly due to the increase in cl-promoting the anode reaction. In addition, since the solubility of oxygen decreases with the increase of salt concentration, the corrosion rate decreases significantly when the salinity in the solution continues to increase.

(3) Temperature: The oxidation reaction of iron and steel occurs in seawater. Generally speaking, the reaction speed increases when the temperature rises. However, this mutual relationship is very complicated, and the corrosion rate does not increase proportionally with the increase in temperature. It is also related to other factors such as oxygen diffusion. The corrosion rate is dominated by oxygen diffusion. At a temperature of 1.2 L, the solubility of oxygen in the solution is reduced, which slows down the reaction process of the cathode. In a closed system, when the temperature rises, the oxygen in the solution does not decrease, and the corrosion rate increases linearly with the rise of the temperature; but in an open system, the oxygen content in the water gradually decreases as the temperature rises. When the water temperature is between 80 and 90 °C, the corrosion rate is significantly reduced. When the temperature reaches the boiling point of 100 °C, the corrosion rate drops to the lowest value.

(4) pH value: Generally speaking, the increase of the pH value of seawater is beneficial to inhibiting the corrosion of steel by seawater. However, the pH value of seawater has a small change, which will not have a significant impact on the corrosion of steel and seawater (far from it with a large oxygen content). Although the pH value of surface seawater is higher than that of deep seawater, surface seawater has higher oxygen content than deep seawater, so surface seawater is more corrosive to steel than deep seawater. The pH value of seawater mainly affects the deposition of calcareous scale, which affects the corrosiveness of seawater. Under the condition of the pH value of seawater, the carbonate in the seawater is generally saturated, so even if the pH value does not change much, it will affect the deposition of the calcium carbonate scale. As the pH value increases, calcium deposits are easily formed, and seawater is less corrosive. When applying cathodic protection, this deposited layer is beneficial to cathodic protection.

(5) Flow rate: The flow of liquid on the metal surface can promote the circulation of corrosion products in the solution, accelerate the diffusion of oxygen, and also remove the corrosion products attached to the metal surface, thereby promoting metal corrosion. However, this refers to steel that is difficult to form a passivation film on the surface. The steel that easily forms a passive film on the surface is different, such as stainless steel. Due to the flow of seawater, a passive film is easily formed on the surface, and the corrosion rate will decrease instead. In a nearly neutral aqueous solution, since the corrosion reaction of the metal is controlled by the reduction of oxygen, the higher the flow rate, the more severe the corrosion. No matter what the situation, a thin water film will always adhere to the metal surface. When the flow rate becomes larger, at this time, the thickness of the film will be reduced, making it easier to diffuse oxygen through the film to the metal surface.

(6) Marine life: The impact of marine life on steel corrosion is complex. Sometimes the attachment of some organisms can reduce the corrosion rate of steel, but soon it will accelerate the corrosion, produce pitting corrosion, or damage the coating. First of all, the surface of steel: the part covered by the organism becomes the anode because the supply of oxygen is controlled, and the part not covered by the organism becomes the cathode, which will cause local corrosion, or the inside and outside of the adhesion layer may produce oxygen concentration cell corrosion; secondly, due to biological life activities, the composition of the seawater on the surface of the steel is changed,

which changes the nature of the water and accelerates the corrosion of the steel. In addition, certain sea creatures can penetrate the protective layer when they grow, and directly destroy the protection. The adhesion of certain marine organisms to the protective layer is even greater than the adhesion of the protective layer to the metal. Therefore, under the action of mechanical loads such as seawater impact, the marine organisms peel off with the protective layer, causing the protective layer to be damaged, and the corrosion of steel is changed.

2.2. Corrosion Mechanism of Steel in Various Corrosion Zones in the Marine Environment

From the perspective of corrosion, the marine environment is generally divided into five corrosive zones: the ocean atmosphere zone, wave splash zone, tidal range zone, sea umbrella flood zone, and the submarine soil zone. There are three corrosion peaks in the marine corrosion environment. One peak is located in the spray splash area at the average high tide level. It is the most severe area of steel corrosion and the most severe marine corrosion environment. The second peak usually occurs 0.5–1.0 m below the average low tide line. The third peak occurs below the junction with sea and mud [16,17].

(1) Corrosion of steel in the marine atmosphere: the marine atmosphere refers to the atmosphere above the splash zone and the coastal atmosphere. For steel structures in the ocean, it refers to the parts that are not in contact with seawater all year round. The ocean atmosphere has high humidity, and water vapor easily adheres to the surface of the steel to form a water film invisible to the naked eye. The standard electrode potential of the main element of steel and the trace element carbon is different. They form when they are in the electrolyte solution (water film) at the same time. In galvanic cells, iron is oxidized as an anode and loses electrons, turning into rust. This is basically the same as the corrosion in the inland atmosphere. However, due to the high relative humidity of the ocean atmosphere, the thick water film, the high salt content, and the strong electrolytic capacity of the water film, the corrosion of steel is accelerated. At the same time, the steel in the ocean atmosphere is exposed to sunlight during the day and the water evaporation increases the surface salinity. With the formation of a wet surface, this dry-wet cycle makes the corrosion rate greatly accelerated;

(2) Corrosion of steel in the splash zone: the splash zone refers to the marine environment. Seawater can splash on the surface of the structure, which is the part of the section that cannot be submerged by the seawater when the seawater is at high tide. For many metal materials, the splash zone is the most corroded part of all marine environments. Foreign scholars believe that the reason the splash zone has become the most severely corroded part of all marine environments, is due to sea water splashingasit is difficult to form a protective rust layer on the surface of steel with a short drying time; and compared with the marine atmosphere, its sunlight exposure is the same. This is due to the movement and evaporation of seawater so that the accumulation of sea salt particles within a certain range of the average high tide level is far greater than the accumulation in the ocean atmosphere. In general, the large number of salt particles, the long water film retention time, and the high frequency of dry and wet alternates are external factors that cause severe corrosion of steel in the splash zone. The internal factor is that the steel in the splash zone is corroded due to surface rust during the corrosion process.

(3) The corrosion of steel in the tidal range refers to the area between the average high tide level and the average low tide level of seawater. There are two main types of steel corrosion in the tidal range. One is the corrosion of steel components that are isolated in the tidal range, for example, the corrosion of the sewage gate in the tidal range; the other is the steel pile type. The corrosion + experiment proved that the corrosion rate of the respective tufted pieces in the tidal range is much greater than that of the long-length coupons. Through the corrosion current measurement experiment, the main reason for the above phenomenon is that the macroscopic battery is formed

between the underwater part and the tidal range of the long-length coupon. The tidal range is the cathode area where oxygen is fully supplied to form the macro battery, and the underwater part becomes the anode area of the macro battery. The anode area provides protection current to the cathode area to reduce corrosion in the tidal range. It should be pointed out that although the specimens in the tidal range are protected to a certain extent, they still corrode. Although all the specimens in the tidal range get the protection current of the specimens in the seawater full immersion zone, the upper part of the specimens has a short immersion time in the seawater, and the time to obtain the current is short, plus the time in the air. Longer immersion timemeans the free corrosion time is also longer; while the corrosion of the lower part of the specimen is just the opposite. Therefore, the corrosion rate of the upper part of the specimen in the tidal range is greater than that of the lower part of the specimen.

(4) Corrosion of steel in the seawater full immersion zone: the seawater full immersion zone refers to the area below the low tide level all year-round to the seabed. According to different sea depths, it is divided into shallow water area (within 20 m–30 m below the low tide level), continental shelf full immersion area (in the water depth area of 30 m to 200 m), and the deep sea area (>200 m water depth area): the three areas affect the corrosion of steel structures. The elements of this water are different due to the water depth. In the shallow sea area, the seawater velocity is relatively high, and there is offshore chemical and sediment pollution. Steel corrosion is mainly electrochemical, and the physical and chemical corrosion is supplemented. The corrosion in this water area is lighter than that in the shallow sea area; the pressure increases with the depth of the water, the dissolved mineral salt decreases, the water flow, and the temperature aeration are low, and the steel corrosion is mainly electrochemical corrosion and stress corrosion, and chemical corrosion is the second. Therefore, generally speaking, due to the high content of oxygen in seawater and the almost neutral pH, the corrosion mechanism of metals in seawater is mainly controlled by the cathodic reaction produced by the reduction of oxygen.

(5) Corrosion of iron and steel in the submarine soil zone. The sea cement soil zone refers to the part below the seawater flooding zone, which is mainly composed of seabed sediments. The physical, chemical, and biological properties of seabed sediments vary with the sea area and sea depth. Compared with terrestrial soil, the submarine mud area has high salt content and low resistivity. The submarine mud is a good electrolyte and corrodes steel more strongly than in terrestrial soil. In addition, the bottom soil area usually contains bacteria, mainly anaerobic sulfate-reducing bacteria, which can grow and multiply under anoxic environmental conditions. The static pressure of seawater will increase the activity of bacteria.

2.3. Intelligent Image Monitoring Technology for Corrosive Pollution in the Marine Environment

Relying on the integrated data collection of intelligent digital remote sensing technology and water quality sensor monitoring technology, the pollution information is fully extracted. Because of the huge amount of extracted data, a comparative analysis is difficult. To solve the above problems, we optimize the big data comparative analysis method to process the collected data. First, redefine the type of data source to be collected. By extracting image information and data sources, and comparing big data with standard pollution images and pollution parameters, comprehensive monitoring results can be obtained. A water quality sensor is one of the important methods of marine environmental pollution monitoring technology. In this paper, the dissolved oxygen, salinity, temperature, and pH value of seawater are monitored by a water quality sensor.

The introduction of intelligent digital remote sensing technology is to rely on remote sensing satellites to build intelligent data modules to monitor marine environmental pollution and obtain available information through screening and analysis of multi-layer databases. Intelligent digital remote sensing technology structure includes image layer, ocean information display layer, and ocean analysis display layer. The function of the image

layer is to use remote sensing satellites to remotely sense the marine environment, to simply process and package the captured pictures, and to send them to the marine information processing interface through wireless transmission [18–20]. The marine information processing layer digitally displays the monitored information in the image layer and processes it by relying on the marine object database and the marine environment physical field analysis database. The data is passed to the analysis display layer for data analysis. The analysis display layer accepts the data information of the ocean information display layer and uses the data link mode, image data module, and data mining technology to perform image processing. The intelligent data remote sensing database structure process is shown in Figure 1. The main function of the marine satellite image database is to process and segment satellite images, identify objects, construct multi-dimensional image organization, and calculate the physical distance between images. The main function of the marine object database is to analyze the manifolds of the marine environment physical field, the embedded dimensions of the marine physical field manifolds, the low-micro distribution analysis, and the feature extraction of marine objects [21].

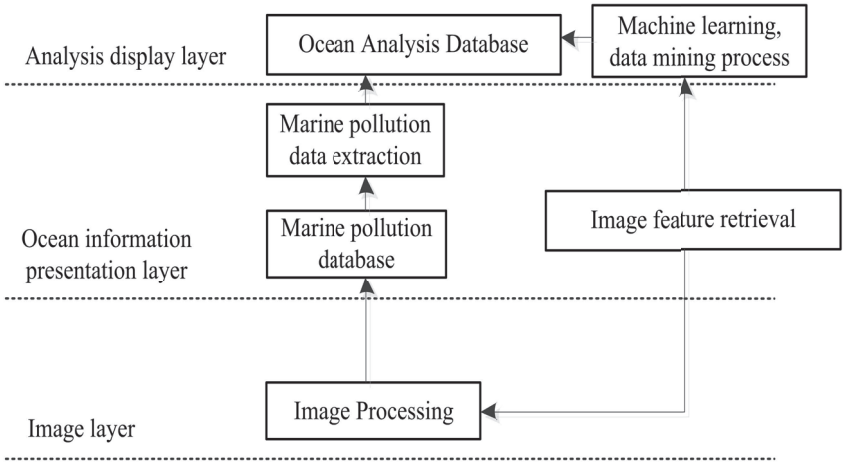


Figure 1. Intelligent remote sensing monitoring structure of corrosive pollution information in marine environment.

3. Improvement of Monitoring Technology for Corrosive Pollution in the Marine Environment Based on Cloud Computing Platform

On the basis of the above-mentioned intelligent image monitoring technology of marine environmental pollution and corrosive information, a cloud computing platform is introduced. The proposed ocean environment system for the cloud computing platform provides a brand-new architecture process in sample collection, data synchronization, and data transmission processing. The extraction and distribution of corrosive pollution in the ocean environment are carried out by using the phase space distributed reconstruction method. For reconstruction, extract the corrosive pollution characteristics of the ocean environment of the cloud computing center, and realize the synchronous monitoring of data.

3.1. Functional Modules of the Marine Environment Corrosive Pollution Monitoring System

The function of the ocean monitoring system of the cloud computing platform is divided into two parts: the system client and the mobile terminal [22]. The entire ocean monitoring system is divided into the following four types of functions according to functions:

(1) System management. Including system management and task management, it can realize the addition and deletion of the overall system functions.
(2) Data recruitment and processing. Including data collection, recruitment, classification, and processing, it is the core of the entire system.

(3) Data encoding and encryption. Since the marine environmental monitoring systems of various countries may contain secret level information, the collected data needs to be encrypted and the data must be encoded at the same time.
(4) Data synchronization function. Keep the data of the monitoring system synchronized with the data of the marine ship information center and storage server.

3.2. Design of a Monitoring System for Corrosive Pollution in the Marine Environment Based on a Cloud Computing Platform

3.2.1. System Total Module

The client of the entire system is mainly divided into five functions: environmental monitoring sample data collection, function parameter configuration, data synchronization, various tool integration, and environmental monitoring task configuration [23–25]. Among them, environmental monitoring sample data collection is classified according to various types of monitoring information, including marine water quality data collection, marine mineral data collection, marine microbial organism data collection, and marine meteorological data collection. Each data collection package sets different types of keys. It also performs synchronous interaction in the data center to complete the issuance of collection commands and the upload of collected data [26].

Function parameter configuration and task configuration are the basic configurations of the ship before going to sea, including the general task of going to sea; tool integration includes all kinds of tools that the ship needs to carry for environmental monitoring tasks (see Figure 2).

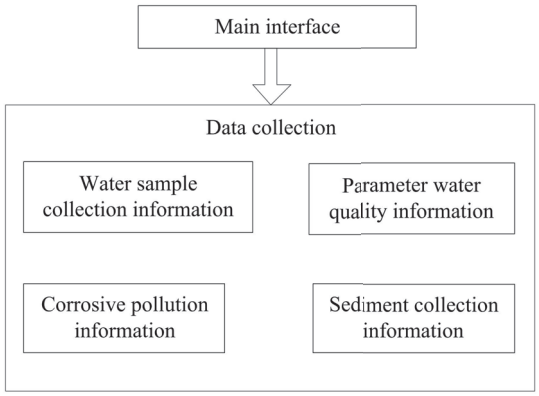


Figure 2. Functional module diagram of the marine environment corrosive pollution monitoring system.

3.2.2. Jump to Each Activity Task on the Mobile Terminal

The start and jump of each task between the mobile terminal are realized through Intent. Its essence is to bind the port of different task processes. It can bind the same port of multiple processes at the same time, and send the opening and closing of the task component through the Intent and the mobile terminal. The client activity program is based on data collection, coefficient parameter setting, data collection handover, tool integration, environmental monitoring task initialization, and client main program. The designed components include: MainAxtivity, SampleActivity, SetActivity, HandoverActivity, SynchroActivity, ToolActivity, TaskActivity, UserActivity, InputActivity, TsiActivity. Process switching between tasks through Intent.

After the mobile client is opened, it first executes the MainAxtivity task, and at the same time sends task instructions to MainAxtivity, which can directly jump to any other components. This kind of jump does not involve data interaction, which is called a single jump. The mobile client program contains multiple UIs, and each UI (User Interface) corresponds to an Activity. The switching of these Activity activities is also switched through the Intent process. The intent process carries the jump message, which contains the following content:

(1) Action: Used to identify the specific jump type, such as the jump initiate Action_Call, data synchronization Action_Sync.
(2) Category: Activity behavior type of this UI, formulate specific Intent type.
(3) Data: The data to be transmitted.
(4) Component: Various components are included in the action behavior. The Intent process parses the jump behavior, all data is packaged in the Manifest.xml file, and all actions are registered during initialization. The Intent then parses out the type of Action and makes a response jump, while data transmission is performed.

3.2.3. Data Synchronization

The phase-space distributed reconstruction method is used to construct the cloud computing center sample sequence distribution structure model, and the fuzzy information fusion method is used to extract and distribute the corrosive pollution of the marine environment, and extract the characteristic value of the corrosive pollution of the marine environment of the cloud computing center:

$$j \in N_i(k), N_i(k) = \left\{ \left\| x_j(k) \right\| < r_d(k) \right\} \tag{1}$$

In the formula, $N_i(k)$ is the sample sequence distribution, $x_j(k)$ is the output limit deviation rate, $r_d(k)$ is the cumulative distribution function of the standard normal distribution.

The matched filter detection method is used to obtain the statistical distribution matrix C_2 of corrosive pollution in the marine environment of the cloud computing center, and its element $C_2(m,n)$ is:

$$C_2(m,n) = cum\left\{ x_m^*(t+1), x_{m+1}(t), x_{n+1}^*(t), x_n(t) \right\} \tag{2}$$

In the formula, m,n is the corrosive pollution surface distribution and depth distribution, $x(t)$ is the corrosion area, $*$ is the conjugate function.

Using the method of information fusion filtering analysis, the marine environment corrosive pollution information fusion is carried out [27], and the following matrix is constructed to represent the characteristic quantity of the corrosive pollution in the marine environment of the cloud computing center:

$$C = \begin{bmatrix} C_1 & C_2 & C_5 & C_4 \\ C_2^H & C_1 & C_6 & C_7 \\ C_5^H & C_6^H & C_1 & C_3^H \\ C_4^H & C_7^H & C_3 & C_1 \end{bmatrix} = \overline{A} C_{4s} \overline{A}^H \tag{3}$$

In the formula $\overline{A} = \left[A^H, (A\Lambda)^H, (A\Omega)^H, (A\Phi)^H \right]^H$, it represents the characteristic quantity of the similarity of the corrosive pollution of the marine environment of the cloud computing center.C_i is the various corrosion parameters, H is the weight, Λ, Ω, Φ is the similarity.

Calculate the maximum utility merging set, establish a fitness function for adaptive optimization of marine environment corrosive pollution monitoring, in the frequent item [28], obtain the fusion function of the cloud computing center for marine environment corrosive pollution detection:

$$\begin{cases} a(H_{ac}) = 1 - \frac{H_{ac}}{\max(H_{ac}) + l} \\ \max(H_{ac}) = \log_2 k \end{cases} \tag{4}$$

In the formula, H_{ac} is the fuzzy attribute value of similarity, l is the minimum utility threshold, k is the adaptive degree.

The adaptive optimization algorithm is used to perform multi-dimensional search and fuzzy clustering of corrosive pollution in the marine environment of the cloud computing center, and improve the detection capability of corrosive pollution in the marine environment.

In this paper, the client data synchronization based on the cloud platform is implemented based on a message-driven mechanism. The design concept is as follows:

(1) Message: The specific message object has a unique ID and is managed by Message Queue.
(2) Message Queue: Message queue, which receives the message sent by the Handler and saves it; at the same time, the Looper polls, and if it is not processed, the Handler is notified to process it, otherwise it is deleted.
(3) Handler: The process of sending and receiving messages.
(4) Looper: The polling process of messages. In the marine environment, each activity data needs to be synchronized with the central server. This article uses a WIFI network for data transmission. First, turn on the WIFI, and the client process sends a 0×0000 confirmation command to the server to confirm whether the server program is ready; if it is ready, the client process subpackages the collected data process and performs MD5 verification. The subpackage package needs to include the synchronization number.

4. Experimental Analysis

4.1. The Purpose of the Experiment

To test the monitoring effect of the marine environment corrosive pollution monitoring technology under the cloud computing platform of this paper, the methods of Wu and Liao and Qin et al. are used as experimental comparison methods to compare the monitoring effects of the marine environment corrosive pollution and analyze the experimental results [6,7].

4.2. Experimental Parameters

In a fixed sea area, a 1000 km^2 monitoring area is selected, and different simulated pollution sources are monitored simultaneously through traditional ocean monitoring technology and intelligent image monitoring technology. After recording the monitoring results, change to another fixed sea area, select a different flow velocity and different contrast environment, and then conduct different simulated pollution source monitoring tests, and record the monitoring results. Collect seawater pH, seawater dissolved oxygen, seawater conductivity, seawater temperature, salinity, pH value, flow rate, and marine organism types, observe the degree of corrosion pollution of steel at regular intervals, and form a data set.

4.3. Experimental Results and Analysis

The detection and identification degree calculation is performed on the monitoring results, and the identification degree-simulated pollution source area curve is shown in Figure 3.

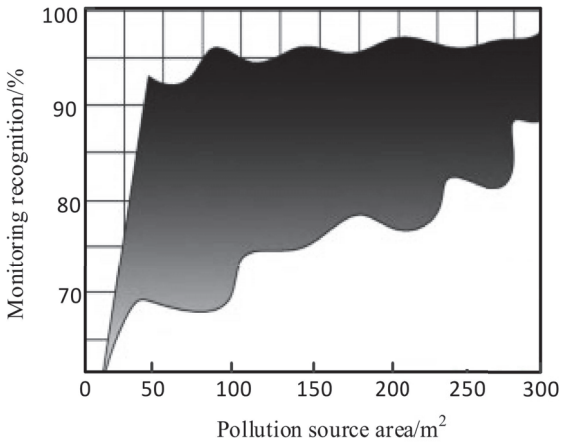


Figure 3. Identification degree-simulated pollution source area curve.

From the identification degree-monitoring range curve, it can be concluded that the traditional marine pollution monitoring system is not suitable for monitoring small pollution sources. When the monitored pollution source is less than 300 m^2, its identification degree is less than 85%, and when the monitored pollution source is less than 200 m^2, its identification degree is low at 80%, and the degree of identification is largely limited by the size of the monitored pollution source. In intelligent image monitoring technology, when the monitoring pollution source is equal to 75 m^2, its recognition degree is higher than 90%. As the area of the pollution source increases, the monitoring recognition rate remains balanced.

According to the above-mentioned monitoring model for experimental comparison, the monitoring effect of the marine environment corrosive pollution monitoring technology under the cloud computing platform of this paper is compared with the monitoring effect of the methods of Wu and Liao and Qin et al., and the obtained monitoring accuracy comparison chart and as shown in Figure 4 [6,7]:

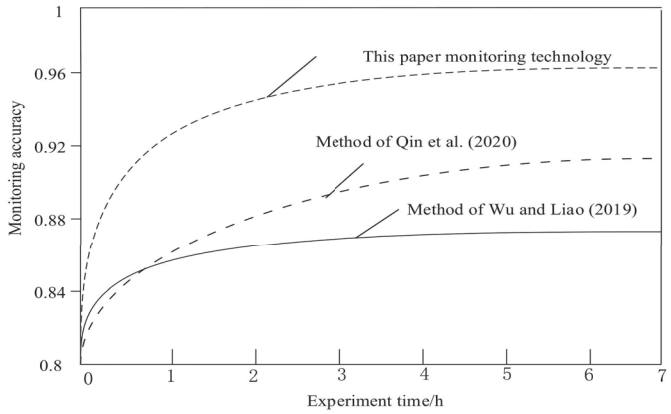


Figure 4. Comparison of monitoring accuracy.

Comparing Figure 4, it can be seen that under the same parameter conditions, the monitoring accuracy of the method of Wu and Liao is 86% on average, and the monitoring accuracy of the method of Qin et al. is 90% on average [6,7]. However, the marine environment under the cloud computing platform in this paper is corrosive. The monitoring accuracy of pollution monitoring technology is relatively high, at about 96% on average. The main reason for this difference is that this article collects data on corrosive pollution in the marine environment, strengthens the control of the data, and at the same time facilitates the development of monitoring experiments under the same conditions, and so, can better obtain effective data. The interference of factors reduces the influence of unfavorable factors, and finally obtains a more complete monitoring image, which is convenient for the research of monitoring objects, enhances experimental concentration, reduces monitoring errors, further improves the monitoring performance of the monitoring system, and finally obtains a higher monitoring accuracy rate. However, traditional methods deal with this aspect poorly, the initial data processing is imperfect, and the monitoring accuracy rate is low.

Comparing Figure 5, it can be seen that when the number of monitoring samples is 100, the complete rate of monitoring image collection of the method of Wu and Liao is 20%, and the complete rate of monitoring image collection in the method of Qin et al. is 30%. The image collection integrity rate is 60% [6,7]. When the number of monitoring samples is 200, the monitoring image collection integrity rate of the method of Wu and Liao is 25%, and the monitoring image collection integrity rate of the method of Qin et al. is 38% [6,7]. The monitoring image collection integrity rate of the monitoring technology in this paper is 68%, and the average monitoring image collection integrity rate of the monitoring technology in this paper is 82%. Because this paper performs secondary processing on the corrosive pollution data collected in the marine environment, cloud computing is used to strengthen the processing and analysis of the data. In this way, we can further realize the large-

scale processing of data, increase the processing rate, strengthen the completeness of the monitoring image reproduction operation, complete the high-level processing of the data, enhance the clarity of the image, increase the intake of useful image data, and improve the image collection degree of completeness.

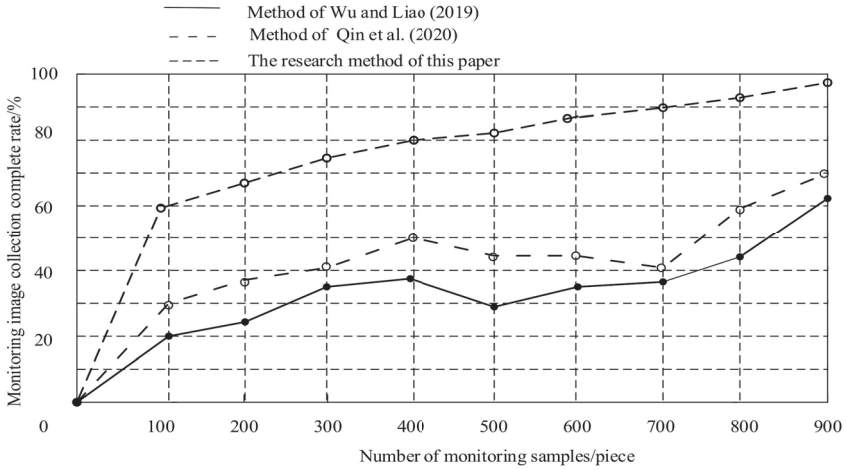


Figure 5. Comparison of complete rate of monitoring image collection.

5. Conclusions

The improvement of the marine environment corrosive pollution monitoring technology proposed in this paper under the cloud computing platform analyzes the corrosion influencing factors and corrosion mechanism of steel in the marine environment. The cloud computing platform of the marine environment monitoring system realizes online real-time monitoring, real-time transmission of marine environmental corrosive pollution data, and provides comprehensive, safe, and reliable monitoring data for marine environmental planning, environmental management, and total pollutant control. The system can meet the development requirements of marine environment monitoring systems such as security, wireless, intelligence, miniaturization, integration, and networking. It is a breakthrough in marine environment monitoring system technology. However, it is alimitation of this study that a wider database is not used for testing, which will be improved in future work to improve the applicability of the method proposed in this paper.

Author Contributions: Y.J. and J.D. collected the samples. X.Q. and F.W. analysed the data. Y.J. and J.D. conducted the experiments and analysed the results. All authors have read and agreed to the published version of the manuscript.

Funding: The research is supported by: Fund Project: project source: basic scientific research business fee research project of Heilongjiang Provincial Colleges and universities in 2019, project name: Research on Key Technologies of software development of intelligent cloud platform for Internet of things of CNC machine tools (No. 135409608); basic scientific research business fee research project of Heilongjiang Provincial Colleges and universities in 2021, project name: Development of NC machine tool machining process simulation monitoring system based on digital twin (No. 145109404); basic scientific research business fee research project of Heilongjiang Provincial Colleges and universities in 2021, project name: 3D design and motion analysis of bridge CNC gantry milling machine (No. 145109402).

Institutional Review Board Statement: Not applicable.

Informed Consent Statement: Not applicable.

Data Availability Statement: All data generated or analysed during this study are included in this published article.

Conflicts of Interest: The authors declare no conflict of interests.

References

1. Li, H.T.; Shao, Z.D. Marines ediment quality evaluation based on IGWO and BP neural network. *Comput. Simul.* **2020**, *37*, 350–353.
2. Barua, P.; Rahman, S.H. Aquatic health index of coastal aquaculture activities at South-Eastern coast of Bangladesh. *Water Conserv. Manag.* **2020**, *4*, 51–57. [CrossRef]
3. Peng, D.; Yang, Q.; Yang, H.J.; Liu, H.; Zhu, Y.; Mu, Y. Analysis on the relationship between fisheries economic growth and marine environmental pollution in China's coastal regions. *Sci. Total Environ.* **2020**, *713*, 136641. [CrossRef] [PubMed]
4. Celis-Hernández, O.; Enrique, V.; Ward, R.D.; Amparo, R.S.M.; Alberto, A.T.J. Microplastic distribution in urban vs pristine mangroves: Using marine sponges as bioindicators of environmental pollution. *Environ. Pollut.* **2021**, *284*, 117391. [CrossRef]
5. Wang, L.; Yang, T.; Wang, B.Q.; Lin, Q.L.; Zhu, S.R.; Li, C.Y.; Ma, Y.C.; Tang, J.; Xing, J.J.; Li, X.S.; et al. RALF1-FERONIA complex affects splicing dynamics to modulate stress responses and growth in plants. *Sci. Adv.* **2020**, *6*, eaaz1622. [CrossRef]
6. Wu, W.F.; Liao, Q.L. The application of laser induced technology in marine pollution detection. *Laser J.* **2019**, *10*, 36–39.
7. Qin, X.G.; Lin, X.R.; Gong, W.Q.; Yang, T. Status of hazardous chemical classification system and its application in marine environmental emergency monitoring. *Adm. Tech. Environ. Monit.* **2020**, *32*, 5–9.
8. Xu, D.; Liu, J.; Ma, T.; Zhao, X.; Ma, H.; Li, J. Coupling of sponge fillers and two-zone clarifiers for granular sludge in an integrated oxidation ditch. *Environ. Technol. Innov.* **2022**, *26*, 102264. [CrossRef]
9. Yu, C.; Chen, X.; Li, N.; Zhang, Y.; Li, S.; Chen, J.; Yao, L.; Lin, K.; Lai, Y.; Deng, X. Ag_3PO_4-based photocatalysts and their application in organic-polluted wastewater treatment. *Environ. Sci. Pollut. Res.* **2022**, *29*, 18423–18439. [CrossRef]
10. Ma, Z.; Zheng, W.; Chen, X.; Yin, L. Joint embedding VQA model based on dynamic word vector. *PeerJ Comput. Sci.* **2021**, *7*, e353. [CrossRef]
11. Yin, L.; Wang, L.; Keim, B.D.; Konsoer, K.; Zheng, W. Wavelet Analysis of Dam Injection and Discharge in Three Gorges Dam and Reservoir with Precipitation and River Discharge. *Water* **2022**, *14*, 567. [CrossRef]
12. Shi, D.; Chen, Y.; Li, Z.; Dong, S.; Li, L.; Hou, M.; Liu, H.; Zhao, S.; Chen, X.; Wong, C.; et al. Anisotropic Charge Transport Enabling High-Throughput and High-Aspect-Ratio Wet Etching of Silicon Carbide. *Small Methods* **2022**, *2022*, 2200329. [CrossRef]
13. Yang, Y.; Yang, X.J.; Jia, J.H.; Cheng, X.Q.; Xiao, K.; Li, X. Effect of Sb and Sn on the corrosion behavior of low alloy steel in simulated polluted marine atmosphere. *Surf. Technol.* **2021**, *50*, 224–237.
14. Guo, H.C.; Wei, H.H.; Yang, D.X.; Liu, Y.H.; Wang, Z.S.; Tian, J.B. Experimental research on fatigue performance of Q690 high strength steel in marine corrosive environment. *J. Civ. Eng.* **2021**, *54*, 36–45.
15. Zhang, X.; Hu, H.Y.; Gong, L.; Wang, Z.Y.; Peng, D.; Zhu, C.J.; Wei, W.Z.; Wu, K.M. Study on the corrosion behavior of rare earth/niobium microalloyed steels in marine atmospheric environments. *Mater. Prot.* **2021**, *54*, 7–15+33.
16. Li, Z.Y.; Wang, G.; Luo, S.W.; Deng, P.C.; Hu, J.Z.; Deng, J.h.; Xu, J.M. Early corrosion behavior of eh36 ship plate steel in tropical marine atmosphere. *J. Chin. Soc. Corros. Prot.* **2020**, *40*, 463–468.
17. Xu, S.H.; Song, C.M.; Li, H. Difference in surface characteristics of corroded steel under simulated marine and general atmosphere environment. *Mater. Rev.* **2021**, *35*, 125–132.
18. Fang, X.; Wang, Q.; Wang, J.; Xiang, Y.; Wu, Y.; Zhang, Y. Employing extreme value theory to establish nutrient criteria in bay waters: A case study of Xiangshan Bay. *J. Hydrol.* **2021**, *603*, 127146. [CrossRef]
19. Wang, Y.; Wang, H.; Zhou, B.; Fu, H. Multi-dimensional prediction method based on Bi-LSTMC for ship roll. *Ocean. Eng.* **2021**, *242*, 110106. [CrossRef]
20. Dai, L.; Wang, Z.; Guo, T.; Hu, L.; Chen, Y.; Chen, C.; Yu, G.; Ma, Q.; Chen, J. Pollution characteristics and source analysis of microplastics in the Qiantang River in southeastern China. *Chemosphere* **2022**, *293*, 133576. [CrossRef]
21. Sanahuja, A.B.; Casado-Coy, N.; Simó-Cabrera, L.; Sanz-Lázaro, C. Monitoring polymer degradation under different conditions in the marine environment. *Environ. Pollut.* **2020**, *259*, 113836. [CrossRef]
22. Ha, M.G.; Jeon, S.H.; Jeong, Y.S.; Mha, H.S.; Ahn, J.H. Corrosion environment monitoring of local structural members of a steel truss bridge under a marine environment. *Int. J. Steel Struct.* **2021**, *21*, 167–177. [CrossRef]
23. Mousavi, A.A.; Zhang, C.; Masri, S.F.; Gholipour, G. Damage detection and characterization of a scaled model steel truss bridge using combined complete ensemble empirical mode decomposition with adaptive noise and multiple signal classification approach. *Struct. Health Monit.* **2021**, *2021*, 84049285. [CrossRef]
24. Bai, B.; Rao, D.; Chang, T.; Guo, Z. A nonlinear attachment-detachment model with adsorption hysteresis for suspension-colloidal transport in porous media. *J. Hydrol.* **2019**, *578*, 124080. [CrossRef]
25. Zheng, W.; Liu, X.; Yin, L. Research on image classification method based on improved multi-scale relational network. *PeerJ Comput. Sci.* **2021**, *7*, e613. [CrossRef]
26. Montrucchio, B.; Giusto, E.; Vakili, M.G.; Quer, S.; Fornaro, C. A densely-deployed, high sampling rate, open-source air pollution monitoring WSN. *IEEE Trans. Veh. Technol.* **2020**, *69*, 15786–15799. [CrossRef]
27. Jo, J.; Jo, B.W.; Khan, R.; Kim, J.H. A cloud computing-based damage prevention system for marine structures during berthing. *Ocean. Eng.* **2019**, *180*, 23–28. [CrossRef]
28. Saxena, D.; Singh, A.K. Security embedded dynamic resource allocation model for cloud data centre. *Electron. Lett.* **2020**, *56*, 1062–1065. [CrossRef]

coatings

MDPI

Article

Evolution of Microstructure and Mechanical Properties of Al-Zn-Mg-Cu Alloy by Extrusion and Heat Treatment

Jun Li [1,†], Yayun He [2,†], Xi Zhao [2,*] and Chankyung Kim [3,*]

[1] School of Chemical Engineering and Technology, North University of China, Taiyuan 030051, China; lijun2015@nuc.edu.cn
[2] College of Mechatronics Engineering, North University of China, Taiyuan 030051, China; hyy798646088@163.com
[3] Department of Chemistry and Chemical Engineering, Inha University, 100 Inha-ro, Michuhol-gu, Inchenon 22212, Korea
* Correspondence: zhaoxi_1111@163.com (X.Z.); kckyung@inha.ac.kr (C.K.)
† These authors contributed equally to this work.

Abstract: Herein, composite extrusion deformation and heat treatment process at various temperatures were studied on a new type of Al-Zn-Mg-Cu alloy billet. The influence of pre-deformation and the final forming of extrusion and heat treatment of annular channel corner extrusion on the microstructure evolution and mechanical properties were explored. The results show that the extrusion process could further refine the structure and break the coarse θ phase. The grains can be refined again after the deformed sample was treated by solution-aging treatment. At the same time, a fine, dispersed second phase is precipitated around the fine recrystallized grains. This is the main reason for the increase in alloy elongation and tensile strength. The best heat treatment process parameters for the formed cup-shaped structure are 480 °C × 1 h solid solution and 120 °C × 24 h aging. The strengthening of the alloy mainly includes three mechanisms: fine grain strengthening, precipitation strengthening, and dispersion strengthening.

Keywords: new Al-Zn-Mg-Cu alloy; annular channel corner extrusion; heat treatment; strengthening mechanisms of alloy

1. Introduction

Lightweight is an important development direction in the fields of aerospace and national defense. Aluminum alloy has become an ideal structural material in the aerospace field by its easy processing, lightweight, corrosion resistance, and high strength and toughness [1]. Cup-shaped components are important basic load-bearing components in the aerospace, so how to manufacture high-performance aluminum alloy cabin components has become the focus and difficulty of research in the aerospace field. Although traditional back extrusion has the advantages of simple mold and easy operation, this method of deformation has large forming force, small plastic deformation, and uneven deformation, so this method is not suitable [2,3]. The annular channel corner extrusion process can use small-diameter billets to form large-diameter cabin shells at one time, which can shorten the process flow and improve production efficiency. The shear deformation applied by the corners of the mold obtains a large amount of plastic deformation, which can be significantly thinner. The crystal grains are reduced, and the overall mechanical properties of the components are greatly improved [4–7]. Zhao et al. [8,9] used AZ80 alloy to compare the traditional reverse extrusion and annular channel angular extrusion process. They found that the annular channel angular extrusion process can better refine the grain structure and make the structure more uniform and at the same time obtain better tensile properties. The billet needs to be prefabricated before the component is prepared. To keep the shape of the billet unchanged after pre-deformation, pier extrusion is selected as the pre-deformation

process of the billet. Therefore, the final forming method of cabin components is cyclic pier extrusion and annular channel angular extrusion.

The new Al-Zn-Mg-Cu alloy is a heat-treatable aluminum alloy. The heat treatment process of aluminum alloy components can improve the alloy structure and performance and meet the requirements of use [10–14]. The structure of the metal will change to a certain extent after plastic deformation and will have a certain impact on the subsequent heat-treatment process. Therefore, this paper discusses the influence of the forming process on the alloy structure and properties of the formed aluminum alloy components, studies the heat treatment process, and explores the relationship between the structure and properties formed by the heat treatment. A theoretical basis for the popularization and application of the new Al-Zn-Mg-Cu alloy was provided.

2. Materials and Methods

In this experiment, a new type of Al-Zn-Mg-Cu alloy homogenization cast rod provided by Central South University (Changsha, China) was used, and the homogenization parameter was 470 °C × 20 h. The specific chemical composition is shown in Table 1.

Table 1. Aluminum alloy composition (%, mass fraction).

Element	Al	Zn	Mg	Cu	Zr	Fe	Si	Ti
Content	86.0–88.9	8.0–9.3	1.5–2.4	1.2~1.9	0.15	0.06	0.03	0.15

Firstly, the billet was prefabricated by extrusion process, and then the cylindrical component was prepared by the annular channel angular extrusion process. The forming process is shown in Figure 1, and the formed part is shown in Figure 2. First, wire cutting was used to take the initial billet with a size of Φ140 mm × 200 mm, as shown in Figure 2a. The billet was preheated at 470 °C for 3 h. The preheating temperature of the die is 20 °C higher than that of the billet, and the preheating is 3.5 h. The extrusion pre-deformation experiment was carried out by a 630-ton hydraulic press, as shown in Figure 1a, and the billet was upsetting. After that, the billet was extruded as shown in Figure 1b, and the diameter of the billet changed from 140 to 100 mm. The upper and lower ends of the pre-deformed billet were processed into planes and processed into bars of 90 mm × 360 mm, as shown in Figure 2b. Before the angular extrusion of the annular channel, the pre-deformed billet was kept at 430 °C for 2.5 h, and the preheating temperature of the die is 20 °C higher than that of the billet for 3.5 h. After putting the heat-preserved billet into the mold, the annular channel angular extrusion test was carried out by a 630-ton hydraulic press. Figure 1c,d show the beginning and ending stages of annular channel angular extrusion, respectively. The extruded formed parts and the section of formed parts are shown in Figure 2c,d, respectively. The thickness of the cup wall after extrusion is 20 mm, the inner diameter of the cup wall is 160 mm, and the height is 220 mm.

The middle area of the cup wall was taken as a sample to study the heat treatment process. The sample size was 10 mm × 10 mm × 10 mm. According to the DSC (Differential Scanning Calorimetry) test and analysis results, the aging process was formulated, and the specific heat treatment plan is shown in Table 2.

We grind the sample surface with 300#, 500#, 1000#, 2000#, 3000#, 5000#, and 7000# in turn, then perform mechanical polishing, and perform Vickers Hardness (HV) Test on the polished sample. The HV pressure, indenter speed, and pressure holding time are 200 gf, 25 μm/s, and 15 s, respectively. To ensure the accuracy of the HV results, 12 different positions were selected for dispersion. The average value was taken as the hardness value after eliminating maximum and minimum values. The surface of the polished sample was treated with the EMRES102 (Leica, Berlin, Germany) ion thinner with an ion beam voltage of 6.7 kV and a current of 2.7 mA. A scanning electron microscope (SEM, Hitachi SU5000, Tokyo, Japan) was used to characterize the structure, including the morphology, distribution, and size of the second phase. The element content was

determined using energy dispersive spectroscopy (EDS, Hitachi SU5000, Tokyo, Japan), and the sample structure was analyzed and processed using electron backscatter diffraction (EBSD Mahwah, NJ, USA) and EDAX-OIM v7.3 (Post-processing analysis) software.

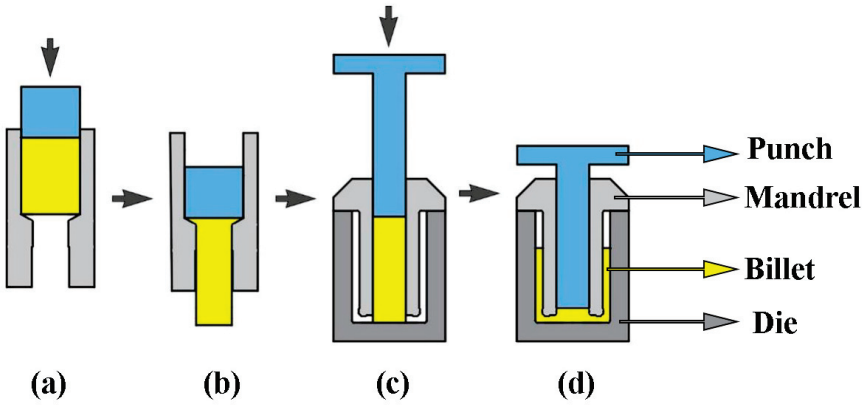


Figure 1. Diagram of forming process (**a**) upsetting, (**b**) extrusion, and (**c**,**d**) the beginning and ending stage of annular channel angular extrusion.



Figure 2. Schematic diagram of the formed part. (**a**) initial billet, (**b**) after upsetting and extrusion billet, (**c**) formed parts, and (**d**) the section of formed parts.

Table 2. The plan of the heat treatment process.

Solution Temperature (°C)	Solution Time (h)	Aging Temperature (°C)	Aging Time (h)
480	1	120, 130, 145, 160	0–60

The solid solution model of Al-Zn-Mg-Cu alloy was constructed according to the specific situation of the experiment as shown in Figure 3. Firstly, the unit cell of the alloy was built by referring to the composition of each metal in Table 1, i.e., Zn: 9.3%, Mg: 2.4, Cu: 1.9, and Al: 86.4%. Then, the solid alloy model was built by extending the unit cell and was simulated by molecular dynamics (MD) with the help of the Forcite module in Materials Studio (MS) software [15,16]. COMPASS (Condensed-phase Optimized Molecular Potentials for Atomistic Simulation Studies) was selected because Al, Zn, Mg, and Cu metals can be properly described in this force field [17,18]. NVT (Constant volume/constant temperature dynamics) ensemble was used to simulate for a short time to balance the pressure of the system. Velocity Scale thermostat, which can quickly correct kinetic energy, was used. NPT (Constant pressure/constant temperature dynamics) ensemble was used for MD simulation of the system after the system was balanced, and the total simulation time was 500 ps. The NHL (Nosé-Hoover-Langevin (NHL) thermostat is a method for performing constant-temperature dynamics) thermostat [19] and Andersen barostat were used to control temperature and pressure, respectively. Next, the Al-Zn-Mg-Cu liquid alloy

model was built using the Amorphous Cell module. The size of the liquid alloy model was consistent with that of the solid alloy model. MD simulations of NVT and NPT were also performed for the liquid alloy model using the same method applied to the solid model, to confirm the density of liquid alloy. Next, an equal amount of liquid alloy was added on top of the solid alloy. Then MD simulations were performed at different temperatures, and the parameter settings were the same as before. The temperature setting was the same as that of heat treatment, as shown in Table 2. Finally, the mechanical properties of the Al-Zn-Mg-Cu alloy model at different temperatures were calculated to study the effect of heat treatment on the alloy.

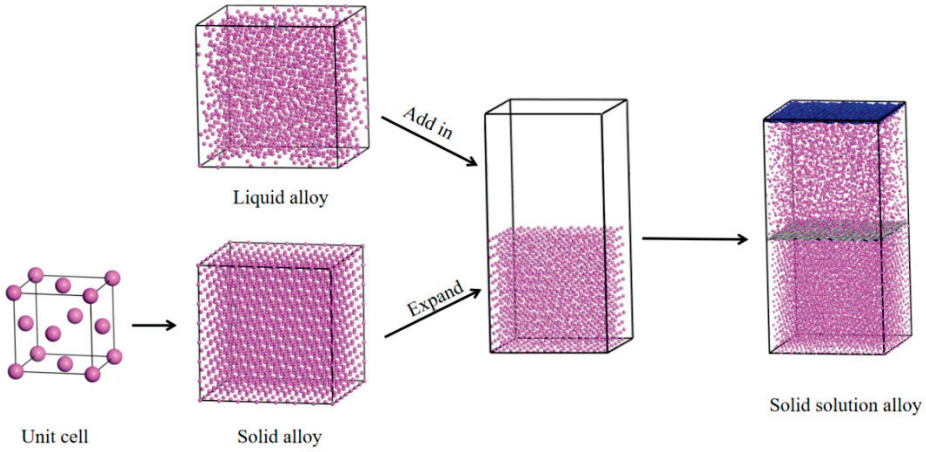


Figure 3. The solid solution model of the Al-Zn-Mg-Cu alloy construction process.

Tensile test is used to measure the axial load of the specimen. Mechanical indexes such as tensile strength, yield strength, and elongation can be measured with an extensometer. The equipment used is Instron 3382 (Instron, Boston, MA, USA) universal tensile testing machine. In this paper, the tensile rate is unified as 1 mm/min, the lower end of the stretching rod is clamped with the chuck, and the upper end of the stretching rod is clamped after the load was adjusted to zero. Take three tensile rods in the same state were taken and their average value was taken as the test result. In this paper, the stretching rod sampling always ensures that the extension rod axis is parallel to the extrusion direction.

Vickers Hardness was used for hardness measurement in this paper. The specific parameters were as follows: pressure 200 gf, pressing speed 25 μm/s, and holding time 15 s. The polished sample was measured 12 times at different positions of the sample, and the average value was taken after removing the two maximum values.

The sample preparation process is as follows: $7 \times 7 \times 7$ samples with flat upper and lower surfaces are cut by the all-in-one finishing machine; The samples were roughed, polished, roughed and polished in turn until no obvious polishing marks were found 200 times under the optical microscope. After confirming that there is no wear and debris throwing, put it into the ion thinning instrument and thin the test surface. To prevent oxidative contamination of the sample surface, the prepared sample should be tested as soon as possible.

The observation test process is as follows: stick the sample in the center of the sample table with a 70° tilt with conductive adhesive, push it into the experimental chamber and vacuum; The scanning position (generally center) was determined under the electron microscope, and the working distance was adjusted to 15mm. According to the grain size and distribution, the image magnification and focal length were adjusted until the sample morphology was clear. Map in EBSD system, determine scan step size according to need, and finally collect spectrum to complete the test. It is generally considered that the orientation of a grain is best determined by 3–5 step sizes. According to the metallographic image, choose 200–400 magnification, scanning step size is $0.5-0.6$ μm. Each scan takes about 4–5 h. OIM analysis software was used to analyze EBSD data.

3. Results and Discussion

3.1. Influence of Extrusion on the Microstructure of the Alloy

The homogenized state and deformed morphology structure are shown in Figure 4. From Figure 4a, it can be observed that the original grain structure of the homogenized state is relatively coarse and equiaxed, and the average diameter of the crystal grains is about 400 μm. Figure 4b shows that the alloy is affected by the extrusion force during the pre-deformation. The grains appear to have a fibrous distribution along the extrusion direction—the grain boundaries and grains. A fine recrystallized structure was produced inside, discontinuous large-angle grain boundaries were formed in the middle of some grains, and the average grain size of the alloy was reduced to 200 μm. This is because, in the process of extrusion deformation, the dislocation cross-slip and climbing occurred with the continuous deformation. The cellular substructure in the grain gradually absorbed the dislocations accumulated on the subgrain boundary, the orientation difference of the adjacent subgrain increases gradually, and the subgrain boundary was transformed into a large-angle grain boundary, which promoted the generation of continuous dynamic recrystallization. Figure 4c shows the structure after annular channel angular extrusion. In this structure, the grain boundary of elongated fibrous grains was flatter, the grain width was further reduced, and the size of some recrystallized grains grew. According to statistical analysis, the proportion of recrystallized grains was increased, and the average grain size was decreased to 132 μm. This was due to the continuous production of new fine dynamic recrystallized grains. To reduce the surface energy and keep the recrystallized grains in a stable and low free energy state, the newly recrystallized grains were absorbed by the migration movement of the grain boundaries, and the recrystallized grains grew up. More recrystallized grains were produced in the fibrous deformation grains and at grain boundaries.

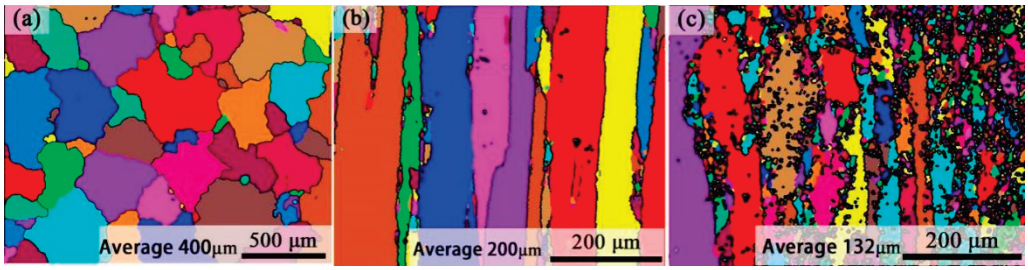


Figure 4. EBSD diagram of alloy microstructure. (**a**) original grain structure. (**b**) pre-deformed structure. (**c**) cup-shaped structure after annual channel angular extrusion.

The sample orientation difference is calculated after pre-deformation and annular channel angular extrusion deformation. As shown in Figure 5, the proportion of misorientation angle greater than 45° is higher for cup-shaped component than pre-deformation one. The results show that the recrystallization occurs further after the angular extrusion of the annular channel, which further increases the orientation difference in the sample and the degree of dynamic recrystallization.

The proportion of large misorientation angle of the cup-shaped structure is higher than that of the pre-deformed one. This is because the forming temperature of the cup-shaped component is lower than that of the pre-deformation structure, which strengthens the work-hardening effect to a certain extent. Therefore, in the grain orientation difference diagram, the proportion of smaller and larger misorientation angle is increased.

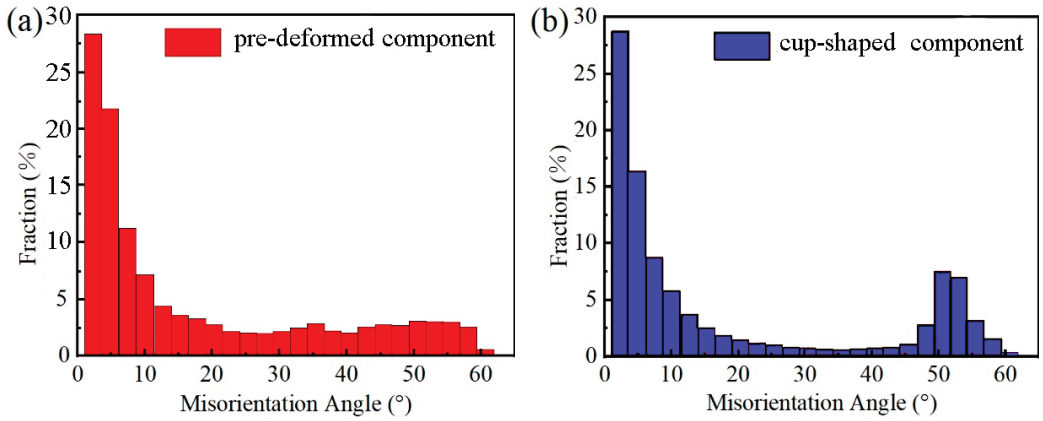


Figure 5. Distribution map of misorientation angle of the deformed structures. (**a**) pre-deformed component. (**b**) cup-shaped component.

SEM pictures of the microstructures of sample materials are shown in Figure 6. The homogenized scanning structure, Figure 6a, shows some coarse network phases in the sample. Scanning specific points through EDS can measure the element distribution ratio. The atomic ratio of Al, Zn, Mg, and Cu is 59.2:6.76:5.85:28.2. The atomic ratio of Al to Cu is close to 1:2. Therefore, the composition at this point is $CuAl_2$, which is the θ phase. Small rod-like phases are distributed on its edge. Figure 6b is the scanned structure of the sample after pre-deformation. It can be observed that the coarse θ phases in the network are broken because of extrusion deformation, distributed along the extrusion direction, and the θ phases are no longer observed in the network structure. Figure 6c shows that with the progress of the angular extrusion deformation of the annular channel, these coarse θ phases are further fragmented. The size is further reduced, and they are more evenly distributed in various places. Compared with Figure 6a,b, the fine second phase in Figure 6c has a higher degree of dispersion. These dispersed second phases can effectively pin the movement of grain boundaries, hinder the growth of recrystallization, and achieve the effect of grain refinement.

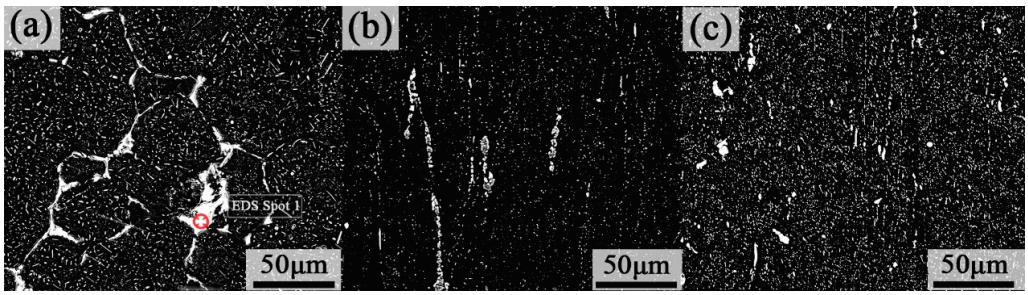


Figure 6. Backscattered electron micrographs (**a**) homogenization state, (**b**) after pre-deformation, and (**c**) after angular extrusion deformation of the annular channel.

3.2. Effect of Heat Treatment on Alloy Structure and Properties

The solid solution and aging heat treatment process (T6) of the formed structures were studied. The solution process was done at 480 °C for 1 h, and the aging temperature was determined according to the DSC curve. As shown in Figure 7, there is an obvious endothermic peak at 123.1 °C in the DSC curve. This peak is the dissolution peak in the GP zone, and the exothermic peak at 165.7 is the η′-phase precipitation peak. The η′-phase is the main strengthening phase of the Al-Zn-Mg-Cu alloy, so the aging treatments were performed at 120, 130, 145, and 160 °C with different aging time scales.

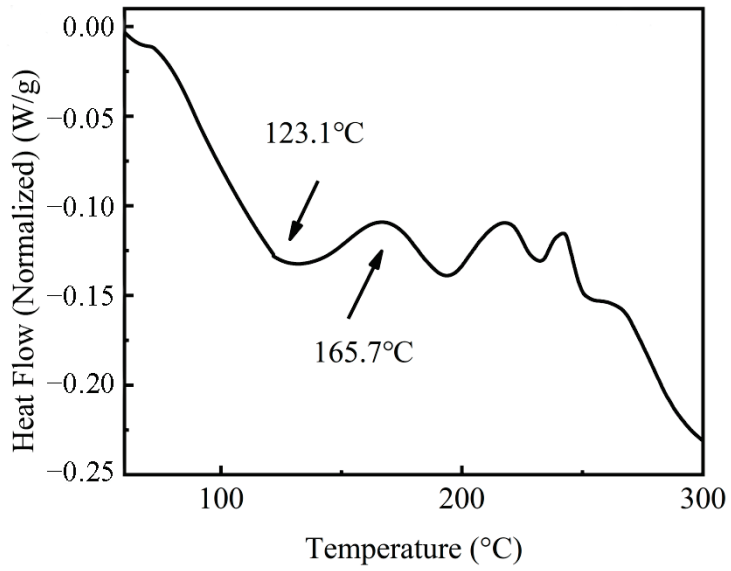


Figure 7. DSC curve for the solid solution.

The aging experiments for the solid solution samples were divided into four sets. The first set is aging at 120 °C, five times every 12 h. The second set is aging at 130 °C, six times every 4 h. The third set is aging at 145 °C, six times every 3 h. The fourth set is aging at 160 °C, 6 times every 2 h. The Vickers Hardness values of the heat-treated samples were measured, as shown in Figure 8. This figure shows that changes in the HV values exhibit a similar trend under different aging temperatures. In proportion to the aging time, the hardness increases rapidly at the initial stage and then gradually decreases after reaching the peak value. This is because as the aging progresses, the precipitation ratio of the second phase gradually increases to enhance the precipitation strengthening, making the alloy hardness reach the peak. When the aging time increases further, the solute elements Mg and Zn in the matrix are gradually consumed, and the precipitated phases grow to a certain extent, which reduces the degree of dispersion between the precipitated phases and weakens the precipitation strengthening effect, resulting in a decrease in the hardness of the alloy. Comparison of the time to reach the peak at different temperatures reveals that the higher the aging temperature, the shorter the time for the hardness to reach the peak. For the four experimental sets, the times to reach the peak hardness are 24, 12, 9, and 4 h and the corresponding hardness values are 211.6, 202.8, 203.8, and 202.6 HV for the sets 1, 2, 3, and 4, respectively. This is due to the increase of the aging temperature, which accelerates the precipitation behavior of the second phase and makes the sample reach the peak hardness earlier. As the highest aging hardness of 211.6 HV is achieved at 120 °C × 24 h, this condition is selected as the best aging parameter, which is greatly improved compared with the 75 HV hardness value of the cup-shaped sample.

The model of Al-Zn-Mg-Cu solid solution alloy was simulated by the MD method at four different temperatures, and its mechanical property parameters were calculated, as summarized in Table 3. E, G, and K are the tensile modulus, shear modulus, and bulk modulus of the material, respectively. K/G value is used to evaluate the toughness of the material. The larger the value, the better the toughness of the material. It can be seen from Table 3 that with the increase of temperature, the toughness of the Al-Zn-Mg-Cu solid solution alloy first increases and then decreases. The reason is that with the initial increase of temperature, the precipitation of the second phase accelerates, which increases the toughness of the material. But, with the continuous increase of the temperature, the precipitated phase will weaken the precipitation effect accompanied by the decrease in toughness, which is consistent with the previous finding.

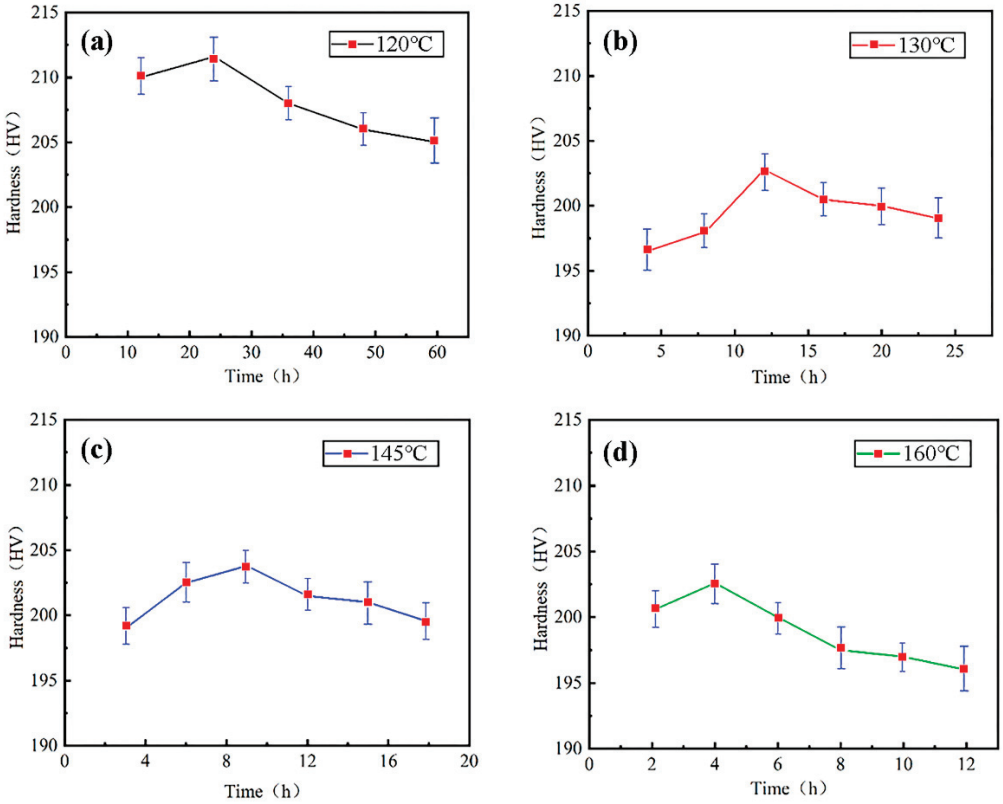


Figure 8. Aging hardness curve under different temperatures (**a**) 120 °C, (**b**) 130 °C, (**c**) 145 °C, and (**d**) 160 °C.

Table 3. Mechanical property parameters of Al-Zn-Mg-Cu solid solution alloy at different heat treatment temperatures.

Temperature (°C)	E	G	K	K/G
120	80.35	49.96	19.24	0.39
130	81.80	47.83	21.14	0.44
145	78.92	50.71	18.22	0.36
160	79.07	51.06	18.15	0.36

The scanning organization of the peak-aged samples is observed from the experiment at different aging temperatures. It can be seen from Figure 9 that, under different temperature conditions, fine precipitated phases are precipitated after heat treatment, and the precipitated phases are in a state of dispersion, mainly distributed at the grain boundary, which shows that the grain boundary of the crystal grain provides a favorable position for the precipitation of the phase. These fine dispersed second phases can effectively pin the dislocations, hinder the movement of the dislocations, and achieve the effect of strengthening the properties of the alloy. After the aging process, some larger size of precipitated phases (pointed by the arrow) appears and the lengths of the η′-phase shown in Figure 9a–d are 0.43, 0.83, 1.21, and 1 μm, respectively. It is found that as the aging temperature increases, the size of the precipitated phase increases, which will reduce the degree of dispersion of the precipitated phase to a certain extent.

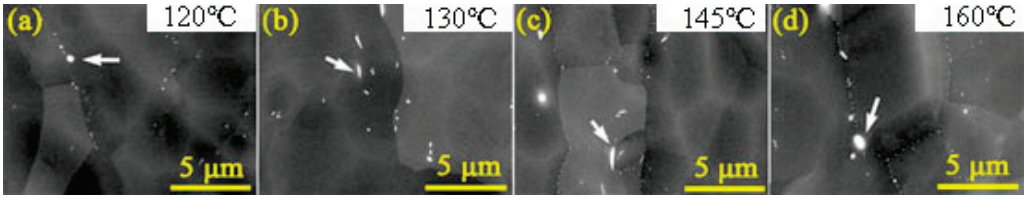


Figure 9. SEM images of Peak aging microstructure at different aging temperatures. (**a**) 120 °C; (**b**) 130 °C; (**c**) 145 °C; (**d**) 160 °C.

Close examination of the microstructure of the cup-shaped structure under the best aging parameters (see Figure 10) shows that a large amount of static recrystallization occurred after the T6 process treatment of the formed structure, and the average grain size of the static recrystallization is 6 μm. It can be seen from Figure 5b that the dislocation density inside the crystal grains of the cup-shaped piece is relatively high, so it has a strong driving force [20]. Under the thermal activation of the heat treatment, the unlike dislocation in the alloy is eliminated, the dislocation density is reduced, and the dislocation cell walls with small misorientation form sub-grain boundaries [21]. The dislocation cells merge into sub-grains and transform into grain boundaries, resulting in many static recrystallized grains. The proportion of recrystallized grains in the alloy is greatly increased, and the overall average grain size is reduced to 112 μm.

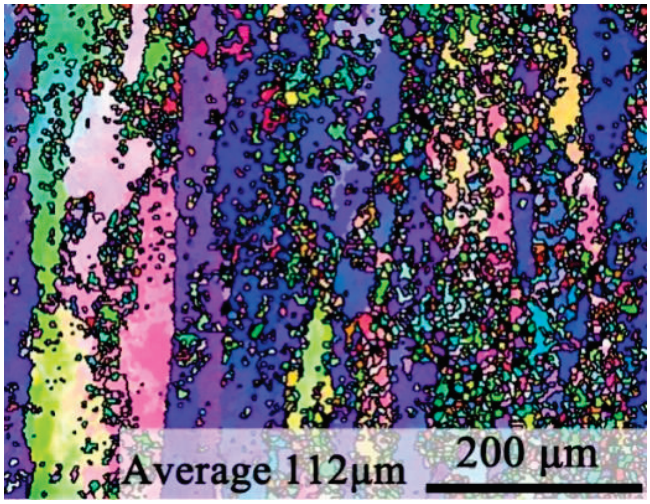


Figure 10. Microstructure after heat treatment (480 °C × 1 h solid solution and 120 °C × 24 h aging).

Figure 11 shows the plots of the mechanical properties of the alloy under the original homogenization state and after the optimal heat treatment. When the initial homogenized billet is heat-treated, the elongation of the alloy changes from 4% to 15.7%, and the tensile strength changes from 289 to 630 MPa, which suggests that the material obtained better tensile strength and elongation. Grain refinement enables the material to disperse the force on more crystal grains when plastic deformation occurs so that the plastic deformation is uniform, the stress concentration is reduced, and the metal obtains a better deformation coordination ability, thereby improving the elongation of the material. According to Hall-Petch formula theory [22], grain refinement can improve alloy strength. After heat treatment, the fine and dispersed precipitated phase greatly improves the strength performance of the alloy material. Therefore, the alloy strengthening mainly includes three mechanisms: fine-grain strengthening, precipitation strengthening, and dispersion strengthening.

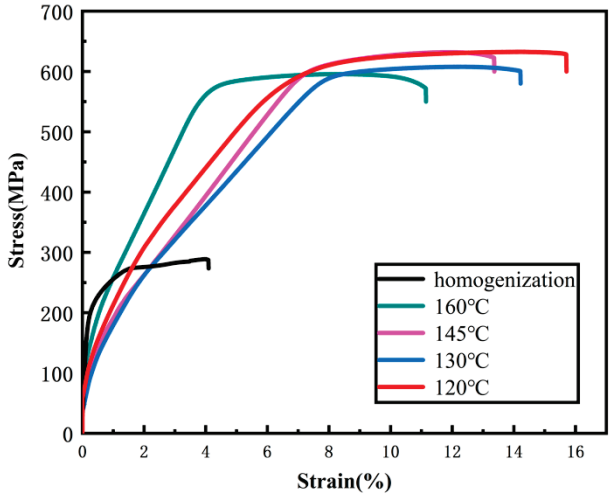


Figure 11. Mechanical properties of the alloy under the homogenization state and heat treatment parameters of the Cup-shaped component.

4. Conclusions

(1) A new type of Al-Zn-Mg-Cu alloy cup-shaped component is prepared by high- and low-temperature composite extrusion deformation, and continuous dynamic recrystallization. The cooling ring channel corner extrusion process has stronger grain refinement and crushing θ coarse phase effects, and the average grain size reaches 180 μm after deformation.

(2) The corner extrusion process enables the sample to obtain a higher dislocation density, which provides a strong driving force for the static recrystallization and the precipitation of the second phase after aging. The size of the aging precipitates increases with the increase of temperature.

(3) In order to maximize the strength and toughness of the new Al-Zn-Mg-Cu alloy cup-shaped components, the best heat treatment process is 480 °C × 1 h solid solution and 120 °C × 24 h aging. The tensile strength reached 630 MPa after heat treatment, and the elongation reached 15.7%. The strengthening mechanisms of the alloy mainly include fine-grain strengthening, precipitation strengthening, and dispersion strengthening.

Author Contributions: Investigation, C.K.; Resources, X.Z.; Writing—original draft, Y.H.; Writing—review & editing, J.L. All authors have read and agreed to the published version of the manuscript.

Funding: This research was funded by the Shanxi Scholarship Council of China, grant number 2020-107, Natural Science Foundation of Shanxi Province, grant number 201901D111129, and Inha University Research Fund.

Institutional Review Board Statement: Not applicable.

Informed Consent Statement: Not applicable.

Data Availability Statement: Not applicable.

Conflicts of Interest: The authors declare no conflict of interest.

References

1. Lavernia, E.J.; Srivatsan, T.S.; Mohamed, F.A. Mohamed, Strength, deformation, fracture behaviour and ductility of aluminium-lithium alloys. *J. Mater. Sci.* **1990**, *25*, 1137–1158. [CrossRef]
2. Furukawa, M.; Horita, Z.; Langdon, T.G. Factors influencing microstructural development in equal-channel angular pressing. *Met. Mater. Int.* **2003**, *9*, 141–149. [CrossRef]
3. Masoudpanah, S.M.; Mahmudi, R. The microstructure, tensile, and shear deformation behavior of an AZ31 magnesium alloy after extrusion and equal channel angular pressing. *Mater. Des.* **2010**, *31*, 3512–3517. [CrossRef]
4. Shatermashhadi, V.; Manafi, B.; Abrinia, K.; Faraji, G.; Sanei, M. Development of a novel method for the backward extrusion. *Mater. Des.* **2014**, *62*, 361–366. [CrossRef]

5. Hosseini, S.H.; Abrinia, K.; Faraji, G. Applicability of a modified backward extrusion process on commercially pure aluminum. *Mater. Des.* **2015**, *65*, 521–528. [CrossRef]
6. Hong, L.; Yong, X.; Xi, Z. Comparative study on technology of new type of backward extrusion with traditional backward extrusion. *Forg. Stamp. Technol.* **2016**, *41*, 34–37.
7. Xue, Y.; Li, H.; Zhang, Z.M.; Zhou, X.J. Effects of annular channel structure on backward extrusion forming of a cup shell. *J. Plast. Eng.* **2017**, *24*, 15–23.
8. Zhao, X.; Li, S.; Xue, Y.; Zhang, Z. An investigation on microstructure, texture and mechanical properties of AZ80 Mg alloy processed by annular channel angular extrusion. *Materials* **2019**, *12*, 1001. [CrossRef] [PubMed]
9. Zhao, X.; Li, S.; Yan, F.; Zhang, Z. Microstructure evolution and mechanical properties of AZ80 Mg alloy during annular channel angular extrusion process and heat treatment. *Materials* **2019**, *12*, 4223. [CrossRef]
10. Ditta, A.; Wei, L.J.; Xu, Y.J.; Wu, S.J. Microstructural characteristics and properties of spray formed Zn-rich Al-Zn-Mg-Cu alloy under various aging conditions. *Mater. Charact.* **2020**, *161*, 110133. [CrossRef]
11. Li, H.; Cao, F.; Guo, S.; Ning, Z.; Liu, Z.; Jia, Y.; Scudino, S.; Gemming, T.; Sun, J. Microstructures and properties evolution of spray-deposited Al-Zn-Mg-Cu-Zr alloys with scandium addition. *J. Alloys Compd.* **2017**, *691*, 482–488. [CrossRef]
12. Wang, F.; Xiong, B.; Zhang, Y.; Zhu, B.; Liu, H.; He, X. Effect of heat treatment on the microstructure and mechanical properties of the spray-deposited Al-10.8Zn-2.8Mg-1.9Cu alloy. *Mater. Sci. Eng. A* **2008**, *486*, 648–652. [CrossRef]
13. Ditta, A.; Wei, L.; Xu, Y.; Wu, S. Effect of hot extrusion and optimal solution treatment on microstructure and properties of spray-formed Al-11.3Zn-2.65Mg-1Cu alloy. *J. Alloys Compd.* **2019**, *797*, 558–565. [CrossRef]
14. Chen, Z.; Mo, Y.; Nie, Z. Effect of Zn Content on the microstructure and properties of super-high strength Al-Zn-Mg-Cu alloys. *Metall. Mater. Trans. A* **2013**, *44*, 3910–3920. [CrossRef]
15. Tang, L.; Wen, T.Q.; Wang, N.; Sun, Y.; Zhang, F.; Yang, Z.J.; Ho, K.M.; Wang, C.Z. Structural and chemical orders in $Ni_{64.5}Zr_{35.5}$ metallic glass by molecular dynamics simulation. *Phys. Rev. Mater.* **2018**, *2*, 033601. [CrossRef]
16. Yang, Z.J.; Tang, L.; Wen, T.Q.; Ho, K.M.; Wang, C.Z. Effects of Si solute on the glass formation and atomic structure of Pd liquid. *J. Phys. Condens. Matter* **2019**, *31*, 135701. [CrossRef]
17. Sun, H. COMPASS: An ab Initio force-field optimized for condensed-phase applications-overview with details on alkane and benzene compounds. *J. Phys. Chem. B* **1998**, *102*, 7338–7364. [CrossRef]
18. Sun, H.; Ren, P.; Fried, J.R. The COMPASS force field: Parameterization and validation for phosphazenes. *Comput. Theor. Polym. Sci.* **1998**, *8*, 229–246. [CrossRef]
19. Leimkuhler, B.; Noorizadeh, E.; Penrose, O. Comparing the efficiencies of stochastic isothermal molecular dynamics methods. *J. Stat. Phys.* **2011**, *143*, 921–942. [CrossRef]
20. Meng, Y.; Ren, Q.; JU, X.H. Evaluation of dislocation density by local grain misorientation in deformed metals. *Trans. Mater. Heat. Treat.* **2014**, *35*, 122–128.
21. Zheng, J.; Chen, Z.; Yan, Z.M.; Zhang, Z.M.; Xue, Y. An alternating ageing-annealing process for enhancing strength and ductility of a Mg-Gd-Y-Zn-Zr alloy. *Mater. Sci. Eng. A* **2021**, *828*, 142103. [CrossRef]
22. Cordero, Z.C.; Knight, B.E.; Schuh, C.A. Six decades of the Hall-Petch effect—A survey of grain-size strengthening studies on pure metals. *Int. Mater. Rev.* **2016**, *61*, 495–512. [CrossRef]

coatings

MDPI

Article

Performance and Application of Geocell Reinforced Sand Embankment under Static and Cyclic Loading

Ang Gao [1,*] and Mengxi Zhang [2]

[1] School of Architecture and Engineering, Zhejiang Industry Polytechnic College, Shaoxing 312000, China
[2] Department of Civil Engineering, Shanghai University, Shanghai 200072, China; mxzhang@i.shu.edu.cn
* Correspondence: gaoangv@126.com

Abstract: As reinforcement material, geocells are widely used in various types of embankment reinforcement. A lot of practical experience shows that geocell reinforced embankment has good reinforcement effect, but the theoretical research lags behind the engineering practice, and the reinforcement mechanism under cyclic loading under various reinforcement conditions needs to be further studied. In this paper, the reasonable reinforcement condition of geocell reinforced embankment under static and cyclic loading is proposed by using a physical model and numerical simulation comparative analysis method. The research findings include: under cyclic loading, the inhibition effect of the number of reinforced layers on the vertical cumulative settlement is better than that under static loading, but the effect of two-layer reinforcement and three-layer reinforcement is relatively close, and both can reduce the vertical settlement by more than 40%. The inhibition effect of the increase of geocell height on the horizontal deformation of slope surface is better than that of the decrease of welding spacing under cyclic loading, and the reinforcement effect of the middle and upper part of embankment is better. Increasing the height of geocell and reducing the welding spacing can improve the limit bearing capacity of embankment, and the former is better. The optimal reinforcement condition of sandy soil embankment under cyclic loading obtained from the comparative analysis is case 3, that is, the reinforced layers is 2, the geocell height is 10 mm, and the welding distance is 50 mm.

Keywords: cyclic load; numerical simulation; model experiment; geocell; settlement

1. Introduction

Geocell, a reinforcement material with optimal corrosion resistance, integrity, and aging resistance, has played a vital role in the construction engineering since one century ago, in particular in the reinforced embankment. The material has been adopted in numerous projects, achieving optimal economic effects and social benefits—due to the three-dimensional structure, the geocell results in side enclosure of the particles of soil inside the cells. In addition, geocell reinforcement causes the vertical enclosure of the soil within the geocells in two ways—firstly, through the friction between the soil-cellular materials formed by the walls of the cell. Secondly, the geocell reinforcement acts like a soil enclosure layer that prevents soil movement outside of the loading zone. The decorative effect of the geocell layer is also enhanced by the force of tensile strength in the geocell's reinforcement due to resistance to vertical loads (Figure 1). Astaraki et al. [1] constructed six 1:20 scaled down railway embankments in the lab environment, by changing the number of reinforced layers of geocell. It is found that the bearing capacity of embankment is the largest and the settlement is the smallest when four layers of geocell are reinforced. Han et al. [2] concluded that the geocell can reduce the amount of soil loss by 20–40%, and can effectively play a role in preventing the slope erosion. After combining with the function of plants, the amount of soil loss can be reduced by more than 90%. Isik et al. [3] concluded that the pullout capacity of geocell reinforcement in cohesion less soils is limited to the seam

peel strength at junctions of longitudinal and transverse of geocell strips. Ardakani et al. [4] conducted three-dimensional numerical simulation of the elastic-plastic behavior of soil and geocell, the results show that pocket size, thickness, and soil compactness have a considerable impact on the performance of geocell reinforced slope. Tiwari et al. [5] investigated the behavior of lime and silica fume treated coir geotextile reinforced expansive soil subgrade. They found that the upward swelling pressure decreased 52.19% in single-layer and 81.89% in double-layer with the lime treated coir geotextile. Sofiyev et al. [6] investigated the effect of heterogeneity on parametric instability of axially excited orthotropic conical shells, similar to the vertical stress distribution effect of the geocell, and stated that the area of the main instability regions decreases with increasing L/R1 (slant length/small mean radii) ratio. Mehdipour et al. [7] investigated the performance and efficiency of reinforced slope in the stability of geocell layers in unsaturated soil conditions; the results show that the geocell's reinforcing efficiency depends on the number of layers and depth of its placement. Song et al. [8] proposed a new numerical approach to model geocell reinforced soils, and the study results show that reducing the geocell pocket size has a strong effect on improving the bearing capacity. Mehrjardi et al. [9] studied the application of geocell in granular soil and found that geocell can effectively improve the shear strength characteristics at the interface of granular soil. Hou et al. [10] analyzed the friction and hoop constraints encountered by the geocell on its sidewall by establishing the finite element model of a single high strength geocell reinforced and non-reinforced foundation. Zhou et al. [11] analyzed the impact imposed by the varying shapes of geocell and confined forms on the bearing and deformation features of individual geocell through constant velocity compression experiments. The above scholars have studied the reinforcement effect of geocell through different methods, but they have not studied the effect under dynamic loading. Venkateswarlu et al. [12] found that the lateral spreading of vibrations can be significantly controlled in the presence of geocell reinforcement. Zhu et al. [13] used the FLAC3D nonlinear, finite-difference method to study the failure mechanism of geocell-reinforced retaining walls under earthquake; the results show that the geocell can effectively reduce the horizontal displacement of the retaining wall, and the effect is better than the geogrid. Zadehmohamad et al. [14] performed eight physical model tests to investigate the effect of backfill soil reinforcement with geocell under a cyclic loading condition; the results of the tests show that soil reinforcement with geocell significantly decreased the peak lateral soil coefficient of the soil behind the wall. The above scholars have studied the performance of geocell reinforcement under dynamic loading, but they all use physical models or numerical models alone. Tafreshi et al. [15] established laboratory model tests; the results indicate that, for the same quantity of geotextile material, the geocell reinforcement system behaves much stiffer and carries greater loading and settles less than does the equivalent planar reinforcement system. Bathurst et al. [16] conducted a series of numerical simulations using a large strain nonlinear finite element model to study the load deformation response of span and eccentrically loaded steel conduits with and without reinforced geocell soil cover; the research shows that, compared with the traditional unreinforced method, this kind of reinforcement technology can make the soil cover thinner. Biabani et al. [17] presented the experimental and numerical studies of geocell-reinforced subballast subjected to cyclic loading; the research shows that geocell could effectively decrease the lateral and axial deformations of the reinforced subballast and the lateral displacement decreased further by increasing geocell stiffness, and geocell with a relatively low stiffness performs very well compared to the geocell with a higher stiffness. Leshchinsky et al. [18] constructed a series of embankment model tests and numerical simulations; the results show that geocell confinement effectively increased stiffness and strength of a gravel embankment while reducing vertical settlement and lateral spreading. Zheng et al. [19] verified the role played by the geocell in enhancing foundation bearing capacity and diminishing foundation settlement through multiple model experiments. Jin et al. [20] elaborated on the damage mode of geocell reinforced cushion embankment in extreme cases through conducting an extensive range of experiments and analyses,

and put forward recommendations for stability assessment accordingly. Avesani Neto et al. [21] conducted experiments by reinforcing the embankments on soft soil with geocell through varying approaches and the proposed method considers the factor of safety of the unreinforced system calculated by two methods; the results thus obtained were compared with those from a three-dimensional finite element computer analysis for both unreinforced and reinforced cases. Zhao et al. [22] established nonlinear algebraic equations and an interaction model for "embankment-geocell-reinforced body-pile-soil reinforcement area" by introducing the proposed soil arch effect model, and a new method for calculating the pile–soil stress ratio, the settlement of embankment and the differential settlement of piles and soil is obtained. Lu et al. [23] conducted an experimental analysis on the geocell reinforced sand particle flow; the results show that the displacement direction of the soil particles in the geocell and its influence area are more concentrated and neater. It is basically along the principal stress direction, spreading outward in the geocell impact area outside the soil particles. The above scholars have studied various properties of geocell reinforced embankment through different research methods, but the research on different reinforcement conditions of geocell is not systematic.

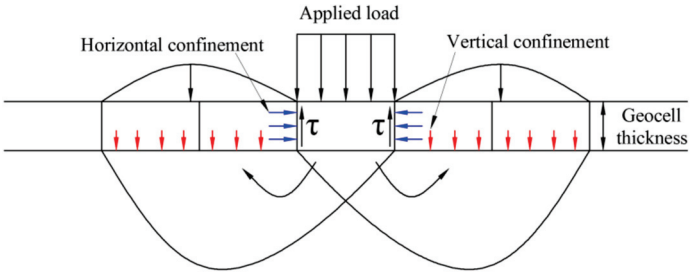


Figure 1. Soil enclosure characteristic by geocell.

In this paper, series model experiments and three-dimensional numerical simulation are performed on geocell reinforced embankment by changing the number of reinforced layer, the height of the geocell, and the welding spacing of geocell. The deformation law and internal soil pressure variation characteristics of embankment under different geocell conditions are analyzed by physical model and numerical simulation, and then the optimal reinforcement conditions of sandy embankment under cyclic load are proposed.

2. Experimental Scheme

2.1. Model Experiment

2.1.1. Experimental Instrument

The loading device of GCTS dynamic triaxial system (Geotechnical Consulting & Testing Systems, Tempe, AZ, USA), which is capable of generating sinusoidal, rectangular, triangular, and self-defining waves, respectively, was adopted in the experiment for loading. Two vertical rods were used to fix the system to the model box with net length, width and height of 600 mm × 290 mm × 400 mm and high-strength tempered glass as the sidewall, as illustrated in Figure 2. The half sine wave is used to simulate the traffic load, the load amplitude is 76 kPa, the load frequency is 1 Hz, and the number of cycles of cyclic load is 5000.

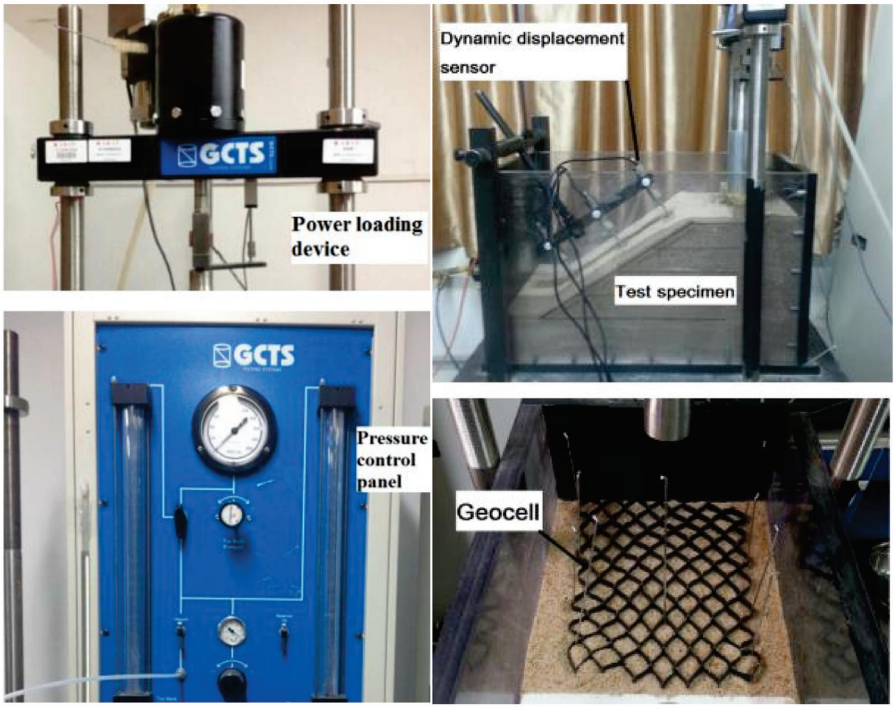


Figure 2. Test equipment and specimen.

2.1.2. Experimental Material

Standard sand, with the particle size ranging between 0.5 and 2 mm, was selected as the sand sample of model experiment, whereas the indicators measuring its physical property are specified in Table 1. High strength geocell, with thickness of (0.45 ± 0.1) mm, was adopted as the reinforcement material, and the indicators measuring its performance are specified in Table 2. A Ctm8050 universal material testing machine (Xie Qiang Instrument Manufacturing (Shanghai) Co., Ltd., Shanghai, China) is used to conduct tensile tests on the geocell used for the test. The stress–strain curve of the geocell can be obtained through the sorting of test data, as shown in Figure 3.

Table 1. Physical property indicators of sand.

Weight/γ (kN/m^3)	Specific Gravity/G_s	Relative Density/d	Void Ratio/e	Moisture Content/ω (%)	Coefficient of Uniformity/C_u	Coefficient of Curvature/C_c
15.81	2.65	0.849	0.586	0.15	1.39	0.94

Table 2. Performance indicators of geocell.

Strength of Strip (MPa)	Elongation at Break of Strip (%)	Tensile Strength of Connection Point (MPa)	Strip Height (mm)
≥244	≤15%	≥244	0.45 ± 0.1

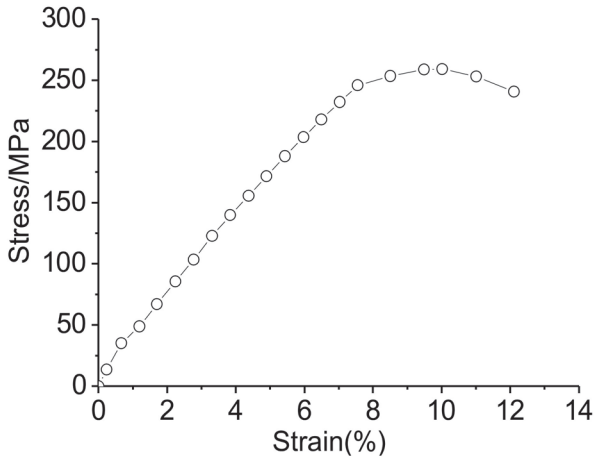


Figure 3. Geocell stress–strain curve.

2.1.3. Experimental Model and Working Conditions

Considering the symmetry of the embankment in the actual project, the half width embankment model is built by the model box test; the width, height, and height ratio on slope of the model specimen are 600 mm, 300 mm, and 1:1.5, respectively. The embankment section and reinforcement conditions are illustrated in Figure 4 and Table 3.

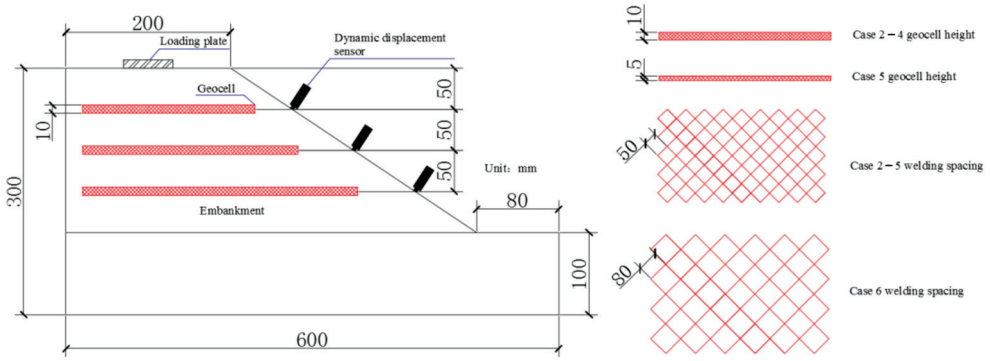


Figure 4. Equipment and specimen.

Table 3. Reinforcement test condition.

Case	Reinforced Layers	Geocell Height (mm)	Welding Spacing (mm)	Reinforcement Spacing (mm)
1	Unreinforced			
2	1	10	50	-
3	2	10	50	50
4	3	10	50	50
5	2	5	50	50
6	2	10	80	50

According to JTG D30-2015 specification for the design of highway subgrade, the compactness of highway embankment is ≥94%; therefore, the compactness and relative compactness of the embankment in the test are 97.23% and 0.849, respectively. In the process of model embankment filling, the filling quality of the embankment is mainly controlled by controlling the compactness of the embankment. Through the maximum dry density test of Fujian standard sand, the maximum dry density of sand is 1.876 g/cm^3. Considering the control compactness of embankment, the dry density of the model is controlled to be 1.824 g/cm^3. The calculation shows that the total mass of sand filling in the model is 70.9 kg.

2.2. Numerical Model

2.2.1. Identification of the Parameters of Numerical Model

The height of the simulated embankment is 300 mm, the width of the top of the embankment is 200 mm, the width of the bottom of the embankment is 500 mm, and the width of the foundation is 600 mm. The length of the strip load is 288 mm and the width is 60 mm. The load is applied in the middle of the embankment with a distance of 70 mm on both sides. The reinforcement position is from the top of the embankment downward, and a layer of reinforcement material is placed every 50 mm, which is divided into three layers. The dimensions of embankment section are illustrated in Figure 4. The width of the embankment amounted to 300 mm. In addition, the reinforcement conditions are specified in Table 3.

(1) Soil model

The soil of the embankment, which was oftentimes merely subject to pressure, was simulated by the eight-node three-dimensional isoparametric element, i.e., C3D8R, and each node of the element has three translational degrees of freedom. C3D8R compared with the complete integration element, and the linear reduced integration element contains only one integration point in the center of the element, while the number of integration points of the quadratic reduced integration element is the same as that of the linear complete integration element. The linear reduced integral unit has the following advantages: (1) Shear self-locking is not easy to occur under bending load. (2) The solution of displacement is accurate. (3) When the mesh is distorted, the accuracy of the analysis will not be greatly affected. The elastoplastic properties of the embankment soil itself were simulated based on the extended Drucker–Prager criterion. The simulated parameters of soil are specified in Table 4. Drucker–Prager is also called generalized Mises yield criterion. The model overcomes the inherent defect that the Mohr–Coulomb model is not easy to converge in plastic analysis. The model is also conducive to numerical calculation and determination of the direction of plastic strain increment.

Table 4. Simulated parameters of soil.

Density (kg/m^3)	Elastic Modulus (kPa)	Poisson Ratio	Internal Friction Angle (°)	Cohesion Force (kPa)	Mechanical Model
1824	5×10^3	0.3	39	0	D-P model

(2) Geocell model

Geocell was simulated through the continuum-based shell elements, and the shell element has six degrees of freedom (three translational degrees of freedom and three rotational degrees of freedom) at each node. The simulated parameters of geocell are specified in Table 5. The continuum-based shell elements degraded from solid elements are able to reflect the changes of the material itself in higher precision, and to more effectively simulate the double-sided contact [24]. It can be seen from Figure 3 that, when the geocell strain is less than or equal to 8%, the stress–strain curve presents a linear distribution, and then the stress–strain curve has nonlinear deformation. It can be seen that, under the action of ultimate load, the stress variable before the geocell fracture in the nonlinear stage is about 5%, and the geocell material can be approximately considered as a linear elastic material. The constitutive equation of linear elastic materials is the generalized Hooke's law.

Table 5. Simulated parameters of geocell.

Density (kg/m^3)	Elastic Modulus (kPa)	Poisson Ratio	Thickness (mm)	Mechanical Model
1700	2.8×10^5	0.25	0.45 ± 0.1	Linear elasticity

(3) Contact simulation

In this study, the embedded constraint was adopted to simulate the interaction between soil and reinforcement material. It is found that the computation of friction units oftentimes failed to converge for numerous contact surfaces of the three-dimensional numerical model. Given the computational cost, it is thus feasible to simulate the geocell reinforced embankment using the embedded constraint when assuming no relative sliding between soil and reinforcement material, as evidenced by the study of Saad et al. [25].

(4) Model meshing

The embankment is meshed. The pure sand embankment is divided into 5852 soil units. The three-layer reinforced units are divided into 1736, 2112, and 2486 units, respectively. The soil units and reinforced units are shown in Figure 5.

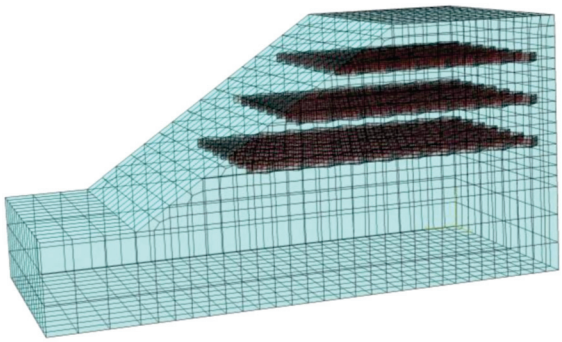


Figure 5. Embankment and reinforced element mesh model.

2.2.2. Loading and Boundary Condition

(1) Loading

The simulated loading, either the static or the dynamic one, was consistent with the experimental loading. The scheme of loading is specified in Table 6.

Table 6. Loading scheme.

Loading Mode	**Load Characteristics**		
Static load	Initial load/kPa	Loading speed/N/s	
	0	4	
Fixed amplitude cyclic load	Loading amplitude/kPa	Frequency/Hz	Cycle numbers
	76	1	5000

(2) Boundary condition

Combined with the features of the box test of physical model, constraints in x, y, and z directions were adopted at the bottom of the numerical model, whereas merely normal constraints were adopted at the middle, left, and right boundaries of the numerical model.

3. Comparative Analysis and Application

3.1. Deformation Analysis

3.1.1. Vertical Settlement of the Embankment Top under Static Loading

The loading scheme under static loading is referred to as the experimental loading scheme, with a maximum amount of loading reaching 253 kPa, which is set as the limit bearing capacity of non-reinforced embankment. Such configuration would facilitate comparison and analysis of data at the same loading amount.

Figure 6 has illustrated that, under static loading, the changing law of the simulated values of vertical cumulative settlement at a specific load was consistent with that of the experimental values. In other words, as the number of reinforcement layers increased at a specific load, the vertical cumulative settlement experienced declines. In addition, with the same number of reinforcement layers, the geocell height grew larger and the vertical cumulative settlement experienced declines. With the same number of reinforcement layers and geocell height, both the welding spacing and the vertical embankment settlement experienced declines. The simulated values of the vertical cumulative settlement, which amounted to 0.66%, 10.9%, 20.9%, 59.8%, 8.2%, and 8.7% under working conditions one to six, respectively, all exceeded the experimental values. When the embankment was not reinforced, the simulated values of vertical cumulative settlement basically consisted with the experimental values. As the number of reinforcement layers increased, the increasing ratio of the simulated values exceeded that of the experimental values, indicating that the ratio of reinforcement could impose a huge impact on the simulated vertical cumulative settlement. The numerical simulation of the geocell reinforced embankment is able to effectively reflect the net isolation effect imposed by the geocell on soil, whereas the net isolation effect was more evident when the ratio of reinforcement grew larger. However, the numerical simulation is unable to reflect the frictional effect existing between reinforcement layers and upper and lower contact surfaces. Hence, though the numerical simulation could not reveal the reinforcement effect in a holistic manner, it has a good reference value while reflecting the overall regularity.

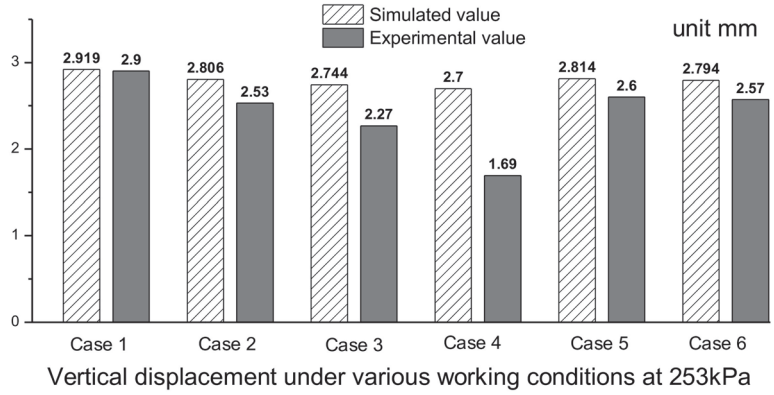


Figure 6. Simulated values and experimental values of vertical cumulative settlement under different conditions.

Under the action of static loading, the number of reinforced layers has a great impact on the vertical settlement of the embankment. The vertical cumulative settlement of experimental values in case 2, case 3, and case 4 is 12.8%, 21.7%, and 41.7% lower than that in case 1, respectively, while the change of geocell height and welding spacing also has a certain impact on the vertical settlement of the embankment. The vertical cumulative settlement of experimental values in case 5 and case 6 is 14.5% and 13.2% higher than that in case 3, respectively. The control of settlement of reinforced embankment under static loading can mainly consider the number of reinforced layers of geocell, and the economy of reinforcement on the basis of meeting the settlement. In practical engineering, the control of embankment vertical settlement should also focus on the situation under cyclic loading, which will be studied in the subsequent sections.

3.1.2. Vertical Cumulative Settlement of the Embankment Top under Cyclic Loading

As shown by Figure 7a, the changing law of the simulated values of vertical cumulative settlement consisted with that of the experimental values. As the number of reinforced layers increased, the vertical cumulative settlement experienced declines accordingly. In addition, the simulated values of vertical cumulative settlement were similar to the experimental values under each reinforcement condition subsequent to 5000 vibrations. However,

the simulated values during loading were smaller than the experimental values, whereas the simulated values under the non-reinforcement condition were smaller than the experimental values. As shown by Figure 7b,c, after altering the geocell height and welding spacing, the changing law of the simulated values of vertical cumulative settlement basically consisted of that of the experimental values. Nevertheless, the amount of settlement after vibration varied to a significant extent. Therefore, since the relative sliding between soil and reinforcement material derived from friction was not taken into account, the simulated values of vertical cumulative settlement were smaller than the experimental values.

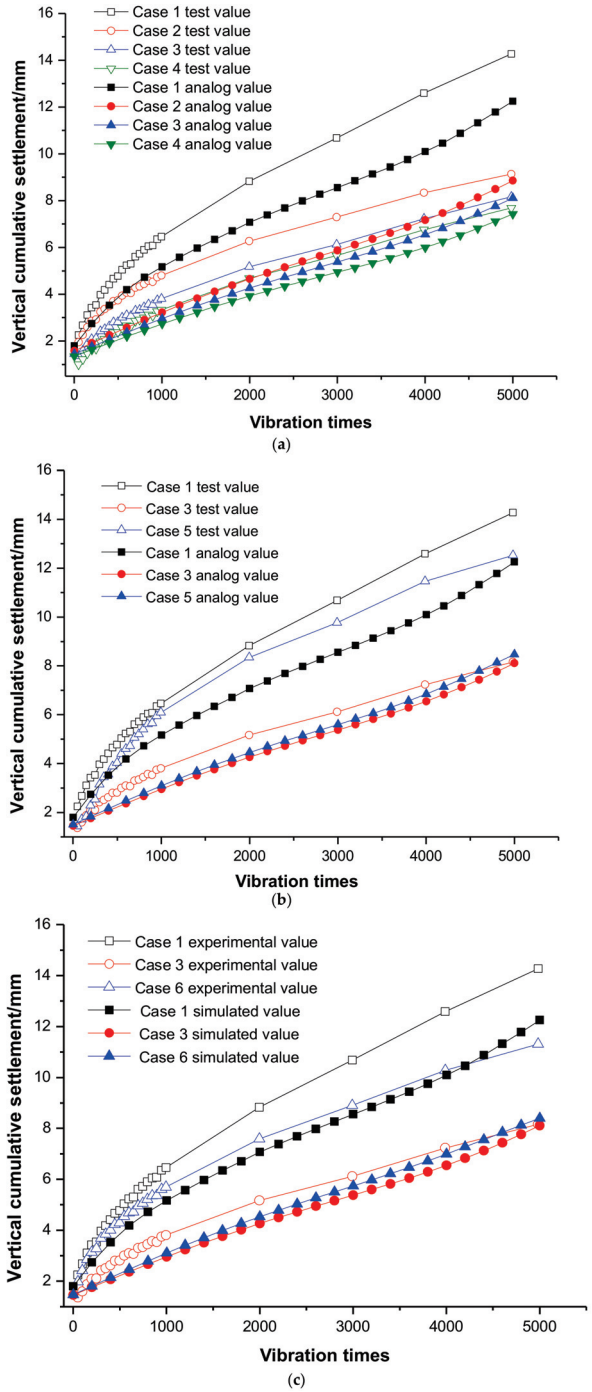


Figure 7. Settlement changing with vibration times under cyclic loading under different conditions. (**a**) different reinforcement layers; (**b**) different geocell heights; (**c**) different welding spacing.

The number of reinforced layers of geocell plays a very important role in the vertical cumulative settlement of embankment under cyclic loading. At 5000 vibrations, the vertical cumulative settlement of experimental values in case 2, case 3, and case 4 is reduced by 36%, 42.8%, and 46.2%, respectively, compared with case 1. It can be seen that the inhibition effect of the number of reinforced layers on the vertical cumulative settlement under cyclic loading is better than that under static loading, but the effect of two-layer reinforcement and three-layer reinforcement is relatively close, and the reinforcement effect of the upper part of the embankment is more significant. Under the action of cyclic loading, reducing the geocell heights and increasing the welding spacing have a significant impact on the reinforced embankment. At 5000 vibrations, the vertical cumulative settlement of the experimental value in case 5 increases by 53.4% compared with case 3, and the vertical cumulative settlement of the experimental value in case 6 increases by 38.6% compared with case 3. Both conditions significantly reduce the inhibition effect on the vertical cumulative settlement of embankment, and this weakening effect is more obvious than that under static loading. The optimal reinforcement condition considering economy is condition 3, that is, the reinforced layers is 2, the geocell height is 10 mm, and the welding distance is 50 mm. In practical engineering, the load of road embankment is mostly cyclic loading. According to the research results of this paper, when studying the vertical cumulative settlement of road embankment under cyclic loading, we should focus on the selection of embankment geocell height and welding spacing on the basis of considering the economy of the number of reinforced layers.

The comparison between the test value and simulation value of static load and cyclic load has been analyzed in the previous section, respectively. This part mainly compares and analyzes the difference percentage (test value and analog value) between static load and cyclic load. As shown by Table 7, the difference percentage under cyclic load is positive and under static load is negative. The main reason is that the middle and upper parts of sandy embankment will become relatively loose under cyclic load and compacted under static load in the model test; however, the numerical simulation is relatively less affected.

Table 7. Percentage difference between test and analog value of vertical settlement.

Case	1	2	3	4	5	6
Cyclic Load (5000 vibrations)	16.5%	3.2%	6.2%	3.4%	47.9%	34.6%
Static Load	−0.7%	−10.0%	−17.2%	−37.4%	−7.5%	−7.9%

3.1.3. Horizontal Displacement of Embankment Slope under Cyclic Loading

As shown by Figure 8a, under cyclic loading, the horizontal deformation of embankment slope under all working conditions increases with the increase of vibration times. With the increase of the number of reinforced layers, the inhibition effect on slope deformation is better. This effect becomes more significant with the increase of load vibration times and is more obvious at the place closest to the slope top. By analyzing the data of the observation surfaces I (as illustrated in Figure 8) closest to the slope top, at 5000 vibrations, the horizontal deformation of case 3 is reduced by 10.4% compared with case 2, and the horizontal deformation of case 4 is reduced by 4.0% compared with case 3. It can be seen that the effect of two-layer reinforcement is better, and the middle and upper part of embankment should be preferentially reinforced if conditions permit. Because the soil in the upper part of the embankment is disturbed more obviously than that in the lower part of the embankment under cyclic loading, resulting in the maximum horizontal deformation of the upper slope of the embankment, the effect of reinforcement in the upper part of the embankment is better. Judging from Figure 8b,c, when the number of reinforcement layers is the same, the increase of geocell height and the decrease of welding spacing can also inhibit the slope deformation, and it is more obvious at the place closest to the slope top. At 5000 vibrations, the horizontal deformation of case 3 at the observation surfaces I is reduced by 10.0% and 3.1%, respectively, compared with case 5 and case 6. It can be seen

that the inhibition effect of the increase of geocell height on the horizontal deformation of slope surface is better than that of the decrease of welding spacing. The increase of geocell height improves the reinforcement rate of embankment, while the smaller geocell welding distance can only improve the reinforcement effect of embankment reinforcement layer, but cannot improve the reinforcement rate of embankment, so the effect of restraining horizontal displacement of slope is worse.

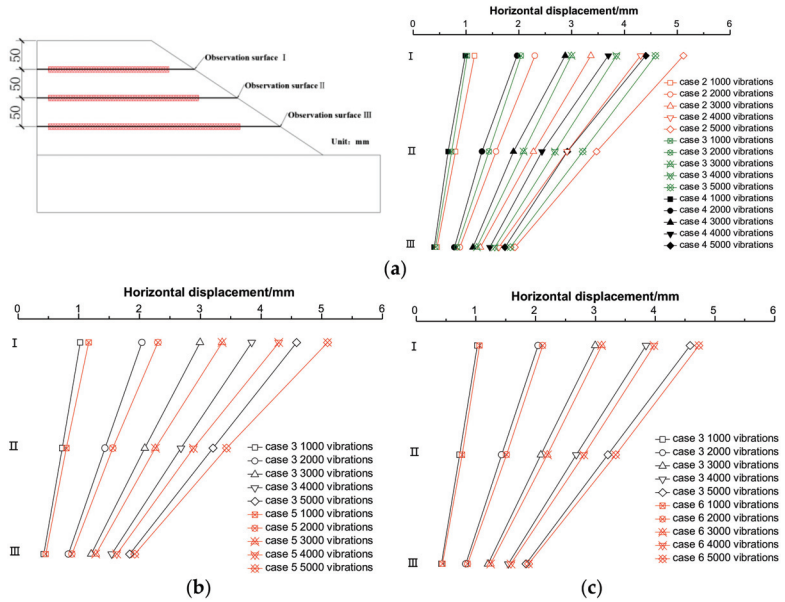


Figure 8. Horizontal displacement of slope changing with vibration times under cyclic loading under different conditions. (**a**) different reinforcement layers; (**b**) different geocell heights; (**c**) different welding spacing.

Geocell reinforcement has a significant inhibitory effect on the horizontal displacement of the embankment, especially in the middle and upper part of the embankment. The optimal reinforcement condition considering economy is condition 3, that is, the reinforced layers is 2, the geocell height is 10 mm, and the welding distance is 50 mm. In practical engineering, the load on the middle and upper part of the embankment is more direct, and it is easier to produce large horizontal displacement. Therefore, geocell is a very ideal reinforcement material to inhibit the horizontal displacement of the embankment.

3.2. Soil Pressure Analysis

3.2.1. Vertical Soil Pressure and Limit Bearing Capacity of the Embankment under Static Loading

Judging from Figure 9, the distribution curve of soil pressure at the three observation surfaces reached the peak level at the loading axis and experienced gradual declines to both sides. As the depth increased, the soil pressure adjacent to the peak became smaller, whereas the distribution curve of soil pressure became gentler. In addition, the distribution curve of soil pressure at the three observation surfaces under the 4th working condition was found to be gentler than that under the 1st working condition, whereas the soil pressure of the same observation surface under the 4th working condition was found to be smaller than that under the 1st working condition. The geocell reinforced embankment is able to convert the vertical stress in the soil into the strip tension borne by the geocell, thereby lowering the vertical soil pressure of embankment at each observation surface. In addition, the reinforcement layers of geocell could be leveraged as a flexible raft foundation to further disperse the soil pressure, enabling the distribution curve of the deep soil pressure for reinforced embankment to become gentler.

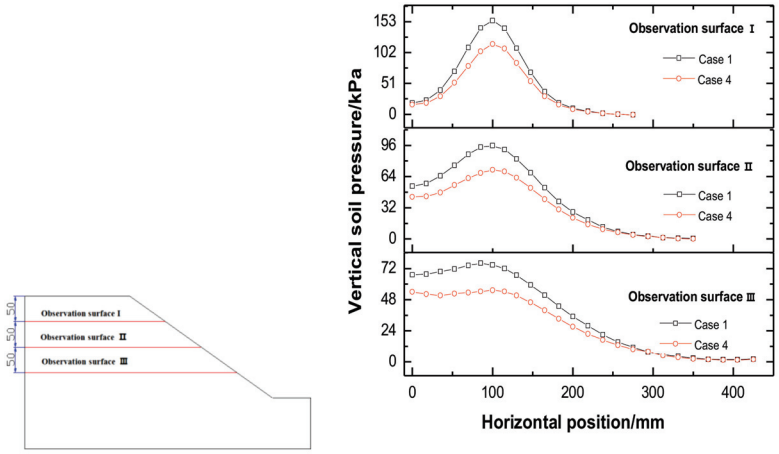


Figure 9. Vertical soil pressure of embankment under different conditions.

Under static loading, the number of reinforced layers of geocell has a significant effect on improving the limit bearing capacity of embankment (as illustrated in Figure 10). The limit bearing capacity of experimental values in case 2, case 3, and case 4 is 12.7%, 36.4% and 44.4% higher than that in case 1, respectively. The change of geocell heights and welding spacing also has a significant impact on the ultimate bearing capacity of embankment (as illustrated in Figure 10). The limit bearing capacity of experimental values in case 3 is increased by 29.3% and 23.0%, respectively, compared with case 5 and case 6. According to the above research results, in practical engineering, the limit bearing capacity of the embankment under static loading can be improved by increasing the number of reinforcement layers, and the reinforcement effect of the upper part of the embankment is more significant. Increasing the geocell height and reducing the welding spacing can also improve the limit bearing capacity of the embankment, and the effect of the former is better.

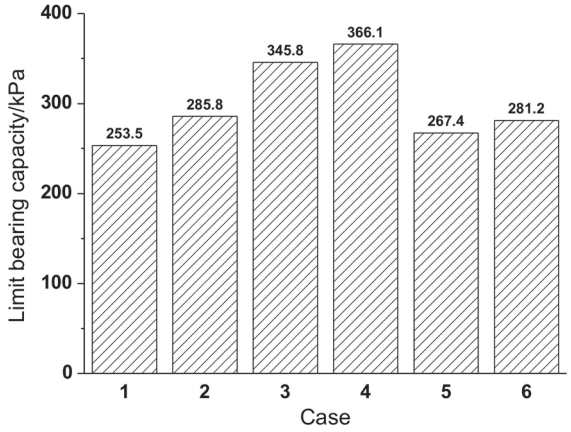


Figure 10. Experimental values of limit bearing capacity under different conditions.

3.2.2. Vertical Soil Pressure of the Embankment under Cyclic Loading

As shown by Figure 11, the vertical soil pressure at the three observation surfaces reached the peak level at the loading axis and experienced gradual declines to both sides. As the loading times multiplied, the vertical stress of the soil also experienced increases accordingly. In addition, the distribution curve of vertical soil pressure at the three observation surfaces was gentler under the 4th working condition than under the 1st working condition. As the depth increased, the vertical soil pressure of the three observation surfaces experienced gradual declines at the loading axis, and the distribution curve of soil pressure became gentler accordingly. Judging from the analysis, as the vibration of cyclic loading increased, the embankment also became more compact, thus contributing to greater soil pressure of the embankment adjacent to the loading axis. Furthermore, the confined

action of geocell is able to convert the vertical stress in the soil into the strip tension. As a result, the embankment would feature the enhanced ultimate bearing capacity, whereas the vertical soil pressure of reinforced embankment at the same position would grow smaller than that of non-reinforced embankment. After the cyclic loading of geocell reinforced embankment in case 4, it has a certain pre tension effect on the reinforcement, which improves the action effect of reinforcement. At the same time, the reinforced layer has a dispersive effect on the vertical loading, resulting in the vertical soil pressure at the same position after reinforcement being less than that in case 1.

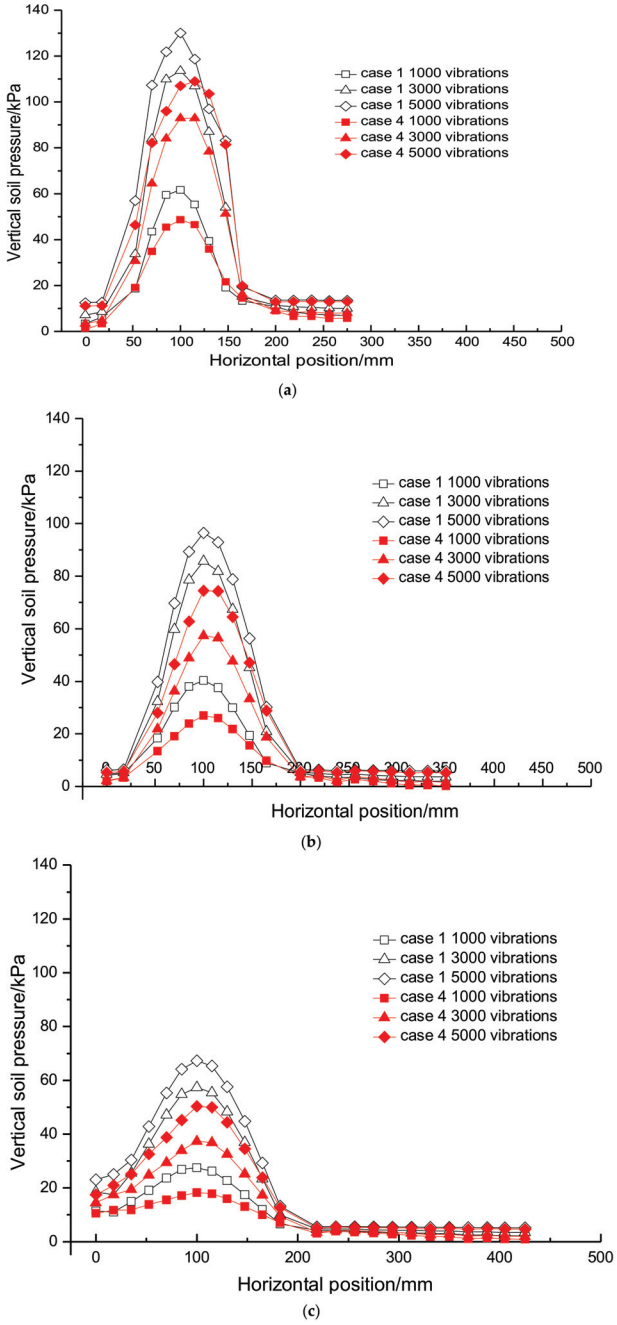


Figure 11. Vertical soil pressure in embankment under different conditions. (**a**) observation surfaces I; (**b**) observation surfaces II; (**c**) observation surfaces III.

Under different loading times, the internal soil pressure of geocell reinforced embankment is significantly lower than that of unreinforced embankment, which reflects that the excavated geocell can still disperse the soil pressure well under cyclic loading.

This also provides a theoretical basis for the application of Engineering geocell reinforced embankment.

4. Conclusions

(1) Under static loading, the changing law of the simulated values of vertical cumulative settlement at a specific load was consistent with that of the experimental values under each of the working conditions. The numerical simulation is unable to reflect the frictional effect existing between reinforcement layers and upper and lower contact surfaces, while in the physical model experiment, the friction effect between the reinforced layer and the upper and lower contact surfaces has a great impact on the vertical settlement; as a result, the percentage difference between the simulated value and the test value under different reinforcement conditions of the embankment reaches 59.8%.

(2) Under cyclic loading, the inhibition effect of the number of reinforced layers on the vertical cumulative settlement under cyclic loading is better than that under static loading, but the effect of two-layer reinforcement and three-layer reinforcement is relatively close, and the vertical cumulative settlement of experimental values in case 4 is reduced by 5.9% compared with case 3. At the same time, reducing the height of geocell and increasing the welding spacing weakened the inhibition of embankment settlement by 53.4% and 38.6%, respectively. The optimal reinforcement condition considering economy is condition 3, that is, the reinforced layers is 2, the geocell height is 10 mm, and the welding distance is 50 mm.

(3) Under cyclic loading, the horizontal deformation of embankment slope under all working conditions increases with the increase of vibration times. With the increase of the number of reinforced layers, the inhibition effect on slope deformation is better. This effect becomes more significant with the increase of load vibration times; at 5000 vibrations, the horizontal deformation of case 3 is reduced by 10.4% compared with case 2, and the horizontal deformation of case 4 is reduced by 4.0% compared with case 3. The optimal reinforcement condition considering economy is condition 3, that is, the reinforced layers is 2, the geocell height is 10 mm, and the welding distance is 50 mm.

(4) Under static loading, as the depth increased, the vertical soil pressure reached the peak level at the loading axis and experienced gradual declines to both sides, and the maximum soil pressure reached 154.31 kPa. Furthermore, the vertical soil pressure adjacent to the peak became smaller, and the distribution curve of soil pressure became gentler accordingly. The reinforcement layers of geocell could be leveraged as a flexible raft foundation to further disperse the soil pressure, enabling the distribution curve of the deep soil pressure for reinforced embankment to become gentler. The limit bearing capacity of experimental values is increased by 29.3% and 23.0%, respectively, through increasing the height of geocell and reducing the welding spacing.

(5) Under cyclic loading, the vertical soil pressure reached the peak level at the loading axis. As the loading times multiplied, the vertical soil pressure also experienced increases at the loading axis correspondingly, the maximum soil pressure reached 130.12 kPa. The embankment also became more compact, thus contributing to greater soil pressure of the embankment adjacent to the loading axis. With the increase of depth, the confined action of geocell is able to convert the vertical stress in the soil into the strip tension, resulting in the vertical soil pressure of the three observation surfaces experiencing gradual declines at the loading axis, and the distribution curve of soil pressure became gentler.

Author Contributions: Conceptualization, A.G. and M.Z.; Data curation, A.G. and M.Z.; Formal analysis, A.G. and M.Z.; Writing—original draft, A.G.; Writing—review & editing, A.G. All authors have read and agreed to the published version of the manuscript.

Funding: The work was financially supported by the National Natural Science Foundation of China (Grant No. 41372280).

Institutional Review Board Statement: Not applicable.

Informed Consent Statement: Not applicable.

Data Availability Statement: Data is contained within the article.

Conflicts of Interest: The authors declare that there is no conflict of interest regarding the publication of this paper.

References

1. Astaraki, F.; Esmaeili, M.; Reza, R.M. Influence of geocell on bearing capacity and settlement of railway embankments: An experimental study. *J. Geomech. Geoengin.* **2022**, *17*, 630–646. [CrossRef]
2. Han, Y.K.; Lu, Z.; Yao, H.L.; Liu, B.; Fan, Y.F.; Lu, Q.; Zhao, D.Q. Study on erosion resistance of geocell reinforced slope. *J. Chin. J. Rock Mech. Eng.* **2021**, *40*, 3425–3433.
3. Isik, A.; Gurbuz, A. Pullout behavior of geocell reinforcement in cohesionless soils. *J. Geotext. Geomembr.* **2020**, *48*, 71–81. [CrossRef]
4. Ardakani, A.; Namaei, A. Numerical investigation of geocell reinforced slopes behavior by considering geocell geometry effect. *J. Geomech. Eng.* **2021**, *24*, 589–597.
5. Tiwari, N.; Satyam, N. An experimental study on the behavior of lime and silica fume treated coir geotextile reinforced expansive soil subgrade. *J. Eng. Sci. Technol.* **2020**, *23*, 1214–1222. [CrossRef]
6. Sofiyev, A.H.; Pancar, E.B. The effect of heterogeneity on the parametric instability of axially excited orthotropic conical shells. *J. Thin-Walled Struct.* **2017**, *115*, 240–246. [CrossRef]
7. Mehdipour, B.; Hashemolhosseini, H.; Nadi, B.; Mirmohamadsadeghi, M. Investigating the effect of geocell changes on slope stability in unsaturated soil. *J. Teh. Glas.* **2020**, *14*, 66–75. [CrossRef]
8. Song, F.; Tian, Y.H. Three-dimensional numerical modelling of geocell reinforced soils and its practical application. *J. Geomech. Eng.* **2019**, *17*, 1–9.
9. Mehrjardi, G.T.; Motarjemi, F. Interfacial properties of Geocell-reinforced granular soils. *J. Geotext. Geomembr.* **2018**, *46*, 384–395. [CrossRef]
10. Hou, J.; Zhang, M.X.; Han, X.; Li, R. Mechanism of a high-strength geocell using FEM. *Chin. J. Geotech. Eng.* **2015**, *37*, 26–30.
11. Zhou, Y.M.; Zhang, M.X.; Wu, Y. Factors influencing the behavior of single geocell-reinforced sand. *J. Shanghai Jiaotong Univ.* **2015**, *49*, 983–987.
12. Venkateswarlu, H.; Ujjawal, K.N.; Hegde, A. Laboratory and numerical investigation of machine foundations reinforced with geogrids and geocells. *J. Geotext. Geomembr.* **2018**, *46*, 882–896. [CrossRef]
13. Zhu, Y.L.; Tan, K.; Hong, Y.; Tan, T.; Song, M.R.; Wang, Y.X. Nimbalkar sanjay. Deformation of the geocell flexible reinforced retaining wall under earthquake. *J. Adv. Civil. Eng.* **2021**, *4*, 8897009.
14. Zadehmohamad, M.; Bolouri, B. Cyclic behaviour of geocell-reinforced backfill behind integral bridge abutment. *Int. J. Geotech. Eng.* **2019**, *13*, 438–450. [CrossRef]
15. Tafreshi, S.N.M.; Dawson, A.R. Comparison of bearing capacity of a strip footing on sand with geocell and with planar forms of geotextile reinforcement. *J. Geotext. Geomembr.* **2010**, *28*, 72–84. [CrossRef]
16. Bathurst, R.J.; Knight, M.A. Analysis of geocell reinforced-soil covers over large span conduits. *J. Comput. Geotech.* **1998**, *22*, 205–219. [CrossRef]
17. Biabani, M.M.; Indraratna, B.; Ngo, N.T. Modelling of geocell-reinforced subballast subjected to cyclic loading. *J. Geotext. Geomembr.* **2016**, *44*, 489–503. [CrossRef]
18. Leshchinsky, B.; Ling, H. Effects of geocell confinement on strength and deformation behavior of gravel. *J. Geotech. Geoenvironmental Eng.* **2013**, *139*, 340–352. [CrossRef]
19. Zheng, C.Y.; Zhang, M.X.; Jiang, S.W.; Han, X.; Sun, Z. Deformation analysis of model test of sand foundation reinforced with high strength geocell. *J. Shanghai Univ.* **2015**, *21*, 606–616.
20. Jin, J.Q.; Xu, C.; Liang, C.; Liu, R.T. Failure mode and stability evaluation of geocell-reinforced cushion embankment. *Hydrogeol. Eng. Geol.* **2019**, *46*, 86–94.
21. Avesani Neto, J.O.; Bueno, B.S.; Futai, M.M. Evaluation of a calculation method for embankments reinforced with geocells over soft soils using finite-element analysis. *Geosynth. Int.* **2015**, *22*, 439–451. [CrossRef]
22. Zhao, M.H.; Zhen, D.X.; Liu, M.; Ou, Q. Deformation analysis of geocell-reinforced body under embankment load considering soil arch effect. *Chin. J. Geotech. Eng.* **2020**, *42*, 601–609.
23. Lu, S.K.; Xia, X.H.; Zhang, M.X.; Yang, J.M. Triaxial analysis of particle flow in geocell reinforced sand samples. *J. Shanghai Univ.* **2019**, *25*, 132–140.
24. Wang, J.; Jiang, Z.J. Application of ABAQUS shell element in roll forming. *Manuf. Informatiz.* **2008**, *2*, 118–120.
25. Saad, B.; Mitri, H.; Poorooshasb, H. 3D FE analysis of flexible pavement with geosynthetic reinforcement. *J. Transp. Eng.* **2006**, *132*, 402–415. [CrossRef]

MDPI AG
Grosspeteranlage 5
4052 Basel
Switzerland
Tel.: +41 61 683 77 34

MDPI Books Editorial Office
E-mail: books@mdpi.com
www.mdpi.com/books



Disclaimer/Publisher's Note: The title and front matter of this reprint are at the discretion of the Topic Editors. The publisher is not responsible for their content or any associated concerns. The statements, opinions and data contained in all individual articles are solely those of the individual Editors and contributors and not of MDPI. MDPI disclaims responsibility for any injury to people or property resulting from any ideas, methods, instructions or products referred to in the content.





Academic Open
Access Publishing

mdpi.com

ISBN 978-3-7258-4220-9